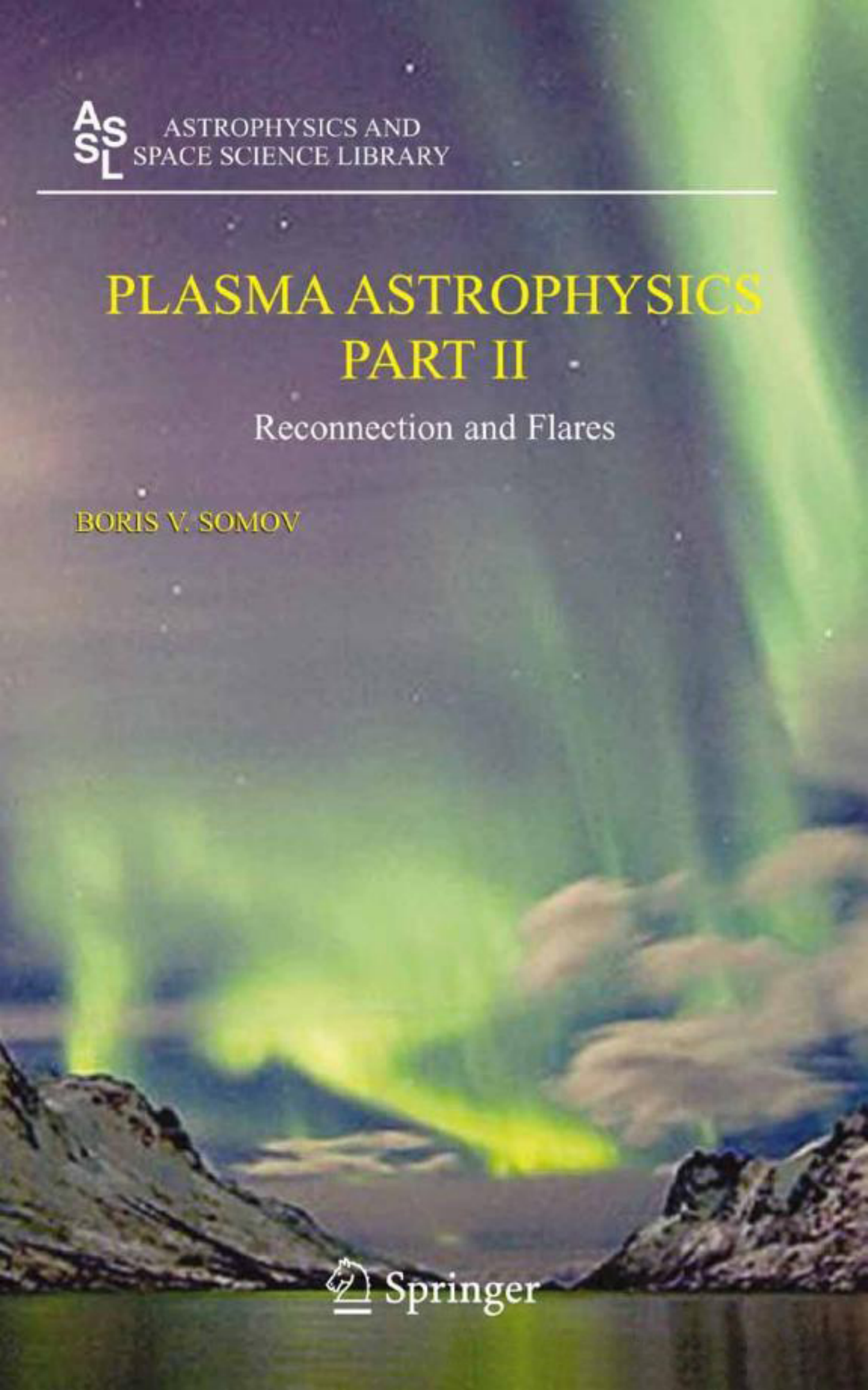
ASSL
ASTROPHYSICS AND
SPACE SCIENCE LIBRARY
PLASMA ASTROPHYSICS
PART II
Reconnection and Flares
BORIS V. SOMOV
Springer

PLASMA ASTROPHYSICS, PART II

PLASMA ASTROPHYSICS

2. Reconnection and Flares

Boris V. Somov

Astronomical Institute and Faculty of Physics

Moscow State University

Springer, 2006

ASTROPHYSICS AND SPACE SCIENCE LIBRARY

VOLUME 341

PLASMA ASTROPHYSICS, PART II

Reconnection and Flares

BORIS V. SOMOV
Moscow State University
Moscow, Russia

Springer

Boris V. Somov
Astronomical Institute
And Faculty of Physics
Moscow State University
Moscow, Russia
somov@sai.msu.ru

Cover illustration: The background is an image of the auroras over Tromsoe, Norway on January 18, 2005, that are the spectacular manifestations of substorms in the Earth's magnetosphere due to reconnection in the geomagnetic tail after a large solar flare.

Photograph reproduced with kind permission by Bjorn Jorgensen (Bjorn Jorgensen/www.arcticphoto.no).

Library of Congress Control Number: 2006926924

ISBN-10: 0-387-34948-0
ISBN-13: 978-0387-34948-0

Printed on acid-free paper.

9 8 7 6 5 4 3 2 1

springer.com

Contents

Reconnection and Flares
Introduction

Magnetic fields are easily generated in astrophysical plasma owing to its high conductivity. Magnetic fields, having strengths of order few 10^{-6} G, correlated on several kiloparsec scales are seen in spiral galaxies. Their origin could be due to amplification of a small seed field by a turbulent galactic dynamo. In several galaxies, like the famous M51, magnetic fields are well correlated (or anti-correlated) with the optical spiral arms. These are the weakest large-scale fields observed in cosmic space. The strongest magnets in space are presumably the so-called *magnetars*, the highly magnetized (with the strength of the field of about 10^{15} G) young neutron stars formed in the supernova explosions.

The energy of magnetic fields is accumulated in astrophysical plasma, and the sudden release of this energy – an original electrodynamical 'burst' or 'explosion' – takes place under definite but quite general conditions (Peratt, 1992; Sturrock, 1994; Kivelson and Russell, 1995; Rose, 1998; Priest and Forbes, 2000; Somov, 2000; Kundt, 2001). Such a 'flare' in astrophysical plasma is accompanied by fast directed ejections (jets) of plasma, powerful flows of heat and hard electromagnetic radiation as well as by impulsive acceleration of charged particles to high energies.

This phenomenon is quite a widespread one. It can be observed in flares on the Sun and other stars (Haisch et al., 1991), in the Earth's magnetosphere as **magnetic storms** and substorms (Nishida and Nagayama, 1973; Tsurutani et al., 1997; Kokubun and Kamide, 1998; Nagai et al., 1998; Nishida et al., 1998), in coronae of accretion disks of cosmic X-ray sources (Galeev et al., 1979; Somov et al., 2003a), in nuclei of active galaxies and quasars (Ozernoy and Somov, 1971; Begelman et al., 1984). However this process, while being typical of astrophysical plasma, can be directly and fully studied on the Sun.

The Sun is the only star that can be imaged with spatial resolution

high enough to reveal its key (fine as well as large-scale) structures and their dynamic behaviours. This simple fact makes the Sun one of the most important objectives in astronomy. The solar atmosphere can be regarded as a natural 'laboratory' of astrophysical plasmas in which we can study the physical processes involved in cosmic **electrodynamical explosions**.

We observe how magnetic fields are generated (strictly speaking, how they come to the surface of the Sun, called the photosphere). We observe the development of **solar flares** (e.g., Strong et al., 1999) and other non-stationary large-scale phenomena, such as a gigantic arcade formation, coronal transients, coronal mass ejections into the interplanetary medium (see Crooker et al., 1997), by means of ground observatories (in radio and optical wavelength ranges) and spaceships (practically in the whole electromagnetic spectrum). For example, on board the *Yohkoh* satellite, (Ogawara et al., 1991; Acton et al., 1992) two telescopes working in soft and hard X-ray bands (Tsuneta et al., 1991; Kosugi et al., 1991) allowed us to study the creation and development of non-steady processes in the solar atmosphere (Ichimoto et al., 1992; Tsuneta et al., 1992; Tsuneta, 1993), acceleration of electrons in flares.

The LASCO experiment on board the *Solar and Heliospheric Observatory*, *SOHO* (Domingo et al., 1995) makes observations of such events in the solar corona out to 30 solar radii. Moreover *SOHO* is equipped with an instrument, the full disk magnetograph MDI (Scherrer et al., 1995), for observing the surface magnetic fields of the Sun. Following *SOHO*, the satellite *Transition Region and Coronal Explorer* (*TRACE*) was launched to obtain high spatial resolution X-ray images (see Golub et al., 1999). With the solar maximum of 2000, we had an unprecedented opportunity to use the three satellites for coordinated observations and study of solar flares.

The *Reuven Ramaty High-Energy Solar Spectroscopic Imager* (*RHESSI*) was launched in 2002 and observes solar hard X-rays and gamma-rays from 3 keV to 17 MeV with spatial resolution as high as 2.3 arc sec (Lin et al., 2002; 2003). Imaging of gamma-ray lines, produced by nuclear collisions of energetic ions with the solar atmosphere, provides direct information of the spatial properties of the ion acceleration in solar flares (Hurford et al., 2003). *RHESSI* observations allow us to investigate physical properties of solar flares in many details (e.g., Fletcher and Hudson, 2002; Krucker et al., 2003).

The link between the solar flares observed and **topology** of the magnetic field in *active* regions, in which these flares occured, was investigated by Gorbachev and Somov (1989, 1990). They developed the first model of an actual flare, the flare on 1980, November 5, and have shown that the all large-scale characteristic features of this flare can be explained by the

presence of a current layer formed on the so-called *separator* which is the intersection of the separatrix surfaces. In particular, the flare ribbons in the chromosphere as well as the 'intersecting' soft X-ray loops in the corona are the consequences of a topological structure of a magnetic field near the separator.

An increasing number of investigations clearly relates the location of a 'chromospheric flare' – the flare's manifestation in the solar chromosphere – with the topological magnetic features of active regions (Mandrini et al., 1991 and 1993; Démoulin et al., 1993; Bagalá et al., 1995; Longcope and Silva, 1998). In all these works it is confirmed that the solar flares can be considered as a result of the interaction of large-scale magnetic structures; the authors derived the location of the separatrices – surfaces that separate cells of different field line connectivities – and of the *separator*.

These studies strongly support the concept of **magnetic reconnection** in solar flares (Giovanelli, 1946; Dungey, 1958; Sweet, 1958). Solar observations with the Hard X-ray Telescope (HXT) and the Soft X-ray Telescope (SXT) on board the *Yohkoh* satellite clearly showed that

> the magnetic reconnection process is common to impulsive (compact) and gradual (large scale) solar flares

(Masuda et al., 1994, 1995). However, in the interpretation of the *Yohkoh* data, the basic physics of magnetic reconnection in the solar atmosphere remained uncertain (see Kosugi and Somov, 1998). Significant parts of the book in your hands are devoted to the physics of the reconnection process, a fundamental feature of astrophysical and laboratory plasmas.

Solar flares and coronal mass ejections (CMEs) strongly influence the interplanetary and terrestrial space by virtue of shock waves, hard electromagnetic radiation and accelerated particles (Kivelson and Russell, 1995; Miroshnichenko, 2001). That is why the problem of 'weather and climate' prediction in the *near space* becomes more and more important. The term 'near space' refers to the space that is within the reach of orbiting stations, both manned and automated. The number of satellites (meteorological, geophysical, navigational ones) with electronic systems sensitive to the ionizing radiation of solar flares is steadily growing.

It has been established that adverse conditions in the space environment can cause disruption of satellite operations, communications, and electric power distribution grids, thereby leading to broad socioeconomic losses (Wright, 1997). **Space weather** (e.g., Hanslmeier, 2002) is of growing importance to the scientific community and refers to conditions at a particular place and time on the Sun and in the solar wind, magnetosphere, ionosphere, and thermosphere that can influence the performance and relia-

bility of spaceborne and ground-based technological systems and can affect human life or health.

It is no mere chance that solar flares and coronal mass ejections are of interest to physicians, biologists and climatologists. Flares influence not only *geospace* – the terrestrial magnetosphere, ionosphere and upper atmosphere (Hargreaves, 1992; Horwitz et al., 1998; de Jager, 2005) but also the biosphere and the atmosphere of the Earth. They are therefore not only of pure scientific importance; they also have an applied or **practical relevance**.

The latter aspect is, however, certainly beyond the scope of this text, the second volume of the book "Plasma Astrophysics", lectures given the students of the Astronomical Division of the Faculty of Physics at the Moscow State University in spring semesters over the years after 2000. The subject of the present book "Plasma Astrophysics. 2. Reconnection and Flares" is the basic physics of the magnetic reconnection phenomenon and the reconnection related flares in astrophysical plasmas. The first volume of the book, "Plasma Astrophysics. I. Fundamentals and Practice" (referred in the text as vol. 1), is unique in covering the main principles and practical tools required for understanding and work in modern plasma astrophysics.

Acknowledgements

The author is grateful to his young colleagues Sergei I. Bezrodnykh, Sergei A. Bogachev, Sergei V. Diakonov, Irina A. Kovalenko, Yuri E. Litvinenko, Sergei A. Markovskii, Elena Yu. Merenkova, Anna V. Oreshina, Inna V. Oreshina, Alexandr I. Podgornii, Yuri I. Skrynnikov, Andrei R. Spektor, Vyacheslav S. Titov, Alexandr I. Verneta, and Vladimir I. Vlasov for the pleasure of working together, for generous help and valuable remarks. He is also happy to acknowledge helpful discussions with many of his colleagues and friends in the world.

Moscow, 2006 Boris V. Somov

Chapter 1

Magnetic Reconnection

Magnetic reconnection is a fundamental feature of astrophysical and laboratory plasmas, which takes place under definite but quit general conditions and creates a sudden release of magnetic energy, an original electrodynamical explosion or *flare*. Surprisingly, the simplest approximation – a single particle in given force fields – gives us clear approach to several facets of reconnection and particle acceleration.

1.1 What is magnetic reconnection?

1.1.1 Neutral points of a magnetic field

The so-called *zeroth* or *neutral* points, lines and surfaces of magnetic field, which are the regions where magnetic field equals zero:

$$\mathbf{B} = 0\,, \tag{1.1}$$

are considered to be important for plasma astrophysics since Giovanelli (1946). They are of interest for the following reasons. First, **plasma behaviour is quite specific** in the vicinity of such regions (Dungey, 1958). Second, they predetermine a large number of astrophysical phenomena. We shall be primarily concerned with non-stationary phenomena in the solar atmosphere (such as flares, coronal transients, coronal mass ejections), accompanied by particle acceleration to high energies. Analogous phenomena take place on other stars, in planetary magnetospheres, and pulsars.

Neutral points of magnetic field most commonly appear in places of the interaction of magnetic fluxes.

The simplest way to recognize this is to consider the emerging flux in the solar atmosphere.

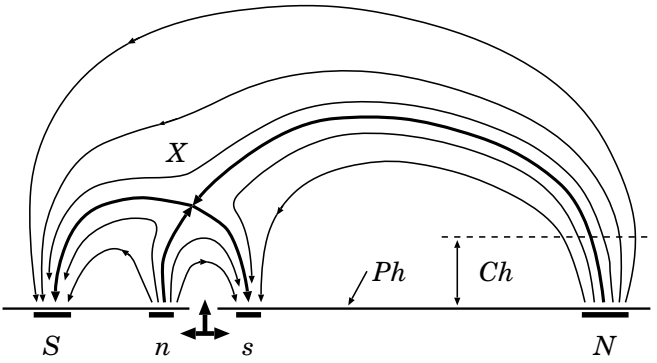

Figure 1.1: The emergence of a new magnetic flux (n, s) from under the photosphere Ph inside an active region whose magnetic field is determined by the sources S and N.

Figure 1.1 shows the sources N and S corresponding to the active region's magnetic field. The sources n and s play the role of a new flux emerging from under the photosphere Ph. The chromosphere is shown by the dashed line Ch. We consider an arrangement of the sources along a straight line, although the treatment can well be generalized (Section 3.2.1) to consider arbitrary configurations of the four sources in the photosphere.

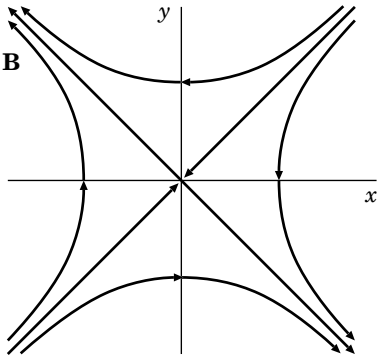

Figure 1.2: A hyperbolic zeroth point (line along the axis z) of a potential magnetic field.

Obviously a point can be found above the emerging flux, where oppositely directed but equal in magnitude magnetic fields 'meet'. Here the total field, that is the sum of the old and the new ones, is zero. Let us

denote this point by X, bearing in mind that the field in its vicinity has the hyperbolic structure shown in Figure 1.2.

In order to convince oneself that this is the case, we can consider the magnetic field in the simplest approach which is the *potential* approximation (see vol. 1, Section 13.1.3). This will be done, for example, in Section 1.1.4. However, at first, we shall recall and illustrate the basic definitions related to the magnetic reconnection process in simplest situations.

1.1.2 Reconnection in vacuum

The X-type points constitute the most important topological peculiarity of a magnetic field. They are the places where redistribution of magnetic fluxes occurs, which changes the connectivity of field lines. Let us illustrate such a process by the simplest example of two parallel electric currents **I** of equal magnitude I in vacuum as shown in Figure 1.3.

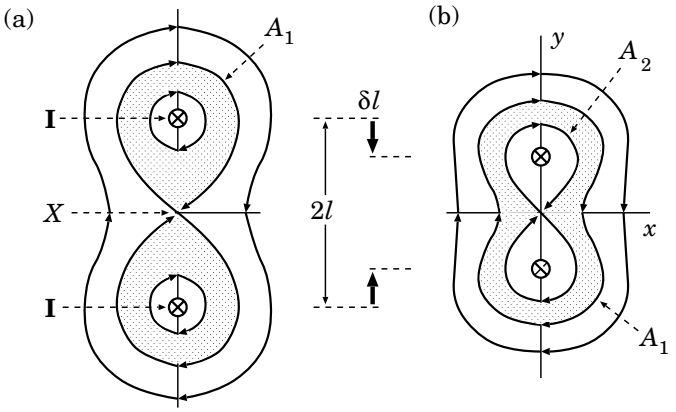

Figure 1.3: The potential field of two parallel currents **I**: (a) the initial state, $2l$ is a distance between the currents; (b) the final state after they have been drawn nearer by a driven displacement δl.

The magnetic field of these currents forms three different fluxes in the plane (x, y). Two of them belong to the upper and the lower currents, respectively, and are situated inside the *separatrix* field line A_1 which forms the eight-like curve with a zeroth X-point. The third flux situated outside this curve belongs to both currents and is situated outside the separatrix.

If the currents are displaced in the direction of each other, then the following redistribution of a magnetic flux will take place. The current's proper fluxes will diminish by the quantity δA (shown by two shadowed

rings in Figure 1.3a), while their common flux will increase by the same quantity (shown by the shadowed area in Figure 1.3b), So the field line A_2 will be the separatrix of the final state.

This process is realized as follows. Two field lines approach the X-point, merge there, forming a separatrix, and then they *reconnect* forming a field line which encloses both currents. Such a process is termed reconnection of field lines or *magnetic reconnection*. A_2 is the last reconnected field line.

Magnetic reconnection is of fundamental importance for the nature of many non-stationary phenomena in astrophysical plasma. We shall discuss the physics of this process more fully in Chapters 2 to 14. Suffice it to note that **reconnection is inevitably associated with electric field generation**. This field is the inductive one, since

$$\mathbf{E} = -\frac{1}{c}\,\frac{\partial \mathbf{A}}{\partial t}\,, \tag{1.2}$$

where $\mathbf{A}$ is the vector potential of magnetic field,

$$\mathbf{B} = \operatorname{curl} \mathbf{A}\,. \tag{1.3}$$

In the above example the electric field is directed along the z axis. It is clear that, if δt is the characteristic time of the reconnection process shown in Figure 1.3, then according to (1.2)

$$E \approx \frac{1}{c}\,\frac{\delta A}{\delta t} \approx \frac{1}{c}\,\frac{A_2 - A_1}{\delta t}\,; \tag{1.4}$$

the last equality is justified in vol. 1, Section 14.2.

Reconnection in vacuum is a real physical process: magnetic field lines move to the X-type neutral point and reconnect in it as well as

> the electric field is induced and can accelerate a charged particle or particles in the vicinity of the neutral point.

In this sense, a *collisionless* reconnection – the physical process in a high-temperature *rarefied* plasma such as the solar corona, geomagnetic tail, fusion plasmas, and so on – is simpler for understanding than reconnection in a highly-conducting collisional space plasma.

1.1.3 Reconnection in plasma

Let us try to predict plasma behaviour near the X-point as reconnection proceeds on the basis of our knowledge about the motion of a charged particle in given magnetic and electric fields.

The first obvious fact is that, given the non-zero electric field **E**, the plasma begins to drift in the magnetic field **B**, in a way shown in Figure 1.4a. The electric drift velocity

$$\mathbf{v}_{\mathrm{d}} = c\,\frac{\mathbf{E}\times\mathbf{B}}{B^{2}} \tag{1.5}$$

is shown in four points. The magnetic field is considered as a uniform field in the vicinity of these points.

The second fact consists of the inapplicability of the adiabatic drift approximation near the zeroth point, since the Larmor radius

$$r_{\mathrm{L}} = \frac{cp_{\perp}}{eB} \tag{1.6}$$

increases indefinitely as $B \to 0$. We have to solve the exact equations of motion. This will be done later on. However we see at once that in this region an electric current **J** can flow along the z axis. The proper magnetic field of the current changes the initial field topology, so that there will be two symmetric zeroth points X_1 and X_2 on the x axis in Figure 1.4b instead of one X-point.

The same arguments concerning drift flows and X-point bifurcation are applicable to the new X-points. We easily guess that the result of the interaction of line currents with the external hyperbolic field is a *current layer* in the region of reconnection. The **reconnecting current layer** (RCL) is shown by thick solid straight line in Figure 1.4c. Note that the direction of the electric current can change at the external edges of the layer. Here the currents can flow in the opposite direction (the *reverse* currents) with respect to the main current (the *direct* current) in the central part.

RCLs are, in general, at least *two-dimensional* and *two-scale* formations. The former means that one-dimensional models are in principle inadequate for describing the RCL: both plasma inflow in the direction perpendicular to the layer and plasma outflow along the layer, along the x axis in Figure 1.5, have to be taken into account.

The existence of two scales implies that usually (for a sufficiently strong field and high conductivity like in the solar corona) the RCL width $2b$ is much greater than its thickness $2a$. This is essential since

> the wider the reconnecting current layer, the larger the magnetic energy which is accumulated

in the region of reconnecting fluxes interaction. On the other hand, a small thickness is responsible for the high rate of accumulated energy dissipation, as well as for the possibility of non-stationary processes (for instance, tearing instability) in the RCL. It is generally believed, on a very serious basis (see Chapter 3), that the solar flares and similar phenomena in space

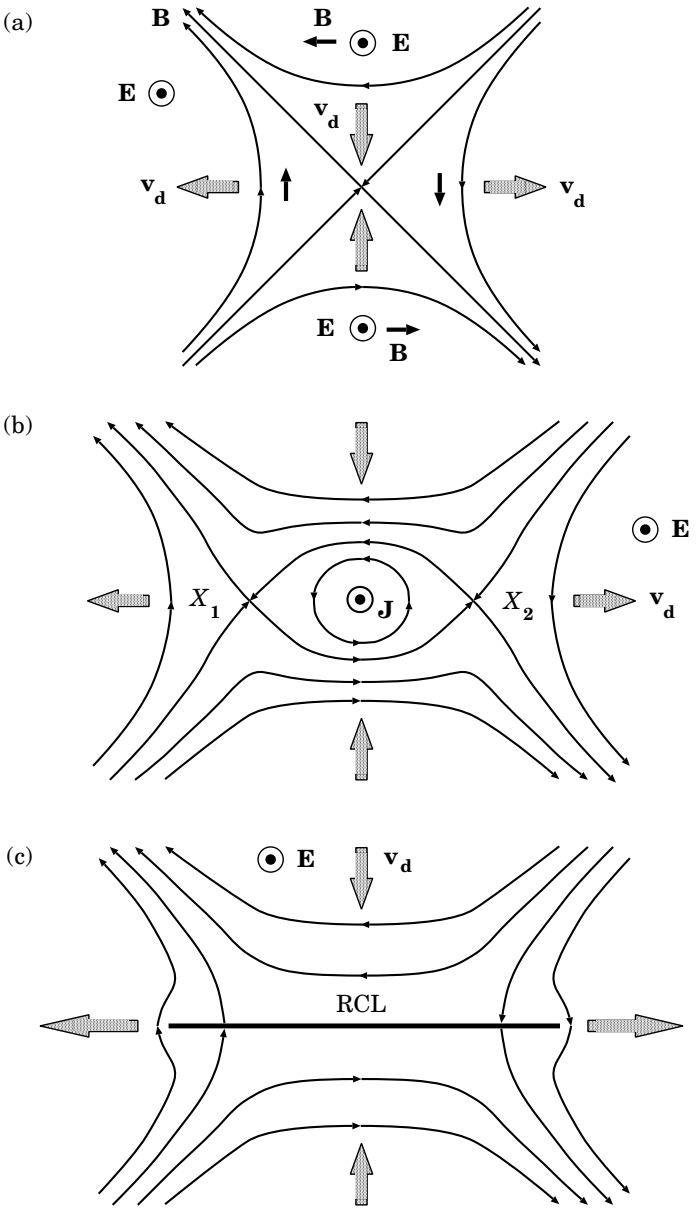

Figure 1.4: (a) Plasma flows owing to the electric drift in the vicinity of a zeroth point. (b) The appearance of secondary X-points – bifurcation of the initial zeroth line, given the current **J** flowing along it. (c) A thin reconnecting current layer (RCL).

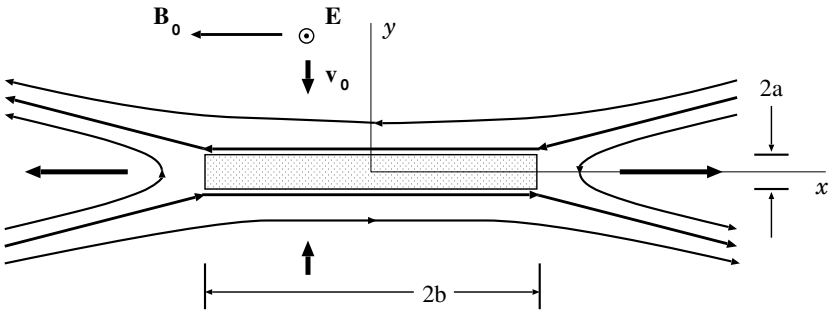

Figure 1.5: The simplest model of a RCL – the neutral layer.

plasma result from the fast conversion of the excess magnetic energy into heat and bulk plasma motions and kinetic energy of accelerated particles.

1.1.4 Three stages in the reconnection process

Now we come back to the example of magnetic reconnection considered in Section 1.1.2. Let the parallel electric currents **I** move to each other with velocity 2**u** as shown in Figure 1.3. Let us describe the electric field induced in the space between the currents.

The magnetic field of two parallel currents is expressed with the aid of the vector-potential **A** having only the z component:

$$\mathbf{A} = \{\, 0,\, 0,\, A\,(x, y, t)\,\}\,. \tag{1.7}$$

The magnetic field **B** is defined by the z-component of the vector-potential:

$$\mathbf{B} = \operatorname{curl} \mathbf{A} = \left\{ \frac{\partial A}{\partial y}\,,\; -\frac{\partial A}{\partial x}\,,\; 0 \right\}. \tag{1.8}$$

The scalar function $A\,(x, y, t)$ is termed the *vector potential*. In the case under consideration

$$A\,(x, y, t) = \frac{I}{c}\left\{ \ln\left[\, x^2 + (y - l(t))^2 \,\right] + \ln\left[\, x^2 + (y + l(t))^2 \,\right] \right\}. \tag{1.9}$$

For a sake of simplicity, near the zeroth line of the magnetic field, situated on the z axis, formula (1.9) may be expanded in a Teylor series, the zeroth order and square terms of the expansion being sufficient for our purposes:

$$A\,(x, y, t) = A\,(0, 0, t) + \frac{2I}{c}\,(x^2 - y^2)\,. \tag{1.10}$$

Here

$$A\,(0,0,t) = \frac{4I}{c}\,\ln l(t)\; = A\,(t) \tag{1.11}$$

is the time-dependent part of the vector potential.

From formula (1.11) the electric field induced along the zeroth line and in its vicinity can be found

$$\mathbf{E} = -\frac{1}{c}\,\frac{\partial \mathbf{A}}{\partial t}\; = -\frac{4I}{c}\,\frac{1}{l}\,\frac{dl}{dt}\,\mathbf{e}_z\,, \tag{1.12}$$

where the half-distance between currents $l = l - ut$ with $u = |\,\mathbf{u}\,|$. Hence

$$\mathbf{E} = \frac{4I}{c}\,\frac{1}{l}\,u\,\mathbf{e}_z\,. \tag{1.13}$$

Therefore

> the electric field induced between two parallel currents, that move to each other, is anti-parallel to these electric currents and induces the current layer in plasma

as shown in Figure 1.6.

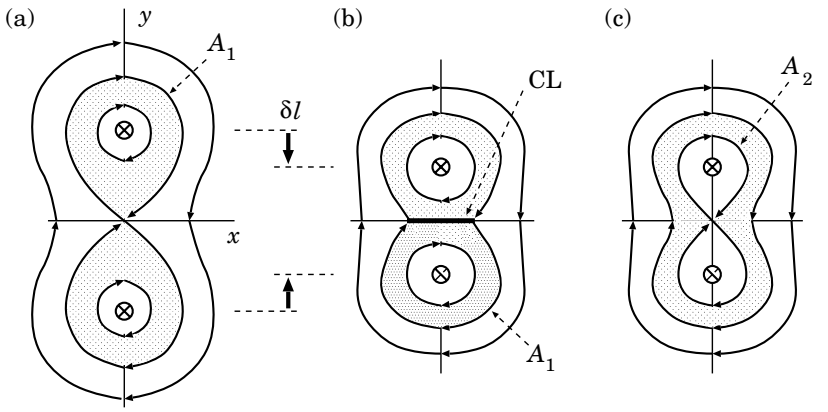

Figure 1.6: Three states of magnetic field: (a) the initial state; (b) the *pre-reconnection* state with a 'non-reconnecting' current layer CL; (c) the final state after reconnection.

So two parallel currents are displaced from the initial state (a) in Figure 1.6 to the final state (c) in plasma, which is the same as the state (b) in Figure 1.3. However, contrary to the case of reconnection in vacuum,

in astrophysical plasma of *low resistivity* we have to add an intermediate state. We call it the *pre-reconnection state*.

At this state, coming between the initial and final one, the electric currents have been displaced to the final positions, but the magnetic field lines have not started to reconnect yet, if the plasma conductivity can be considered as *infinite*. **The current layer** along the X-type neutral line **protects the interacting fluxes from reconnection**. The energy of this interaction called the *free magnetic energy* is just the energy of the magnetic field of the current layer.

Because of the *finite* conductivity, magnetic reconnection proceeds slowly (or rapidly) depending on how high (or low) the conductivity of plasma is. Anyway, the final state (c) after reconnection is the same as the state (b) in Figure 1.3 with the line A_2 as the separatrix of the final state or the last reconnected line. The following analogy in everyday life is appropriate to the process under discussion. A glass of hot water will invariably cool from a given temperature (the initial state) to a room temperature (the final state), independently of the mechanism of heat conductivity, i.e. the heat exchange with the surrounding air; the mechanism determines only the rate of cooling.

1.2 Acceleration in current layers, why and how?

1.2.1 The origin of particle acceleration

The formation and properties of current layers will be considered in Chapters 2 to 14 in different approximations. However one property which is important from the standpoint of astrophysical applications can be understood just now by considering the motion of a charged particle in given magnetic and electric fields. This property is particle acceleration.

In accordance with Figure 1.5, let the magnetic field $\mathbf{B}$ be directed along the x axis, changing the sign at $y = 0$ (the current layer plane). That is why the $y = 0$ plane is called the *neutral* surface (or neutral plane) and the model under consideration is called the *neutral* current layer. Certainly this simplest model is not well justified from physical point of view but mathematically convenient. Moreover, even being a strong idealization, the model allows us to understand why particles are accelerated in a reconnecting current layer.

The electric field $\mathbf{E}$ is directed along the z axis, to the right in Figure 1.7,

being constant and homogeneous. Thus

$$\mathbf{B} = \{ -hy,\, 0,\, 0 \}\,, \qquad \mathbf{E} = \{ 0,\, 0,\, E \}\,, \tag{1.14}$$

where h and E are constants. We assume that the magnetic field changes its value gradually inside the current layer with a gradient $h = |\,\nabla B\,|$.

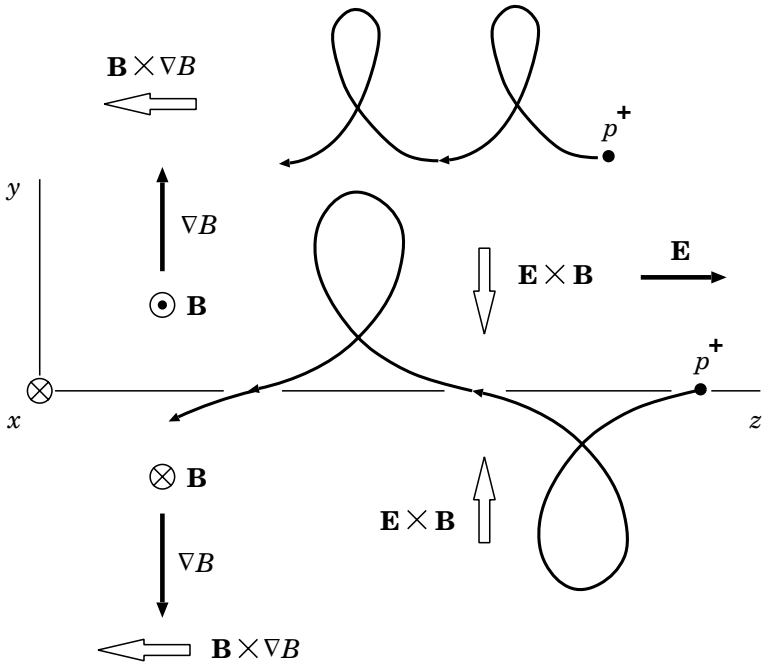

Figure 1.7: The drift motions of a positively charged particle near the neutral plane $y = 0$. The electric field $\mathbf{E}$ induces a particle drift towards the neutral plane from both above and below. The case of the slow gradient drift is shown high above the plane and for a particle crossing the plane.

Let us consider the particle motion in such crossed fields.

At sufficiently large distances from the neutral plane $y = 0$, the motion is a sum of electric and gradient drifts (see Appendix 3). The electric drift makes a particle move to the neutral plane from both sides of this plane. So the electric drift creates some confinement of a particle near the neutral plane.

The gradient drift drives a positively charged particle (an ion) along the negative direction of the z axis, to the left in Figure 1.7, i.e. in the direction opposite to the electric field $\mathbf{E}$. Hence the energy of an ion decreases. A

negatively charged particle (an electron) moves in opposite direction to the ion's drift, i.e. along the electric field; so its energy also decreases due to the gradient drift.

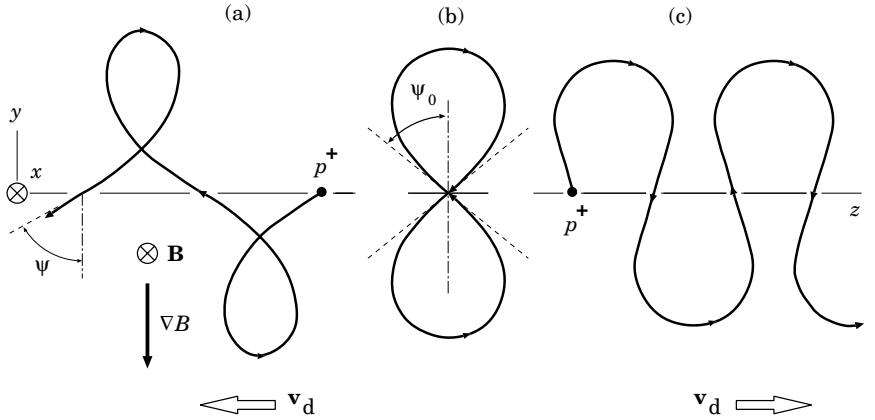

Figure 1.8: The serpentine-type orbits of a positively charged particle crossing the neutral plane $y = 0$.

Particles that cross the neutral plane have more complex orbits. An ion can drift to the left, as shown in Figure 1.8a, or to the right, as shown in Figure 1.8c, depending on the angle at which it crosses the neutral plane. There is only one angle ψ_0 for which the ion moves in a figure-eight pattern (Figure 1.8b) and has no net motion. It stays (in the absence of electric field along the plane, of course). Any ion that crosses the plane with a velocity vector closer to the normal than the ion which stays still, will drift to the right (Cowley, 1986). Such ions moving along the electric field increase their energy. Hence an acceleration of particles crossing the neutral plane is possible.

Therefore the electric field induces the particle drift toward the neutral plane. On reaching the neutral plane, the particles become unmagnetized, since the magnetic field is zero there, and are accelerated in the electric field: ions to the right along the electric field and electrons to the left.

1.2.2 Acceleration in a neutral current layer

As we have seen above, on the basis of the gradient drift consideration, one might think that the neutral current layer is perhaps not the best place for a particle acceleration. However this is not true. First, in an isotropic velocity distribution, this must be a majority of the particles,

resulting in a net rightward current, along the electric field, as required for acceleration. Second, as the particle approaches the neutral plane, the Larmor radius $r_{\text{L}} = \mathcal{R}_\perp / B$ increases indefinitely. Hence the drift formalism is not applicable here. We have to solve the exact equation of particle motion. In the non-relativistic case, it is of the form

$$m\,\dot{\mathbf{v}} = e\,\mathbf{E} + \frac{e}{c}\,\mathbf{v}\times\mathbf{B}\,. \tag{1.15}$$

With the electric and magnetic fields given by (1.14) we have the following three equations in the coordinates x, y, and z:

$$\ddot{x} = 0\,, \qquad \ddot{y} = -\frac{eh}{mc}\,y\,\dot{z}\,, \qquad \ddot{z} = \frac{e}{m}\left(E + \frac{h}{c}\,y\,\dot{y}\right).$$

Let us rewrite these equations as follows:

$$\ddot{x} = 0\,, \qquad \ddot{y} + \frac{eh}{mc}\,\dot{z}\,y = 0\,, \qquad \ddot{z} = \frac{eE}{m} + \frac{eh}{mc}\,y\,\dot{y}\,. \tag{1.16}$$

The last equation is integrated to give

$$\dot{z} = \frac{eE}{m}\,t + \frac{eh}{2mc}\,y^2 + \text{const}\,. \tag{1.17}$$

The motion along the y axis is *finite*. This is a result of the above analysis of the character of motion in the drift approximation which applies when the particle is far enough from the neutral plane $y = 0$. That is the reason why, for large t (the ratio $y^2/t \to 0$), the first term on the right of Equation (1.17) plays a leading role. So we put asymptotically

$$\boxed{\dot{z} = \frac{eE}{m}\,t\,.} \tag{1.18}$$

As we shall see below, (1.18) is the *main* formula which desribes the effect of **acceleration by the electric field inside the neutral layer**.

After substituting (1.18) into the second equation of (1.16) we obtain

$$\ddot{y} + \frac{e^2hE}{m^2c}\,t\,y = 0\,.$$

Introducing the designation

$$\frac{e^2hE}{m^2c} = a^2\,,$$

we have

$$\boxed{\ddot{y} + \omega^2(t)\, y = 0\,,} \tag{1.19}$$

where $\omega^2(t) = a^2 t$.

Let us try to find the solution of Equation (1.19) in the form

$$y\,(t) = f(t)\, \cos\varphi(t)\,, \tag{1.20}$$

where $f(t)$ is a slowly changing function of the time t. Substituting (1.20) in Equation (1.19) results in

$$\ddot{f}\cos\varphi - 2\dot{f}\,\dot{\varphi}\,\sin\varphi - f\,\ddot{\varphi}\,\sin\varphi - f\,(\dot{\varphi})^2\cos\varphi + a^2 t\, f\cos\varphi = 0\,.$$

Since f is a slow function, the first term, containing the second derivative of f with respect to time, can be ignored. The remaining terms are regrouped in the following way:

$$f\,\left[\,-(\dot{\varphi})^2 + a^2 t\,\right]\,\cos\varphi - \left(\,2\dot{f}\,\dot{\varphi} + f\,\ddot{\varphi}\,\right)\sin\varphi = 0\,.$$

By the orthogonality of the functions $\sin\varphi$ and $\cos\varphi$, we have a set of two independent equations:

$$(\dot{\varphi})^2 = a^2\, t\,, \tag{1.21}$$

$$2\dot{f}\,\dot{\varphi} + f\,\ddot{\varphi} = 0\,. \tag{1.22}$$

The first equation is integrated, resulting in

$$\varphi = \frac{2}{3}\, a\, t^{3/2} + \varphi_0\,, \tag{1.23}$$

where φ_0 is a constant. Substitute this solution in Equation (1.22):

$$\frac{\dot{f}}{f} = -\frac{1}{2}\,\frac{\ddot{\varphi}}{\dot{\varphi}} = -\frac{1}{4}\, t^{-1}\,.$$

From this it follows that

$$f = C\, t^{-1/4}\,, \tag{1.24}$$

where C is a constant of integration.

On substituting (1.23) and (1.24) in (1.20), we obtain the sought-after description of the particle trajectory in a current layer:

$$y\,(t) = C\, t^{-1/4}\cos\left(\,\frac{2}{3}\, a\, t^{3/2} + \varphi_0\right), \tag{1.25}$$

$$z\,(t) = \frac{eE}{m}\,\frac{t^2}{2} + z_0\,. \tag{1.26}$$

Eliminate the variable t between formulae (1.25) and (1.26). We have

$$y\,(z) = C\left[\frac{2m}{eE}\,(z-z_0)\right]^{-1/8}\cos\left\{\frac{2}{3}\,a\left[\frac{2m}{eE}\,(z-z_0)\right]^{3/4}+\varphi_0\right\}. \quad (1.27)$$

The amplitude of this function

$$A_y \sim z^{-1/8} \sim t^{-1/4} \quad (1.28)$$

slowly decreases as z increases.

Let us find the 'period' of the function (1.27): $\varphi \sim z^{3/4}$, hence $\delta\varphi \sim z^{-1/4}\,\delta z$. If $\delta \simeq 2\pi$, then

$$\delta z\,\big|_{2\pi} \sim z^{1/4}. \quad (1.29)$$

Thus the period of the function (1.27) is enhanced as shown in Figure 1.9.

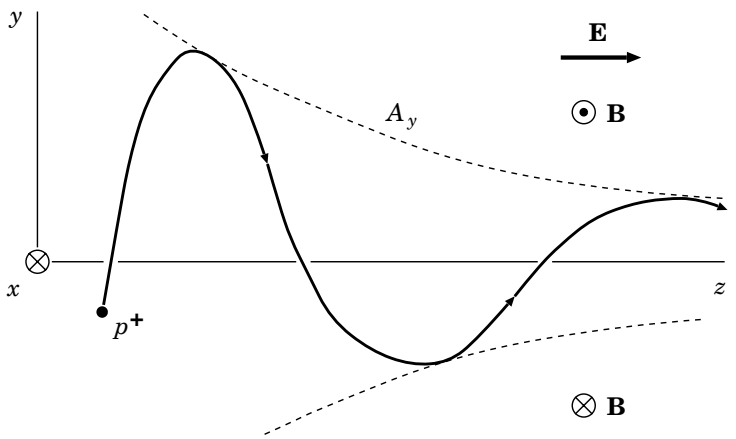

Figure 1.9: The trajectory of a particle accelerated by the electric field **E** in the neighbourhood of the neutral plane inside a neutral current layer.

Note that the transversal velocity

$$\dot{y} \sim t^{-1/4}\,\dot{\varphi} \sim t^{1/4} \quad (1.30)$$

grows with time, but slower than the velocity component parallel to the electric field. From the main formula (1.18) it follows that

$$\dot{z} \sim t\,. \quad (1.31)$$

As a result, the particle is predominantly accelerated in the electric field direction along the current layer.

An exact analytical solution to Equation (1.19) can be expressed as a linear combination of Bessel functions (Speiser, 1965). It has the same properties as (it asymptotically coincides with) the approximate solution. Equation (1.19) corresponds to the equation of a linear oscillator, with the spring constant becoming larger with time. In the neutral current layer, the magnetic force returns the particle to the neutral plane: the larger the force, the higher the particle velocity.

> The electric field provides particle acceleration along the reconnecting current layer. This is the main effect.

Needless to say, the picture of acceleration in real current layers is more complicated and interesting. In particular, acceleration efficiency depends strongly upon the small *transversal* component of the magnetic field which penetrates into the reconnecting current layer (RCL) and makes the accelerated particles be ejected from the layer (Speiser, 1965). This effect, as well as the role of the *longitudinal* (along the z axis) component of a magnetic field inside the current layer, will be considered in Chapters 9 and 11. Magnetical non-neutrality of the current layer is of great significance for acceleration of electrons, for example, in the solar atmosphere.

In fact, real current layers are *non-neutral* not only in the sense of the magnetic field. They are also *electrically* non-neutral; they have an additional electric field directed towards the layer plane from both sides. This electric field is necessary for ion acceleration and will be considered in Chapter 9.

1.3 Practice: Exercises and Answers

Exercise 1.1. [Section 1.1.2] Consider the Lorentz force acting between two parallel electric currents in vacuum.

Answer. One of the currents, for example the upper current $\mathbf{I}$ in the place $y = l$ in Figure 1.3, generates the magnetic field

$$\mathbf{B} = \frac{I}{2\pi R}\,\mathbf{e}_\varphi\,. \tag{1.32}$$

This field circulates around the upper current as shown in Figure 1.10. In the place of the second current, the magnetic field is

$$\mathbf{B} = -\frac{I}{\pi l}\,\mathbf{e}_x\,. \tag{1.33}$$

The Lorentz force acting on the second current, on its unit length, is equal to

$$\mathbf{F} = \mathbf{I} \times \mathbf{B} = \frac{I^2}{\pi l}\,\mathbf{e}_y\,. \tag{1.34}$$

Therefore two parallel currents attract each other.

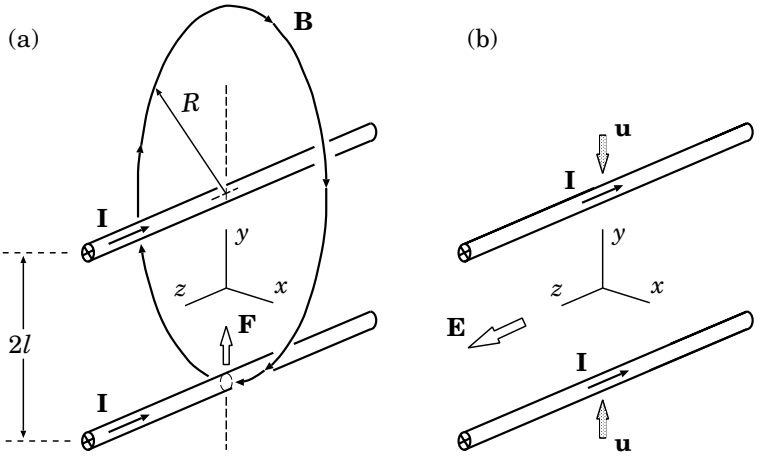

Figure 1.10: Two parallel currents: (a) $2l$ is a distance between the currents; (b) the currents are drawn nearer with velocity $\mathbf{u}$ and induce the electric field $\mathbf{E}$.

Exercise 1.2. [Section 1.1.2] Under conditions of the previous problem discuss how the energy of interaction between two parallel currents depends on the distance between them.

Answer. According to formula (1.34), the force between the interacting current is proportional to $1/l$. Hence the energy of interaction is proportional to $\ln l$ with the sign (-) for the parallel currents but with the sign (+) for the anti-parallel electric currents.

Exercise 1.3. [Section 1.1.2] Show that the electric field (1.13) between two parallel electric currents is proportional to the rate of reconnection of magnetic field lines.

Hint The term $A(t)$, defined by formula (1.11), represents the reconnected magnetic flux as a function of time.

Exercise 1.4. [Section 1.1.2] What happens if we move the parallel currents in opposite directions?

Chapter 2

Reconnection in a Strong Magnetic Field

When two oppositely directed magnetic fields are pressed together, the conductive plasma is squeezed out from between them, causing the field gradient to steepen until a reconnecting current layer (RCL) appears and becomes so thin that the resistive dissipation determines the magnetic reconnection rate. In this Chapter, the basic magnetohydrodynamic properties of such a process are considered in the approximation of a strong magnetic field.

2.1 Small perturbations near a neutral line

2.1.1 Historical comments

The notion of *reconnection* of magnetic field lines, magnetic reconnection, came into existence in the context of the interpretation of solar flare observations. The review of early works in the field is contained, for example in the eminent paper by Sweet (1969). From the viewpoint of reconnection, **points and lines where the magnetic field is zero are peculiarities**. This special feature, which is of a topological nature, has already been mentioned in Section 1.1 (see Figure 1.2).

Giovanelli (1947) pointed out that a *highly concentrated* electric current appears readily at an X-type zeroth point in a highly conducting plasma. This is true and important. Dungey (1958) put forward the idea that

unusual *electrodynamic* properties of a plasma emerge in the vicinity of a neutral (or zeroth) point of type X.

Since there was no clear view of the physical essence of reconnection, the notion has been accepted uncritically. It was assumed, for instance, that the mere existence of a zeroth point inevitably leads to spontaneous compression of a magneto-plasma configuration and rapid dissipation of the magnetic field, i.e. a flare (Dungey, 1958; Severny, 1962).

However, as was shown by Syrovatskii (1962), given magnetostatic equilibrium near a zeroth point, the plasma is stable with respect to spontaneous compression. The situation changes once **the plasma near the zeroth point is subject to an outside action due to an electric field** as shown in Figure 1.4 or due to a MHD wave which is created, for instance, by changes of the magnetic field sources at the photosphere (Figure 1.1).

This action gives rise to an original *cumulative effect* (Syrovatskii, 1966a). We attempted to understand this fundamental property at the qualitative level in Section 1.1. Let us illustrate it by the example of the behaviour of *small* MHD perturbations near the zeroth line. Bearing the solar flare case in mind, we consider the reconnection process in the approximation of a strong magnetic field at first.

2.1.2 Reconnection in a strong magnetic field

Let us start from the set of the ideal MHD equations:

$$\frac{\partial \mathbf{v}}{\partial t} + (\mathbf{v} \cdot \nabla)\, \mathbf{v} = -\frac{\nabla p}{\rho} - \frac{1}{4\pi\rho}\, \mathbf{B} \times \operatorname{curl} \mathbf{B}\,, \tag{2.1}$$

$$\frac{\partial \mathbf{B}}{\partial t} = \operatorname{curl} (\mathbf{v} \times \mathbf{B})\,, \tag{2.2}$$

$$\frac{\partial \rho}{\partial t} + \operatorname{div} \rho\, \mathbf{v} = 0\,, \tag{2.3}$$

$$\frac{\partial s}{\partial t} + (\mathbf{v} \cdot \nabla)\, s = 0\,, \tag{2.4}$$

$$\operatorname{div} \mathbf{B} = 0\,, \tag{2.5}$$

$$p = p\,(\rho, s)\,. \tag{2.6}$$

Here $\mathbf{v}$ is the macroscopic velocity of plasma considered as a continuous medium, s is the entropy per unit mass, other notations are also conventional.

We shall consider a two-dimensional (2D) problem of the second type. The problems of this type treat the plane plasma flows with the velocity field of the form

$$\mathbf{v} = \{\, v_x(x,y,t),\, v_y(x,y,t),\, 0 \,\} \tag{2.7}$$

associated with the plane magnetic field

$$\mathbf{B} = \{\, B_x(x,y,t),\, B_y(x,y,t),\, 0 \,\}\,. \tag{2.8}$$

The electric currents corresponding to this field are parallel to the z axis

$$\mathbf{j} = \{\, 0,\, 0,\, j\,(x,y,t) \,\}\,. \tag{2.9}$$

The vector-potential $\mathbf{A}$ of such a field has as its only non-zero component:

$$\mathbf{A} = \{\, 0,\, 0,\, A\,(x,y,t) \,\}\,.$$

The magnetic field $\mathbf{B}$ is defined by the z-component of the vector-potential:

$$\mathbf{B} = \operatorname{curl} \mathbf{A} = \left\{ \frac{\partial A}{\partial y}\,,\; -\frac{\partial A}{\partial x}\,,\; 0 \right\}. \tag{2.10}$$

The scalar function $A\,(x,y,t)$ is termed the *vector potential*. This function is quite useful, owing to its properties (for more detail see vol. 1, Section 14.2.2).

In the strong-field-cold-plasma approximation, the MHD equations for a plane two-dimensional flow of ideally conducting plasma (for second-type problems) are reduced, in the zeroth order in the small parameter (vol. 1, Section 13.1.1)

$$\varepsilon^2 = \frac{v^2}{V_A^2}\,, \tag{2.11}$$

to the following set of equations (see vol. 1, Section 14.3):

$$\Delta\, A = 0\,, \tag{2.12}$$

$$\frac{d\mathbf{v}}{dt} \times \nabla A = 0\,, \tag{2.13}$$

$$\frac{dA}{dt} = 0\,, \tag{2.14}$$

$$\frac{\partial \rho}{\partial t} + \operatorname{div} \rho\mathbf{v} = 0\,. \tag{2.15}$$

A solution of this set is completely defined inside some region G on the plane (x,y), once the boundary condition is given at the boundary S

$$A\,(x,y,t)\,\big|_{\,S} = f_1\,(x,y,t) \tag{2.16}$$

together with the initial conditions inside the region G

$$\mathbf{v}_{\parallel}(x,y,0)\,\big|_{G} = \mathbf{f}_2(x,y)\,, \tag{2.17}$$

$$\rho(x,y,0)\,\big|_{G} = f_3(x,y)\,. \tag{2.18}$$

Here $\mathbf{v}_{\parallel}$ is the velocity component along field lines. Once the potential $A(x,y,t)$ is known, the transversal velocity component is uniquely determined by the freezing-in Equation (2.14) and is equal, at any moment including the initial one, to

$$\mathbf{v}_{\perp}(x,y,t) = (\mathbf{v}\cdot\nabla A)\,\frac{\nabla A}{|\,\nabla A\,|^2} = -\frac{\partial A}{\partial t}\,\frac{\nabla A}{|\,\nabla A\,|^2}\,. \tag{2.19}$$

From Equation (2.12) and boundary condition (2.16) we find the vector potential $A(x,y,t)$ at any moment of time. Next, from Equations (2.13) and (2.14) and the initial condition (2.17), the velocity $\mathbf{v}(x,y,t)$ is determined; the density $\rho(x,y,t)$ is found from the continuity Equation (2.15) and the initial density distribution (2.18).

However such a procedure is not always possible (see Somov and Syrovatskii, 1972). This means that continuous solutions to the Equations (2.12)–(2.15) do not necessarily exist. Let the boundary and initial conditions be given. The vector potential $A(x,y,t)$ is uniquely determined by Equation (2.12) and the boundary condition (2.16). The latter can be chosen in such a way that the field $\mathbf{B}$ will contain zeroth points:

$$\mathbf{B} = \left\{\frac{\partial A}{\partial y}\,,\ -\frac{\partial A}{\partial x}\,,\ 0\right\} = 0\,. \tag{2.20}$$

Among them, there can exist ones in which the electric field is distinct from zero

$$\mathbf{E} = -\frac{1}{c}\,\frac{\partial \mathbf{A}}{\partial t} \neq 0\,. \tag{2.21}$$

Such points contradict the freezing-in Equation (2.14). We will call them the *peculiar* points.

> The freezing-in condition allows continuous deformation of the strong magnetic field and the corresponding continuous motion of plasma everywhere except at peculiar zeroth points,

i.e. the lines parallel to the z axis of the Cartesian system of coordinates, where the magnetic field is zero while the electric field is nonzero.

Note that simultaneous vanishing of both fields is quite unlikely. This is the reason why the peculiar points occur rather frequently. They will receive much attention in what follows because they represent the places where a reconnecting current layer (RCL) is formed as will be shown below. Here we only stress that

> if there is not a zeroth point inside the region G at the initial time, it does not mean that such a point will never appear there.

An initial field can even be an homogeneous one (Parker, 1972). Following the continuous evolution of the boundary condition (2.16), a zeroth point may appear on the boundary S and, if the electric field at this point does not equal zero, it will create a magnetic field discontinuity which prevents a change of magnetic field topology in the approximation of an ideal plasma. This discontinuity is a *neutral* layer of infinitesimal thickness. In a plasma of finite conductivity, the RCL of finite thickness is formed at a peculiar zeroth point.

The creation of a current layer at the zeroth point which appears on the boundary S was used in the model of coronal streamers driven by the solar wind (Somov and Syrovatskii, 1972). Just the same occurs in the model for interacting magnetic fluxes, compressed by a converging motion of magnetic footpoints in the photosphere (Low, 1987; Low and Wolfson, 1988).

Another case is an appearance of a couple of neutral points inside the region G. Anyway, and in all cases,

> the interaction of magnetic fluxes in the peculiar point changes the field topology and creates the reconnecting current layer.

This kind of MHD discontinuous flows is of great importance for plasma astrophysics.

Let two equal currents I flow parallel to the axis z on lines $x = 0$, $y = \pm\, l$ as shown in Figure 1.3. The magnetic field of these currents is expressed with the aid of the vector-potential $\mathbf{A}_0$ having only the z component:

$$\mathbf{A}_0 = \{\, 0,\, 0,\, A_0\,(x, y)\,\}\ ,$$

where

$$A_0\,(x, y) = \frac{I}{c}\left\{ \ln\left[\, x^2 + (y - l)^2\,\right] + \ln\left[\, x^2 + (y + l)^2\,\right]\right\}. \tag{2.22}$$

Near the zeroth line situated on the z axis, formula (2.22) may be expanded in a Teylor series, the square terms of the expansion being sufficient for our purposes:

$$A_0\,(x, y) = \frac{2I}{c}\,(x^2 - y^2)$$

or

$$A_0\,(x, y) = \frac{h_0}{2}\,(x^2 - y^2)\,. \tag{2.23}$$

Here $h_0 = 4I/c$ is the magnetic field gradient in the vicinity of the zeroth line. The gradient of the field is an important characteristic of a reconnection region. In fact,

$$\mathbf{B}_0 = \operatorname{curl} \mathbf{A}_0 = \left\{ \frac{\partial A_0}{\partial y} \,,\, -\frac{\partial A_0}{\partial x} \,,\, 0 \right\} = \{ -h_0 y \,,\, -h_0 x \,,\, 0 \} \,. \tag{2.24}$$

The field lines of the hyperbolic field (2.24) are shown in Figure 1.2.

Let us assume the field $\mathbf{B}_0$ to be sufficiently strong, so that the Alfvén speed V_{A} should be much greater than that of sound V_{s} everywhere, the exception being a small region near the zeroth line. On the strength of formula (2.24),

$$V_{\text{A}}^{\,2} = \frac{h_0^2 \, r^2}{4\pi\rho_0} \,,$$

where $r = (x^2 + y^2)^{1/2}$ is the radius in the cylindrical frame of reference, i.e. in the plane (x, y). Hence the condition

$$V_{\text{A}}^{\,2} \gg V_{\text{s}}^{\,2}$$

can be rewritten in the form:

$$r \gg r_{\text{s}} \,. \tag{2.25}$$

Here

$$r_{\text{s}} = \left(\frac{4\pi \, n_0 k_{\text{B}} T_0}{h_0^2} \right)^{1/2} , \tag{2.26}$$

n_0 and T_0 being the number density and temperature of the plasma at the initial stage of the process, k_{B} is Boltzmann's constant.

Let $l = 1$ in formula (2.22). Then the assumed condition (2.25), together with the condition for applicability of the approximate expression (2.23) for the potential $\mathbf{A}_0$, means that the domain of admissible values is

$$r_{\text{s}} \ll r \ll 1 \,. \tag{2.27}$$

We shall consider the MHD processes in this domain, related to magnetic reconnection at the X-type zeroth point.

2.1.3 A linearized problem in ideal MHD

Of concern to us are *small perturbations* in the region (2.27) relative to the initial equilibrium state

$$\mathbf{v}_0 = 0 \,, \quad \rho_0 = \text{const} \,, \quad p_0 = \text{const} \,, \quad \Delta A_0 = 0 \,.$$

Let us consider plane flows of a plasma with a frozen magnetic field in the plane (x, y):

$$\mathbf{v} = \{\, v_x(x,y,t),\ v_y(x,y,t),\ 0\,\}\,, \qquad \mathbf{B} = \mathbf{B}_0 + \mathbf{b}\,,$$

the small perturbation of magnetic field being

$$\mathbf{b} = \{\, b_x(x,y,t),\ b_y(x,y,t),\ 0\,\}\,.$$

Thus, from the mathematical standpoint (see vol. 1, Section 14.2.2), the problem at hand belongs to the two-dimensional problems of the *second* type.

For small perturbations $\mathbf{v}$, p, ρ, and A (instead of $\mathbf{b}$), the linearized equations of ideal MHD can be written in the form

$$\begin{aligned} \frac{\partial A}{\partial t} &= -\,\mathbf{v}\cdot\nabla A_0\,, \\ \frac{\partial\,\mathbf{v}}{\partial t} &= -\,\frac{\nabla p}{\rho_0} - \frac{1}{4\pi\rho_0}\,\nabla A_0\,\Delta A\,, \\ \frac{\partial \rho}{\partial t} &= -\,\rho_0\,\mathrm{div}\,\mathbf{v}\,. \end{aligned} \tag{2.28}$$

The gas pressure gradient in the region (2.27) can be ignored. If we did not ignore the term ∇p, the set of Equations (2.28), on differentiating with respect to t, could be transformed to give us

$$\begin{aligned} \underline{\frac{\partial^2 A}{\partial t^2} = \frac{(\nabla A_0)^2}{4\pi\rho_0}\,\Delta A} + \frac{{V_{\mathrm{s}}}^2}{\rho_0}\,\nabla A_0\cdot\nabla\rho\,, \\ \frac{\partial^2\mathbf{v}}{\partial t^2} = \frac{\nabla A_0}{4\pi\rho_0}\,\Delta\,(\mathbf{v}\cdot\nabla A_0) + {V_{\mathrm{s}}}^2\,\nabla\,\mathrm{div}\,\mathbf{v}\,, \\ \frac{\partial^2\rho}{\partial t^2} = \frac{1}{4\pi}\,\nabla A_0\cdot\nabla\,\Delta A + {V_{\mathrm{s}}}^2\,\Delta\rho\,. \end{aligned} \tag{2.29}$$

So perturbations in the region (2.27) are seen (see the underlined terms in the first equation) to propagate with the *local* Alfvén velocity V_{A}:

$$V_{\mathrm{A0}}^2 = V_{\mathrm{A0}}^2\,(r) = \frac{\left(\nabla A_0\,(r)\right)^2}{4\pi\rho_0}\,, \tag{2.30}$$

the result being accurate to small corrections of the order of ${V_{\mathrm{s}}}^2/V_{\mathrm{A0}}^2$. This is the case of astrophysical plasma with a strong magnetic field; see the mostly *isotropic* wave V_+ in vol. 1, Figure 15.3.

The displacement of the plasma under the action of the perturbation, $\boldsymbol{\xi}$, is convenient to introduce instead of the velocity perturbation $\mathbf{v}$:

$$\mathbf{v} = \frac{\partial \boldsymbol{\xi}}{\partial t}\,. \tag{2.31}$$

Dropping the terms depending on the pressure gradient, the initial set of Equations (2.29) is recast as follows (Syrovatskii, 1966b):

$$\frac{\partial^2 A}{\partial t^2} = V_{\mathrm{A}0}^{\,2}\,(r)\,\Delta A\,, \tag{2.32}$$

$$\frac{\partial^2 \boldsymbol{\xi}}{\partial t^2} = \frac{V_{\mathrm{A}0}^{\,2}\,(r)}{\sqrt{4\pi\rho_0}}\,\Delta\,(\,\boldsymbol{\xi}\cdot\nabla A_0)\,, \tag{2.33}$$

$$\rho = -\,\rho_0\,\mathrm{div}\,\boldsymbol{\xi}\,, \tag{2.34}$$

$$A = -\,(\,\boldsymbol{\xi}\cdot\nabla\,)\,A_0\,. \tag{2.35}$$

Rewrite Equation (2.32) in the cylindrical frame of reference

$$\frac{\partial^2 A}{\partial t^2} = \frac{h_0^2}{4\pi\rho_0}\left[\,r\,\frac{\partial}{\partial r}\left(r\,\frac{\partial A}{\partial r}\right) + \frac{\partial^2 A}{\partial \varphi^{\,2}}\right]\,.$$

On substituting $x = \ln r$, this equation is reduced to the usual wave equation in the variables (x, φ)

$$\frac{\partial^2 A}{\partial t^2} = V_{\mathrm{a}}^{\,2}\left(\frac{\partial^2 A}{\partial x^2} + \frac{\partial^2 A}{\partial \varphi^{\,2}}\right), \tag{2.36}$$

where

$$V_{\mathrm{a}} = h_0/\sqrt{4\pi\rho_0}$$

is a constant playing the role of the wave velocity.

2.1.4 Converging waves and the cumulative effect

Let us consider an initial perturbation of the potential, which is independent of the cylindrical-frame angle φ:

$$A\,(r, \varphi, 0) = \Phi\,(r)\,,$$

where $\Phi\,(r)$ is an arbitrary function of r. In this case the general solution of Equation (2.36) is

$$A\,(r, t) = \Phi\,(\,\ln r + V_{\mathrm{a}}\,t)\,. \tag{2.37}$$

The sign +, which we have chosen, by $V_{\rm a}\,t$ corresponds to the *converging* cylindrical wave, its velocity being

$$V(r) = \frac{dr}{dt} = -\,r\,V_{\rm a} = -V_{\rm A0}(r)\,,$$

i.e. the wave propagates with the Alfvén velocity (see definition (2.30)). The following properties of the wave are of interest.

(a) The magnetic field intensity in such a wave is

$$B_r = \frac{1}{r}\,\frac{\partial A}{\partial \varphi} = 0\,, \qquad B_\varphi = -\frac{\partial A}{\partial r} = -\frac{\Phi}{r}\,.$$

As the wave approaches the zeroth line, the field intensity grows

$$B\,(r) = B\,(R)\,\times\,\frac{R}{r}\,.$$

Here $B\,(R)$ is the field intensity in the wave when its front is at a distance R from the zeroth line.

(b) The magnetic field gradient increases as well

$$\frac{\partial B}{\partial r}(r) = \frac{\partial B}{\partial r}(R)\,\times\left(\frac{R}{r}\right)^2.$$

Thus

> as the cylindrical wave converges to zero it gives rise to a *cumulative* effect in regard to the magnetic field and its gradient.

(c) The character of the plasma displacement $\boldsymbol{\xi}$ in such a wave can be judged from the motion Equation (2.33). It contains the scalar product $\boldsymbol{\xi}\cdot\nabla A_0$. Hence the displacements directed along the field lines are absent in the wave under consideration. The perpendicular displacements

$$\boldsymbol{\xi} = -\,\frac{A}{(\nabla A_0)^2}\,\nabla A_0\,, \tag{2.38}$$

whence, in view of (2.37), it follows that $|\,\boldsymbol{\xi}\,| \sim r^{-1}$. So

> the quantity of the displacement also grows, as the wave approaches the zeroth line of the magnetic field.

(d) As for the change in plasma density, we find from Equation (2.34), using formulae (2.38) and (2.37), that

$$\rho = -\,\rho_0\,\mathrm{div}\,\boldsymbol{\xi} \sim \frac{1}{r^2}\,\cos 2\varphi\,. \tag{2.39}$$

The plasma density increases in a pair of opposite quadrants while decreasing in the other pair (Figure 2.1). The first pair of quadrants ($-\pi/4 \le \varphi \le \pi/4$ and $3\pi/4 \le \varphi \le 5\pi/4$) corresponds to the regions where the plasma flows are convergent. In the second pair ($\pi/4 < \varphi < 3\pi/4$ and $5\pi/4 < \varphi < 7\pi/4$) of quadrants, the trajectories of the fluid particles diverge, resulting in a decrease of the plasma density.

Therefore, even in a linear approximation,

> small perturbations grow in the vicinity of the magnetic field zeroth line. As this takes place, regions appear in which the field and its gradients increase, whereas the plasma density decreases.

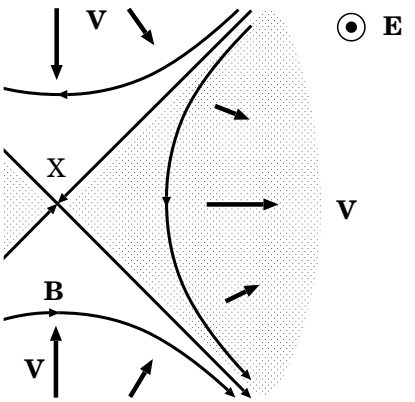

Figure 2.1: Plasma flows and the density change in small perpurbations in the vicinity of a hyperbolic zeroth point X. Shadow shows two regions of converging flows; here the plasma density increases.

The so-called linear-reconnection theory takes into account the dissipative processes in the linear approximation (see Sections 13.1 and 13.2.3).

2.2 Large perturbations near the neutral line

Let us relax the assumption concerning the smallness of the perturbations in the vicinity of a zeroth line. Then, instead of linearized MHD equations, we shall deal with the exact set of two-dimensional equations in the approximation of the strong field and the cold plasma, taken in a zeroth order with respect to the small parameter $\varepsilon^2 = v^2/V_{\text{A}}^2$, i.e. Equations (2.12)–(2.15):

$$\Delta A = 0\,, \tag{2.40}$$

$$\frac{d\mathbf{v}}{dt} \times \nabla A = 0\,, \tag{2.41}$$

$$\frac{dA}{dt} = 0\,, \tag{2.42}$$

$$\frac{\partial \rho}{\partial t} + \operatorname{div} \rho \mathbf{v} = 0\,. \tag{2.43}$$

Here it is implied that the region in the vicinity of the zeroth line is to be restricted by the condition (2.25).

2.2.1 Magnetic field line deformations

As was shown in vol. 1, Section 14.2.2, Equations (2.42) and (2.43) are integrated on passing to Lagrangian coordinates

$$\mathbf{r}\,(\mathbf{r}_0, t) = \mathbf{r}_0 + \boldsymbol{\xi}\,(\mathbf{r}_0, t)\,. \tag{2.44}$$

Here $\mathbf{r}_0$ is the coordinate of a fluid particle before displacement, i.e. at the initial moment, $\mathbf{r}$ is its coordinate at a moment of time t, $\boldsymbol{\xi}(\mathbf{r}_0, t)$ is the *displacement vector* (cf. definition (2.31)). Let us rewrite Equation (2.44) as the inverse transformation

$$\mathbf{r}_0\,(\mathbf{r}, t) = \mathbf{r} - \boldsymbol{\xi}\,(\mathbf{r}, t)\,.$$

Then the continuity Equation (2.43) can be written in its Lagrangian form:

$$\rho\,(\mathbf{r}, t) = \rho_0\,(\mathbf{r} - \boldsymbol{\xi}\,(\mathbf{r}, t))\ \frac{\mathcal{D}\,(\mathbf{r} - \boldsymbol{\xi}(\mathbf{r}, t))}{\mathcal{D}\,(\mathbf{r})}\,, \tag{2.45}$$

where $\mathcal{D}\,(\mathbf{r}_0)/\mathcal{D}\,(\mathbf{r})$ is the Jacobian transformation from $\mathbf{r}_0$ coordinates to $\mathbf{r}$ coordinates.

The integral of the freezing-in Equation (2.42) is

$$A\,(\mathbf{r}, t) = A_0\,(\mathbf{r} - \boldsymbol{\xi}\,(\mathbf{r}, t))\,, \tag{2.46}$$

where $A_0\,(\mathbf{r}_0)$ is an initial value of the vector-potential.

Had the displacement $\boldsymbol{\xi}\,(\mathbf{r}, t)$ been known, formulae (2.46) and (2.45) would have allowed us to uniquely determine the field line deformation and plasma density change in the vicinity of the zeroth line, given the displacement of the currents I. However, to find $\boldsymbol{\xi}(\mathbf{r}, t)$ generally, we must simultaneously solve Equations (2.40) and (2.41), i.e. the set of equations

$$\Delta A = 0\,, \tag{2.47}$$

$$\frac{\partial^2 \boldsymbol{\xi}}{\partial t^2} \times \nabla A = 0\,. \tag{2.48}$$

As a rule, to integrate Equation (2.48), we must have recourse to numerical methods (Somov and Syrovatskii, 1976b). Let us try to circumvent the difficulty.

Let us suppose the displacement of the currents occurs sufficiently fast as compared with the speed of sound but sufficiently slow as compared with the Alfvén speed. With these assumptions, the boundary conditions of the problem (see (2.16)) change slowly in comparison with the speed of fast magnetoacoustic waves, which allows us to **consider the field as being in equilibrium at each stage** of the process (see Equation (2.47)).

The latter assumption actually means that the total displacement $\boldsymbol{\xi}$ can be held to be a sum of successive small perturbations $\delta\boldsymbol{\xi}$ of the type (2.38), each of them transferring the system to a close equilibrial state. Since the small displacement $\delta\boldsymbol{\xi}$ is directed across the magnetic field lines, the total displacement $\boldsymbol{\xi}$ is also orthogonal to the picture of field lines. To put it another way, the lines of the plasma flow constitute a family of curves orthogonal to the magnetic field lines, i.e. the family of hyperbolae

$$x\,y = x_0\,y_0\,. \tag{2.49}$$

A numerical solution of the problem (Somov and Syrovatskii, 1976b) shows that such a flow is actually realized for comparably small t or sufficiently far from the zeroth line.

Let us make use of the freezing-in Equation (2.46) to find another equation relating the coordinates of a fluid particle (x, y) with their initial values (x_0, y_0). In view of the formula (2.22) for the initial vector-potential $A_0\,(x, y)$, the magnetic field potential of displaced currents is

$$A\,(x, y) = \frac{h_0}{4}\left\{\ln\left[\,x^2 + (y - 1 + \delta)^2\,\right] + \ln\left[\,x^2 + (y + 1 - \delta)^2\,\right]\right\}\,. \tag{2.50}$$

Relative to formula (2.22), $I/c = h_0/4$, $l = 1$, and $\delta l = \delta$.

Near the zeroth line, with the accuracy of the terms of order δ, we find

$$A\,(x, y) = \frac{h_0}{2}\left(x^2 - y^2 - 2\delta\right). \tag{2.51}$$

Substitution of (2.51) in (2.46) gives

$$y^2 - x^2 + 2\delta = y_0^2 - x_0^2\,. \tag{2.52}$$

Equations (2.49) and (2.52) allow us to express the initial coordinates of a fluid particle (x_0, y_0) in terms of its coordinates (x, y) at the moment of time t (Syrovatskii, 1966a):

$$x_0^2 = \frac{1}{2}\left\{\left[\left(x^2 - y^2 - 2\delta\right)^2 + 4x^2y^2\right]^{1/2} + \left(x^2 - y^2 - 2\delta\right)\right\},$$

$$y_0^2 = \frac{1}{2}\left\{\left[\left(x^2 - y^2 - 2\delta\right)^2 + 4x^2y^2\right]^{1/2} - \left(x^2 - y^2 - 2\delta\right)\right\}. \tag{2.53}$$

The displacements determined by these expressions are such that the field lines which crossed the y axis at points 0, $\sqrt{\delta}$, $\sqrt{2\delta}$, would take the place of the field lines which crossed the x axis at points $\sqrt{2\delta}$, $\sqrt{\delta}$, 0, respectively (see Figure 2.2 in the region $r \gg r_s$).

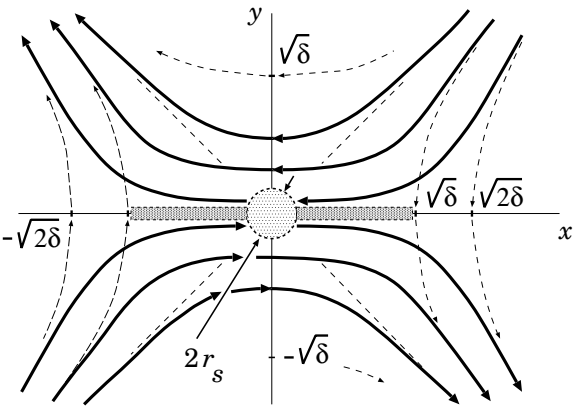

Figure 2.2: The deformation of the magnetic field lines in the neighbourhood of a zeroth line.

The plasma displacements and frozen-in field line deformations obtained pertain only to the region $r \gg r_s$. The approximation of a strong field and a cold plasma is inapplicable outside this region, i.e. $r \leq r_s$. It must also be considered that a region of *strong plasma compression* can arise in the course of the displacement. The conditions for applicability of the strong-field-cold-plasma approximation can be broken down in such regions, thus making it necessary to solve a more general problem. In particular, field deformations can be distinctly different here, owing to *strong electric currents* flowing in these regions. They will be discussed in the next Section.

The main effect demonstrated above is the deformation of the field lines which is schematically shown as two long dashed areas along the x axis. Here

> a current layer formation is confirmed by the presence of oppositely directed magnetic field lines

near the origin of the coordinates in Figure 2.3. The current inside the current layer is parallel to the z axis, i.e. parallel to the electric field **E**

related to the magnetic field line motion (cf. Figure 1.4). However, at the edges of the layer, the currents are sometimes opposite in direction (the so-called reverse currents) to the one inside the main current layer which is formed at the zeroth line as shown above.

2.2.2 Plasma density variations

Let us find the density distribution (2.45) by calculating the Jacobian of the reverse transformation of the Lagrangian variables, with the aid of the formulae (2.53). Assuming an homogeneous initial distribution of plasma, we have

$$\frac{\rho\,(x,y)}{\rho_0} = \frac{x^2+y^2}{\left[\,(x^2+y^2)^2 + 4\delta\,(y^2-x^2) + 4\delta^2\,\right]^{1/2}}\,. \tag{2.54}$$

The formula obtained shows that in the region

$$x^2 < y^2 + \delta \tag{2.55}$$

the displacement of the currents leads to plasma rarefaction. As this takes place, the largest rarefaction occurs for small r ($r^2 \ll \delta$):

$$\frac{\rho\,(x,y)}{\rho_0} \sim \frac{r^2}{2\delta}\,. \tag{2.56}$$

By contrast, in the region $x^2 > y^2 + \delta$ the plasma is compressed, its density tending to infinity at the points (Figure 2.3):

$$y = 0\,, \qquad x = \pm\sqrt{2\delta}\,. \tag{2.57}$$

The approximation of a strong field and a cold plasma is inapplicable in the vicinity of these points, and the actual deformation of the field lines can differ significantly from that found above.

Figure 2.3 illustrates a characteristic distribution of plasma near a current layer ($-\sqrt{\delta} \le x \le \sqrt{\delta}$), dissipation of magnetic field being neglected. The regions of strong plasma compression near the points (2.57) are shown by the shadowed regions C_1 and C_2 outside of the layer.

2.3 Dynamic dissipation of magnetic field

2.3.1 Conditions of appearance

In the region between the points (2.57), where the plasma density formally tends to infinity, the character of the displacements can be determined

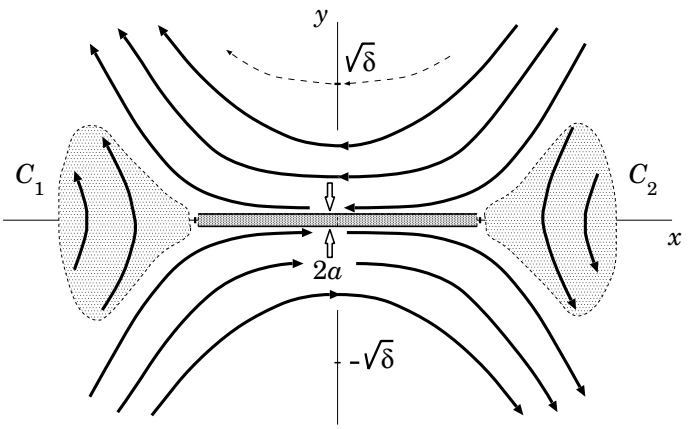

Figure 2.3: The plasma distribution near a forming current layer. $2a$ is the thickness of the current layer.

by using the freezing-in condition for the magnetic field lines and taking into account that, as was mentioned in the previous section, plasma spread along the field lines during the rapid displacement of the currents may be neglected. Under these assumptions, the magnetic field deformation is of the form shown in Figures 2.2 and 2.3. Definition of the current displacement δ is given in formula (2.50).

It is important for the following discussion that the whole magnetic flux which crossed the axis y in the region

$$0 < y < \sqrt{2\delta}\,,$$

namely

$$\Phi = A_0\,(0, \sqrt{2\delta}) - A_0\,(0,0) = h_0\,\delta\,, \tag{2.58}$$

is now confined to the strip $y \leq r_{\rm s}$. The thickness of this strip $r_{\rm s} \approx a$ in Figure 2.3. The field lines of this flux 'spread' along the x axis in the negative direction. The same flux of field lines, but oppositely directed, is situated along the x axis in the lower half-plane.

Therefore, in the region

$$|\,x\,| \leq \sqrt{\delta}\,, \qquad |\,y\,| \leq r_s\,,$$

the magnetic field lines of opposite directions are compressed to form a thin *reconnecting current layer* (RCL). The region of the magnetic field

compression is shown in Figures 2.2 and 2.3 as the long dashed area along the x axis. The magnetic field gradient in this region is evaluated as

$$h \approx \frac{B}{r_\mathrm{s}} \approx \frac{\Phi}{r_\mathrm{s}^2} \approx \frac{h_0}{r_\mathrm{s}^2}\,\delta\,. \tag{2.59}$$

The field gradient h in the region of the magnetic compression is δ/r_s^2 times its initial value h_0. In other words,

> the magnetic field gradient inside the current layer is proportional to the value of the external currents displacement δ,

with the proportionality coefficient, by virtue of definition (2.26), being larger, the smaller is the gas pressure as compared with the magnetic one in the reconnecting plasma.

At the same time, according to (2.56) the plasma density in the region $r^2 < \delta$ decreases by a factor of $r^2/2\delta$. This conclusion applies for $r \gg r_\mathrm{s}$ and is of a qualitative character. Nonetheless it is of fundamental importance that we can make an order-of-magnitude evaluation of the ratio of the field gradient to the plasma concentration in the region of the magnetic compression ($r \approx r_\mathrm{s}$)

$$\frac{h}{n} \approx \frac{h_0}{n_0}\,\frac{\delta^2}{r_\mathrm{s}^4}\,. \tag{2.60}$$

Recall that in the MHD approximation we usually neglect the displacement current $(1/c)\,\partial\mathbf{E}/\partial t$ as compared with the conductive one

$$\mathbf{j} = ne\,\mathbf{u}\,.$$

Here e is the charge on a particle, $\mathbf{u}$ is the current velocity, i.e. the velocity of current carriers. Subject to this condition, we may use the 'truncated' Maxwell equation

$$\operatorname{curl}\mathbf{B} = \frac{4\pi}{c}\,\mathbf{j}\,, \tag{2.61}$$

whence, on setting $|\operatorname{curl}\mathbf{B}| \approx h$, the following estimate is obtained

$$\frac{h}{n} \approx 4\pi e\left(\frac{u}{c}\right).$$

Since the particle velocity u cannot exceed the speed of light c, the current density is limited by the value $j = nec$ and the ratio

$$\frac{h}{n} < 4\pi e\,. \tag{2.62}$$

On the other hand, from (2.60) this ratio is determined by the value of the displacement δ and by the parameters r_s and h_0/n_0. Once the condition (2.62) breaks down, by virtue of (2.60), i.e.

$$\frac{h_0}{n_0}\,\frac{\delta^2}{r_s^4} \geq 4\pi e\,, \tag{2.63}$$

the displacement current $(1/c)\,\partial\mathbf{E}/\partial t$ must be accounted for in Equation (2.61). It means that, under condition (2.63),

> a strong electric field of an inductive nature arises in the region where magnetic fluxes interact.

A quantitative description of the physical processes in the region involved is difficult and is the subject of the theory of reconnection in current layers. The qualitative effects are as follows.

2.3.2 The physical meaning of dynamic dissipation

The appearance of the inductive electric field, independent of the plasma motion, signifies the violation of the freezing-in condition. Thus the motion of the field lines relative to the plasma, which is necessary for their reconnection in the region of interaction of the magnetic fluxes, is allowed. The important aspect of the situation under discussion is that these processes are *independent* of Joule dissipation and can take place in a collisionless plasma. This is the reason why this phenomenon may be termed *dynamic dissipation* (Syrovatskii, 1966a) or, in fact, *collisionless reconnection* (see Section 2.4.3).

An essential peculiarity of the dynamic dissipation of a magnetic field is that the inductive electric field is directed along the main current $\mathbf{j}$ in the reconnection region. Hence the electric field does positive work on charged particles, thus increasing their energy. It is this process that provides the transformation of the magnetic energy into the kinetic one, i.e. dynamic dissipation.

As opposed to Joule dissipation, there is no direct proportionality of the current density $\mathbf{j}$ to the electric field intensity $\mathbf{E}$ in the case of dynamic dissipation. Given the condition (2.63),

> the current density is saturated at the value $j \approx nec$, the field energy going to increase the total energy of a particle,

$$\mathcal{E} = \frac{mc^2}{\sqrt{1 - v^2/c^2}}\,, \tag{2.64}$$

i.e. the acceleration by the electric field. Thus, under the conditions considered, the field energy converts directly to that of the accelerated particles.

Acceleration occurs along zeroth lines (parallel to the z axis) which are formed in the current layer region. Recall that the particle motion along a neutral plane (see Section 1.2) is stable: the magnetic field returns deviating particles to the neutral plane, as is clear from immediate consideration of the Lorentz force $(e/c)\,\mathbf{v} \times \mathbf{B}$. More realistic analysis of the acceleration problem will be given in Chapter 9.

The condition (2.63) is, in fact, extreme. This implies the regular acceleration of particles to relativistic energies. In fact, acceleration may take place under much more modest conditions, when the dynamic dissipation of a magnetic field is, in essence, related to the known phenomenon of the electric runaway of particles (primarily electrons; see vol. 1, Section 8.4.2). The condition which in this case replaces the extreme condition (2.63) was derived by Syrovatskii (1966b).

Needless to say, relativistic energies are not always reached in the acceleration process. Some instabilities are, as a rule, excited in the plasma-beam system in the acceleration region. As this takes place, particle scattering and acceleration with the created wave turbulence must be accounted for. However it is important that the general inference as to the possibility of **particle acceleration by an electric field in the magnetic reconnection region** (i.e. dynamic dissipation of the magnetic field) remains valid, in particular, when applied to the solar flare problem (see Section 3.1, Chapters 6 and 9).

2.4 Nonstationary analytical models of RCL

2.4.1 Self-similar 2D MHD solutions

In connection with the 2D problem of the equilibrium state of a plasma near the X-type zeroth point of magnetic field, Chapman and Kendall (1963) had obtained the exact particular solution of the ideal MHD equations for an *incompressible* fluid. This *self-similar* analytical solution has a perfectly defined character. A fixed mass of a plasma near the zeroth point receives energy from the outside in the form of an electromagnetic-field energy flux. Finally, a *cumulative effect* is developed and arbitrarily large energy densities are attained. The solution demonstrates the tendency to form a current layer near the zeroth point.

Imshennik and Syrovatskii (1967) had found a self-similar solution for an ideal *compressible* fluid. Let us also start from the set of the ideal MHD Equations (2.1)–(2.6). Consider the 2D MHD problem of the second

type (see vol. 1, Section 14.2.2). Substitute definition (2.10) of the vector potential **A** in the first three equations, we have the following set:

$$\rho \frac{d\mathbf{v}}{dt} = -\nabla p - \frac{1}{4\pi} \Delta A \nabla A \,, \tag{2.65}$$

$$\operatorname{curl} \frac{d\mathbf{A}}{dt} = 0 \,, \tag{2.66}$$

$$\frac{d\rho}{dt} + \rho \operatorname{div} \mathbf{v} = 0 \,. \tag{2.67}$$

We assume that the pressure p is a function of the density ρ only. This condition is satisfied by any politropic equation of state. Moreover, as it was shown by Imshennik and Syrovatskii, for the class of solutions of interest to us, the plasma density ρ depends only on time. Hence, by virtue of the foregoing assumption, the pressure p depends only on time too. Therefore the pressure gradient ∇p in Equation (2.65) vanishes. So we have equations:

$$\rho \frac{d\mathbf{v}}{dt} = -\frac{1}{4\pi} \Delta A \nabla A \,, \tag{2.68}$$

$$\operatorname{curl} \frac{dA}{dt} = 0 \,, \tag{2.69}$$

$$\frac{d\rho}{dt} + \rho \operatorname{div} \mathbf{v} = 0 \,. \tag{2.70}$$

Let us seek a solution of the set of Equations (2.68)–(2.70) under the following initial conditions.

(a) The plasma density is constant:

$$\rho\,(x, y, 0) = \rho_0 \,, \tag{2.71}$$

(b) The magnetic field is a hyperbolic one (cf. formula (2.23) where put $h_0/2 = a_0$):

$$A\,(x, y, 0) = a_0 \left(x^2 - y^2\right) , \tag{2.72}$$

(c) The initial velocity depends linearly on the coordinates, so that there is no flow of plasma across the coordinate axes:

$$v_x\,(x, y, 0) = Ux \,, \qquad v_y\,(x, y, 0) = Vy \,. \tag{2.73}$$

Thus the initial conditions are defined by the four independent quantities ρ_0, a_0, U, and V. We can construct from them three independent combinations with the dimension of time:

$$t_x = \frac{1}{U} \,, \qquad t_y = \frac{1}{V} \,, \qquad t_0 = \frac{(\pi\rho_0)^{1/2}}{\mid a_0 \mid} \tag{2.74}$$

and not even one combination with the dimension of length. We introduce new variables with dimensions equal to a certain power of the length:

$$\tau = \frac{t}{t_0}\,, \qquad u_x = t_0 v_x\,, \qquad u_y = t_0 v_y\,, \qquad a = \frac{A}{a_0}\,, \qquad g = \frac{\rho}{\rho_0}\,. \tag{2.75}$$

In terms of these variables, Equations (2.68)–(2.70) take the form

$$\frac{\partial}{\partial x}\frac{da}{d\tau} = 0\,, \qquad \frac{\partial}{\partial y}\frac{da}{d\tau} = 0\,, \tag{2.76}$$

$$g\,\frac{du_x}{d\tau} = -\frac{1}{4}\,\frac{\partial a}{\partial x}\,\Delta a\,, \qquad g\,\frac{du_y}{d\tau} = -\frac{1}{4}\,\frac{\partial a}{\partial y}\,\Delta a\,, \tag{2.77}$$

$$\frac{dg}{d\tau} + \left(\frac{\partial u_x}{\partial x} + \frac{\partial u_y}{\partial y}\right) g = 0\,. \tag{2.78}$$

The initial conditions (2.71)–(2.73) then become

$$g\,(x, y, 0) = 1\,, \qquad a\,(x, y, 0) = x^2 - y^2,$$

$$u_x(x, y, 0) = \varepsilon_x x\,, \qquad u_y(x, y, 0) = \varepsilon_y y\,, \tag{2.79}$$

where

$$\varepsilon_x = U\,\frac{(\pi\rho_0)^{1/2}}{\mid a_0 \mid}\,, \qquad \varepsilon_y = V\,\frac{(\pi\rho_0)^{1/2}}{\mid a_0 \mid}\,. \tag{2.80}$$

Thus the problem is completely determined by the two dimensionless parameters (2.80) which are similar to the parameter ε in (2.11). As to the choice of the unit of length, Equations (2.76)–(2.78) impose no limitations whatever. So the length unit can be chosen arbitrarily; and both the coordinates x and y, together with all the variables in definition (2.75), can be chosen dimensionless.

Therefore we consider the problem as a *self-similar* one, more exactly, as the self-similar problem of the *first type* (Zel'dovich and Raizer, 1966, 2002, Chapter 12). It means that the set of equations in partial derivatives, (2.76)–(2.78), can be reduced to the set of ordinary differential equations. Let us do it. Substitute in Equations (2.76)–(2.78) the following solution:

$$a\,(x, y, \tau) = a_x(\tau)\,x^2 - a_y(\tau)\,y^2, \tag{2.81}$$

$$g\,(x, y, \tau) = g\,(\tau)\,, \tag{2.82}$$

$$u_x(x, y, \tau) = f_x(\tau)\,x\,, \qquad u_y(x, y, \tau) = f_y(\tau)\,y\,. \tag{2.83}$$

We obtain the following set of five ordinary differential equations for the five unknown functions $a_x(\tau)$, $a_y(\tau)$, $g\,(\tau)$, $f_x(\tau)$ and $f_y(\tau)$:

$$\dot{a}_x + 2a_x f_x = 0\,, \qquad \dot{a}_y + 2a_y f_y = 0\,,$$

$$\dot{g} + (f_x + f_y)\, g = 0\,, \tag{2.84}$$

$$\left(\dot{f}_x + f_x^2\right) g = a_x\,(a_y - a_x)\,, \qquad \left(\dot{f}_y + f_y^2\right) g = a_y\,(a_x - a_y)\,.$$

The dot denotes differentiation with respect to the dimensionless time τ. The initial conditions (2.79) give us the following initial conditions:

$$a_x(0) = 1\,, \qquad a_y(0) = 1\,, \qquad g(0) = 1\,,$$

$$f_x(0) = \varepsilon_x\,, \qquad f_y(0) = \varepsilon_y\,. \tag{2.85}$$

Let us eliminate the functions f_x and f_y from the first two and last equations of the set (2.84). As a result we get the equation

$$\frac{\dot{a}_x}{a_x} + \frac{\dot{a}_y}{a_y} - 2\,\frac{\dot{g}}{g} = 0\,. \tag{2.86}$$

From this, assuming that the functions a_x, a_y and g are not equal to zero and using the initial conditions (2.85), we obtain an integral of the set of ordinary Equations (2.84):

$$g = (a_x a_y)^{1/2}\,. \tag{2.87}$$

Since the initial values of these three functions are positive, the subsequent results will pertain to a time interval τ for which these quantities remain positive.

2.4.2 Magnetic collapse at the zeroth point

To illustrate the behaviour of the solutions (2.81)–(2.83), it is convenient to introduce two functions $\zeta_x(\tau)$ and $\zeta_y(\tau)$ such that

$$a_x = \frac{1}{\zeta_x^2}\,, \qquad a_y = \frac{1}{\zeta_y^2}\,. \tag{2.88}$$

Without loss of generality, we assume that these new functions are positive.

From the first two equations of the set (2.84) and from the integral (2.87) we obtain formulae for the other three unknown functions:

$$f_x = \frac{\dot{\zeta}_x}{\zeta_x}\,, \qquad f_y = \frac{\dot{\zeta}_y}{\zeta_y}\,, \qquad g = \frac{1}{\zeta_x\,\zeta_y}\,. \tag{2.89}$$

The set of five equations (2.84) then reduces to two second-order differential equations for $\zeta_x(\tau)$ and $\zeta_y(\tau)$:

$$\ddot{\zeta}_x = -\zeta_y \left(\frac{1}{\zeta_x^2} - \frac{1}{\zeta_y^2}\right), \qquad \ddot{\zeta}_y = \zeta_x \left(\frac{1}{\zeta_x^2} - \frac{1}{\zeta_y^2}\right), \tag{2.90}$$

with the initial conditions

$$\zeta_x(0) = 1\,, \qquad \zeta_y(0) = 1\,,$$
$$\dot{\zeta_x}(0) = \varepsilon_x\,, \qquad \dot{\zeta_y}(0) = \varepsilon_y\,. \tag{2.91}$$

For definiteness, let $\varepsilon_x > \varepsilon_y$. Then a solution of the problem has a singular point which is reached after a finite time τ_0. When $\tau \to \tau_0$ the quantity ζ_x tends to a finite value $\zeta_x(\tau_0)$, and $\zeta_y(\tau) \to 0$. So we retain in Equations (2.90) only the principal terms:

$$\ddot{\zeta_x} = \frac{1}{\zeta_y}\,, \qquad \ddot{\zeta_y} = -\frac{\zeta_x}{\zeta_y^2}\,. \tag{2.92}$$

In the region $\tau < \tau_0$ of interest to us, the solution of these equation is

$$\zeta_x(\tau) = \zeta_x(\tau_0) + \dots\,,$$
$$\zeta_y(\tau) = \left(\frac{9}{2}\,\zeta_x(\tau_0)\right)^{1/3} (\tau_0 - \tau)^{2/3} + \dots\,. \tag{2.93}$$

Here the terms of higher order of smallness in $(\tau_0 - \tau)$ have been omitted.

Returning to the variables (2.88) and (2.89), we obtain the asymptopic behaviour of the unknown functions near the singularity as $\tau \to \tau_0$:

$$a_x \to a_x(\tau_0)\,, \qquad a_y \to \left(\frac{2}{9}\right)^{2/3} (a_x(\tau_0))^{1/3}\ \frac{1}{(\tau_0 - \tau)^{4/3}}\,,$$
$$f_x \to \varepsilon_x(\tau_0)\,, \qquad f_y \to -\frac{2}{3(\tau_0 - \tau)}\,, \tag{2.94}$$
$$g \to \left(\frac{2}{9}\right)^{1/3} (a_x(\tau_0))^{2/3}\ \frac{1}{(\tau_0 - \tau)^{2/3}}\,.$$

Here the quantities τ_0, $a_x(\tau_0)$, and $\varepsilon_x(\tau_0)$ depend on the initial conditions (2.79) and can be determined by numerical integrating (Imshennik and Syrovatskii, 1967) the complete set of Equations (2.76)–(2.78).

Let us consider the fraction of the plasma that is located within a circle of radius equal to unity (Figure 2.4) at the initial instant $\tau = 0$. The corresponding Lagrange line is the circle

$$a_x(0)\, x^2 + a_y(0)\, y^2 = 1\,.$$

Therefore at any subsequent instant of time this plasma will be located inside the ellipse

$$a_x(\tau)\, x^2 + a_y(\tau)\, y^2 = \frac{x^2}{\zeta_x^2(\tau)} + \frac{y^2}{\zeta_y^2(\tau)} = 1\,, \tag{2.95}$$

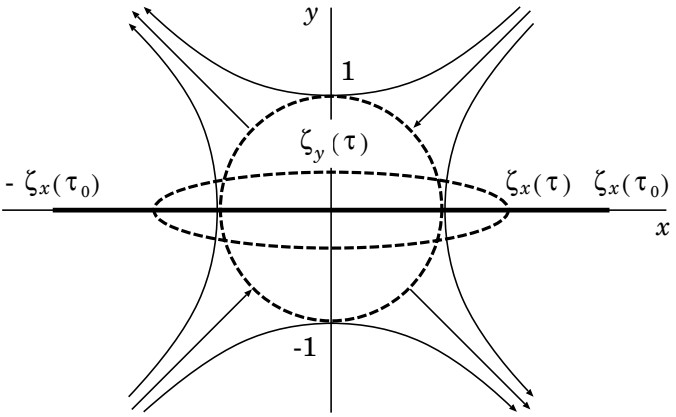

Figure 2.4: Magnetic collapse in the vicinity of a hyperbolic zeroth point.

where $\zeta_x(\tau)$ and $\zeta_y(\tau)$ introduced above have the simple meaning of semi-axes of this deforming ellipse.

As follows from the obtained solution, the semi-axis whose direction corresponds to a smaller initial velocity vanishes at the instant τ_0. At the same time, the second semi-axis remains different from zero and bounded. Thus any initial circle is transformed at the instant τ_0 into a segment of the x axis with the ends $x = \pm\zeta_x(\tau_0)$ as shown in Figure 2.4.

Let us consider the behaviour of the magnetic field (see definitions (2.72) and (2.81)):

$$\mathbf{B} = h_0 \{ -a_y(\tau)\, y,\, -a_x(\tau)\, x,\, 0 \} , \tag{2.96}$$

where $h_0 = 2a_0$ is the gradient of the initial field near the zeroth point. In the limit as $\tau \to \tau_0$ the field is equal to

$$\mathbf{B} = h_0 \left\{ \mp \frac{1}{\zeta_y(\tau)} , -\frac{x}{\zeta_x(\tau)} , 0 \right\} , \tag{2.97}$$

where the minus and plus signs correspond to the regions $y > 0$ and $y < 0$ respectively. Therefore, when $\tau \to \tau_0$, the magnetic field is always tangent to the x axis segment into which the ellipse (2.95) degenerates, increases in magnitude without limit, and experiences a discontinuity on the x axis:

$$B_x(y = +0) - B_x(y = -0) = -\frac{2h_0}{\zeta_y(\tau)} \to \infty . \tag{2.98}$$

The appearance of the discontinuity in the magnetic field corresponds

to an unbounded increase in the density of the electric current:

$$j_z = \frac{c}{4\pi} \, (\operatorname{curl} \mathbf{B})_z = -\frac{c}{4\pi} \, \Delta A \, . \tag{2.99}$$

Substituting (2.81) and (2.88) into (2.99), we calculate the current density

$$j_z(\tau) = \frac{ch_0}{4\pi} \left(\frac{1}{\zeta_y^2(\tau)} - \frac{1}{\zeta_x^2(\tau)} \right) . \tag{2.100}$$

From this and from the solution (2.93) it follows that when $\tau \to \tau_0$ the current density increases like

$$j_z(\tau) \sim \frac{1}{(\tau_0 - \tau)^{4/3}} \, . \tag{2.101}$$

So, when $\tau \to \tau_0$ a kind of *magnetic collapse* occurs. The x component of the magnetic field and the z component of the current density become infinite. The magnetic field is tangential to the x axis everywhere and changes its sign when passing the plane $y = 0$. Therefore

> the magnetic collapse results in the generation of a *neutral* current layer after a finite amount of time.

As we mentioned above, a similar solution for imcompressible plasma was obtained by Chapman and Kendall (1963). In that solution the quantities ζ_x and ζ_y depend exponentially on time τ. Thus the magnetic collapse in an *incompressible* fluid requires an *infinite* amount of time.

In general, it is difficult to determine the exact conditions under which the derived plasma motion can occur. The most difficult question is that of the realization of the assumed initial linear distribution of velocity (2.73). In practice, such a distribution could be realized as a small perturbation of an stationary initial state. One might therefore assume, as was done by Chapman and Kendall, that the entire process has the same character as an ordinary instability. However Imshennik and Syrovatskii showed that

> the plasma flow under consideration – magnetic collapse – is caused by external forces and has a cumulative nature

(as we saw in Section 2.1.4). Syrovatskii (1968) showed that the self-similar solutions obtained in both Chapman and Kendall (1963) and Imshennik and Syrovatskii (1967) can be set in correspondence with exact boundary conditions that have a physical meaning. These conditions are a particular case of the conditions considered in Sections 2.1 and 2.2. They correspond to a change of the potential of the external currents producing the hyperbolic field in accordance with a fully defined law (Syrovatskii, 1968).

2.4.3 From collisional to collisionless reconnection

An essential circumstance in magnetic collapse is that the current density (2.101) increases more rapidly than the plasma density and accordingly the particle density

$$n(\tau) \sim g(\tau) \sim \frac{1}{(\tau_0 - \tau)^{2/3}} \,. \tag{2.102}$$

The specific (per one particle) current density is

$$\frac{j_z}{n} = \frac{ch_0}{4\pi\, n_0} \left(\frac{\zeta_x}{\zeta_y} - \frac{\zeta_y}{\zeta_x} \right), \tag{2.103}$$

where n_0 is the initial plasma density. In the limit as $\tau \to \tau_0$

$$\frac{j_z}{n} = \frac{ch_0}{4\pi\, n_0} \left(\frac{2}{9\, a_x(\tau_0)} \right)^{1/3} \left(\frac{1}{\tau_0 - \tau} \right)^{2/3} . \tag{2.104}$$

So the ratio j_z/n tends to infinity when $\tau \to \tau_0$ within the frame of the solution desribed above. Of course, the solution has no physical meaning near the singularity where a number of quantities increase infinitely.

> When a sufficiently high current density is attained, new effects arise, not accounted from by MHD.

Here they are. First, when the current density

$$j_z \geq \sigma E_{\text{Dr}} \,, \tag{2.105}$$

where E_{Dr} is the Dreicer field, an intense electric runaway of electrons begins and causes current instabilities inside the reconnecting current layer. This process leads to a decrease in an effective conductivity of the plasma inside the current layer (Section 6.3), but still does not impose essential limitations on the applicability of MHD to the description of the macroscopic plasma flows.

If, however,

$$j_z \gg \sigma E_{\text{Dr}} \,, \tag{2.106}$$

direct acceleration of the particles by the strong electric field can set in. This is the case of **dynamic dissipation** of the magnetic field, for example, in solar flares (see the estimations in Section 6.1.1). The particle inertia (usually combined with anomalous resistivity due to wave-particle interactions) replaces the classical resistivity in allowing the magnetic reconnection to occur very quickly and practically without any Coulomb collisions.

Fast collisionless reconnection seems to be often observed in a high-temperature, rarefied cosmic plasma in the presence of a strong magnetic field, for example, in solar flares. At a first sight, to describe the collisionless reconnection process, one may try to use an ordinary resistive MHD with a generalized Ohm's law (see vol. 1, Chapter 11) by simply including the electron inertia:

$$E_z = \sigma_{\rm ef}^{-1}\, j_z + \frac{4\pi}{\left(\omega_{pl}^{(\rm e)}\right)^2}\,\frac{d}{dt}\, j_z\,. \tag{2.107}$$

Here $\sigma_{\rm ef}$ is an anomalous conductivity originated from the wave-particle interaction or the stochasticity of the particle orbits.

The problem will appear soon, however, in such an over-simplified approach because inside actual reconnecting current layers the magnetic field is not equal to zero. This internal (transversal and longitudinal) magnetic field has a strong influence on the particle acceleration by the strong electric field E_z related to the fast collisionless reconnection. This problem will be discussed in Chapter 9.

Chapter 3

Evidence of Reconnection in Solar Flares

The physics of flares on the Sun now becomes 'an étalon' for contemporary astrophysics, in particular for gamma and X-ray astronomy. In contrast to flares on other stars and to many analogous phenomena in the Universe, solar flares are accessible to a broad variety of observational methods to see and investigate the magnetic reconnection process in high-temperature strongly-magnetized plasma of the corona as well as in low-temperature weakly-ionized plasma in the photosphere.

3.1 The role of magnetic fields

3.1.1 Basic questions

Understanding solar flares has been a major goal of astrophysics since frequent observations of solar flares became available in the 1920s. Early studies showed that flares were preferentially associated with strong complicated magnetic fields. Estimates of the energy required to power large flares, together with their association with magnetic fields, led to the conclusion that flares must be electromagnetic in origin. Step by step it bacame more and more clear that a flare is the result of the reconnection of magnetic field lines in the corona.

However there were and still exist three objections to the hypothesis that the energy of a solar flare can be stored in the form of a magnetic field of one or several reconnecting current layers (RCLs).

(1) First, it is claimed that measurements of photospheric magnetic fields do not demonstrate an unambiguous relation between flares and the changes of the magnetic fields. More exactly, the changes in question are those that occur immediately before a flare to creat it. These changes were supposed to be the cause but not the consequence of the flare.

(2) The second objection is related to the time of dissipation of the magnetic field in a volume that would contain the energy necessary for the flare. If this time is estimated in a usual way as the diffusion time in a solar plasma of a finite conductivity, then it is too long compared with the observed duration of the flare.

(3) The third objection is the most crucial one: the observers have never seen real RCLs in solar flares.

For more than four decades, starting from Severny (1964), solar observers have been studying flare-related changes in photospheric magnetic fields, which would provide crucial information as to how an active region stores and releases its energy (see also Lin et al., 1993; Wang, 1999). However the role of photospheric fields is still far from being fully understood and is an area of ongoing research (e.g., Liu et al., 2005; Sudol and Harvey, 2005; Wang et al., 2005). What are the answers on the reconnection theory to the objections mentioned above?

3.1.2 Concept of magnetic reconnection

According to contemporary views, the principal flare process is contingent on the accumulation of the *free magnetic energy* in the corona and chromosphere. At least, this is one of basic concepts (see Chapter 14). By 'free' we mean the **surplus energy above that of a potential magnetic field** having the same sources (sunspots, background fields) in the photosphere. In other words, the free energy is related to the electric currents in the solar atmosphere above the photosphere. The flare correspondes to rapid changes of these currents. So we distinguish between two processes: **(1)** the slow accumulation of flare energy and **(2)** its fast release, a flare.

Let us see these distinctions in the following classical example – the evolution of the quadrupole configuration of sunspots shown in the *two-dimensional* (2D) Figure 3.1. Four sunspots of pairwise opposite polarity are shown: N and S represent a bipolar group of sunspots in an active region, n and s model a new emerging flux. All four sunspots are placed along the axis x placed in the photospheric plane Ph at the bottom of the chromosphere Ch.

As in Figure 1.6, **three consequent states of the potential field** are shown. In Figure 3.1a the field line A_1 is the separatrix line of the initial

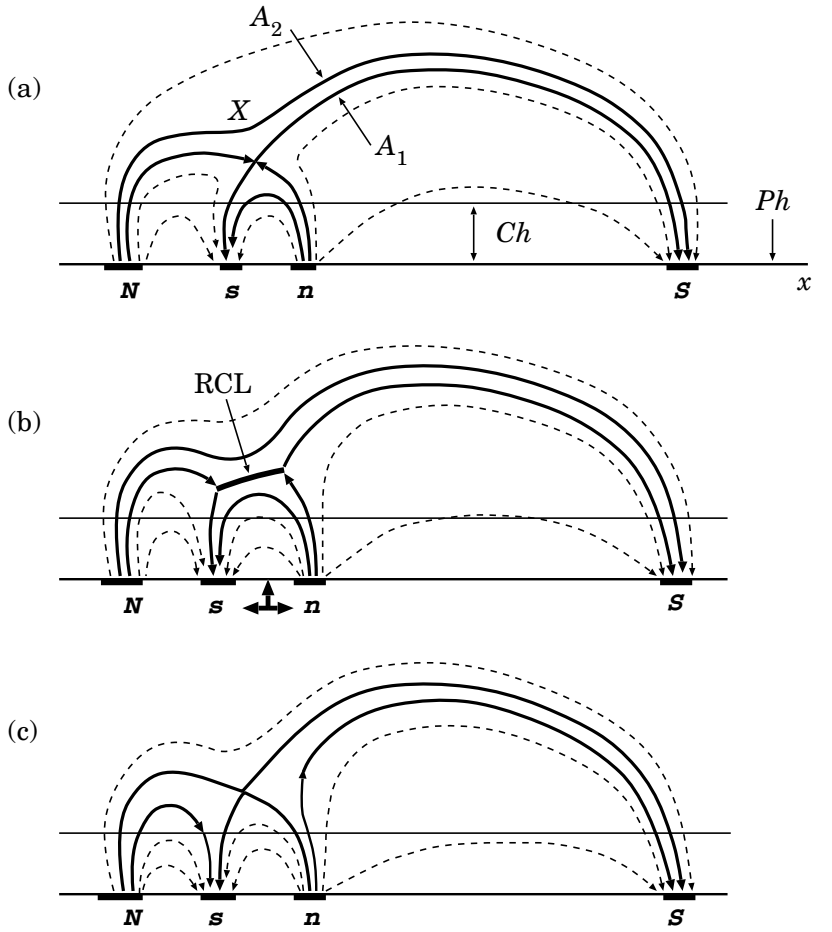

Figure 3.1: The classical 2D cartoon of magnetic reconnection in a solar flare. Three states of the potential field: (a) the initial state, (b) the *pre-reconnection* state, (c) the final state after reconnection.

state (a), this field line will reconnect first; X is the neutral point (line along the z axis) of the potential field at the initial state, here the RCL is created at the state (b). The magnetic field line A_2 is the separatrix of the final state (c) or the last reconnected field line. Therefore $\delta A = A_2 - A_1$ is the reconnected magnetic flux.

In Figure 3.1b three solid arrows under the photosphere show an emergence of the new magnetic flux (the sunspots n and s); the sunspots have been emerged, but the field lines do not start to reconnect.

In general, the redistribution of fluxes appears as a result of the **slow motions and changes of magnetic field sources** in the photosphere. These changes can be either the emergence of a new flux tube from below the photosphere (Figure 3.1) or many other **flows of photospheric plasma**, in particular the *shear flows* – inhomogeneous horizontal flows along the neutral line of the photospheric magnetic field. For this reason,

> an actual reconnection of magnetic fields in the solar atmosphere is always a three-dimensional process

(see next Section). Sometimes the 2D problems still give a simple illustration of an effect, for example, the formation and dissipation of the RCL at the X point under action of the photospheric shear (Kusano and Nishikawa, 1996; Karpen et al., 1998), see also Sections 14.3 and 14.4. The term '2.5-dimensional' frequently refers to such 2D MHD problems (in two spatial variables x and y) to point out the presence of the longitudinal field B_z related to the shear flow.

3.1.3 Some results of observations

Let us come back to the first objection **(1)** in Section 3.1.1 to the reconnection theory of solar flares. According to the theory, the free magnetic energy is related to the electric current J inside the RCL. The flare corresponds to rapid changes of this current. It is clear, however, that the magnetic flux through the photospheric plane Ph (Figure 3.1) can change only little over the whole area of a flare during this process, except in some particular places, for example, between close sunspots N and s.

It means that sunspots and other magnetic features in the photosphere are weakly affected by the occurrence of a flare because the plasma in the photosphere is almost 10^9 times denser than the plasma in the corona where the flare originates. Therefore it is difficult (but still possible) for disturbances in the tenuous corona and upper chromosphere to affect the extremely massive plasma in the photosphere. Only small MHD perturbations penetrate into the photosphere.

The same is true in particular for the vertical component of the magnetic field, which is usually measured. Therefore

> in the first approximation, the photospheric magnetic field changes a little during the solar flare over its whole area.

As a consequence, it is not surprising that after a flare the large-scale structure in the corona can remain free of noticeable changes, because it is determined essentially by the potential part of the magnetic field above the photospheric sources. More exactly, even being disrupted, the large-scale structure will come to the potential field configuration corresponding to the post-flare position of the photospheric sources (see discussion in Section 14.5.1).

On the other hand, in the Bastille day flare on 2000 July 14 (see Chapters 4 and 5) as well as in some other large solar flares, it was possible to detect the real changes in the sunspot structure just after a flare. The outer penumber fields became more vertical due to magnetic reconnection in the corona (Liu et al., 2005; Wang et al., 2005). One can easily imagine such changes by considering, for example, Figure 3.1 between sunspots N and s.

Sudol and Harvey (2005) have used the Global Oscillation Network Group (GONG) magnetograms to characterize the changes in the photospheric vertical component of magnetic field during 15 large solar flares. An abrupt, significant, and persistent change in the magnetic field occured in at least one location within the flaring active region during each event after its start. Among several possible interpretations for these observations, Sudoh and Harvey favour one in which the magnetic field changes result from the penumber field relaxing upward by reconnecting magnetic field above the photoshere. This interpretation is very similar to than one given by Liu et al. (2005) and Wang et al. (2005).

As for the second objection **(2)** to the hypothesis of accumulation of energy in the form of magnetic field of slowly-reconnecting current layers in the solar atmosphere, the rapid dissipation of the field necessary for the flare is naturally explained by the theory of current layers presented in what follows, especially in Chapters 6 and 7).

3.2 Three-dimensional reconnection in flares

3.2.1 Topological model of an active region

Gorbachev and Somov (1989, 1990) have developed a three-dimensional model for a potential field in the active region AR 2776 with an extended flare of 1980 November 5. Before discussing the flare, let us consider, at

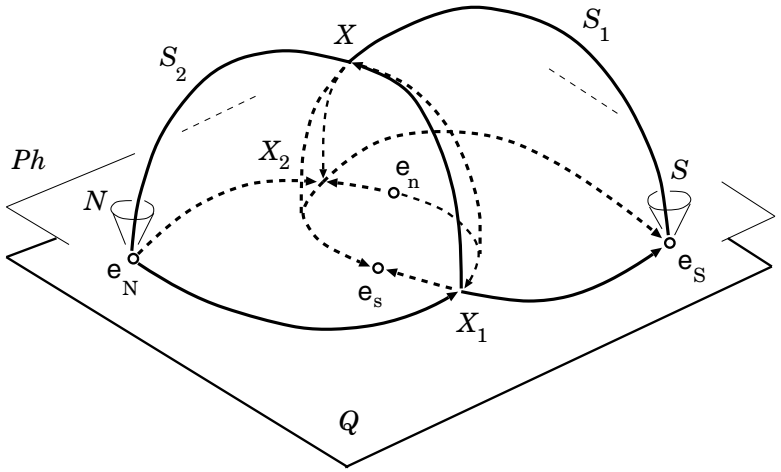

Figure 3.2: The model for the magnetic field of four sunspots of pairwise opposite polarity. The sunspots N and S in the photospheric plane Ph. The separatrices S_1 and S_2 cross at the separator X_1XX_2 above the plane Q of the effective magnetic 'charges' $e_{\rm N}$, $e_{\rm S}$, etc.

first, the general properties of this model called *topological*. Four magnetic field sources – the magnetic 'charges' $e_{\rm N}$ and $e_{\rm S}$, $e_{\rm n}$ and $e_{\rm s}$, located in the plane Q under the photosphere Ph (Figure 3.2) – are used to reproduce the main features of the observed field in the photosphere related to the four most important sunspots: N, S, n and s. As a consequence, the model reproduces only the large-scale features of the actual field in the corona related to these sunspots.

The features are two magnetic surfaces, the boundary surfaces called the *separatrices* S_1 and S_2 (Figure 3.2), that divide the whole space above the under-photospheric plane Q into four regions and, correspondingly, the whole field into four magnetic fluxes having different linkages. The field lines are grouped into four regions according to their termini. The separatrices of the potential magnetic field are formed from field lines beginning or ending at magnetic zeroth points X_1 and X_2 rather than the magnetic charges, of course. The field lines originating at the point X_1 form a separatrix surface S_1 (for more detail see Gorbachev et al., 1988).

There is a topologically singular field line X_1XX_2 lying at the intersection of the two separatrices, it belongs to all four fluxes that interact at this line – the 3D magnetic *separator*. So **the separator separates the interacting magnetic fluxes by the separatrices** (see also Sweet, 1969,

Lau, 1993).

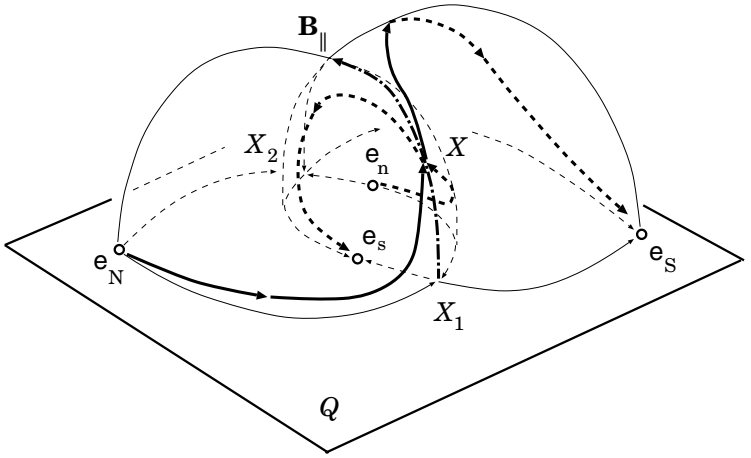

Figure 3.3: The same model for the magnetic field. The field lines located at the separatrices and connected to the separator due to the reconnection process at the point X, the vector $\mathbf{B}_{\parallel}$ is the longitudinal component of a magnetic field.

The potential field model does not include any currents and so cannot model the energy stored in the fields and released in the flares. Therefore here we introduce some currents and energetics to a flare model. The linkage of real field lines connected to the separator is shown in Figure 3.3. This Figure does not mean, of course, that we assume the existance of real magnetic charges under the photosphere as well as the real X-type zeroth points X_1 and X_2 in the plane Q which does not exist either. We only assume that above the photospheric plane the large-scale magnetic field can be described in terms of such a model. We also assume that the actual conditions for reconnection are better at some point X of the separator rather than at its other points. If the magnetic sources move or/and change, the field also changes.

> It is across the separator that the magnetic fluxes are redistributed and reconnected so that the magnetic field could remain potential, if there were no plasma.

In the presence of the solar plasma of low resistivity, the separator plays the same role as the hyperbolic neutral line of magnetic field, familiar from 2D MHD problems (see Syrovatskii, 1966a; Sweet, 1969; Brushlinskii et al., 1980; Biskamp, 1986 and 1997). In particular, as soon as the separator

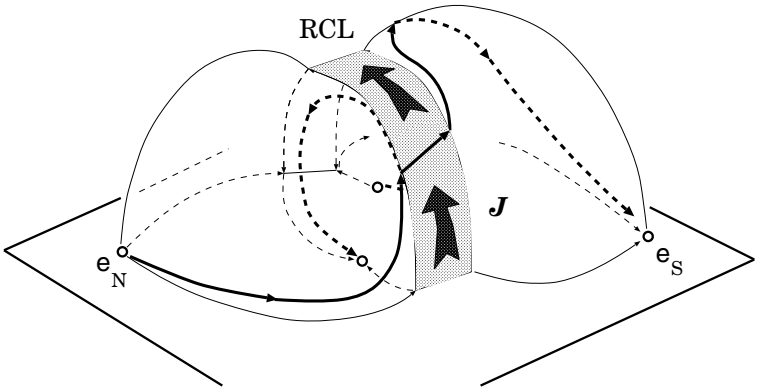

Figure 3.4: The current layer RCL with a total current J at the separator.

appears, the electric field $\mathbf{E}_0$ induced by the varying magnetic field produces an electric current $\mathbf{J}$ along the separator. The current interacts with the potential magnetic field in such a way (Section 1.1.3) that the current assumes the shape of a **thin wide current layer** (see RCL in Figure 3.4).

> In the high-conductivity plasma the current layer hinders the redistribution of the magnetic fluxes.

This results in an energy being stored in the form of magnetic energy of a current layer – the *free* magnetic energy.

Therefore the model assumes that the slowly-reconnecting current layer appears at the separator (Syrovatskii, 1981; Gorbachev and Somov, 1989; Longcope and Cowley, 1996) in a pre-flare stage. If for some reason (see Somov, 1992) the reconnection process becomes fast, then the *free* magnetic energy is rapidly converted into kinetic energy of particles. This is a *flare*. The rapidly-reconnecting current layer, being in a high-temperature turbulent-current state (Section 6.3), provides the flare energy fluxes along the reconnected field lines.

* * *

It is important for what follows in Chapters 9, 11, and 14 that

> actual 3D reconnection at the separator proceeds in the presence of an increasing (or decreasing) longitudinal magnetic field $\mathbf{B}_\parallel$

(Figure 3.3), which is parallel to the electric current $\mathbf{J}$ inside the RCL (Figure 3.4). What factors do determine the increase (or decrease) of the longitudinal field? – The first of them is the global field configuration, i.e.

the relative position of the magnetic field sources in an active region. It determines the position of the separator and the value of the longitudinal field at the separator and in its vicinity. This field is not uniform, of course, near the separator.

The second factor is the evolution of the global magnetic configuration, more exactly, the electric field $\mathbf{E}_0$ related to the evolution and responsible for driven reconnection at the separator. The direction of reconnection – with an increase (or decrease) of the longitudinal magnetic field – depends on the sign of the electric field projection on the separator, i.e. on the sign of the scalar product $(\mathbf{E}_0 \cdot \mathbf{B}_\parallel)$. In general, this sign can be plus or minus with equal probabilities, if there are no preferential configurations of the global field or no preferential directions of the active region evolution. This statement as well as the whole model must be examined by future observations and their analysis.

3.2.2 Topological portrait of an active region

Because the topological model uses a minimal number of magnetic sources – four, which is necessary to describe the minimal number of interacting magnetic fluxes – two, we call it the *quadrupole-type* model. This label is not an exact definition (because in general $e_{\mathrm{N}} \neq -e_{\mathrm{S}}$ and $e_{\mathrm{n}} \neq -e_{\mathrm{s}}$) but it is convenient for people who know well the *exact-quadrupole* model by Sweet (1969). In fact, the difference – the presence of another separator in the model by Gorbachev and Somov – is not small and can be significant for actual active regions on the Sun. The second separator may be important to give accelerated particles a way to escape out of an active region in interplanetary space.

Figure 3.5 shows the topologically important magnetic-field lines in the plane (x', y') which is the plane Q of the effective sources e_1, e_2, e_3, and e_4. They reproduce the large-scale features of the observed magnetic field in the photosphere related to the four largest sunspots in the active region AR 2776 where the extended 1B/M4 flare of 1980 November 5 was observed by the SMM satellite. Positions and magnitudes of the sources are adjusted to fit the main topological features of the magnetogram (see Figures 1 and 3 in Gorbachev and Somov, 1989).

The field lines shown in Figure 3.5 play the role of separatrices (cf. Figure 3.2) and show the **presence of two separators** in the active region. Two zeroth points X_1 and X_2 are located in the vicinity of the magnetic sources and are connected by the first separator shown by its projection, the thin dasched line L_1. Near this separator, the field and its gradient are strong and determine the flare activity of the region. Another separator starts from the zeroth point X_3 far away from the magnetic sources and

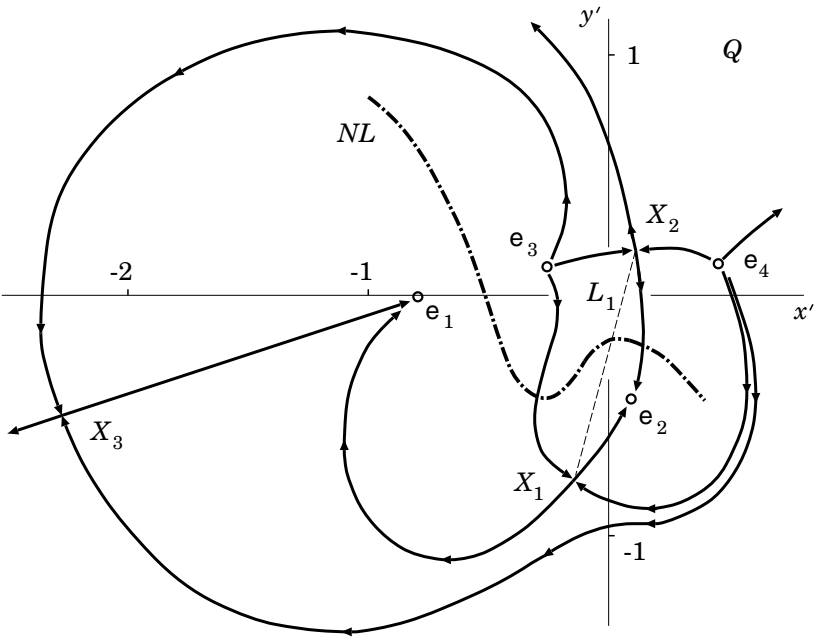

Figure 3.5: The topological portrait of the active region AR 2776 where the solar flare of 1980 November 5 occurred.

goes much higher above the active region. The second separator can be responsible for flares in weaker magnetic fields and smaller gradients high in the corona.

Let us suppose that a part of the flare energy is initially released in some compact region $\mathcal{E}$ near the apex of the main separator X_1X_2. Then energy fluxes F_ε will propagate *along* the field lines connecting the energy source with the photosphere. Projections of the energy source $\mathcal{E}$ on the photospheric plane Ph along the field lines are shown as two 'flare ribbons' FR_1 and FR_2 in Figure 3.6. Therefore we identify flare brightenings, in the hydrogen $H\alpha$ line as well as in EUV and hard X-rays, with the ribbons located at the intersection of the separatrices with the chromosphere which is placed slightly above the photospheric plane (x, y).

The characteristic *saddle* structure of the field in the vicinity of the reconnecting point X at the separator (cf. vol. 1, Figure 14.1) leads to a spatial redistribution of the energy flux F_ε of heat and accelerated particles. This flux is efficiently split apart in such a way that it creates the observed long-narrow Hα ribbons in the chromosphere (see FR_1 and FR_2

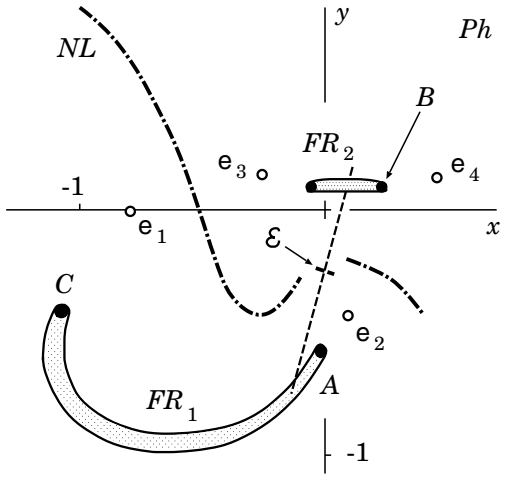

Figure 3.6: The flare ribbons at both sides of the photospheric neutral line NL in the flare of 1980 November 5.

in Figure 3.7).

For the first time, the model by Gorbachev and Somov (1989, 1990) had reproduced the observed features of the M4/1B flare of 1980 November 5. In particular, the model predicts the simultaneous flaring of the two chromospheric ribbons. Moreover it predicts that a concentration of the field lines that bring energy into the ribbons in the chromosphere is higher at the edges of the ribbons, i.e. at relatively compact regions indicated as A, B, and C. Here the Hα brightenings must be especially bright. This prediction of the model is consistent with observations of Hα 'kernels' in this flare.

3.2.3 Features of the flare topological model

The topological model also predicts another signature of flares. Since in the Hα kernels the flare energy fluxes are more concentrated, the impulsive heating of the chromosphere must create a fast expansion of high-temperature plasma upwards into the corona (see Somov, 1992). This effect is known as the chromospheric 'evaporation' observed in the EUV and soft X-ray (SXR) emission of solar flares. Evaporation lights up the SXR coronal loops in flares.

Moreover the topological model shows that the two flare ribbons as well as the four of their edges with Hα kernels are magnetically connected to the common region of energy release at the separator (see $\mathcal{E}$ in Figure 3.7). Note that Figure 3.7 demonstrates only the field lines connected to one of the ribbons. Through the same region all four Hα kernels are magnetically

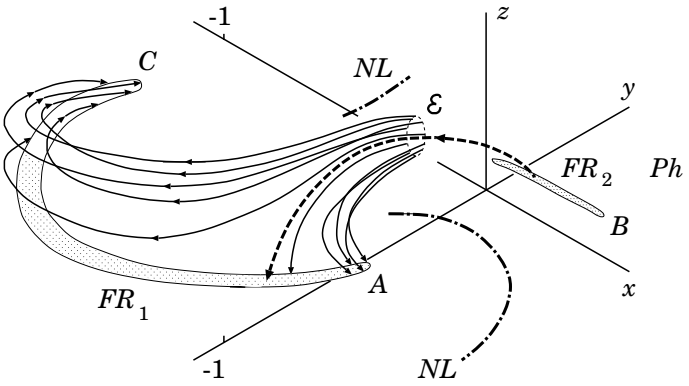

Figure 3.7: A picture of potential field lines crossing the region of primary energy release $\mathcal{E}$, which is situated at the apex of the main separator (boldface dashed curve). The flare ribbons are formed where these field lines cross the photosphere (plane $z = 0$).

connected to one another. Therefore the SXR loops look like they are crossing or touching each other somewhere in the region of energy release as shown in Figure 3.8 from Somov et al. (2001, 2002b).

So the quadrupole-type model predicts that the reconnecting magnetic fluxes are distributed in the corona in such a way that the **two SXR loops may look like that they interact with each other**. That is why the SXR observations demonstrating such structures are usually considered as direct evidence in favour of the model of two interacting loops (Sakai and de Jager, 1996). The difference, however, exists in the primary source of energy. High concentrations of electric currents and twisted magnetic fields are created inside the interacting loops by some under-photospheric mechanism. If these currents are mostly parallel they attract each other giving an energy to a flare (Gold and Hoyle, 1960). On the contrary, according to the topological model, the flare energy comes from an interaction of magnetic fluxes that can be mostly potential.

Note that the **S-shaped structures**, when they are observed in SXRs (e.g., Figure 2 in Pevtsov et al., 1996) or in hydrogen Hα-line, are usually interpreted in favour of non-potential fields. In general, the shapes of coronal loops are signature of the helicity (Section 12.1) of their magnetic fields. The S-shaped loops match flux tubes of positive helicity, and inverse S-shaped loops match flux tubes of negative helicity (Pevtsov et al., 1996). As we see in Figure 3.8, the S-shaped structure $C\mathcal{E}B$ connecting the bright

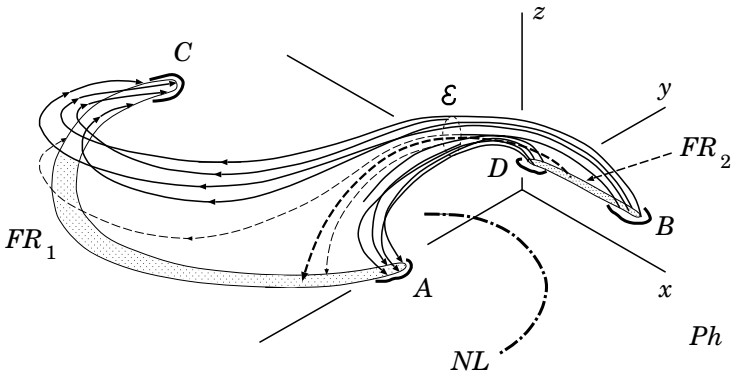

Figure 3.8: Field lines that connect the Hα kernels A, B, C, and D. Chromospheric evaporation creates a picture of the crossing SXR loops predicted by the topological model for a flare in an active region with the quadrupole-type configuration of magnetic sources in the photosphere.

points C and B results from the computations of the potential field in the frame of the topological model.

Not surprisingly, the potential field produced by four sources may be even more complicated and may look as a strongly non-potential field. Severely **kinked Ω-type loops**, sometimes connecting two active regions, might be understood in terms of a simple topological model, see Figure 8 in Pevtsov and Longcope (1998).

In the active region AR 2776 where the flare of 1980 November 5 was observed, Den and Somov (1989) had found a considerable **shear of a potential field** above the photospheric neutral line near the region of the brightest flare loop AB. Many authors concluded that an initial energy of flares is stored in magnetic fields with large shear. However, such flares presumably were not the case of potential field having a minimum energy. This means that the presence of magnetic shear is not a sufficient condition for generation of a large flare in an active region.

The topological model by Gorbachev and Somov postulated a global topology for an active region consisting of four fluxes. Reconnection between, for example, the upper and lower fluxes transfers a part of the magnetic flux to the two side systems. Antiochos (1998) addresses the following question: 'What is the minimum complexity needed in the magnetic field of an active region so that a similar process can occur in a fully three-dimensional geometry?' He starts with a highly sheared field near the photospheric neutral line held down by an overlying unsheared field. Anti-

ochos concludes that a real active region can have much more complexity than very simple configurations. We expect that

> the topology of four-flux systems meeting along a coronal separator is the basic topology underlying eruptive activity of the Sun.

It is unlikely that more than four fluxes would share a common boundary, a separator. This four-flux topology is precisely what is needed for a flare to occur.

On the other hand, magnetic configurations with more separators would have more opportunity to reconnect and would thus more likely to produce flares. Such complicated configuration would presumably produce many small flares to release a large excess of magnetic energy in an active region rather than one large flare.

It is also clear that, in order to accomplish different aims of topological modeling, different methods have to be used. In general, it is not a simple task to implement one or another topological model for a time series of vector magnetograms, paying particular attention to distinguishing real evolution of the photospheric magnetic fluxes from changes due to variations in atmospheric seeing, as well as uncorrelated noise. Barnes et al. (2005) investigated the reliability of one of such methods and have estimated the uncertainties in its results.

3.2.4 The S-like morphology and eruptive activity

The appearance of separators in the solar atmosphere was initially attributed to the emergence of a new magnetic flux from the photosphere in the region where a magnetic flux already exists as illustrated by Figure 3.1. In fact, the presence of separators must be viewed as a much more general phenomenon. Figure 3.9a taken from Somov (1985) exhibits the simplest model of the uniform distribution of the vertical component B_z of the magnetic field in the photosphere. The neutral line NL divides the region of the field source along the y axis. In accordance with the fact that it is often visible in solar magnetograms, this region is deformed by photospheric flows with velocity $\mathbf{v}$ in such a way that the neutral line gradually acquires the S-shape as shown in Figure 3.9b.

At first glance it seems that the magnetic field with such simple sources cannot in principle have any topological peculiarities. However this is not so. Beginning with some critical bending of the neutral line, the field calculated in the potential approximation contains a separator as shown in Figure 3.10 (Somov, 1985, 1986). In this figure, the separator X is located above the photospheric NL like a *rainbow* above a river which makes a bend. The separator is nearly parallel to the NL in its central part. The

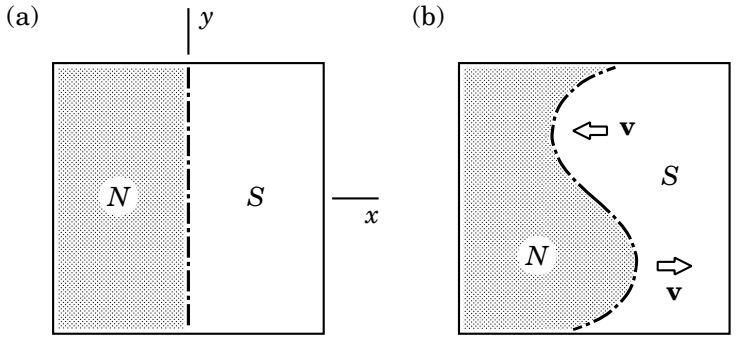

Figure 3.9: Model distribution of the vertical component of the magnetic field in the photosphere. A vortex flow distorts the photospheric neutral line so that it takes the shape of a letter S.

potential field lines just above the NL are orthogonal to it. This is important to make the simplest 2D models.

By using the topological model, Gorbachev and Somov (1988) demonstrated the appearance and growth of the separator as a result of photospheric vortex flows in the locality of the photospheric neutral line. They showed that the vortex flows or any other photospheric magnetic field changes, creating the S-shape of the neutral line, produce a special topological structure in the field above the photosphere. The peculiarity of this structure is the separator.

The topological 'rainbow reconnection' model explains some reliably established properties of two-ribbon flares.

First,

> the rainbow reconnection model reveals a connection of large solar flares with the S-shaped bend of photospheric neutral line.

It shows that the neutral line bend must be greater than some critical value. Then it leads to appearance of the separator above the photosphere. So that a necessary condition for magnetic reconnection in the solar atmosphere is satiesfied.

Second, the model explains the bipolar picture of a flare: its development simultaneously in regions of different photospheric magnetic field polarities. Moreover it naturally explains the arrangement and shape of the flare ribbons in the chromosphere, the structure observed in X-ray bands like two intersecting loops, and the early appearance of bright flare kernels on the flare ribbon ends.

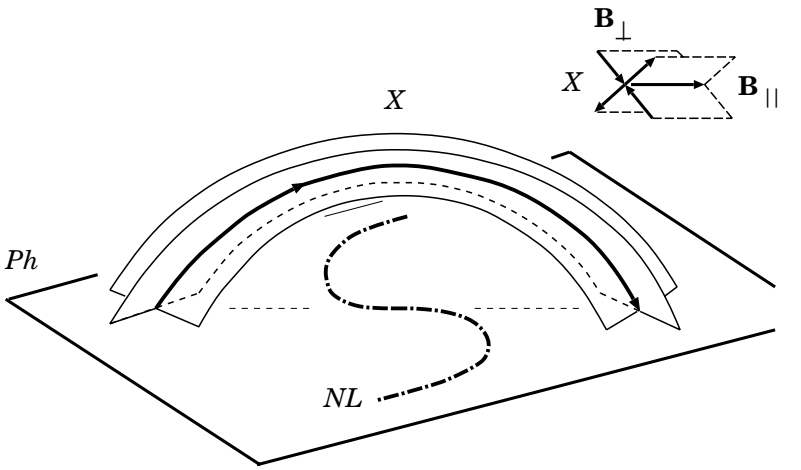

Figure 3.10: The 'rainbow reconnection' model: the separator X above the S-shaped bend of the photospheric neutral line NL. The inset in the upper right-hand corner shows the structure of the magnetic field near the top of the separator.

As viewed in SXRs, the coronal part of active regions consists of discrete bright loops. These loops often collectively form **sinuous S shapes** similar to that one which we saw in Section 3.2.3 (see also Acton et al., 1992). This shape has been named 'sigmoidal' by Rust and Kumar (1996) who studied the characteristic of such brightenings in SXRs and found that they are typically evolve from a bright, sharp-edges sigmoidal features into either an arcade of loops or a diffuse cloud. We can expect that such transient arcades of loops (loop prominence systems) and long-duration events (LDEs) are related to coronal mass ejections (CMEs).

Using the *Yohkoh* SXR images, Hudson et al. (1998) considered the implications of this scenario in the context of 'halo' CMEs. These may correspond to events near the solar disk center. Incorporating data from the SOHO Large Angle Spectroscopic Coronagraph (LASCO), this survey found the 'sigmoid-to-arcade' development a common feature of active regions associated with the onset of a halo CME.

Canfield et al. (1999), Glover et al. (2000) performed a similar study incorporating a much wider range of data and observations over an increased range in wavelength. A high proportion of active regions were reviewed with the intention of clarifying which SXR features possess the highest probability of eruption. The results suggest a strong relationship between

an overall S-like morphology and the potential of an active region to erupt.

We assume that

> the S-like SXR morphology results from the reconnection process in a high-temperature current layer located at the separator of a quadrupole-type magnetic field of an active region

as was illustrated in Figure 3.8. Since a pre-event sigmoid disappears leaving a SXR arcade and two 'transient coronal holes' (Sterling and Hudson, 1997), opening a closed configuration (see Syrovatskii and Somov, 1980; Syrovatskii, 1982) seems to be an important element of the CME onset, which drives reconnection at the separator.

3.3 A current layer as the source of energy

3.3.1 Pre-flare accumulation of energy

Potential field has no free energy. Given common and obvious assumptions, the free energy in the quadrupole-type model described above is simply the magnetic energy of the total electric current J in the reconnecting current layer (RCL) in the solar atmosphere (Figure 3.4):

$$\mathcal{E}_f = \frac{1}{2c^2}\, LJ^2. \tag{3.1}$$

Here

$$L \approx 2l\, \ln \frac{2l}{b} \tag{3.2}$$

is the *self-inductance* of the current layer, l is the distance taken along the separator from the zeroth point X_1 to the point X_2 in Figure 3.3, and b is the half-width of the layer.

Since we know the physical properties of a pre-flare current layer (see Section 6.1.2), we estimate the total current inside the layer as well as its free magnetic energy (Syrovatskii, 1976b, 1981), the energy of a flare.

If we did not know the properties of the pre-flare reconnection process, we should have considered as an open question the following one. Why can the considerable excess energy be accumulated in the coronal magnetic field during the pre-flare stage without contradicting the natural tendency that lower energy states are more favourable? – We should look for an answer to this question, for example, in a *bifurcation* structure of force-free fields in the corona (e.g., Kusano and Nishikawa, 1996). However we may continue our consideration of the pre-flare stage as the creation and existence of the slowly-reconnecting current layer. In this way, we see that

slowly-reconnecting current layers in the solar atmosphere can store the magnetic energy $\mathcal{E}_f$ necessary for flares.

Moreover in a quasi-stationary case (e.g., in the pre-flare state) their output can account for the energetics of the whole active region (Somov and Syrovatskii, 1977; Den and Somov, 1989). We may call such a state the **minimum current corona**.

Note that from (3.1) a simple formula follows for the total current J necessary for a solar flare to release the energy $\mathcal{E}_f$:

$$J = c\left(\frac{2\mathcal{E}_f}{L}\right)^{1/2} \approx (1-6)\times 10^{11}\ \text{Ampere}\,. \tag{3.3}$$

In this estimate the length l is set equal to the characteristic size of a large active region, $l \approx 10^{10}$ cm, and the flare energy to $\mathcal{E}_f \approx (1-3)\times 10^{32}$ erg. The result agrees with the estimates of the total electric current based on measurements of the magnetic field components in the photospheric plane (Moreton and Severny, 1968).

The vector magnetographs determine the transversal field at lower atmospheric levels; the curl of this field yields the vertical current density (Gopasyuk, 1990; Zhang, 1995; Wang et al., 1996). Distributions of the intensity of the vertical current inferred from the horizontal magnetic field evolve only gradually and demonstrate two possibilities. One is the emergence of a new electric current from the sub-photosphere. The other is the rearrangement of the current systems in the solar atmosphere.

3.3.2 Flare energy release

The reconnecting current layers in the pre-flare state can suffer many instabilities: thermal instability caused by radiative energy losses (Field, 1965), resistive instability caused by temperature dependence of plasma conductivity, two-steam instabilities of various types, structural instability (Chapter 10), tearing instability (Chapter 11) etc. It is assumed that, as a result of one of these instabilities, the magnetic energy of the RCL is rapidly released and a flare starts. For example, a flare occurs when the current carried on a separator exceeds some threshold.

At present there are several open questions related to these instabilities: what is the relative importance of each of them, which of them can develop first, and whether an external action upon the current layer is necessary or whether the layer gradually evolves towards an unstable equilibrium or a non-equilibrium state by itself. Some attempts to answer these questions using relatively simple models will be demonstrated in what follows. In general, however, answers to these questions depend on the internal structure

of the RCL. In its turn this structure depends on the initial and boundary conditions, and on the current layer evolution during previous stages.

Therefore the investigation of RCL dynamics is important for cosmic plasma physics. This investigation must include the formation stage, the pre-flare evolution, and the rapid realignment (rupture of the current layer) with transition to a new state characterized by high temperatures and high resistivity (Chapter 6).

In the process of solving this problem many numerical (Brushlinskii et al., 1980; Antiochos et al., 1996) and laboratory (Altyntsev et al., 1977; Stenzel and Gekelman, 1984; Bogdanov et al., 1986, 2000) experiments have been performed. The hydrodynamic stage of the rise and evolution of pre-flare current layers has been studied in detail. Experiments have shown that a thin, extended current layer can be formed, even in laboratory conditions. To some approximation it has been possible to study the structures of the magnetic field inside the layer and in the ambient plasma, to find the current distribution, the electron density and other plasma parameters.

> The laboratory experiments have demonstrated the possibility of a substantial accumulation of free magnetic energy and the explosive disruption of the thin wide reconnecting current layer.

The cause of such disruption, which is accompanied by fast reconnection, may be a local resistivity increase related to the development of plasma turbulence.

Future experiments will probably, more than hitherto, concentrate on the study of the conditions for current layer disruption, of nonlinear interactions in the fast reconnection region, and of particle acceleration (see Chapter 9). This would help us to solve the most difficult problem in the reconnection theory and, in particular, give us information necessary to investigate experimentally the characteristics of current layers as the source of flare energy during the impulsive phase.

The disruptive stage of the evolution cannot be described in hydrodynamic terms only: it requires a kinetic description in the disruption region. The impulsive electric field induced there efficiently accelerates charged particles (Somov and Syrovatskii, 1975). During this process, plasma turbulence is generated. Its intensity depends on the fast particle flux and governs plasma resistivity, reconnection rate, and, as a consequence, the electric field intensity. There is thus a nonlinear feedback. Of course, to solve such a self-consistent problem is not easy. We shall, however, bear two limiting cases in mind.

First, low-energy particles interact effectively with the plasma, and most of their energy is rapidly lost by heating the plasma to very high temperatures, the so-called 'super-hot' plasma. Second, in the high-energy region, a

part of the accelerated particles enters into the *electric runaway* regime (see vol. 1, Section 8.4.2). i.e. it virtually ceases to interact with the plasma.

3.3.3 The RCL as a part of an electric circuit

We have not discussed yet another problem of the theory of reconnecting current layers as a source of energy for solar flares. This problem has been nicely called *global electrodynamic coupling* (Spicer, 1982; Kan et al., 1983) and it essentially consists in the question about the role of inductance and resistance in an equivalent electric circuit one of whose components is a current layer in the solar atmosphere. In its simplest form (Baum et al., 1978), the corresponding task can be illustrated by the elementary equation

$$L\,\frac{d}{dt}\,J(t) + J(t)R_{_0} = V(t)\,. \tag{3.4}$$

Here $V = V(t)$ is the external *electromotive force* (emf) due to variations of photospheric magnetic fields, or simply the potential difference between the points X_1 and X_2 at the ends of the separator in Figure 3.2. The unknown quantity V depends on the strength of the photospheric sources and in the simplest approach it is treated as a given function of time.

Let us assume that at the initial moment $t = 0$, the current $J(0)$ along the separator was zero. At this point the external emf $V(0)$ was completely used up by acting against the self-induction emf:

$$L\,\frac{dJ}{dt} + 0 = V(0)\,. \tag{3.5}$$

So the current $J(t)$ will appear.

As soon as a nonzero current $J(t)$ appears, the voltage drop on the total separator resistance $R_{_0}$, according to Equation (3.4), makes the rate of current increase dJ/dt in the circuit smaller, which amounts to decreasing the rate of magnetic energy accumulation prior to a flare. The final steady current J_s depends on the resistance $R_{_0}$ and the external emf V:

$$J_s = \frac{V}{R_{_0}}\,. \tag{3.6}$$

The characteristic time of the process is proportinal to the self-inductance L:

$$\tau_a = \frac{L}{R_{_0}}\,. \tag{3.7}$$

Note that $L \sim l$ and $R_{_0} \sim \sigma^{-1} l$. Therefore $\tau_a \sim \sigma$ does not depend of the length scale l.

The maximum accumulated energy (3.1) is also proportional to the inductance L of the equivalent circuit comprising the separator current layer:

$$\mathcal{E}_f = \frac{1}{2c^2}\,\frac{LV^2}{R_0^2}\,. \tag{3.8}$$

It is important that the free magnetic energy $\mathcal{E}_f$ and the energy accumulation time τ_a depend also on the total resistance R_0. In the pre-flare state, the RCL with low Coulomb resistivity has low resistance. For this reason, the accumulated energy can be sufficiently large. The accumulation time is long enough: $\tau_a \sim 3 \times 10^4$ s (Syrovatskii, 1976b).

Schrijver et al. (2005) compared *TRACE* EUV images of 95 active regions and potential-field source-surface extrapolations based on *SOHO* MDI magnetograms. It appears that the electric currents associated with coronal nonpotentiality have a characteristic timescale $\tau_{obs} \sim 10 - 30$ hr. Thus the flare-energy accumulation time $\tau_a \sim \tau_{obs}$.

TRACE observations of an emerging active region in the vicinity of an existing active region have been used by Longcope et al. (2005) in order to quantify magnetic reconnection between two active regions. Comparison of the observed EUV loops with the magnetic field lines computed in a topological model (for more detail see Section 3.4.4) revealed that the interconnecting EUV loops are consistent with those produced by reconnection at a separator overlying the volume between the active regions. The net energy released is consistent with the amount that could be stored magnetically during the 24 hr delay between emergence and reconnection.

From what we have seen it is evident that

> to release the accumulated energy in a time $\tau_f \approx 10^2 - 10^3$ s corresponding to the solar flare duration, the total current layer resistance must be increased by 2 to 3 orders of magnitude.

Such an effect can be well the result of the appearance of plasma turbulence (Section 6.3). An alternative possibility (see Chapter 14) is an appearance of one or many local current disruptions which have large enough resistance, *electric double layers*.

Earlier the possibility of formation of the double layers was, for some reason, treated as being alternative or even more in conflict with the concept of reconnection. However, after the laboratory experiment by Stenzel and Gekelman (1984), it became clear that double layers may form inside the RCL. The hypothesis of the formation of electric double layers inside the separator-related RCL can prove useful for the explanation of the extremely rapid energy release observed sometimes during solar flares. However, the concept of collisionless reconnection seems to be a more natural and more realistic alternative.

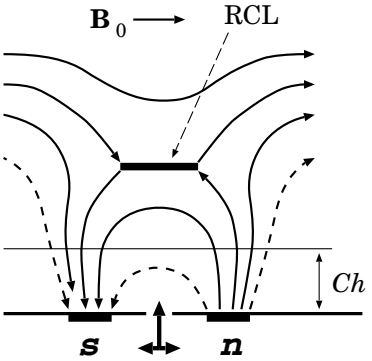

Figure 3.11: The Syrovatsky model of a solar flare. n and s represent a bipolar source of a new emerging flux in the chromosphere Ch. The uniform field $\mathbf{B}_0$ models a large-scale magnetic field in the corona. RCL is a reconnecting current layer between the interacting magnetic fluxes.

3.4 Reconnection in action

3.4.1 Solar flares of the Syrovatsky type

Much of the activity in the solar corona is related to the emergence of magnetic flux from the solar interior. Flux emergence episodes are continually injecting magnetic fields into the solar atmosphere over a wide range of length- and timescales, from small magnetic elements on a granular size all the way up to the emergence of large active regions.

Emerging active regions interact with preexisting magnetic systems by establishing magnetic links to them, well visible in image series taken by the *TRACE* satellite. They also cause the ejection of fast, high-temperature flows often seen, for example, with the soft X-ray telescope (SXT) on board the *Yohkoh* satellite.

> Observed changes of connectivity and high-temperature jet emission clearly point to reconnection of magnetic field lines

as being effective whenever an upcoming and a preexisting magnetic flux system meet in the corona in spite of the low resistivity of the coronal plasma.

It is essential to understand how the magnetic field emerged from the solar interior interacts with the overlying coronal field. The simplest two-dimensional (2D) model suggested by Syrovatsky (1972) had provided a first glimpse at the physics of a solar flare as a result of emergence of a bipolar magnetic region from under the photosphere into a model corona containing a large-scale *uniform horizontal* magnetic field (Figure 3.11).

A horisontal reconnecting current layer (RCL) was assumed to be formed at the interface between the rising magnetic flux and the ambient coronal field which is antiparallel to the topmost field lines of the upcoming

magnetic flux. The field lines of the initial coronal field reconnect to those of the rising flux, so that the corona and the photosphere become magnetically connected. This process is repeatedly observed in modern space missions like *SOHO* and *TRACE*.

Syrovatsky (1972) estimated the magnetic energy which can be accumulated by the RCL before a solar flare as well as the characteristic time and other basic parameters of the 2D reconnection process in the flare. However, even in the simplest configuration, the accumulation and release of magnetic energy are highly time dependent, have an intrinsically complex three-dimensional geometry, and contain a wide range of length- and timescales. Hence numerical simulations are necessary to provide better physical insight.

The three-dimentional (3D) time-dependent resistive MHD equations have been integrated numerically by Archontis et al. (2005) in order to model the process of reconnection between an emerging bipolar region and a preexisting horizontal uniform field in the corona. In the initial stages of contact of the two systems, the magnetic configuration across a forming current layer is similar to the classical X-point type, with mutually antiparallel field lines on both sides of the current layer being joined and ejected sideways.

The RCL is formed with the shape of a narrow arch distributed all around a rising 'dome' of the massive emergence from the photosphere of magnetic flux and plasma. The numerical experiment shows the structure and evolution of the RCL. It changes from a structure resembling the simple tangential discontinuity to another structure resembling the simple rotational discontinuity. Most of the original subphotospheric flux becomes connected to the coronal field lines.

The ejection of plasma from the RCL gives rise to high-speed and high-temperature jets. The acceleration mechanism for those jets is akin to that found in previous 2D models, but the geometry of the jets bears a clear 3D imprint, having a curved-layer appearance with a sharp interface to the overlying coronal field system. Temperatures and velocities of the jets in the numerical experiment are commensurate with those observed by the *Yohkoh* SXT.

3.4.2 Sakao-type flares

Sakao et al. (1998) studied the spatial evolution of 14 impulsive flares that clearly show the typical double-source structure (Figure 3.12) at the peak of the M2 band (33-53 keV) emission in the hard X-ray (HXR) images obtained by the Hard X-ray Telescope (HXT) onboard *Yohkoh*. The distance l between the sources has been analyzed as a function of time. As

a result, two subclasses of flares – *more impulsive* (MI) and *less impulsive* (LI) – have been discovered. We assume that in both subclasses, the three-dimensional reconnection process occurs in the corona at the separator with a longitudinal field.

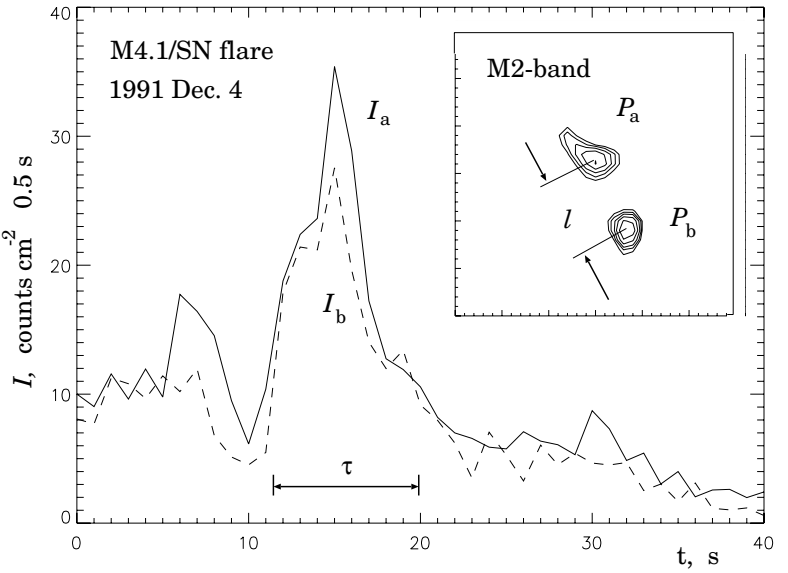

Figure 3.12: Typical HXR structure of a selected impulsive flare is shown in the right top corner: P_a and P_b are the footpoint sources, l is a distance between them. I_a and I_b are the HXR flux from the footpoint sources as a function of time, τ is a total duration of the impulsive phase.

The difference between the LI and MI flares presumably appears because in the LI flares the reconnection process accompanies an increase of the longitudinal field at the separator (Somov et al., 1998). In contrast, in the MI flares the reconnection proceeds with a decrease of the longitudinal field. Hence the reconnection rate is higher in the MI flares.

To illustrate that the observed variations of the footpoint separation depend on the longitudinal field $\mathbf{B}_\parallel$, this field is shown near the separator X in Figure 3.13. The arrows $\mathbf{v}_0$ and $\mathbf{v}_1$ indicate the reconnection velocity pattern (the inflows and outflows) during the impulsive phase of a flare.

Two reconnecting field lines f_1 and f_2 arrive at the separator X and pass through it, the second one after the first. They bring different values of the longitudinal field $\mathbf{B}_\parallel$. If the second field line f_2 arrives with a stronger longitudinal field than the first one, i.e. $B_{\parallel 2} > B_{\parallel 1}$, then the length of the

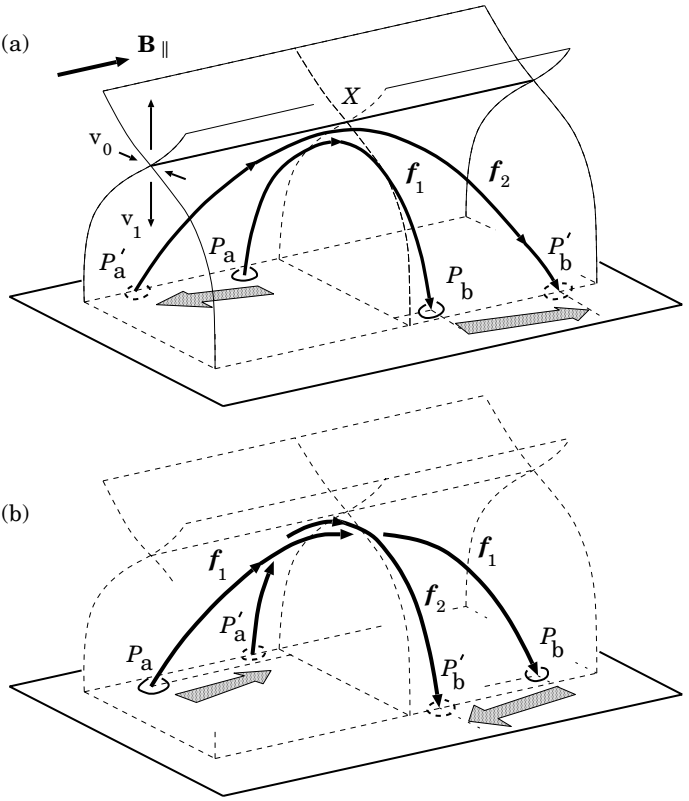

Figure 3.13: An apparent motion of the HXR footpoints during the fast reconnection: (a) the footpoint separation rapidly increases in the LI flares, (b) a decreasing footpoint separation in the MI flares.

line f_2 after reconnection is obviously larger than the length of the line f_1 as shown in Figure 3.13a.

Figure 3.13a also shows positions of the footpoints in the chromospheric plane for the same field lines. The footpoints $P_{\rm a}$ and $P_{\rm b}$, being impulsively heated by accelerated particles, became bright in HXR earlier than the footpoints $P'_{\rm a}$ and $P'_{\rm b}$. Figure 3.13a demonstrates that, if the longitudinal field becomes stronger at the separator, then the footpoint separation will increase during the fast reconnection. If, on the contrary, the line f_2 brings a weaker longitudinal field, i.e. $B_{\parallel 2} < B_{\parallel 1}$, then the distance between footpoints rapidly becomes shorter as shown in Figure 3.13b.

The topological model makes intelligible the observed decrease (in-

crease) of the separation between the HXR sources in the MI (LI) flares (Somov and Merenkova, 1999). Let us consider two configurations (a) and (b) in Figure 3.14 for the four magnetic sources in the source plane Q. To a different extent they differ from the ideal configuration when all the four sources are placed along the symmetry axis x. The longitudinal magnetic field at the separator is equal to zero in the ideal symmetrical case.

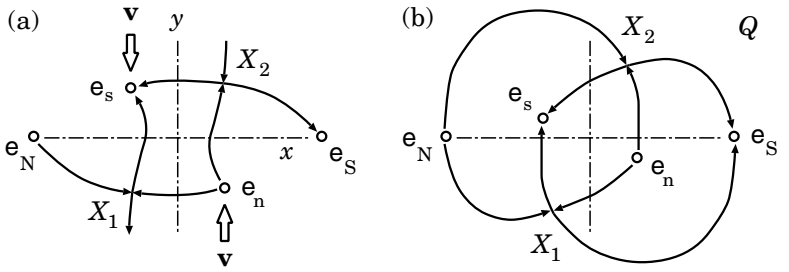

Figure 3.14: Two configurations of magnetic sources in the plane Q.

In general, the pre-reconnection state differs from the ideal configuration, of course. So the longitudinal field already exists at the separator. This field always presents under condition of actual 3D reconnection in the solar atmosphere, and it will increase (or decrease) depending on the direction of evolution of the magnetic field in an active region. For example, the configuration evolves from the less-ideal initial state (a) to a more-ideal one (b) as shown in Figure 3.14. Under this direction of evolution, indicated by vector **v** in Figure 3.14, the reconnection process decreases the longitudinal field at the separator.

Following Gorbachev and Somov (1988, 1990), let us suppose that a part of the flare energy is initially released in some compact region $\mathcal{E}$ near the apex of the separator. Then the energy fluxes will propagate *along* the field lines connecting the energy source with the photosphere. Projections of the energy source $\mathcal{E}$ on the photospheric plane Ph along the field lines are shown as the two 'flare ribbons' FR in Figure 3.15. Therefore we identify flare brightenings, in the hydrogen $H\alpha$ line etc., with the ribbons located at the intersection of the separatrices with the chromosphere which is placed slightly above the photospheric plane.

As in the model of the 1B/M4 flare of 1980 November 5, shown in Figure 3.8, the *saddle* structure of the field near the separator splits the flux of heat and accelerated particles in such a way that it creates the long-narrow Hα ribbons in the chromosphere (FR in Figure 3.15). Moreover the model predicts that a concentration of the field lines that bring energy into

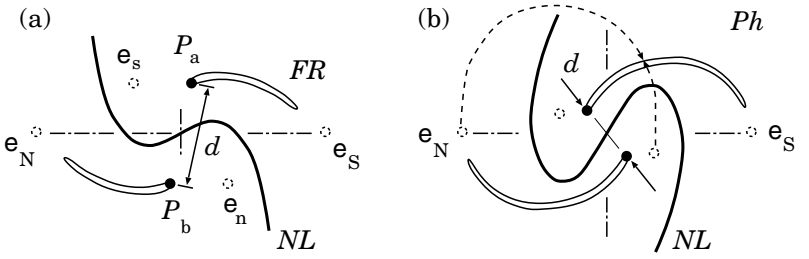

Figure 3.15: The long-narrow Hα ribbons FR and Hα kernels P_a and P_b projected in the photospheric plane Q both sides of the photospheric neutral line NL.

the flare ribbons in the chromosphere is higher at the edges of the ribbons, i.e. at relatively compact regions shown by dark points P_a and P_b. Here the Hα brightenings must be especially bright. This prediction of the model is consistent with observations of Hα kernels in a flare.

Figure 3.15 shows that the foot-point separation, which is the distance d between the points P_a and P_b, decreases if the magnetic configuration evolves from the state (a) to state (b), id. when the longitudinal magnetic field decreases during the reconnection process at the separator. So the reconnection rate is higher in the MI flares of the Sakao type. In contrast, in the LI flares the magnetic configuration evolves from (b) to (a). This means that the reconnection proceeds with an increase of the longitudinal field, more slowly, and with an increase of the foot-point separation. Therefore we may conclude that

> if the evolution of the sunspot configuration goes to a more ideal state with a smaller displacement from the symmetry axies, then the MI flares should occur.

This statement must, however, be examined by future observations and their analysis.

3.4.3 New topological models

When the photospheric magnetic field of active regions was extrapolated into the corona, it was found in many cases (e.g., Aulanier et al., 2000; Bentley et al., 2000) that the large-scale magnetic field of active regions was close to being potential indeed. The basic ingradients for reconnection to occur were present. Moreover the observed photospheric field evolution is expected to drive reconnection and to produce flares in such active regions.

After Gorbachev and Somov (1988, 1989, 1990), a series of similar investigations have sought observational evidence for reconnection in flares (Mandrini et al., 1991, 1993; Mandrini and Machado, 1993; Démoulin et al., 1993; Bagalá et al., 1995; Longcope, 1996; Antiochos, 1998; Longcope and Silva, 1998). The results of these investigations were summarized as follows. Flare brightenings are located at the intersection of the separatrices with the chromosphere and are magnetically connected to one another as well as to a common region close to the separator (cf. Figure 3.8). In particular, Longcope (1996), Longcope and Silva (1998) demonstrated clearly how

> motions of the photospheric sources (magnetic charges) lead to the build-up of 'ribbon-like' current layers parallel to the separator

or two separators (Section 3.2.2), as it is in the case of the solar flare on 7 January 1992.

The magnitude of the current J at the separator (see formula (3.2)) is related through the self-inductance L to the magnetic flux change which would have occured in a potential field in the corona (Syrovatskii, 1966a, 1981). By calculating approximate self-inductances of the separator, the topological model, called now the *minimum current corona*, provides an estimate of the current and the associated free energy from a given displacement of the magnetic sources.

The model developed by Longcope and Silva (1998) applies a topological approach to the magnetic field configuration for 7 January 1992. A new bipole ($\sim 10^{21}$ Mx) emerges amidst a pre-existing active region flux. This emergence gives rise to two current layers along the separators separating the distinct, new and old, magnetic flux systems. Sudden reconnection across the separators transfers $\sim 10^{20}$ Mx of flux from the bipole into the surrounding flux. The locations of current layers in the model correspond with observed soft X-ray loops. In addition the footpoints and apexes of the current layers correspond with observed sources of microwave and hard X-ray emission. The magnitude of the magnetic energy stored by the current layers compares favourably to the inferred energy content of accelerated electrons.

The occurrence of flares in a quadrupolal magnetic configuration is a well studied topic. Ranns et al. (2000) present multi-wavelength observations of two homologous flares observed by *SOHO* and *Yohkoh*. The preflare conditions are reformed after the first flare by emerging flux. With the continual advancements in image resolution, at all wavelengths, we will learn progressively more about the reconnection process in flares.

3.4.4 Reconnection between active regions

An active region is generally assumed to be produced by the buoyant emergence of one or more magnetic flux tubes from below the photosphere. Under this assumption, any coronal field interconnecting two distinct regions must have been produced through magnetic reconnection after emergence. Thus the coronal loops connecting between two active regions offer some of the most compelling evidence of large-scale reconnection in the solar corona (Sheeley et al., 1975; Pevtsov, 2000).

The *TRACE* high-cadence observations in the 171 A passband show numerous loops interconnecting two active regions and thereby provide a good opportunity to quantify magnetic reconnection. Longcope et al. (2005) have analyzed data from the period 2001 August 10–11, during which active region 9574 emerged in the vicinity of existing active region 9570. They have identified each extreme-ultaviolet (EUV) loop connecting the emerging polarity to a nearby existing active region over the 41 hr perion beginning at emergence onset.

The topology of the coronal field was modeled as a potential field anchored in 36 point sources (i.e., the topological model similar to that one introduced in Section 3.2 but with many magnetic charges) representing each of the magnetic field concentrations. Geometrical resemblance of the identified EUV loops to post-reconnection (see Figure 3.1c) field lines from the topological model of the active region pair implicates separator reconnection in their production. More exactly, comparison of the observed EUV loops with computed field lines reveals that the interconnecting loops are consistent with those produced by reconnection at a separator overlying the volume between the active regions.

The computed field included a domain of magnetic flux interconnecting one specific charge from the emerging region to another charge of opposite polarity in the pre-existing region. The magnetic flux in this domain increases steadily, in contrast to the EUV loop observations showing that during the first 24 hr of emergence, reconnection between the active regions proceeded slowly.

The lack of reconnection caused magnetic stress to accumulate as current layer along the separator (see Figure 19 in Longcope et al., 2005). When the accumulated current had reached $J \approx 1.2 \times 10^{11}$ A, a brief reconnection process was triggered, leading to the transfer of $\approx 10^{21}$ Mx across the separator current layer. The stressed field had accumulated at least $\approx 1.4 \times 10^{31}$ ergs, which was then released by the reconnection. According to interpretation given by Longcope et al. (2005), only a small fraction of this energy was dissipated directly at the separator. The released energy was converted instead into small-scale fluctuations such as a turbulence of

Alfvén waves etc.

The reconnection rate was relatively small for the first ~ 24 hr of emergence and then rapidly increased to a peak as high as 10^{17} Mx s^{-1} (10^9 V). Thus the most intense period of reconnection occured after a 1 day delay. The net energy released, and ultimately dissipated, is consistent with the amount that could be stored magnetically during this delay between emergence and reconnection.

Chapter 4

The Bastille Day 2000 Flare

The famous 'Bastille day 2000' flare was well observed by several space- and ground-based observatories and stidied extensively by many researchers. The modern observations in multiple wavelengths demonstrate, in fact, that the Bastille day flare has the same behavior as many large solar flares. In this Chapter, the flare is studied from observational and topological points of view in terms of three-dimentional magnetic reconnection.

4.1 Main observational properties

4.1.1 General characteristics of the flare

On 14 July 2000 near 10:10 UT, a large solar flare with the X-ray importance of X5.7 launched near disk center in the active region NOAA 9077. The event comprised a 3B flare as revealed by bright emission throughout the electromagnetic spectrum, the eruption of a giant twisted filament, an extended Earth-directed CME, and a large enhancement of accelerated particle flux in interplanetary space. This well-observed flare was called the 'Bastille day 2000' flare.

The *Yohkoh* satellite (Ogawara et al., 1991; Acton et al., 1992) observed an early phase (∼10:11 - 10:13 UT) and some of the impulsive phase (from ∼10:19 UT) of this famous flare classified as a long duration event (LDE). The Soft X-ray Telescope (SXT; Tsuneta et al., 1991) observed a large arcade. The width and length of the arcade were ∼30 000 km and

$\sim$120 000 km, respectively. The Hard X-ray Telescope (HXT; Kosugi et al., 1991) clearly showed a two-ribbon structure in the energy ranges $33-53$ and $53-93$ keV. This structure corresponds to a series of footpoints of the SXR arcade (Figure 4.1).

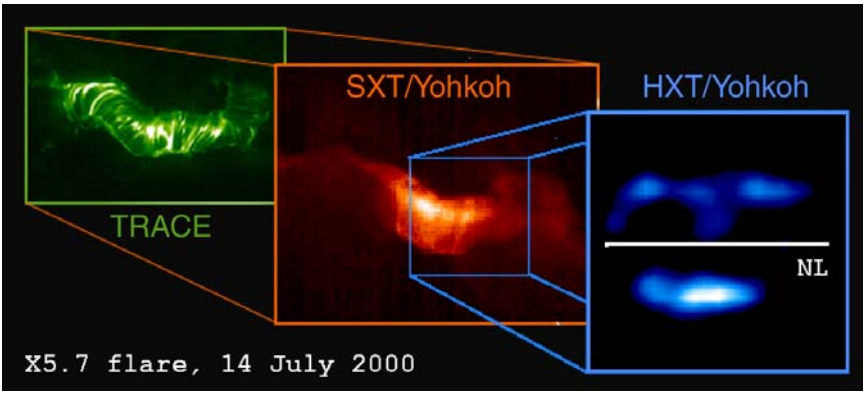

Figure 4.1: *Yohkoh* and *TRACE* observations of the Bastille day flare. The right panel shows HXR (53-93 keV) sources aligned along the flare ribbons, which lie at the feet of the arcade loops in the center of the left panels.

Solar flares often exhibit a two-ribbon structure in the chromosphere, observed for example in Hα (Svestka, 1976; Zirin, 1988; Strong et al., 1999), and this pattern becomes especially pronounced for LDEs of the type often associated with CMEs. In the Bastille day flare, the two ribbons were well seen in Hα and Hβ (Yan et al., 2001; Liu and Zhang, 2001). Fletcher and Hudson (2001) describe the morphology of the EUV ribbons of this flare, as seen in *SOHO*, *TRACE*, and *Yohkoh* data. The two-ribbon structure, however, had never before been observed so clearly in HXR as presented in Masuda et al. (2001).

Masuda et al. analyzed the motions of bright HXR kernels (compact intense sources) in the two ribbons of the Bastille day flare during the first and second bursts (S1 and S2) of emission in the HXT bands M1, M2, and H; they cover the energy range of 23-33, 33-53, and 53-93 keV, respectively. Even without an overlay of the HXR images of the flare on the photospheric magnetograms, Masuda et al. speculated that "these bright kernels are footpoints of newly reconnected loops" and that "lower loops, reconnecting early, are highly sheared; the higher loops, reconnecting later, are less sheared".

This key supposition well supports the idea of three-dimensional reconnection in the corona at a separator with a longitudinal magnetic field. Being introduced to explain the so-called Sakao-type impulsive flares (Sakao et al., 1998), which have double footpoint sources observed in HXR (see Figure 3.12), the idea consists in the following. It is easy to imagine that two reconnecting field lines f_1 and f_2 pass through the separator, the second after the first; see Figure 3.13. If the first line f_1 has the stronger longitudinal field than the second one, then the length of the line f_2 in the corona after reconnection becomes shorter than the length of the line f_1. Therefore the distance between bright HXR footpoints in the chromosphere also becomes shorter as shown in Figure 3.13b.

In general, such a scenario (Section 3.4) is consistent with the observed motions of the HXR kernels in the Bastille day flare. However, to make a judgement about it we need to investigate possible relationships between the HXR kernels (their appearance positions and further dynamics) and the photospheric magnetic field (its structure and evolution).

With the aim of finding such relations, let us adopt the following procedure. First, we overlay the HXR images of the flare on the full-disk magnetograms by the Michelson Doppler Imager (MDI; Scherrer et al., 1995) on board the Solar and Heliospheric Observatory (*SOHO*; Domingo et al., 1995). Second, we overlay the obtained results of the first step on the vector magnetograms of high quality (Liu and Zhang, 2001; Zhang et al., 2001) obtained with the Solar Magnetic Field Telescope (SMFT) at Huairou Solar Observing Station (HSOS).

The coalignment of the HXT images with the MDI and SMFT data allows us (Somov et al., 2002a): (a) to identify the most important MDI sunspots with the SMFT spots, whose properties, morphology and evolution have been carefully studied; and (b) to examine the relationships between the HXR kernel behavior during the impulsive phase of the Bastille day flare and the large-scale displacements of the most impotant sunspots during the two days before the flare, based on precise measurements of the proper motions (Liu and Zhang, 2001). The most important findings will be described below; their interpretation will be given in Chapter 5.

4.1.2 Overlay HXR images on magnetograms

Since we wish to study the relationship between the HXR kernels and the underlying magnetic field, we must accurately coalign the *Yohkoh* data with simultaneous magnetic field data, first of all, the magnetograms from the MDI instrument on the *SOHO*. In principle, such coalignment is possible using the pointing information of the two instruments. In practice, however, there are always quantified and unquantified errors in the pointing of

different satellites and even different instruments on the same satellite.

Concerning the Bastille day flare, as observed by *SOHO* and *TRACE*, Fletcher and Hudson (2001) have determined the coalignment of data from the two instruments via cross-correlation of an image made in the white-light channel of *TRACE* and the MDI continuum image of the active region NOAA 9077. This has allowed the authors to locate the EUV ribbon positions on the photospheric magnetic field. Then the HXT and MDI images have been coaligned. When this has been done, the strongest HXR M2 sources occur at the same locations as the strongest EUV sources. This result is reasonable from the physical point of view (see Chapter 2 in Somov, 1992).

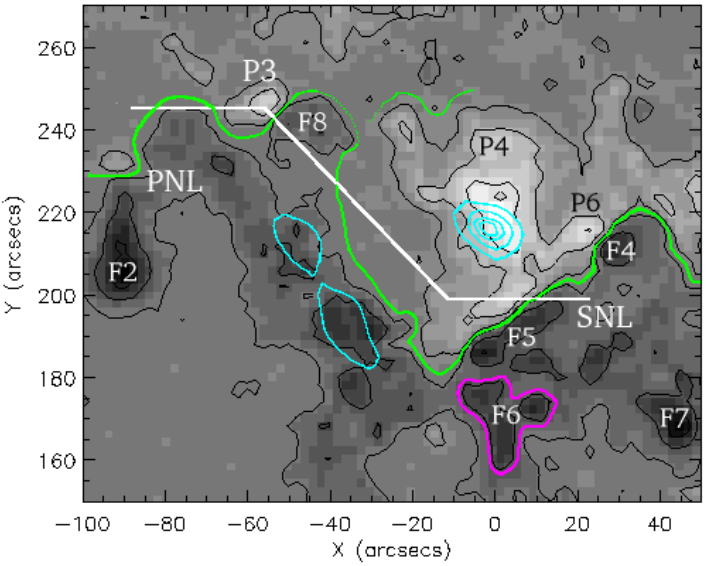

Figure 4.2: The HXR source contours (blue curves) at the HXR maximum of the Bastille day flare overlaid on the MDI magnetogram. The green curve PNL represents the photospheric neutral line. SNL is the simplified neutral line.

Figure 4.2 shows the HXR source image synthesized during the peak of the flare at 10:27:00 - 10:27:20 UT; the blue contours are at 25, 50, 75 and 90 % of the maximum HXR intensity. The sources are superimposed by Fletcher and Hudson (2001) on the MDI magnetic field. The magnetogram is taken at 11:12 UT. White indicates positive line-of-sight field, and black negative; the contours are at ± 100, 500 and 1000 G. The broken straight

line SNL indicates the so-called "simplified neutral line" of the photospheric magnetic field, as introduced by Masuda et al. (2001). This effective line does not coincide with an actual photospheric neutral line PNL (or the polarity inversion line) but it is used to describe dynamic behavior of the HXR sources during the flare. The physical meaning of the SNL will be given in Section 5.1 where we discuss a model of the flare.

We have added to this overlay the notations of some sunspots in the field according to Liu and Zhang (2001). They describe the spots on the photospheric magnetograms obtained with the SMFT by the polarities with "P" and "F" representing the preceding (positive) and following (negative) magnetic polarities respectively. There is a good spatial correspondence between the spots as seen in the MDI magnetogram and the spots in the gound-based magnetogram obtained with the SMFT on July 14 at 08:43:19 UT. This allows us to identify the MDI spots with corresponding spots in the SMFT magnetograms. In this way, we use the sunspot notations taken from Figure 8 in Liu and Zhang (2001) and from Figure 3 in Liu and Zhang (2002). For example, the "triangular" negative spot F6 in the MDI magnetogram at 11:12 UT in Figure 4.2 is the same spot F6 in the SMFT magnetogram at 08:43:19 UT shown in Figure 4.3.

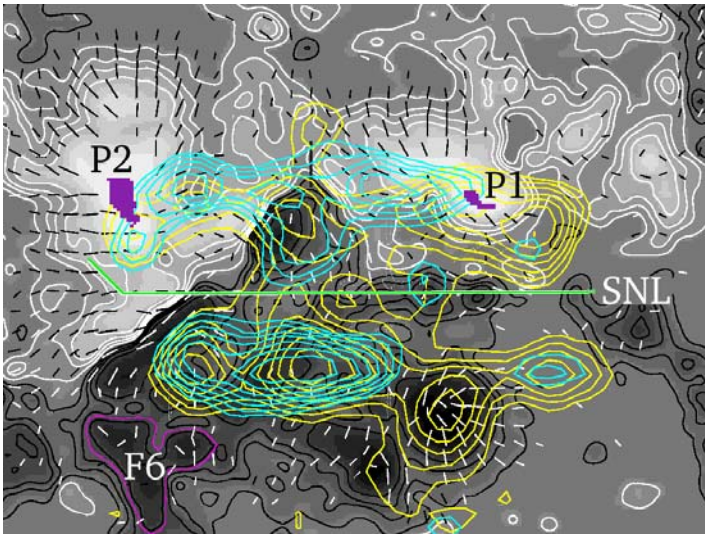

Figure 4.3: The HXR source positions in the beginning of the first HXR spike S1 (yellow contours) and near its end (blue contours).

The underlying magnetic field in Figure 4.3 is the SMFT vector mag-

netogram at 08:43:19 UT on July 14, taken from Figire 8d in Liu and Zhang (2001). The contour levels of the line-of-sight field are 160, 424, 677 and 1071 G. White contours represent positive polarity and black represent negative. The bars are transverse components with their length proportional to intensity. P1 and P2 are the most important positive sunspots.

To overlay the HXT data on the SMFT magnetogram we have used the pointing information for the same satellite and the same instrument, HXT. This procedure gave us the relative position of the HXR images taken in the same energy band during the different HXR spikes: S2 and S1, that is with a small difference in time. Since we already have the coalignment of the HXT data during the spike S2 at 10:27 UT and the magnetogram shown in Figure 4.2, we simply find the HXR source positions during the spike S1 at 10:19 - 10:24 UT according to Masuda et al. (2001) on the SMFT magnetogram.

The two overlays in Figure 4.3 are the HXT H-band images during the first HXR spike S1 in its rising and decay phases. The contour levels are 70.7, 50.0, 35.4, 25.0, 17.7, 12.5 and 8.8 % of the peak intensity for each of two images. The first one, shown by yellow contours, is reconstructed in the beginning of the spike S1 at 10:19:37 - 10:20:27 UT. The second, shown by blue contours, is synthesized just after a peak (at about 10:22 UT) of the spike, at 10:22:17 - 10:22:45 UT. In this way, Figure 4.3 allows us to study the evolution of the HXR sources during the first spike.

4.1.3 Questions of interpretaion

Several comments should be made here. First, as mentioned before, the two-ribbon structure is really well seen during the first spike. Two ribbons are most clearly observed in the rising phase and the decay phase of S1. Moreover the bright compact kernels in HXR are observed along the ribbons separated by the simplified magnetic neutral line SNL which is almost exactly aligned in the E-W direction in Figures 4.3 and 4.1. The appearance of the HXR kernels is not a surprisingly unexpectable result. The chromospheric Hα-ribbons typically demonstrate several bright patches, called kernels. However the intensity dynamical range of the *Yohkoh* HXT was not high enough to observe the HXR ribbons in many flares as a typical phenomenon.

Second, if the whole structure, the HXR ribbons and kernels together with the ridge of the huge arcade as it seen in Figures 2 and 5 in Masuda et al. (2001), is illuminated by fast electrons, then they seem to be accelerated (or, at least, trapped) in a large-scale system of magnetic loops. If we accept the standard two-dimensional MHD model of the two-ribbon flares, which was well known as successful in interpretation of the *Yohkoh* SXT

observations (Forbes and Acton, 1996; Tsuneta, 1996; Tsuneta et al., 1997), then this result seems to be consistent with the hypothesis of a large-scale reconnection process in the corona, involved in the flare energy release. Moreover, because of a large scale and large energetics of the system of interacting magnetic fluxes, the reconnected parts of magnetic fluxes should be also large. This is clear even if we do not know the exact links of the magnetic field lines before and after reconnection. Therefore the problem of identification and measurement of the reconnected fluxes becomes essential (Fletcher and Hudson, 2001).

Third, the brightest HXR kernels do not coincide with the regions of highest line-of-sight field strength, with umbrae of sunspots. The question where the HXR kernels appear and disappear requires a special investigation. Since the HXR kernels are produced as a result of direct bombardment by powerful beams of fast electrons, nonthermal and presumably quasi-thermal, we expect the fast hydrodynamic and radiative response of the transition zone and chromosphere to an impulsive heating by these electrons and secondary XUV emission as discussed in Chapter 2 in Somov (1992).

4.1.4 Motion of the HXR kernels

To see the strongest sources of HXR during the first spike S1, we show in Figure 4.4 only the contours with levels 70.7, 50.0, 35.4 and 25.0 % of the peak intensity. For this reason, the lower HXR background disappears. However, two HXR ribbons are still well distinguished as two chains of the HXR kernels on either side of the SNL. We shall consider the apparent displacements of the brightest sources.

The most intense kernel K2 in the southern ribbon reappears to the east. However this displacement is much slower in comparison with that of the brightest kernel K1 in the northern ribbon. The displacement of the kernel K1 is shown by the large green arrow. The source K1 moves to the north, that is outward from the simplified neutral line SNL, and to a larger extent it moves to the east, parallel to the SNL. An exact description of the motion of the centroid of the most intensive HXR source in the northern and southern ribbons is presented in Figure 4 in Masuda et al. (2001). However, what is important for the following discussion is shown above in our Figure 4.4.

We shall show that the observed displacement of the brightest HXR kernel K1 during the first spike S1 can be related to the magnetic field evolution before the Bastille day flare. It was reasonable to assume that some relationships between the kernel motion and magnetic field structure and evolution do exist (Somov et al., 1998). However it has not been known

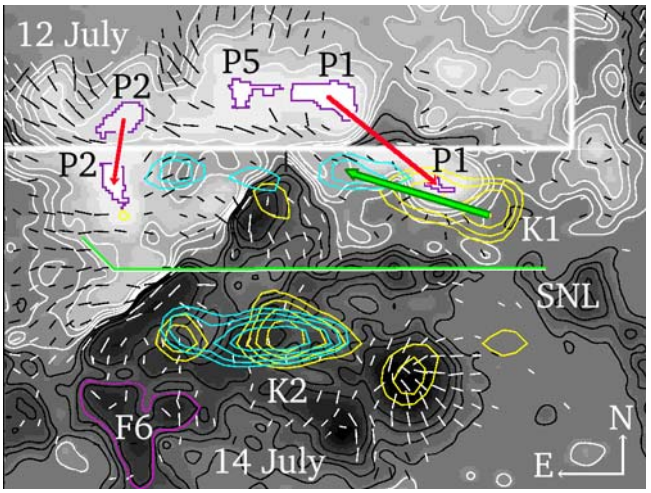

Figure 4.4: The position and motion of the strongest HXR sources K1 and K2 relative to the SMFT magnetogram on 14 July.

how these relations manifest themselves in actual flares or at least in the models which are more realistic than the ideal 'standard model' of the two-ribbon flare (see discussion in Fletcher and Hudson, 2001).

4.1.5 Magnetic field evolution

The active region (AR) NOAA 9077 had one of the most complex magnetic field structures; it was in a typical $\beta\gamma\delta$ class (Liu and Zhang, 2001, 2002). It produced nearly 130 flares, including 3 flares of the X-class, the largest of those being the X5.7 flare on July 14. The next one in terms of X-ray importance was the X1.9 flare on July 12. We assume that after this very large flare the AR had a minimum of magnetic energy and that two days were necessary for the AR to accumulate an energy sufficient for the Bastille day flare.

The motions of the sunspots cause the footpoints of magnetic fluxes to move and interact between themselves in the chromosphere and corona. In the absence of reconnection this process increases the non-potential part of the magnetic energy, the excess available for the next flare or flares. When the original (say on July 12) magnetic configuration is deformed, magnetic gradients and stresses (including the magnetic shear) become enhanced. Moreover, slowly reconnecting current layers (RCL) are created at the sur-

faces that divide different magnetic flux systems, and fast reconnection would be able to release the free magnetic energy as a flare (Sections 3.1 and 3.3).

Liu and Zhang (2001, 2002) have described the morphology of AR 9077, the proper motions of many spots, and the evolution of the magnetic fields. They have found many interesting peculiarities of the sunspot motions, including a suggested trigger of the fv2, lare etc. However we shall restrict ourselve to large scales related to the HXR structure of the Bastille day flare. Let us compare two magnetograms from a time sequence of magnetograms presented in Figure 8 in Liu and Zhang (2001). We overlay the magnetogram on July 12 in the top panel in our Figure 4.4 on the magnetogram on July 14 in the bottom panel in the same Figure. We see that the largest positive spot P1 rapidly moves southwest as shown by the large red arrow. Other big umbrae seem more stable or, at least, do not move so quickly as P1. This is well seen from comparison with the displacement of the second positive spot P2 shown by the small red arrow.

Detail descriptions of the proper motions with precise measurements and results are given by Liu and Zhang (2001, 2002). For example, a small part P5 (shown in our Figure 4.4) of the umbra P1 moved away from the east end of P1 on July 12, but P5 still followed P1 on July 13 and 14. P1 became smaller but tiny satellite spots formed around it. Figure 5 in Liu and Zhang (2001) shows a variety of spot proper motion velocities. The small spots P5, A1, B2 and B3 were short-lived relative to spot P1 but all of them moved in the same direction as one group.

So the southwest motion of the large spot P1 together with its group 1 is certainly one of the dominant motions in the AR. The other motions and changes of the magnetic field are presented in Liu and Zhang (2001) but they are presumably more important for the second spike S2 and many other manifestations of the Bastille day flare. In this Chapter, we shall discuss only the first spike S1. More exactly, we shall consider its position and dynamics with relation to the spot P1 displacement shown above.

4.1.6 The HXR kernels and field evolution

The observed displacement of the brightest kernel K1 during the first spike S1 (as shown by the large green arrow in Figure 4.4) is directed nearly anti-parallel to the displacement of the strongest positive spot P1 during the two days between two largest flares. An interpretation of this fact will be given in the next Section. First, let us consider the fact in more detail, as shown in Figure 4.5.

As in Figure 4.4, the HXR kernel is shown with four contour levels: 70.7, 50.0, 35.4 and 25.0 % of the peak intensity. In the rising phase of

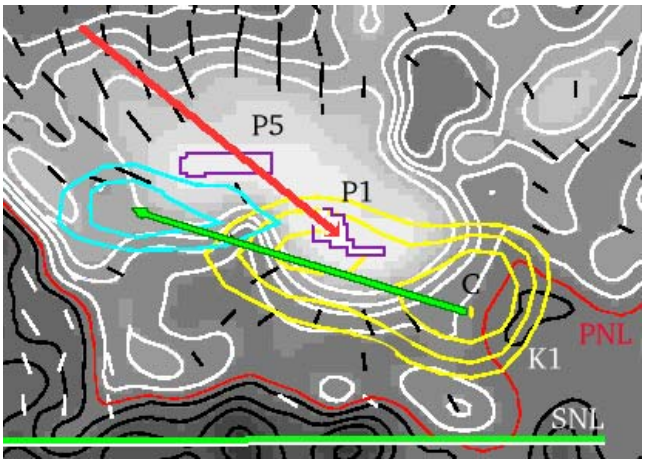

Figure 4.5: H-band images of the brightest kernel K1 in the rise and decay of the first HXR spike S1 overlaid on the SMFT magnetogram on July 14.

the spike, the kernel K1 appears in front of the moving spot P1, in its vicinity but not in the umbra. The brightest part of the kernel, indicated as the yellow 'point' C in the beginning of the green arrow, locates in a region of weak line-of-sight field: between the contour of the 160 G and the actual photospheric neutral line (the red curve PNL in Figure 4.5). This is consistent with observations of several flares at Hα by a fast CCD camera system installed at Big Bear Solar Observatory (BBSO). Wang and Qiu (2002) compared the initial brightening of flare kernels at Hα-1.3 A with photospheric magnetograms and found that initial brightenings avoided the regions of a strong line-of-sight magnetic field. The observed Hα flare morphology and evolution suggest that that emission near a magnetic neutral line may come from footpoints of flare loops of small height, where the first accelerated electrons precipitate.

Figure 4.5 also shows that, later on,

> the centroid of the most intense HXR source moves ahead, mostly anti-parallel to the spot P1 displacement arrow,

but avoids the strongest field area. In the decay phase of the spike, the centroid arrives at the end of the green arrow in the vicinity of the spot P5 but still remains outside of the line-of-sight field level 1071 G. One of the possible reasons of such behavior may be in the magnetic-mirror interpretation (Somov and Kosugi, 1997). Further investigation is necessary to under-

stand the actual conditions of propagation, trapping, and precipitation of accelerated electrons from the corona into the chromosphere.

However the main problem in the flare physics still remains the primary release of energy. This is the transformation of the excess magnetic energy into kinetic and thermal energy of particles. Such transformation can be done by the reconnection process which occurs at the separator (one or several) with a longitudinal magnetic field. On the basis of the simultaneous multiwavelength observations, we are interested to understand how such a mechanism can work in the Bastille day flare.

4.2 Simplified topological model

4.2.1 Photospheric field model. Topological portrait

Following Section 3.2.1, we model the photospheric field by using several magnetic "charges" q_i located in a horizontal plane Q beneath the photosphere. For example, in order to study the large-scale structure and dynamics of the 3B/X5.7 flare on 14 July 2000, we replace the five most important regions, in which the magnetic field of a single polarity is concentrated in the *SOHO* MDI magnetogram (Figure 4.6a), by two sources of northern polarity (n_1 and n_2) and three of southern polarity (s_1, s_2, and s_3) as shown in Figure 4.6b. One characteristic feature of the observed and model magnetograms is the ω-shaped structure of the photospheric neutral line NL, shown by the thick curve.

Figure 4.6b also shows contours of the vertical component B_z of the field in the photospheric plane Ph, $z = 0$, calculated in the potential field approximation. $B_z = 0$ at the calculated neutral line NL. The magnetic charges are located in the source plane Q at $z = -0.1$.

Figure 4.7 represents the same magnetic charges in the source plane Q and the structure of the magnetic field in this plane. The arrows show the directions of the magnetic-field vectors in Q. The points X_1, X_2, X_3, and X_4 are the zero-field points (or neutral points), where $B = 0$. They are important topological features of the field. The magnetic-field separatrix lines (separatrices), shown by solid curves, pass through these points and the magnetic charges. Thus the separatices separate the magnetic fluxes connecting different magnetic charges. At the same time, they are the bases of the separatric surfaces in the half-space above the plane Q. Therefore Figure 4.7 contains all the information about the topology of the large-scale field of the active region. So we refer to this figure as the *topological portrait* of the active region.

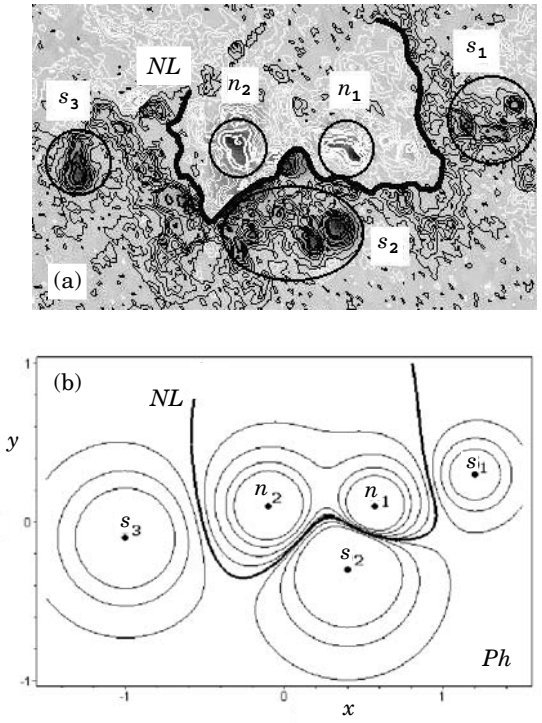

Figure 4.6: (a) The *SOHO* MDI magnetogram of the active region NOAA 9077 on July 14, 2000. The most important large-scale sources of the photospheric magnetic field are indicated as n_1, n_2, s_1, s_2, and s_3. NL is the photospheric neutral line. (b) The model magnetogram of the same active region.

4.2.2 Coronal field model. Separators

Figure 4.8 demonstrates the three-dimentional structure of magnetic field above the plane of topological portrait. The field lines are shown at different separatrix surfaces that have the forms of "domes" of various size, with their basis being located on separatrix lines in the plane Q.

The separatrix surfaces intersect along the field lines connecting the neutral points. Each of these critical lines belongs simultaneously to four magnetic fluxes with different connectivity; thus it is called *separator*. During the flare, there is a redistribution of magnetic fluxes - magnetic reconnection at the separators. For example, one of the separators connects the points X_1 and X_2 (see Figure 4.9). Here, at the separator (X_1X_2), re-

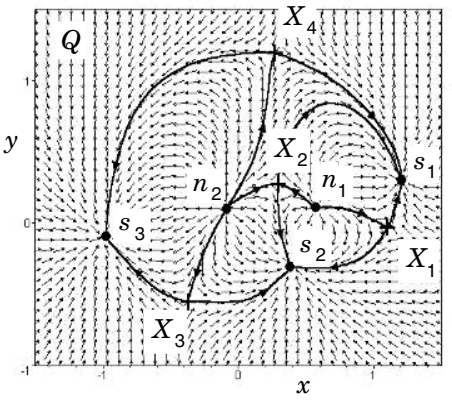

Figure 4.7: Topological portrait of the active region NOAA 9077 on July 14, 2000. The magnetic field directions are shown in the source plane Q at the height $z = -0.1$ beneath the photospheric plane Ph. The solid curves with arrows are the separatrices that separate the magnetic fluxes connecting different magnetic sources.

connection occurs during the first stage S1 in the impulsive phase of the Bastille-day flare.

4.2.3 Chromospheric ribbons and kernels

Reconnection at the separators transforms the accumulated magnetic energy of coronal currents into the thermal and kinetic energy of plasma and accelerated particles. Propagating along the field lines and reaching the chromosphere, these energy fluxes give rise to a complex hydrodynamic and radiative response (see vol. 1, Section 8.3.2). Secondary processes in the chromospheric plasma result in the basic flare behavior observed in the optical, UV, EUV, soft and hard X-rays.

Following Gorbachev and Somov (1990), let us assume that the most powerful release of energy and particle acceleration take place near the tops of the two separators. We calculate the magnetic-field lines passing through such sources of energy until their intersection with the photospheric plane Ph. These field lines form narrow flare ribbons in the chromosphere.

It is natural that different parts of the complex active region NOAA 9077 were important during different stages of the large Bastille-day flare in progress. In fact, the two pairs of field sources (n_1, n_2) and (s_1, s_2) played the main role during the first stage S1 of the impulsive phase of the flare

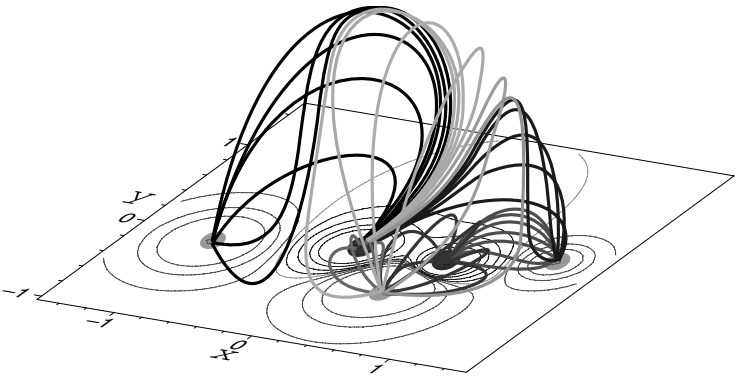

Figure 4.8: The magnetic-field lines forming the separatrix surfaces that are the domes bounding the magnetic fluxes of different pairs of sources.

as illustrated by Figure 4.9, while the large-scale structure of the flare during the second stage S2 was mainly determined by the pairs (n_1, n_2) and (s_2, s_3). In other words, the region of the most powerful release of energy and acceleration of electrons was initially located in the western part of the active region without any influence of the spot s_3, then moves to the eastern part, closer to s_3. This is clearly visible in the hard and soft X-ray *Yohkoh* images and the *TRACE* EUV images (Aschwanden and Alexander, 2001; Fletcher and Hudson, 2001; Masuda et al., 2001).

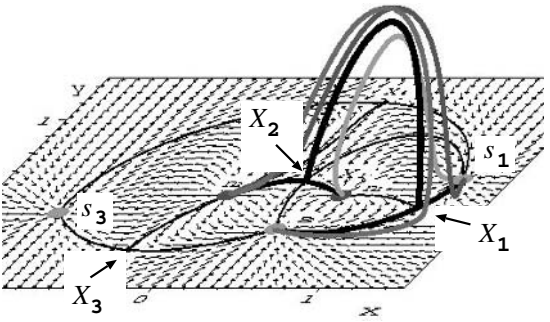

Figure 4.9: The magnetic-field lines in the vicinity of the separator (the solid dark curve) connecting the neutral points X_1 and X_2.

We assume that, during the second stage S2, the spot s_1 has not its primary influence anymore. Instead, the sources (n_1, n_2) and (s_2, s_3) are

efficiently involved in the flare in a way similar to that one shown in Figure 4.9. Figure 4.10a, presents similar calculations for chromospheric ribbons during the stages S1 and S2. The calculated ribbons are shown by the dashed curves. The ribbon between sources s_1 and s_2 corresponds to the first stage, and the ribbon between sources s_2 and s_3 to the second. However two calculated ribbons are located between the field sources n_1 and n_2. The lower ribbon corresponds to the stage S1, and the upper one to the second stage.

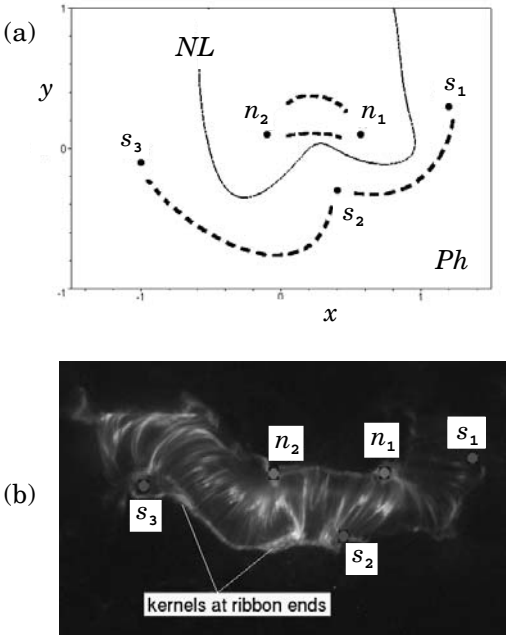

Figure 4.10: (a) Calculated chromospheric ribbons are shown by the dashed curves. (b) *TRACE* image of the Balstille-day flare at 171 A.

Figure 4.10b presents a *TRACE* image of the flare at 171 Å obtained during the second stage S2. The eastern part (the left site of the image) of the flare is somewhat brighter that the western part. A chromospheric ribbon is clearly visible between the field sources s_2 and s_3. Bright kernels at the ends of the ribbon are also visible. The observed ribbons are arc-shaped and are in a reasonable agreement with the locations and shapes of the calculated ribbons. However the calculated ribbons are not reproducing some portions of the observed ribbons. This is especially clear when we

consider the calculated ribbons in the northern polarity. Two small parallel ribbons between the sources n_1 and n_2 are given by the model while the *TRACE* observations show one very elongated ribbon.

This discrepancy presumably has the following origins. First, in order to illustrate the effect of a primary energy source at a separator, we have taken a small circle encompassing the separator near its top in a plane perpendicular to the separator. Such a simplistic approach seems to be good for relatively simple active regions with one dominating separator (see Section 3.2.2), which is not the case of the active region NOAA 9077. It is no easy task to investigate how the rate of magnetic reconnection (and the related dissipation rate) is distributed along the separators in the active region with a complex topology. Second, the topological model based on the potential field approximation completely neglects the nonpotential components of magnetic field in the active region. This approximation is not justified in places where strong electric cirrents flow (see Section 5.1). And finally, we use only five charges while the observed photospheric field is much more complex.

In principle, one could try to achieve a better agreement between the observed chromospheric ribbons and the calculated ones, for example, by introducing an additional magnetic charge n_3 in the most eastern part of the active region (see the spot p_3 in Figures 1, 3 and 7 in Liu and Zhang, 2001). This would allow to reproduce the eastern wing of the northern chromospheric ribbon between sources n_2 and n_3. One could add more charges q_i or replace them with more precise distributions of the magnetic-field sources, thereby increasing the number of separators. However, in this way, the model becomes too complicated.

Moreover there is another principal restriction. The real magnetic field and real velocity field in the photosphere always contain at least two components: regular, large-scale and chaotic, small-scale. The topological model should take into account only the first component, with the aim of describing the global reconnection mechanism behind a large flare. The small number of the charges in the model under consideration, five, allows us to reproduce only the most important large-scale features of the *SOHO* MDI magnetogram and keeps the model being simple and clear.

Using the nonpotential, for example, force-free methods to extrapolate the surface field would also be likely to improve the agreement between the topological model and the observations. The most logical next approximation would be to take into account the current layers along the separators. The magnetic field containing the current layer is in force-free equilibrium. An expression can be found for the net current induced in the layer in response to displacement of the photospheric sources (Longcope and Cowley, 1996; Longcope, 1996).

4.2.4 Reconnected magnetic flux. Electric field

As we made it above, the topology of the active region was defined by partitioning of the observed photospheric field into a set of discrete sources and determining which pairs were interlinked by coronal field lines. The level of topological activity then can be quantified through the transfer of magnetic flux between domains of differing field line connectivity.

The magnetic fields in the active region NOAA 9077 were observed during several days before and after the Bastille-day flare (Liu and Zhang, 2001; Zhang, 2002). There were many flares in this active region over this period. The largest one (X5.7) was on July 14 and the next largest in the magnitude (X1.9) was on July 12. It was suggested by Somov et al. (2002a) that the magnetic energy of the active region reached its minimum after this flare and that the energy necessary for the Bastille-day flare was accumulated over the following two days (July 12-14).

We have made the model of the photospheric and coronal magnetic fields in the active region NOAA 9077 on July 12 just in the same way as presented above for July 14. It appears that the topological portrait of the active region and the structure of its coronal field did not change significantly during two days. For example, in the western part of the active region on July 12, there was also the separator (X_1X_2) connecting in the corona the neutral points X_1 and X_2 in the plane Q of five magnetic sources. We have calculated the magnetic flux beneath this separator and above the source plane Q, Ψ_{12} on July 12 and Ψ_{14} on July 14. The difference of these fluxes is $\delta\Psi = \Psi_{14} - \Psi_{12} \sim 6 \times 10^{21}$ Mx.

What is the physical meaning of $\delta\Psi$? – If there were a vacuum without plasma above the plane Q, then the flux $\delta\Psi$ would reconnect at the separator (X_1X_2) over the two day evolution of the photospheric field sources, and the magnetic field would remain potential without any excess of magnetic energy. In the low-resistivity plasma, changes in the photospheric sources induce an electric current at the separator in the corona. This current in the coronal plasma forms a current layer which will prevent the reconnection of the flux $\delta\Psi$. Thus, the energy will be accumulated in the magnetic field of the current layer.

There are several important questions related to this scenario.

First, why reconnection cannot destroy the current layer during the long pre-flare state? In principle, the current layer in this state can suffer many instabilities: thermal instability due to the radiative energy losses, resistive overheating instability caused by the temperature dependence of plasma conductivity, two-stream instabilities of various types, tearing instability, structural instability etc. Fortunately, many of these instabilities can be well stabilized or have a high threshold in many cases of interest.

For example, the tearing instability is an integral part of magnetic reconnection. The theory of resistive MHD instabilities developed for the case of the neutral current layers predicts very low threshold (Furth et al., 1963). However laboratory and numerical experiments, as well as some astrophysical observations, show that the reconnecting current layers can be stable for a long time because the tearing mode is suppressed by a small transversal magnetic field, i.e., by a small component of magnetic field which is perpendicular to the current layer (see Section 11.4).

The second question is why reconnection is sufficiently slow to permit the current layer build-up during the slow evolution before flaring and fast enough during the flare? In the pre-flare state, the current layer with the classical Coulomb conductivity has very low resistance R_0. For this reason, the characteristic time of the energy accumulation process at the separator in the corona, $\tau_a = L/R_0$ (with the self-inductance L which is proportional to the separator length l_s), can be long enough (say 3×10^4 s) in order to accumulate the sufficiently large energy for a large flare (see discussion in Section 3.3.3).

It is assumed that, as a result of one of the instabilities mentioned above, the magnetic energy related to the current layer is rapidly released and a flare starts. It is clear that, in order to release the accumulated energy in a time $\tau_f \sim 10^2 - 10^3$ s, the total resistance of the current layer must be increased by 2 or 3 orders of magnitude. Such an effect can be well the result of the appearance of plasma turbulence or local current disruptions that have large enough resistance, electric double layers.

Note that the highly-concentrated currents are necessary to generate plasma turbulence or double layers. This fact justifies the pre-flare storage of magnetic energy in current layers rather than distributed currents in the full volume. The smoothly-distributed currents can be easily generated in a plasma of low resistivity but they dissipate too slowly. On the contrary, the current density inside the pre-flare current layers usually grows with time and reaches one or another limit. For example, wave exitation begins and wave-particle interaction becomes efficient to produce high resistance, or the collisionless dynamic dissipation allows the fast process of collisionless reconnection (Section 6.3.1).

The energy released during the first stage S1 of the Bastille-day flare was estimated to be $\varepsilon_f \sim (1-3) \times 10^{31}$ erg (e.g., Aschwanden and Alexander, 2001). If this energy was accumulated as the magnetic energy of the current layer at the separator, then it corresponds to the total current $J_f \sim (1-2) \times 10^{11}$ Ampere along the separator in the corona (Somov et al., 2002a). This value does not contradict to the high level of non-potentiality of the active region NOAA 9077, which was estimated from measurements of the three components of the photospheric magnetic field

(see Figure 5 in Deng et al., 2001). More exactly, the estimated total vertical current in the photosphere, $J_z \sim (1-2) \times 10^{13}$ Ampere, is significantly larger than the coronal current J_f at the separator. Note, however, that the nonpotential components of the field in this active region are presumably (see Section 5.1) related to the following currents: (a) the pre-flare slowly-reconnecting current layers which are highly-concentrated currents flowing along the separators, (b) the smoothly distributed currents which are responsible for magnetic tension generated by the photospheric shear flows, (c) the concentrated currents at the separatrices, also generated by the shear flows.

Anyway, the flare energy ε_f is much smaller than the energy of potential field, which we calculated by using the topological model: $\varepsilon_{ar} \sim (3-6) \times 10^{33}$ erg on July 12 and $\varepsilon_{ar} \sim (1-2) \times 10^{34}$ erg on July 14. We see that the potential field really dominates the global energetics of the active region and, therefore, determines the large-scale structure of its magnetic field. However, in smaller scales, especially in the vicinity of the main neutral line of the photospheric magnetic field, the energy of nonpotential field has to be taken into account in modeling of the Bastille-day flare (Deng et al., 2001; Tian et al., 2002; Zhang, 2002). A two-step reconnection scenario for the flare energy process was suggested by Wang and Shi (1993). The first step takes place in the photosphere and manifests as flux cancellation observed in the photospheric magnetograms. The second-step reconnection is explosive in nature and directly responsible for the coronal energy release in flares.

The most rapid reconnection of the flux $\delta\Psi$ in the corona occurs during the impulsive phase of the Bastille-day flare. Taking the duration of the first impulsive stage of electron acceleration (during the burst S1 of the hard X-rays with energies exceeding 33 keV) to be $\delta t \sim 3$ min (Masuda et al. 2001), we estimate the electric field

$$\mathbf{E} = -\frac{1}{c}\frac{\partial \mathbf{A}}{\partial t}\,. \tag{4.1}$$

Here $\mathbf{A}$ is the vector potential, i.e. $\mathbf{B} = \operatorname{curl} \mathbf{A}$, c is the speed of light. The magnetic flux Ψ is written as a function of $\mathbf{A}$ as follows:

$$\Psi = \oint\limits_L \mathbf{A}\, d\,\mathbf{l}, \tag{4.2}$$

where L is the closed contour: the separator plus the line connecting its feet, the neutral points in the source plane Q. First, we have calculated directly the magnetic flux beneath the separator and above the plane Q, Ψ_{12} on July 12 and Ψ_{14} on July 14. We just integrated the flux of magnetic field across

a surface bounded by the contour L. Second, in order to be sure in the final results, we also made numerical integration over a "separator loop" as defined by Longcope (1996): (a) from one neutral point along the separator above the plane Q and parallel to the magnetic field $\mathbf{B}$ at the separator to another neutral point and then (b) back from the second neutral point to the first one along the separator below the plane Q and anti-parallel to the magnetic field $\mathbf{B}$. In this way, we have found the magnetic fluxes on July 12 and 14, and we have estimated the value of electric field $E \sim 30$ V/cm. This value does not contradict to the electric-field estimates obtained for impulsive flares using the theory of reconnecting SHTCL (Chapter 6.3).

The reconnected magnetic flux can be also estimated in another way. Since the energy fluxes from the separator reconnection region result in the formation of chromospheric ribbons, these ribbons correspond to newly reconnected field lines. In a two-dimensional MHD model for a two-ribbon flare with a vertical current layer (the standard model, see Forbes and Acton, 1996), the ascending region of reconnection gives rise to chromosphertic ribbons moving in opposite directions from the photospheric neutral lines. In general, a ribbon's motion with respect to the photospheric neutral line can be used to estimate the reconnected magnetic flux.

In the Bastille-day flare, Fletcher & Hudson (2001) analyzed the motions of the northern and southern EUV ribbons observed by *TRACE* at the maximum of the HXR burst S2. They estimated the value of the reconnected flux as the total magnetic flux traversed by the ribbons in the north and the south in the eastern part of the active region. During the time interval from 10:26:15 UT to 10:28:58 UT, which is a part of the stage S2, $\delta\Psi \approx -(14.5 \pm 0.5) \times 10^{20}$ Mx for the southern ribbon and $\delta\Psi \approx (8.6 \pm 1.4) \times 10^{20}$ Mx for the northern ribbon with the inclusion of the mixed-polarity fields to the north from the photospheric neutral line. It is not clear whether the ribbons are actually passing through this region or just suddenly form. Anyway, the magnetic flux reconnected during the stage S2 and estimated by Fletcher & Hudson at the level of the photosphere is of the same order of magnitude as the magnetic flux which we have found for the stage S1 and which is the flux reconnected at the separator (X_1X_2) in the corona.

4.2.5 Discussion of topological model

The use of the topological model requires that the relevant magnetic polarities are well taken into account. So, at least, they should be spatially well resolved. It is also obvious that the topological model can be relevant for large flares, since it neglects fine temporal behavior and small-scale processes. The model is relatively simple if it concentrates on general evolution

of the global structure of large flares. The topological model for large-scale magnetic fields remains simple and clear for such a complex active region as the NOAA 9077 (the $\beta\gamma\delta$ configuration, according to Liu and Zhang, 2001), which gave rise to the Bastille-day flare. At the same time, the topological model explains the main features of this well-studied flare.

First, the simplified topological model approximately predicts the location of the flare energy source in the corona and, with a reasonable accuracy, reproduces the locations and shapes of chromospheric ribbons and bright kernels on the ribbons. More accurate models should be constructed, with account of nonpotential components of magnetic field in the active region, in order to reach a better agreement between the model and observations.

Second, the topological model explains the observed large-scale dynamics of the Bastille-day flare as the result of fast reconnection in the reconnecting current layers at separators. It allows us to estimate roughly the reconnection rate and the strength of the large-scale electric fields that presumably accelerate charged particles along the separators. All these effects can be carefully investigated in many flares by using the *Ramaty High Energy Solar Spectroscopic Imager (RHESSI)* high-resolution HXR and gamma- imaging data (Krucker et al., 2003; Lin et al., 2003).

In order to interpret the temporal and spectral evolution and spatial distribution of HXRs in flares, a two-step acceleration was proposed by Somov and Kosugi (1997) with the second-step acceleration via the collapsing magnetic-field lines. The *Yohkoh* HXT observations of the Bastille-day flare (Masuda et al., 2001) clearly show that, with increasing energy, the HXR emitting region gradually changes from a *large diffuse source*, which is located presumably above the ridge of soft X-ray arcade, to a two-ribbon structure at the loop footpoints. This result suggests that electrons are in fact accelerated in the large system of the coronal loops, not merely in a particular one. This seems to be consistent with the *RHESSI* observations of large coronal HXR sources; see, for example, the X4.8 flare of 2002 July 23 (see Figure 2 in Lin et al., 2003).

Efficient trapping and continuous acceleration also produce the large flux and time lags of microwaves that are likely emitted by electrons with higher energies, several hundred keV (Kosugi et al., 1988). Somov et al. (2005c) believe that the lose-cone instabilities (Benz, 2002) of trapped mildly-relativistic electrons in the system of many collapsing field lines (each line with its proper time-dependent lose cone) can provide exitation of radio-waves with a very wide continuum spectrum as observed.

Qiu et al. (2004) presented a comprehensive study of the X5.6 flare on 2001 April 6. Evolution of HXRs and microwaves during the gradual phase in this flare exhibits a separation motion between two footpoints, which reflects the progressive reconnection. The gradual HXRs have a harder

and hardening spectrum compared with the impulsive component. The gradual component is also a microwave-rich event lagging the HXRs by tens of seconds. The authors propose that the collapsing-trap effect is a viable mechanism that continuously accelerates electrons in a low-density trap before they precipitate into the footpoints (see Section 7.3).

Chapter 5

Electric Currents Related to Reconnection

The topological model of a flare, with a reasonable accuracy, predicts the location of a flare energy source in the corona. In order to clarify an origin of this energy, we have to consider the non-potential part of magnetic field in an active region. In this Chapter, we discuss the main electric currents related to magnetic reconnection in a large solar flare. More specificaly, we continue a study of the Bastille day 2000 flare which topological model was considered in a previous Chapter

5.1 Magnetic reconnection in the corona

5.1.1 Plane reconnection model as a starting point

The two-dimensional (2D) reconnection models for solar flares, including the standard model, are definitely an over-simplification that cannot explain all features of actual flares. However they have to be considered to find a missing element of the flare modeling and to demonstrate how this element should be introduced into the flare interpretation. Moreover some features and predictions of the 2D models still have to be studied and clarified.

5.1.1 (a) Pre-flare evolution and energy accumulation

As in Section 3.4.2, we shall consider a *three*-component reconnection in *two* dimensions, at first. With this simplification, which will be discussed in Section 5.2.3, the separator is a straight line X in the corona as shown

in Figure 5.1a by dashed vectors X above the photospheric plane Ph. In the case of the Bastille day 2000 flare, this configuration of magnetic field corresponds to a central part of the two-dimensional cartoon picture with two magnetic dipoles (Wang et al., 2005).

To clarify notation, we start here from the classical example of 'reconnection in the plane', in the plane (x, z). A 2D model means, as usual, that all the unknown functions do not depend of the coordinate y. In addition we assume here that there is no the magnetic field component B_y which is perpendicular to the plane (x, z).

In this case illustrated by Figure 5.1a, the straight line NL is the neutral line in the photospheric plane (x, y). Above this plane, six magnetic surfaces are shown to discuss the reconnection model. In the scheme, that is usual and sufficient to describe the plane reconnection (e.g., Figure 3.1), we do not introduce the magnetic surfaces because we simply consider reconnection of magnetic field lines just in one plane, the reconnection plane (x, z), that is $y = 0$. And we 'remember' that, in all other planes with $y \neq 0$, we have the same process. This is not necessarily true in general and never true in reality, in three-dimensional configurations of the magnetic fields in solar active regions.

So it is instructive to introduce the magnetic surfaces even in the simplest situation considered here. The magnetic surface 1 in Figure 5.1a consists of the field lines which are similar to the line f_1 starting at the point a with coordinates $x = x_a$, $y = 0$, $z = 0$. The surface 2 consists of the field lines similar to f_2. For the sake of simplicity, we consider here a symmetrical case with the symmetry plane $x = 0$ for the magnetic surfaces. Hence the field lines f_1', f_2' etc have the vertical component B_z of the opposite sign with respect to the similar field lines on the opposite side of NL. Morover we have put $B_y = 0$ to see the ordinary 2D magnetic field configuration in the simplest approach to the reconnection problem.

Among the magnetic surfaces shown in Figure, two are topologically important: separatrices S_1 and S_2 cross at the separator straight line X which is parallel to NL. The separator separates the interacting magnetic fluxes by the separatrices. In addition, it is across the separator that the interacting fluxes are redistributed (more exactly, reconnected) so that the magnetic field would tend to keep a minimum energy, to remain potential, if there were no plasma.

Let Figure 5.1a describe an 'initial state' of the magnetic configuration in evolution. Starting from this state, let us introduce the *converging flow* of the photospheric footpoints (for example, two magnetic dipoles join as proposed by Wang et al., 2005). This converging flow is illustrated by Figure 5.1b by the displacement vector δx related to the photospheric velocity

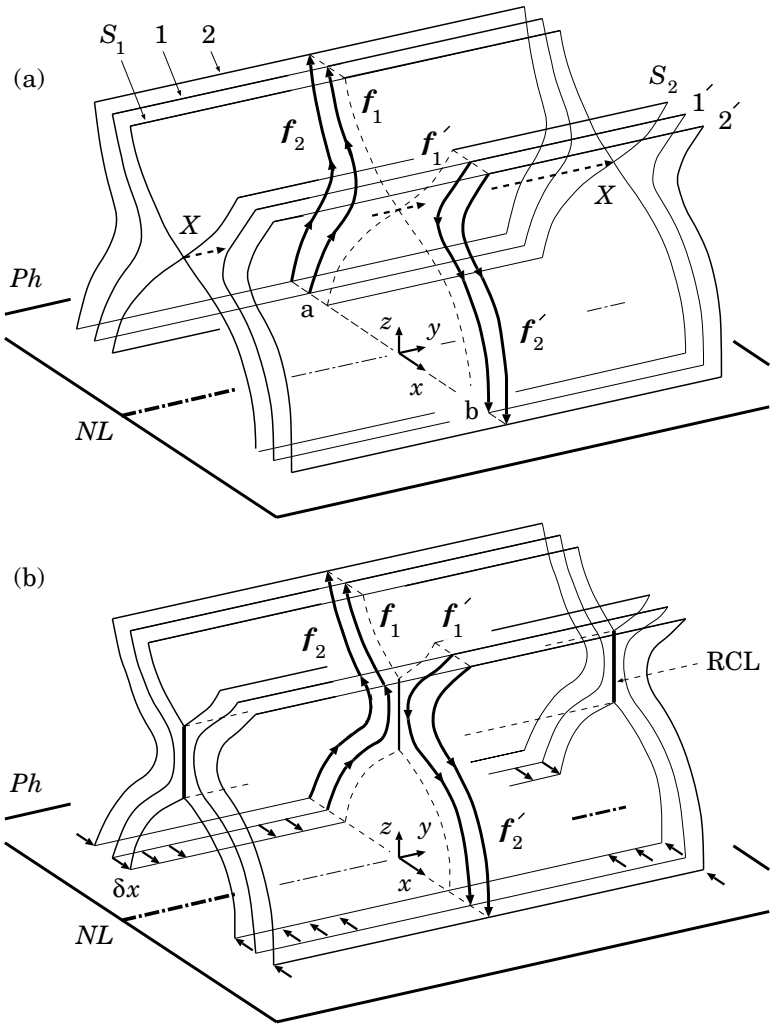

Figure 5.1: (a) An initial state of magnetic field. The separatrices S_1 and S_2 cross at the separator X. (b) The converging flows in the photosphere induce a reconnecting current layer (RCL) in the corona.

component $v_\perp$

$$\delta x = v_\perp \times \tau\,, \tag{5.1}$$

where τ is the duration of a pre-reconnection stage in the active region evolution. Some part of the magnetic fluxes, δA, would reconnect across the separator X. Here A is the y-component of the vector potential $\mathbf{A}$ defined by relation $\mathbf{B} = \mathrm{curl}\,\mathbf{A}$.

In a plasma of low resistivity, like coronal plasma, the separator plays the same role as the hyperbolic neutral line (Section 3.2.1). The slowly-reconnecting current layer (see RCL in Figure 5.1b) is developing and growing (we may call this process a 'pile-up regime') to hinder the redistribution of interacting magnetic fluxes. This results in an excess energy being stored in the form of magnetic energy of a RCL. If J is the total electric current in the RCL, b is the half-width of the current layer, then the surplus energy above that of a potential magnetic field, having the same sources in the photosphere (see Section 3.3), is equal to

$$\mathcal{E}_f = \frac{1}{2c^2} \times LJ^2\,. \tag{5.2}$$

Here

$$L \approx 2l\,\ln\,\frac{2l}{b} \tag{5.3}$$

is the self-inductance of the RCL, l being its length along the separator.

In the case of the Bastille day 2000 flare, the length of the SXR arcade was ∼120 000 km. So $l \sim 10^{10}$ cm. With a typical RCL width $b \sim 10^9$ cm (see Section 7.1), we have $\ln\,(2l/b) \approx 3$ and

$$\mathcal{E}_f \approx \frac{3}{c^2} \times l\,J^2 \sim \frac{J^2}{3 \times 10^{10}} \tag{5.4}$$

or

$$\mathcal{E}_f \sim 3 \times 10^8\,J(\mathrm{Ampere})^{\,2},\ \mathrm{erg}\,. \tag{5.5}$$

Hence the total current $J \sim 3 \times 10^{11} - 10^{12}$ Ampere is necessary for a large flare, like the Bastille day flare, to release the energy

$$\mathcal{E}_f \sim 3 \times 10^{31} - 3 \times 10^{32}\ \mathrm{erg}\,.$$

These estimates do not contradict to the estimates of the electric current based on measurements of the magnetic field components in the photosphere in the active region NOAA 9077 (Deng et al., 2001; Zhang, 2002). More exactly, a level of magnetic non-potentiality in AR NOAA 9077 seemed to be even higher before 14 July than that after the Bastille day flare and that predicted by formula (5.5). This presumably means that

some part of free energy is accumulated in surplus to the magnetic energy of the current layer, as an additional energy related to the photospheric shear and photospheric reconnection (Sections 5.2 and 5.3).

On the other hand, during the Bastille day flare, the total integrated thermal energy was $\lesssim 3\times10^{31}$ erg (Aschwanden and Alexander, 2001) which is smaller than the total energy of the flare predicted by formula (5.5). This means that significant part of the flare energy goes to the kinetic energy of the fast plasma motions (i.e. CME) and accelerated particles (Share et al., 2001).

5.1.1 (b) Flare energy release

What could be expected as a result of fast reconnection in the RCL during a flare? – Figure 5.2 illustrates such expectations. Being in a high-temperature turbulent-current state (Section 6.3) the *rapidly*-reconnecting current layer provides the powerful fluxes of the flare energy along the reconnected field lines. These fluxes, when they arrive in the upper chromosphere, create very impulsive heating of the chromospheric plasma to high temperatures. Fast electrons (accelerated and super-hot) lose their energy by Coulomb collisions with the thermal electrons of the chromospheric plasma. This creates a quick hydrodynamic and radiative response of the chromosphere (see vol. 1, Section 8.3.2) observed in SXR, EUV, and optical emission. Inelastic collisions of the fast electrons with thermal protons and other ions generate the HXR bremsstrahlung radiation. For this reason, the footpoints of the reconnected field lines also become bright in HXR.

We adopt the hypothesis that the EUV and HXR flare ribbons observed by *TRACE* and *Yohkoh* in the Bastille day flare map out the chromospheric footpoints of magnetic field lines newly linked by reconnection in the corona (Fletcher and Hudson, 2001; Masuda et al., 2001). So the bright kernels in the flare ribbons allow us to find the places in the corona where the magnetic reconnection process has the highest rate and produces the most powerful fluxes of energy.

Since the magnetic field lines f_1 and f_1' reconnect first, they create the *first reconnected line* f_1f_1' and the first pair of the chromospheric bright footpoints P_a and P_b related to this line as shown in Figure 5.2. In fact, two field lines being reconnected create two other field lines of different magnetic linkage. In Figure 5.2, there are two field lines f_1f_1': one goes down, the second moves up. In order not to obscure the simplest situation, we do not discuss in this Section the upward-moving field lines. Depending on conditions, they have complicated structure and behaviour in the upper corona and interplanetary space.

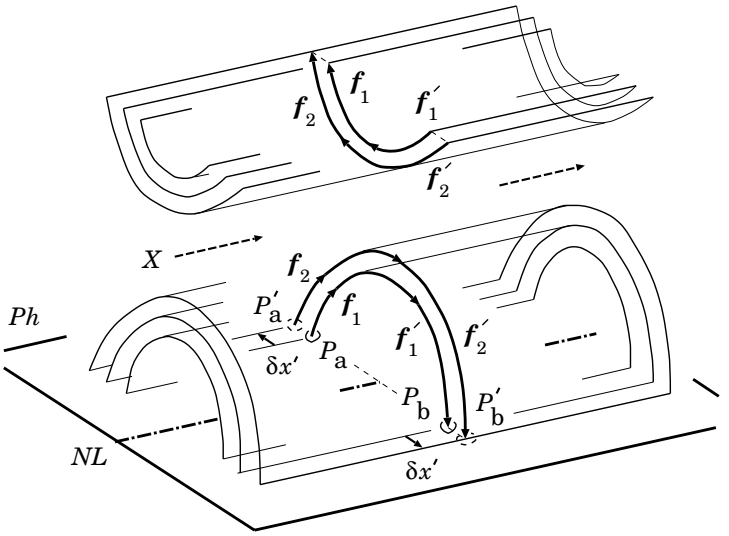

Figure 5.2: Apparent motion of footpoints during the fast reconnection process. The footpoint separation increases with time.

The field lines f_2 and f_2' will reconnect later on, for example at the end of the first HXR spike S1 described in Section 4.1. So they will create a new pair of footpoints P_a' and P_b' in different locations. Obviously the distance between the footpoints of the reconnected field lines will become larger. This is the well-known prediction of the standard model of two-ribbon flares, which is also the well-observed effect of the increasing distance between flare ribbons (Svestka, 1976; Zirin, 1988).

Wang et al. (2005) compared two *TRACE* images of the active region NOAA AR 9077 before and after the Bastille day flare on 2000 July 14. They marked the magnetic field line connections based on the *TRACE* flux loop structures. Figure 8 in Wang et al. (2005) clearly shows that, before the flare, magnetic fields connect outward in the outer border of the active region. After the flare, connectivity is most obvious between fields inside the active region and close to the photospheric neutral line. Naturally, the simple 2D model does not allow the authors to identify the two far footpoints with where the preflare fields were connected.

From the physical point of view, the predicted and observed displacement $\delta x'$, as illustrated in Figure 5.2, represents the effect of fast relaxation of the non-potential component of the magnetic field related to the RCL which has been generated by the photospheric converging motion. Note

that, in general,

$$\delta x' \neq \delta x\,. \tag{5.6}$$

In the simplest example under consideration, the reason is obvious. Let the field lines f_1 and f_1' coincide with the separatrices S_1 and S_2 of the initial state shown in Figure 5.1a. Then δx represents a photospheric displacement of the initial separatrices. For this reason, the first pair of the bright footpoints $P_{\rm a}$ and $P_{\rm b}$ shows us the real displacement of the footpoints of the initial separatrices. This is important for interpretation of the flare onset, the beginning of the first HXR spike S1.

On the other hand, the apparent footpoint displacement $\delta x'$ is directed to the new positions of the bright kernels $P_{\rm a}'$ and $P_{\rm b}'$. These are related to the footpoints of the separatrices in a final state of the magnetic field after reconnection. And the final state, in general, does not coincide with the initial one for many reasons. The main one is that presumably the magnetic field changes during a flare (Anwar et al., 1993, Kosovichev and Zharkova, 2001). It is natural to assume that

$$\delta x' \lesssim \delta x \tag{5.7}$$

since dissipation of the electric currents in solar flares is presumably never complete.

Therefore the plane reconnection model with a vertical RCL, considered here, predicts that the flare bright kernels, as they are seen in EUV, HXR or Hα, should separate in opposite directions from the photospheric neutral line, if the photospheric magnetic fields converge to this line before a flare. Note that the plane-reconnection models of solar flares with a new emerging flux and with a horizontal RCL (Syrovatskii, 1972) predict a decreasing footpoint separation (see Section 3.4.1).

From the observational point of view, however, actual solar flares are not so simple. Initially, on the basis of *Yohkoh* SXT observations, the flares with the so-called 'cusped arcade' (e.g., the well-known 21 February 1992 flare) were often considered as a clear evidence in favour of the standard 2D MHD model; see Shibata et al. (1995), Tsuneta (1996) and references there. In a deeper examination of the SXT data, Uchida et al. (1998), Morita et al., (2001) noted that there are some essential features inexplicable by the standard model. Morita et al. showed that the magnetic structure responsible for these flares, including the homologous flares, turned out to be a structure with 3D quadruple-type magnetic fields (Section 3.2.1).

5.1.2 Three-component reconnection

In the above we neglected the component of the magnetic field parallel to the separator in order to discuss the classical example of 2D reconnection.

However, under actual conditions in the solar atmosphere, reconnection always occurs in the presence of a longitudinal component. Moreover the longitudinal component of magnetic field in the vicinity of a separator has several important physical consequences for the reconnection process in solar flares (Section 6.2.2). Only those of them will be discussed below that are important for understanding the apparent motions of chromospheric ribbons and bright kernels during a large two-ribbon flare.

As in the previous example, illustrated by Figures 5.1 and 5.2, we assume that all the geometrical properties of the magnetic field are uniform in the y-direction. Now we allow the y-components of the unknown vector functions, for example the magnetic field vector $\mathbf{B}$. So the problem under consideration still remains a two-dimensional one, at least in the initial and pre-reconnection stages, until we shall make new assumption that something depends on the coordinate y. For example, we shall assume in the following Sections that the conditions for field dissipation depend on y. In this case, the problem becomes essentially three-dimensional when dissipation acts quickly at a certain region determined by a given value of y. Before we make such an assumption, the problem remains two-dimensional because there is no need and no reason to assume that the longitudinal (parallel to the separator X) magnetic field component $B_\parallel = B_y$ is uniform in the plane, i.e. in variables (x, z). On the contrary, Somov et al. (1998) assumed that each field line arrives to the separator with its own value of $B_\parallel$. The only restriction up to now is that the component $B_\parallel$ does not depend on y.

Near the separator X the longitudinal component $B_\parallel$ naturally dominates because the orthogonal (perpendicular to the separator) field $\mathbf{B}_\perp$ vanishes at the separator. For this obvious reason, the field lines passing very close to the separator become elongated in the y-direction; the separator by itself is a unique field line. This and other properties of the separator are well known since the classical work by Gorbachev et al. (1988); they will not be discussed here except one of them which is essential. The reconnection process in the RCL at the separator will just conserve the flux of the longitudinal component $B_\parallel$ (Section 6.2.2).

In other words, at the separator, the orthogonal components (i.e. the magnetic field $\mathbf{B}_\perp$) are reconnected. Therefore the orthogonal components of the magnetic field actively participate in the connectivity change, but the longitudinal one does not. Hence the longitudinal component plays a relatively passive role in the topological aspect of the process but it influences the physical properties of the RCL, in particular the reconnection rate (see Section 6.2.2). The only exception constitutes a neutral point of the magnetic field, which can appear on the separator above the photospheric plane. Gorbachev et al. (1988) showed that even very small changes in the

configuration of the magnetic field sources can lead to a rapid migration of such a neutral point along the separator and to a *topological trigger* of a solar flare.

So, in general, a three-component reconnection, i.e. the reconnection process inside a RCL which has three components of magnetic field, at the separator can proceed with an increase (or decrease) of the longitudinal component of magnetic field and, as a consequence, with an increase (or decrease) of the length of the reconnected field lines. According to Somov et al. (1998), in the more impulsive (MI) flares, the reconnection process proceeds with a decrease of the longitudinal component and hence with a decrease of the footpoint separation. The physical origin of this kind of flare is discussed in the next Section.

5.2 Photospheric shear and coronal reconnection

5.2.1 Accumulation of magnetic energy

Figure 5.3 demonstrates the action of a specified photospheric velocity field on different field lines f_1, f_2 etc placed at different magnetic surfaces 1, 2 etc. As in the previous Section, a converging flow is present in opposite sides of the neutral line NL in the photosphere Ph and creates the RCL along the separator X in the corona as shown in Figure 5.3b. In addition, now a shear flow is superposed on the converging flow in the photosphere. So the separatrices S_1 and S_2 are involved in the large-scale shear flow together with nearby surfaces 1, 2 and $1'$, $2'$. When a field line, for example the line f_1, moves in direction to NL, it becomes longer along the NL under action of the shear flow.

Figure 5.3b shows the field lines which were initially in the plane (x, z) as indicated in Figure 5.3a. Under action of the shear flow, these lines move out of the plane (x, z), except for an upper corona boundary, which is assumed, for the sake of simplicity of illustration, to be unaffected by the photospheric shear.

We assume again that reconnection is too slow to be important yet. We call this stage of the magnetic field evolution the 'pre-reconnection state'. At this stage, coming between the initial and final one, the magnetic field sources in the photosphere have been displaced to their final pre-flare positions, but the magnetic field lines have not started to reconnect yet because the plasma conductivity still can be considered as infinite. Therefore the RCL prevents the interacting fluxes from reconnection. The energy of this interaction is just the energy of the magnetic field of the current layer, as

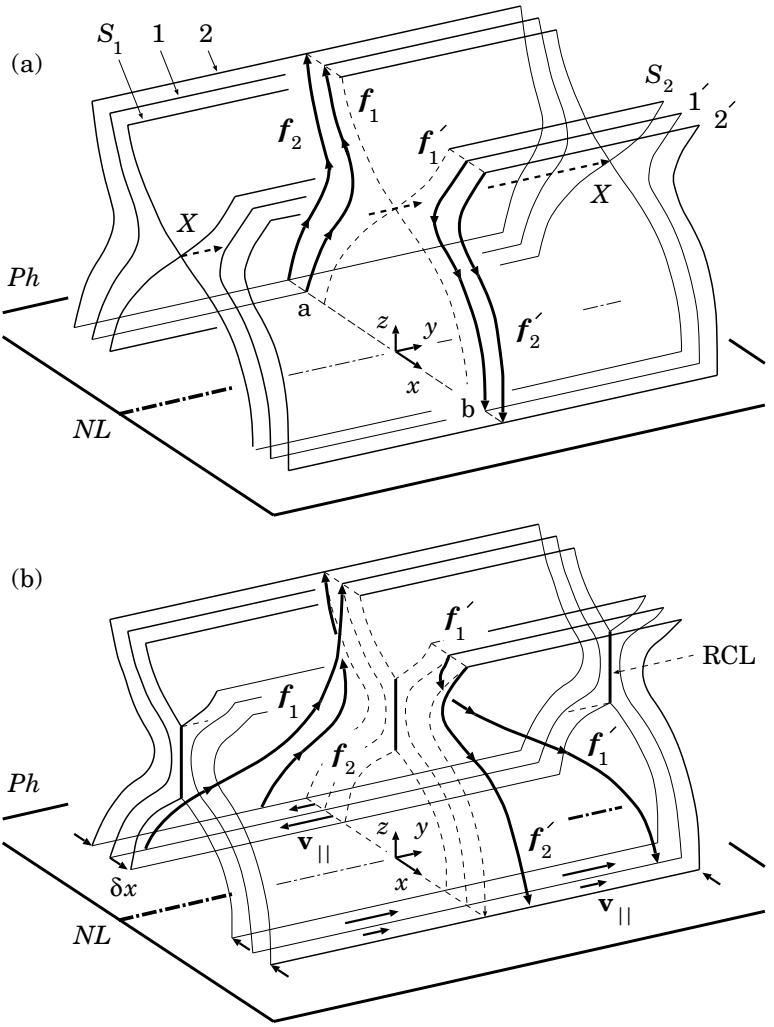

Figure 5.3: (a) The initial configuration of the magnetic field is the same as in Figure 5.1. (b) The converging photospheric flow creates the RCL at the separator X. In addition, the shear flow with velocity $\mathbf{v}_{\parallel}$ in the photosphere makes the field lines longer, thus increasing the energy in the magnetic field.

in Section 1.1.4.

Photospheric shear flows add to the energy of the pre-reconnection state an additional energy. This is the energy of magnetic tension generated by the shear because of the 'freezing-in' property of the solar plasma. The flow works on the field-plasma system, making the field lines longer. This is always true, even if there are not a separator. In addition, if the pre-flare magnetic-field configuration contains the separator, and

> if the bases of the field separatrices are involved in the large-scale photospheric shear flows, then the shear flows induce current layers extending along the separatrices, with the concentrated current flowing parallel to the orthogonal field $\mathbf{B}_\perp$

(see Sections 14.3 and 14.4). The origin of this current lies in the discontinuity of the longitudinal component $B_\parallel$ on the separatrices, created by the photospheric shear flows in the presence of the separator in the corona. Dissipation of the current during a flare leads to a decrease of the discontinuity. We call such a process the '*shear relaxation*'.

From a mathematical point of view, if the magnetic force dominates all the others, the potential or force-free field is a solution of the MHD equations for an ideal medium in the approximation of a strong field (see vol. 1, Section 13.3.1). Such a field, changing in time according to the boundary conditions in the photosphere, sets the chromospheric and coronal plasma in motion. The field remains mainly potential but accumulates non-potential components related to electric currents: (a) slowly-reconnecting current layers which are highly-concentrated currents, flowing parallel to the separator, (b) the smoothly distributed currents which are responsible for magnetic tension generated by the photospheric shear flows, (c) the concentrated currents at the separatrices, generated by the shear flows too.

As for the fast reconnection process which tends to release these excesses of magnetic energy during a flare, the main difference is that now a longitudinal magnetic field is present inside and outside the RCL. Hence we shall have a three-component reconnection as mentioned in Section 5.1.2.

5.2.2 Flare energy release and CMEs

The fast reconnection stage of a flare, that is the flare impulsive phase, is illustrated by Figure 5.4. As in the case of plane reconnection demonstrated by Figure 5.2, in Figure 5.4b only two pairs of the reconnected field lines are shown. How were they selected among the continuum of the field lines at each magnetic surface before reconnection, as they are shown in Figure 5.4a?

Note that Figure 5.4a differs from Figure 5.3b in one important respect. These figures show the same magnetic surfaces but different field lines. An additional assumption used here is that the physical conditions along the y-direction are not uniform any longer. More exactly it is assumed that the fastest reconnection place is located in vicinity of the point $y = 0$ in the RCL at the separator. For this reason, those field lines are selected which have the nearest distance to the RCL under condition $y = 0$. So just these field lines will reconnect first and quickly.

Usually, in three-dimensional topological models, the place of fast reconnection is chosen at the top of the separator. This is assumed, for example, in the model for the well-studied flare of 1980 November 5 (Sections 3.2.2 and 3.2.3). In this Section we shall not consider the upward-moving reconnected field lines in detail. They are just indicated in Figure 5.4b by a velocity vector $\mathbf{U}$. As a consequence of the three-component reconnection at the separator, the upward-moving lines may take a twisted-flux-tube shape, which may correspond to a central helical part of a CME (see Hirose et al., 2001). This seems to be consistent with observations of a rapid halo-type CME generated by the Bastille day flare (Klein et al., 2001, Manoharan et al., 2001, Zhang et al., 2001).

In general, the upward disconnection pictured in Figure 5.4b plays a central role in observed expansion of arcade loops into the upper corona and interplanetary space by creating helical fields which may still be partially connected to the Sun (Gosling et al., 1995; Crooker et al., 2002). It is now commonly used to interpret white-light signatures of CMEs. On the other hand, the low-lying SXR-arcade events associated with CMEs are interpreted as the consequent brightening of the newly formed arcade (see Figure 2 in Crooker et al., 2002). In terms of the model under consideration, the reconnected field lines below the separator shrink to form magnetic arcade loops. This part is discussed below.

5.2.3 Flare and HXR footpoints

The quickest release of energy at the top of the separator creates, at first, the pair of the chromospheric bright points $P_{\rm a}$ and $P_{\rm b}$ related to the *first* reconnected line $f_1 f_1'$. Later on the field lines f_2 and f_2', being reconnected at the point $y = 0$ in the RCL, create the field line $f_2 f_2'$ with the pair of the bright footpoints $P_{\rm a}'$ and $P_{\rm b}'$. Figure 5.4a shows only two pairs of the field lines that reconnect in the plane $y = 0$. Being reconnected, they create two pairs of the bright footpoints shown in Figure 5.4b.

The apparent displacement of the footpoints, from $P_{\rm a}$ to $P_{\rm a}'$ and from $P_{\rm b}$ to $P_{\rm b}'$, now consists of two parts: $\delta x'$ and $\delta y'$. The first one has the same meaning as in the classical 2D reconnection process (Section 5.1.1). The

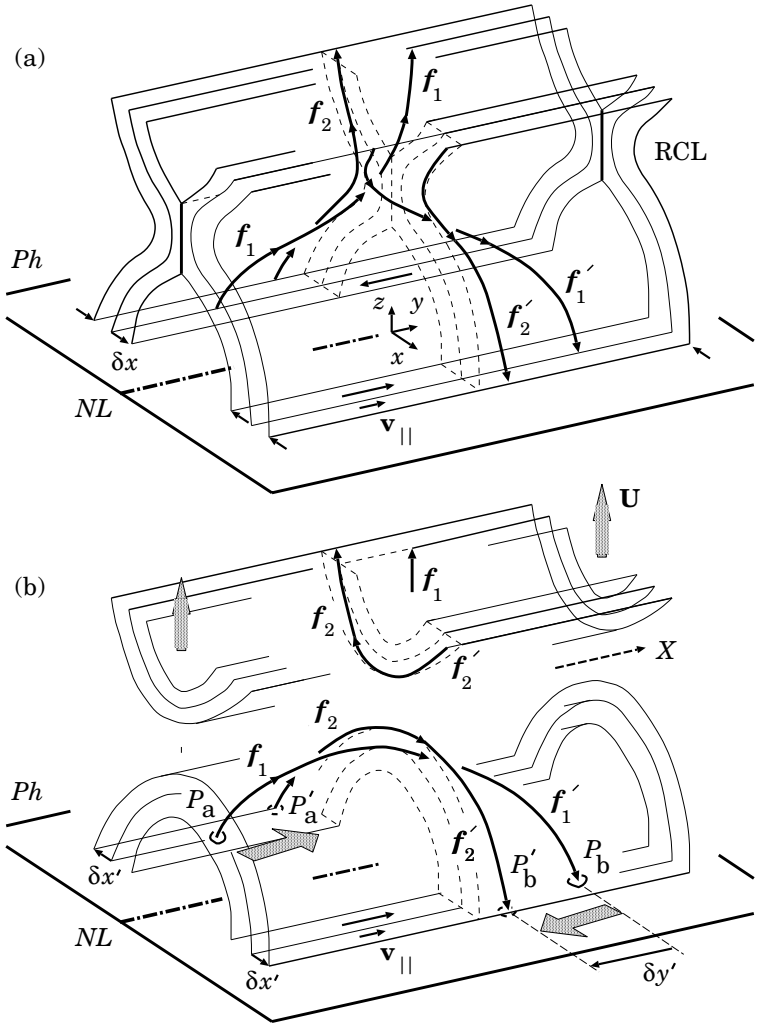

Figure 5.4: (a) A pre-reconnection state of the magnetic field in an active region with the converging and shear flows in the photosphere. The field lines are shown which are nearest to the fastest reconnection place ($y = 0$) in the RCL. (b) Rapidly decreasing footpoint separation during the 'more impulsive' Sakao-type flares.

second apparent displacement $\delta y'$ equals a distance along the y axis between footpoints of the reconnected field lines $f_1 f_1'$ and $f_2 f_2'$. This value is related to an increase of the length of the field lines on two different magnetic surfaces, generated by the photospheric shear flow along these surfaces. Therefore the displacement $\delta y'$ during a flare (or a part of its energy release as the first HXR spike S1 in the Bastille day flare) represents the effect of relaxation of the non-potential component of the magnetic field related to the photospheric shear flow.

In fact, the 'rainbow reconnection' model (Section 3.2.4) or the topological model with photospheric vortex flows (Gorbachev and Somov, 1988), which is mainly the same, predicts the existence of the converging and shear flows in the central region under the top of the separator.

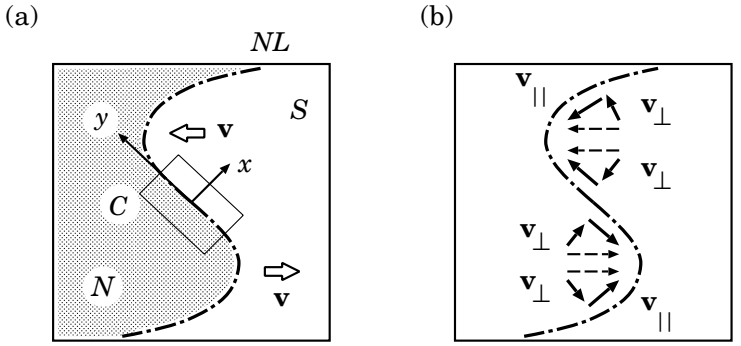

Figure 5.5: (a) A photospheric vortex flow distorts the neutral line NL. (b) A schematic decomposition of the velocity field $\mathbf{v}$ into the components parallel and perpendicular to the neutral line.

Figure 5.5 illustrates a character of the photospheric velocity field which deforms the neutral line NL. The vortex-type flow generates two components of the velocity field: parallel to NL and directed to NL. The velocity components $\mathbf{v}_{\|}$ and $\mathbf{v}_{\perp}$ are parallel and perpendicular to the photospheric neutral line NL. The first component of the velocity field provides a shear of magnetic field lines above the photospheric neutral line. The second one tends to compress the photospheric plasma near the NL and in such a way it can drive magnetic reconnection in the corona and in the photosphere (Section 5.3).

To demonstrate the basic physics in the simplest way, we considered only a central region C in the vicinity of the S-shaped neutral line NL in Figure 5.3b. Here we put the y-direction along the NL; the separator is nearly parallel to NL as was shown in Figure 5.1. In actual flares this

'central part' can be long enough to be considered in this way. The Bastille-day flare seems to be a good example of such flares because of its extremely regular appearance as a beautifully 'cylindrical arcade' in EUV and SXR (Figure 4.1), which extends more than 10^{10} cm.

In the region C, the converging flow generates the RCL in the corona above the photospheric neutral line. The shear flow creates the longer magnetic loops which must be reconnected by the RCL. Such loops, being reconnected first, provide the bright footpoints, flare kernels, with a large footpoint separation. Later on, the bright footpoints with shorter separation appear. In this way, the *more impulsive* (MI) Sakao-type flares (see definitions and properties of two sub-classes, *more impulsive* (MI) and *less impulsive* (LI) flares, in Section 3.4.2) with a decreasing footpoint separation can appear in active regions. This is consistent with the model by Somov et al. (1998).

Why does the footpoint separation increase in the LI flares? – This may be the case when the velocity of the photospheric shear flow decreases near NL. Hence the second field line f_2 arrives to the separator with a stronger longitudinal field than the first, i.e. $B_{\parallel 2} > B_{\parallel 1}$. This can make the reconnection process slower, because the longitudinal field makes the solar plasma less compressible, and the flare less impulsive. However the longitudinal field does not have an overwhelming effect on the parameters of the current layer and the reconnection rate (Section 6.2.2). This might be especially true if the compression of the plasma inside the current layer is not high since its temperature is very high.

What seems to be more efficient is the following. In the LI flares, after reconnection, the reconnected field line f_2 will be longer than the line f_1 as illustrated by Figure 3.13a. (It means that reconnection proceeds in the direction of a stronger shear in the LI flares.) So the energy of a longitudinal component of magnetic field becomes larger after reconnection of the shear-related currents (Section 14.4). On the contrary, in the MI flares, the reconnection process tends to decrease both excesses of energy: (a) the magnetic energy which comes from the converging flows in the photosphere, i.e. the magnetic energy of RCL, and (b) the energy taken by coronal magnetic fields from the photospheric shear flows. Presumably this circumstance makes the MI flares more impulsive.

We have proposed above that, before the large two-ribbon flares with observed decrease of footpoint separation,

> the separatrices are involved in a large-scale shear photospheric flow in the presence of an RCL generated by a converging flow.

This seems to be consistent with conclusion by Schrijver et al. (2005) that shear flows do not by themselves drive enhanced flaring or coronal

nonpotentiality. These properties related to coronal free energy require appropriately complex and dynamic flux emergence within the preceding $\sim 10 - 30$ hr. The magnetic and velocity field distributions in the photosphere, more complicated than the simple shear, are necessary to create large solar flares.

For example, Hénoux and Somov (1987) considered an active complex with four magnetic sources of interchanging polarities in the photosphere and vortex-type flows in the photosphere around each source. Two systems of large-scale coronal currents are distributed inside two different magnetic cells. These currents are interacting and reconnecting at the separator together with reconnecting magnetic-field lines (see Section 14.2.1). Such a process may play a significant role in the dynamics of large solar flares because of a topological interruption of the electric currents.

Even the scenario with the converging and shear flows considered above (Somov et al., 2002a) is still incomplete unless it does not take into account the presence and eruption of a long twisted filament along the photospheric neutral line before the flare (Liu and Zhang, 2001; Yan et al., 2001; Zhang et al., 2001). Bearing this morphological fact in mind, we are going to consider some physical processes in the close vicinity of the polarity reversal line NL in the photosphere.

5.3 Shear flows and photospheric reconnection

Let us return to Figure 5.3 and consider only the nearest vicinity of the photospheric neutral line NL. So, on the one hand, the separatrices are outside of the region under consideration but, on the contrary, the effects related directly with NL become dominant. In the case of the Bastille day flare, the typical distance between the separatrices is $\sim 3 \times 10^9$ cm. The width of the region which we are going to consider $\lesssim 3 \times 10^8$ cm.

The converging flow toward the polarity reversal line can cause the opposite-polarity magnetic fields to collide in the photosphere and subsequently drive magnetic reconnection there. Converging flows in the photosphere have been reported from many observations (see Martin, 1998; Kosovichev and Zharkova, 2001). Morover the flux cancellation - defined by the mutual disappearance of positive magnetic flux and negative one - has been frequently observed in association with the formation of a quiet pre-flare filament prominence (Martin et al., 1985, Martin, 1986; Chae et al., 2001; Zhang et al., 2001).

Figure 5.6 illustrates the possibility of a photospheric reconnection pro-

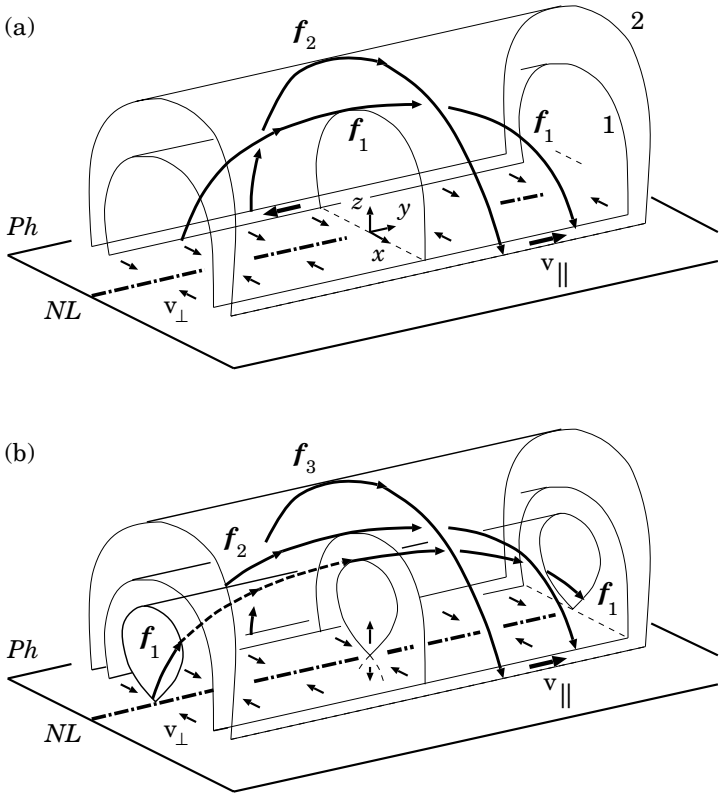

Figure 5.6: (a) The converging and shear flows in the photosphere act on the magnetic field lines near the neutral line NL. (b) Photospheric reconnection and filament formation.

cess in the presence of the photospheric shear flow. We assume that the initial magnetic field is mainly a potential one sufficiently high above the photosphere, so that the field lines pass above the photospheric neutral line NL more or less at right angles. However, due to a shear flow, the footpoints on either side of the NL are displaced along it in opposite directions. This process produces a non-potential magnetic structure, shown in Figure 5.6a, in which the projections of the field lines onto the photospheric plane Ph are more closely aligned with the NL. A motion toward the NL brings the footpoints closer together and further enhances the magnetic shear. Moreover the converging flow makes the opposite-polarity magnetic fluxes interact and subsequently drives their reconnection in the photo-

sphere, shown in Figure 5.6b.

The reconnection changes the topology of the field lines arriving at the neutral line NL. They become disconnected from the photospheric plane inside the prominence body. Since the reconnection conserves the flux of the longitudinal magnetic field generated by the shear flow, the photospheric reconnection leads to the formation of helical field lines which are capable, in principle, of supporting the prominence plasma (van Ballegooijen and Martens, 1989).

Filament eruptions in active regions are sometimes an integral part of the phenomena associated with a large two-ribbon flare. Let us assume that, at the beginning of a flare, the prominence erupts and disrupts the magnetic field configuration shown in Figure 5.6b. In this case, because of fast energy transport along the field lines, the first field line f_1 will be energized first and will creates the bright footpoints $P_{\rm a}$ and $P_{\rm b}$ as shown in Figure 5.4b. More exactly, the upward-directed reconnection outflow produces a long low loop with the footpoints $P_{\rm a}$ and $P_{\rm b}$. However the downward-directed reconnection outflow creates a short loop (cf. Figure 1 in van Ballegooijen and Martens, 1989), which submerges, remaining under the photospheric RCL. Next the field line f_2 will become bright and will create the bright footpoints $P'_{\rm a}$ and $P'_{\rm b}$.

Hence a general tendency in the kernel behaviour should be similar to that one as for the coronal collisenless reconnection, but such kinetic phenomena as acceleration of charged particles, their trapping and precipitation are questionable because of high density and low ionization of the photospheric plasma. An essential aspect of photospheric reconnection is that the atoms have no trouble flowing accross the magnetic field lines, the ions are not entirely constrained to follow the field lines as this should be in ordinary MHD.

The remarkable thing about photospheric reconnection is predicted by the model (Litvinenko and Somov, 1994b): reconnection effectively occurs only near the temperature minimum. Here the resistivity is especially high, and an RCL forms where reconnection proceeds at a rate imposed by the horizontal converging flows of the photospheric plasma. Magnetic energy is transformed into the thermal and kinetic energy of the resulting vertical motions as shown in the central part of Figure 5.6b. The upward flux of matter through the photospheric RCL into corona is capable of supplying 10^{17} g of cold weakly-ionized plasma in a time of 10^5 s. This is amply sufficient for the formation of a huge filament prominence.

However, in the pre-flare stage, when the height h of such a filament is presumably comparable with its width, so $h \lesssim 10^9$ cm, see Figure 2 in Liu and Zhang (2001) or Figure 1 in Zhang et al. (2001), the gravitational

energy of the filament

$$\mathcal{E}_{grav} = mgh \lesssim 10^{17}\,\mathrm{g} \times 3 \times 10^{4}\,\mathrm{cm\ s^{-2}} \times 10^{9}\,\mathrm{cm} \sim 3 \times 10^{30}\,\mathrm{erg} \quad (5.8)$$

is large but still much smaller than the total energy of a large two-ribbon flare $\mathcal{E}_{fl} \sim (1-3) \times 10^{32}$ erg. Moreover this mass requires an additional energy to accelerate it outwards, as typically observed. Therefore the flare energy has to be accumulated in other forms to push plasma upward (see Litvinenko and Somov, 1994a, 2001).

In the Bastille day flare, the observations of TRACE in 171 and 195 A together with the synchronous ground-based Hβ observations at HSOS showed that the filament rupture at some point at 09:48 UT activated the south-west part of the active region. At 10:10 UT a surge erupted, and a two-ribbon flare started to develop rapidly along the photospheric neutral line (Liu and Zhang, 2001). For this reason, we believe that the photospheric reconnection and filament eruption played a triggering role in this flare.

5.4 Motions of the HXR footpoints in flares

5.4.1 The footpoint motions in some flares

It is well known that the standard model of a flare (see Kopp and Pneuman, 1976; Forbes and Acton, 1996) predicts an increasing separation motion of the footpoint (FP) sources as new field lines reconnect at higher and higher altitudes. First results of *RHESSI* observations (Fletcher and Hudson, 2002; Krucker et al., 2003) confirm regular but more complex FP motions than the standard model predicts. Krucker et al. (2003) studied the HXR source motions in the 2002 July 23 flare. Above 30 keV, at least three sources were observed during the impulsive phase. One FP source moved along the photospheric neutral line (NL) at a speed of about 50 km/s.

Asai et al. (2003) examined the fine structure inside Hα-ribbons during the X2.3 flare on 2001 April 10. They identified the conjugate Hα-kernels in both ribbons and found that the pairs of the kernels were related to the FPs of the postflare loops seen in the *TRACE* 171 Å images. As the flare progresses, the loops and pairs of Hα kernels moved from the strongly-sheared to the less-sheared configuration. For the X5.7 two-ribbon "Bastille-day" flare on 2000 July 14, the motions of bright HXR kernels from strong-to-weak sheared structure were also observed in the HXR ribbons (Masuda et al., 2001; Somov et al., 2002a). This fact is consistent with the FP motions predicted by the Somov et al. (1998) model for the MI flares.

Somov et al. (2002a) suggested that, during two days before the Bastille-day flare, the bases of magnetic separatrices were slowly moved by the large-scale photospheric flows of two types. First, the shear flows, which are parallel to the NL, increase the length of field lines in the corona and produce an excess of energy related to magnetic shear. Second, the converging flows, i.e. the flows directed to the NL, create preflare current layers in the corona and provide an excess of energy as a magnetic energy of these layers. During the flare, both excesses of energy are quickly released. Thus, the structure of magnetic field (its topology) and its slow evolution during the days before a flare determine the nature of the flare, more exactly the way of magnetic energy accumulation in an active region and energy release during the flare.

5.4.2 Statistics of the footpoint motions

From 1991 September to 2001 December, the *Yohkoh* Hard X-Ray Telescope (HXT) observed about 2000 flares in an energy range above 30 keV. According to the results of analysis of 28 flares, Sakao (1994) inferred that a double source structure (Figure 3.12) is the most frequent type in an energy range above 30 keV. Sakao et al. (1998) studied the spatial evolution of 14 flares around the peaking time of the M2-band (33–53 keV) emission. For all the flares selected, the separation between the sources was analyzed as a function of time. In 7 flares, the FPs moved from each other (the separation velocity $v_{sep} > 0$). The rest of the flares showed decreasing FP separation ($v_{sep} < 0$) or did not show either increasing or decreasing separation of the FPs ($v_{sep} \sim 0$).

These two types of the FP motions were related to the two subclasses of impulsive flares (Sakao et al., 1998). The flares with $v_{sep} > 0$ are *less impulsive* (LI): they have a longer duration in the impulsive phase. The flares with a decreasing FP separation are *more impulsive* (MI). However the electron acceleration proceeds with the same high efficiency in the both subclasses of flares; that seemed to be a little bit strange.

Somov et al. (2005a) selected 72 flares according to the following criteria: (a) the integral photon count of HXRs in the M2-band is greater than 1000 counts per subcollimator, (b) an active region is within 45° of the center of the solar disk.

The important result is that about 80 % of the sources studied have $V > 3\,\sigma$. Here the average velocity V and the velocity dispersion σ were determined by a linear regression for each of the 198 intense sources that are presumably the chromospheric footpoints (FPs) of flare loops. This fact strongly suggests that: (a) the *moving* sources are usually observed rather than stationary ones, and (b) the *regular* motion of HXR sources during

the impulsive phase of flares is rather a general rule than an exception.

In order to reveal the observable types of the FP motions, a significant part of the HXT images (for 43 of 72 flares) were overlayed on the *SOHO* MDI photospheric magnetograms. To relate the source motions to magnetic fields, the fields were characterized by a photospheric neutral line (NL) or a *smoothed*, *simplified* neutral line (SNL; Gorbachev and Somov, 1989). By so doing, the following types of FP motions relative to the SNL can be conditionally distinguished.

5.4.3 The FP motions orthogonal to the SNL

In the type I, the HXR sources move mainly away and nearly perpendicular to the SNL. A fraction of such flares appears to be very small: only 2 out of 43 flares. One of them, the M7.1 flare on 1998 September 23 at 06:56 UT, is shown in Figure 5.7.

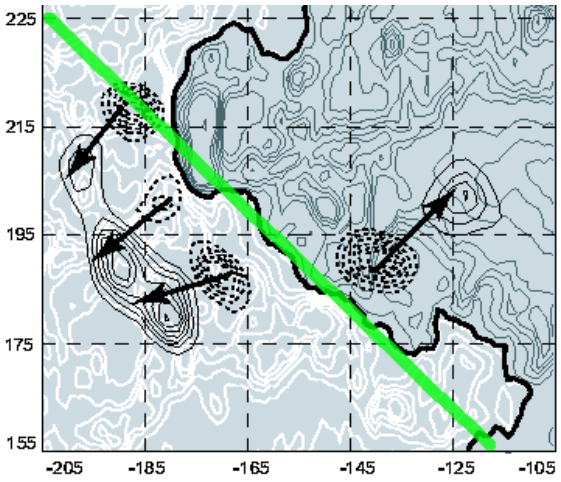

Figure 5.7: Position and motion of the HXR sources in the flare on 1998 September 23. The field of view is $100'' \times 83''$. The beginnings of arrows correspond to the time 06:56:09 UT, the ends are at 07:08:54 UT. The straight semi-transparent line represents the simplified neutral line (SNL).

The maximal value of velocity in this flare, $V \approx 20$ km s^{-1}, does not contradict to the typical velocities of the Hα-ribbon separation in solar flares (e.g., Svestka, 1976). However, even in this flare, the question appears how to draw a simplified NL. Presumably the flare does not represent a

clear example of the type I flares. The second flare, the X1.0 flare on 2001 November 4 at 16:09 UT, is not free from the same question either. The simple (arithmetical) mean value of the HXR source motion velocity equals 15 $\mathrm{km\,s^{-1}}$ in two flares of the type I.

In general, the direction of HXR source motions in a flare depends mainly on the magnetic field configuration. During a flare, reconnection provides powerful fluxes of energy along the reconnected field lines. As the flare progresses, the FPs of newly reconnected lines move away from the NL with a velocity which is proportional to the rate of reconnection. This is the well-known prediction of the standard model, explaining the effect of the increasing separation between flare ribbons. However we see that actual flares are usually not so simple as the standard model predicts. Under actual conditions in the solar atmosphere, reconnection always occurs in a more complicated configuration of field: at least, in the presence of the field component which is parallel to the SNL. As a consequence, the other types of FP motions dominate in flares.

5.4.4 The FP motions along the SNL

In many flares, the apparent displacements of FPs are directed mainly along the SNL. There are two types of such motions: the FP sources move in anti-parallel directions (type II) or they move in the same direction (type III).

5.4.4 (a) The type II of FP motions

The type II motions were found in 11 out of the 43 flares. Figure 5.8 shows the M4.4 flare on 2000 October 29 at 01:46 UT as a clear example of the type II. In this flare, the maximal value of the FP motion velocity, $V \approx 65$ $\mathrm{km\,s^{-1}}$, is significantly larger than that for the flare Hα ribbons. This implies that the FPs mainly move along the ribbons, i.e. along the SNL, similar to the 2000 July 14 flare.

Note that, in general, it may be not simple to distinguish a flare with an increasing FP separation from a flare with a decreasing separation. Both kinds of separations can be present in the same flare of the type II. In the onset of a flare, the HXR sources move one to another and the distance between them decreases. Then they pass through a 'critical point'. At this moment, the line connecting the sources is nearly perpendicular to the SNL. After that moment, the sources move one from other with increasing separation between them. All these stages are seen in Figure 5.8. Such a motion pattern seems to be close to that one predicted by the rainbow reconnection model (a sheared vortex flow in the photosphere) assumed by Somov et al. (2002a) for the Bastille day flare.

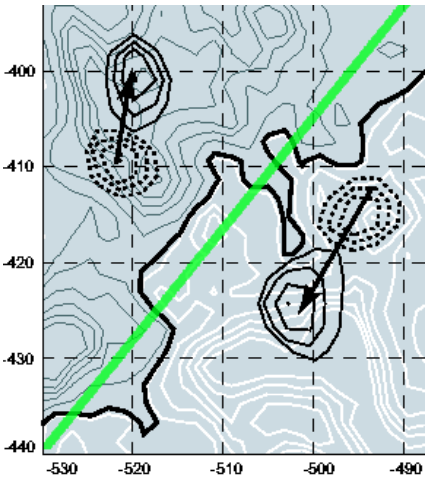

Figure 5.8: Position and motion of the HXR sources in the flare on 1998 September 23. The field of view is $100'' \times 83''$. The beginnings of arrows correspond to the time 06:56:09 UT, the ends are at 07:08:54 UT. The straight semi-transparent line represents the simplified neutral line (SNL).

Note also that, in some flares (e.g., the flare on 1991 November 15 at 22:37 UT), the separation between the FP sources does not increase monotonically but rather shows repeated episodes of small increase and small decrease, while the overall separation increasing. Recall that our simple code makes such deviations smooth and provides only the average velocity, $V \approx 58$ km s^{-1}. Thus it is not possible to give a physical classification of flares by dividing them into two wide categories (with converging or diverging FP motions) without considering how these motions are orientated relative to the SNL.

As for the physical interpretation of the type II motions, the antiparallel motions of the HXR sources presumably represent the effect of relaxation of the non-potential shear component of magnetic field (Somov et al., 2003b). In contrast to the standard model, such configurations accumulate a sufficient amount of energy for a large flare in the form of magnetic energy of a sheared field.

How are such sheared 3D structures formed? – Large-scale photospheric flows of vortex type play a leading role in this process. They deform the SNL in such way that it acquires the shape of the letter S, as shown in Figure 5.5, proved that such distortion of the NL leads to the separator appearance in the corona above the NL (see Figure 3.10). Developing this idea, we

assume that a causal connection exists between the type I and type II flares and the S-shaped bend of the SNL. The vortex flow generates two components of the velocity. The first one is directed to the NL and tends to compress the photospheric plasma near the NL. In such a way, it can drive magnetic reconnection in the corona and photosphere (Section 5.1). The second component is parallel to the NL and provides a shear of coronal magnetic-field lines above the photospheric NL (Section 5.2).

5.4.4 (b) The type III of FP motions

Contrary to the type II, in the type III flares, the HXR sources move along the SNL in the same direction as shown in Figure 5.9.

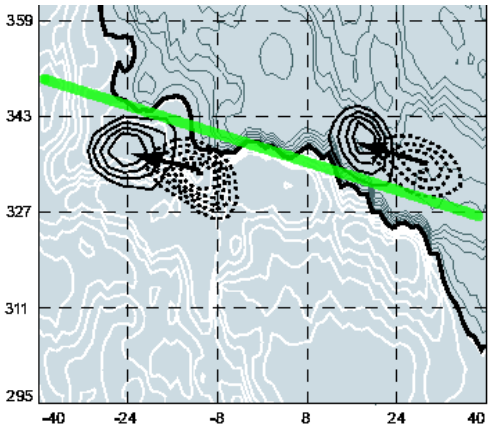

Figure 5.9: The type III motions of the HXR sources in the X1.2 flare on 2000 June 7 at 15:44:06 – 15:46:46 UT. The field of view is $80'' \times 66''$.

We can see here the X1.2 flare on 2000 June 7 at 15:44 UT, in which both FP sources move with velocity of about 60 km s^{-1} parallel to the SNL. This fact suggests that an acceleration region in the corona also moves in the same direction during the flare. In terms of the rainbow reconnection model, it means that the fastest reconnection place located at the separator moves along the separator. This pattern of motions was found in 13 flares.

In addition, there were 8 flares in which the motions away from the SNL were mixed with the other type motions. For example, in the X2.0 flare on 2001 April 12 at 10:15 UT, shown in Figure 5.10, the projections of the motion vectors on the SNL are not small. This flare represents a superposition of the types I and II. The maximal value of velocity is not large:

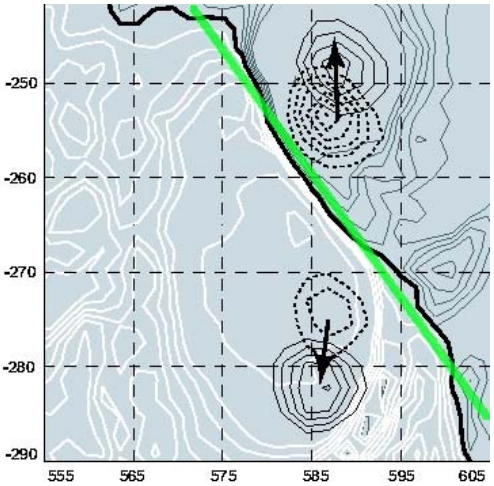

Figure 5.10: The motions of HXR sources representing a combination of the type I and type II in the X2.0 flare on 2001 April 12 at 10:15:34 – 10:20:19 UT. The field of view is $50'' \times 48''$.

$V \approx 21$ km s^{-1}. In the absence of information about the photospheric magnetic field, this flare would be classified as a typical LI flare.

5.4.5 Discussion of statistical results

Following the rainbow reconnection model of a two-ribbon flare, we consider the HXR source motions during the impulsive phase of a flare as the chromospheric signature of the progressive reconnection in the corona. Since the FPs of newly reconnected field lines move from those of previously reconnected lines, the places of electron precipitation into the chromosphere change their position during the flare. In order to study the relationship between the direction of motions and the configuration of magnetic field in an active region, we have coaligned the HXT images in 43 flares with MDI magnetograms. In this way, we have inferred that there are three main types of the FP motions (Somov et al., 2005a; for more detail and better statistics see Bogachev et al., 2005).

The type I represents the motions of FP sources away from and nearly perpendicular to the SNL, predicted by the standard model of a flare. However only less than 5 % of flares show this pattern of motions. The standard model is a strong oversimplification that cannot explain even the main fea-

tures of actual flares. The evolution of the HXR emitting sources is so complex that it is hardly explained with a simplified model such as the standard model.

In the type II flares, the HXR sources on the both sides of the SNL move along the SNL in the opposite directions. Such motions were found in 26 % of the flares. This type of motions indicates that the reconnected field lines are highly sheared and the shear angle changes as the flare evolves.

We assume that, before a flare, the shear flows in the photosphere add to the energy of the pre-flare state of an active region an additional energy. It is the energy of magnetic tension generated by the shear because of the freezing-in property of the solar plasma. The photospheric flows work on the field-plasma system, making the field lines longer. This is always true, even if there are neither a separator nor separatrices of the magnetic field above the photosphere. In such a case, the electric currents responsible for tension are smoothly distributed in a coronal volume above a region of photospheric shear.

If the pre-flare configuration of magnetic field contains separatrices, then the shear flows induce the layers of concentrated currents extending along the separatrices. The origin of these currents lies in the discontinuity of magnetic field on the separatrices (see Section 14.3.3). During a flare, reconnection and dissipation of the concentrated current leads to a decrease of the discontinuity. We call such a process the 'shear relaxation' (e.g., Somov et al. 2003b). At the same time, the observed evolution from "sheared-" to "less-sheared-" and "relaxed-" HXR pairs also demonstrates the evolution of the flare and post-flare loops.

The simple mean value of the FP source velocity in the type II flares is of about 35-40 $\mathrm{km\,s^{-1}}$ is significantly larger than the mean velocity in the type I flares, $\approx$15 $\mathrm{km\,s^{-1}}$. Statistics is not sufficiently high to say whether or not the HXR sources are distributed over velocities by the Gaussian law however the maximum of distribution is well located near the mean velocity. The difference which we have found between numbers of flares of the type I and type II means that the highly-sheared magnetic structures are much more favorable for flare production than simple 2D configurations without the shear flows in the photosphere.

The type III is similar to the type II except the HXR sources move in the same direction along the SNL. This happens in about 30 % of flares. The parallel motions of the FPs is presumably the chromospheric signature of a 'horizontal' displacement of the particle acceleration region in the corona during a flare. The simple mean velocity is also of about 35-40 $\mathrm{km\,s^{-1}}$. The Hα observations by Wang et al. (2003) indicate that an electric field in the corona is not uniform along the RCL at the separator. The peak point of the electric field (related to a region of the most powerful energy release

and particle acceleration) can change its position during the flare, moving along the separator. Corollary, all three HXR sources (the loop-top source and two FP sources) move in the same direction along the SNL.

We have not found any flare in that both HXR sources move towards the SNL. Thus all the other motion patterns could be described in the first approximation as a combination of these three basic types. In fact, 19 % of flares show the FP motions away from the SNL mixed with other two type motions. Only about 20 % of flares seem to be more complicated in the motion scale under consideration. This is not surprizing since we know that large and well resolved flares involve multiple loops with complex structure. For such flares, the loop top and associated FP sources are not readily identified and separated.

A dominant part (≈ 80 %) of the 43 flares shows a clear or mixed pattern of the HXR source motions, leading us to the idea that the types I to III are really the three fundamental components of the FP motions. This seems to be reasonable because of the following three relationships. The type I represents the reconnection in the corona. The type II motion indicates the shear relaxations. And the type III is presumably related with a motion of the fastest reconnection place along the arcade, along the separator.

What are the reasons of the apparent prevalence of one or two components over the other in different flares? We hope to find an explanation in different topological and physical conditions, we expect that this will help reveal the underlying physics. We have studied the relationship between the HXR sources in a flare and the configuration of magnetic field in an active region. However, it is clear that not only the structure of magnetic field (more exactly, its topology) but also its slow evolution before a flare determines the nature of the flare, at least the way of magnetic energy accumulation in an active region and energy release during the flare. Therefore, in a future research, we have to analyze not only distribution of photospheric magnetic fields (in order to reconstruct topology of coronal fields) but also their evolution during sufficiently long time before a flare.

5.5 Open issues and some conclusions

On the basis of what we saw above, we assume that the Bastille day 2000 flare energy was accumulated in the following forms.

(a) Magnetic energy of the slowly-reconnecting current layer (RCL) at the separator in the corona. This excess energy in the amount sufficient to produce a large two-ribbon flare, like the Bastille day flare, can be accumulated in the pre-flare active region and can be quickly transformed into observed forms of the flare energy if the RCL becomes a super-hot

turbulent-current layer (SHTCL, see Section 6.3).

(b) The magnetic energy of the current layers at the separatices and the distributed currents generated in the pre-flare active region by the photospheric shear flows, seems to be sufficiently high to influence the main reconnection process at the separator in the Bastille day flare. In general, the energy of a large-scale ($\gtrsim 10^9$ cm) sheared component of magnetic field participates in energetics of the main reconnection process in the corona presumably with a positive (negative) contribution in more (less) impulsive Sakao-type flares.

(c) In the vicinity of the photospheric neutral line, some part of energy is also accumulated as the energy of the sheared magnetic field and twisted filament. It is not clear, however, if we could consider this to be a part of the pre-flare configuration in the force-free approximation which would be the simplest model for a magnetic field configuration to compute and analyze its surplus energy. But the non-magnetic forces, including the gas pressure gradient in a high-β (high-density and high-temperature) plasma, the inertia-type (proportional to $\partial \mathbf{v}/\partial t + (\mathbf{v} \cdot \nabla)\mathbf{v}$) term, in particular the centrifugal force (Shibasaki, 2001), can make the non-force-free part locally significant in the pre-flare structure of an active region. Unfortunately we do not know the value of the related energy excess either observationally or theoretically.

The non-force-free component participates in the flare development process, but we do not know from observations whether it playes the primary role in a flare triggering or it is initiated somehow by reconnection at the separator (e.g., Uchida et al., 1998). For example, Antiochos et al. (1999), Aulanier et al. (2000) proposed that reconnection in the corona, above a sheared neutral line, removes a magnetic flux that tends to hold down the sheared low-lying field and thereby allows the sheared field to erupt explosively outward. *Yohkoh*, *SOHO* and *TRACE* data do not seem to be capable of providing the necessary information to make a choice between these two possibilities. We hope this problem will be well investigated with the coming *Solar-B* mission (see Section 14.6).

Reconnection at two levels (in the corona and in the photosphere) plays different roles in solar flares. Photospheric reconnection seems to be mainly responsible for supply of a cold dense plasma upward, into pre-flare filament prominences. Wang and Shi (1993) suggested however that the photospheric reconnection transports the magnetic energy and complexity into the rather large-scale structure higher in the corona. According to Deng et al. (2001), the effect of photospheric reconnection was manifested by the change of non-potentiality at least nine hours before the Bastille day flare. The energy was gradually input into the higher solar levels. Therefore the slow magnetic reconnection in the photosphere, observed as magnetic flux

cancellation, seems to play a key role in the energy build-up process.

Two level reconnection in solar flares has been modeled by Kusano (2005) by numerical integration of the 3D dissipative MHD equations, in those the pressure gradient force and the density variation are neglected. The simulation is initiated by adding a small 3D perturbation to a quasi-static 2D equilibrium, in which the magnetic shear is reversed near the magnetic neutral line in the photosphere. This initial state is given by the solution of the linear force-free field equation.

The simulation results indicate that magnetic reconnection driven by the resistive tearing mode instability (see Chapter 11) growing on the magnetic shear inversion layer (cf. Figure 5.6) can cause the spontaneous formation of sigmoidal structure. The reconnection of the tearing instability works to eliminate the reversed-shear magnetic field in the lower corona. Furthermore, it is also numerically demonstrated that the formation of the sigmoids can be followed by the explosive energy liberation, if the sigmoids contain sufficient magnetic flux.

Coronal reconnection, being slow before a flare, allows to accumulate a sufficient amount of magnetic energy. During a flare, the fast reconnection process in the corona, converts this excess of energy into kinetic and thermal energies of fast particles and super-hot plasma. As for the physical mechanism of the Bastille day flare, we assume that it is the collisionless three-component reconnection at the separator in the corona (Somov et al., 1998, 2002a).

More specifically, we assume that before the large-scale two-ribbon flares with an observed significant decrease of the footpoint separation, like the Bastille day flare, two conditions are satisfied. First, the separatrices are involved in the large-scale shear photospheric flow, which can be traced by proper motions of main sunspots. The second condition is the presence of an RCL generated by large-scale converging motion of the same spots. These two conditions seem to be sufficient ones for an active region to produce a huge two-ribbon flare similar to the Bastille day flare. Other realizations of large solar flares are possible, of course, but this one seems to be the most favourable situation. At least, in addition to the flare HXR ribbons and kernels, it explains formation of the twisted filament prominences along the photospheric neutral line before and after the Bastille day flare.

This page intentionally blank

Chapter 6

Models of Reconnecting Current Layers

Reconnection in cosmic plasma serves as a highly efficient engine to convert magnetic energy into thermal and kinetic energies of plasma flows and accelerated particles. Stationary models of the reconnection in current layers are considered in this Chapter. Properties of a stationary current layer strongly depends on a state of plasma turbulence inside it.

6.1 Magnetically neutral current layers

6.1.1 The simplest MHD model

Let us consider two consequent approximations used to study the reconnection process in current layers. The first of them was the *neutral* current layer model (Sweet, 1969; Parker, 1979; Syrovatskii, 1981). This was initially the simplest two-dimensional (2D) configuration of steady reconnection. Two oppositely directed magnetic fields are pushed together into the neutral layer as shown in Figure 6.1. The uniform field $\mathbf{B}_0$ immediately outside the layer is frozen into the uniform plasma inflow with a velocity $\mathbf{v}_0$ perpendicular to the field. The plasma flows out of the neutral layer through its edges with a large velocity $\mathbf{v}_1$ perpendicular to the velocity $\mathbf{v}_0$.

The strength of the magnetic field, B_0, on the inflow sides of the neutral layer can be found out, for example, from the analytical solution of the problem for the vertical current layer in the solar corona above a dipole source of the field in the photosphere (Somov and Syrovatskii, 1972). This

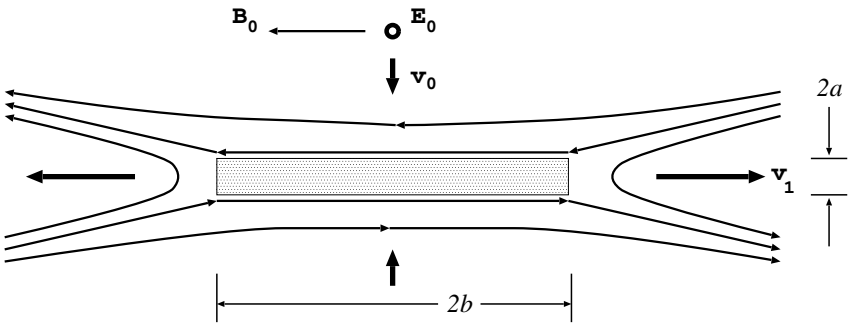

Figure 6.1: A schematic drawing of the field lines undergoing reconnection across the neutral current layer according to Sweet-Parker model.

would be just the case of the so-called 'standard model' for a two-ribbon flare (see Tsuneta, 1996, and references there). The strength of the electric field, E_0, near the current layer can be estimated for a given value of the velocity v_0 for the coronal plasma inflow into the reconnecting current layer (RCL) and for a given value of the magnetic field B_0.

By definition, there is no magnetic field inside the neutral layer; that is why it is called a *neutral* or, more exactly, a *magnetically neutral* RCL. This oversimpified approximation seems to be good, however, only for a low-temperature RCL, for example, for cold dense pre-flare current layers because heat conduction does not play any role in the energy balance for such RCL (Section 6.1.2). Although it is a strong idealization, the approximation of a neutral layer is still useful for several reasons.

First, the neutral layer approximation demonstrates the existence of two linear scales corresponding to two different physical processes. (a) The layer half-thickness

$$a \approx \frac{\nu_m}{v_0} \tag{6.1}$$

is the dissipative scale responsible for the rate of reconnection; here $\nu_m = c^2\,(4\pi\sigma)^{-1}$ is the magnetic diffusivity. (b) The layer width $2b$ is responsible for the accumulation of magnetic energy (Syrovatskii, 1976a). The wider the reconnecting layer, the larger is the energy accumulated in the region of the reconnecting magnetic fluxes interaction.

Second, the neutral layer approximation indicates that very efficient acceleration of particles can work in the RCL (Section 1.2). Let us take as the low limits for the magnetic field $B_0 \approx 50$ G and for the inflow velocity $v_0 \approx 20$ km s^{-1}. These values are smaller than those estimated from the *Yokhoh* SXT and HXT observations of the well studied impulsive

flare on 1992 January 13 – the magnetic field strengh in the supposed Petschek-type (Exercise 10.1) upstream plasma 50 G and the inflow speed range 40-140 km s^{-1}, respectively (Tsuneta et al., 1997). So the lower limit for the electric field can be estimated as

$$E_0 = \frac{1}{c}\, v_0 B_0 \approx 1 \text{ V cm}^{-1}\,. \tag{6.2}$$

This field is much stronger than the Dreicer's field – the electric field strength for which the critical runaway speed is equal to the electron thermal velocity (see Appendix 3):

$$E_{\text{Dr}} = \frac{4\pi e^3}{k_{\text{B}}}\,(\ln\Lambda)\,\frac{n}{T} \approx 10^{-4} \text{ V cm}^{-1}\,. \tag{6.3}$$

Here we have assumed that the density and temperature of the plasma near the RCL $n_0 \approx 4 \times 10^8\,\text{cm}^{-3}$ and $T_0 \approx 3 \times 10^6\,\text{K}$. In fact, near the RCL in solar flares, the magnetic field B_0 can be as high as 100–300 G. So the electric field E_0 can be even stronger by one order of magnitude (Somov, 1981).

Since $E_0 \gg E_{\text{Dr}}$, we neglect collisional energy losses (Dreicer, 1959, Gurevich, 1961) as well as wave-particle interaction of fast particles (Gurevich and Zhivlyuk, 1966). So

> the neutral layer model predicts very impulsive acceleration of charged particles by the direct strong electric field $\mathbf{E}_0$.

This advantage of the RCL will be discussed in Chapter 9 with account of the fact that real reconnecting layers are always magnetically non-neutral: they always have an internal magnetic field. The influence of this three-component field inside the RCL on the particle acceleration is considered in Chapter 9. The main disadvantage of the neutral layer model is that it does not explain the high power of the energy release in solar flares. The reason will be explained in Section 6.2 by using a less idealized model of the RCL.

6.1.2 The current layer by Syrovatskii

To establish relations between the parameters of a neutral layer in *compressible* plasma let us use the equations of continuity and momentum. Under conditions of the strong magnetic field (see vol. 1, Section 13.1.3) these equations are rewritten as the following *order-of-magnitude* relations:

$$n_0 v_0\, b = n_s v_1\, a\,, \tag{6.4}$$

$$\frac{B_0^2}{8\pi} = 2n_s k_{\rm B} T, \tag{6.5}$$

$$2n_s k_{\rm B} T = \frac{1}{2}\, M n_s v_1^2\,. \tag{6.6}$$

Here n_0 and n_s is plasma density outside and inside the layer, respectively. T is temperature of the plasma inside the layer.

It follows from Equations (6.5) and (6.6) that the velocity of outflow from the current layer

$$\boxed{v_1 = V_{\rm A,S} = \frac{B_0}{\sqrt{4\pi M n_s}}\,.} \tag{6.7}$$

Note that the value of the magnetic field is taken outside the layer, for plasma density it is taken *inside* the neutral layer. So the outflow velocity (6.7) *differs* from the Alfvén speed outside the layer

$$V_{\rm A,0} = \frac{B_0}{\sqrt{4\pi M n_0}}\,. \tag{6.8}$$

The downstream flow velocity v_1 of a compressed plasma is *not* equal to the upstream Alfvén speed outside the layer $V_{\rm A,0}$.

The inflow velocity equals the velocity of the plasma drift to the neutral layer

$$v_0 = V_d = c\,\frac{E_0}{B_0}\,. \tag{6.9}$$

Hence we have to add an equation which relates the electric field E_0 with the current layer parameters. From the Maxwell equation for curl $\mathbf{B}$ and Ohm's law, we find

$$\frac{cB_0}{4\pi a} = \sigma E_0\,. \tag{6.10}$$

Here $\sigma = \sigma_0\, T^{3/2}$ is the Coulomb conductivity.

Following Syrovatskii (1976b), from Equations (6.4)–(6.6) and (6.10) the layer half-thickness a, its half-width b, and the plasma density inside the layer n_s can be expressed in terms of three 'external' (assumed known) parameters n_0, $h_0 = B_0/b$, E_0 and the unknown equilibrium temperature T of the plasma inside the current layer:

$$a = b\,\frac{c}{4\pi\sigma_0}\left(\frac{h_0}{E_0}\right)\frac{1}{T^{3/2}}\,, \tag{6.11}$$

$$b = 4\pi \left(\frac{k_{\text{B}} \sigma_0^2 M}{4\pi^2} \right)^{1/6} \left(\frac{n_0 E_0^2}{h_0^4} \right)^{1/3} T^{2/3} , \tag{6.12}$$

$$n_s = \left(\frac{\pi \sigma_0^2 M}{4 k_{\text{B}}^2} \right)^{1/3} \left(\frac{n_0 E_0^2}{h_0} \right)^{2/3} T^{1/3} . \tag{6.13}$$

To determine the temperature T let us add the energy equation in the following form:

$$\frac{B_0^2}{4\pi} V_d \, b = L(T) \, n_s^2 \, ab . \tag{6.14}$$

It is assumed here that the temperature of the neutral layer is not high; so the energy transfer from the layer by plasma outflow and by heat conduction play a secondary role. The principal factors are the influx of magnetic energy into the current layer and radiative cooling. The radiative loss function $L(T)$ can be taken, for example, from Cox and Tucker (1969). More justifications for simple Equation (6.14) follow from the more detailed numerical model by Oreshina and Somov (1998); see also a comparison between different models in Somov and Oreshina (2000).

Substituting the solution (6.11)–(6.13) in Equation (6.14) we obtain the following equation for the temperature of the plasma inside the current layer:

$$T = \sigma_0^{2/5} \left(\frac{\pi M}{4 k_{\text{B}}^2} \right)^{4/5} \Gamma_{\text{S}}^{4/5} L^{6/5}(T) . \tag{6.15}$$

Here

$$\Gamma_{\text{S}} = \frac{n_0^2 E_0}{h_0^2} \tag{6.16}$$

is the dimensional parameter which characterizes the reconnection conditions. Therefore the values n_0, h_0, and E_0 must be specified in advance. The other quantities can be determined from the solution (Exercise 6.1).

Figure 6.2 shows a solution of Equation (6.15) with two unstable branches indicated by dashed curves. On these branches a small deviation of the temperature from equilibrium will cause the deviation to increase with time. It means that the *thermal instability* of the current layer occurs.

The first appearance of the thermal instability, at $T \approx 2 \times 10^4$ K, is caused by emission in the Lα line of hydrogen. It can hardly be considered significant since the function $L(T)$ was taken from Cox and Tucker (1969) without allowance for the absorption of radiation, which may be important for the hydrogen lines in the solar atmosphere. On the contrary, the second break, at

$$T \approx 8 \times 10^4 \text{ K} , \quad \Gamma_{\text{S}} \approx 3.8 \times 10^{26} , \tag{6.17}$$

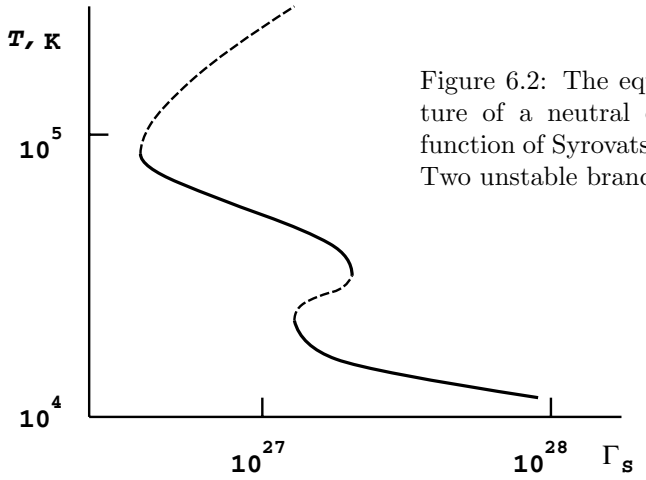

Figure 6.2: The equilibrium temperature of a neutral current layer as a function of Syrovatskii's parameter $\Gamma_{\rm S}$. Two unstable branches are dashed.

will necessarily occur because of the maximum in the radiative cooling function $L(T)$. Near this maximum, in the region where $L(T) \propto T^{\alpha}$ with $\alpha < 1$, the condensation mode of the thermal instability (Field, 1965) occurs (see also Somov and Syrovatskii, 1976a and 1982).

Syrovatskii (1976b) assumed that the temperature T of a *cold dense* current layer in the solar atmosphere gradually increases in the pre-flare stage until the critical values (6.17) are reached. Then the current layer can no longer stay in equilibrium; the radiative losses cannot balance the Joule heating, and the temperature of the layer rapidly rises. This leads to a flare. In this way, Syrovatskii suggested to identify the thermal instability of a cold dense current layer with the onset of the eruptive phase of a solar flare.

Whether such a *thermal trigger* for solar flares occurs or not is unclear yet (Somov and Syrovatskii, 1982). It is clear only that heating of the reconnecting current layer (RCL) leads to the powerful heat-conductive cooling of the plasma electron component. This effect is important for energy balance of a 'super-hot' ($T \gtrsim 3 \times 10^7$ K) turbulent-current layer (SHTCL) discussed in Section 6.3.

6.1.3 Simple scaling laws

In order to determine the parameters of a stationary driven reconnection configuration, the stationary resistive MHD equations must be solved for given boundary conditions. Unfortunately it appears that the problem is too complicated to permit analytical solutions without severe approxima-

tions. The severest of them are called the scaling 'laws'.

Let us come back to **the Sweet-Parker model** of reconnection in *incompressible* plasma. The *order-of-magnitude* relations introduced above become simpler:

$$v_0\, b = v_1\, a\,, \tag{6.18}$$

$$v_0 = \frac{\nu_m}{a}\ , \tag{6.19}$$

$$v_1 = V_{\mathrm{A},0}\,. \tag{6.20}$$

These equations follow from (6.4)–(6.13) and give us the ratio of the inflow (upstream) velocity of the incompressible plasma to the upstream Alfvén speed:

$$\frac{v_0}{V_{\mathrm{A},0}} = \left(\frac{\nu_m}{V_{\mathrm{A},0}\, b}\right)^{1/2}. \tag{6.21}$$

The left-hand side of the relation (6.21) is called the Alfvén-Mach number M_{A} and is conventionally used as a dimensionless measure of the reconnection rate. The right-hand side is simply related to the magnetic Reynolds number (see Appendix 3), more exactly

$$\mathrm{Re_m}(V_{\mathrm{A},0}, b) = \frac{V_{\mathrm{A},0}\, b}{\nu_{\mathrm{m}}} \equiv N_{\mathrm{L}}\,. \tag{6.22}$$

Here N_{L} is called the Lundquist number. Therefore the Sweet-Parker reconnection rate

$$\boxed{M_{\mathrm{A}} = N_{\mathrm{L}}^{-1/2}\,.} \tag{6.23}$$

Order-of-magnitude relations similar to (6.23) are often called scaling 'laws'. They certainly do not have a status of any law but are useful since they simply characterize the *scaling properties* of stationary reconnecting configurations as a proper dimensionless parameter.

Since in formula (6.22) the linear scale L is taken to be equal to the large half-width b of the Sweet-Parker neutral layer, the Lundquist number (6.23) is rather a *global* parameter of the reconnection problem. In the most cases of practical interest the Lundquist number is too large, typically $10^{14} - 10^{15}$ in the solar corona (Exercise 6.1), such that the Sweet-Parker rate would lead to reconnection times many orders of magnitude longer than observed in flares. This means that

> slowly-reconnecting current layers can exist in the solar corona for a long time.

In general, scaling relations are useful to summarize and classify different regimes and configurations of reconnection as they are observed, for example, in numerical simulations (see Chapter 6 in Biskamp, 1997; Horiuchi and Sato, 1994).

6.2 Magnetically non-neutral RCL

Magnetic neutrality of the RCL, as assumed in the previous Section, means that there is no penetration of magnetic field lines through the layer (the transversal field $\mathbf{B}_\perp = 0$) as well as no longitudinal magnetic field parallel to the electric current inside the RCL (the longitudinal field $\mathbf{B}_\parallel = 0$). In general, both assumptions are incorrect (see Somov, 1992). The first of them is the most important for what follows in this Chapter.

6.2.1 Transversal magnetic fields

As it reconnects, every field line penetrates through the current layer as shown in Figure 6.3. So the reconnecting layer is magnetically non-neutral by definition because of physical meaning of the reconnection process. In many real cases (for example, the magnetospheric tail or interplanetary sectorial current layers) a small transversal component of the magnetic field is well observed. This is also the case of laboratory and numerical experiments (Hesse et al., 1996; Ono et al., 1996; Horiuchi and Sato, 1997; Horiuchi et al., 2001).

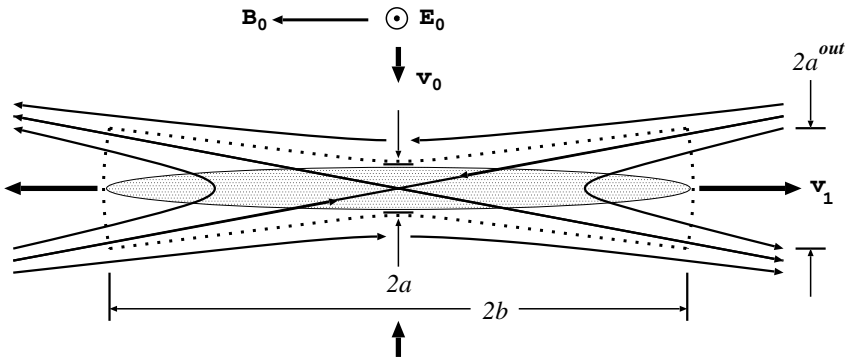

Figure 6.3: A magnetically non-neutral reconnecting layer: the electric current distribution is schematically shown by the shadow, the dotted boundary indicates the field lines going through the current layer.

We characterize the penetration of the magnetic field into the current layer by the parameter $\xi_\perp = B_\perp/B_0$ which is the relative value of the transversal component $\mathbf{B}_\perp$. As distinguished from the neutral-layer approximation, we assume that $\xi_\perp \neq 0$ and satisfies the inequality

$$a/b \ll \xi_\perp \ll 1\,. \tag{6.24}$$

What are the consequences of such a penetration?

The penetration of even a very small transversal field into the high-temperature layer essentially increases the outflows of energy and mass from the layer along the field lines. The effective cross-section for the outflows of energy and mass is proportional to the outflow scale

$$a^{out} \approx \xi_\perp b \gg a\,. \tag{6.25}$$

Hence, corresponding to three different physical processes, the magnetically **non-neutral current layer is characterized by three different linear scales:** $2a$ is a small dissipative thickness of the layer, $2b$ is the scale responsible for the energy accumulation process, and $2a^{out}$ is the linear scale which determines the outflow of energy and mass along the field lines into the surrounding plasma.

As we shall see in Section 6.3, even a very small (like $\xi_\perp \approx 10^{-3}$) transversal field $\mathbf{B}_\perp$ **significantly increases the plasma outflows** as well as the heat-conductive cooling of the non-neutral super-hot turbulent-current layer (SHTCL). As a result, its energy output is much larger than that of the neutral SHTCL. (In the neutral-layer approximation $a^{out} = a$.) The last reason will enable us to consider the SHTCL with a small transversal component of the magnetic field as the source of energy in flares.

6.2.2 The longitudinal magnetic field

As we saw in Section 3.1, the reconnection process under the actual conditions in the solar atmosphere is released at the separator which differs from the X-type neutral line in that the separator has a longitudinal field $\mathbf{B}_\parallel$. In this context, it is necessary to understand the physical effects that are created by the longitudinal field inside the RCL and its vicinity.

It is intuitively clear that the longitudinal field at the separator decreases the reconnection rate

$$\mathbf{v}_0 = c\,\frac{\mathbf{E}_0 \times (\,\mathbf{B}_0 + \mathbf{B}_{\parallel 0}\,)}{B_0^{\,2} + B_{\parallel 0}^{\,2}} = c\,\frac{\mathbf{E}_0 \times \mathbf{B}_0}{B_0^{\,2}\,\left[1 + (B_{\parallel 0}/B_0)^{\,2}\right]}\,. \tag{6.26}$$

Here $\mathbf{B}_0$ and $\mathbf{B}_{\parallel 0}$ are the strengths of the reconnecting component and of the longitudinal component of the magnetic field on the inflow side of the

layer, respectively; they are not *free* parameters, they have to be determined from a self-consistent solution of the problem on the RCL properties.

The appearance of the longitudinal field changes, first of all, the balance of forces across the layer. The pressures of the plasma and the magnetic field outside the RCL should balance not only the plasma pressure but also the magnetic pressure of the longitudinal field inside it:

$$2n_0 k_{\rm B} T_0 + \frac{B_0^2}{8\pi} + \frac{B_{\parallel 0}^2}{8\pi} = 2n_s k_{\rm B} T + \frac{B_{\parallel s}^2}{8\pi}\,. \tag{6.27}$$

Here n_0 and n_s are the plasma densities outside and inside the current layer. T_0 is the temperature of inflowing plasma outside the layer, T is the temperature of plasma inside the layer. In the right-hand side of Equation (6.30) $B_{\parallel s}$ is the strength of the longitudinal field inside the current layer.

If the longitudinal field could be effectively accumulated inside the current layer, its pressure would impose strong limitations on the layer compression and, hence, on the rate of reconnection. In terms of the ideal MHD approximation, the longitudinal field must increase proportionally to the plasma density n_s inside the layer because the field is frozen in the plasma:

$$B_{\parallel s} = B_{\parallel 0}\,\frac{n_s}{n_0}\,. \tag{6.28}$$

On the contrary, in a real finite-conductivity plasma, the increase of the longitudinal field is accompanied by dissipative effects. As soon as the longitudinal field inside the layer becomes stronger than outside the layer, a gradient of the longitudinal field $\mathbf{B}_\parallel$ will appear and give rise to an electric current. In turn, the dissipation of this current produced by the field compression affects the $\mathbf{B}_\parallel$ field value. Thus the compression of the longitudinal field seems to facilitate its dissipation. In reality, however, this problem proves to be more delicate; see Somov and Titov (1985a, 1985b), Somov (1992).

The essence of the effect is that any compression of the longitudinal field $\mathbf{B}_\parallel$ within a current layer does create a gradient of the longitudinal field, $\nabla\mathbf{B}_\parallel$. By so doing, compression generates an associated electric current $\mathbf{J}_\perp$ which circulates in the transversal (relative to the main current $\mathbf{J}$ in the layer) plane. The ohmic dissipation of the current $\mathbf{J}_\perp$, circulating around the layer, gives rise to an outward diffusion of the longitudinal field from the current layer and to the Joule heating of the plasma. It is of importance that **the total flux of the longitudinal field is conserved**, while

> the Joule heating due to the $\mathbf{B}_\parallel$ field compression is produced by the dissipation of the reconnecting magnetic field $\mathbf{B}_0$.

This effect is certainly valid for collisionless reconnection in the RCL.

On the one hand, the magnetic field compression decreases the velocity v_0 of plasma inflows. On the other hand, due to the large magnetic diffusion in the small scale of the current layer thickness $2b$, the longitudinal field $\mathbf{B}_\parallel$ does not have an overwhelming effect on the parameters of the current layer and the reconnection rate. For this reason, we regard as likely that

> the longitudinal field $\mathbf{B}_\parallel$ at the separator changes the reconnection rate in the current layer not too strongly.

This can be especially true if the compression of the plasma inside the RCL, n_s/n_0, is not high, for example, in super-hot turbulent-current layers (SHTCL) of solar flares. Therefore, in the first approximation, we neglect the longitudinal magnetic field in the next Section.

6.3 Basic physics of the SHTCL

6.3.1 A general formulation of the problem

Coulomb collisions do not play any role in the SHTCL. So the plasma inside the SHTCL has to be considered as essentially collisionless (Somov, 1992). The concept of an anomalous resistivity, which originates from wave-particle interactions, is then useful to describe the fast conversion from field energy to particle energy. Some of the general properties of such a **collisionless reconnection** can be examined in a frame of a self-consistent model which makes it possible to estimate the main parameters of the SHTCL. Basing on the mass, momentum and energy conservation laws, we write the following relations (valid for a quarter of the current layer and a unit length along the electric current):

$$n_0 v_0\, b = n_s v_1\, a^{out}, \tag{6.29}$$

$$2n_0 k_{\rm B} T_0 + \frac{B_0^2}{8\pi} = n_s k_{\rm B} T \left(1 + \frac{1}{\theta}\right), \tag{6.30}$$

$$n_s k_{\rm B} T \left(1 + \frac{1}{\theta}\right) = \frac{1}{2}\, M n_s v_1^2 + 2n_0 k_{\rm B} T_0\,, \tag{6.31}$$

$$\chi_{\rm ef}\, \mathcal{E}_{mag}^{\,in} + \mathcal{E}_{th,e}^{\,in} = \mathcal{E}_{th,e}^{\,out} + \mathcal{C}_\parallel^{\,an}\,, \tag{6.32}$$

$$(1 - \chi_{\rm ef})\, \mathcal{E}_{mag}^{\,in} + \mathcal{E}_{th,i}^{\,in} = \mathcal{E}_{th,i}^{\,out} + \mathcal{K}_i^{\,out}\,. \tag{6.33}$$

Here n_0 and n_s are the plasma densities outside and inside the current layer. T_0 is the temperature of inflowing plasma outside the layer, $T = T_e$ is an

effective electron temperature (the mean kinetic energy of chaotic motion per single electron) inside the SHTCL, the ratio $\theta = T_e/T_i$, T_i is an effective temperature of ions.

$$v_0 = V_d = c\,\frac{E_0}{B_0} \tag{6.34}$$

is the velocity of the plasma drift to the current layer, and

$$v_1 = V_{\text{A,S}} = \frac{B_0}{\sqrt{4\pi M n_s}} \tag{6.35}$$

is the velocity of the plasma outflow from the layer. Compare this approximate formula with (6.7).

The continuity Equation (6.29) as well as the energy Equations (6.32) and (6.33) are of integral form for a quarter of the current layer assumed to be symmetrical and for a unit length along the electric current.

The left-hand sides of the energy equations for electrons (6.32) and ions (6.33) contain the magnetic energy flux (see vol. 1, formula (12.74))

$$\mathcal{E}^{\,in}_{mag} = \frac{B_0^2}{4\pi}\,v_0\,b\,, \tag{6.36}$$

which coincides with the direct heating of the ions and electrons due to their interactions with waves. A relative fraction χ_{ef} of the heating is consumed by electrons, while the remaining fraction $(1-\chi_{\text{ef}})$ goes to the ions.

The electron and ion temperatures of the plasma inflowing to the layer are the same. Hence, the fluxes of the electron and ion thermal energies are also the same:

$$\mathcal{E}^{\,in}_{th,e} = \mathcal{E}^{\,in}_{th,i} = \frac{5}{2}\,n_0 k_{\text{B}} T_0 \cdot v_0 b\,. \tag{6.37}$$

Because of the difference between the effective temperatures of electrons and ions in the outflowing plasma, the electron and ion thermal energy outflows also differ:

$$\mathcal{E}^{\,out}_{th,e} = \frac{5}{2}\,n_s k_{\text{B}} T \cdot v_1 a^{out}\,, \qquad \mathcal{E}^{\,out}_{th,i} = \frac{5}{2}\,n_s k_{\text{B}}\,\frac{T}{\theta} \cdot v_1 a^{out}\,. \tag{6.38}$$

The ion kinetic energy flux from the layer

$$\mathcal{K}_i^{\,out} = \frac{1}{2}\,M n_s v_1^2 \cdot v_1 a^{out} \tag{6.39}$$

is important in the energy balance (6.33). As to the electron kinetic energy, it is negligible and disregarded in (6.32). However, electrons play the dominant role in the heat conductive cooling of the SHTCL:

$$\mathcal{C}^{\,an}_{\parallel} = f_{\text{M}}(\theta)\,\frac{n_s (k_{\text{B}} T)^{3/2}}{M^{1/2}}\,a^{out}. \tag{6.40}$$

Here

$$f_{\rm M}(\theta) = \begin{cases} \frac{1}{4}\left(\frac{M}{m}\right)^{1/2} & \text{at } 1 \le \theta \le 8.1\,, \\ \left(\frac{M}{m}\right)^{1/2} \theta^{3/2} \left[\left(1+\frac{3}{\theta}\right)^{1/2} - \frac{1}{\theta^{1/2}}\right] \times & \\ \times \exp\left[-\frac{2\,(\theta+3)}{5}\right] + \left(1+\frac{3}{\theta}\right)^{1/2} & \text{for } \theta > 8.1 \\ & \text{or } \theta < 1\,. \end{cases} \tag{6.41}$$

is the Manheimer function which allows us to consider the anomalous magnetic-field-aligned thermal flux depending on the the effective temperature ratio θ.

Under the coronal conditions derived from the *Yohkoh* data, especially in flares, contributions to the energy balance are not made either by the energy exchange between the electrons and the ions due to collisions, the thermal flux across the magnetic field, and the energy losses for radiation. The magnetic-field-aligned thermal flux becomes anomalous and plays the dominant role in the cooling of electron component inside the layer. All these properties are typical for collisionless 'super-hot' ($T_e \gtrsim 30$ MK) plasma.

Under the same conditions, the effective anomalous conductivity $\sigma_{\rm ef}$ in the Ohm's law

$$\frac{cB_0}{4\pi a} = \sigma_{\rm ef} E_0\,, \tag{6.42}$$

as well as the relative fraction $\chi_{\rm ef}$ of the direct heating consumed by electrons, are determined by the wave-particle interaction inside the SHTCL and depend on the type of plasma turbulence and its regime (Ch. 3 in Somov, 1992). For example, if the resistivity was caused by Coulomb collisions, it would depend on the electron temperature only. However, when the plasma is in a **collisionless turbulent state**, the electrons carring the current and the ions interact with the field fluctuations in the waves, which changes the resistivity and other transport coefficients of the plasma in a way that depends on the type of waves that grow.

6.3.2 Problem in the strong field approximation

Let the conditions of a strong magnetic field (see vol. 1, Section 13.1.3) be satisfied. Then, the set of Equations (6.29)–(6.33) takes the following form:

$$n_0 V_d = n_s V_{\rm A,S}\, \xi_\perp, \tag{6.43}$$

$$\frac{B_0^2}{8\pi} = n_s k_{\rm B} T \left(1 + \frac{1}{\theta}\right), \tag{6.44}$$

$$n_s k_{\rm B} T \left(1 + \frac{1}{\theta}\right) = \frac{1}{2}\, M n_s V_{\rm A,S}^2\,, \tag{6.45}$$

$$\chi_{\rm ef}\, \frac{B_0^2}{4\pi}\, V_d = \frac{5}{2}\, n_s k_{\rm B} T \cdot V_{\rm A,S}\, \xi_\perp + f_{\rm M}(\theta)\, \frac{n_s \left(k_{\rm B} T\right)^{3/2}}{M^{1/2}}\, \xi_\perp\,, \tag{6.46}$$

$$(1 - \chi_{\rm ef})\, \frac{B_0^2}{4\pi}\, V_d = \left(\frac{5}{2}\, n_s k_{\rm B}\, \frac{T}{\theta} + \frac{1}{2}\, M n_s V_{\rm A,S}^2\right) V_{\rm A,S}\, \xi_\perp\,. \tag{6.47}$$

In Ohm's law (6.42) it is convenient to replace the effective conductivity $\sigma_{\rm ef}$ by effective resistivity $\eta_{\rm ef}$:

$$\frac{cB_0}{4\pi a} = \frac{E_0}{\eta_{\rm ef}}\,. \tag{6.48}$$

In general, the partial contributions to the effective resistivity may be made simultaneously by several processes of electron scattering by different sorts of waves, so that the resistivity proves to be merely a sum of the contributions:

$$\eta_{\rm ef} = \sum_k \eta_k\,. \tag{6.49}$$

The relative share of the electron heating $\chi_{\rm ef}$ is also presented as a sum of the respective shares χ_k of the feasible processes taken, of course, with the weight factors $\eta_k/\eta_{\rm ef}$ which defines the relative contribution from one or another process to the total heating of electrons inside the SHTCL:

$$\chi_{\rm ef} = \sum_k \frac{\eta_k}{\eta_{\rm ef}}\, \chi_k\,. \tag{6.50}$$

In usual practice (e.g., Somov, 1992), the sums (6.49) and (6.50) consist of no more than two terms, either of which corresponds to one of the turbulent types or states. Note also that more detailed numerical results (Somov and Oreshina, 2000) confirm validity of the assumptions made above.

6.3.3 Basic local parameters of the SHTCL

We shall assume that the magnetic field gradient h_0 locally characterizes the potential field in the vicinity of the separator or X-type neutral line. It means that we consider a less specific configuration of reconnecting magnetic fluxes in comparison with the 2D MHD 'standard model' mentioned in Section 6.1.1. We shall also assume that, at distances larger than the current layer width $2b$, the magnetic field structure becomes, as it should be, the same as the structure of the potential field of 'external sources', for example, of sunspots in the solar photosphere. So the gradient h_0 is

the local parameter which 'remembers' the global structure of the potential field.

Under the assumptions made, the field B_0 on the inflow sides of the current layer may be estimated as

$$B_0 = h_0 b\,. \tag{6.51}$$

The second local parameter of the reconnection region is the inflow velocity v_0 or, alternatively, the electric field E_0 determined by formula (6.2). We shall use E_0 in what follows.

In the approximation of a strong magnetic field, the pressure p_0 (or temperature T_0) of inflowing plasma is negligible, but its density n_0 certainly has to be prescribed as a local parameter of the reconnection region. In fact, as we shall see below, all characteristics of the SHTCL depend on n_0.

The dimensionless parameter $\xi_\perp$ could be, in principle, obtained as a result of the solution of the more self-consistent problem on the current layer structure (Section 3.4 in Somov, 1992). However in order to keep the problem under consideration as simple as possible, here we shall consider the small (see Inequalities (6.24)) parameter $\xi_\perp$ as the specified one.

Summarizing the formulation of the problem, we see that the set of Equations (6.43)–(6.48) becomes closed if the particular expressions (6.49) and (6.50) are added to this set. This allows us to find the following parameters of the SHTCL: a, b, n_s, T, and θ.

6.3.4 The general solution of the problem

The input set of Equations (6.43)–(6.47) exibits a remarkable property which facilitates the solution of the problem as a whole. The property consists of the fact that the first three Equations (6.43)–(6.45) allow us to transform the last two Equations (6.46) and (6.47) into a simpler form:

$$2\,\chi_{\rm ef}\,\frac{n_s}{n_0} = \frac{2.5}{1+\theta^{-1}} + \frac{f_{\rm M}(\theta)}{\sqrt{2}\,(1+\theta^{-1})^{3/2}}\,, \tag{6.52}$$

$$2\,(1-\chi_{\rm ef})\,\frac{n_s}{n_0} = 1 + \frac{2.5}{1+\theta}\,. \tag{6.53}$$

From these two Equations we find the plasma compression and the relative share of the total heating of the electrons in the current layer:

$$\frac{n_s}{n_0} = N(\theta) = 1.75 + \frac{f_{\rm M}(\theta)}{\sqrt{8}\,(1+\theta^{-1})^{3/2}}\,, \tag{6.54}$$

$$\chi_{\rm ef} = f_\chi(\theta) = 1 - \frac{3.5+\theta}{2N(\theta)\,(1+\theta)}\,. \tag{6.55}$$

Now we use Equations (6.43)–(6.45) together with (6.48) to find the general solution of the problem, which determines the following parameters of the SHTCL: the layer half-thickness

$$a = \frac{c\,m^{1/2}}{e\,(2\pi)^{1/2}} \left[\left(\frac{1+\theta^{-1}}{N(\theta)} \right)^{1/2} \frac{1}{U_k\,(\theta)} \right] \times \frac{1}{n_0^{1/2}}\,, \tag{6.56}$$

its half-width

$$b = (2c)^{1/2}\,(\pi M)^{1/4} \left[\frac{1}{N(\theta)} \right]^{1/4} \times n_0^{1/4}\,\frac{1}{h_0} \left(\frac{E_0}{\xi_\perp} \right)^{1/2}\,, \tag{6.57}$$

the effective temperature of electrons

$$T = \frac{cM^{1/2}}{4k_{\text{B}}\pi^{1/2}} \left[\frac{1}{(1+\theta^{-1})\,N^{3/2}(\theta)} \right] \times \frac{1}{n_0^{1/2}} \left(\frac{E_0}{\xi_\perp} \right), \tag{6.58}$$

the effective anomalous resistivity

$$\eta_{\text{ef}} = \frac{2\,m^{1/2}\,\pi^{1/4}}{e\,c^{1/2}M^{1/4}} \left[\frac{(1+\theta^{-1})^{1/2}}{N^{1/4}(\theta)\,U_k\,(\theta)} \right] \times \frac{1}{n_0^{3/4}}\,(\xi_\perp E_0)^{1/2}\,. \tag{6.59}$$

Thus to complete the solving this problem, we have to find a form of the function $U_k\,(\theta)$ which depends on the regime of the plasma turbulence. This will be done in Section 6.3.5.

In addition, from definitions (6.51), (6.34), (6.35), and (6.36), by using the obtained solutions (6.56)–(6.59), we have the following formulae: the magnetic field near the current layer

$$B_0 = (2c)^{1/2}\,(\pi M)^{1/4} \left[\frac{1}{N(\theta)} \right]^{1/4} \times n_0^{1/4} \left(\frac{E_0}{\xi_\perp} \right)^{1/2}\,, \tag{6.60}$$

the reconnection inflow velocity

$$v_0 = \frac{c^{1/2}}{2^{1/2}\,\pi^{1/4}M^{1/4}}\,[\,N(\theta)\,]^{1/4} \times \frac{1}{n_0^{1/4}}\,(\xi_\perp E_0)^{1/2}\,, \tag{6.61}$$

the outflow velocity

$$v_1 = \frac{c^{1/2}}{2^{1/2}\,\pi^{1/4}M^{1/4}} \left[\frac{1}{N(\theta)} \right]^{3/4} \times \frac{1}{n_0^{1/4}} \left(\frac{E_0}{\xi_\perp} \right)^{1/2}\,, \tag{6.62}$$

the power of energy release per unit length along the current layer length l_j

$$\frac{P_s}{l_j} = \frac{B_0^2}{4\pi}\,v_0\,4b = \frac{2c^2M^{1/2}}{\pi^{1/2}} \left[\frac{1}{N(\theta)} \right]^{1/2} \times n_0^{1/2}\,\frac{1}{h_0} \left(\frac{E_0^2}{\xi_\perp} \right), \tag{6.63}$$

the rate of high-temperature plasma production by the SHTCL per unit length along the current layer length l_j

$$\frac{\dot{N}}{l_j} = n_s v_1 \, 4a^{out} = n_0 v_0 \, 4b = 4c \times n_0 \, \frac{1}{h_0} \, E_0 \, . \tag{6.64}$$

Formula (6.64) demonstrates a high level of self-consistency for the SHTCL model under consideration. It shows that the total flux of plasma through the reconnecting current layer depends only on the plasma density n_0 on the inflow sides of the layer, the driving electric field E_0, and the gradient h_0 of potential magnetic field in the vicinity of the X-type neutral point. It is remarkable that other parameters, like the dimensionless parameter $\xi_\perp$, as well as the assumptions on the plasma turbulence inside the SHTCL, discussed in the next Section, do not influence the total flux of plasma passing through the current layer.

6.3.5 Plasma turbulence inside the SHTCL

In the case of the marginal regime (e.g., Duijveman et al., 1981), the electron current velocity

$$u = \frac{E_0}{e n_s \eta_{\rm ef}} \tag{6.65}$$

coincides with the critical velocity u_k of the k-type wave excitation. Hence, in formulae (6.56) and (6.59), the unknown function

$$U_k \, (\theta) = U_k^{mar} \, (\theta) = \frac{u_k}{V_{\rm Te}} \, . \tag{6.66}$$

For example, the ion-cyclotron instability becomes enhanced when the electron current velocity u is not lower than the critical value u_{ic} of the ion-cyclotron (ic) waves. In the marginal regime of the ion-cyclotron instability

$$U_{ic}^{mar} \, (\theta) = \frac{u_{ic}}{V_{\rm Te}} \, . \tag{6.67}$$

As long as the ion-cyclotron waves are not saturated, the electron current velocity u remains approximately equal to u_{ic} and thus it is possible to calculate the effective resistivity $\eta_{\rm ef}$ from Equation (6.65).

In the saturated turbulence regime, $U_k \, (\theta)$ must be replaced by certain functions $U_{ic}^{sat}(\theta)$ and $U_{ia}^{sat}(\theta)$ for the ion-cyclotron and ion-acoustic turbulence, respectively (see Section 3.3 in Somov, 1992).

6.3.6 Formulae for the basic parameters of the SHTCL

So we rewrite the general solution (6.56)–(6.59) as follows: the SHTCL half-thickness

$$a = 7.5 \times 10^5 \, f_a(\theta) \times \frac{1}{n_0^{1/2}} \, , \ \mathrm{cm} \, ; \tag{6.68}$$

the half-width of the layer

$$b = 3.7 \times 10^{-1} \, f_b(\theta) \times n_0^{1/4} \, \frac{1}{h_0} \left(\frac{E_0}{\xi_\perp} \right)^{1/2} \, , \ \mathrm{cm} \, ; \tag{6.69}$$

the effective temperature of electrons

$$T = 4.0 \times 10^{13} \, f_{_T}(\theta) \times \frac{1}{n_0^{1/2}} \left(\frac{E_0}{\xi_\perp} \right) \, , \ \mathrm{K} \, ; \tag{6.70}$$

the effective anomalous resistivity

$$\eta_{\,\mathrm{ef}} = 8.5 \times 10^{-4} \, f_\eta(\theta) \times \frac{1}{n_0^{3/4}} \, (\xi_\perp E_0)^{1/2} \, , \ \mathrm{s} \, . \tag{6.71}$$

Here we write separatelly the functions which are determined by the plasma turbulence inside the current layer:

$$f_a(\theta) = \left(\frac{1 + \theta^{-1}}{N(\theta)} \right)^{1/2} \frac{1}{U_k \, (\theta)} \approx 2.9 \, , \tag{6.72}$$

$$f_b(\theta) = \frac{1}{N^{1/4}(\theta)} \approx 6.8 \times 10^{-1} \, , \tag{6.73}$$

$$f_{_T}(\theta) = \frac{1}{(1 + \theta^{-1}) \, N^{3/2}(\theta)} \approx 8.2 \times 10^{-2} \, , \tag{6.74}$$

$$f_\eta(\theta) = \frac{(1 + \theta^{-1})^{1/2}}{N^{1/4}(\theta) \, U_k \, (\theta)} \approx 4.3 \, . \tag{6.75}$$

Bearing in mind the discussion of solar flares in Section 7.1, we calculate the right-hand sides of functions (6.72)–(6.75) in the marginal regime of the ion-acoustic turbulence:

$$\theta \approx 6.5 \, , \quad N \approx 4.8 \, , \quad U_k = U_{ia}^{mar} \approx 0.17 \, ,$$

see Section 3.3 in Somov (1992).

The magnetic field on the inflow sides of the current layer can be found from formula (6.60):

$$B_0 = 3.7 \times 10^{-1}\, f_b(\theta) \times n_0^{1/4} \left(\frac{E_0}{\xi_\perp}\right)^{1/2} ,\ \mathrm{G}\,. \tag{6.76}$$

From (6.61) it follows that the reconnection inflow velocity

$$v_0 = 8.1 \times 10^5\, N^{1/4}(\theta) \times \frac{1}{n_0^{1/4}} \left(\xi_\perp E_0\right)^{1/2} ,\ \mathrm{km\ s^{-1}}\,. \tag{6.77}$$

From (6.62) and (6.63) we obtain the outflow velocity

$$v_1 = 8.1 \times 10^5\, N^{-3/4}(\theta) \times \frac{1}{n_0^{1/4}} \left(\frac{E_0}{\xi_\perp}\right)^{1/2} ,\ \mathrm{km\ s^{-1}}\,, \tag{6.78}$$

and the power of energy release per unit length along the current layer length l_j

$$\frac{P_s}{l_j} = 6.0 \times 10^8\, N^{-1/2}(\theta) \times n_0^{1/2}\, \frac{1}{h_0} \left(\frac{E_0^2}{\xi_\perp}\right) ,\ \mathrm{erg\ s^{-1}\,cm^{-1}}\,. \tag{6.79}$$

The rate of super-hot plasma production by the SHTCL is found from (6.64):

$$\frac{\dot{N}}{l_j} = 1.2 \times 10^{11}\ \times n_0\, \frac{1}{h_0}\, E_0\,,\ \mathrm{s^{-1}\,cm^{-1}}\,. \tag{6.80}$$

The applicability scope of the SHTCL model has been considered in Somov (1992) with account of the ion-acoustic and ion-cyclotron instabilities in marginal and saturated regimes. It follows from this consideration that the best agreement between the average quantities predicted by the model and those observed in solar flares can be achieved in the marginal regime of ion-acoustic turbulence. A small parameter of the model, $\xi_\perp$, is really small; on average $\xi_\perp \leq 3 \times 10^{-3}$. With this value taken into account, we finally have the following approximate formulae: the current-layer half-thickness

$$a = 2.2 \times 10^6\ \times \frac{1}{n_0^{1/2}} ,\ \mathrm{cm}\,; \tag{6.81}$$

the half-width of the current layer

$$b = 4.6\ \times n_0^{1/4}\, \frac{1}{h_0}\, E_0^{1/2} ,\ \mathrm{cm}\,; \tag{6.82}$$

the effective temperature of electrons

$$T = 1.1 \times 10^{15} \times \frac{1}{n_0^{1/2}} E_0 \,, \ \mathrm{K} \,; \tag{6.83}$$

the effective anomalous resistivity

$$\eta_{\mathrm{ef}} = 2.0 \times 10^{-4} \times \frac{1}{n_0^{3/4}} E_0^{1/2} \,, \ \mathrm{s} \,; \tag{6.84}$$

the magnetic field on the inflow sides of the current layer

$$B_0 = 4.6 \times n_0^{1/4} E_0^{1/2} \,, \ \mathrm{G} \,; \tag{6.85}$$

the reconnection inflow velocity

$$v_0 = 6.6 \times 10^4 \times \frac{1}{n_0^{1/4}} E_0^{1/2} \,, \ \mathrm{km\ s^{-1}} \,; \tag{6.86}$$

the outflow velocity of super-hot plasma

$$v_1 = 4.6 \times 10^6 \times \frac{1}{n_0^{1/4}} E_0^{1/2} \,, \ \mathrm{km\ s^{-1}} \,; \tag{6.87}$$

the power of energy release per unit length along the current layer length l_j

$$\frac{P_s}{l_j} = 2.0 \times 10^{11} \times n_0^{1/2} \frac{1}{h_0} E_0^2 \,, \ \mathrm{erg\ s^{-1}\,cm^{-1}} \,; \tag{6.88}$$

and the rate of high-temperature plasma production by the SHTCL

$$\frac{\dot{N}}{l_j} = 1.2 \times 10^{11} \times n_0 \frac{1}{h_0} E_0 \,, \ \mathrm{s^{-1}\,cm^{-1}} \,. \tag{6.89}$$

Formulae (6.81)–(6.89) depend on **three principal parameters of the reconnection region**: the gradient of the magnetic field h_0 in the vicinity of separator, the value of the inductive electric field E_0 and the plasma density n_0. For applications to the solar flares in the next Chapter.

We also introduce the *heating time* t_h which is the time for a given magnetic-field line to be connected to the SHTCL. In other words, during the time t_h, the thermal flux from the SHTCL along the field line heats the high-temperature plasma flowing out of the current layer along this field line. Let us take by definition

$$t_h = \frac{2b}{v_1} = 4(\pi M)^{1/2} \, [\, N(\theta) \,]^{1/2} \times n_0^{1/2} \frac{1}{h_0} = \\ = 2.0 \times 10^{-11} \times n_0^{1/2} \frac{1}{h_0} \,, \ \mathrm{s} \,. \tag{6.90}$$

In all these formulae all the quantities, except the temperature, are measured in CGS units; the temperature is given in degrees Kelvin.

6.4 Open issues of reconnection in flares

The existing models of magnetic reconnection in the solar atmosphere can be classified in two wide groups: global and local ones (Figure 6.4).

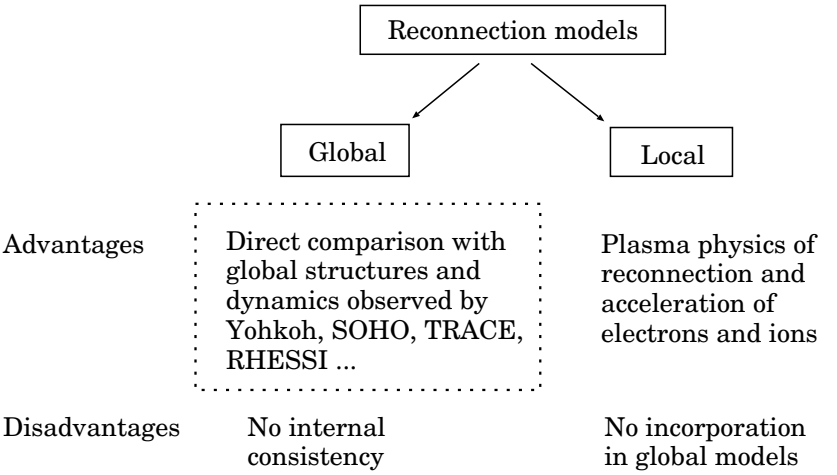

Figure 6.4: Models of magnetic reconnection in the solar atmosphere.

The global models are used to describe actual active regions or even complexes of activity on the Sun in different approximations and with different accuracies (Somov, 1985, 1986; Gorbachev and Somov, 1989, 1990; Demoulin et al., 1993; Bagalá et al., 1995; Tsuneta, 1996; Tsuneta et al., 1997; Antiochos, 1998; Longcope and Silva, 1998; Aschwanden et al., 1999; Somov, 2000; Morita et al., 2001; Somov et al., 2002a). We make no attempt to review all these models, stationary or non-stationary, 3D or 2D, but just remark that

> the main advantage of the global models for magnetic reconnection in solar flares is a direct comparison between the results of computation and the observed large-scale patterns.

For example, the 'rainbow reconnection' model (Section 3.2.4) is used to reproduce the main features of the observed magnetic and velocity fields in the photosphere related to the large-scale photospheric vortex flows. As a consequence, the model reproduces, in the potential approximation, the large-scale features of the actual field in the corona, related to these flows before a flare.

The advantage of the local models is that they take kinetic effects into account and allow us to develop the basic physics of the magnetic reconnection process in solar flares. In general, many analytical, numerical, and combined models of reconnection exist in different approximations and with different levels of self-consistency (e.g., Biskamp, 1994; Somov, 2000). It becomes more and more obvious that *collisionless* reconnection in a 'superhot' rarefied plasma is an important process in considering active phenomena like solar flares. This process was introduced by Syrovatskii (1966a, 1966b) as a *dynamic dissipation* of magnetic field in a reconnecting current layer (RCL) and leads to fast conversion from field energy to particle energy, as well as a topological change of the magnetic field (e.g., Horiuchi and Sato, 1997; Horiuchi et al., 2001).

General properties and parameters of the collisionless reconnection can be examined in a frame of local models based on the mass, momentum, and energy conservation laws. As discussed in this Chapter, a particular feature of the models is that electrons and ions are heated by wave-particle interactions in a different way; contributions to the energy balance are not made by energy exchange between electrons and ions. The magnetic-field-aligned thermal flux becomes anomalous and plays the role in the cooling of the electrons in the *super-hot turbulent-current layer* (SHTCL). These properties are typical for collisionless plasmas under the coronal conditions derived from the *Yohkoh* data. Unfortunately, the local models, like the SHTCL, are not incorporated yet in the global 3D consideration of the reconnection process in the corona. Only a few first steps have been made in this direction (e.g., Somov and Kosugi, 1997; Somov et al., 1998).

Future models should join 'global' and 'local' properties of the magnetic reconnection process under solar coronal conditions. For example, chains of plasma instabilities, including kinetic instabilities, can be important for our understanding of the types and regimes of plasma turbulence inside the collisionless current layer. In particular it is necessary to evaluate anomalous resistivity and selective heating of particles in the SHTCL. Heat conduction is also anomalous in the high-temperature plasma of solar flares. Self-consistent solutions of the reconnection problem will allow us to explain the energy release in flares, including the open question of the mechanism or combination of mechanisms which explains the observed acceleration of electrons and ions to high energy (see Chapter 9). One can be tempted to use, however, the MHD approximation to describe the energy release in solar flares, since this approximation may give a global picture of plasma motions.

To understand the 3D structure of actual reconnection in flares is one of the most urgent problems. Actual flares are 3D dynamic phenomenon of electromagnetic origin in a highly-conducting plasma with a strong mag-

netic field. The Sakao-type flares (Section 3.4.2) are a clear example which shows that 3D models of flares should be involved in treatment of *Yohkoh* data. It does not seem possible to explain these flares in the framework of 2D MHD models.

Yohkoh observations with HXT, SXT, and BCS had offered us the means to check whether phenomena predicted by solar flare models of a definite type (such as the 2D MHD standard model or the quadrupole-type model described in Section 3.2) actually occur. There are apparent successes of the standard model, for example, in the morphology of flares with cusp geometries. However some puzzling discrepancies also exist, and further development of more realistic 3D models is required.

6.5 Practice: Exercises and Answers

Exercise 6.1. Evaluate the characteristic value of the global Lundquist number (6.22) for a current layer with the classical Coulomb conductivity in the solar corona before an impulsive flare. Compare a predicted reconnection rate with the real one.

Answer. First, let us formally apply the Sweet-Parker scaling property (6.23) to the Syrovatskii current layer (see Section 6.1.2). Consider the main parameters of the neutral layer at the limit of thermal stability (6.17). The values $n_0 \approx 5 \times 10^8$ cm^{-3}, $h_0 \approx 5 \times 10^{-7}$ Gauss cm^{-1}, and $E_0 \approx 1.2 \times 10^{-1}$ V cm^{-1} have been specified in advance. The other quantities have been determined from the Syrovatskii solution. For example, the half-width of the current layer $b \approx 7 \times 10^8$ cm, the magnetic field near the layer $B_0 = h_0 b \approx 340$ Gauss, the plasma density inside the neutral layer $n_s \approx 2 \times 10^{14}$ cm^{-3}.

The upstream Alfvén speed (6.8):

$$V_{\mathrm{A},0} = 2.18 \times 10^{11} \, \frac{B_0}{\sqrt{n_0}} \approx 3 \times 10^9 \text{ cm s}^{-1} \approx 0.1 \, c \,. \tag{6.91}$$

Here c is the light speed.

The global Lundquist number (6.22):

$$N_{\mathrm{L}} = \frac{V_{\mathrm{A},0} b}{\nu_{\mathrm{m}}} \approx 2.3 \times (10^{14} - 10^{15}) \,.$$

Therefore the Sweet-Parker reconnection rate (6.23) predicted for the Syrovatskii neutral layer is extremely low:

$$M_{\mathrm{A}} = N_{\mathrm{L}}^{-1/2} \approx (2.1 - 6.7) \times 10^{-8} \,.$$

Let us compare this rate with the one which directly corresponds to the Syrovatskii model. According to formula (6.9) the inflow velocity

$$v_0 = V_d = c\,\frac{E_0}{B_0} \approx 3.5 \times 10^4 \text{ cm s}^{-1} = 0.35 \text{ km s}^{-1}\,.$$

Hence an actual reconnection rate in the Syrovatskii neutral layer

$$M_{\text{A,S}} = \frac{v_0}{V_{\text{A},0}} \approx 1.1 \times 10^{-5} \gg M_{\text{A}}.$$

Obviously a difference in the reconnection rate is related to the compressibility of the plasma in the Syrovatskii model. With account the plasma compressibility inside the reconnecting current layer, the actual reconnection rate

$$\boxed{M_{\text{A,S}} = \frac{v_0}{V_{\text{A},0}} = \left(\frac{n_s}{n_0}\right)^{1/2} N_{\text{L}}^{-1/2}.} \tag{6.92}$$

In the frame of Syrovatskii's model for the neutral layer

$$\left(\frac{n_s}{n_0}\right)^{1/2} > 10^2.$$

So the astrophysical plasma compressibility is really very important factor in the magnetic reconnection theory.

Chapter 7

Reconnection and Collapsing Traps in Solar Flares

The super-hot turbulent-current layer (SHTCL) model fits well for solar flares with different properties: impulsive and gradual, compact and large-scale, thermal and non-thermal. Reconnection in SHTCLs creates collapsing magnetic traps. In this Chapter, we discuss the possibility that coronal HXR emission is generated as bremsstrahlung of the fast electrons accelerated in the collapsing traps due to joint action of the Fermi-type first-order mechanism and betatron acceleration.

7.1 SHTCL in solar flares

7.1.1 Why are flares so different but similar?

Even if one considers the flares driven by reconnection in the SHTCL with the same kind of plasma turbulence, then one can see from the solution described above that very different physical processes will dominate in a flare depending on physical conditions. The advantage which this analytical solution gives us is that we can estimate the most important parameters which determine the physical difference in solar flares.

7.1.1 (a) Magnetic reconnection rate in SHTCL

Let us consider, first, the reconnection inflow velocity v_0 of plasma in the vicinity of the SHTCL. According to formula (6.86), v_0 does not depend on the magnetic-field gradient h_0. For given values of the plasma density n_0 and the electric field E_0, the inflow velocity is shown in Figure 7.1. On aver-

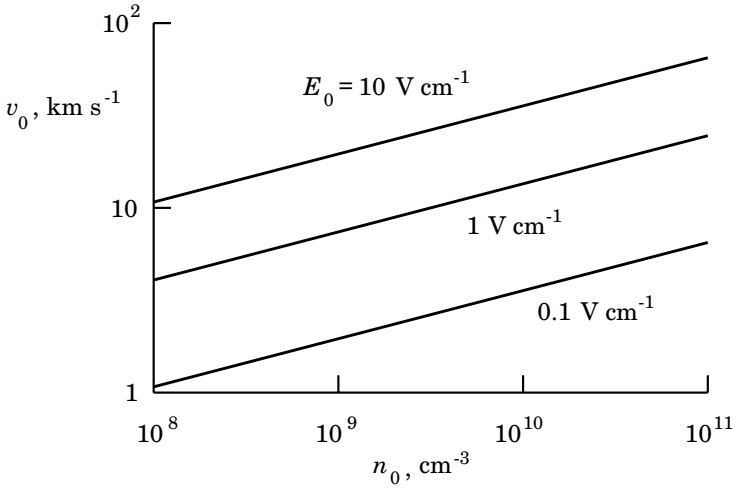

Figure 7.1: The reconnection inflow velocity v_0 in the vicinity of the SHTCL as a function of the plasma density n_0 and the electric field E_0.

age, the characteristic value of the reconnection velocity is $v_0 \sim 10$ km s^{-1}.

So the reconnection inflow velocity during the 'main' or 'hot' phase of solar flares is much higher than that one in the pre-flare state (cf. Exercise 6.1).

Second, if the characteristic value of the upstream Alfvén speed in the undisturbed solar corona $V_{A,0} \approx 3 \times 10^4$ km s^{-1} (see (6.91)), then the parameter $\varepsilon \approx 3 \times 10^{-4}$. Hence the parameter $\varepsilon^2 \approx 10^{-7}$ is really very small. Therefore the approximation of a strong magnetic field (see vol. 1, Section 13.1.3) is well applicable to the SHTCL in solar flares. Except, the parameter γ^2 is small but not so small as ε^2:

$$\gamma^2 \approx \frac{V_s^2}{V_{A,0}^2} \sim 10^{-4} \gg \varepsilon^2 \sim 10^{-7}\,.$$

So the condition (13.20) in vol. 1 would be well satisfied in the undisturbed corona near the SHTCL.

This means that, in a first approximation, the parameter γ^2 is more important than the ε^2 (see vol. 1, Equation (13.22)). Hence we cannot neglect the gas-pressure-gradient effects in the vicinity of the SHTCL.

> We have to take into account a compression of the plasma by a magnetic field near the SHTCL.

That is why we use in the SHTCL model the plasma density $n_0 \sim 10^9 - 10^{11}\,\mathrm{cm}^{-3}$ which is different from the plasma density in the undisturbed corona. In other words, the thin SHTCL, being in equilibrium considered here, is presumably embedded into a thicker plasma layer.

7.1.1 (b) Magnetic-field gradient effects

Let us distinguish *impulsive* and *gradual* flares in the following way. If the difference in the time scale of a flare t_f would be mainly determined by the difference in its linear size l_f, then the impulsive flares should have the stronger gradient h_0 near the separator of the potential field in an active region (see Section 3.2.1). By thinking so, we would believe that **the impulsive flares are the compact flares in strong magnetic fields**, for example, flares in the low corona not far from sunspots. On the contrary, the gradual or long-duration flares may occur in a large-scale region placed high in the corona at a significant distance above the strong sunspots.

For definiteness, let us put $l_f \approx 3 \times 10^9$ cm as a typical value at an imaginary boundary between compact (impulsive) and large-scale (long-duration or gradual) flares. In that case, the typical value of the field gradient $h_f = B_f/l_f$, where B_f is a typical value of the external (with respect to the reconnecting current layer) magnetic field in the photosphere. Since in sunspots $B_f \approx 10^3$ G, we take

$$h_f = \frac{B_f}{l_f} \approx 3 \times 10^{-7}\,\mathrm{G\ cm}^{-1} \tag{7.1}$$

as a boundary value of the field gradient. Therefore, by our conventional definition, which is not always true, in impulsive flares $h_0 > h_f$ but in gradual flares $h_0 < h_f$.

Note that the half-thickness a of the current layer, its temperature T and effective anomalous resistivity η_{ef}, the magnetic field B_0 on the inflow sides of the current layer, the inflow and outflow velocities v_0 and v_1 do *not* depend on the gradient h_0. This remarkable feature follows from formulae (6.81), (6.83)–(6.87), respectively. Perhaps, that is why

> there still exists some similarity between solar flares, in spite of the great difference in their observed scales and shapes.

On the contrary, the current-layer half-width b and, as a consequence, the power of energy release per unit length along the current P_s/l_j and the rate of high-temperature plasma production by the SHTCL $\dot{N}/l_j$ are inverse proportional to the field gradient h_0, see formulae (6.82), (6.88) and (6.89). The plasma production rate is proportional to the electric field E_0, which is typical for driven reconnection.

7.1.1 (c) The role of the plasma density

Also conventionally, we shall distinguish *thermal* and *non-thermal* flares. Plasma heating is an unavoidable phenomenon in all flares. The relative role of the thermal part of a flare certainly depends on collisional relaxation processes mainly in the secondary (Somov, 1992) transformations of the flare energy. It is natural to assume that

> the plasma density n_0 determines the importance of collisions in flares: the higher the density, the faster is the thermalization.

The thermal flares, having the high plasma density, have to produce very efficient heating but inefficient acceleration. The opposite seems to be true for the non-thermal flares.

The solutions (6.56)–(6.63) show that all parameters of the SHTCL depend on the density n_0. Generally, this dependence is not strong ($n_0^{1/2}$, $n_o^{1/4}$ etc.), but the difference in density can be large. This is important for what follows. For example, Figure 7.2 shows the effective temperature of electrons (6.83) as a function of the plasma density n_0 and electric field E_0.

As we see, **temperatures greater than 10^8 K can be easily reached in flares**. Moreover the effective temperature of electrons does not depend on the field gradient h_0. So the SHTCL may well exist in both impulsive and gradual flares.

In the conditions of the 'main' or 'hot' phase of solar flares the characteristic parameters of such collisionless current layers, computed in the frame of the model described above (see also Table 3.3.3 in Somov, 1992), are the followings.

(a) The effective electron temperature inside the current layer $T_e \approx 100 - 200$ MK, the temperature ratio $\theta = T_e/T_p \approx 6.5$. The plasma compression $n_s/n_0 \approx 4.8$ is not high.

(b) The effective dissipative thickness of the current layer $2a \approx 20$ cm is very small but its width $2b \approx (1-2) \times 10^9$ cm is large, for this reason the linear scale (6.25) for the outflows of energy and mass $2a^{out} \approx (3-6) \times 10^6$ cm is not small. This scale should be considered as actual thickness of the SHTCL.

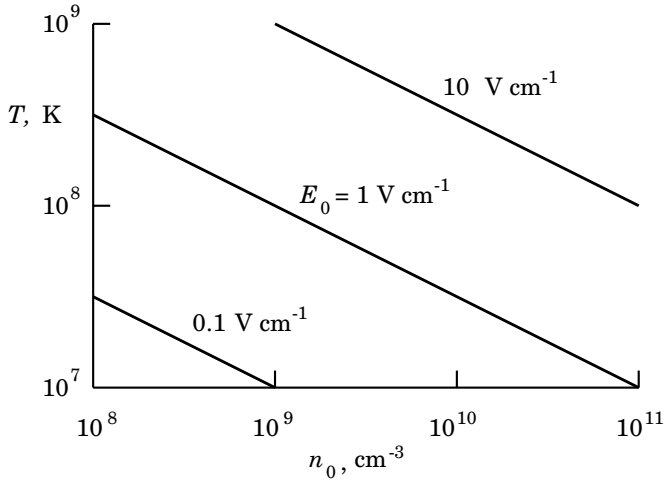

Figure 7.2: The effective temperature of electrons inside the SHTCL as a function of the plasma density n_0 and the driving electric field E_0.

(c) The anomalously high resistivity $\eta \approx (3-10)\times 10^{-13}$ s is induced by the ion-acoustic turbulence in a marginal regime inside the SHTCL. Under this condition, the energy release power per unit layer length l_j (along the direction of current inside the layer) is $P_s/l_j \approx (1-7)\times 10^{19}$ erg (s cm)$^{-1}$, if the plasma inflow velocity $v_0 \approx 10-30$ km s^{-1}. Hence, if the current layer length $l_j \approx 3\times 10^9$ cm, then the power of energy release

$$P_s \approx 3\times 10^{28} - 2\times 10^{29} \text{ erg s}^{-1}\,.$$

The outflow velocity equals $v_1 \approx 1400 - 1800$ km s^{-1}.

7.1.2 Super-hot plasma production

How much super-hot plasma is generated by the SHTCL? – According to formula (6.89), for the impulsive flares with the field gradient $h_0 \approx 5\times 10^{-7}$ G cm^{-1}, the rate of high-temperature plasma production by the SHTCL (per unit length along the current layer length l_j) is

$$\dot{N}/l_j \approx 2\times 10^{17}\, n_0\, E_0\,,\ \text{s}^{-1}\,\text{cm}^{-1}.$$

If we take the maximum value of the electric field $E_0 \approx 10$ V cm^{-1} and plasma density $n_0 \approx 10^9 - 10^{10}$ cm^{-3}, then we estimate the rate of plasma production as $\dot{N}/l_j \approx 10^{25} - 10^{26}$ s^{-1} cm^{-1}.

Let us take the characteristic length $l_j \sim l_f \approx 3 \times 10^9$ cm and the characteristic value of the impulsive phase duration $\tau \approx 30$ s. Then the amount of super-hot plasma produced by the SHTCL can be estimated as

$$N = \frac{\dot{N}}{l_j} \times l_j \, \tau \approx \left(10^{36} - 10^{37}\right) \text{ particles}. \tag{7.2}$$

> This amount of high-temperature (super-hot) particles seems to be comparable with the total number of accelerated electrons

having energies larger than ≈ 10 keV during the impulsive phase of a typical flare. So, in principle, the SHTCL can produce an observable amount of the super-hot plasma (Section 7.3) and pre-accelerated particles: protons and other ions.

Let us estimate the emission measure of the super-hot plasma. The 2D distributions of temperature and pressure, that follow from the *Yohkoh* SXT and HXT observations (Tsuneta et al., 1997), do not allow us to estimate the volume V_{sh} occupied by super-hot plasma. So we have to start from a rather arbitrary assumption frequently used in this situation as a first approximation. If this plasma would be distributed uniformly over the large volume of a flare $V_f = {l_f}^3$, then the emission measure should be

$$EM_{min} = \frac{N^2}{{l_f}^3} \approx 3 \times \left(10^{43} - 10^{45}\right) \text{ cm}^{-3}. \tag{7.3}$$

This is not the case. The emission measure can be much higher because the super-hot plasma is concentrated in a much smaller volume, more exactly, in a compact source above the soft X-ray (SXR) loops (see Figures 7.8 and 7.9). So the value (7.3) is only a *lower limit* to the emission measure of the super-hot plasma in real flares. A reasonable value of the volume filling factor V_{sh}/V_f, which we may assume, is of about $3 \times 10^{-4} - 10^{-3}$. That is why the super-hot plasma was observed in flares by the HXT on board *Yohkoh*.

* * *

Before *Yohkoh*, a little indirect evidence of the super-hot plasma was known. First, the high-resolution (≈ 1 keV) spectral measurements (Lin et al., 1981) from 13 to 300 keV of a flare on June 27, 1980 have shown, at energies below ≈ 35 keV, an extremely steep spectrum which fits to that from the Maxwellian distribution with an electron temperature $T_e \approx 34$ MK and an emission measure $EM \approx 3 \times 10^{48}$ cm^{-3}. Second, statistical properties of a large number of solar flares detected with the Hard X-Ray Burst Spectrometer (HXRBS) on the satellite *Solar Maximum Mission* (*SMM*)

allowed to confirm the existence of super-hot thermal flares (Type A) with temperatures 30-40 MK (Dennis, 1985, 1988).

Third, the 2D distributions of electron temperature and emission measure of the 'hot' (say $10 \leq T_e \leq 30$ MK) and super-hot plasma (Den and Somov, 1989) were calculated for the 1B/M4 flare on November 5, 1980 on the basis of data obtained with the Hard X-ray Imaging Spectrometer (HXIS) on board *SMM*. It was shown that

> the large and small SXR 'interacting loops' do not coincide with the location of super-hot plasma in a long structure (≈ 1 arc min) during the long after-impulsive phase of the flare.

The emission measure of the super-hot plasma in this flare was of about $EM \sim 10^{47}$ cm^{-3}. In two maxima, the electron temperature reaches enormous values, $T_{\rm e} \approx$ 50-60 MK, determined with accuracy better than 20 %.

Hard X-ray imaging telescopes on *Hinotori* observed a super-hot plasma of 30-35 MK with an emission measure of the order of 10^{49}cm^{-3} (Tsuneta et al., 1984, Tanaka, 1987). The same super-hot plasma was detected by the Bragg-type spectrometer (Tanaka, 1987).

Fast flows of the hot plasma can produce a symmetrical broadening of the optically thin SXR lines observed during solar flares. This broadening is larger than the thermal one. A comparison of the observed profiles of the Fe XXV emission lines with the predictions of the SHTCL model suggests that the presence in the flare region of several small-scale or one (or a few) large-scale curved SHTCL (Antonucci et al., 1996).

* * *

The *Yohkoh* data obtained simultaneously with the HXT, SXT, and BCS offered an opportunity for a detailed analysis which is necessary to distinguish the super-hot plasma components of different origins in different classes of flares as well as at different phases of the flare development.

Fast outflows of super-hot plasma create complicated dynamics of plasma in an external (relative to the current layer) region (see Section 7.3.2). If the distance between the SHTCL and the magnetic obstacle is not large, then the outflow becomes wider but does not relax in the coronal plasma before reaching the obstacle. Moreover, if the plasma velocity still exceeds the local fast-magnetoacoustic-wave velocity, a fast MHD shock wave appears ahead the obstacle (see Figure 7.6).

If, on the contrary, the distance is large, the outflow of super-hot plasma relaxes gradually with (or even without) a collisinal shock depending on the height and the conditions in an active region where a flare occurs (e.g., Tsuneta, 1996). For example, collisional relaxations can be fast just near

the SHTCL if the plasma density is relatively high but its temperature inside the reconnecting current layer is relatively low.

We do not discuss in this Chapter an existance of slow or fast MHD shocks (or other MHD discontinuities) which may be attached to external edges of the collisionless SHTCL. It will be reasonable to discuss such structures as a part of the current layer evolutionarity problem in Chapter 10, see also Exercise 10.1.

7.1.3 On the particle acceleration in a SHTCL

The collisionless transformation of the magnetic energy into kinetic energy of particles inside the non-steady 2D reconnecting current layer (RCL) was introduced by Syrovatskii (1966a) as a *dynamic dissipation*. An essential peculiarity of the dynamic dissipation is that

> the inductive electric field $\mathbf{E}_0$ is directed along the current in the RCL; this field does positive work on charged particles, thus increasing their energy.

Naturally, some instabilities are excited in the plasma-beam system in the RCL. Wave-particle interactions transform a part of this work into direct heating of ions and electrons.

Three-component collisionless reconnection (Ono et al., 1996; Horiuchi and Sato, 1997) includes several natural complications. For example, large ion viscosity possibly contributes to the thermalization process of the ion kinetic energy. However the general inference as to the possibility of particle acceleration and heating inside the collisionless RCL (i.e. dynamic dissipation of the magnetic field) remains valid and is used in the SHTCL model. This allows us to consider the SHTCL as the primary source of flare energy and, at least, the first-step acceleration mechanism.

7.2 Coronal HXR sources in flares

7.2.1 General properties and observational problems

An unexpected feature of solar flares is the presence of a HXR source located in the corona (Figure 7.3). Such emission interpreted as the bremsstrahlung of fast electrons was not predicted by theory because of very low density of coronal plasma. Space observations before the *Yohkoh* satellite had not sufficient sensitivity to observe these relatively faint emissions.

At first, a coronal source of HXRs was detected in the impulsive flare which occurred at the limb on 1992 January 13 and is well known as Masuda's flare (Masuda et al., 1994). The source was observed in the HXT

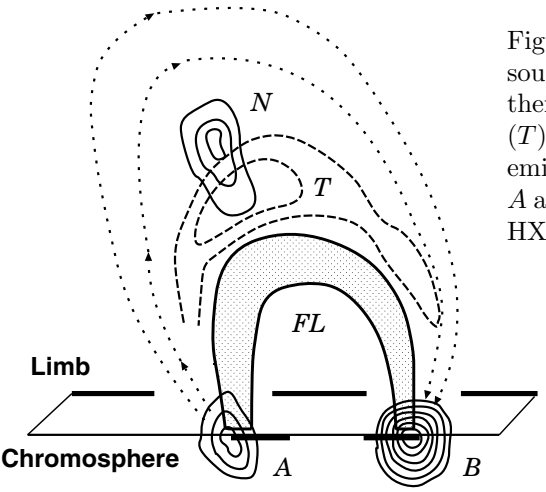

Figure 7.3: A coronal HXR source in a flare: the non-thermal (N) and quasi-thermal (T) components of the HXR emission above a flare loop FL. A and B are the chromospheric HXR footpoints.

energy bands M1 (23-33 keV) and M2 (33-53 keV) and had a relatively hard spectrum with index $\gamma \sim 4$. It was located above a SXR flare loop. Another source was observed in the L-band (14-23 keV), had a very soft spectrum, and looked similar to the SXR loop. This quasi-thermal emission of a 'superhot' (with electron temperature $T_e \gtrsim 30$ MK) plasma started in the impulsive phase and became dominant in the gradual phase of the flare. In some flares, non-thermal sources seemed to be too weak and only such quasi-thermal component was observed during almost the whole flare period. For example, in the flare of 1992 February 6, the HXR spectrum was fitted by the thermal spectrum with $T_e \sim 40$ MK (Kosugi et al., 1994).

Masuda's analysis was extended by Petrosian et al. (2002). Of 18 X-ray-bright limb flares analyzed, 15 showed detectable loop top (LT) emission. The absence of LT emission in the remaining cases was most likely due to the finite dynamic range of the HXT. The coronal LT emission is presumably a common feature of all flares. This is one of the important properties of flares, which has to be investigated by using high resolution data of the *Reuven Ramaty High Energy Solar Spectroscopic Imager* (*RHESSI*) satellite (Lin et al., 2002).

Different types of coronal HXR sources may exist simultaneously even in a single flare (Masuda, 2002). Some sources *slowly move upward* during a flare. For example, in the flare of 1992 October 4, a clear upward motion was observed in the impulsive phase as shown in Figure 2 in Masuda et al. (1998). The flare had a multiple spikes in the HXR time profile. The position of the footpoints (FPs) changed at the time of each spike. This observation suggests that the energy release process proceeds not only in

a vertical direction, like reconnection in the 'standard' model, but also in horizontally-different places.

The number of impulsive flares, in which the presence of the above-the-loop-top (ALT) source was well confirmed, was small. Mainly, these were three flares: 1992 January 13, 1993 February 17, 1994 January 16. Their L-band images had been synthesized by Sato et al. (1999). However, these flares did not look intense enough for an analysis of motion of the coronal source.

Due to the work in recalibrating the HXT and improvement of the software, it became possible to study the coronal source in long-duration events (LDEs). The size of LDEs is generally larger than that of impulsive flares. In a typical LDE, the extended HXR source lies above or slightly overlapping the SXR loops (Sato, 1997; Masuda et al., 1998). The source observed in the L-band has two components – thermal and non-thermal. The source is maintained for a much longer time than the compact sources in impulsive flares. The shape of the HXR source is indicative of a high-temperature cusp region tracing an arcade of loops (Sato, 1997).

In the X1.2 flare on 1998 April 23, coronal HXR sources showed complex structure unlike any previously observed (Sato, 2001). Dominant thermal and nonthermal sources did not come from the same loop-top region. Non-thermal sources included two sources in the low corona ($\sim 3 \times 10^3$ km) and an extended source in the high corona ($\sim 5 \times 10^4$ km). The low and high coronal sources had common features such as a hard spectrum and a related evolution of spatial structures. The high coronal source showed a delayed peak. These observations suggest that energetic phenomena occur in the low corona at first, and energized electrons are then injected into a high coronal region (Sato, 2001).

7.2.2 Upward motion of coronal HXR sources

Harra-Murnion et al. (1998) analyzed two LDEs observed by *Yohkoh*. They concluded that the SXR loops were located below the HXR emission of the ALT source. For the LDE of 1992 November 2, the ALT source rose with a velocity of $\approx$ 3 km/s. For the 28 June 1992 event, it was not possible to follow the HXR images for a long time due to the poor count statistics. So the ascent velocity was not estimated. The improved L-band images synthesized with the revised MEM for three LDEs, including the 1992 November 2 event, have been published (see Figure 13 in Sato et al., 1999) but the ascent velocity was not estimated.

The *RHESSI* mission provides high-resolution imaging from soft X-rays to γ-rays and allows the HXR source motions to be studied in detail. For example, the HXR observations of the 2002 July 23 flare show FP emissions

originating from the chromospheric ribbons of a magnetic arcade and a coronal (LT or ALT) source moving with a velocity of ~ 50 km/s (Krucker et al., 2003; Lin et al., 2003). Some part of this velocity is presumably directed upward, another part along the ribbons. LT and FP sources are also seen in the limb X28 flare on November 4, 2003. The limb flare on 2002 April 15, demonstrates that, after the HXR peak, the coronal HXR source moved upward at velocity $\sim$ 300 km/s, presumably indicating a *fast* upward outflow from reconnecting current layer (RCL) or its upward expansion (Sui and Holman, 2003).

Sui et al. (2004) studied the *RHESSI* imagies of three homologous flares that occurred between April 14 and 16, 2002. The flares share the following common features: (a) The higher energy loops are at higher altitude than those of lower energy loops, indicating the hotter loops are above the cooler ones. (b) Around the start of the HXR impulsive phase, the altitude of the looptop centroid decreases with time. (c) Then the altitude increases with time with velocities up to 40 km/s. (d) A separate coronal source appears above the flare loop around the start time and stays stationary for a few minutes. (e) The looptop centroid moves along a direction which is either away from or toward the coronal source above the loop.

These features are presumably associated with the formation and development of a RCL between the looptop and the coronal source. Physical parameters of such RCL seem to be consistent with the model of super-hot turbulent-current layer (SHTCL). Moreover Sui et al. (2004) found a correlation between the loop growth rate and the HXR (25-50 keV) flux of the flare. The faster the reconnection site moves up, the faster the reconnection rate. More energetic electrons are produced and, therefore, more HXR emission is observed.

Different parts of the flare 'mechanism' in the corona can be seen in HXR emission, depending on conditions. These parts are the reconnection downflows in a cusp area, the reconnection site itself and with its vicinity, the reconnection upflows with or without 'plasmoid'. They certainly have different physical properties and demonstrate different observational signatures of the flare mechanism, that should be studied in detail. We start such a study from the simplest situation, a slow upward motion of the coronal HXR source above the SXR loop in a limb flare.

7.2.3 Data on average upward velocity

Somov et al. (2005b) have searched through the *Yohkoh* HXT/SXT Flare Catalogues (Sato et al., 2003) for appropriate limb flares using Masuda's two criteria: (a) The heliocentric longitude of an active region must be greater than 80°. This ensures maximum angular separation between the LT and

FP sources. (b) The peak count rate in the M2-band must be greater than 10 counts per second per subcollimator (counts s^{-1} SC^{-1}). Thus at least one image can be formed at energies 33-53 keV, where thermal contribution is expected to be lower.

Masuda (1994) found 11 such limb flares before 1993 September. After 1993 September up to 1998 August, Petrosian et al. (2002) found additional 8 flares. Thus there were 19 flares from 1991 October through 1998 August that satisfy these conditions. Only 15 of these flares show detectable LT emission. We (in this Section Somov et al., 2005b) have added some limb flares after 1998 August, that met Masuda's criteria. However, for the study of the upward motion of a coronal HXR source, we selected from this set only 6 flares that have a relatively simple structure: a compact LT source moving upward during sufficiently long time.

Some flares have complex behavior and structure with multiple LT and FP sources (see Aschwanden et al., 1999; Petrosian et al., 2002). The coronal sources may appear and disappear, change direction of motion, or combine with another source as a flare evolves (e.g., the limb flare of 1993 February 17 at 10:35 UT); this can lead to erroneous interpretations if the spatial and time resolution is not sufficiently high. After all removings, we limited our analysis to the 6 flares. For 5 of these flares $V > 3\,\sigma$, where the average velocity V and the velocity dispersion σ were determined by a linear regression. Two of them are presented below.

1991 December 02.— The M3.6 flare at approximately 04:53 UT with the location coordinates N16° E87° occurred in the active region 6952, which just started to appear from the East limb (Figure 7.4).

Two upper panels show the HXT images in the M2 band (33–53 keV) integrated from 04:52:48.2 UT to 04:53:22.7 UT (*left*) and from 04:53:47.7 UT to 04:54:09.2 UT (*right*). The eight contour levels are 12 %, 24 %, 36 %, 48 %, 60 %, 70 %, 82 % and 98 % of the peak intensity for each panel. The arrows show the direction of the HXR source motions. The lower panel shows the height of the upper source centroid as a function of time. The dashed straight line represents the averaged upward motion derived by the method of least squares to estimate the average upward velocity. The dashed thin curve is the HXR emission coming from the selected coronal source area as a function of time.

Presumably, a low part of the flare was partially occulted by the solar limb and, for this reason, it did not show significant chromospheric emission in the M2-band (33-53 keV) at first. Alternatively, the chromospheric emission in the beginning of the flare was weak indeed. The HXT images show two sources (Figure 7.4) associated with a compact flaring SXR loop. One of them that appears high above the limb was probably an LT source. It was observed rather inside the SXT loop than above it (see Petrosian

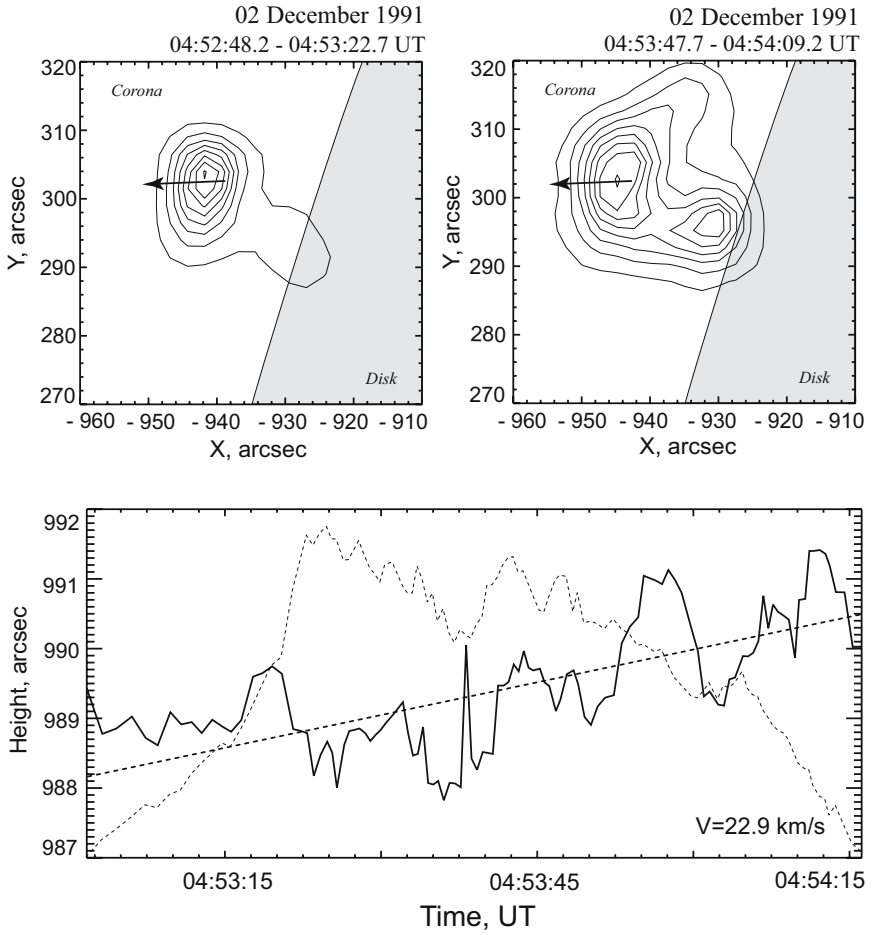

Figure 7.4: The HXR sources and their motions during the 1991 December 2 flare. *Upper panels*: HXT images in two different times. *Lower panel*: Height of the upper source as a function of time. The dashed straight line shows the averaged upward motion. The dashed thin curve is the HXR emission coming from the upper coronal source.

et al., 2002). The other fainter source lay at lower altitudes and could be either an LT or an FP source. This source also shifted its position but we were not able to investigate its motion with sufficient accuracy.

In contrast to the Masuda flare, the coronal HXR source here was bright and long lived (see the dashed thin curve which shows the HXR emission coming from the coronal source area as a function of time). During the initial phase, the average height of the source did not change significantly. The motion seems to be downward in the beginning of the flare like the LT centroid motion in the homologous flares observed by RHESSI (Sui et al., 2004). The height of the LT source begun to increase only after 04:53:20–04:53:30 UT. We tried to make the downward part of a motion track. However an accuracy was not sufficient to study this part. It is enough only to estimate the average velocity during the HXR flare. The average upward velocity of the LT source is $\approx 23 \pm 7$ km/s. The lower (FP) source showed the most strong emission at the time when the LT source rose.

1992 January 13.— Masuda's flare started at approximately 17:27 UT, it was one the most famous events and had been studied extensively. The flare occurred close to the west limb of the Sun. In Figure 7.5 we see three bright sources here, one LT-source and the other two at the footprints. The coronal HXR source located well above the apex of the SXR loop. So this is an ALT source. Its emission was weaker than the FP emission. From 17:28:03 to 17:28:07 UT the LT source disappeared, then arose again for several seconds and faded away completely. Its displacement was about $2''$. The corresponding upward velocity is $\approx 16 \pm 2$ km/s.

Slow ascending motions of sources can be seen in several flares. However, only in five flares, it was possible to estimate the velocity of the upward motion with values between 10 and 30 km/s. These results do not mean, of course, that the HXR source moves monotonically upward. We simply calculated just the average upward velocity expected in view of the standard model of flares. On the other hand, the motion seems to be downward, for example, in the beginning of the flare shown in Figure 7.4. The accuracy of the *Yohkoh* HXT data was not sufficiently high to investigate this actual effect discovered by *RHESSI* (Sui and Holman, 2003). Therefore, the motion of the coronal HXR sources in flares should be studied statistically better by using the *RHESSI* high-resolution imaging data.

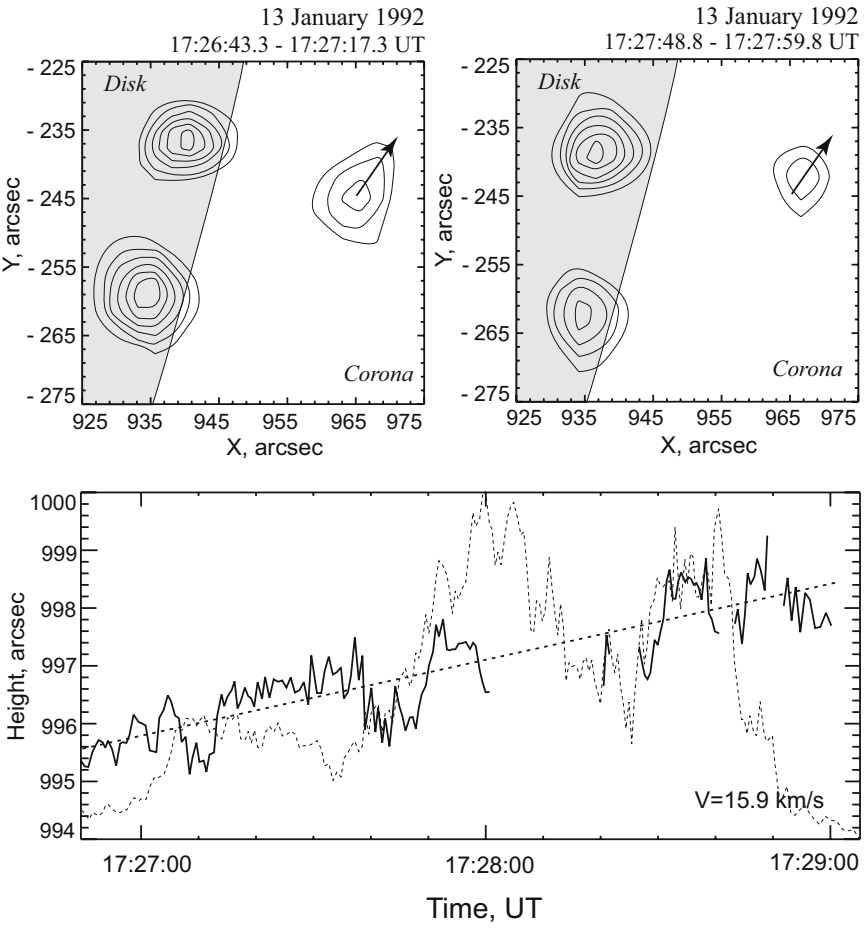

Figure 7.5: The same as Figure 7.4 for the 1992 January 13 flare, Masuda's flare.

7.3 The collapsing trap effect in solar flares

7.3.1 Fast electrons in coronal HXR sources

Fletcher (1995) proposed that the coronal HXR sources as well as the FP sources are nonthermal in origin and are generated by the same population of electrons, with enhanced emission near the top of loops due to initially high pitch-angle distribution of accelerated electrons orbiting the magnetic field near their site of injection before being scattered into the lose-cone. Hudson and Ryan (1995) argued that the impulsive part of the coronal source cannot be thermal, because the thermalization timescale for the superhot plasma with the inferred temperature and density is longer than the observed timescale of variations of emission.

According to Kosugi (1996), the trapped fast electrons create the coronal ALT source of HXR. Meanwhile, the electrons precipitating from the trap generate the thick-target bremsstrahlung in the chromosphere, observed as the FP sources of HXR near the feet of a flare loop. The collapsing trap model, where mirroring particles become energized by the first-order Fermi-type acceleration mechanism in the cusp region between the superhot turbulent-current layer (SHTCL) and the fast oblique collisionless shock (FOCS) front, explains several observed properties of the coronal HXR source (Somov and Kosugi, 1997). One of the questions in the context of this Section is whether or not the observed upward motion of the coronal HXR source in limb flares can be related to the upward motion of the FOCS. An answer to this question depends on two factors: (a) physical properties of the FOCS, and (b) physical and geometrical properties of a magnetic obstacle (MO), the region of strong magnetic field, which stops the fast downflow of superhot plasma and which is observed in SXR as a coronal loop or an arcade of loops.

7.3.2 Fast plasma outflows and shocks

Reconnection serves as a highly efficient engine to convert magnetic energy into thermal and kinetic energies of plasma flows and accelerated particles (Section 3.1). The collisionless reconnection theory (more exactly, the model of a super-hot turbulent-current layer (SHTCL, Section 6.3) under the coronal conditions derived from the *Yohkoh* data) shows that the SHTCL can be considered as the source of flare energy and, at least, the first-step mechanism in a two-step acceleration of electrons and ions to high energies (Somov and Kosugi, 1997).

Fast outflows of super-hot collisionless plasma create complicated dynamics in an external (relative to the SHTCL) region; this dynamics should

be a topic of special research. From the physical point of view, it is difficult to find a proper approximation which takes into account both collisionless and collisional effects. From the mathematical point of view, it is not simple to construct a self-consistent model of the collapsing trap even in a simple kinematic 2D MHD approximation (Giuliani at al., 2005).

It is clear, however, that the interaction of the fast flow of super-hot plasma with an external plasma and magnetic field strongly depends on the initial and boundary conditions, especially on the relative position of the outflow source (the SHTCL) and the magnetic 'obstacle' – the region of the strong external field. Near the boundary of this region the energy density of the outflow becomes equal to the energy density of the field which tries to stop the flow. In Figure 7.6 the magnetic obstacle is shown as a shadowed loop placed schematically above two sunspots N and S in the photosphere Ph.

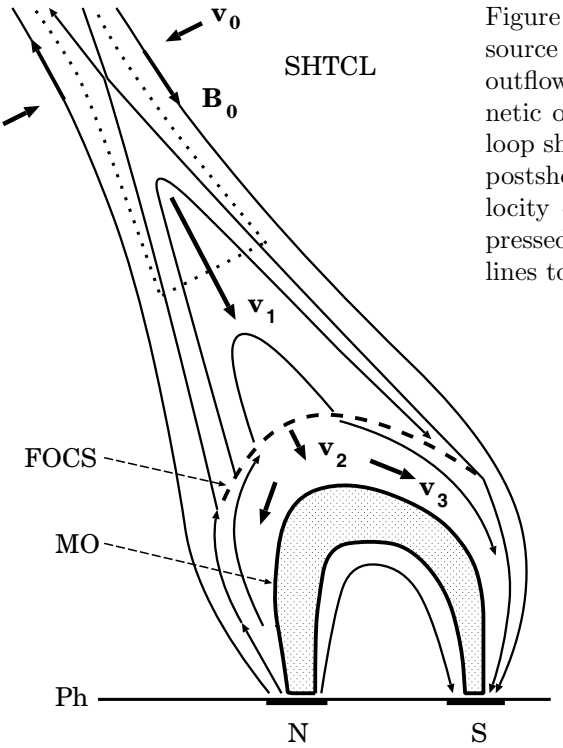

Figure 7.6: A SHTCL as the source of the super-hot plasma outflow with velocity $\mathbf{v}_1$. Magnetic obstacle (MO) is the SXR loop shown by shadow. $\mathbf{v}_2$ is the postshock velocity, $\mathbf{v}_3$ is the velocity of expansion of the compressed plasma along the field lines toward the feet of the loop.

Something similar was observed by the SXT on the *Yohkoh* during the limb flare in 1999 January 20. Images from the SXT show the formation of

a large arcade of loops as well as high-speed flows in the region immediately above the flare loops (McKenzie and Hudson, 1999). Downward-traveling dark voids appear in the SXR images. They presumably represent the cross-section of flux tubes; their downward motion would be interpretable as shrinkage of the field lines due to magnetic tension. Some of the voids slow down and stop as they approach the top of the arcade.

The coronal imaging instruments on *SOHO* study fast (> 1000 km/s) coronal mass ejections (CMEs) which may be responsible for accelerating some of the energetic particles very high in the corona. The LASCO coronagraphs identify motion of plasma in both directions along a radius vector. Simnett (2000) has suggested that such bi-directional flows seen by LASCO are evidence for reconnection in coronal streamers (Somov, 1991). Therefore the *SOHO* observations have identified the sites of reconnecting magnetic fields in the high corona.

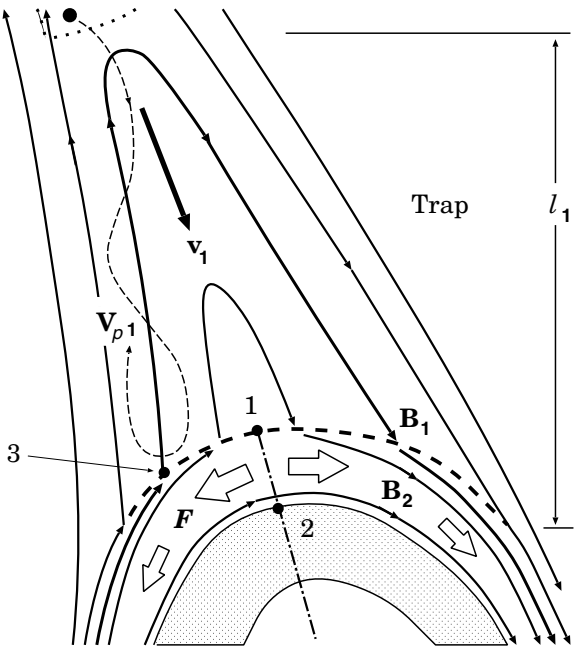

Figure 7.7: A magnetic trap between the SHTCL and the shock front; an accelerated particle moves with velocity $\mathbf{v}_{p1}$ along the field lines. Big arrows F show heat fluxes, directed along the field lines.

Let us assume that the distance l_1 between the source of a fast outflow (an edge of the HTTCS) and the stagnation point 2 at the obstacle is not too

large (Figure 7.7). This means that the outflow becomes *wider* but does not relax in the coronal plasma before reaching the obstacle. Moreover, if the flow velocity still exceeds the local fast magnetoacoustic wave velocity, a fast MHD shock appears ahead the obstacle, which is similar to the terrestrial bow shock ahead the magnetosphere.

By analogy with the ordinary hydrodynamics of supersonic flows, we assume that the shock front reproduces the shape of the obstacle smoothly and on a larger scale (Figure 7.7), more exactly, the shape of the upper part of the obstacle facing the incoming flow. This is true if the incoming flow is uniform or quasi-uniform. Generally, the incoming flow may significantly differ from a quasi-uniform one. Hence the shock may have a more complicated shape. This is, however, not crucial to the effect of the collapsing magnetic trap discussed below. For simplicity, in Figure 7.7, all the field lines ejected by the SHTCL penetrate through the shock. Therefore all super-hot plasma and all particles pre-accelerated by the SHTCL, being frozen into the reconnected field lines, interact with the shock.

For what follows the most important point is that, with respect to the particles pre-accelerated and to superhot particles energized by the SHTCL, the shock should be considered as a *fast oblique collisionless* shock (FOCS).

7.3.3 Particle acceleration in collapsing trap

Being frozen into super-hot plasma, the reconnected field lines move out of the SHTCL and form magnetic loops at the height l_1 above the magnetic obstacle. The top of each loop moves with a high velocity $v_1 \approx 1400 - 2000\ \mathrm{km\,s^{-1}}$. The local fast magnetoacoustic wave speed $\approx 1000\ \mathrm{km\,s^{-1}}$. Therefore a fast shock may appear between the SHTCL and the obstacle. Let us assume that both feet of a loop penetrate through the shock front ahead the obstacle.

Depending on the velocity and pitch-angle, some of the particles pre-accelerated by the SHTCL may pass directly through the magnetic field jump related to the shock. Others may either be simply reflected by the shock or interact with it in a more complicated way.

For the particles reflected by the shock the magnetic loop represents a trap whose length decreases from the initial length $L_0 \approx 2l_1$ to zero (*collapses*) with the velocity $v_m \approx 2v_1$. Therefore the lifetime of each magnetic field line – of each collapsing trap – is equal to

$$t_1 \approx l_1/v_1 \sim 10\ \mathrm{s}\,, \tag{7.4}$$

if $l_1 \approx 10^4$ km and $v_1 \approx 10^3\ \mathrm{km\ s^{-1}}$ are taken as the characteristic values for the length and velocity.

During the trap lifetime t_1 the reflected fast particles move between two magnetic corks – the reflecting points where the field line crosses the shock front. Since these corks (or magnetic mirrors) move to each other with the velocity v_m, the particles trapped inside the trap are 'heated' quickly by the first-order Fermi-type mechanism.

For the electrons pre-accelerated by the SHTCL we estimate the characteristic value of the velocity as $V_{e,1} \approx 10^{10}$ cm s^{-1}. Hence the characteristic time between two subsequent reflections of a particle is estimated as

$$\tau_1 \approx 2l_1/V_{e,1} \sim 0.1 \text{ s}\,. \tag{7.5}$$

Since $\tau_1 \ll t_1$, the conditions of the periodic longitudinal motions change *adiabatically* slowly (see vol. 1, Section 6.1). Then the *longitudinal* adiabatic invariant is conserved (vol. 1, Section 6.2):

$$I = \oint p_{\parallel}\, dl \approx p_{\parallel}(t) \cdot 4\, l(t) = \text{const}\,. \tag{7.6}$$

Here $p_{\parallel} = p\cos\theta$ is the particle longitudinal momentum, θ is its pitch angle. From (7.6) it follows that

$$p_{\parallel}(t) = p_{\parallel}(0)\,\frac{l_1}{l(t)} \approx p_{\parallel}(0)\,\frac{1}{1-(t/t_1)}\,. \tag{7.7}$$

> When the magnetic trap collapses, the longitudinal momentum of a particle grows *infinitely* within the *finite* lifetime t_1.

Neglecting an unknown change of the transversal momentum, we see that the particle kinetic energy of longitudinal motion increases within the time scale t_1:

$$\mathcal{K}_{\parallel}(t) = \frac{1}{2m}\,p_{\parallel}^2 = \mathcal{K}_{\parallel}(0)\,\frac{1}{[1-(t/t_1)]^2}\,. \tag{7.8}$$

That is why we can assume, for example, that just the trap lifetime t_1 is responsible for the observed few-second delay in the higher energies of the hard X-ray (HXR) and gamma-ray emission (Bai et al., 1983).

The main objection usually raised against Fermi acceleration is that the Fermi mechanism is 'neither efficient nor selective'. A magnetic mirror reflects particles on a non-selective basis: thermal particles may be reflected as well as supra-thermal ones. Hence most of the primary energy – the kinetic energy of the fast flow of super-hot plasma – goes into bulk heating of the plasma rather than the selective acceleration of only a small minority of the fast particles. This 'disadvantage' appears to be the main *advantage* of the Fermi mechanism when applied to solar flares in the frame of the collapsing trap model (Somov and Kosugi, 1997).

First, the collapsing trap heats and compresses the super-hot plasma. Thus it becomes visible in HXR emission. Second, the same mechanism lifts some electrons from a quasi-thermal distribution and accelerates them to higher energies; even better, it can further accelerate the electrons pre-accelerated by the SHTCL. The trap of the accelerated electrons is seen as the non-thermal component of the coronal HXR source in flares. Third,

> being non-selective, the collapsing magnetic trap can accelerate not only electrons but also protons and other ions to high energies.

This is a big problem for many other acceleration mechanisms.

Super-hot plasma trapped inside the collapsing loops certainly also contributes to the HXR and radio emission above the SXR loop. The total coronal HXR emission consists of two parts: non-thermal and quasi-thermal. The model predicts, however, a significant difference between them. Being more collisional, the super-hot plasma is less confined inside the trap. For this reason the non-thermal emission dominates at higher energies and occupies a more compact 'vertical' (Figure 7.8) HXR source in comparison with more extended 'horizontal' distribution of a quasi-thermal emission at lower energies. This seems to be consistent with the *Yohkoh* results (Tsuneta et al., 1997).

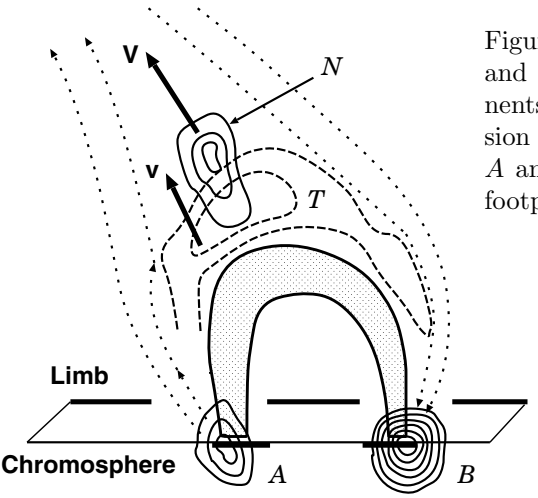

Figure 7.8: The non-thermal (N) and quasi-thermal (T) components of the coronal HXR emission and their apparent motion. A and B are the chromospheric footpoints.

Electron acceleration in the collapsing trap seems to be consistent with the results of the wavelet analysis of the solar flare HXR (Aschwanden et al., 1998). This analysis yields a dynamic decomposion of the power at different timescales τ. The lifetime t_1 may correspond to the dominant peak

time $\tau_{\rm peak}$ detected in the wavelet scalegrams. The collapsing trap scenario is also consistent with the observed correlations, because the acceleration time is proportional to the spatial size of the collapsing trap ($\tau_{\rm min} \sim l_1$).

7.3.4 The upward motion of coronal HXR sources

Further development required for the collapsing trap model is a quantitative consideration of the upward motion of the coronal X-ray sources predicted by the model (Somov et al., 1999). It is clear that the super-hot plasma heated and compressed inside the trap will unavoidably relax in the downstream flow behind the shock. This relaxation is strongly influenced by thermal conductive cooling, hydrodynamic expansion as well as by radiative energy losses. The dynamics of relaxation may not be simple and will depend on the initial and boundary conditions.

The behaviour of the magnetic field behind the shock seems to be more determined – the incoming field lines simply accumulate between the obstacle and the shock. Hence the shock must move upward together with the HXR source in the upstream side (Figure 7.8) and the SXR source in the downstream side.

In the adiabatic approximation, the postshock pressure reach extremely high values. As a result, the shock is accelerated to speeds of order 1000 km/s. This value exceeds by two orders of magnitude the upward speed of the coronal HXR source observed in flares, which usually does not exceed 10–20 km/s.

Postshock energy losses considerably change shock parameters. Bogachev et al., (1998) have considered three mechanisms of energy losses from the shock-compressed super-hot plasma: anomalous heat conduction, hydrodynamic expansion, and radiation. According to estimates, timescales of the first two processes do not exceed a few seconds, whereas radiative losses are much slower and can be initially neglected.

A fast removal of heat from the postshock super-hot plasma and its expansion lead to a considerable decrease of the temperature and, as a consequence, of the gas pressure. As a result, the shock speed v_2 noticeably decreases. For large flow speeds v_1, the shock speed v_2 is proportional to the Alfvén speed upstream, i.e. directly proportional to the field B_1, frozen into the plasma, and inversely proportional to the square root of electron number density n_1. In particular, if we adopt $n_1 \approx 2 \times 10^9$ cm^{-3} and $B_1 \approx 0.5$ G, then the shock is moving at a speed of order 10 km/s, which coincides with the observed upward speed. Of course, this combination of n_1 and B_1 is not unique; we give it here just as the most plausible one on the basis of the *Yohkoh* observations.

However, if we assume higher densities of the flow, we have to assume

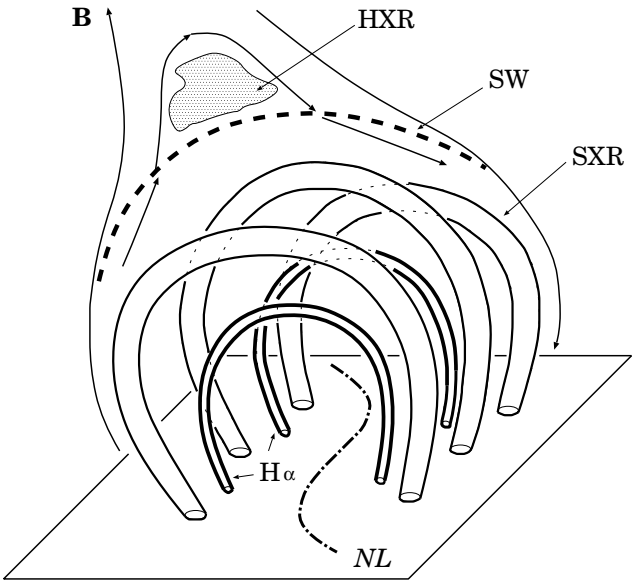

Figure 7.9: The two level structure of the SXR and Hα loops in the solar corona, created as a result of an instability of the magnetic obstacle. NL is the photospheric neutral line, **B** represents the magnetic field lines in the corona.

stronger fields frozen into super-hot plasma. This is acceptable. On the other hand, the shock speed only very weakly depends on the temperature and on the upstream speed. For this reason, a considerable uncertainty in these quantities (especially in the latter one) practically does not affect the results. Moreover, taking into account that the magnetic obstacle is not ideal (Somov et al., 1999) and hence some of plasma with the frozen-in field can 'filter through' it (Figure 7.9) with speeds $v_4 \approx v_2$, allows us to obtain better agreement of the upward shock speed v_2 with observations for stronger magnetic fields in the corona above the shock.

To conclude, a fast MHD or collisionless shock wave with heat-conduction cooling of the postshock plasma may play an important role in the dynamics of a coronal source of HXR during a solar flare. The upward speed of the shock is determined by two processes: accumulation of magnetic flux behind the shock and 'filtering' of cold dense filaments (toghether with the frozen-in field) through the magnetic obstacle. This scenario agrees with the observed hierarchy of hot (SXR) and cool (Hα) loops. For a more detailed comparison of the observed distributions of temperature and emis-

sion measure of the source, a more accurate model is required: it must take into account the actual structure of interaction of the super-Alfvén flow of super-hot magnetized plasma with a magnetic obstacle.

7.3.5 Trap without a shock wave

If, on the contrary to the assumption made above, the distance l_1 between the SHTCL and the stagnation point is large enough, then the fast flow of 'super-hot' plasma relaxes gradually with (or without) collisional shock depending on the height of the reconnection site and other conditions in an active region where the flare occurs. F or example, collisional relaxation can be very fast near the SHTCL if the plasma density is relatively high but the temperature inside the RCL is relatively low.

Let us consider the configuration of a magnetic trap with field lines rapidly moving down but without any shock (Figure 7.10). The strongly de-

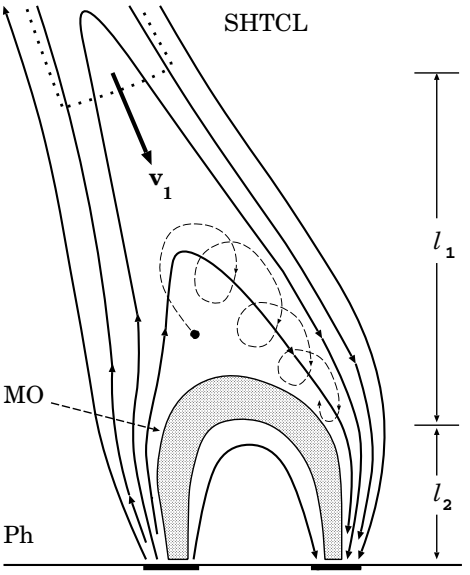

Figure 7.10: Trap without a shock. A SHTCL provides the plasma outflow. The stretched field lines are carried away from the SHTCL by reconnection outflow and relax to a lower energy state. Since the magnetic field strength increases with decreasing coronal height, particles can be trapped within this configuration.

creasing length of the field lines leads to a decrease of the distance between the mirror points and a consequent Fermi-type acceletation of charged particles, while the general increase of the magnetic field strength gives rise to the betatron acceleration. Both effects are considered in Section 7.4 in the adiabatic approximation by using two adiabatic invariants. For the sake of simplicity, let us consider the first effect as a starting point.

In this case, instead of formula (7.7), we have for the collapsing trap without a shock wave another simple formula:

$$p_{\parallel}(t) \approx p_{\parallel}(0)\,\frac{(l_1+l_2)}{l_2+(l_1-v_1 t)}$$

$$\Rightarrow p_{\parallel}(0)\,\frac{(l_1+l_2)}{l_2}\,, \quad \text{when} \quad t \to t_1\,. \tag{7.9}$$

So the trap does not collapse.

If the height l_2 of the magnetic obstacle is not small, the adiabatic heating of fast particles inside the trap is less efficient than in the collapsing trap with the shock. The small height l_2 is probably the case of the so-called 'shrinkage' of X-ray loops, as observed by the *Yohkoh* SXT (e.g. McKenzie and Hudson, 1999). Such situation is expected when magnetic reconnection takes place high in the corona, far from photospheric magnetic-field sources, as follows, for example, from the *SOHO* observations made with LASCO (e.g. Wang and Sheeley, 2002; see also discussion in Section 7.3.2).

7.4 Acceleration mechanisms in traps

7.4.1 Fast and slow reconnection

Collapsing magnetic traps are formed by the process of collisionless reconnection in the solar atmosphere. Figure 7.11 illustrates two possibilities. Fast (Figure 7.11a) and slow (Figure 7.11b) modes of reconnection are sketchy shown in the corona above the magnetic obstacle, the region of a strong magnetic field, which is observed in SXRs as a flare loop (shaded).

In the first case, let us assume that both feet of a reconnected field loop path through the shock front (SW in Figure 7.11a) ahead the obstacle. Depending on the velocity and pitch-angle, some of the particles preaccelerated by the SHTCL may penetrate through the magnetic-field jump related to the shock or may be reflected. For the particles reflected by the shock, the magnetic loop represents a trap whose length $L(t)$, the distance between two mirroring points at the shock front, measured along a magnetic-field line, decreases from its initial value $L(0) \approx 2L_0$ to zero (the top of the loop goes through the shock front) with the velocity $\approx 2v_1$. Therefore, the lifetime of each collapsing trap $t_1 \approx L_0/v_1$.

In the case of slow reconnection, there is no a shock wave, and the trap length $L(t)$ is the distance between two mirroring points (M_1 and M_2 in Figure 7.11b), measured along a reconnected magnetic-field line. In both cases, the electrons and ions are captured in a trap whose length decreases. So the particles gain energy from the increase in parallel momentum.

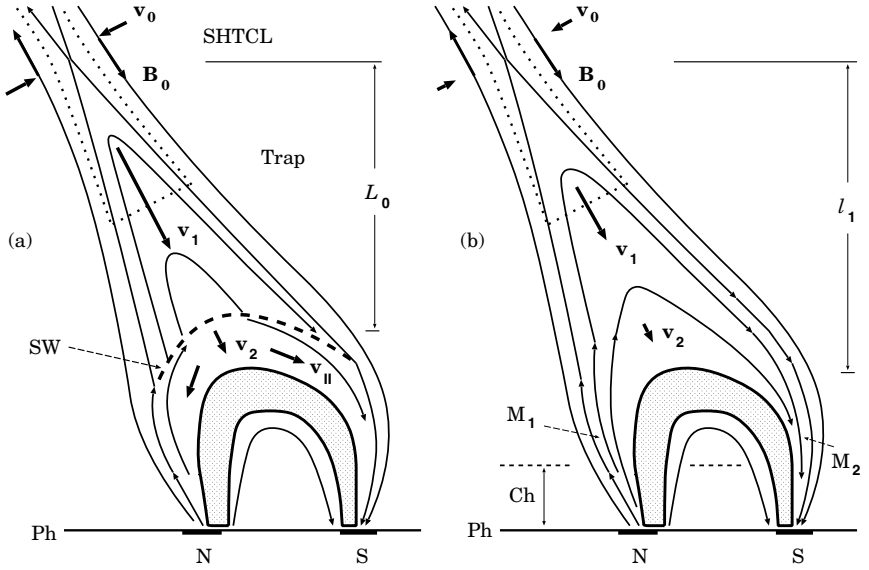

Figure 7.11: Plasma flows related to a super-hot turbulent-current layer (SHTCL): the inflows with a relatively low velocity $\mathbf{v}_0$, the downward outflow with a super-Alfvén velocity $\mathbf{v_1}$. (a) SW is the shock wave above the magnetic obstacle. $\mathbf{v}_2$ is the postshock velocity, $\mathbf{v}_{\|}$ is the velocity of spreading of the compressed plasma along the field lines toward the feet of the loop. (b) The supra-arcade downflow and collapsing trap without a shock. M_1 and M_2 are the mirroring points where the field becomes sufficiently strong to reflect fast particles above the chromosphere (Ch).

Note that the opposite effect – a decrease in parallel momentum and the related adiabatic cooling – should occur for particles trapped between two slow shocks in the Petschek-type MHD reconnection model (see Tsuneta and Naito (1998), Figure 1) because the length of the trap (the distance between the two slow shocks in the reconnection downflow) increases with time. However, Tsuneta and Naito considered acceleration by a fast termination shock; more exactly, they assumed that nonthermal electrons in solar flares can be efficiently accelerated at the fast shock (see the same Figure) by the first-order Fermi-type process if the diffusion length is sufficiently small. The opposite limiting case will be assumed in what follows.

Thus, in the first approximation, we shall neglect collisions of particles ahead of the shock wave (Figure 7.11a) or in the trap without a shock (Figure 7.11b). In both cases, the particle acceleration can be demonstrated

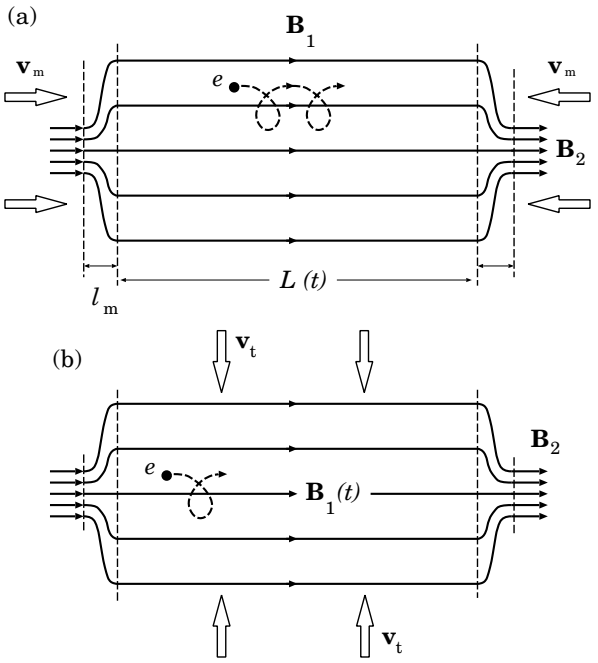

Figure 7.12: Two main effects in a collapsing trap. (a) Magnetic mirrors move toward each other with velocity $\mathbf{v}_m$. (b) Compression of the trap with velocity $\mathbf{v}_t$.

in a simple model – a long trap with short mirrors (Figure 7.12). The decreasing length $L(t)$ of the trap is much larger than the length l_m of the mirrors; the magnetic field $\mathbf{B} = \mathbf{B}_1$ is uniform inside the trap but grows from $\mathbf{B}_1$ to $\mathbf{B}_2$ in the mirrors. The quantity B_2/B_1 is called the mirror ratio; the larger this ratio, the higher the particle confinement in the trap. The validity conditions for the model are discussed by Somov and Bogachev (2003).

7.4.2 The first-order Fermi-type acceleration

We consider the traps for those the length scale and timescale are both much larger than the gyroradius and gyroperiod of an accelerated particle. Due to strong separation of length and timescales, the magnetic field inside the trap can be considered as uniform and constant (for more detail see Somov and Bogachev, 2003). If so, then the longitudinal momentum of a particle

increases with a decreasing length $L(t)$, in the adiabatic approximation, as

$$p_{\parallel}(l) = \frac{p_{\parallel 0}}{l}\,. \tag{7.10}$$

Here $l = L(t)/L(0)$ is the dimensionless length of the trap. The transverse momentum is constant inside the trap,

$$p_{\perp} = p_{\perp 0}\,, \tag{7.11}$$

because the first adiabatic invariant is conserved:

$$\frac{p_{\perp}^2}{B} = \text{const}\,. \tag{7.12}$$

Thus the kinetic energy of the particle increases as

$$K(l) = \frac{p_{\parallel}^2 + p_{\perp}^2}{2\,m} = \frac{1}{2\,m}\left(\frac{p_{\parallel 0}^2}{l^2} + p_{\perp 0}^2\right). \tag{7.13}$$

The time of particle escape from the trap, $l = l_{es}$, depends on the initial pitch-angle θ_0 of the particle and is determined by the condition

$$\text{tg}\,\theta_0 = \frac{p_{\perp 0}}{p_{\parallel 0}} \le \frac{1}{R\,l_{es}}\,, \tag{7.14}$$

where

$$R = \left(\frac{B_2}{B_1} - 1\right)^{1/2}\,. \tag{7.15}$$

The kinetic energy of the particle at the time of its escape is

$$K_{es} = \frac{p_{\perp 0}^2}{2\,m}\,\left(R^2 + 1\right) = \frac{p_{\perp 0}^2}{2\,m}\,\frac{B_2}{B_1}\,. \tag{7.16}$$

One can try to obtain the same canonical result by using more complicated approaches. For example, Giuliani et al. (2005) numerically solved the drift equations of motion (see vol. 1, Section 5.2). However it is worthwhile to explore first the simple analytical approach presented in this Chapter to investigate the particle energization processes in collapsing magnetic traps in more detail before starting to use more sophisticated methods and large-scale simulations.

7.4.3 The betatron acceleration in a collapsing trap

If the thickness of the trap also decreases with its decreasing length, then the strength of the field $\mathbf{B}_1$ inside the trap increases as a function of l, say

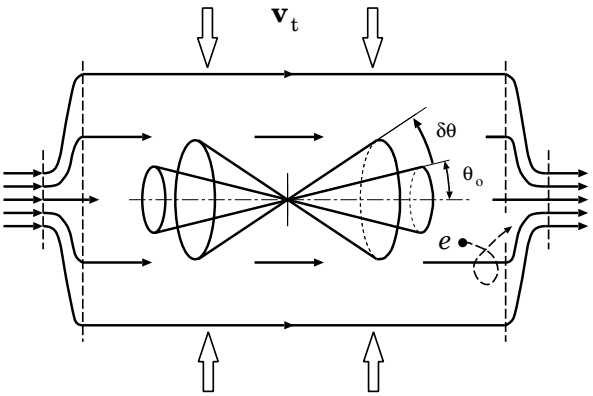

Figure 7.13: The betatron effect in a collapsing magnetic trap. As the trap is compressed with velocity $\mathbf{v}_t$, the loss cone becomes larger. A particle escapes from the trap earlier with an additional energy due to betatron acceleration.

$B_1(l)$. In this case, according to (7.12), the transverse momentum increases simultaneously with the longitudinal momentum (7.10):

$$p_{\perp}(l) = p_{\perp 0} \left(\frac{B_1(l)}{B_1} \right)^{1/2} . \tag{7.17}$$

Here $B_1 = B_1(1)$ is the initial (at $l = 1$) value of magnetic field inside the trap.

The kinetic energy of a particle

$$K(l) = \frac{1}{2\,m} \left(\frac{p_{\parallel 0}^2}{l^2} + p_{\perp 0}^2 \, \frac{B_1(l)}{B_1} \right) \tag{7.18}$$

increases faster than that in the absence of trap contraction, see (7.13). Therefore it is natural to assume that the acceleration efficiency in a collapsing trap also increases.

However, as the trap is compressed, the loss cone becomes larger (Figure 7.13),

$$\theta_{es}(l) = \arcsin \left(\frac{B_1(l)}{B_2} \right)^{1/2} . \tag{7.19}$$

Consequently, the particle escapes from the trap earlier.

On the other hand, the momentum of the particle at the time of its escape satisfies the condition

$$p_{\parallel}(l) = R(l)\, p_{\perp}(l) \,, \tag{7.20}$$

where

$$R(l) = \left(\frac{B_2}{B_1(l)} - 1 \right)^{1/2} . \tag{7.21}$$

Hence, using (7.17), we determine the energy of the particle at the time of its escape from the trap

$$K_{es} = \frac{p_\perp(l)^2}{2\,m} \left(R(l)^2 + 1 \right) = \frac{p_{\perp 0}^2}{2\,m} \frac{B_1(l)}{B_1} \frac{B_2}{B_1(l)} = \frac{p_{\perp 0}^2}{2\,m} \frac{B_2}{B_1} . \tag{7.22}$$

The kinetic energy (7.22), that the particle gains in a collapsing trap with compression, is equal to the energy (7.16) in a collapsing trap without compression, i.e. without the betatron effect.

Thus the compression of a collapsing trap (as well as its expansion or the transverse oscillations) does not affect the final energy that the particle acquires during its acceleration.

> The faster gain in energy is *exactly* offset by the earlier escape of the particle from the trap

(Somov and Bogachev, 2003).

The acceleration efficiency, which is defined as the ratio of the final ($l = l_{ls}$) and initial ($l = 1$) energies, i.e.

$$\frac{K_{es}}{K(1)} = \frac{p_{\perp 0}^2}{p_{\perp 0}^2 + p_{\parallel 0}^2} \frac{B_2}{B_1} = \left(\frac{p_{\perp 0}}{p_0} \right)^2 \frac{B_2}{B_1} , \tag{7.23}$$

depends only on the initial mirror ratio B_2/B_1 and the initial particle momentum or, to be more precise, on the ratio $p_{\perp 0}/p_0$. The acceleration efficiency (7.23) does not depend on the compression of collapsing trap and the pattern of decrease in the trap length either.

It is important that

> the acceleration time in a collapsing trap with compression can be much shorter than that in a collapsing trap without compression.

For example, if the cross-section area $S(l)$ of the trap decreases proportionally to its length l:

$$S(l) = S(1)\, l , \tag{7.24}$$

then the magnetic field inside the trap

$$B_1(l) = B_1(1) \,/\, l , \tag{7.25}$$

and the effective parameter

$$R(l) = \left(R^2 - \frac{1 - l}{l} \right)^{1/2} , \tag{7.26}$$

where R is define by formula (7.15). At the critical length

$$l_{cr} = \frac{1}{1+R^2}\,, \tag{7.27}$$

the magnetic field inside the trap becomes equal the field in the mirrors, and the magnetic reflection ceases to work. If, for certainty, $B_2/B_1 = 4$, then $l_{cr} = 1/4$. So contraction of the collapsing trap does not change the energy of the escaping particles but this energy is reached at an earlier stage of the magnetic collapse when the trap length is finite. In this sense, the betatron effect increases the actual efficiency of the main process – the particle acceleration on the converging magnetic mirrors.

7.4.4 The betatron acceleration in a shockless trap

If we ignore the betatron effect in a shockless collapsing trap, show in Figure 7.11b, then the longitudinal momentum of a particle is defined by the formula (instead of (7.10))

$$p_{\parallel}(t) \approx p_{\parallel}(0)\,\frac{(l_1+l_2)}{l_2+(l_1-v_1 t)} \Rightarrow p_{\parallel}(0)\,\frac{(l_1+l_2)}{l_2}\,, \quad \text{when} \quad t \to t_1\,. \tag{7.28}$$

The particle acceleration on the magnetic mirrors stops at the time $t_1 = l_1/v_1$ at a finite longitudinal momentum that corresponds to a residual length (l_2 in Figure 7.11b) of the trap.

Given the betatron acceleration due to compression of the trap, the particle acquires the same energy (7.16) by this time or earlier if the residual length of the trap is comparable to a critical length l_{cr} determined by a compression law (see Somov and Bogachev, 2003). Thus the acceleration in shockless collapsing traps with a residual length becomes more plausible. The possible observational manifestations of such traps in the X-ray and optical radiation are discussed by Somov and Bogachev (2003). The most sensitive tool to study behaviour of the electron acceleration in the collapsing trap is radio radiation. We assume that wave-particle interactions are important and that two kinds of interactions should be considered in the collapsing trap model.

The first one is resonant scattering of the trapped electrons, including the loss-cone instabilities and related kinetic processes (e.g., Benz (2002), Chapter 8). Resonant scattering is most likely to enhance the rate of precipitation of the electrons with energy higher that hundred keV, generating microwave bursts. The lose-cone instabilities of trapped mildly-relativistic electrons (with account taken of the fact that there exist many collapsing field lines at the same time, each line with its proper time-dependent

loss cone) would provide exitation of waves with a very wide continuum spectrum. In a flare with a slowly-moving upward coronal HXR source, an ensemble of the collapsing field lines with accelerated electrons would presumably be observed as a slowly moving type IV burst with a very high brightness temperatures and with a possibly significant time delay relative to the chromospheric footpoint emission.

The second kind of wave-particle interactions in the collapsing trap-plus-precipitation model is the streaming instabilities (including the current instabilities related to a return current) associated with the precipitating electrons.

7.5 Final remarks

In order to interpret the temporal and spectral evolution and spatial distribution of HXRs in flares, a two-step acceleration was proposed by Somov and Kosugi (1997) with the second-step acceleration via the collapsing magnetic-field lines. The *Yohkoh* HXT observations of the Bastille-day flare (Masuda et al., 2001) clearly show that, with increasing energy, the HXR emitting region gradually changes from a *large diffuse source*, which is located presumably above the ridge of soft X-ray arcade, to a two-ribbon structure at the loop footpoints. This result suggests that electrons are in fact accelerated in the large system of the coronal loops, not merely in a particular one. This seems to be consistent with the *RHESSI* observations of large coronal HXR sources; see, for example, the X4.8 flare of 2002 July 23 (see Figure 3 in Lin et al., 2003).

Efficient trapping and continuous acceleration also produce the large flux and time lags of microwaves that are likely emitted by electrons with higher energies, several hundred keV (Kosugi et al., 1988). We believe that the lose-cone instabilities (Benz, 2002) of trapped mildly-relativistic electrons in the system of many collapsing field lines (each line with its proper time-dependent lose cone) can provide exitation of radio-wave with a very wide continuum spectrum.

Qiu et al. (2004) presented a comprehensive study of the X5.6 flare on 2001 April 6. Evolution of HXRs and microwaves during the gradual phase in this flare exhibits a separation motion between two footpoints, which reflects the progressive reconnection. The gradual HXRs have a harder and hardening spectrum compared with the impulsive component. The gradual component is also a microwave-rich event lagging the HXRs by tens of seconds. The authors propose that the collapsing-trap effect is a viable mechanism that continuously accelerates electrons in a low-density trap before they precipitate into the footpoints.

Imaging radio obsevations (e.g., Li and Gan, 2005) should provide another way to investigate properties of collapsing magnetic traps. It is not simple, however, to understand the observed phenomena relative to the results foreseen by theory. With the incessant progress of magnetic reconnection, the loop system newly formed after reconnection will grow up, while every specific loop will shrink. Just because of such a global growth of flare loops, it is rather difficult to observe the downward motion of newly formed loops. The observations of radio loops by Nobeyama Radioheliograph (NoRH) are not sufficient to resolve specific loops. What is observed is the whole region, i.e., the entire loop or the loop top above it. Anyway, combined microwave and HXR imaging observations are essential in the future.

7.6 Practice: Exercises and Answers

Exercise 7.1. Consider the velocity and magnetic fields in the vicinity of the shock front locally at two points. One of them is point 1 related to the stagnation point 2 at the surface of the magnetic obstacle in Figure 7.7. The other is point 3 located somewhere far from point 1.

Answer. Near point 3 the reconnection outflow with velocity $\mathbf{v}_1$ crosses the shock front and continues to move downwards relative to the front with a small perpendicular component $\mathbf{v}_{2\perp}$ and a large velocity component $\mathbf{v}_{2\parallel}$, which is parallel to the surface of the front (see Figure 7.14a). In the presence of the obstacle MO, the first component is compensated by a slow upward motion of the shock with velocity $\mathbf{v}_2^{sw} = -\mathbf{v}_{2\perp}$.

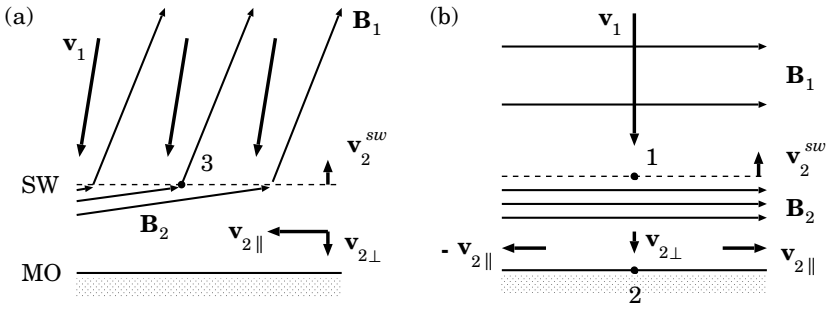

Figure 7.14: The velocity and magnetic fields in the vicinity of: (a) an arbitrary point 3 and (b) point 1 related to the stagnation point 2 at the magnetic obstacle MO.

Near point 1 the flow crosses the front and diverges in such a way that

the velocity $\mathbf{v}_2 = 0$ at the stagnation point 2. So the plasma mainly flows out of the vicinity of this point (Figure 7.14a). On the contrary, new field lines arrive through the shock but, being unidirectional, they cannot disappear there. They are accumulated between the front and the magnetic 'wall'. Magnetic field $\mathbf{B}_2$ increases. Thus we expect the upward motion of the shock with some velocity $\mathbf{v}_2^{sw}$.

Exercise 7.2. Derive an Equation which relates the parameters of the plasma and magnetic field upstream and downstream the shock in the vicinity of point 1 in Figure 7.14b.

Answer. Let us write the MHD continuity Equations for the fluxes of mass, momentum, and energy across the shock front. Considering a pure-hydrogen plasma, we write its pressure and density in terms of the electron number density n and temperature T:

$$p = 2nk_{\text{B}}T, \quad \rho = m_{\text{p}}n, \tag{7.29}$$

m_{p} is the proton mass, k_{B} is the Boltzmann constant; we also assume that $T_{\text{e}} = T_{\text{p}} = T$. With (7.29), the conservation laws become:

$$n_1 (v_1 + v_2) = n_2 v_2, \tag{7.30}$$

$$2n_1 k_{\text{B}} T_1 + m_{\text{p}} n_1 (v_1 + v_2)^2 + \frac{B_1^2}{8\pi} = \\ = 2n_2 k_{\text{B}} T_2 + m_{\text{p}} n_2 v_2^2 + \frac{B_2^2}{8\pi}, \tag{7.31}$$

$$\frac{\gamma}{\gamma - 1} \frac{2k_{\text{B}} T_1}{m_{\text{p}}} + \frac{(v_1 + v_2)^2}{2} + \frac{B_1^2}{4\pi m_{\text{p}} n_1} = \\ = \frac{\gamma}{\gamma - 1} \frac{2k_{\text{B}} T_2}{m_{\text{p}}} + \frac{v_2^2}{2} + \frac{B_2^2}{4\pi m_{\text{p}} n_2}. \tag{7.32}$$

Freezing of the field into the plasma is described by the Equation

$$\frac{B_1}{n_1} = \frac{B_2}{n_2}. \tag{7.33}$$

Here v_1 is the speed of the outflow from the RCL in the immovable reference frame, connected with the 'immovable' obstacle. We neglect the slow proper motion of the obstacle because the SXR loops move upwards much slower than the coronal HXR source. In Equations (7.30)–(7.32) velocity $v_2 \equiv v_2^{sw}$ is directed upward and represents the velocity of the shock with respect to the obstacle. Hence, $v_1 + v_2$ is the velocity of the plasma inflow to the shock;

n_1 and n_2, T_1 and T_2, B_1 and B_2 are electron number density, temperature, and magnetic field upstream and downstream the shock, γ is the adiabatic exponent.

Equations (7.30)–(7.33) yield a relationship, allowing us to determine the front velocity v_2 from the known onflow parameters n_1, T_1, B_1, and v_1:

$$2v_2^3 + (3-\gamma)\, v_2^2 v_1 - (\gamma-1)\, v_2 v_1^2 -$$

$$- (2-\gamma)\, V_{\rm A}^2 v_1 - 2\left(V_{\rm A}^2 + V_s^2\right) v_2 = 0. \qquad (7.34)$$

Here $V_{\rm A}$ and V_s are the Alfvén and sound speeds in the upstream plasma.

Exercise 7.3. The shock-heated plasma inevitably loses energy because of fast heat-conduction cooling. Fast expansion of the compressed super-hot plasma along the field lines also reduces its temperature and pressure. Both cooling mechanisms play an important role in the energy balance, leading to a fast decrease of the postshock temperature. Radiative cooling of the plasma becomes dominating later, at lower temperatures: $T_2 < 10^7$ K. Suppose a rapid fall of the temperature T_2, which must inevitably result in a fast decrease of the gas pressure to values negligible in comparison with the high postshock magnetic pressure:

$$2n_2 k_{\rm B} T_2 \ll \frac{B_2^2}{8\pi}\,. \qquad (7.35)$$

Consider properties of such a shock with fast cooling.

Answer. Condition (7.35) allows us to simplify Equation (7.31):

$$2n_1 k_{\rm B} T_1 + m_{\rm p} n_1 \left(v_1 + v_2\right)^2 + \frac{B_1^2}{8\pi} = m_{\rm p} n_2 v_2^2 + \frac{B_2^2}{8\pi}\,. \qquad (7.36)$$

Moreover Equation (7.32) is no more necessary. From (7.36), (7.30) and (7.33) there follows an Equation for the shock speed:

$$\frac{1}{\gamma}\, V_s{}^2 v_2^2 + v_2^3 v_1 + v_2^2 v_1^2 - V_{\rm A}{}^2 v_2 v_1 - \frac{1}{2}\, V_{\rm A}{}^2 v_1^2 = 0. \qquad (7.37)$$

The shock speed v_2 as a function of the super-hot flow speed and its temperature is shown in Figure 7.15. The dependence of v_2 on the temperature T_1 as well as on the upstream speed v_1 is so weak that in wide ranges of these parameters we see practically the same values of v_2, $10 < v_2 < 20$ km/s.

So the fast shock with fast cooling slowly moves upwards. Morover such shock can provide a significant compression of a magnetic field necessary for particle trapping and acceleration (Somov et al., 1999).

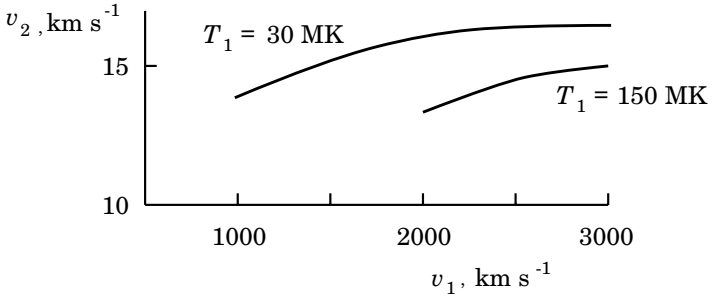

Figure 7.15: Shock speed v_2 versus the speed of the onflowing stream v_1 of the super-hot plasma and its temperature T_1.

Exercise 7.4. Conditions of the second invariant conservation are well satisfied for electrons trapped in collapsing traps of solar flares (Somov and Kosugi, 1997). For ions, however, the acceleration has a more discrete character than for electrons (Somov et al., 2002c). Find how the number of collisions suffered by a trapped ion does depend on the current length of a collapsing trap.

Answer. Each reflection of an ion on a moving mirror leads to an increase of the parallel velocity $\delta V = 2v_m$. After n reflections the parallel velocity of the ion becomes equal to

$$V_n = V_0 + 2nv_m \quad \text{or} \quad V_n = V_{n-1} + 2v_m\,. \tag{7.38}$$

After the reflection number n the ion moves from one mirror with velocity (7.38) to another mirror moving in an opposite direction with velocity v_m. If L_n is the length of the trap at the time of the reflection n, then the time δt_n between consequent reflections can be found from the simple kinematic condition

$$L_n - v_m\,\delta t_n = V_n\,\delta t_n\,. \tag{7.39}$$

Hence the time of flight of the ion between the reflection n and the reflection $n+1$

$$\delta t_n = \frac{L_n}{V_n + v_m}\,. \tag{7.40}$$

During this time, the length of the trap decreases on $2v_m\,\delta t_n$. Thus the length of the trap at the time of the reflection n is

$$L_n - L_{n+1} = 2v_m\,\delta t_n. \tag{7.41}$$

Let us assume that fast ions are injected into the trap in its center at the time $t_0 = 0$. Then, before the first reflection at the time δt_0, each ion

passes the distance $L_0/2 - v_m\,\delta t_0 = V_0\,\delta t_0$. From this condition

$$\delta t_0 = \frac{L_0}{2\,(V_0 + v_m)}\,. \tag{7.42}$$

Substituting (7.42) in formula (7.41) with $n = 0$ gives us the first decrease of the trap length

$$L_0 - L_1 = 2v_m\,\delta t_0 = v_m\,\frac{L_0}{V_0 + v_m}\,. \tag{7.43}$$

Thus

$$L_1 = L_0 - v_m\,\frac{L_0}{V_0 + v_m} = L_0\,\frac{V_0}{V_0 + v_m}\,. \tag{7.44}$$

Acting similarly for any reflection number n we find a general formula which relates the trap length L_n with n:

$$L_n = L_0\,\frac{V_0}{V_0 + v_m}\,\frac{V_0 + v_m}{V_0 + 2nv_m - v_m} = L_0\,\frac{V_0}{V_0 - v_m + 2nv_m}\,. \tag{7.45}$$

From here, the number of reflections as a function of the descrete lengths L_n is equal to

$$n = \frac{L_0V_0 + L_n\,(v_m - V_0)}{2v_mL_n}\,. \tag{7.46}$$

For arbitrary value of the trap length L and for any number n, we introduce the step-function

$$n = \mathcal{N}\left(\frac{L_0V_0 + L\,(v_m - V_0)}{2v_mL}\right), \tag{7.47}$$

where $\mathcal{N}(x) = 0,\ 1,\ 2$, etc. is the integer part of the argument x.

As the trap becomes shorter and shorter, the trapped particle is accelerated, and the number of accelerations per second increases.

Exercise 7.5. How does kinetic energy of a trapped ion increase in a collapsing trap?

Answer. Substituting (7.47) in formula (7.38) gives us a relationship between the ion velocity V and the trap length L:

$$V(L) = V_0 + 2v_m\,\mathcal{N}\left(\frac{L_0V_0 + L\,(v_m - V_0)}{2v_mL}\right). \tag{7.48}$$

By using the dimensionless parameter $l(t) = L(t)/L_0$, we rewrite (7.48) as follows

$$V(l) = V_0 + 2v_m\,\mathcal{N}\left(\frac{V_0\,(1 - l) + lv_m}{2v_ml}\right). \tag{7.49}$$

Since for a nonrelativistic ion, the momentum $\mathbf{p} = m_i \mathbf{V}$, the parallel momentum variation as a function of l is given by

$$p_{\parallel i}(l) = m_i V_{\parallel i}(l) = p_{\parallel i 0} + 2 m_i v_m \mathcal{N}\left(\frac{p_{\parallel i 0}(1-l) + m_i v_m l}{2 m_i v_m l}\right), \quad (7.50)$$

instead of formula (7.7). Here, as above, $\mathcal{N}$ is the step function of its argument or simply the number of mirroring reflections of a given particle. The parallel motion energy of an ion is growing as

$$\mathcal{K}_{\parallel i}(l) = \frac{m_i}{2} V_{\parallel i}(l)^2 = \quad (7.51)$$

$$= \frac{m_i}{2}\left[\left(\frac{2\mathcal{K}_{\parallel i 0}}{m_i}\right)^{1/2} + 2 v_m \mathcal{N}\left(\frac{(1-l)\sqrt{2\mathcal{K}_{\parallel i 0}/m_i} + v_m l}{2 v_m l}\right)\right]^2 .$$

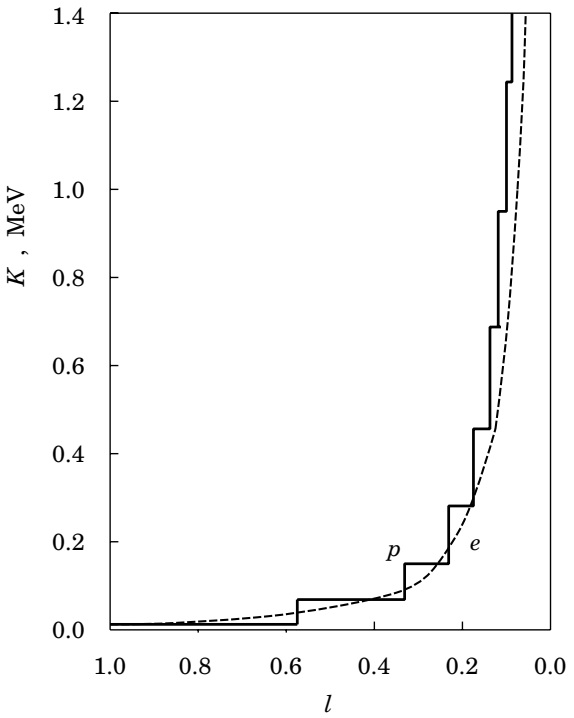

Figure 7.16: Kinetic energy of electrons and protons in a collapsing magnetic trap as a function of its length.

For comparison, we show in Figure 7.16 the kinetic energy of a proton (solid steps) and of an electron (the dashed curve) as a function of l. Initially, the energy steps for the proton are not frequent but follow the second invariant curve of the electron. Later on, when the kinetic energy of the electron becomes close to $m_e c^2$, its energy grows more slowly than the one of the proton. For example, a proton with an initial energy $K_0 \approx k_B T$, where $T \approx 10^8$ K is a typical temperature for a high-temperature turbulent-current layer (see Sections 6.3 and 7.1), has a kinetic energy twice higher than the one of an electron at $l \approx 0.1$ with the same initial energy. At the same time, reflections of the proton on magnetic mirrors become more frequent, and the second adiabatic invariant is conserved. So, conservation of the second invariant is not a bad approximation for trapped protons.

After a number of bounces the ion's pitch angle becomes less than the loss cone pitch angle, and it passes through the mirror, never to return. An accelerated particle escapes from a trap as soon as

$$p_\parallel \geq R\, p_\perp, \quad \text{where } R = \left(\frac{B_2}{B_1} - 1\right)^{1/2}. \tag{7.52}$$

As soon as the increase of its parallel momemtum under the acceleration process is high enough to satisfy this condition, a particle escapes from the trap. Every particle is able to escape the collapsing magnetic trap before the length of the trap shrinks to zero.

This page intentionally blank

Chapter 8

Solar-type Flares in Laboratory and Space

The super-hot turbulent-current layer (SHTCL) theory offers an attractive opportunity for laboratory and astrophysical applications of the magnetic reconnection.

8.1 Solar flares in laboratory

New data on the mechanism of magnetic energy transformation into kinetic and thermal energies of a super-hot plasma at the Sun require new models of reconnection under conditions of anomalous resistivity, which are similar to that ones investigated in toroidal devices performed to study turbulent heating of a collisionless plasma.

8.1.1 Turbulent heating in toroidal devices

The electric resistivity of plasma is the important macroscopic parameter that can be assessed relatively straightforwardly in laboratory experiments. In order to clarify the basic physical mechanisms behind the anomalous resistivity, much effort has been spent. Many experiments were done to investigate the feasibility of using turbulent heating as a means of injecting a large power into toroidal devices: stellarators and tokamaks. Much progress has been made in understanding the anomalous resistivity and concurrent plasma heating by current-driven turbulence (CDT), the turbulence driven by a current parallel to a magnetic field (for a review see de Kluiver et al., 1991). In general,

the electric conductivity σ exhibits an anomalous reduction when the electric field E exceeds a threshold.

The electric conductivities observed in the toroidal devices are highly anomalous, and scales with the electric field as

$$\frac{\sigma}{\sigma_{\rm cl}} \approx 0.1\,\frac{E_{\rm Dr}}{E}\,. \tag{8.1}$$

Here $\sigma_{\rm cl} = \sigma_0\,T^{3/2}$ is the classical conductivity, $\sigma_0 \approx 1.44\times 10^8/\ln\Lambda$, $\ln\Lambda$ is the Coulomb logarithm; the Dreicer's field (see Appendix 3)

$$E_{\rm Dr} \approx 6.4\times 10^{-10}\,\frac{n}{T}\,\ln\Lambda\,,\quad {\rm V}\,. \tag{8.2}$$

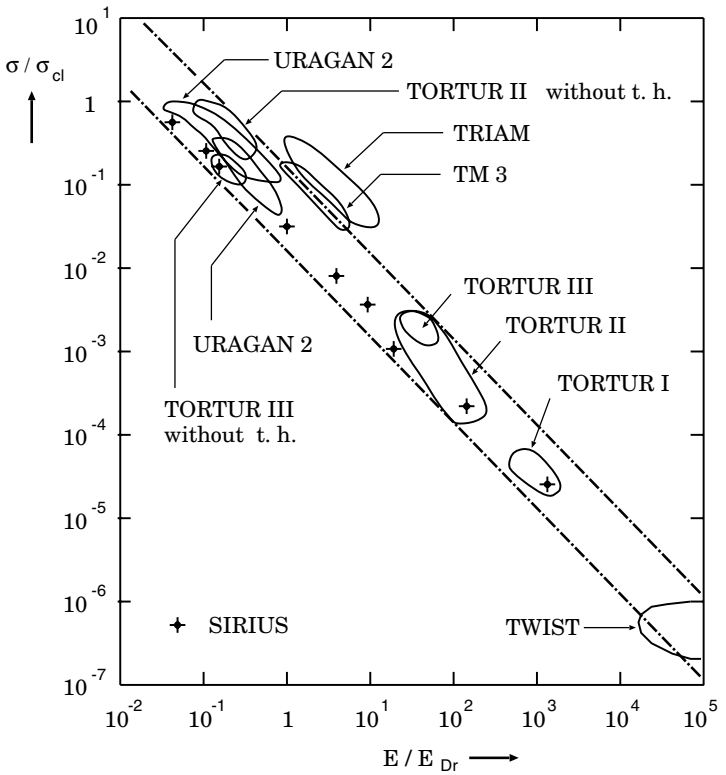

Figure 8.1: Normalized conductivity σ/σ_{cl} versus the normalized electric field $E/E_{\rm Dr}$ in various toroidal devices (de Kluiver et al., 1991).

The scaling law (8.1) is valid in the range of electric fields

$$10^{-2} \leq E/E_{\rm Dr} \leq 10^{5}\,.$$

The corresponding ratio $\sigma/\sigma_{\rm cl}$ varies from 10 to 10^{-6}. Almost all known nonlinear process (from quasilinear to strong turbulence) are likely to be involved in the experiments. However all data points from considerably different devices fall in a narrow band indicated in Figure 8.1.

Formulae (8.1) and (8.2) give us

$$\sigma \approx 3.0 \times 10^{-5}\,\frac{T^{1/2}\,n}{E}\,, \quad {\rm s}^{-1}\,. \tag{8.3}$$

So, instead of using complicated methods to find the anomalous conductivity in different regimes of CDT, as it was done in Section 6.3, we can apply the simple empirical formula (8.3).

8.1.2 Current-driven turbulence in current layers

Let us assume that the electron temperature exceeds significantly the ion one in the super-hot turbulent-current layer (SHTCL):

$$T_{\rm e} \gg T_{\rm i}\,, \quad T = T_{\rm e}\,.$$

In the reconnecting current layer (RCL), magnetic field lines inflow together with plasma at a small velocity v, reconnect inside the layer and then outflow at a large velocity V. It follows from the set of Equations (6.43)–(6.48) that:

$$n_0\,v\,b = n\,V\,\xi\,b\,, \tag{8.4}$$

$$\frac{B_0^2}{8\pi} = n\,k_{\rm B}T\,, \qquad n\,k_{\rm B}T = \frac{1}{2}\,M\,n\,V^2\,, \tag{8.5}$$

$$\frac{c\,B_0}{4\pi\,a} = \sigma\,E_0\,, \tag{8.6}$$

$$\mathcal{E}_{mag}^{\,in} = \mathcal{E}_{th}^{\,out} + K^{\,out} + C_{\parallel}\,. \tag{8.7}$$

In the continuity Equation (8.4), $v = c\,E_0/B_0$ is the plasma drift velocity into the layer. It follows from Equations (8.5) that the velocity of the plasma outflow is

$$V = \frac{B_0}{\sqrt{4\pi\,Mn}}\,. \tag{8.8}$$

The magnetic field near the RCL is estimated as (6.51).

The energy equation (8.7) includes the magnetic enthalpy flux into the layer

$$\mathcal{E}_{mag}^{\,in} = \frac{B_0^2}{4\pi}\, v\, b\,, \tag{8.9}$$

which coincides with the Joule heating of the RCL $(j^2/\sigma)\, a\, b$. The thermal enthalpy flux from the layer along the magnetic field lines is

$$\mathcal{E}_{th}^{\,out} = \left(\frac{5}{2}\, n_{\rm e}\, k_{\rm B} T_{\rm e} + \frac{5}{2}\, n_{\rm i}\, k_{\rm B} T_{\rm i}\right)\, V\, \xi\, b \approx \frac{5}{2}\, n\, k_{\rm B} T \times\, V\, \xi\, b\,, \tag{8.10}$$

where allowance is made for $n_{\rm i} = n_{\rm e} \equiv n$ and $T_{\rm i} \ll T_{\rm e} = T$. The kinetic energy flux of the plasma outflowing from the layer is

$$K^{\,out} = \left(\frac{1}{2}\, Mn\, V^2 + \frac{1}{2}\, mn\, V^2\right)\, V\, \xi\, b \approx \frac{1}{2}\, Mn\, V^2 \times\, V\, \xi\, b\,, \tag{8.11}$$

since the ion mass M exceeds significantly the electron mass m.

The heat flux along the field lines can be taken as (6.40). Therefore, in general, the new models presented below are similar to the simple 'test models' of a SHTCL, described in Chapter 3 in Somov (1992), or, more exactly to an 'one-temperature model' (Somov and Titov, 1983; see also Somov, 1981). We remind that the heat flux in the test model was considered as saturated at $1 \le \theta \le 8.1$; this only approximately satisfies inequality $T_{\rm e} \gg T_{\rm i}$. We shall keep in the next Section the same value of the flux

$$C_{\parallel} = \frac{n\,(k_{\rm B}\, T)^{3/2}}{4\, m^{1/2}}\, \xi\, b\,, \tag{8.12}$$

in order to demonstrate clearly the effect of formula (8.3) for estimating the turbulent conductivity:

$$\sigma = \sigma_1\, \frac{T^{1/2}\, n}{E_0}\,, \quad {\rm s}^{-1}\,, \quad \text{where} \quad \sigma_1 \approx 2.98 \times 10^{-5}\,. \tag{8.13}$$

Later on, the anomalous value of the heat flux will be adopted which corresponds to $\theta \gg 1$. So a better agreement will be reached between the initial assumptions and designed functions; moreover the question will be solved on a sensitivity of the SHTCL model to the heat flux value.

Equation (8.7) does not include the thermal enthalpy flux into the RCL

$$\mathcal{E}_{th}^{\,in} = (5\, n_0\, k_{\rm B} T_0)\, v\, b \ll \mathcal{E}_{th}^{\,out}\,, \tag{8.14}$$

as long as the coronal plasma temperature $T_0 \ll T$, and the kinetic energy flux of the plasma flowing into the layer

$$K^{\,in} = \left(\frac{1}{2}\, Mn_0\, v^2 + \frac{1}{2}\, mn_0\, v^2\right)\, v\, b \ll K^{\,out}, \tag{8.15}$$

as $v^2 \ll V^2$ in the strong field approximation. We neglect also the magnetic enthalpy flux from the current layer

$$\mathcal{E}_{mag}^{out} = \frac{B_y^2}{4\pi} V \xi b \ll \mathcal{E}_{mag}^{in}, \tag{8.16}$$

since $B_y^2 \ll B_0^2$. Moreover, as is shown in the test model, the following factors do not influence the energy balance of the SHTCL under the corona conditions: the energy exchange between electrons and ions due to Coulomb collisions, the heat flux across a magnetic field, and the energy losses due to radiation.

8.1.3 Parameters of a current layer with CDT

Let us find the unknown values a, b, n, and V from Equations (8.4)–(8.6) considering the temperature T as an unknown parameter. We obtain the following formulae:

$$a = 2^{1/6} \pi^{-1/3} k_{\text{B}}^{5/6} M^{-1/6} c^{2/3} \sigma_1^{-1} \left[n_0^{-1/3} E_0^{-1/3} \xi^{1/3} \right] T^{1/3}, \tag{8.17}$$

$$b = 2^{5/6} \pi^{1/3} k_{\text{B}}^{1/6} M^{1/6} c^{1/3} \left[n_0^{1/3} E_0^{1/3} h_0^{-1} \xi^{-1/3} \right] T^{1/6}, \tag{8.18}$$

$$n = 2^{-4/3} \pi^{-1/3} k_{\text{B}}^{-2/3} M^{1/3} c^{2/3} \left[n_0^{2/3} E_0^{2/3} \xi^{-2/3} \right] T^{-2/3}, \tag{8.19}$$

$$V = 2^{1/2} k_{\text{B}}^{1/2} M^{-1/2} T^{1/2}. \tag{8.20}$$

Now from Equation (8.7), we derive the temperature as a function of the parameters n_0, h_0, E_0, and ξ. On this purpose, let us rewrite (8.7):

$$\frac{B_0^2}{4\pi} v b = \frac{1}{2} \left(M n V^2 + 5 n k_{\text{B}} T \right) V \xi b + \frac{n (k_{\text{B}} T)^{3/2}}{4 m^{1/2}} \xi b. \tag{8.21}$$

Transform the terms on the right-hand side:

$$\frac{1}{2} \left(M n V^2 + 5 n k_{\text{B}} T \right) V \xi b = \frac{7}{4} \frac{n_0}{n} \frac{B_0^2}{4\pi} v b, \tag{8.22}$$

$$\frac{n (k_{\text{B}} T)^{3/2}}{4 m^{1/2}} \xi b = \frac{1}{8} \left(\frac{M}{2m} \right)^{1/2} \frac{n_0}{n} \frac{B_0^2}{4\pi} v b. \tag{8.23}$$

Substituting (8.22) and (8.23) in Equation (8.21) yields

$$\frac{n}{n_0} = \frac{7}{4} + \frac{1}{8} \left(\frac{M}{2m} \right)^{1/2} \approx 5.54. \tag{8.24}$$

From this, with allowance for formula (8.19), we find the temperature

$$T = \frac{2}{\left[7 + \sqrt{M/8m}\right]^{3/2}}\ \pi^{-1/2}\, k_{\text{B}}^{-1}\, M^{1/2}\, c\, \left[n_0^{-1/2}\, E_0\, \xi^{-1}\right]. \qquad (8.25)$$

Thus formulae (8.24), (8.25), (8.17), (8.18), and (8.20) determine the current layer characteristics n, T, a, b, and V via the external parameters n_0, E_0, h_0, and the dimensionless parameter ξ. Apart from the SHTCL parameters mentioned above, the energy release power per unit of the layer length has been calculated:

$$\frac{P}{l} = \frac{B_0^2}{4\pi}\, v\, 4b = \frac{1}{\pi}\, c\, E_0\, h_0\, b^2\,. \qquad (8.26)$$

Comparison of the parameters estimated in the framework of the well studied test models with the results of the new models, shows the previous and new results differ only slightly. This indicates an agreement between two different approaches to the estimation of anomalous conductivity: the theoretical one used in the test models, and the empirical one described by de Kluiver et al. (1991). For example, with the electric field $E_0 \approx 0.1 - 6.9$ V/cm the test model predicts the conductivity $\sigma \approx 3{\times}10^{12}{-}6{\times}10^{11}$ s^{-1}, which is the well suitable range for solar flares and CMEs (Somov, 1992). For the same electric field, the new model yields $\sigma \approx 2\times10^{13} - 6\times10^{11}$ s^{-1}.

8.1.4 The SHTCL with anomalous heat conduction

Let now the electric conductivity be determined by formula (8.13) and heat conduction flux by

$$C_{\parallel} = \frac{n\,(k_{\text{B}}T)^{3/2}}{M^{1/2}}\,\xi\, b\,. \qquad (8.27)$$

Here it is taken into account that $f_{M}(\theta) = 1$ at $\theta \gg 1$, see formulae (6.40) and (6.41). Equation (8.7) in this case has the following form:

$$\frac{B_0^2}{4\pi}\, v\, b = \frac{1}{2}\left(Mn\,V^2 + 5\,n\,k_{\text{B}}T\right)\, V\,\xi\, b + \frac{n\,(k_{\text{B}}T)^{3/2}}{M^{1/2}}\ \xi\, b\,. \qquad (8.28)$$

Solving procedure of the set of Equations (8.4)–(8.6) and (8.28) is similar to that one developed earlier. From Equation (8.28) we obtain the ratio

$$\frac{n}{n_0} = \frac{7}{4} + 2^{-3/2} \approx 2.1\,. \qquad (8.29)$$

From here, taking into account (8.19), the RCL temperature is found:

$$T = \frac{1}{4\,\left[(7/4) + 2^{-3/2}\right]^{3/2}}\,\pi^{-1/2}\,k_{\text{B}}^{-1}\,M^{1/2}\,c\,\left[n_0^{-1/2}\,E_0\,\xi^{-1}\right]\,. \qquad (8.30)$$

So, in the framework of the new models of a SHTCL with the anomalous heat conduction, the values describing the RCL (n, T, a, b, and V) are determined by formulae (8.29), (8.30), (8.17), (8.18), and (8.20). Their estimations, obtained for the same initial data as in the test models, show that a replacement of the saturated heat flux by the anomalous one leads to decreasing $C_{\parallel}$ by a factor of 2–3. This slightly influences the results. The RCL becomes hotter and more rarefied, its thickness and width somewhat increase. A factor of changes does not exceed 4. Therefore a choice of the turbulent heat flux (saturated or anomalous) model generally is not a crutial point when a rough comparison is made of the local models of a RCL. However

> the choice of the heat transport regime in a super-hot plasma may be of importance for interpreting HXRs of solar flares

(Somov and Kosugi, 1997; Somov et al., 1998).

The energy release power per unit of length of the layer, depending on conditions, varies over a wide range: from $\sim 10^{15}$ to $\sim 10^{19}$ erg/(cm s), i.e. for the SHTCL with characteristic length $L \sim 10^{10}$ cm, the power is high as 10^{29} erg/s which is sufficient to account for the most powerful flares and CMEs (Somov, 1992). So

> the collisionless 3D reconnection in the solar active phenomena seems to be similar to the reconnection observed in laboratory, in the toroidal devices: tokamaks and stellarators.

Classically, most electrons are expected to run away in strong electric fields. However the experiments in the toroidal devices, most of which have been made in well magnetized plasmas, indicate that effective braking mechanisms exist to retard runaway electrons. In this way, a sufficiently strong electric field creates the state of the CDT. This state is macroscopically characterized by a large decrease of conductivity σ from the classical value σ_{cl}.

With the anomalous decrease of conductivity, Joule dissipation is enhanced by a factor σ_{cl}/σ and leads to rapid plasma heating to extremaly high temperatures. *Yohkoh* observations of super-hot plasma in solar flares presumably indicate that the anomalous conductivity and accompanying turbulent heating are macroscopic manifestations of the CDT in the place of collisionless reconnection (the SHTCL) as well as in the surrounding coronal plasmas heated by anomalous heat fluxes.

8.2 Magnetospheric Physics Problems

8.2.1 Reconnection in the Earth Magnetosphere

The coupling between the solar wind and the magnetosphere is mediated and controlled by the magnetic field in the solar wind through the process of magnetic reconnection as illustrated by Figure 8.2 according to Dungey (1961).

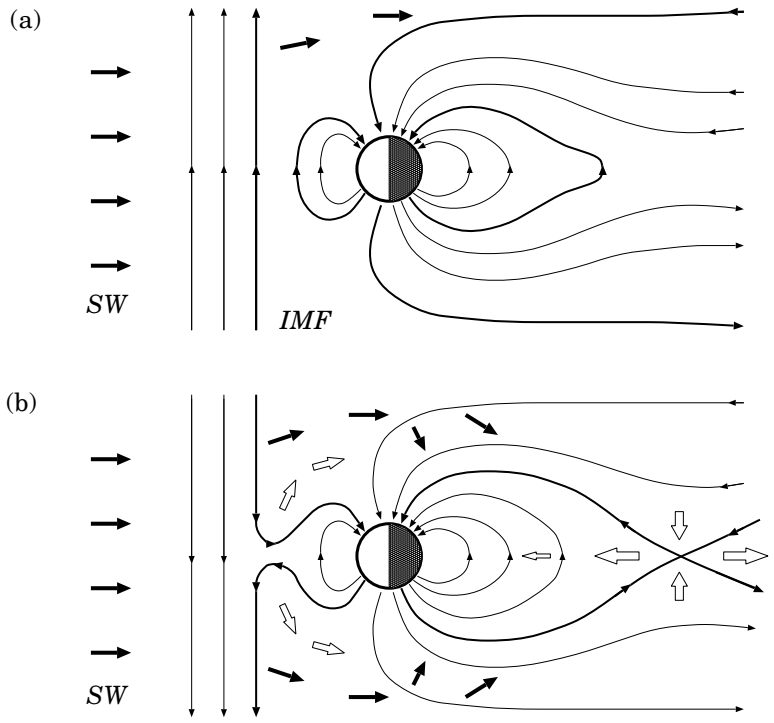

Figure 8.2: Schematic of the process of reconnection in the magnetosphere. (a) No reconnection and no energy flow into the magnetosphere. Energy flow is indicated by solid arrows. (b) Reconnection opens the magnetosphere and allows entry of plasma, momentum, and energy. Magnetospheric convection is indicated by the open arrows.

Reconnection occurs on the dayside if an interplanetary magnetic field (IMF) is directed southwardly. Reconnection turns closed field lines of the Earth into open field lines: one end is connected to the Earth and the other in the solar wind (SW in Figure 8.2). The reconnected field lines

take part in the antisunward motion of the solar wind and get dragged to the nightside. Here they enhance the tail lobes. Hence reconnection must again occur on the nightside, and the new closed field lines must return to the dayside. Therefore, reconnection gives rise to convection of plasma through the magnetosphere.

3D magnetospheric configurations that represent pressure balance across the magnetopause were found for a variety of actual conditions (e.g., Sotirelis and Meng, 1999) allowing for the cross-tail current. Many different configurations were presented for general reference. The magnetospheric magnetic pressure was calculated by using the current systems of the model by Tsyganenko (1996) together with self-consistently calculated magnetopause shapes and currents.

8.2.2 MHD simulations of space weather

As we discussed in Introduction, solar flares and coronal mass ejections (CMEs) strongly influence interplanetary and terrestrial space by virtue of shock waves, hard electromagnetic radiation and accelerated particles (e.g., Kivelson and Russell, 1995). That is why **space weather** is of growing importance to the scientific community and refers to conditions at a particular place and time on the Sun and in the solar wind, magnetosphere, ionosphere, and thermosphere that can influence the performance and reliability of spaceborne and ground-based technological systems and can affect human life or health (Wright, 1997; Hanslmeier, 2002; de Jager, 2005). These influences have prompted efforts to enhance our understanding of space weather and develop effective tools for space weather prediction.

Global MHD simulations have been used for a long time to model the global magnetospheric configuration and to investigate the response of the magnetosphere-ionosphere system to changing solar wind conditions (see review by Lyon, 2000). Variations in the solar wind can lead to disruptions of space- and ground-based systems caused by enhanced electric currents flowing into the ionosphere and increased radiation in the near-Earth environment.

A focus of many MHD investigations was the study of magnetospheric 'events'. In addition to this study, there have been several applications of MHD models to the study of coronal and solar wind plasma flows. For example, the ideal MHD approximation was efficiently used by Groth et al. (2000) to simulate the initiation, structure, and evolution of a CME and its interaction with the magnetosphere-ionosphere system.

Groth et al. have developed a new parallel adaptive mesh refinement (AMR) finite-volume scheme to predict the ideal MHD flows in a complete fully three-dimensional space weather event. So the simulation spans

the initiation of the solar wind disturbance at the surface to its interaction with the Earth's magnetosphere-ionosphere system. Starting with generation of a CME at the Sun, the simulation follows the evolution of the solar wind disturbance as it evolves into a magnetic cloud and travels through interplanetary space and subsequently interacts with the terrestrial magnetosphere-ionosphere system.

8.3 Flares in accretion disk coronae

In this Section we discuss the possibility of applying the theory of magnetic reconnection in solar flares to astrophysical phenomena accompanied by fast plasma ejection, powerful fluxes of heat and radiation, impulsive acceleration of electrons and ions to high energies. We use the well-tested models of the SHTCL to evaluate an ability to release a free magnetic energy in the accretion disk coronae of compact stars, for example, neutron stars.

8.3.1 Introductory comments

The accretion disks presumably have a corona which interacts with a magnetic field generated inside a disk. Drawing on developments in solar flare physics, Galeev et al. (1979) suggested that the corona is heated in magnetic loops which have buoyantly emerged from the disk. Reconnection of buoyant fields in the lower density surface regions may supply the energy source for a hot corona. Another feature related to the disk corona is the possibility of a flare energy release similar to solar flares. They are accompanied by fast directed plasma ejections (jets), coronal mass ejections (CMEs) into interplanetary space, powerful fluxes of hard electromagnetic radiation.

If a plasma in the disk corona is optically thin and has a dominant magnetic pressure, the circumstances are likely to be similar to the solar corona. Therefore it is also possible to imagine some similarity between solar flares and the X-ray flares in the accretion disk coronae. Besides the effect of heating the the disk corona, reconnection is able to accelerate electrons and protons to relativistic energies (Lesch and Pohl, 1992; Bednarek and Protheroe, 1999). Starting from well-tested models for magnetic reconnection in the solar corona during flares, we examine whether the magnetic reconnection may explain the hard X-ray emission of stars.

8.3.2 Models of the star magnetosphere

8.3.2 (a) Global and local magnetic fields

Let us assume that the magnetic fields in the magnetosphere of a star (for example, the pulsar magnetosphere) with an accretion disk consist of two components of different origin. The first, *regular* large-scale magnetic component is related to the proper magnetic field of a star and large-scale electric currents flowing in the accretion disk as a whole. This component is similar to the large-scale quasi-stationary magnetic field in the solar corona, including the coronal streamers, or in the Earth magnetosphere, including the magnetotail.

The second component represents the *chaotic* magnetic fields generated by the differential rotation and turbulence in the accretion disk. The MHD turbulence inside the disk gives rise to the dynamo mechanism with a wide spectrum of scales for magnetic fields emerging at the disk's surfaces into its corona. These fields, interacting between themselves and with the large-scale regular field of the magnetosphere, create flares of different scales in the corona of the disk. We believe that they heat the corona and accelerate particles to very high energy via magnetic reconnection in myriads of large and small flares similar to solar flares.

By analogy with the solar corona or the Earth magnetosphere, we shall assume that, in the magnetosphere of a compact star, the magnetic-field energy density greatly exceeds that of the thermal, kinetic and gravitational energy of the accreting plasma:

$$\frac{B^2}{8\pi} \gg 2nk_{\rm B}T\,, \quad \frac{B^2}{8\pi} \gg \frac{\rho v^2}{2}\,, \quad \text{and} \quad \frac{B^2}{8\pi} \gg \rho\, g\,. \tag{8.31}$$

So the magnetic field can be considered in the strong field approximation. This means, in fact, that the magnetic field is mainly potential in the magnetosphere everywhere outside the field sources: a star, an accretion disk, and the magnetospheric boundaries. At least, the magnetic field is potential in a large scale, in which the field determines the *global* structure of the magnetosphere. This 3D structure is illustrated by Figure 8.3 (Somov et al., 2003a).

Here $\mathbf{m}$ is a magnetic dipole moment of a star which rotates with an angular velocity $\mathbf{\Omega}$. The velocity of plasma flow inside the accretion disk D is shown by vectors $\mathbf{V}$. The large-scale regular magnetic field $\mathbf{B}$ is presented by two pairs of field lines separated by the accretion disk. Such structure seems to be well supported by results of the fully three-dimensional MHD simulations (see Romanova et al., 2004, Figure 4). $S_{\rm u}$ and $S_{\rm d}$ are the upper and bottom boundary surfaces of the magnetosphere. $C_{\rm u}$ is a cusp at the upper boundary. The outer surfaces $S_{\rm u}$ and $S_{\rm d}$ play the role of the

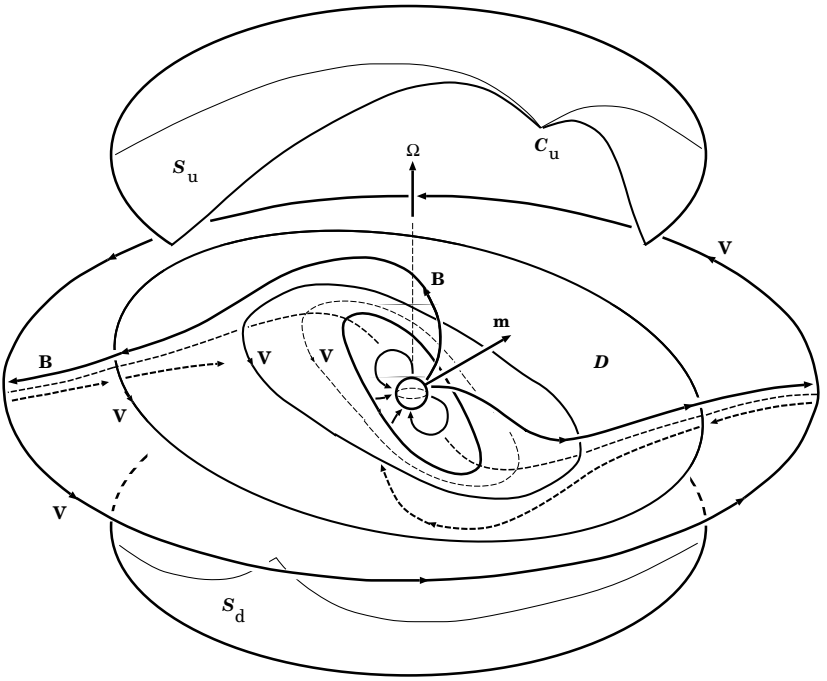

Figure 8.3: A three-dimensional picture of the star magnetosphere. The field lines **B** show the transition from the dipolar field of a rotating magnetized star to the tail-like field above and below an accretion disk D. The solid curves with arrows **V** represent the velocity field of the differentially rotating flows inside the disk.

magnetopause; their location and configuration are determined primarily by the condition of pressure equilibrium. The interaction between the magnetosphere and the surrounding plasma makes the outer boundaries highly asymmetric.

8.3.2 (b) An auxiliary two-dimensional problem

To estimate characteristic values of the large-scale magnetic field and its gradient in the corona of an accretion disk, we have to find the structure of the field inside the magnetosphere created by a dipole field of a star and a regular field generated by the disk. Let us consider a simplified two-dimensional problem on the shape of a magnetic cavity and the shape of the accretion disk under assumption that this cavity, i.e. the magneto-

sphere, is surrounded by a perfectly conducting uniform plasma with a gas pressure p_0.

Two conditions have to be satisfied at the boundary surface S which consists of two surfaces: the upper one S_u and the bottom S_d (compare Figures 8.3 and 8.4). These conditions are the equality of magnetic and gas

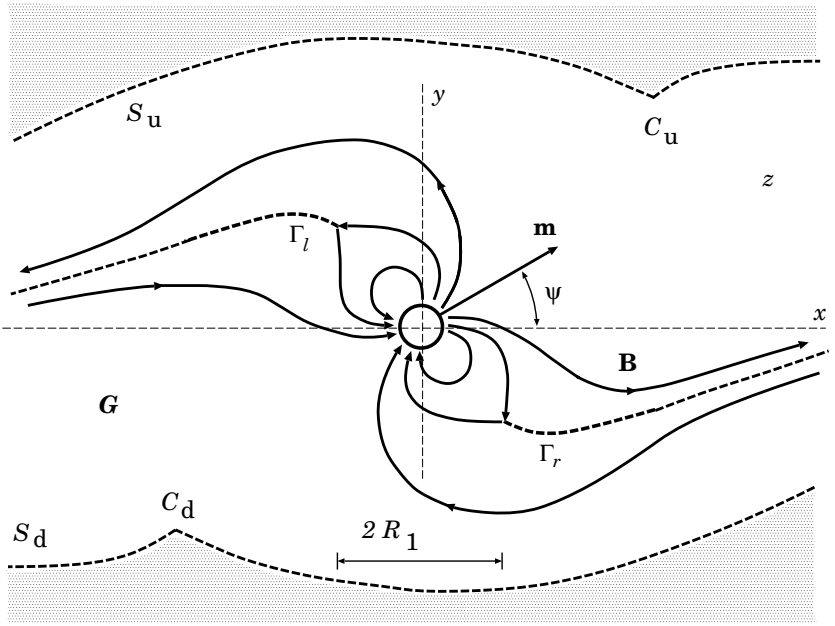

Figure 8.4: A two-dimensional model of the star magnetosphere. Γ_l and Γ_r are the cross sections of the accretion disk D by the plane determined by two vectors: the dipole moment $\mathbf{m}$ of the star and its angular velocity Ω in Figure 8.3. An auxiliary plane z corresponds to the complex variable $z = x+\mathrm{i}y$. R_1 is the inner radius of the disk. S_u and S_d together with Γ_l and Γ_r constitute the boundary of the singly connected domain G in the plane z.

pressure,

$$\left.\frac{B^2}{8\pi}\right|_S = p_0 = \mathrm{const}\,, \tag{8.32}$$

and tangency of the magnetic field along the boundary S,

$$\left.\mathbf{B}\cdot\mathbf{n}\right|_S = 0\,. \tag{8.33}$$

Condition (8.33) means that, along the boundary S,

$$\mathrm{Re}\, F(z) = A\,(x, y) = \mathrm{const}\,. \tag{8.34}$$

Here a complex potential $F(z)$ is an analytic function

$$F\,(z, t) = A\,(x, y, t) + \mathrm{i}\, A^{+}(x, y, t)\,, \tag{8.35}$$

within the domain G in the complex plane z except at the point $z = 0$ of the dipole and the current layers Γ_l and Γ_r related to the accretion disk. $A^{+}(x, y, t)$ is a conjugate harmonic function connected with $A\,(x, y, t)$ by the Cauchy-Riemann condition

$$A^{+}(x, y, t) = \int \left(-\,\frac{\partial A}{\partial y}\, dx + \frac{\partial A}{\partial x}\, dy \right) + A^{+}(t)\,, \tag{8.36}$$

where $A^{+}(t)$ is a quantity independent of the coordinates x and y.

The magnetic field vector, according to definition $\mathbf{B} = \mathrm{curl}\,\mathbf{A}$, is:

$$\mathbf{B} = B_x + \mathrm{i}\, B_y = -\,\mathrm{i} \left(\frac{dF}{dz} \right)^{*}, \tag{8.37}$$

the asterisk denoting the complex conjugation. After introducing the complex potential, we apply the methods of the complex variable function theory, in particular the method of *conform mapping*, to determine the magnetic field. This has been done, for example, to determine the structure of the magnetic field in solar coronal streamers (Somov and Syrovatskii, 1972).

By analogy with the solar coronal streamers or with the Earth magnetotail, we assume that the large-scale regular magnetic field reverses its direction from one side of the accretion disk to the other:

$$\mathbf{B}\,\Big|_{\Gamma+} = -\mathbf{B}\,\Big|_{\Gamma-}\,. \tag{8.38}$$

So, with respect to the large-scale field of the global magnetosphere, the accretion disk electric current is considered, for simplicity, as the large-scale neutral current layer Γ.

We also assume that a conform transformation $w = w(z)$ maps the domain G shown in Figure 8.4 onto the circle $|w| \leq 1$ in an auxiliary complex plane $w = u + \mathrm{i}v$ so that the point $z = 0$ goes into the centre of the circle without rotation of the magnetic dipole as shown in Figure 8.5.

Then the complex potential inside the circle has the following form:

$$F(w) = i\, Q \left(\ln \frac{w - e^{i\alpha}}{w\, e^{i\alpha} - 1} + \ln \frac{w - e^{i(\pi-\alpha)}}{-w\, e^{i(\pi-\alpha)} + 1} \right) + i\, e^{-i\psi}\, w + \frac{i\, e^{i\psi}}{w}\,. \tag{8.39}$$

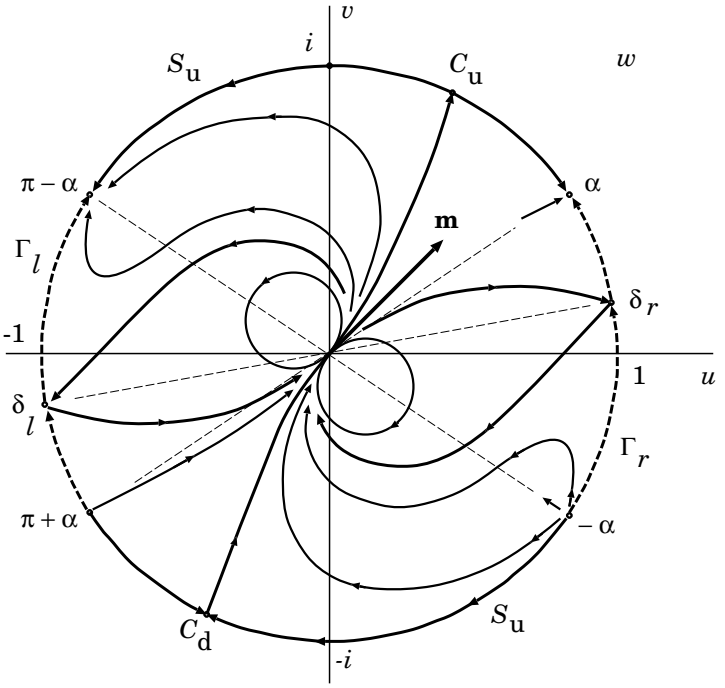

Figure 8.5: A solution of the two-dimensional problem inside the unit circle in the complex plane $w = u + iv$. The domain G in the plane z shown in Figure 8.4 is mapped onto the unit circle.

Here Q is a 'magnetic charge', the value which is proportional to the flux of the 'open' field lines, that go from a star to infinity. An angle α is a free parameter of the problem, which determines the type of a selected solution (for more mathematical details see Somov et al., 2003a).

8.3.3 Power of energy release in the disk coronae

Let us consider some consequences of the solution of the auxiliary two-dimensional problem. For parameters $m \approx 10^{30}$ G cm^3, $\psi = \pi/4$, $p_0 \approx 1.4 \times 10^6$ dynes cm^{-2}, we obtain that the inner radius R_1 of the accretion disk (Figure 8.4) is about 4×10^8 cm. The half-size of the magnetosphere is about 6×10^8 cm. These values seem to be in agreement with those inferred for the 4U 1907+09 neutron star and similar objects (Mukerjee et al., 2001). At a distance of 5×10^8 cm from the star, the magnetic-field strength is

$(1-2)\times10^4$ G while the magnetic-field gradient is $h_0 \sim 10^{-6}-10^{-2}$ G cm^{-1}.

From the solution of the problem on the SHTCL parameters (see Section 8.1.3) we find the power released per one current layer. For example, for the input parameters $n_0 \approx 10^{13}$ cm^{-3}, $h_0 \approx 10^{-2}$ G cm^{-1}, $E_0 \approx 10^3$ CGSE units, and $\xi \approx 0.1$ (Somov et al., 2003a), we obtain $b \approx 5 \times 10^6$ cm and the power released per layer length

$$\frac{P_1}{l} = \frac{B_0^2}{4\pi}\, v\, 4b = \frac{1}{\pi}\, c\, E_0\, h_0\, b^2 \approx 3 \times 10^{24} \text{ erg s}^{-1} \text{ cm}^{-1}. \qquad (8.40)$$

Let us assume that the SHTCL length l has the same order of magnitude as its width $2b$. Then the power released by a single SHTCL is P_1. We assume that new layers are continually forming in the disk corona as a result of permanently emerging new magnetic loops. Let us consider an inner part of the ring-shaped accretion disk. Let the inner radius be $R_1 \sim 4 \times 10^8$ cm while the outer radius is $R_2 \sim 8 \times 10^8$ cm. Its area is thus $S_\mathrm{r} = \pi(R_2^2 - R_1^2)$, while the area of a single RCL is $S_1 = l \times 2b$. Thus, in the inner part of the accretion disk, a number $N \sim 2S_\mathrm{r}/S_1$ of current layers exist simultaneously. The total energy release per second is

$$P \sim N\, P_1 = \frac{2\, S_\mathrm{r}}{S_1} \times P_1 = \frac{2\,\pi\left(R_2^2 - R_1^2\right)}{l\, 2b} \times \frac{c}{\pi}\, E_0\, h_0\, b^2\, l =$$

$$= \left(R_2^2 - R_1^2\right)\, c\, E_0\, h_0\, b \sim 7 \times 10^{35} \text{ erg s}^{-1}. \qquad (8.41)$$

This estimate (which should be, in fact, considered as a lower limit, according to Somov et al., 2003) does not contradict to the total power released by some neutron stars such as Aql X-1, SLX1732-304, 4U0614+09, 4U1915-05, SAX J1808.4-3658 (Barret et al., 2000). So the magnetic reconnection in accretion disk coronae is a powerful mechanism which may explain the observed X-ray emission from neutron stars.

Disk accretion to a rotating star with an inclined dipole magnetic field has been studied by three-dimensional MHD simulations (Romanova et al., 2004). It was shown that the hot spots arise on the stellar surface because of the impact on the surface of magnetically channeled accretion streams. The results are of interest for understanding the variability of classical T Tauri stars, millisecond pulsars, and cataclysmic variables.

8.4 The giant flares

The so-called *giant flares* are produced via annihilation of magnetic fields of a highly magnetized neutron star, a *magnetar*. This annihilation deposits energy in the form of photons and pairs near the surface of the neutron star.

The pair-radiation plasma evolves as an accelerating *fireball*, resulting in a thermal radiation burst carring the bulk of the initial energy with roughly the original temperature and a fraction of energy in the form of relativistic pairs. The thermal spectrum of giant flares and their temperatures support this scenario.

On 2004 December 27, a giant flare from SGR (soft gamma-ray) 1806-20 was the most powerful flare of gamma rays ever measured on Earth (for a review see Nakar et al., 2005). Its energy of 3×10^{46} erg was released at a distance of 15 kpc during about 0.2 s. The spectrum of the flare is consistent with that of a cooling blackbody spectrum with an average temperature of 175 ± 25 keV. Like other giant flares, this flare was followed by a pulsed softer X-ray emission that lasted more than 380 s. Radio afterglow was detected from Very Large Array (VLA) observations. After 1 week the radio source was extended to a size of $(0.6 - 0.9) \times 10^{16}$ cm. Therefore a significant amount of energy was emitted in the form of a relativistic ejecta around the same time that the gamma-ray flare was emitted.

This page intentionally blank

Chapter 9

Particle Acceleration in Current Layers

The inductive electric field is directed along the current inside a collisionless reconnecting current layer (RCL). This strong field does positive work on charged particles, thus increasing their energy impulsively, for example, in solar flares of flares in the accretion disk coronae of compact astrophysical objects.

9.1 Magnetically non-neutral RCLs

9.1.1 An introduction in the problem

Magnetic reconnection determines many phenomena in astrophysical plasma (for a review of pioneering works see Sweet, 1969; Syrovatskii, 1981, 1982). The theory of reconnection in a super-hot turbulent-current layer (SHTCL, see Section 6.3) explains the total amount of energy accumulated before solar flares, the power of energy released during flares and some other parameters of flares (Section 7.1). In particular, it has been shown (Litvinenko and Somov, 1991) that acceleration by the electric field and scattering of particles by ion-acoustic turbulence in an SHTCL lead to the appearance of about $10^{35} - 10^{36}$ electrons with a power-law spectrum and with energies of the order of tens of keV. Future development of the theory should result in models for the total number of accelerated particles, their maximum energy and the rate of particle acceleration (Bai and Sturrock, 1989; Somov, 1992; Hudson and Ryan, 1995; Miroshnichenko, 2001).

In this Section we return to the question of the maximum energy of particles accelerated in a RCL, which has been formulated in Section 1.2. Three points are important here.

(a) The problem of particle motion in a magnetic field which changes the sign of its direction and in the electric field related to reconnection has been considered many times. Speiser (1965) found particle trajectories near the neutral plane where the magnetic field is zero. The physical meaning of the Speiser solution is in the following. Formally speaking,

> a charged particle can spend an *infinite* time near such a neutral plane and can take an infinite energy from the electric field.

However, under real conditions in astrophysical plasma, the probability of such a situation is small; usually the magnetic field in the 'reconnecting plane', i.e. the current layer, has non-zero transversal and longitudinal components. Therefore actual current layers are *magnetically* non-neutral RCLs. This is of importance for their energetics (Chapter 6), stability (Chapter 11), and for the mechanism of acceleration that will be considered in the present Chapter.

(b) Speiser (1965) showed also that

> even a small transversal field changes the particle motion in such a way that the particle leaves the RCL after a *finite* time,

the particle energy being finite. In what follows we show that this time is small and the energy is not sufficient in the context of solar flares.

(c) Can we increase the time spent by the particle inside the RCL? – In the following it will be shown that (Somov and Litvinenko, 1993)

> the longitudinal field increases the acceleration time and, in this way, strongly increases the efficiency of particle acceleration

thus allowing us to explain the first step of acceleration of electrons in solar flares. An iterative method will be presented which gives an approximate general solution of the problem.

9.1.2 Dimensionless parameters and equations

Let us consider a reconnecting current layer placed in the (x, z) plane in Figure 9.1. More exactly, this is a right-hand-side part of the magnetically non-neutral RCL as shown in Figure 6.3. The electric field $\mathbf{E}$ and current density $\mathbf{j}$ are parallel to the z axis; so the associated magnetic field components are parallel to the x axis and change their sign in the plane $y = 0$.

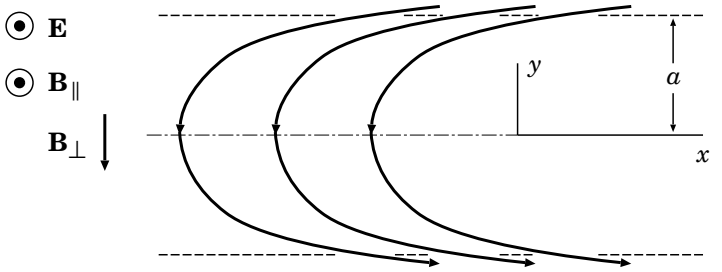

Figure 9.1: The projection of field lines inside the RCL to the plane (x, y); $\mathbf{B}_\parallel$ is the longitudinal magnetic field. $\mathbf{E}$ is the inductive electric field related to magnetic reconnection.

Therefore we prescribe the electric and magnetic fields inside the current layer as follows:

$$\mathbf{E} = \{\, 0,\, 0,\, E_0 \,\}\,, \qquad \mathbf{B} = \left\{\, -y/a\,,\, \xi_\perp,\, \xi_\parallel \,\right\} B_0\,. \tag{9.1}$$

The non-relativistic equation of motion for a particle with mass m and charge $q = Ze$ is

$$m\,\frac{\partial\,\mathbf{v}}{\partial t} = q\left(\mathbf{E} + \frac{1}{c}\,\mathbf{v}\times\mathbf{B}\right). \tag{9.2}$$

Let us take the half-thickness a of the layer as a unit of length and the inverse gyro-frequency $\omega_{\text{B}}^{-1} = mc/qB_0$ as a unit of time. Then Equation (9.2) can be rewritten in the dimensionless form:

$$\frac{\partial^2 x}{\partial t^2} = \xi_\parallel\,\frac{\partial y}{\partial t} - \xi_\perp\,\frac{\partial z}{\partial t}\,, \tag{9.3}$$

$$\frac{\partial^2 y}{\partial t^2} = -\,\xi_\parallel\,\frac{\partial x}{\partial t} - y\,\frac{\partial z}{\partial t}\,, \tag{9.4}$$

$$\frac{\partial^2 z}{\partial t^2} = \varepsilon + \xi_\perp\,\frac{\partial x}{\partial t} + y\,\frac{\partial y}{\partial t}\,. \tag{9.5}$$

Here the dimensionless electric field

$$\varepsilon = \frac{mc^2 E_0}{aqB_0^2}\,. \tag{9.6}$$

The influence of plasma turbulence on particle motions is ignored in (9.2). This is justified provided the time spent by a particle inside the RCL

is less than the inverse frequency of the wave-particle interactions $\nu(v)$. For the typical case, like the ion-acoustic turbulence,

$$\nu(v) = \nu_{eff} \left(\frac{\sqrt{k_{\text{B}} T/m}}{v} \right)^3 , \tag{9.7}$$

T being the temperature in the layer. For typical parameters of SHTCL (Chapter 6), the effective collision frequency can be estimated as

$$\nu_{eff} \approx \xi_{\perp}\, \omega_{\text{B}} \approx 10^6 \text{ s}^{-1} .$$

Hence the turbulence can be ignored for suprathermal particles, once the time spent by a particle inside the SHTCL does not exceed

$$\tau_{eff} = (\xi_{\perp}\, \omega_{\text{B}})^{-1} \approx 10^{-6} \text{ s} .$$

On integrating Equations (9.3) and (9.5) and substituting in (9.4), the set of Equations (9.3)–(9.5) becomes

$$\frac{\partial x}{\partial t} = \xi_{\parallel}\, y - \xi_{\perp} z + c_1 , \tag{9.8}$$

$$\frac{\partial^2 y}{\partial t^2} + \xi_{\parallel}^{\,2}\, y = -\left(\varepsilon\, t + \xi_{\perp}\, x + \frac{1}{2}\, y^2 + c_2 \right) y + \\ + \xi_{\parallel}\, (\xi_{\perp} z - c_1) , \tag{9.9}$$

$$\frac{\partial z}{\partial t} = \varepsilon\, t + \xi_{\perp}\, x + \frac{1}{2}\, y^2 + c_2 . \tag{9.10}$$

Let x_0, y_0, and z_0 be the initial coordinates of the particle. Its initial velocity is assumed to be negligible. In this case the constants of integration are as follows:

$$c_1 = -\xi_{\parallel}\, y_0 + \xi_{\perp} z_0 , \qquad c_2 = -\xi_{\perp} x_0 - \frac{1}{2}\, y_0^2 . \tag{9.11}$$

So, in principle, the problem can be solved.

9.1.3 An iterative solution of the problem

The simple-looking set of ordinary differential Equations (9.3)–(9.5) for the single particle motion inside the RCL is still complex, because the equations are not linear in the variables. As surprising as it may seem, we cannot solve these equations exactly, except for very special cases or with some simplifications.

Until the particle leaves the layer, the value of $y\,(t)$ is small, since the layer is supposed to be thin. The behaviour of the functions $x\,(t)$ and $z\,(t)$ does not depend strongly on the exact form of the solution $y\,(t)$. For this reason the Equations (9.8) and (9.10) can be solved by the following iterative procedure. First, we prescribe some function

$$y\,(t) = y^{(0)}(t)\,.$$

Second, using this function, we calculate $x^{(0)}(t)$ and $z^{(0)}(t)$ from Equations (9.8) and (9.10). Third, we use these functions to find a small correction $y^{(1)}(t)$ from Equation (9.9).

In zeroth approximation Equation (9.9) takes the simplest form

$$\frac{\partial^2 y^{(0)}}{\partial t^2} + \xi_{\parallel}^{\,2}\left(y^{(0)} - y_0\right) = 0\,, \tag{9.12}$$

whence $y^{(0)} = y_0 = \text{const}$. Now, from Equations (9.8) and (9.10), we find the zeroth order functions:

$$\begin{aligned} x^{(0)}(t) &= x_0 + (\sin\xi_{\perp}t - \xi_{\perp}t)\;\varepsilon/\,\xi_{\perp}^{\,2}\,,\\ z^{(0)}(t) &= z_0 + (1 - \cos\xi_{\perp}t)\;\varepsilon/\,\xi_{\perp}^{\,2}\,. \end{aligned} \tag{9.13}$$

In this approximation the projection of the particle's trajectory on the plane (x, z) is a cycloid curve whose shape does not depend on the longitudinal field $B_z = \xi_{\parallel}\,B_0$. Physically, formulae (9.13) describe the particle drift in the perpendicular fields $B_y = \xi_{\perp}B_0$ and $E_z = E_0$ (see Appendix 3), the influence of the B_z component being neglected.

Now let us write an equation which will allow us to find a correction to $y^{(0)}(t)$. Making use of (9.9) and (9.13), we obtain

$$\frac{\partial^2 y}{\partial t^2} + \left(\xi_{\parallel}^{\,2} + \varepsilon\,\frac{\sin\xi_{\perp}t}{\xi_{\perp}}\right) y = \xi_{\parallel}^{\,2}\,y^{(0)} + (1 - \cos\xi_{\perp}t)\,\varepsilon\,\frac{\xi_{\parallel}}{\xi_{\perp}}\,. \tag{9.14}$$

So the character of the particle motion is determined by two dimensionless parameters: $\xi_{\parallel}$ and $\xi_{\perp}$. Depending on them, two cases can be considered.

9.1.3 (a) No longitudinal field

The case $\xi_{\parallel} = 0$ means that there is no longitudinal magnetic field inside the RCL. Equation (9.14) becomes

$$\frac{\partial^2 y}{\partial t^2} + \left(\varepsilon\,\frac{\sin\xi_{\perp}t}{\xi_{\perp}}\right) y = 0\,. \tag{9.15}$$

This is the equation of a one-dimensional oscillator with a time-dependent frequency. From (9.15), together with (9.13), Speiser's results follow. In particular, a particle can remain inside the layer only for the time

$$\tau = \frac{\pi}{\xi_\perp} \,. \tag{9.16}$$

When $t > \tau$, the particle quickly moves out of the layer, since the frequency formally becomes an imaginary value. At this instant,

$$\frac{\partial x\,(\tau)}{\partial t} = -\frac{2\varepsilon}{\xi_\perp} \,, \qquad \frac{\partial z\,(\tau)}{\partial t} = 0 \,. \tag{9.17}$$

Note that in the case of a neutral layer $\xi_\perp = 0$ and the particle acceleration along the z axis is not restricted. According to (9.16), $\tau \to \infty$; the non-relativistic kinetic energy increases as $\mathcal{K} \sim z \sim \tau^2$, while the oscillation amplitude decreases as $A_y \sim \tau^{-1/4}$ (formula (1.28)).

If $\xi_\perp \neq 0$ and the electric field is small enough,

$$\varepsilon < \frac{1}{2}\, \xi_\perp^{\,3} \,, \tag{9.18}$$

then small oscillations near the plane $y = 0$ are stable, and particles are not pushed out of the layer. However, in the SHTCL model pertaining to solar flare conditions (Section 7.1), $\xi_\perp \sim 10^{-3}$ and $\varepsilon \sim 10^{-5}$. Therefore the inequality (9.18) cannot be satisfied and particles go out of the RCL without being accelerated.

9.1.3 (b) Stabilization by the longitudinal field

The case $\xi_\parallel \neq 0$, the RCL with a longitudinal field. Equation (9.14) describes an oscillator the frequency of which changes with time and which is also subject to the action of an external periodic force. Hence the oscillating system represented by Equation (9.14) is not closed and may have resonance increases of $y = y\,(t)$. This corresponds to the particle going out of the layer.

It is important, however, that the particle's motion can become *stable* provided $\xi_\parallel$ is large enough. Here we assume that the domains of stability exist for sufficiently large values of the longitudinal magnetic field. The simple argument is that, if the longitudinal field is strong enough, then the particles tend to follow the orbits mostly parallel to the direction of the longitudinal field, which is also parallel the the electric field. Such particles stay within the RCL and they are accelerated by the electric field.

In this case a particle remains in the vicinity of the layer plane, $y = 0$. For the resonance effects to be absent, the oscillation frequency must always be real:

$$\xi_{\parallel}^{\,2} > \frac{\varepsilon}{\xi_{\perp}} \,. \tag{9.19}$$

Once the inequality (9.19) is valid, some particles do not leave the RCL due to unstable trajectories. Were it not for the turbulence, these particles would simply drift along the RCL, gaining energy. The ion-acoustic turbulence in SHTCL (cf. formula (9.7)) makes the particle motion more complex.

9.1.4 The maximum energy of an accelerated particle

In general, the kinetic energy gain of escaping particles is a function of the physical parameters of the RCL and of the initial conditions that determine the orbits of particles. An issue of great concern is, however, what is the maximum energy to which a particle can be accelerated by the RCL?

For the case of a strong longitudinal magnetic field, the maximum velocity can be evaluated as

$$v_{\max} \approx \xi_{\parallel} \,. \tag{9.20}$$

Here a unit of velocity (Section 9.1.2) is

$$V_1 = a\,\omega_{\text{L}} = \frac{aqB_0}{mc} \,. \tag{9.21}$$

Therefore the longitudinal field qualitatively changes the character of particle motion inside the layer. As an example, let us consider electron acceleration in SHTCL during solar flares.

The SHTCL model allows us to express the characteristics of a current layer through the external parameters of a reconnection region: the concentration of plasma n_0 outside the layer, the electric field E_0, the magnetic field gradient h_0 and the relative value $\xi_{\perp}$ of a transversal magnetic field (Chapter 6). In the case $\xi_{\parallel} = 0$ (no longitudinal field), i.e. (9.17), the maximum electron energy is given by

$$\mathcal{E}_{\max} = 2\,mc^2 \left(\frac{E_0}{\xi_{\perp} B_0} \right)^2 \tag{9.22}$$

or, using the SHTCL model,

$$\mathcal{E}_{\max}\,(\text{keV}) \approx 5 \times 10^{-9}\, T\,(\text{K}) \,. \tag{9.23}$$

Formula (9.23) shows that acceleration in the RCL without a longitudinal field is not efficient: for the temperature inside the layer $T \approx 10^8\,\text{K}$, the maximum energy of accelerated electrons is only 0.5 keV.

Let us consider now the case of a non-zero longitudinal field. The stabilization condition (9.19) can be rewritten in dimensional units as follows:

$$\left(\frac{B_\parallel}{B_0}\right)^2 > \frac{mc^2 E_0}{aq\, B_\perp B_0}\,. \tag{9.24}$$

In the frame of the SHTCL model the last inequality becomes especially simple:

$$B_\parallel > 0.1\, B_0\,. \tag{9.25}$$

Thus the longitudinal component can be one order of magnitude smaller than the reconnecting components related to the electric current in the current layer.

The maximum energy (written in dimensional units) of accelerated electrons in the RCL is

$$\mathcal{E}_{\max} = \frac{1}{2m}\left(\frac{qa\, B_\parallel}{c}\right)^2 \tag{9.26}$$

or, in the SHTCL model,

$$\mathcal{E}_{\max}\,(\mathrm{keV}) \approx 10^{-5}\, \xi_\parallel^{\,2}\, T\,(\mathrm{K})\,. \tag{9.27}$$

If the current-layer temperature $T \approx 10^8$ K and $\xi_\parallel^{\,2} \approx 0.1$, formula (9.27) gives $\mathcal{E}_{\max} \approx 100$ keV. Therefore

> the longitudinal magnetic field increases the acceleration efficiency to such a degree that it becomes possible to interpret the *first stage* or the *first step* of electron acceleration in solar flares

as the particle energization process in a non-neutral SHTCL.

The results obtained are clear. On the one hand, the transversal field turns a particle trajectory in the layer plane (the plane (x, z) in Figure 9.1). At some point, where the projection of velocity v_z on the electric field direction changes its sign, the Lorentz force component associated with the field component $B_x = (-y/a)\, B_0$ pushes the particle out of the layer. This process is described by Equation (9.4) with $\xi_\parallel = 0$, or by Equation (9.15). On the other hand, a non-zero longitudinal magnetic field tries to turn the particle back to the layer. This effect is related to the first term on the right-hand side of Equation (9.4). That is why the maximum velocity of a particle is proportional to the gyro-frequency in the longitudinal field.

9.1.5 The non-adiabatic thickness of current layer

The condition (9.24) is simply understood from the physical point of view. In the absence of a longitudinal magnetic field, there exists a region near

the neutral plane (x, z), where the adiabatic approximation is not valid (see Section 1.2.2). So we had to solve Equation (9.2) to determine the character of the particle motion. The thickness of this region which is called the *non-adiabatic thickness* of a current layer equals

$$d = (r_{\rm L} a)^{1/2} = \left(\frac{mc\, va}{qB_0} \right)^{1/2} . \tag{9.28}$$

Here the maximum velocity $v \approx cE_0/\xi_\perp B_0$ is substituted in the formula for the Larmor radius $r_{\rm L}$ (see Appendix 3).

The longitudinal magnetic field tends to keep particles 'frozen' and to confine them inside the layer. Obviously such a confinement can become efficient, once

$$r_{\rm L} \left(B_\parallel \right) < d \,, \tag{9.29}$$

where

$$r_{\rm L} \left(B_\parallel \right) = \frac{mcv}{qB_\parallel} = \frac{r_{\rm L}}{\xi_\parallel} \,. \tag{9.30}$$

This last expression coincides with condition (9.24).

The condition given by Inequality (9.19) or (9.24), which is the same, is not sufficient to ensure stability of the orbits, of course. A detailed study of the solutions of Equation (9.14) shows that the instability domains of considerable width exist for relatively low values of $B_\parallel$ (Efthymiopoulos et al., 2005). For super-Dreicer electric fields, these domains are very narrow so that the criterion (9.19) is an acceptable approximation in order to consider the particle acceleration in solar flares.

* * *

Let us remind that, in the solar atmosphere, reconnection usually takes place at the separators with the non-zero transversal and longitudinal components of the magnetic field (Section 3.1). This effect was already considered in the MHD approximation from the viewpoint of the RCL energetics (Chapter 6). The longitudinal and transversal components of the magnetic field are also important for the current layer stability (Chapter 11). As was shown in this Section, the longitudinal field has strong influence on the kinetics of suprathermal particles: the magnetically non-neutral SHTCL does efficient work as an electron accelerator and, at the same time, as a trap for fast electrons in solar flares.

9.2 Regular versus chaotic acceleration

Considerable attention is focused on the phenomenon of *dynamic chaos*. The stochastic behaviour of a dynamic system is due to its intrinsic non-

linear properties rather than some external noise (Lichtenberg and Lieberman, 1983). A particular example of such a system is a particle moving in the RCL.

So far both numerical (Chen and Palmadesso, 1986) and analytic (Büchner and Zelenyi, 1989) treatments of the particle's motion have concentrated on a current layer with a small magnetic field component perpendicular to the layer. This small transversal component has been shown to give rise to chaotic particle behaviour. However current layers in the solar atmosphere usually have also longitudinal (parallel to the electric field inside the RCL) magnetic field components. The purpose of this section is to illustrate the influence of the longitudinal field on the character of particle motion in non-neutral current layers.

9.2.1 Reasons for chaos

Let us consider the RCL with the electric and magnetic fields (9.1). An approximate solution to Equations (9.3)–(9.5) of particle motion in such current layer was discussed above. Now we consider some general properties of this set of equations, starting from the fact that it possesses three exact constants of motion – the invariants of particle motion:

$$C_x = \dot{x} - \xi_{\parallel}\, y + \xi_{\perp} z\,, \tag{9.31}$$

$$C_z = \dot{z} - \xi_{\perp} x - \frac{1}{2}\, y^2 - \varepsilon\, t\,, \tag{9.32}$$

$$H = \frac{1}{2}\left(\dot{x}^{\,2} + \dot{y}^{\,2} + \dot{z}^{\,2}\right) - \varepsilon\, z\,. \tag{9.33}$$

Here H is the usual Hamiltonian (see Landau and Lifshitz, *Mechanics*, 1976, Chapter 7, § 40).

Rewrite the set of master Equations (9.3)–(9.5) in the Hamiltonian form. The usual way to do this is to introduce the four generalized coordinates

$$Q = \{\, t\,,\, x\,,\, y\,,\, z\,\} \tag{9.34}$$

and the generalized momenta

$$P = \left\{ -H,\ \dot{x} - \xi_{\parallel}\, y\,,\ \dot{y}\,,\ \dot{z} - \xi_{\perp} x - \frac{1}{2}\, y^2 \right\}. \tag{9.35}$$

Then the equations of motion take the form

$$\dot{Q}_i = \frac{\partial \mathcal{H}}{\partial P_i}\,, \qquad \dot{P}_i = -\,\frac{\partial \mathcal{H}}{\partial Q_i} \qquad (\, i = 0, 1, 2, 3\,)\,, \tag{9.36}$$

where

$$\mathcal{H} = H(P, Q) + P_0 \,. \tag{9.37}$$

The *transformed* Hamiltonian $\mathcal{H}$ is formally time-independent since t is treated as another coordinate variable. The constants of motion are now as follows:

$$C_x = P_x + \xi_\perp z \,, \tag{9.38}$$

$$C_z = P_z - \varepsilon\, Q_0 \,, \tag{9.39}$$

$$\mathcal{H} = \frac{1}{2}\left(P_x + \xi_\parallel y\right)^2 + \frac{1}{2}\,P_y^2 + \frac{1}{2}\left(P_z + \xi_\perp x + \frac{1}{2}\,y^2\right)^2 - \varepsilon\, z + P_0 \,. \tag{9.40}$$

> The Hamiltonian system (9.36) is integrable if the three constants of motion are in *involution*, i.e. their Poisson brackets are zero

(see Landau and Lifshitz, *Mechanics*, 1976, Chapter 7, § 42). Otherwise the system is likely to demonstrate *chaotic* behaviour, i.e. the particle trajectory inside the current layer is unpredictable.

Straightforward calculation, based on the definition (see vol. 1, Exercise 1.2) for the Poisson brackets, shows that

$$[\,\mathcal{H}\,,\, C_x\,] = 0 \quad \text{and} \quad [\,\mathcal{H}\,,\, C_z\,] = 0 \,.$$

However, for C_x and C_z we find

$$\boxed{[\,C_x\,,\, C_z\,] = \xi_\perp \,,} \tag{9.41}$$

so that the constants C_x and C_z are not in involution.

Chen and Palmadesso (1986) have obtained this result for the case $\xi_\parallel = 0$ and numerically showed the particle trajectory to be chaotic. In what follows our attention will be drawn to the fact that a non-zero longitudinal magnetic field leaves the result (9.41) unchanged. This means that **the chaos is entirely due to the transversal field** which is proportional to $\xi_\perp$ inside the RCL.

Moreover, as will be proved below,

> the longitudinal magnetic field tends to make the particle trajectory bounded and integrable inside the RCL.

Therefore an additional constant of motion must be present in the set of equations under consideration for a sufficiently large value of the parameter $\xi_\parallel$ (Litvinenko, 1993). Seemingly, this constant cannot be expressed in terms of elementary functions.

9.2.2 The stabilizing effect of the longitudinal field

Because of the presence of three constants of motion, the phase trajectory – the particle trajectory inside a six-dimensional phase space X – is restricted to a three-dimensional surface. It follows from Equations (9.31)–(9.33) that the particle coordinate and velocity components are subject to the relation

$$H = \frac{1}{2}\,\dot{y}^2 + \frac{1}{2}\left(\xi_{\parallel}\,y - \xi_{\perp} z\right)^2 + \frac{1}{2}\left(\varepsilon\,t + \xi_{\perp}\,x + \frac{1}{2}\,y^2\right)^2 - \varepsilon\,z = \text{const}\,, \quad (9.42)$$

where zero initial conditions are assumed for simplicity.

A useful way to study the character of the particle motion is to calculate the curvature of the *energy surface* $H = H(P, Q)$.

> The negative curvature K implies the exponentially fast divergence with time of initially close trajectories.

In its turn, that gives rise to chaos. Analogous inferences can be drawn concerning the particle motion in the usual coordinate space (Anosov, 1967). Provided the curvature $K \leq 0$, the asymptotic (for large t) behaviour of the trajectory is indistinguishable from that of random motion, which corresponds to stochasticity.

As was shown by Speiser (1965, 1968), particle motions in the current layer plane and across it occur almost independently. Thus, while studying the instability in the y direction, it is justifiable to consider the two-dimensional energy surface $H = H(y, \dot{y})$, treating x and z as some time-dependent constants. Attention must be centred on the motion along the y axis, which is known to possess the strongest instability (Speiser, 1965). Therefore the quantity to be calculated is

$$K = \frac{H_{\dot{y}\dot{y}} H_{yy} - {H_{\dot{y}y}}^2}{\left(1 + {H_{\dot{y}}}^2 + {H_y}^2\right)^2}\,. \quad (9.43)$$

Assuming that $\xi_{\parallel}^{\,2} \ll 1$ and that the particle is near the layer plane (i.e., $y \ll 1$), we show that the denominator of formula (9.43) approximately equals unity. Anyway, being positive, it does not influence the sign of K. The curvature of the energy surface is calculated to be

$$K(t) \approx \xi_{\parallel}^{\,2} + \varepsilon\,t + \xi_{\perp}\,x + \frac{3}{2}\,y^2\,, \quad (9.44)$$

or on making use of the invariant (9.32),

$$K(t) \approx \xi_{\parallel}^{\,2} + \dot{z}(t) + y^2(t)\,. \quad (9.45)$$

It is known that $\dot{z} \geq -\varepsilon/\xi_\perp$ (Speiser, 1965). Thus **strong chaos is expected** in the vicinity of the neutral plane $y = 0$, provided $\xi_\parallel = 0$. In this case the model of Büchner and Zelenyi (1989) is applicable. On the other hand, inside the RCL and in its vicinity,

> a sufficiently strong longitudinal magnetic field tends to suppress chaos and make the particle motion regular.

The necessary condition for such a suppression is $K > 0$, that is

$$\xi_\parallel > \left(\frac{\varepsilon}{\xi_\perp}\right)^{1/2}. \tag{9.46}$$

So, in another way, we arrive at an inequality which coincides with (9.19). The inequality (9.46) gives $\xi_\parallel > 0.1$ for typical solar flare conditions if the particles under consideration are electrons (Somov, 1992; Somov et al., 1998; Somov and Merenkova, 1999). Litvinenko and Somov (1993) have been the first to pay attention to this important property of the magnetically non-neutral current layer.

9.2.3 Characteristic times of processes

It might seem surprising that $\xi_\parallel$ in inequality (9.46) should tend to infinity for $\xi_\perp \to 0$. However, it is incorrect to consider such a limiting case. The point is that the time needed for the instability to start developing is of the order of ${\xi_\perp}^{-1}$ (Speiser, 1965). Hence, while being formally unstable, the particle's motion in the limit of small $\xi_\perp$ is regular for all reasonable values of time.

The result (9.46) is easy to understand from the physical viewpoint. A typical time for destabilization of the y-motion, i.e. the time for divergence of initially close trajectories inside the current layer, is (in dimensional units)

$$t_\perp = \left(\frac{am}{F}\right)^{1/2}, \tag{9.47}$$

where the Lorentz force component is evaluated to be

$$F \approx \frac{1}{c}\, q\, v B_0 = \frac{1}{c}\, q\, \frac{cE}{B_\perp}\, B_0 = \frac{qE}{\xi_\perp} \tag{9.48}$$

and some typical value of $v = cE/B_\perp$ is assumed; $q = Ze$. The instability creating the chaos becomes suppressed once it has no time for developing, i.e.

$$t_\perp > t_\parallel, \tag{9.49}$$

$t_{\parallel}$ being the time scale introduced by the longitudinal magnetic field:

$$t_{\parallel} = \frac{mc}{qB_{\parallel}} = \frac{mc}{\xi_{\parallel} qB_0} \,. \tag{9.50}$$

Once (9.49) is valid, the particle becomes magnetized inside the current layer and its trajectory is no longer chaotic. Clearly the inequality (9.49) is equivalent to condition (9.46).

9.2.4 Dynamics of accelerated electrons in solar flares

A question at this point is: What observational data can be used to verify the above-presented results? To put it another way: What are the observational consequences of chaotic particle dynamics? – Such consequences do exist.

Consider electron acceleration in solar flares. The accelerated electrons spiral in the coronal magnetic field and produce flare radio emission. Using the data on radio pulsations, Kurths and Herzel (1986), Kurths et al. (1991), Isliker (1992) have calculated the dimension of the pseudo-phase space related to the electron source. The technique for reconstructing phase space from a one-dimensional data array is described by Schuster (1984), where also the references to original works can be found.

> The dimension of the pseudo-phase space serves as a measure of chaos: the larger the dimension, the more chaotic is the system.

Using the data on ms-spikes, Isliker (1992) has found that the degree of chaos varied from flare to flare and during the course of a flare. He conjectured that such behaviour was due to some *exterior* (to the electron source) parameter which could change with time. Based on the above discussion, the role of this parameter may be ascribed to the value of the longitudinal magnetic field.

This conclusion is in agreement with previous findings. From the theoretical viewpoint, the longitudinal field is determined by the photospheric sources and does change in time. It is this change that can be responsible for flare onset, i.e., the longitudinal field can be the 'topological trigger' of a solar flare (Section 3.2.1). As far as observations are concerned, the electron acceleration during flares is likely to occur at the separators with a strong longitudinal field, where magnetically non-neutral current layers are formed (Section 3.1). As indicated above, the relative value of this field, $\xi_{\parallel} = B_{\parallel} / B_0$, determines whether the acceleration occurs in a regular or stochastic manner. To summarize,

> the motion of electrons in magnetically non-neutral current layers of solar flares becomes **regular rather than chaotic**, once the relative value of the longitudinal magnetic field $\xi_{\parallel} > 0.1$.

This fact has important implications for the dynamics of the electron acceleration in solar flares. It would be also of interest to perform calculations analogous to those of Isliker (1992), in the context of the geomagnetic tail.

Recommended Reading: Froyland (1992).

9.2.5 Particle simulations of collisionless reconnection

A particle simulation study (e.g., Horiuchi and Sato, 1997) has investigated collisionless driven reconnection in a sheared magnetic field by modeling the response of a collisionless plasma to an external driving flow. They specifically studied the effects of the transversal and longitudunal magnetic fields on the rate of reconnection and the acceleration of electrons.

Litvinenko (1997) has used our model for electron acceleration in a magnetically non-neutral current layer to interpret the results of the simulation. He explained the electron energization in both two-dimensional ($\xi_{\perp} \neq 0$, $\xi_{\parallel} = 0$) and three-dimensional ($\xi_{\perp} \neq 0$, $\xi_{\parallel} \neq 0$) magnetic fields. An agreement was obtained between the analytical predictions and the numerical results for the electron energy gain, the acceleration time, the longitudinal field diving rise to adiabatic particle motion, and the scaling with $B_{\parallel}$ of the collisionless resistivity due to particle escape from the RCL.

The particle simulation, therefore, has substantiated the theoretical modeling presented in Section 9.1. This is important both for future more general analytical models of particle acceleration and for the application of the existing models, for example, to the electron acceleration in solar flares (Sections 9.1.4 and 9.2.4).

Although the particle simulation (Horiuchi and Sato, 1997) had not been run for a sufficient time to study the acceleration of protons, it did show that the question of proton acceleration is more complicated. Their motion, as we shall see in the next Section, is influenced by the polarization electric field arising due to charge separation. Because it is much more difficult to magnetize a proton than an electron, the protons tend to escape the current layer across its border even when the electrons are well magnetized by the longitudinal field $B_{\parallel}$. This leads to the generation of a transversal electric field $E_{\perp}$ directed towards the plane of the layer. This field may have important consequences for the proton motion as we discuss below.

9.3 Ion acceleration in current layers

9.3.1 Ions are much heavier than electrons

In Section 9.1 we considered the particle acceleration in a current layer, taking into account not only the reconnecting field $\mathbf{B}_0$, parallel to the x axis, but also a small transversal field component $B_\perp = \xi_\perp B_0$, parallel to the y axis as shown in Figure 9.1. A typical relative value of the transversal field is $\xi_\perp \sim 10^{-3} \div 10^{-2}$ (see Somov, 1992). In what follows we adopt the value of $\xi_\perp \approx 3 \times 10^{-3}$ for our estimates. The basic Speiser's (1965) result is that both the energy gain $\delta\mathcal{E}$ and the time that the particles spend in the magnetically non-neutral RCL, $\delta t_{\rm in}$, are finite.

> The transversal magnetic field makes the particle turn in the plane of the layer, and then a component of the Lorentz force expels it from the RCL plane almost along the field lines

(see Figure 3 in Speiser, 1965). The distance that the particle can travel along the layer equals the Larmor diameter determined by the transversal field and a typical speed of the particle.

Litvinenko and Somov (1993) generalized the results of Speiser (1965) by including into consideration the *longitudinal* (parallel to the main electric field $\mathbf{E}$ in Figure 9.1) magnetic field $\mathbf{B}_\parallel$ in the layer.

> The longitudinal field efficiently magnetizes fast electrons in the RCL, but it cannot influence the motion of the accelerated protons and heavier ions.

The Larmor radius of ions is much larger than the Larmor radius of electrons having the same velocity because ions are much heavier than electrons. As a consequence of this fact, the critical longitudinal field, necessary to magnetize a particle and to accelerate it, is proportional to the square root of the particle mass (see (9.24)). Hence we can use, first, the Speiser's non-relativistic formulae, derived for the case when an ion of mass m and charge $q = Ze$ enters the RCL with a negligible velocity:

$$\delta\mathcal{E} = 2\,mc^2 \left(\frac{E_0}{B_\perp}\right)^2, \tag{9.51}$$

$$\delta t_{\rm in} = \frac{\pi\, mc}{q\, B_\perp}\,. \tag{9.52}$$

Generalizations of these formulae to particles with nonzero initial velocities are given in Section 9.3.3.

Thus, on the one hand, electrons can acquire even relativistic energies in current layers with a nonzero longitudinal field $B_{\parallel}$ (Litvinenko and Somov, 1993). On the other hand, application of formulae (9.51) and (9.52) to the RCL, formed, for example, behind a rising coronal mass ejection – CME (see Section 9.4), shows that a nonzero field $B_{\perp}$ radically restricts the energy of heavier particles: $\delta\mathcal{E}$ for protons cannot exceed 20 MeV if a typical value of $\xi_{\perp} = 3 \cdot 10^{-3}$ ($B_{\perp} = 0.3$ G) is assumed.

Therefore the relativistic energies cannot be reached after a single 'interaction' of a proton with the layer (cf. Martens, 1988). To overcome this difficulty, Martens conjectured that the relativistic acceleration could take place in RCL regions where $B_{\perp} \to 0$ (the neutral layer approximation), and the protons are freely accelerated by the electric field. This conjecture, however, does not seem to be adequate for actual RCLs, where reconnection always occurs in the presence of a transversal magnetic field. Though we expect the latter to vary somewhat along the RCL (Somov, 1992), the region with a vanishing $B_{\perp}$ is so small that a particle will quickly leave the region (and hence the RCL) before being accelerated. Thus we are led to modify the classic Speiser's model significantly.

Let us propose that a proton (or another ion) interacts with the RCL more than once, each time gaining a finite, relatively small amount of energy. The effect could be the required relativistic acceleration. A similar model was considered in the context of acceleration in the geomagnetic tail (see Section 2.4 in Schabansky, 1971). However, the magnetic structures in the solar atmosphere are quite different from that of the geomagnetic tail; and conditions also differ. Therefore formulae given by Schabansky are inapplicable to the problem at hand. For this reason, we have to consider another model in application to the solar atmosphere.

9.3.2 Electrically non-neutral current layers

The factor that makes positively charged particles return to the RCL is the *transversal* electric field $\mathbf{E}_{\perp}$, which is parallel to the y axis in Figure 9.2 and directed toward the layer plane from both sides (cf. Figure 9.1). What is the origin of this electric field?

As we saw in the previous Section, protons and other ions, having much larger masses than the electron mass, have significanly larger Larmor radii. Both electrons and protons try to escape from magnetic confinement inside the RCL. They are deflected by the magnetic field when they move out of the layer. However the trajectories of electrons are bent to a much greater degree owing to their smaller mass. As for the much heavier protons and ions, they stream out of the layer almost freely. Hence the charge separation arises, leading to the electric field $\mathbf{E}_{\perp}$ at both sides of the layer.

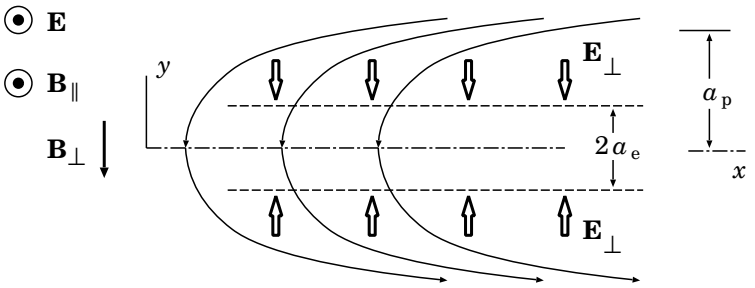

Figure 9.2: An electrically non-neutral current layer: $\mathbf{E}_\perp$ is the transversal component of the electric field. $\mathbf{E}$ is the electric field related to the reconnection process.

This field detains the protons and ions in the vicinity of the electron current layer (Harris, 1962; see also Chapter 5 in Longmire, 1963; Hoh, 1966; Dobrowolny, 1968).

In an exact self-consistent one-dimensional model of the *electrically* non-neutral current layer due to Harris (1962), this field equals

$$E_\perp = 2\pi\,\sigma^q\,. \tag{9.53}$$

Here the magnitude of the electric charge density integrated over the layer thickness is

$$\sigma^q = \left(\frac{u}{c}\right)^2 nea\,, \tag{9.54}$$

u is the current velocity of electrons in the RCL.

Let us estimate the velocity u from the Maxwell Equation for $\operatorname{curl}\mathbf{B}$ as

$$u = \frac{c}{4\pi}\,\frac{B_0}{nea}\,. \tag{9.55}$$

On substituting (9.55) and (9.54) in (9.53), we obtain

$$E_\perp \approx \frac{k_{\rm B}T}{e\,a}\,, \tag{9.56}$$

where the equation $B_0^2/8\pi \approx nk_{\rm B}T$ has been used, T being the plasma temperature in the layer.

It is not obvious *a priori* that Harris's solution applies to actual RCLs with nonzero $\xi_\perp$ and finite conductivity σ. It should be valid, however, for small $\xi_\perp$, at least as a first approximation. In fact all we need for our calculations is the electric potential

$$\phi = \int E_\perp\,{\rm d}y\,, \tag{9.57}$$

which we take to equal $k_{\rm B}T/e$, the usual value owing to spread of a 'cloud' of charged particles.

The following point is worth emphasizing here. The charge separation that gives rise to the potential ϕ mainly stems from the motion of protons perpendicular to the layer plane. At the same time, some protons are known to leave the layer almost along its plane. This property is a characteristic feature of the Speiser's mechanism of acceleration. It seems obvious that

> even a modest transversal electric field will considerably influence the motion of the particles, leaving the layer, because they always move almost perpendicular to this field.

Having made this qualitative remark, we now proceed to calculating the energy gain rate and maximum energy for the protons being accelerated in the RCL, taking into account both the main components of electromagnetic field ($\mathbf{B}_0$ and $\mathbf{E}_0$) and the transversal ones ($\mathbf{B}_\perp$ and $\mathbf{E}_\perp$).

9.3.3 Maximum particle energy and acceleration rates

According to the model delineated above, a positively charged particle ejected from the RCL may be quickly reflected and moves back to the layer. The reason for this is the electric field $\mathbf{E}_\perp$, directed perpendicular to the current layer, which always exists outside the RCL (Harris, 1962). It is of importance for what follows that the accelerated protons and other ions are ejected from the layer almost *along* the field lines (Speiser, 1965). The transversal electric field efficiently locks the particles in the RCL because they always move almost in the plane of the layer. On getting into the layer again, the particles are further accelerated and the cycle repeats itself.

In order to find the properties of the acceleration mechanism, we need to dwell at some length on the particle motion outside the RCL. Let us consider a proton leaving the RCL plane with energy $\mathcal{E}$ and momentum $\mathbf{p}$. According to Speiser (1965), the component of the momentum perpendicular to the layer is

$$p_\perp \approx \xi_\perp p \ll p \tag{9.58}$$

for such a proton. The perpendicular component of the equation of motion for the particle outside the electron current layer is

$$\frac{\mathrm{d}}{\mathrm{d}t}\, p_\perp(t) = -\,qE_\perp\,. \tag{9.59}$$

Here we neglect the magnetic force, in order not to obscure the essential physical point made in this Section. Equation (9.59) allows us to estimate

the time spent by the proton between two successive interactions with the RCL,

$$\delta t_{\,\mathrm{out}} = \frac{2\,p_{\,\perp}}{qE_{\,\perp}} \approx \frac{2\,\xi_{\,\perp}\,p}{qE_{\,\perp}}\,. \tag{9.60}$$

The largest energy attainable is determined by the condition that the potential (9.57) is just enough to prevent the proton from leaving the RCL. In other words, the field $\mathbf{E}_{\,\perp}$ must cancel the perpendicular momentum $\mathbf{p}_{\,\perp}$. The energy conservation gives:

$$\mathcal{E}_{\,\mathrm{max}} = \left(\,\mathcal{E}^{\,2}_{\,\mathrm{max}} - p^{\,2}_{\,\perp}\,c^{\,2}\,\right)^{1/2} + q\phi\,, \tag{9.61}$$

where

$$p^{\,2}_{\,\perp}\,c^{\,2} = \xi^{\,2}_{\,\perp}\,\left(\,\mathcal{E}^{\,2}_{\,\mathrm{max}} - (mc^2)^2\right). \tag{9.62}$$

Eliminating the unknown $p_{\,\perp}$ between (9.61) and (9.62), we get the maximum energy

$$\mathcal{E}_{\,\mathrm{max}} = q\phi\,\frac{1}{\xi^{\,2}_{\,\perp}}\left[1 + \left(\,1 - \xi^{\,2}_{\,\perp} + \frac{\xi^{\,4}_{\,\perp}\,(mc^2)^2}{q^2\phi^{\,2}}\right)^{1/2}\right]. \tag{9.63}$$

According to formulae (9.56) and (9.57), here the electric field potential $\phi \approx k_{\mathrm{B}}T/e$. Formula (9.63) shows that

> protons can actually be accelerated to GeV energies in the super-hot turbulent-current layers (SHTCLs) in solar flares

(see Chapter 6): for instance $\mathcal{E}_{\,\mathrm{max}} \approx 2.4$ GeV provided $T_{\mathrm{e}} \approx 10^8$ K. Even larger energies can be reached in RCL regions with a smaller transversal magnetic field.

Note in passing that if a particle leaves the layer with the velocity that is perpendicular to the magnetic field lines outside the RCL, the magnetic reflection is very efficient too. In this case it occurs in a time of order the inverse gyrofrequency in the field $\mathbf{B}_{\,0}$.

The resulting acceleration rate can be estimated as

$$\frac{\mathrm{d}\mathcal{E}}{\mathrm{d}t} \approx \frac{\langle\,\delta\mathcal{E}\,\rangle}{\delta t_{\,\mathrm{in}} + \delta t_{\,\mathrm{out}}}\,. \tag{9.64}$$

Here

$$\langle\,\delta\mathcal{E}\,\rangle = 2\mathcal{E}\left(\frac{E_{\,0}}{B_{\perp}}\right)^2 \tag{9.65}$$

is the relativistic generalization of the Speiser formula (9.51) for the average energy gain. The averaging needs to be introduced because, in general,

a term linear in a component of the particle momentum appears in the expression for $\delta\mathcal{E}$ (cf. Speiser and Lyons, 1984).

In much the same way

$$\delta t_{\,\mathrm{in}} = \frac{\pi\mathcal{E}}{c\,qB_{\perp}} \tag{9.66}$$

is the relativistic generalization of the Speiser formula (9.52). The approach using the differential equation (9.64) is quite justified once the inequality $\langle\,\delta\mathcal{E}\,\rangle \ll \mathcal{E}_{\max}$ holds.

Equation (9.64), with account taken of the formulae (9.60), (9.65), and (9.66), can be integrated in elementary functions. To simplify the problem further, we note that

$$\frac{\delta t_{\,\mathrm{in}}}{\delta t_{\,\mathrm{out}}} = \frac{\pi\,E_{\perp}}{2\,\xi_{\perp}\,B_{\perp}}\left(\frac{\mathcal{E}}{pc}\right) \approx 10^3\,\frac{\mathcal{E}}{pc} \gg 1\,. \tag{9.67}$$

Hence it is justifiable to ignore the second term in the denominator of Equation (9.64). The simplified equation is integrated to give the kinetic particle energy

$$\mathcal{K}\,(t) \equiv \mathcal{E} - mc^2 = \frac{2}{\pi}\,c\,qE_0\,\left(\frac{E_0}{B_{\perp}}\right)t\,, \tag{9.68}$$

whence the time of the particle acceleration is

$$t_{\,\mathrm{ac}}\,(\mathcal{K}) \approx 0.03\,\left(\frac{\mathcal{K}}{1\,\mathrm{GeV}}\right)\,\mathrm{s}\,. \tag{9.69}$$

This result demonstrates the possibility of very efficient acceleration of protons and other ions by the direct electric field in the RCL (Litvinenko and Somov, 1995). At the same time, taking care of the actual magnetic field structure has considerably diminished (by a factor of $E_0/B_{\perp} = V/(\xi_{\perp}\,c) \approx 10^{-1}$) the magnitude of the energy gain rate, as compared with the case $B_{\perp} = 0$.

Alternatively, we could rewrite formula (9.68) to obtain the energy $\mathcal{E}$ as a function of the number of particle entries to the RCL, N_{int}:

$$\mathcal{E}\,(N_{int}) = mc^2\,\exp\left[2\left(\frac{E_0}{B_{\perp}}\right)^2 N_{int}\right]. \tag{9.70}$$

Therefore the particle must interact with the RCL

$$N_{\max} \approx \left(\frac{B_{\perp}}{E_0}\right)^2 \approx 10^2 \tag{9.71}$$

times in order to reach a relativistic energy. As was shown above (see Equation (9.63)), the transversal electric field outside the RCL is actually capable of providing this number of reentries into the current layer.

In principle, the protons and other ions could leave the RCL along its plane rather than across it. This is not likely, however, because of a very short acceleration time $t_{\rm ac}$; the distance a proton can travel along the layer when being accelerated is less than $c\,t_{\rm ac} \approx 10^9$ cm, that does not exceed a typical RCL width and length $10^9 \div 10^{10}$ cm.

Therefore we have estimated the efficiency of the acceleration process in the frame of the simple RCL model which contains several taciturn assumptions. One of them is a modification of the steady two-dimensional model for the SHTCL (Chapter 6) with account of the Harris type equilibrium across the layer. Such a possibility does not seem surprising one *a priory*, but it certainly has to be considered in detail somewhere else.

Another assumption is that the initially assumed conditions of the layer equilibrium are not changed due to the acceleration, more exactly, during the characteristic time of the acceleration of a particle. In fact, we consider the number of particles accelerated to high energies as a small one in comparison with the number of current driving thermal electrons inside the RCL. However, in general, it remains to be seen that this assumption can be well justified without careful numerical modelling of the real plasma processes in the region of reconnection and particle acceleration.

9.4 How are solar particles accelerated?

9.4.1 Place of acceleration

It was widely believed that the most-energetic and longest-lasting *solar energetic particle* events (SEPs) observed in interplanetary space result from acceleration by the bow shocks of coronal mass ejections (CMEs). However, using gamma-ray, X-ray and radio diagnostics of interacting (with the solar plasmas and magnetic fields) particles and spaceborne and ground-based detection of $\gtrsim$ 20 MeV protons at 1 AU during two large events (1989 September 29 and October 19), Klein et al. (1999) demonstrated that time-extended acceleration processes **in the low and middle corona**, far behind the CME, leave their imprints in the proton intensity time profiles in interplanetary space for one or several hours after the onset of the solar flare. So the bow shock is not the main accelerator of the high-energy protons.

Electrons accelerated to $\sim 1 - 100$ keV are frequently observed in interplanetary space. The energy spectrum has a power-law shape, often extend-

ing down to $\lesssim 2$ keV without clear signatures of collisional losses. Electron events showing enhanced electron fluxes at energies as low as 0.5 keV were observed by Lin et al. (1996). This requires an acceleration in a low-density coronal plasma.

Low-energy (2-19 keV) impulsive electron events observed in interplanetary space have been traced back to the Sun, using their interplanetary type III radiation and metric-decimetric radio-spectrograms (Benz et al., 2001). The highest frequencies and thus the radio signatures closest to an acceleration region have been studied. All the selected events have been found to be associated with the interplanetary type III bursts. This allows to identify the associated coronal radio emission. The start frequency yields a lower limit to the density in the acceleration region of the order of 3×10^8 cm^{-3}.

It is obvious that a 3D reconstruction of source locations depends on a chosen model of the coronal density in terms of absolute heights. However the relative positions are not altered by changing the atmospheric models. The trajectories of the type III bursts may be stretched and shifted in height but the topology of the birst remains the same. Figure 9.3 (cf. Paesold et al., 2001) displays a sketch depicting a possible location of acceleration with respect to two simultaneous bursts.

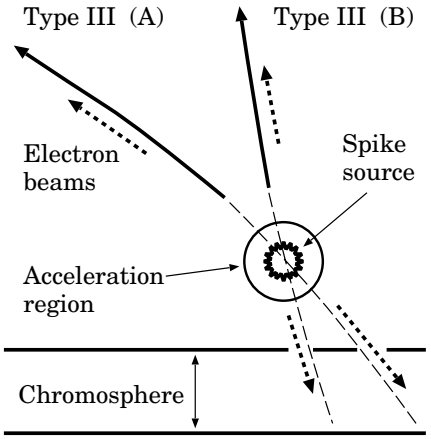

Figure 9.3: Location of the acceleration region with respect to a type III burst (labeled A) and an associated spike source. A second type III (labeled B) is displayed in a case of two simultaneous bursts. The upward moving electrons produce type III bursts and the downward moving electrons lose their energy in the chromosphere.

The spatial association of narrow band metric radio spikes with type III bursts has been analyzed by using data provided by the Nancay Radioheliograph (NRH) and the Phoenix-2 spectrometer (ETH Zurich), see Paesold et al. (2001). It has been found that the spike source location, presumably an acceleration region, is consistent with the backward extrapolation of a trajectory of the type III bursts, tracing a magnetic field line. In one of the five analyzed events, type III bursts with two different trajectories

originating from the same spike source were identified.

These findings support the hypothesis that narrow metric spikes are closely related to the acceleration region (Krucker et al., 1997). Escaping beams of electrons cause the type III emission. Energetic electrons appear to be injected into different and diverging coronal structures from one single point as illustrated in Figure 9.3. Such a diverging magnetic field geometry is a standard ingradient of reconnection.

9.4.2 Time of acceleration

Litvinenko and Somov (1995) have suggested that the time-extended (or late, or second) acceleration of protons and perhaps heavier ions to relativistic energies during the late phase of large-scale solar flares (e.g., Akimov et al., 1996) occurs in a 'vertical' RCL (Figure 9.4). Here the field lines are driven together and forced to reconnect below erupting loop prominences. The time of RCL formation corresponds to the delay of the **second phase of acceleration** after the first (or early), impulsive phase. The mechanism invoked (the direct electric field acceleration) is, in fact, quite ordinary in studies of the impulsive phase (Syrovatskii, 1981; Chupp, 1996). There are good reasons to believe that the same mechanism also efficiently operates during the second phase of the acceleration in large-scale flares occuring high in the corona.

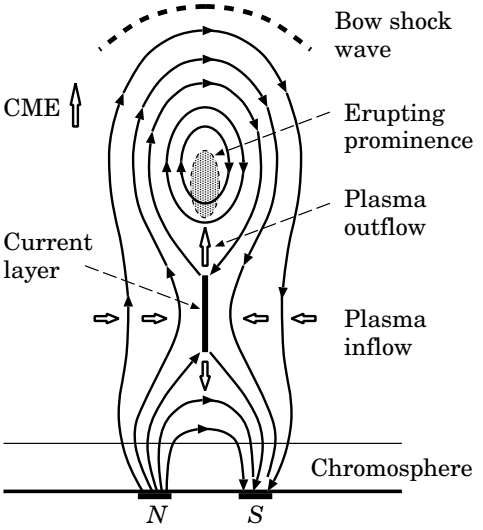

Figure 9.4: When passing through the corona, a prominence strongly disturbs magnetic field and creates a CME. The disturbed field will relax to its initial state via reconnection. This is assumed to accompany by a prolongated energy release and particle acceleration (Litvinenko and Somov, 1995).

First, early radio imaging observations of solar flares (Palmer and

Smerd, 1972; Stewart and Labrum, 1972) were indicative of particle acceleration at the cusps of helmet magnetic structures in the corona. These are exactly the structures where RCLs are expected to form according to the *Yohkoh* observations in soft and hard X-rays (see Kosugi and Somov, 1998).

Note that the acceleration by Langmuir turbulence inside the RCL in the helmet structure, invoked by Zhang and Chupp (1989) to explain the electron acceleration in the flare of April 27, 1981, is too slow to account for the generation of relativistic protons and requires an unreasonably high turbulence level.

Specific models have been designed to explain the particle acceleration in magnetic cusp geometry, in particular the two-step acceleration model with a RCL and magnetic collapsing trap, described in Section 7.3.

Second, gamma-emission during large flares consists of separate peaks with a characteristic duration of 0.04–0.3 s (Gal'per et al., 1994; Akimov et al., 1996). If this behaviour is interpreted in terms of a succession of separate acts of the acceleration, then the shock mechanism is also too slow since the acceleration time would be

$$t_{\,\mathrm{ac}} = 50 \left(\frac{100\,\mathrm{G}}{B_0}\right) \left(\frac{\mathcal{E}}{1\,\mathrm{GeV}}\right) \mathrm{s} \approx 50 \mathrm{\ s} \tag{9.72}$$

(Colgate, 1988). By contrast, as we saw above,

> the direct electric field inside the RCL provides not only the maximum energy but also the necessary energy gain rate

(see formula (9.69)). High velocities (up to the coronal Alfvén speed) of erupting filaments and other CMEs imply a large direct electric field in the RCL. This is the reason why the acceleration mechanism considered is so efficient in *fast transient phenomena* in the corona (Somov, 1981). Strong variability of gamma-emission may reflect the regime of impulsive, bursty reconnection in the RCL.

An interesting feature of the mechanism considered is that neither the maximum energy nor the acceleration rate depend upon the particle mass. Hence the mechanism may play a role in the preferential acceleration of heavy ions during solar flares.

Recall that Martens (1988) applied the Speiser (1965) model when considering relativistic acceleration of protons during the late phase of flares. However it turned out necessary to assume an idealized geometry of the magnetic field in the RCL, viz. $\mathbf{B}_\perp \to 0$, in order to account for the relativistic acceleration. We have seen that the difficulty can be alleviated by allowing for the transversal electric field $\mathbf{E}_\perp$ outside the layer. This field necessarily arises in the vicinity of the RCL (Harris, 1962).

Though MHD shocks are usually thought to be responsible for the relativistic generation of protons during the late phase of extended (gradual) gamma-ray/proton flares (Bai and Sturrock, 1989), another mechanism – the direct electric field acceleration in RCL – can explain the proton acceleration to the highest energies observed, at least in flares with strong variability of gamma-emission. Of course, the same sudden mass motions that lead to formation of current layers also give rise to strong shock waves, so the two mechanisms of acceleration can easily coexist in a solar flare.

9.5 Cosmic ray problem

The cosmic ray energy spectrum extends from 1 GeV to 100 EeV (the prefix "E" is for "exa", i.e. 10^{18}). To be accelerated at such high energies, a particle has to be submitted to powerful electromagnetic fields. Such energies hardly can be reached by any one-shot mechanism. In the late forties, the Fermi mechanism was introduced as the stochastic and repetitive scattering by "magnetic clouds". However such a process is a very slow one and to reach the highest energies under "normal conditions", the necessary acceleration time often exceeds the age of the universe.

Many models with extreme parameters or assumptions were proposed in the past. They mostly relay on relativistic shock acceleration such as in hot spots of powerful radio-galaxies. However such galaxies are rare objects. The second type models relate the ultra-high-energy cosmic rays to another long-lasting astrophysical puzzle, the Gamma Ray Bursts (GRBs). These are characterized by the emission of huge amounts of energies (a non-negligible fraction of the mass energy of the Sun) over a very short time, minutes.

GRBs are observed as gamma rays but with, in some cases, X-ray and optical counterparts. Their distribution is uniform over the sky; and they happen at a rate of 2-3 per day. Young black holes, neutron stars and magnetars were proposed as putative sources of cosmic rays, because these rapidly rotating compact objects possibly are the sources of the most intense magnetic fields in the universe. The capability of such relativistic systems to reach the required energies has to be investigated in the context of the magnetic reconnection concept.

Chapter 10

Structural Instability of Reconnecting Current Layers

The interrelation between the stability and the structure of current layers governs their nonlinear evolution and determines a reconnection regime. In this Chapter we study the structural instability of the reconnecting current layer, i.e. its evolutionarity.

10.1 Some properties of current layers

10.1.1 Current layer splitting

The continuous MHD flow of a perfectly conducting medium is impossible in the zeroth point of a magnetic field, in which the electric field differs from zero. In the vicinity of this peculiar point the frozen-in condition breaks down (Section 2.1.2), and the reconnectiong current layer (RCL in Figure 10.1) – the discontinuity dividing magnetic fields of opposite directions – forms there in compliance with the statement of Syrovatskii (1971). Later on Brushlinskii et al. (1980), Podgornii and Syrovatskii (1981), Biskamp (1986, 1997) observed the splitting of the RCL into other MHD discontinuities in their numerical experiments.

This splitting (or bifurcation) of the RCL is usually discussed in relation to the configuration suggested by Petschek (1964), which appears in particular during the reconnection of uniform magnetic fluxes (see Exercise 10.1).

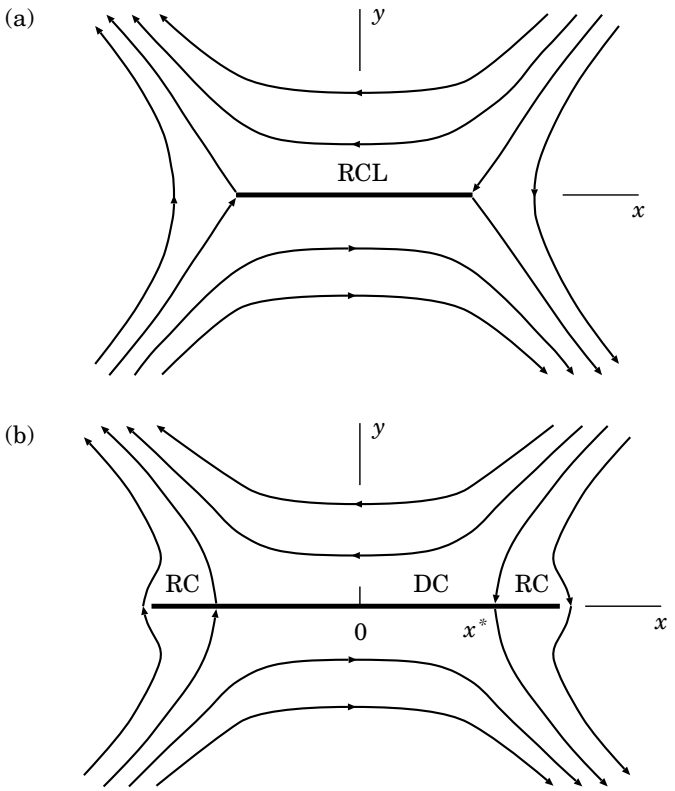

Figure 10.1: Thin current layers: (a) without reverse electric currents, and (b) with two reverse currents (RC), DC is a region of direct current.

It consists of a system of MHD discontinuities, crossing in the small central diffusion region D.

As distinct from Petschek's configuration, the thin wide current layer forms in the vicinity of a hyperbolic zeroth point of a strong magnetic field as shown in Figure 10.2. Just this case (and more complicated ones) has been realized in the numerical MHD experiments carried out by Brushlinskii et al. (1980), Podgornii and Syrovatskii (1981), Biskamp (1986), Antiochos et al. (1996), Karpen et al. (1998) and will be considered below.

The splitting of the current layer means a change of the regime of magnetic reconnection, since the distribution of electric current becomes two-dimensional. In the present Chapter we consider the conditions under which the splitting takes place and point out its possible reason. This reason is

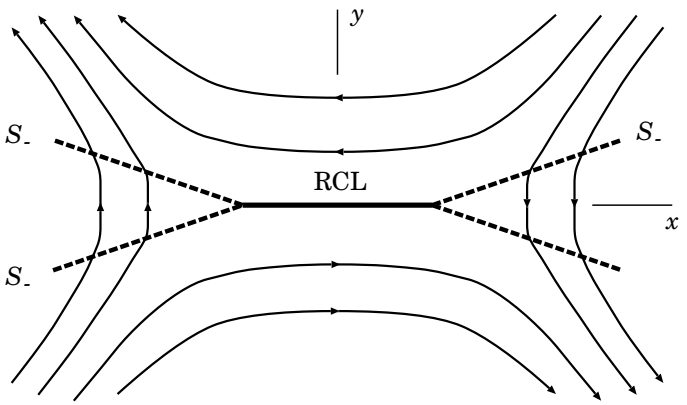

Figure 10.2: A splitted current layer (RCL) with the attached MHD discontinuities – the four slow shock waves (S_-).

the *non-evolutionarity* of the RCL as a discontinuity or its *structural* instability, as people sometimes say.

10.1.2 Evolutionarity of reconnecting current layers

The one-dimensional equations of ideal MHD have discontinuous solutions: fast and slow shock waves, tangential, contact and Alfvén discontinuities, peculiar shocks (vol. 1, Chapter 16). As was shown, a steady discontinuity may exist in a real plasma only if it is stable with respect to the break up into other discontinuities or the transition to some unsteady flow (vol. 1, Chapter 17).

Let the MHD quantities be subjected to an infinitesimal perturbation at the initial instant of time. Then a linear passage of waves out from the discontinuity occurs. If the amplitudes of these waves and the displacement of the discontinuity are uniquely determined from the linearized boundary conditions, then the problem of the *time evolution* of the initial perturbation has a single solution. If this problem does not have a single solution, then the supposition that the initial perturbation is small is not valid. In this case

> the infinitesimal perturbation results in an instant (in the approximation of an ideal medium) non-linear change of the original flow.

This is a *non-evolutionary* discontinuity. Note that, as distinct from a non-evolutionary discontinuity, the perturbation of an unstable evolutionary discontinuity remains infinitesimal during a small enough period of time.

The criterion of evolutionarity results from the comparison of two numbers. N_w is the number of the independent unknown parameters: the amplitudes of outgoing, i.e. reflected and refracted, waves and the displacement of the discontinuity, describing infinitesimal perturbation. And N_e is the number of independent boundary conditions (equations) which infer the unknown parameters by the amplitudes of the incident waves. If these numbers are equal, then the discontinuity satisfies the requirement of evolutionarity. Otherwise the problem of the time evolution of an initial infinitesimal perturbation does not have a solution, or else it has an infinite amount of solutions. Such a discontinuity cannot exist in a real medium.

As the direction of the propagation of a wave depends on the relationship between its group velocity and the flow velocity,

> the requirement of evolutionarity gives the restriction on the unperturbed MHD quantities on both sides of the discontinuity.

In particular, the shock waves turn out to be evolutionary when either the upflow and the downflow velocities are larger than the Alfvén speed (fast shocks) or smaller than it (slow shocks).

The RCL cannot be reduced to a one-dimensional flow, since the inhomogeneity of velocity in it is two-dimensional, and is characterized by two spatial parameters. The thickness of the layer, i.e. the distance $2a$ between the reconnecting magnetic fluxes (see Figure 1.5), determines the rate of magnetic field dissipation in it, but the width $2b$ characterizes the storage of magnetic energy in the domain of the flux interaction.

In what follows we obtain the conditions under which, in a plasma of high conductivity, infinitesimal perturbations interact with the RCL as with a discontinuity, and the problem of its evolutionarity with respect to such perturbations can be solved.

10.1.3 Magnetic field near the current layer

Consider the thin current layer, appearing in the vicinity of the zeroth point of a magnetic field

$$\mathbf{B}_0 = (\, h_0 y, h_0 x, 0\,) \ ,$$

at which the electric field

$$\mathbf{E} = (\, 0,\, 0,\, E\,)$$

differs from zero. The magnetic field lines, frozen into the plasma, drift along the y axis into the layer, where the frozen-in condition breaks down, reconnect in it, and flow out along the x axis. Syrovatskii (1971) represented the coordinate dependence of the field $\mathbf{B}$ outside the layer in a complex

form, supposing that the half-thickness of the current layer a (size along the y axis) equals zero (see Figure 10.1),

$$B_y + \mathrm{i}B_x = h_0 \left(\zeta^2 - (x^*)^2\right) \left(\zeta^2 - b^2\right)^{-1/2} \tag{10.1}$$

(see also Chapter 3 in Somov and Syrovatskii, 1976b). Here the complex variable $\zeta = x + \mathrm{i}\, y$, b is the half-width of the layer (size along the x axis), c is the speed of light, and I is the total current in the layer. The quantity I varies through the range $0 \le I \le ch_0 b^2/4$. At the points

$$x^* = \pm \sqrt{\frac{1}{2} b^2 + \frac{2I}{ch_0}} \tag{10.2}$$

the magnetic field changes its sign (see formula (10.1) and Figure 10.1b).

For $\mid x \mid < \mid x^* \mid$ the direction of the current coincides with the direction of the electric field. This is direct (DC) current in Figure 10.1b. However for $\mid x^* \mid < \mid x \mid < b$ it has the opposite direction (*reverse* currents RC). If $x \sim b$ and $b - \mid x^* \mid \sim b$, then the reverse current is comparable with the forward one. Suppose that precisely this configuration appears. In so doing all MHD quantities outside (but near) the RCL may be treated as quasi-homogeneous everywhere, except in some neighborhood of the points $x = x^*$ and $x = \pm b$, which are excluded from the further consideration.

Given the plasma conductivity σ is infinite the quantity b increases indefinitely with time. If σ is limited, then the finite width $2b$ settles in finite time (Syrovatskii, 1976a) and $a/b \neq 0$, although $a \ll b$. In this case, as distinct from (10.1), $B_y \neq 0$ on the surface of the current layer. However, when σ is large enough, $B_x \gg B_y$ outside some neighborhood of the points (10.2). Later on B_y is assumed to be zero. More general formulation of the problem is given in Section 3.4 in Somov (1992).

10.1.4 Reconnecting current layer flows

Let the flow of the plasma satisfy the MHD approximation. If $a \ll b$, all quantities except the velocity $\mathbf{v}$ are quasi-homogeneous along the x axis inside the layer. As for the inhomogeneity of the velocity, it is two-dimensional, since it follows from the mass conservation equation that at the point $x = 0$, $y = 0$

$$\frac{\partial v_x}{\partial x} = -\frac{\partial v_y}{\partial y}$$

because of the flow symmetry. Therefore the RCL cannot be reduced to a one-dimensional flow. This is obvious because

> two reconnecting magnetic fluxes move towards each other and the plasma flow inside the current layer is thus two-dimensional.

If the conductivity is infinite it becomes a tangential discontinuity in the limit $t \to \infty$.

Let us consider a settled RCL. Then the electric field $\mathbf{E}$ is independent of time. This being so the ratio a/b was estimated by Syrovatskii (1976a) from the steady-state Ohm's law

$$\frac{a}{b} \sim \frac{\nu_m h_0}{cE}, \tag{10.3}$$

where ν_m is the magnetic diffusivity. Besides, in the stationary model, the electric field is independent of the coordinates. Hence

> in the region of direct current the plasma flows into the layer, but in the regions of reverse currents it flows out along the y axis.

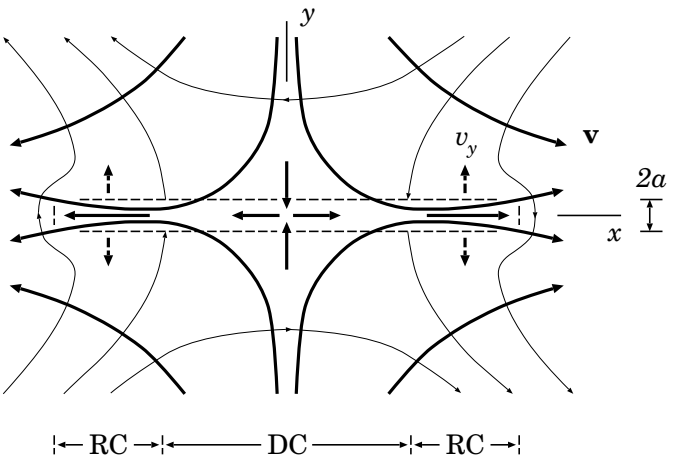

Figure 10.3: Plasma flows inside the RCL and in its vicinity.

Such character of the conductive plasma flows is shown schematically in Figure 10.3. The velocity component v_y changes the sign when the plasma flows from the region DC of direct current into two regions RC of reverse current, which are the same regions as in Figure 10.1b. This is important for counting the number N_w of the outgoing small-amplitude waves.

10.1.5 Additional simplifying assumptions

Let us suppose that all dissipative factors except the magnetic diffusivity ν_m equal zero, but ν_m is so small that

$$\frac{cE}{h_0 b} \ll \frac{h_0 b}{\sqrt{4\pi\rho}}. \tag{10.4}$$

The left side of this inequality represents the characteristic value of the drift velocity directed to the current layer v_y, the right side gives the value of the Alfvén speed $V_{\rm A}$.

Consider also that

$$\rho^{in} \sim \rho^{ex}. \tag{10.5}$$

Here the indexes 'in' and 'ex' denote the quantities inside and outside the layer. Such a distribution was, for example, in the numerical experiment by Brushlinskii et al. (1980).

On the surface of the current layer the magnetic field increases without bound but the drift velocity tends to zero, if the conductivity is infinite. At the same time the quantity of the pressure p outside the RCL is close to its value for $\zeta = \infty$ and does not equal zero or infinity for all σ. On this basis it may be thought that, outside the neighborhood of the point (10.2), the sound velocity V_s satisfies the condition

$$\boxed{v_y^{ex} \ll V_s^{ex} \ll V_{\rm A}^{ex},} \tag{10.6}$$

when the conductivity is large enough. Inequalities (10.6) are well consistent with the magnetostatic approximation (see vol. 1, Section 13.1.3).

Taking the characteristic values of these quantities for an active region in the solar corona:

$$v_y \sim 10 \text{ km/s}\,, \quad V_s \sim 100 \text{ km/s}\,, \quad V_{\rm A} \sim 1000 \text{ km/s}\,,$$

we see that the approximation (10.6) well holds there.

As far as the component of the velocity v_x is concerned, its modulus grows from zero for $x = 0$ to

$$\mid v_x^{in} \mid \sim \frac{h_0 b}{\sqrt{4\pi\rho}} \tag{10.7}$$

for $x = x^*$ (Syrovatskii, 1971) and then reduces to zero for $\mid x \mid = b$. Outside, the component v_x also does not exceed the characteristic Alfvén speed.

Let us now investigate the infinitesimal perturbation of the RCL using the outlined properties of the plasma flow.

10.2 Small perturbations outside the RCL

10.2.1 Basic assumptions

Let us assume that the MHD quantities Q are subjected to an infinitesimal perturbation δQ. Suppose that $\delta v_z \equiv 0$ and $\delta B_z \equiv 0$, and outside the current layer the perturbation satisfies the WKB approximation. Then its wave vector $\mathbf{k}$, in the zeroth order in terms of the small parameter $1/kb$, is determined from the dispersion equation

$$\omega_0 \Big[\mathrm{i}\, k^2 V_s^{\,2} \left(\mathbf{k}\mathbf{V}_{\mathrm{A}} \right)^2 - V_s^{\,2} k^2 \omega_0 \left(\mathrm{i}\,\omega_0 - \nu_m k^2 \right) - \\ - \mathrm{i}\, k^2 V_{\mathrm{A}}^{\,2} \omega_0^2 + \omega_0^3 \left(\mathrm{i}\,\omega_0 - \nu_m k^2 \right) \Big] = 0 \,, \tag{10.8}$$

where $\omega_0 = \omega - \mathbf{k}\mathbf{v}$.

Let us impose the following restriction on the frequency ω:

$$\boxed{\frac{v_y}{a} \ll \omega_{\parallel} \ll \frac{V_s}{a} \,,} \tag{10.9}$$

where

$$\omega_{\parallel} = \omega - k_x v_x \,. \tag{10.10}$$

Besides, for the sake of simplicity, we put

$$v_y \sim \frac{V_s^{\,3}}{V_{\mathrm{A}}^{\,2}} \,. \tag{10.11}$$

We will show in Section 10.5.3 that precisely this velocity appears in the criterion of evolutionarity for the RCL.

10.2.2 Propagation of perturbations normal to a RCL

At first, let us consider the case of the propagation of the perturbations normal to the current layer, i.e. the perturbations with $k_x = 0$. In the zeroth order in terms of the small parameters, given by inequality (10.9), the solutions of Equation (10.8) take the form

$$k_y^d = -\,\mathrm{i}\, \frac{v_y}{\nu_m} \frac{V_{\mathrm{A}}^{\,2}}{V_s^{\,2}} \,, \tag{10.12}$$

$$k_y^0 = \frac{\omega}{v_y} \,, \tag{10.13}$$

$$k_y^- = \frac{\omega}{v_y}\,, \tag{10.14}$$

$$k_y^+ = \pm\frac{\omega}{V_{\rm A}}\,. \tag{10.15}$$

Here the root (10.14) is twofold.

The WKB approximation (see Landau et al., *Electrodynamics of Continuous Media*, 1984, Chapter 10, § 85, Geometrical optics) holds for these perturbations if

$$1/k_y^+ b \ll 1$$

since $\mid k_y^+ \mid$ is the least wave number. This is equivalent to the following condition for the frequency ω:

$$\omega \gg \frac{h_0}{\sqrt{4\pi\rho}}\,. \tag{10.16}$$

When condition (10.16) is true, the derivatives of the unperturbed quantities over the coordinates in the linear MHD equations are negligible and the dispersion Equation (10.8) is valid.

To obtain the criterion of evolutionarity it is necessary to classify the perturbations according to whether they are incoming to the current layer or outgoing from it. Generally, such a classification has to be made by the sign of the sum of the projections of the velocity $\mathbf{v}$ of the medium and the *group* velocity on the normal to the layer. However, as it was mentioned by Kontorovich (1959), in the case of normal propagation it is sufficient to determine only the sign of the phase velocity, since in the absence of frequency dispersion the latter coincides with the projection of the group velocity on the direction of the vector $\mathbf{k}$ in the system of coordinates, where the plasma is at rest.

The perturbation with the wave vector k_y^0 from formula (10.13) corresponds to an entropy wave (see vol. 1, Section 15.2.1), but k_y^- from (10.14) corresponds to the slow magnetoacoustic wave propagating perpendicularly to the magnetic field. In the system of coordinates, where the moving plasma is at rest, their phase velocities equal zero, but in the laboratory system they coincide with the plasma velocity $\mathbf{v}$. This being so,

> both perturbations are incoming to the RCL when the plasma flows into it, and are outgoing ones when the plasma flows out.

Besides, by virtue of the left side of inequality (10.9), we have conditions

$$k_y^0 \gg 1/a \quad \text{and} \quad k_y^- \gg 1/a.$$

Hence the RCL is not a discontinuity for the perturbations (10.13) and (10.14).

The perturbation with the wave vector k_y^+ from (10.15) represents fast magnetoacoustic waves. Their phase velocity ω/k_y^+ satisfies the condition $V_{ph}^+ \gg v_y$ (see (10.6) and (10.15)) and is aligned with the normal to the RCL or opposed to it. So one of them is always incoming to the layer and the other is outgoing from it, regardless of the sign of v_y. As distinct from k_y^0 and k_y^-, the quantity $k_y^+ \ll 1/a$, and the waves (10.15) interact with the RCL as with a discontinuity.

The perturbation k_y^d from (10.12) is a dissipative wave and it damps within a distance which is much smaller than the layer half-thickness a. Consequently, as was pointed out by Roikhvarger and Syrovatskii (1974), its amplitude does not appear in the boundary conditions on the surface of a discontinuity. This being so, the dissipative effects outside the RCL are negligible.

Thus, in the case of normal propagation,

> there is one outgoing wave on each side of the current layer when the plasma flows into it (in the region DC of forward current),

and there are four of such waves, when the plasma flows out (in the domains RC of the reverse currents).

10.2.3 The inclined propagation of perturbations

Let us now turn to the inclined propagation. To solve the problem of the evolutionarity of the current layer as a discontinuity, it is necessary to obtain the solution of Equation (10.8) with common ω and k_x. Kontorovich (1959) showed that, for a given flow, the number of waves incoming to the x axis and outgoing from it, with common ω and k_x, is independent of k_x, i.e. of the angle of propagation (see also Chapter 3 in Anderson, 1963). Thus it is sufficient to determine the number of such waves for $k_x = 0$. From the preceding it follows that, when the plasma flows into the layer (the region DC of the forward current in Figure 10.1b), there is one outgoing wave on each side of it. But when the plasma flows out there are four of them.

For the RCL under condition (10.9), however, the number of the perturbations with $k_y \ll 1/a$ (i.e. those for which the amplitudes are discontinuous across it) depends on k_x. If $k_x = 0$, then there are two of such perturbations, determined by the wave vector k_y^+ from (10.15). As will be shown below, there are three for the inclined propagation. This fact is important in our further considerations.

The wave vector of a slow magnetoacoustic wave is given by the formula

$$| \mathbf{k}^- | = \frac{\omega}{v_y \sin\theta + v_x \cos\theta \pm | V_{ph}^- |}, \tag{10.17}$$

where V_{ph}^{-} is the phase velocity, and θ is the angle between $\mathbf{k}^{-}$ and the x axis. Here the scalar product $\mathbf{kv}$ is represented in the form

$$\mathbf{kv} = \mid \mathbf{k}^{-} \mid \times (v_y \sin\theta + v_x \cos\theta) .$$

With $V_s \ll V_{\mathrm{A}}$ the following expression for $\mid V_{ph}^{-} \mid$ is valid:

$$\mid V_{ph}^{-} \mid = \frac{V_{\mathrm{A}} V_s}{V_\perp} \mid \cos\theta \mid \left[1 + \frac{1}{2} \frac{V_{\mathrm{A}}^2 V_s^2}{V_\perp^4} \cos^2\theta + o\left(\frac{V_{\mathrm{A}}^2 V_s^2}{V_\perp^4} \right) \right], \quad (10.18)$$

where $V_\perp^2 = V_{\mathrm{A}}^2 + V_s^2$.

Let us choose the angle θ_0 in such a way that $\mid V_{ph}^{-} \mid \sim V_s$, i.e. $\mid \cos\theta_0 \mid$ is not small, and find the solutions of Equation (10.8) for fixed ω and

$$k_x = \mid \mathbf{k}^{-} \mid \cos\theta_0 . \quad (10.19)$$

For this purpose let us separate out the unknown variable k_y

$$\begin{aligned} (\omega_\parallel - k_y v_y) \left[\left(\nu_m v_y V_s^2 \right) k_y^5 + \left(\mathrm{i} v_y^2 V_\perp^2 - \nu_m \omega_\parallel V_s^2 \right) k_y^4 - \right. \\ - \left(2\mathrm{i} \omega_\parallel v_y V_\perp^2 \right) k_y^3 + \mathrm{i} \left(\omega_\parallel^2 V_\perp^2 - k_x^2 V_{\mathrm{A}}^2 V_s^2 \right) k_y^2 - \\ - \left[2\mathrm{i} \omega_\parallel v_y \left(V_\perp^2 k_x^2 - 2\omega_\parallel^2 \right) \right] k_y + \\ \left. + \mathrm{i} k_x^2 \left(\omega_\parallel^2 V_\perp^2 - k_x^2 V_{\mathrm{A}}^2 V_s^2 \right) - \mathrm{i} \omega_\parallel^4 \right] = 0 . \end{aligned} \quad (10.20)$$

Here condition (10.9) is used.

In the zeroth order in terms of the small parameters, given by Inequality (10.9), this equation has the following solutions: (10.12) and

$$k_y^0 = \frac{\omega_\parallel}{v_y} , \quad (10.21)$$

$$k_y^{1-} = \frac{2\omega_\parallel}{v_y} , \quad (10.22)$$

$$k_y^{2-} = k_x \tan\theta_0 , \quad (10.23)$$

$$\begin{aligned} k_y^s = \frac{1}{2} \left[\frac{\omega_\parallel V_s^2 \cos^2\theta_0}{2 v_y V_{\mathrm{A}}^2} \pm \left(-\frac{4\omega_\parallel^2}{V_s^2} + \right. \right. \\ \left. \left. + \frac{\omega_\parallel^2 V_s^4 \cos^4\theta_0}{4 v_y^2 V_{\mathrm{A}}^4} \pm 2 \sin\theta_0 \mid \cos\theta_0 \mid \frac{\omega_\parallel^2 V_s}{v_y V_{\mathrm{A}}^2} \right)^{1/2} \right] . \end{aligned} \quad (10.24)$$

The sign in the round brackets in (10.24) coincides with the sign in front of $\mid V_{ph}^{-} \mid$ in formula (10.17), but that in front of the round brackets specifies two different solutions of Equation (10.20). From inequality (10.9) it follows that for the perturbations (10.21) and (10.22) $k_y \gg 1/a$, but for (10.23) and (10.24), on the contrary, $k_y \ll 1/a$.

The waves k_y^{1-} and k_y^{2-} are slow magnetoacoustic ones, here with the angle between $\mathbf{k}^{2-}$ and the x axis equals θ_0 for k_x from (10.19). As for the waves k_y^s, they may be either slow magnetoacoustic or the *surface* ones, depending on the ratio $v_y V_{\text{A}}^2/{V_s}^3$. Recall that if the perturbations are characterized by a common θ, but not k_x, as in the present case, then there are always two slow waves, but the rest are fast magnetoacoustic waves.

If the expression in the round brackets in formula (10.24) is negative, then k_y^s has an imaginary part and the corresponding perturbations increase or decrease exponentially with the characteristic length, which is much smaller than a, while propagating away from the surface.

Investigation of the polynomial of the second degree in v_y in the round brackets in formula (10.24) shows that it equals zero at the points

$$v_y = \frac{{V_s}^3}{4\,V_{\text{A}}^2} \mid \cos\theta_0 \mid \times (\pm \sin\theta_0 \pm 1)\ . \tag{10.25}$$

Here the sign in front of $\sin\theta_0$ is given by the sign in formula (10.17). Two signs in front of 1 determine two ends of the length on the axis of v_y, within which the perturbations (10.24) are slow magnetoacoustic waves. Outside this length they become surface waves. The one of them, which increases, while propagating away from the surface, should be rejected as it does not satisfy the boundary condition at infinity. As was stated by Kontorovich (1959), the decreasing perturbation should be classified as outgoing from the discontinuity surface.

Below we will use the fact that for large enough velocities, v_y, the waves (10.24) are surface ones, independent of θ_0. It may be shown that the function $v_y(\theta_0)$, determined by formula (10.24), is restricted by modulus from above by the quantity

$$v_y^{max} = \frac{3\sqrt{3}}{16}\ \frac{{V_s}^3}{V_{\text{A}}^2}\,, \tag{10.26}$$

here the maximum value (10.26) is reached for $\theta_0 = \pi/6$. If

$$\mid v_y \mid > v_y^{max}\,, \tag{10.27}$$

the waves (10.24) are surface ones for all θ_0.

The surface perturbation, which decreases with distance from the x axis, does not transfer energy away from the layer surface, because its amplitude equals zero at $y = \infty$. However this

> surface wave enters into the total perturbation of the RCL and its amplitude must be determined from the boundary conditions. In this sense the wave is classified as an outgoing one.

As for the increasing perturbation, it is formally an incoming wave, but it must be discarded, since it tends to infinity as $y \to \infty$. Note that for this reason in the domain of the plasma outflow, where only one incoming wave is possible, the incoming waves are absent, for a given θ_0, when $\mid v_y \mid > v_y^{max}$.

Note that v_y^{max} coincides with the maximum value of the projection of the group velocity of a slow magnetoacoustic wave on the y axis, which in the approximation $V_s \ll V_{\text{A}}$ has the form

$$(V_{gr}^{-})_y = \frac{V_s^3}{V_{\text{A}}^2} \sin\theta \cos^3\theta \,. \tag{10.28}$$

Moreover this value is also reached for the angle $\theta = \pi/6$. So inequality (10.27) means that

> all slow waves are either incoming or outgoing, provided the plasma flows into or out of the RCL.

To solve the problem of evolutionarity of the current layer we now have to derive boundary conditions. They relate the amplitudes of the perturbations with $k_y \ll 1/a$ (that interact with the layer as with a discontinuity) on two sides of the surface.

However, as distinct from a one-dimensional discontinuity, the waves with $k_y \ll 1/a$ outside the current layer may lead to the perturbations for which the inverse inequality is valid in the interior. Furthermore, since inside the layer the dissipative effects are essential, the wave numbers of these perturbations have imaginary parts that tend to infinity in the limit $a/b \to 0$. This means that the magnitude of the perturbation increases without bound, and therefore

> the linearized one-dimensional boundary conditions generally do not hold at the reconnecting current layer (RCL)

(Markovskii and Somov, 1996). This fact can be understood in the next Section from the analysis of the perturbations inside the current layer.

10.3 Perturbations inside the RCL

10.3.1 Linearized dissipative MHD equations

Let us deduce the equations for the perturbed MHD quantities δQ inside the current layer. In this case $y \lesssim a$. We linearize the dissipative MHD equations (see vol. 1, Section 12.2.2).

For $Q_z \equiv 0$ and $\partial\,\delta Q/\partial z \equiv 0$ the equations for δv_z and δB_z, which we put equal to zero, are separated from the equations for the other small quantities. In the latter we may neglect the derivatives $\partial p/\partial x$, $\partial\,\mathbf{B}/\partial x$, and $\partial\rho/\partial x$ in the approximation $a \ll b$. The left side of inequality (10.9) allows us also to neglect the derivative $\partial v_x/\partial x$.

Consider, for example, the linear equation of mass conservation

$$\frac{\partial\,\delta\rho}{\partial t} + \delta\rho\,\frac{\partial v_x}{\partial x} + \rho\,\frac{\partial\,\delta v_x}{\partial x} + \delta v_x\,\frac{\partial\,\rho}{\partial x} + v_x\,\frac{\partial\,\delta\rho}{\partial x} + \\ + v_y\,\frac{\partial\,\delta\rho}{\partial y} + \delta\rho\,\frac{\partial v_y}{\partial y} + \delta v_y\,\frac{\partial\rho}{\partial y} + \rho\,\frac{\partial\,\delta v_y}{\partial y} = 0\,. \qquad (10.29)$$

Since, inside the RCL, the inhomogeneity of the velocity is two-dimensional then, together with the terms proportional to $\partial v_x/\partial x$, we have to neglect the terms with $\partial v_y/\partial y$.

Let us choose the sign in formula (10.17) coinciding with the sign of v_x. Inside the layer $\mid v_x \mid$ is a growing function of $\mid y \mid$, but k_x is constant. So from formulae (10.10) and (10.17) it follows that $\mid \omega_{\parallel} \mid$ increases, while $\mid y \mid$ decreases, and satisfies the condition

$$\mid \omega_{\parallel} \mid > \mid \omega_{\parallel}^{ex} \mid\,. \qquad (10.30)$$

Estimating

$$\frac{\partial\,\delta\rho}{\partial t} + v_x\,\frac{\partial\,\delta\rho}{\partial x} \sim \omega_{\parallel}\,\delta\rho\,, \qquad \frac{\partial v_y}{\partial y} \sim \frac{v_y^{ex}}{a}\,,$$

we get from (10.30) and the left side of (10.9) that

$$\frac{\partial\,\delta\rho}{\partial t} + v_x\,\frac{\partial\,\delta\rho}{\partial x} \gg \delta\rho\,\frac{\partial v_y}{\partial y}\,, \quad \text{q.e.d.}$$

If the other sign in (10.17) is chosen, then a value of y exists for which $\omega_{\parallel} = 0$ and this inequality does not hold.

Similar reasoning is valid for the other equations. Hence $\partial Q/\partial x = 0$ in the zeroth order in terms of the small parameters given by relation (10.9). Besides, we put $\partial Q/\partial t = 0$ in all equations.

Following Syrovatskii (1956), let us substitute $\partial\,\delta Q/\partial t$ by

$$-\,\mathrm{i}\,\omega\left(\delta Q-\xi\,\frac{\partial Q}{\partial y}\right)\equiv-\,\mathrm{i}\,\omega\,\hat{\mathcal{D}}Q\,, \tag{10.31}$$

and $\partial\,\delta Q/\partial x$ by $\mathrm{i}\,k_x\,\hat{\mathcal{D}}Q$, where ξ is the displacement of the layer as a unit. Then we obtain the set of *linear ordinary* differential equations with respect to y

$$\mathrm{i}\,\omega_{\parallel}\,\hat{\mathcal{D}}\rho=\mathrm{i}\,k_x\,\rho\,\hat{\mathcal{D}}v_x\,+(\,\rho\,\delta v_y\,)'\,+v_y\,\delta\rho'\,, \tag{10.32}$$

$$\mathrm{i}\,k_x\,\hat{\mathcal{D}}B_x\,+\delta B_y'\,=0\,, \tag{10.33}$$

$$\mathrm{i}\,\omega_{\parallel}\,\rho\,\hat{\mathcal{D}}v_x=\mathrm{i}\,k_x\,\hat{\mathcal{D}}p+\rho\,v_y\,\delta v_x'\,-\,\frac{B_x'\,\delta B_y}{4\pi}+v_x'\,\rho\,\delta v_y\,, \tag{10.34}$$

$$\mathrm{i}\,\omega_{\parallel}\,\rho\,\delta v_y=\delta\left(p+\frac{B_x^2}{8\pi}\right)'+\rho\,v_y\,\delta v_y'-\mathrm{i}\,k_x\,\frac{B_x\,\delta B_y}{4\pi}\,, \tag{10.35}$$

$$\begin{aligned}\mathrm{i}\,\omega_{\parallel}\,\hat{\mathcal{D}}p&=\mathrm{i}\,k_x\,\gamma p\,\hat{\mathcal{D}}v_x\,+\gamma p\,\delta v_y'+\\&+\delta\,(\,p'v_y\,)-\frac{(\gamma-1)}{2\pi}\,\nu_m\,B_x'\,\delta B_x'\,,\end{aligned} \tag{10.36}$$

$$\mathrm{i}\,\omega_{\parallel}\,\hat{\mathcal{D}}B_x=(B_x\,\delta v_y)'\,+v_y\,\delta B_x'-v_x'\,\delta B_y\,-\nu_m\,\delta B_x''\,, \tag{10.37}$$

where the prime denotes the differentiation with respect to y. Here we make use of the equality

$$p+\frac{B_x^2}{8\pi}=\mathrm{const}\,, \tag{10.38}$$

which follows from the y component of the unperturbed momentum equation.

10.3.2 Boundary conditions

Under certain restrictions on the unperturbed MHD quantities Q and the frequency ω, the *boundary conditions* (the conservation laws), which relate the amplitudes of the small perturbations on both sides of the current layer, may be deduced from the set of linear Equations (10.32)–(10.37).

For a one-dimensional discontinuity these conditions are obtained as a result of integrating the linear equations over the thickness of the domain in which the unperturbed quantities change substantially, and allowing this thickness (the thickness $2a$ of the layer shown in Figure 10.3) to tend to zero.

Let us integrate, for example, the induction Equation (10.37), substituting $v_x' = -\omega_\parallel' / k_x$ (see definition (10.10)) and δB_y from Equation (10.33)

$$\mathrm{i}\,\omega_\parallel^{ex} \int_{-a}^{+a} \delta B_x \, dy = \left\{ B_x \left(\delta v_y + \mathrm{i}\,\omega_\parallel \xi \right) \right\} + \\ + \int_{-a}^{+a} v_y \, \delta B_x' \, dy - \nu_m \left\{ \delta B_x' \right\}. \tag{10.39}$$

Here and below, the braces denote the jump of a quantity over a discontinuity. Supposing that δQ varies only slightly inside the discontinuity, if $k_y^{ex} a \ll 1$ outside it, we can estimate the integral proportional to $\omega_\parallel^{ex}$:

$$\omega_\parallel^{ex} \int_{-a}^{+a} \delta B_x \, dy \sim \omega_\parallel^{ex} \, \delta B_x^{ex} \, a \,.$$

Let us compare this expression with the jump

$$\left\{ B_x \, \delta v_y \right\} \sim B_x^{ex} \, \delta v_y^{ex}.$$

In the case under study the requirement $k_y^{ex} a \ll 1$ is satisfied for the waves (10.23) and (10.24). The relationship between the perturbations δQ in such waves, in approximation (10.6) and (10.9), is given by the formulae:

$$\delta p \sim {V_s}^2 \, \delta\rho \,, \qquad \delta v_x \sim V_s \, \frac{\delta\rho}{\rho} \,, \qquad \delta B_x \sim B_x \left(\frac{V_s}{V_\mathrm{A}} \right)^2 \frac{\delta\rho}{\rho} \,,$$

$$\delta v_y \sim V_s \left(\frac{V_s}{V_\mathrm{A}} \right)^2 \frac{\delta\rho}{\rho} \,, \quad \text{and} \quad \delta B_y \sim B_x \left(\frac{V_s}{V_\mathrm{A}} \right)^2 \frac{\delta\rho}{\rho} \,. \tag{10.40}$$

Taking (10.40) into account, we find that the condition

$$\omega_\parallel^{ex} \int_{-a}^{+a} \delta B_x \, dy \ll \left\{ B_x \, \delta v_y \right\}$$

coincides with the inequality $k_y^{ex} a \ll 1$, i.e. with the right side of (10.9).

Similar reasoning for the other terms in Equation (10.37) leads to the following boundary condition

$$\left\{ B_x \left(\delta v_y + \mathrm{i}\,\omega_\parallel \xi \right) \right\} = 0 \,. \tag{10.41}$$

The application of this approach to Equation (10.33) gives

$$\{\, \delta B_y \, - \mathrm{i}\, k_x \, B_x \, \xi \,\} = 0\,. \tag{10.42}$$

As in the magnetoacoustic waves, in approximation (10.9)

$$\delta v_y = -\frac{\omega_{\parallel}\, \delta B_y}{k_x \, B_x}\,, \tag{10.43}$$

Equations (10.41) and (10.42) are satisfied if

$$\delta B_y = \mathrm{i}\, k_x \, \xi \, B_x^{ex}\,, \tag{10.44}$$

and, consequently,

$$\delta v_y = -\,\mathrm{i}\, \omega_{\parallel}^{ex}\, \xi\,. \tag{10.45}$$

As distinct from a one-dimensional discontinuity, δQ changes substantially inside the RCL. We will show that the perturbation with $k_y^{ex} \ll 1/a$ outside the RCL may lead to perturbations inside it, for which $k_y^{in} \gg 1/a$ and k_y^{in} has an imaginary part. These perturbations increase or decrease exponentially on the characteristic length which is much smaller than a. So the above estimations of the terms in Equation (10.37) are generally not valid.

10.3.3 Dimensionless equations and small parameters

To deduce the boundary conditions on the RCL as on the surface of a discontinuity, let us obtain the solutions of the set (10.32)–(10.37) inside the layer for given ω and k_x. Assume that outside the layer only the amplitudes of the waves with $k_y^{ex} \ll 1/a$ differ from zero. Let us bring Equations (10.32)–(10.37) to a dimensionless form by the following substitution of variable and unknown functions:

$$y = a\,\tilde{y}\,, \qquad Q = Q^{\,ex}\,\tilde{Q}\,, \qquad \delta Q = \delta Q^{\,ex}\,\delta\tilde{Q}\,, \tag{10.46}$$

$$\xi = \frac{\delta v_y^{ex}}{\omega_{\parallel}^{ex}}\,\tilde{\xi}\,, \qquad k_x = \frac{\omega_{\parallel}^{ex}}{V_s^{ex}}\,\tilde{k}_x\,, \tag{10.47}$$

$$\delta v_y = -\mathrm{i}\,\xi\,\omega_{\parallel} \, + \, \frac{a\,\omega_{\parallel}^{ex}}{V_s^{ex}}\; \delta v_y^{ex}\; \tilde{\omega}_{\parallel}\, \delta\tilde{v}_y\,, \tag{10.48}$$

$$\delta B_y = \mathrm{i}\, k_x\, \xi B_x \, + \, \frac{a\,\omega_{\parallel}^{ex}}{V_s^{ex}}\; \delta B_y^{ex}\, \delta\tilde{B}_y\,. \tag{10.49}$$

Here the quantities $\delta Q^{\,ex}$ are related by formula (10.40), the tilde denotes the dimensionless functions and the expressions for δv_y and δB_y contain the boundary values (10.44) and (10.45) in an explicit form.

Let us insert expressions (10.46)–(10.49) into Equations (10.32)–(10.37) and introduce the following four small parameters in accordance with the basic assumptions (10.9) and (10.11):

$$\varepsilon_0 = \frac{v_y^{ex}}{a\,\omega_\parallel^{ex}}, \quad \varepsilon_1 = \frac{a\,\omega_\parallel^{ex}}{V_s^{ex}}, \quad \varepsilon_2 = \frac{v_y^{ex}}{V_s^{ex}}, \quad \varepsilon_3 = \left(\frac{V_s^{ex}}{V_{\rm A}^{ex}}\right)^2. \tag{10.50}$$

As a result, we obtain equations describing the dimensionless functions,

$$\mathrm{i}\,\tilde\omega_\parallel\,\delta\tilde\rho = \mathrm{i}\,\tilde k_x\,\tilde\rho\,\delta\tilde v_x + \varepsilon_3\,(\,\tilde\rho\,\tilde\omega_\parallel\,\delta\tilde v_y\,)' + \varepsilon_0\,\tilde v_y\,\delta\tilde\rho', \tag{10.51}$$

$$\mathrm{i}\,\tilde k_x\,\delta\tilde B_x + \delta\tilde B_y' = 0, \tag{10.52}$$

$$\mathrm{i}\,\tilde\omega_\parallel\,\tilde\rho\,\delta\tilde v_x = \mathrm{i}\,\tilde k_x\,\delta\tilde p - \frac{1}{\tilde k_x}\,\varepsilon_3\,\tilde\omega_\parallel\,\tilde\omega_\parallel'\,\tilde\rho\,\delta\tilde v_y - $$

$$-\tilde B_x'\,\delta\tilde B_y + \varepsilon_0\,\tilde v_y\,\tilde\rho\,\delta\tilde v_x', \tag{10.53}$$

$$\Big(\delta\tilde p + \tilde B_x\,\delta\tilde B_x\Big)' = \varepsilon_2\,\varepsilon_3\,\tilde\rho\,\tilde v_y\Big[\mathrm{i}\,\tilde\xi\,\tilde\omega_\parallel' - \varepsilon_1\,(\,\tilde\omega_\parallel\,\delta\tilde v_y\,)'\Big] +$$

$$+\varepsilon_1\,\varepsilon_3\,\tilde\omega_\parallel^2\,\tilde\rho\Big(\tilde\xi + \mathrm{i}\,\varepsilon_1\,\delta\tilde v_y\Big) - \varepsilon_1\,\tilde k_x\,\tilde B_x\Big(\tilde k_x\,\tilde\xi\tilde B_x - \mathrm{i}\,\varepsilon_1\,\delta\tilde B_y\Big), \tag{10.54}$$

$$\mathrm{i}\,\tilde\omega_\parallel\,\delta\tilde p = \mathrm{i}\,\tilde k_x\,\tilde p\,\delta\tilde v_x + \varepsilon_3\Big[\tilde p\,\big(\,\tilde\omega_\parallel\,\delta\tilde v_y\big)' + \frac{1}{\gamma}\,\tilde\omega_\parallel\,\tilde p'\,\delta\tilde v_y\Big] +$$

$$+\varepsilon_0\Big[\tilde v_y\,\delta\tilde p' - 2\,(\gamma-1)\,\tilde B_x'\,\delta\tilde B_x'\Big], \tag{10.55}$$

$$\mathrm{i}\,\tilde\omega_\parallel\,\delta\tilde B_x = \Big(\tilde B_x\,\tilde\omega_\parallel\,\delta\tilde v_y\Big)' + \frac{1}{\tilde k_x}\,\tilde\omega_\parallel'\,\delta\tilde B_y +$$

$$+\varepsilon_0\Big(\tilde v_y\,\delta\tilde B_x' - \delta\tilde B_x''\Big). \tag{10.56}$$

This is the complete set of dimensionless equations valid on the RCL as a discontinuity surface.

10.3.4 Solution of the linearized equations

Since we are interested in the solutions of the set of Equations (10.51)–(10.56) in approximation (10.9), let us allow the small parameters ε_i (except the parameter ε_3) to tend to zero. Then the equations reduce to the following simpler ones:

$$\mathrm{i}\,\tilde{\omega}_\parallel\,\delta\tilde{\rho} = \mathrm{i}\,\tilde{\rho}\,\delta\tilde{v}_x\,, \tag{10.57}$$

$$\mathrm{i}\,\delta\tilde{B}_x + \delta\tilde{B}_y' = 0\,, \tag{10.58}$$

$$\mathrm{i}\,\tilde{\omega}_\parallel\,\tilde{\rho}\,\delta\tilde{v}_x = \mathrm{i}\,\delta\tilde{p} - \varepsilon_3\,\tilde{\omega}_\parallel\,\tilde{\omega}_\parallel'\,\tilde{\rho}\,\delta\tilde{v}_y - \tilde{B}_x'\,\delta\tilde{B}_y\,, \tag{10.59}$$

$$\left(\delta\tilde{p} + \tilde{B}_x\,\delta\tilde{B}_x\right)' = 0\,, \tag{10.60}$$

$$\mathrm{i}\,\tilde{\omega}_\parallel\,\delta\tilde{p} = \mathrm{i}\,\tilde{p}\,\delta\tilde{v}_x + \varepsilon_3\left[\tilde{p}\left(\tilde{\omega}_\parallel\,\delta\tilde{v}_y\right)' + \frac{1}{\gamma}\,\tilde{\omega}_\parallel\,\tilde{p}'\,\delta\tilde{v}_y\right], \tag{10.61}$$

$$\mathrm{i}\,\tilde{\omega}_\parallel\,\delta\tilde{B}_x = \left(\tilde{B}_x\,\tilde{\omega}_\parallel\,\delta\tilde{v}_y\right)' + \tilde{\omega}_\parallel'\,\delta\tilde{B}_y\,. \tag{10.62}$$

The terms proportional to ε_3 are retained in Equations (10.59) and (10.61), since inside the current layer the quantities

$$\left(\tilde{\omega}_\parallel',\ \tilde{\omega}_\parallel\right) \lesssim 1/\sqrt{\varepsilon_3}$$

(see (10.7)) and $(\tilde{p},\ \tilde{p}') \sim 1/\varepsilon_3$ (see equality (10.38)). Besides, the expression for $\tilde{k}_x$, which follows from (10.18) and (10.19), is used

$$\tilde{k}_x = 1 + O(\varepsilon_2) + O(\varepsilon_3)\,. \tag{10.63}$$

In the set (10.57)–(10.62) the Equations (10.57) and (10.59) are not differential, but serve as the algebraic definitions of the functions $\delta\tilde{v}_x$ and $\delta\tilde{\rho}$. After the substitution of $\delta\tilde{B}_x$ from Equation (10.58) to (10.62), the latter becomes the full derivative with respect to $\tilde{y}$ and, by integrating, is brought to the form

$$\delta\tilde{B}_y + \tilde{B}_x\,\delta\tilde{v}_y = 0\,. \tag{10.64}$$

The constant of integration in this equation is put equal to zero, as the perturbation outside the layer represents the superposition of magnetoacoustic waves, for which (10.43) holds. The integration of Equation (10.60) gives

$$\delta\tilde{p} + \tilde{B}_x\,\delta\tilde{B}_x = C_0\,. \tag{10.65}$$

The substitution of (10.59), (10.64) and (10.65) in Equation (10.61) reduces it to

$$\left[\varepsilon_3\,\tilde{p} + \tilde{B}_x^2\left(1 - \frac{\tilde{p}}{\tilde{\rho}\,\tilde{\omega}_\parallel^{\,2}}\right)\right]\delta\tilde{v}_y' + \left(\frac{1}{\gamma}\,\varepsilon_3\,\tilde{p}' + \tilde{B}_x\,\tilde{B}_x'\right)\delta\tilde{v}_y =$$

$$= \mathrm{i}\, C_0 \left(1 - \frac{\tilde{p}}{\tilde{\rho}\, \tilde{\omega}_{\parallel}^{\,2}} \right). \tag{10.66}$$

Expressing the dimensionless values in the coefficient in front of $\delta\tilde{v}_y$ in terms of the dimensional ones, we find that they are equal to

$$\left(p + \frac{B_x^2}{8\pi} \right)' \frac{4\pi a}{(\, B_x^{ex}\,)^2} = 0\,. \tag{10.67}$$

(see equality (10.38)).

Hence the solution of the set (10.58), (10.60)–(10.62) is

$$\delta\tilde{v}_y = \mathrm{i}\, C_0 \int \frac{\left(1 - \tilde{p}/\tilde{\rho}\, \tilde{\omega}_{\parallel}^{\,2} \right) d\tilde{y}}{\varepsilon_3\, \tilde{p} + \tilde{B}_x^2 \left(1 - \tilde{p}/\tilde{\rho}\, \tilde{\omega}_{\parallel}^{\,2} \right)} + C\,, \tag{10.68}$$

$$\delta\tilde{B}_y = -\,\tilde{B}_x\, \delta\tilde{v}_y\,, \tag{10.69}$$

$$\delta\tilde{B}_x = -\,\mathrm{i} \left(\tilde{B}_x\, \delta\tilde{v}_y \right)', \tag{10.70}$$

$$\delta\tilde{p} = C_0 - \tilde{B}_x\, \delta\tilde{B}_x\,. \tag{10.71}$$

The solution (10.68)–(10.71) has a singularity at the point $\tilde{y}_0$, in which

$$\tilde{A} \equiv \varepsilon_3\, \tilde{p} + \tilde{B}_x^2 \left(1 - \frac{\tilde{p}}{\tilde{\rho}\, \tilde{\omega}_{\parallel}^{\,2}} \right) = 0\,, \tag{10.72}$$

and the function in the integral in (10.68) turns to infinity. However it may be shown by expressing $\delta Q'$ in terms of δQ in the set (10.32)–(10.37) that it has a singularity only for $y = 0$, where $v_y = 0$. This means that in some neighborhood of $\tilde{y}_0$ we cannot neglect the small parameters in the set (10.51)–(10.56) and turn to (10.57)–(10.62). The vicinity of the point $\tilde{y}_0$ will be considered below.

Let us now find the remaining solutions of the set of Equations (10.51)–(10.56) in the domain where the formulae (10.68)–(10.71) are valid. We suppose, for the sake of definiteness, that $v_x^{in} \sim V_{\mathrm{A}}^{ex}$ (see (10.7)), i.e. $\tilde{\omega}_{\parallel}^{\,2} \sim 1/\varepsilon_3$. Such a relation holds if x is not close to 0 and $\pm\, b$. The solution (10.68)–(10.71) is valid when the expression in the integral in (10.68) is of order of unity. Since, inside the current layer $\tilde{B}_x \lesssim 1$ and $\tilde{p} \sim 1/\varepsilon_3$, it follows from (10.68) and (10.72), that in this case

$$\tilde{A} \sim 1\,. \tag{10.73}$$

Then the remaining solutions of the set (10.51)–(10.56) satisfy the WKB approximation inside the RCL and may be found from the dispersion Equation (10.20).

Let us express the dimensionless quantities in $\tilde{A}$ in terms of the dimensional ones and take into account that

$$k_x = \omega_{\parallel}^{ex} / V_s^{ex} \,.$$

Then we find that the quantity $\tilde{A}$ is related with the coefficient in front of k_y^2 in dispersion Equation (10.20) in the following way:

$$A = \omega_{\parallel}^2 \, V_{\perp}^2 \, - k_x^2 \, V_{\mathrm{A}}^2 \, V_s^2 \, \sim \omega_{\parallel}^2 \, \left(V_{\mathrm{A}}^{ex} \right)^2 \, \tilde{A} \,. \tag{10.74}$$

Under condition (10.73) in the zeroth order in terms of the small parameters ε_i (see definition (10.50)) the solutions of Equation (10.20) take on the form (10.21) and

$$k_y^d = \frac{\omega_{\parallel}}{v_y} \,, \tag{10.75}$$

$$k_y^- = \pm \sqrt{\frac{\mathrm{i}A}{V_s^2 \, \nu_m \, \omega_{\parallel}}} \,, \tag{10.76}$$

$$k_y^* = \frac{1}{A} \left[\omega_{\parallel} \, v_y \, F \pm \sqrt{\omega_{\parallel}^2 \, v_y^2 \, F^2 - A \left(k_x^2 \, A - \omega_{\parallel}^4 \right)} \right] , \tag{10.77}$$

where

$$F = V_{\perp}^2 \, k_x^2 \, - 2 \, \omega_{\parallel}^2 \,.$$

From the basic Inequality (10.9) it follows that the wave vectors (10.21), (10.75), and (10.76) satisfy the WKB approximation inside the RCL. The dispersion equation is valid for them, as in the limit $k_y \gg 1/a$ the terms with the derivatives of unperturbed quantities in Equations (10.32)–(10.37) are negligible.

The expressions (10.42), (10.75), and (10.76) give us four solutions of the set of Equations (10.32)–(10.37). By contrast, the perturbations (10.77) do not satisfy the WKB approximation, since they have $1/k_y \, a \to 0$. In this case we cannot neglect the derivatives of unperturbed quantities in the set of Equations (10.32)–(10.37), so we cannot use Equation (10.20). These perturbations are described by formulae (10.68)–(10.71).

Thus we have shown that

> there are four perturbations, which satisfy the WKB approximation inside the RCL, regardless of the value of k_x.

Recall that outside the current layer there are also four of such perturbations in the case of normal propagation, but in the case of oblique propagation there are three. Therefore in the latter case the perturbations with $k_y \ll 1/a$ and $k_y \gg 1/a$ transform to each other.

10.4 Solution on the boundary of the RCL

In order to obtain the boundary conditions it is necessary to determine the value of the perturbation on the boundary of the current layer, i.e. for $Q = Q^{ex}$. In this case

$$a \ll y \ll 1/k_y^{ex}\,.$$

If $Q = Q^{ex}$, then the solution (10.68)–(10.71) is not valid, since the coefficients in Equation (10.66) are much smaller than unity (see definitions (10.46)) and the small parameters cannot be neglected in deducing of this equation.

Let us find the solutions of Equations (10.51)–(10.56) in the neighborhood of the boundary of the RCL in the domain

$$\tilde{Q} \sim 1\,. \tag{10.78}$$

Note that as $p^{in} \gg p^{ex}$ and $\omega_\parallel^{in} \gg \omega_\parallel^{ex}$, the value of $\tilde{y}$ exists, for which $\tilde{p} \gg 1$ and $\tilde{\omega}_\parallel \gg 1$, although for $\tilde{y} \gg 1$ always $\tilde{Q}'/\tilde{Q} \ll 1$.

Substitute Equation (10.52) in (10.56) and then substitute (10.56) and (10.53) in Equation (10.54), in the same way as for deduction of (10.66), but hold the terms proportional to the small parameter ε_0

$$\mathrm{i}\,\tilde{\omega}_\parallel \left(1 - \frac{\tilde{p}}{\tilde{\rho}\,\tilde{\omega}_\parallel^{\,2}}\right) \delta\tilde{p} = \tilde{\omega}_\parallel\, \varepsilon_3 \left(\tilde{p}\;\delta\tilde{v}_y' + \frac{1}{\gamma}\,\tilde{p}'\;\delta\tilde{v}_y\right) -$$

$$-\frac{\tilde{p}}{\tilde{\rho}\,\tilde{\omega}_\parallel}\,\tilde{B}_x'\,\delta\tilde{B}_y + \varepsilon_0\,\tilde{v}_y \left(\frac{\tilde{p}}{\tilde{\omega}_\parallel}\,\delta\tilde{v}_x' + \delta\tilde{p}'\right). \tag{10.79}$$

Here we use (10.63) and the inequality $\varepsilon_0 \ll (\varepsilon_2, \varepsilon_3)$, which follows from condition (10.9).

As the derivatives $\delta\tilde{v}_x'$ and $\delta\tilde{p}'$ appear in (10.78) with small parameters, in the first order they may be expressed from Equations (10.59) and (10.60), which do not contain small parameters. Let us integrate Equation (10.59) and use (10.64) and (10.65). Then, taking into account that $\tilde{Q}' \ll 1$ and considering (10.67), we find the equation describing the function $\delta\tilde{v}_y$,

$$\mathrm{i}\,\varepsilon_0\,\tilde{B}_x^2\,\tilde{v}_y \left(1 + \frac{\tilde{p}}{\tilde{\rho}\,\tilde{\omega}_\parallel^{\,2}}\right) \delta\tilde{v}_y'' + \tilde{\omega}_\parallel\,\tilde{A}\,\delta\tilde{v}_y' = \mathrm{i}\,C_0\,\tilde{\omega}_\parallel \left(1 - \frac{\tilde{p}}{\tilde{\rho}\,\tilde{\omega}_\parallel^{\,2}}\right) \tag{10.80}$$

(cf. Equation (10.66)). Three cases differ.

(a) Let

$$1 - \tilde{p}/\tilde{\rho}\,\tilde{\omega}_{\parallel}^{\,2} \gg \varepsilon_0\,,$$

then $\tilde{A} \gg \varepsilon_0$ (see definition (10.72)), as in the domain (10.78) $\varepsilon_3\,\tilde{p} \ll \varepsilon_0$, and Equation (10.66) is valid.

(b) Let

$$1 - \tilde{p}/\tilde{\rho}\,\tilde{\omega}_{\parallel}^{\,2} \lesssim \varepsilon_0\,,$$

then $\tilde{A} \lesssim \varepsilon_0$ and all the terms in Equation (10.79) are essential. In this case, in the first order, it is sufficient to substitute $\delta\tilde{p}$ in Equation (10.79) from (10.65), but not from (10.54). So the small parameter ε_1 does not enter in Equation (10.80).

(c) On the boundary of the layer ($\mid \tilde{Q} \mid = 1$),

$$1 - \frac{\tilde{p}}{\tilde{\rho}\,\tilde{\omega}_{\parallel}^{\,2}} = 0\,, \qquad \tilde{A} = 0\,,$$

and Equation (10.80) transforms to $\delta\tilde{v}_y'' = 0$. After integrating, this equality turns to the following one:

$$\delta\tilde{v}_y = C_*\,\tilde{y} + C\,. \tag{10.81}$$

Expression (10.81) together with (10.69)–(10.71) defines three solutions of the set of Equations (10.51)–(10.56). The remaining three solutions for $\mid \tilde{Q} \mid = 1$ satisfy the WKB approximation with the wave vectors (10.12), (10.21), and (10.22).

* * *

Let us now return to the vicinity of the point $\tilde{y}_0$, in which $\tilde{A} = 0$. From Equation (10.38) and condition (10.7) it follows that the point $\tilde{y}_0$ may generally be situated either in the domain $\tilde{y} \lesssim 1$ or $\tilde{y} \gg 1$. If

$$\tilde{y}_0 \lesssim 1\,, \tag{10.82}$$

then the terms containing $\tilde{v}_y'$ appear in the equation for $\delta\tilde{v}_y$ with $\tilde{A} = 0$. As $\tilde{v}_y' \sim 1$, they are found to be comparable with the terms proportional to $\partial v_x/\partial x$, which we have neglected when deducing the set of Equations (10.32)–(10.37). Because of this, to determine $\delta\tilde{v}_y$ in the vicinity of $\tilde{y}_0$, in the present case, it is necessary to solve a partial differential equation.

Let

$$\tilde{y}_0 \gg 1\,, \tag{10.83}$$

then $\tilde{v}_y' \ll 1$ and for $\tilde{y} = \tilde{y}_0$, in the first order, $\delta\tilde{v}_y$ is described by an ordinary differential equation. In particular, in the domain (10.78), it is

the Equation (10.80). It does not have a singularity for $\tilde{A} = 0$ and the solutions of the set of Equations (10.51)–(10.56) in the vicinity of $\tilde{y}_0$ are given by the formulae (10.81), (10.69)–(10.71), (10.12), (10.21), and (10.22).

Finally let us establish the correspondence between the perturbations outside and inside the RCL. Assume that (10.83) holds and, for $\tilde{y} \lesssim 1$ (10.73) is true.

Solving the set of Equations (10.51)–(10.56) in the domain

$$1 \ll \left(\tilde{p}\,,\, \tilde{\omega}_{\parallel}^{\,2} \right) \ll 1/\varepsilon_3\,,$$

it may be shown that the following correspondence takes place. The perturbations, which are described by the wave vectors k_y^d from (10.12) and k_y^0 from (10.21) outside the RCL, *transform* into (10.76) and (10.21) inside it, i.e. represent the same roots of Equation (10.20) for the different values of $\tilde{y}$.

> The wave (10.22) transforms into one of the perturbations (10.76), with the sign '$-$' or '$+$' depending on the sign of v_y.

Hence the superposition of (10.23) and (10.24) corresponds to the superposition of (10.68)–(10.71) and the other perturbation (10.76).

Besides, the frequency $\omega_{\parallel}$ from the interval (10.9) may be chosen in such a way, that the solution proportional to C_0 exists inside the RCL for all $\tilde{y}$. In this case the solution proportional to C_*, in the domain (10.78), transforms, for $\tilde{y} \lesssim 1$ into the perturbation with the wave vector (10.76). Thus

> the three waves with $\lambda_y^{ex} \gg a$ outside the RCL cause the perturbation inside the RCL, for which $\lambda_y^{in} \ll a$.

So now we can formulate the conditions of evolutionarity for the RCL.

10.5 The criterion of evolutionarity

10.5.1 One-dimensional boundary conditions

Let us now turn to the criterion of evolutionarity. With this end in view, we deduce the boundary conditions on the RCL as a surface of a discontinuity. There are two possibilities.

(a) If the amplitudes of the perturbations (10.21), (10.75), and (10.76) with $k_y \gg 1/a$ inside the layer differ from zero, then the boundary conditions, similar to those which hold on one-dimensional discontinuities, do not exist on its surface. If this were not so, then the quantity δv_y would

remain constant after a transition across the layer, by virtue of condition (10.45). However the magnitude of the perturbations (10.21), (10.75), and (10.76) changes substantially within the distance a and (10.45) is not valid in a general case.

(b) We consider below only such perturbations that the amplitudes of the modes (10.21), (10.75), and (10.76) equal zero. This requirement is obeyed by the solution of Equations (10.32)–(10.37), if the constant C_0 differs from zero, but the other constants equal zero (see the end of Section 10.4).

Let us obtain the boundary conditions which the solution proportional to C_0 satisfies. Due to (10.81), formulae (10.48) and (10.49) give the boundary values (10.44) and (10.45) for δv_y and δB_y. From (10.45) it follows that

$$\{\, \delta v_y \,\} = 0\,. \tag{10.84}$$

As for condition (10.44), it is equivalent to (10.45) and does not result in an additional boundary condition. Expression (10.71) determines the second boundary condition

$$\left\{ \delta p + \frac{B_x\, \delta B_x}{4\pi} \right\} = 0\,. \tag{10.85}$$

Finally formula (10.70) means that

$$\delta B_x = 0 \tag{10.86}$$

on both sides of the discontinuity, since $\delta \tilde{v}_y' = 0$ and $\tilde{B}_x' = 0$.

The appearance of the equality (10.86) is caused by the fact that we consider the perturbation, for which only the constant C_0 differs from zero, but not an arbitrary one. Given another perturbation is present inside the RCL, the condition (10.86) is generally not satisfied. As δB_x in magnetoacoustic waves do not equal zero, condition (10.86) together with (10.84) and (10.85) represents four boundary conditions, relating the amplitudes of the waves outside the RCL. Note that equalities (10.57) and (10.58) do not give additional boundary conditions, since they are valid for the perturbations in magnetoacoustic waves.

10.5.2 Solutions of the boundary equations

Now we write Equations (10.84)–(10.86) in an explicit form, i.e. expressing all small quantities in terms of the perturbation of density. As was pointed out at the end of Section 10.4, the superposition of the waves (10.23) and (10.24) outside the RCL corresponds to the superposition of the solutions (10.68)–(10.71) and (10.76) inside it.

This being so, the waves (10.23) and (10.24) are present outside the RCL, but the amplitudes of the waves (10.12), (10.21), and (10.22) equal zero, if inside it only the constant C_0 differs from zero. Using the relationship between the perturbations of MHD quantities in magnetoacoustic waves in approximation (10.9) we obtain from the boundary conditions (10.84)–(10.86), respectively

$$\sum_{i=1}^{3} \frac{k_{y+}^{(i)}}{(\,k^{(i)}\,)^2} \left(\delta\rho_{+}^{(i)} + \delta\rho_{-}^{(i)} \right) = 0\,, \tag{10.87}$$

$$\sum_{i=1}^{3} \frac{1}{(\,k^{(i)}\,)^2} \left(\delta\rho_{+}^{(i)} - \delta\rho_{-}^{(i)} \right) = 0\,, \tag{10.88}$$

$$\sum_{i=1}^{3} \left(\frac{k_y^{(i)}}{k^{(i)}} \right)^2 \delta\rho_{\pm}^{(i)} = 0\,. \tag{10.89}$$

Here the indexes + and − denote the quantities outside the RCL for $y = +\infty$ and $y = -\infty$, the index i specifies three waves (10.23) and (10.24); and it is taken into account that

$$k_{y+}^{(i)} = -\,k_{y-}^{(i)}$$

due to the plasma flow symmetry.

Let us find the solutions of these equations for the cases of the inflowing and the outflowing of a plasma, i.e. determine the amplitudes of outgoing waves versus the amplitudes of incident ones.

If the plasma flows into the layer, then there are two outgoing waves: one on each side. As there are four equations, set (10.87)–(10.89) has solutions only for a definite relationship between the amplitudes of incident waves. If these amplitudes are arbitrary, then the set of Equations (10.87)–(10.89) does not have a solution. It means that for such perturbations condition (10.86) cannot be satisfied. Since equality (10.86) is valid always, when C_0 is the only constant which differs from zero, a violation of this equality results in the fact that the other constants, i.e. the amplitudes of the perturbations with $k_y^{in} \gg 1/a$, differ from zero. Hence, in this case, the boundary conditions do not exist on the surface of the layer, i.e. it is not a discontinuity, and the conclusion of its evolutionarity cannot be obeyed.

Let the plasma flow out from the current layer. In this case there are four outgoing waves (two on each side). Denote them by the indexes $i = 1, 2$. Then their amplitudes $\delta\rho_{\pm}^{(1,2)}$ are expressed in terms of the amplitudes $\delta\rho_{\pm}^{(3)}$ of incident waves in the following way

$$\delta\rho_{\pm}^{(1)} = -\frac{1}{2} \left(\frac{k^{(1)}}{k^{(3)}} \right)^2 \frac{k_y^{(2)} - k_y^{(3)}}{k_y^{(2)} - k_y^{(1)}} \times$$

$$\times\left[\frac{k_y^{(3)}}{k_y^{(1)}}\left(\delta\rho_+^{(3)}+\delta\rho_-^{(3)}\right)\pm\frac{k_y^{(2)}+k_y^{(3)}}{k_y^{(2)}+k_y^{(1)}}\left(\delta\rho_+^{(3)}-\delta\rho_-^{(3)}\right)\right], \qquad (10.90)$$

$$\delta\rho_\pm^{(2)}=-\left(\frac{k^{(2)}}{k_y^{(2)}}\right)^2\left[\left(\frac{k_y^{(3)}}{k^{(3)}}\right)^2\delta\rho_\pm^{(3)}+\left(\frac{k_y^{(1)}}{k^{(1)}}\right)^2\delta\rho_\pm^{(1)}\right]. \qquad (10.91)$$

In formula (10.90) all the quantities $k_y^{(i)}$ are taken for one side of the discontinuity. From (10.90) it follows that if $k_y^{(1)}=k_y^{(2)}$ and $k_y^{(2)}\neq k_y^{(3)}$, then $\delta\rho_\pm^{(1)}$ turns to infinity, i.e. the coefficients of refraction and reflection are not limited.

Let us find the conditions under which the wave vectors of two outgoing waves coincide. In Section 10.2 it was shown that if

$$\mid v_y^{ex}\mid<\frac{3\sqrt{3}}{16}\,\frac{V_s^3}{V_{\rm A}^2}, \qquad (10.92)$$

then the resonant angle θ_0^* exists, for which the expression in the round brackets in formula (10.24) equals zero and two roots (10.24) coincide. This angle is determined by Equation (10.25).

Provided $\theta_0=\theta_0^*$, both waves (10.24) are outgoing, since if the plasma flows out from the current layer, then there is only one incoming wave. In the present case its wave vector is given by formula (10.23) and $k_y^{(2)}\neq k_y^{(3)}$. If condition (10.92) is not valid, then the expression in the round brackets in (10.24) is negative and the corresponding waves are surface ones for all θ_0 (see Section 10.2). In this case all wave vectors are different and $k_y^{(i)}\neq\pm k_y^{(j)}$ for $i\neq j$. So the coefficients of refraction and reflection are limited.

For the definite, but rather general, distribution of the unperturbed MHD properties inside the RCL the expressions describing the perturbation (and thus the transition between the perturbations with $k_y\ll 1/a$ and $k_y\gg 1/a$) can be found in an analytical form (Markovskii and Somov, 1996). These solutions are represented schematically in Figure 10.4.

Horizontal solid and dotted lines represent the solutions with $k_y\ll 1/a$ and $k_y\gg 1/a$ respectively. Inclined lines represent the solutions that do not satisfy the WKB approximation. Superposition of perturbations on one side of the bold line $y=\pm a$ transforms to superposition of perturbations on the other side.

In the case of normal propagation the long waves, $k_y\ll 1/a$, do not transform to the short ones, $k_y\gg 1/a$, (see Figure 10.4a). In this case the long waves interact with the RCL as with a tangential discontinuity, i.e. as if v_y equals zero. The amplitudes of the waves satisfy the linearized boundary

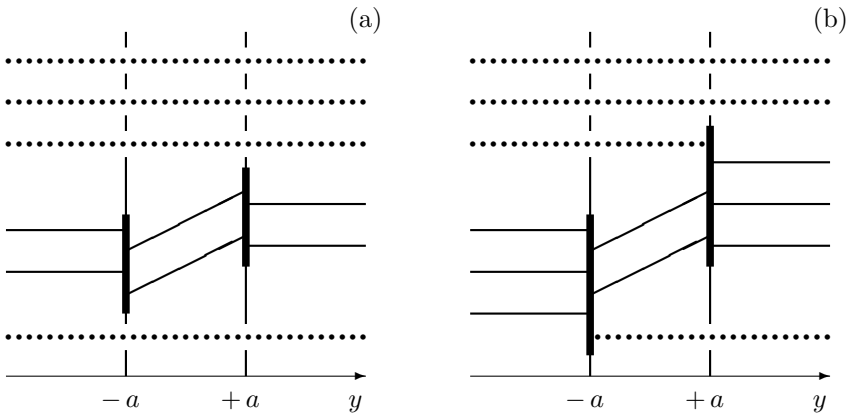

Figure 10.4: Schematic representation of solutions of the linear MHD equations in the case of normal (a) and oblique (b) propagation.

conditions for magnetoacoustic waves at a tangential discontinuity with $v_{x1} = v_{x2}$:

$$\left\{ \delta p + \frac{B_x\, \delta B_x}{4\pi} \right\} = 0\,, \qquad \{\, \delta v_y \,\} = 0\,. \tag{10.93}$$

There are thus two boundary equations and two outgoing waves (see Section 10.2.2) regardless of the sign of v_y. Moreover these equations always have a unique solution, therefore the RCL is evolutionary with respect to normally propagating waves.

Another situation arises in the case of oblique propagation. In this case long waves outside the layer transform inside it to short waves. This imposes two additional boundary conditions on the perturbations that interact with the layer as with a discontinuity, because for such perturbations the amplitudes of short waves must be equal zero. Therefore

> the RCL behaves like a discontinuity only with respect to a specially selected perturbation.

We emphasize that the conditions (10.93) appear as a result of the properties of the solutions of the linearized MHD equations, while the additional conditions occur due to the fact that we consider the perturbation which is not arbitrary. An otherwise additional condition generally does not hold.

With respect to these perturbations the problem of evolutionarity can be posed. However, the conclusions on non-evolutionarity are different for the domain of direct current, where the plasma flows into the RCL, and for the domains of reverse current, where the plasma flows out.

10.5.3 Evolutionarity and splitting of current layers

Thus we have obtained the criterion of evolutionarity for the RCL as a discontinuity.

If the plasma flows into the layer (in the region DC of the direct current in Figures 10.1b and 10.3) or if inequality (10.92) does not hold, then **the conclusion of non-evolutionarity cannot hold**. In this case the current layer either does not behave like a discontinuity or else the problem of its infinitesimal perturbation has a single solution. The last is the case when we can consider an ordinary problem of linear stability. For example, the question on the linear tearing instability always exists concerning the central part (the region of the direct current) of the RCL (see Chapter 11).

Let the relation (10.92) be valid, provided the plasma flows out from the layer (in the regions RC of the reverse current in Figures 10.1b and 10.3), and the outflow velocity is less than the projection of the group velocity of a slow magnetoacoustic wave on the normal to the layer (see (10.92)). Then the perturbation exists, for which, firstly, the boundary conditions on the surface of the layer are true, and, secondly, the amplitudes of the outgoing waves are as large as is wished, compared with the amplitudes of the incident ones in the limit $\varepsilon_i \to 0$, i.e. when the conductivity is large enough.

Such a perturbation inside the RCL is the solution of the set of Equations (10.32)–(10.37) proportional to C_0, and is characterized by the resonant angle θ_0^* from (10.25) outside it. Thus the perturbation is not described by linear equations and the problem of its time evolution does not have a single solution. Hence the current layer is non-evolutionary, as **the initial perturbation of the MHD flow is not small**. This perturbation may be the splitting of the RCL into shock waves that are observed in the numerical experiments carried out by Brushlinskii et al. (1980), Podgornii and Syrovarskii (1981), Biskamp (1986, 1997).

Therefore we have found a possible cause of splitting of the RCL into a set of the one-dimensional MHD discontinuities observed in numerical experiments. Moreover we have obtained the condition under which the splitting takes place. This allows us to unify the two regimes of magnetic reconnection in current layers: with attached shocks and without them. Such a unified model can be used to describe unsteady phenomena in astrophysical plasma, which occur as a result of magnetic reconnection.

10.6 Practice: Exercises and Answers

Exercise 10.1. Discuss basic properties of the Petschek-type reconnecting region with the four slow MHD shocks shown in Figure 10.5 (Petschek, 1964).

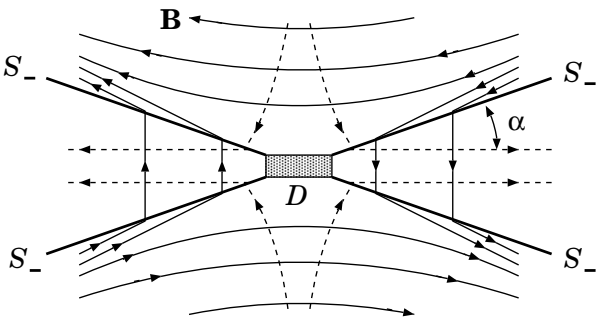

Figure 10.5: The Petschek-type reconnecting flow.

Answer. As shown in Figure 10.5, there is a diffusion region D which occupies a small central part of the area under consideration. Two pairs of the slow MHD shock waves S_- propagate away from the diffusion region. These shocks may be regarded loosely as current layers extending from the reconnecting current layer (RCL) in Figure 10.2.

While plasma flow carries magnetic field through these shock waves, the direction of the magnetic field vector rotates towards the normal, and the strength of the field decreases in this process. When the inflow velocity v_0 is much less than the Alfvén velocity, the angle α becomes very small, which makes the external flow almost uniform. As the inflow velocity increases, the inclination of the waves increase, which in turn decreases the field strength at the diffusion region.

Petschek (1964) estimated the maximum inflow velocity by assuming that the magnetic field in the inflow regions is potential and uniform at large distances. The reconnection rate turns out to be

$$\frac{v_0}{V_{\mathrm{A},0}} \approx \frac{1}{\log \mathrm{Re}_m}\,. \tag{10.94}$$

When the magnetic Reynolds number Re_m is sufficiently large, the Petschek rate would still correspond to a much faster inflow compared to the Sweet-Parker rate given by formula (6.21). In this sense, Petschek (1964) was the first to propose a *fast reconnection* model.

The elegance of this simple model has meant that it has been possible to generalize it in several ways; this has been done by different authors. These further developments cast even more serious doubt on the validity of the Petschek model. Since the reconnection rate may depend sensitively on the boundary conditions, building detailed and realistic models of reconnection is an extremely challenging problem (see Biskamp, 1997).

This page intentionally blank

Chapter 11

Tearing Instability of Reconnecting Current Layers

The tearing instability can play a significant role in reconnecting current layers, but it is well stabilized in many cases of interest. For this reason, quasi-stationary current layers can exist for a long time in astrophysical plasma, for example in the solar corona, in the Earth magnetospheric tail.

11.1 The origin of the tearing instability

11.1.1 Two necessary conditions

Among the host of instabilities appearing in a plasma with magnetic field, the tearing mode is of fundamental value for processes which transform 'free' magnetic energy into other kinds of energy. In a sense, the tearing instability is an integral part of magnetic reconnection. It is conceivable that the instability can play the role of a triggering mechanism for many of its essentially nonstationary manifestations in astrophysical plasma – flares on the Sun and in magnetospheres of the Earth and other astrophysical bodies.

The tearing instability has a universal character and arises in reconnecting current layers over quite a wide range of their parameter values. In fact, it is seen from the 2D picture of the magnetic field lines shown

in Figure 11.1a, that this state with the neutral current layer at $y = 0$ is energetically high and hence it must tend to a lower one, depicted in Figure 11.1b.

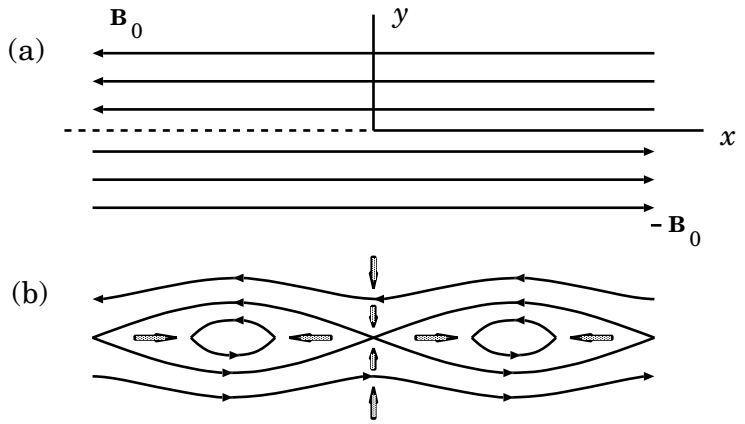

Figure 11.1: (a) Magnetic field 'reversal', a peculiarity of the configuration of field lines in a neutral current layer. (b) Magnetic-field lines in the course of the tearing instability; the arrows show the plasma velocity directions.

Such a transition may be interpreted as a process of coalescence of parallel currents constituting the current layer. However, for ideally conducting plasma, the process is impossible since it implies the displacement of field lines, leading to their tearing and the formation of closed loops – magnetic islands. This transition, i.e. the reconnection of field lines, is known to be forbidden by the condition of magnetic lines freezing into plasma (see vol. 1, Section 12.3.2). Such a restriction is removed given a finite (even if very high) electric conductivity. Thus

> for the tearing instability to develop, two conditions are necessary: (1) magnetic field reversal and (2) the availability of a finite electric conductivity.

The instability is called *tearing* because, as we have seen, its growth, once unbounded, causes the current layer to tear into separate filaments.

11.1.2 Historical comments

Before giving an account of the theory of the tearing instability, let us briefly describe the history of the question. Dungey (1958) supposed that

the availability of a neutral line in a plasma with finite conductivity leads to the instability giving rise to the current concentration. This hypothesis was based on the consideration of a *non-equilibrium* configuration of the magnetic field with an X-line whose separatrix (forming the letter X) lines intersect at an angle not equal to $\pi/2$ (see also discussion of the paper by Zwingmann et al. (1985) in Chapter 14).

The presence of the instability was experimentally found in configurations of a pinch type (Colgate and Furth, 1960), for which stability had been predicted by the ideal MHD theory. Using Dungey's mechanism, Furth (1961) qualitatively explained the current layer tearing instability. Murty (1961) investigated the same process theoretically and found the presence of the tearing mode in a resistive current layer for the low conductivity case. Finally, the theory of resistive MHD instabilities was thoroughly developed for the case of the neutral current layer without plasma flows, in the famous work of Furth et al. (1963).

In the framework of the kinetic approach the first fundamental results on the tearing instability were obtained by Coppi et al. (1966). They showed that the tearing instability arises from coupling between a negative energy wave and a dissipative process. Landau resonance of electrons inside and near the zero magnetic field plane was proposed to provide the appropriate dissipation mechanism (Section 11.6).

In parallel with the investigation of the tearing instability, mechanisms resulting in its stabilization were searched for. Why? – The point is that laboratory and numerical experiments, as well as astrophysical observations, contrary to theoretical predictions, allowed one to conclude that **reconnecting current layers can be stable for a long time**. The appearance of such stable states is of paramount importance, in particular, for the physics of reconnecting current layers (RCLs) in the cosmic plasma.

Furth (1967) proposed the hypothesis that the tearing mode is suppressed by a small transversal magnetic field (i.e., perpendicular to the current layer). As pointed out by Pneuman (1974),

> such a non-neutral current layer, cannot be topologically affected by an infinitesimal displacement,

as opposed to a neutral current layer that does not contain a transversal field. This suggests that a disturbance of *finite* amplitude is necessary to disturb the RCL, i.e. the configuration could be *metastable* (see Section 11.6.3). The stabilizing effect of the transversal field was demonstrated in the frame of the kinetic approach by Schindler (1974), Galeev and Zelenyi (1975, 1976).

Janicke (1980, 1982) considered the same hypothesis in the context of MHD and drew the conclusion that the stabilizing influence was absent.

This is the reason why a fundamental indecision as to the role of the transversal field remained for a long time. On the one hand, Somov and Verneta (1988, 1989) demonstrated a considerable stabilizing effect within the limits of the MHD approach. They also explained the reasons for negative results due to Janicke. Incidentally, on the other hand, Otto (1991), Birk and Otto (1991) once again confirmed the conclusion that, in the context of Janicke's model, the transversal component of the magnetic field does not change the tearing increment. A comparative review of alternative approaches is given, for example, in Somov and Verneta (1993). As we shall also see in Section 11.4, the transversal component of the magnetic field does modify the collisional tearing mode in such a way that it results in its stabilization.

Having finished this brief introduction, we come now to an account of the basic theory of the tearing instability.

11.2 The simplest problem and its solution

In Chapter 10, we obtained the criterion of evolutionarity for the RCL with respect to magnetoacoustic waves. We saw that in the region of the direct current, the current layer either does not behave like a discontinuity or else the problem of its small perturbation has a single solution. Therefore, in this region, we are well motivated to consider an ordinary problem of linear stability.

11.2.1 The model and equations for small disturbances

We begin by obtaining an expression for the growth rate of a *pure* tearing instability without additional stabilizing or destabilizing effects. For this purpose, we consider the case when the instability increment is much larger than the inverse time of magnetic diffusion τ_r. As will be shown in Section 11.5, once these quantities are of the same order, the effect of plasma compressibility becomes decisive. Provided diffusion may be ignored, plasma drift into the reconnecting current layer (RCL) becomes unimportant since its characteristic time is also τ_r. For the case $\omega \gg V/b$ (ω is the instability increment, V is the speed of plasma outflow from the RCL, b is its half-width, see Figure 1.5), the plasma flow along the current layer is negligible as well.

Let us consider the instability in a *linear* approximation:

$$f(\mathbf{r}, t) = f_0(\mathbf{r}) + f_1(\mathbf{r}, t).$$

Unperturbed quantities in the frame of the simplest model depend only upon the y coordinate which is perpendicular to the current layer as shown in Figure 11.1a:

$$f_0 = f_0\,(y)\,.$$

Hence small perturbations are of the form

$$f_1\,(\mathbf{r},t) = f_1\,(y)\,\exp\left[\,\mathrm{i}\,(k_x x + k_z z) + \omega t\,\right], \tag{11.1}$$

provided $1/k_x \ll b$.

The set of the MHD equations for an *incompressible* plasma with a finite conductivity σ is reduced to the following one:

$$\operatorname{curl}\left(\rho\,\frac{d\,\mathbf{v}}{dt}\right) = \operatorname{curl}\left(\frac{1}{4\pi}\operatorname{curl}\mathbf{B}\times\mathbf{B}\right),$$

$$\frac{\partial\,\mathbf{B}}{\partial t} = \operatorname{curl}\,(\mathbf{v}\times\mathbf{B}) - \operatorname{curl}\left(\frac{\eta}{4\pi}\operatorname{curl}\mathbf{B}\right),$$

$$\frac{\partial\rho}{\partial t} + \mathbf{v}\cdot\nabla\rho = 0\,, \qquad \frac{\partial\eta}{\partial t} + \mathbf{v}\cdot\nabla\eta = 0\,,$$

$$\operatorname{div}\mathbf{v} = 0\,, \qquad \operatorname{div}\mathbf{B} = 0\,.$$

Here $\eta = c^2/\sigma$ is the value proportional to magnetic diffusivity (see Appendix 3); the other symbols are conventional. This set gives the following equations for the perturbations:

$$\omega\,\operatorname{curl}\,(\,\rho_0\,\mathbf{v}_1) = \operatorname{curl}\left\{\frac{1}{4\pi}\left[\,(\,\mathbf{B}_0\cdot\nabla\,)\,\mathbf{B}_1 + (\,\mathbf{B}_1\cdot\nabla\,)\,\mathbf{B}_0\,\right]\right\},$$

$$\omega\,\mathbf{B}_1 = (\,\mathbf{B}_0\cdot\nabla\,)\,\mathbf{v}_1 - (\,\mathbf{v}_1\cdot\nabla\,)\,\mathbf{B}_0 - \frac{1}{4\pi}\,(\,\nabla\eta_0\times\operatorname{curl}\mathbf{B}_1 -$$

$$-\,\eta_0\,\Delta\,\mathbf{B}_1 + \nabla\eta_1\times\operatorname{curl}\mathbf{B}_0 - \eta_1\,\Delta\,\mathbf{B}_0)\,,$$

$$\omega\,\rho_1 + \mathbf{v}_1\cdot\nabla\rho_0 = 0\,, \qquad \omega\,\eta_1 + \mathbf{v}_1\cdot\nabla\eta_0 = 0\,,$$

$$\operatorname{div}\mathbf{v}_1 = 0\,, \qquad \operatorname{div}\mathbf{B}_1 = 0\,.$$

These dimensional equations are reduced to two dimensionless equations containing y components of the velocity and magnetic field perturbations as unknown variables:

$$(\,\tilde\rho\,W'\,)' = \alpha^2\,\tilde\rho^{\,2}\,W - \frac{S^{\,2}\alpha^2}{p}\,(\,\alpha^2 F\,\Psi + F''\,\Psi - F\,\Psi''\,)\,, \tag{11.2}$$

$$\Psi'' = \left(\alpha^2 + \frac{p}{\tilde\eta}\right)\Psi + \left(\frac{F}{\tilde\eta} + \frac{\tilde\eta'\,F'}{p\,\tilde\eta}\right)W. \tag{11.3}$$

Here

$$\Psi = \frac{B_{1y}}{B(a)}, \quad W = -\mathrm{i}\, v_{1y}\, k\, \tau_r, \quad \mu = \frac{y}{a},$$

$$F = \frac{\mathbf{k}\cdot\mathbf{B}_0}{k\, B(a)}, \quad k = \left(\mathbf{k}^2\right)^{1/2}, \quad \alpha = k\, a, \quad \tau_r = \frac{4\pi a^2}{\langle\, \eta \,\rangle},$$

$$\tau_{\mathrm{A}} = \frac{a\, (4\pi \langle\, \rho \,\rangle)^{1/2}}{B(a)}, \quad S = \frac{\tau_r}{\tau_{\mathrm{A}}}, \quad p = \omega\, \tau_r, \quad \tilde{\eta} = \frac{\eta_0}{\langle\, \eta \,\rangle}, \quad \tilde{\rho} = \frac{\rho_0}{\langle\, \rho \,\rangle}.$$

Thus we intend to solve Equations (11.2) and (11.3). As will be seen from the final results, the tearing instability is a *long-wave* mode:

$$\alpha^2 \ll 1. \tag{11.4}$$

Hence this case is considered from the beginning. For definiteness, the following distribution of the unperturbed field is chosen:

$$\mathbf{B}_0 = F(\mu)\, \mathbf{e}_x,$$

where

$$F(\mu) = \begin{cases} -1, & \mu < -1, \\ \mu, & -1 < \mu < 1, \\ 1, & \mu > 1. \end{cases}$$

Let us examine the instability mode with the *fastest* growth, for which the condition

$$\mathbf{k} \parallel \mathbf{B}_0$$

holds. Assume that

$$S \gg 1, \tag{11.5}$$

i.e., the plasma is highly-conductive (compare definition of S with definition of the magnetic Reynolds number (Appendix 3) where $v = V_{\mathrm{A}}$, $L = a$). What this means is that

> dissipative processes in such a regime are not large in magnitude, while they play a principle role in the tearing instability,

as was mentioned in the previous Section.

11.2.2 The external non-dissipative region

Starting from some distance y from the neutral plane $y = 0$ of the current layer, the dissipative processes may be ignored. We shall call this region

the *external non-dissipative* one. In the limiting case

$$\boxed{S = \frac{\tau_r}{\tau_{\rm A}} = \frac{V_{\rm A}\, a}{\nu_m} \to \infty\,,}$$

Equation (11.2) is simplified to

$$\Psi'' - \left(\alpha^2 + \frac{F''}{F}\right)\Psi = 0\,. \tag{11.6}$$

The function Ψ should be even for reasons of symmetry:

$$\Psi\,(-\mu) = \Psi\,(\mu)\,. \tag{11.7}$$

The boundary condition for the sought-after function must be formulated for $\mu \to \infty$:

$$\Psi \to 0\,. \tag{11.8}$$

Since $\mu = y/a \neq 0$, Equation (11.6), under conditions (11.7)–(11.8), has the following solution:

$$\Psi = \begin{cases} A\,\exp\left[\,\alpha(\mu+1)\,\right]\,, & \mu < -1\,, \\ A\left\{\left[\,\cosh\alpha + \left(1-\alpha^{-1}\right)\sinh\alpha\,\right]\cosh\alpha\,\mu + \right. & \\ \left. + \left[\,\sinh\alpha + \left(1-\alpha^{-1}\right)\cosh\alpha\,\right]\sinh\alpha\,\mu\right\}\,, & -1 < \mu < 0\,, \\ \Psi\,(-\mu)\,, & \mu > 0\,. \end{cases} \tag{11.9}$$

Here A is an arbitrary constant.

The derivative Ψ' suffers a rupture at the point $\mu = 0$, with

$$\Delta' = \left.\frac{\Psi'}{\Psi}\right|_{-0}^{+0} \approx \frac{2}{\alpha} \tag{11.10}$$

for $\alpha^2 \ll 1$. This fact signifies that the solution applicable in the external non-dissipative region corresponds to a singular current at the $\mu = 0$ plane.

The approximation $S \to \infty$ is not applicable in a neighbourhood of the point $\mu = 0$. This will be called the *internal dissipative* region. Outside this region the solution is described by the function (11.9) which, for $\mu \to 0$ (once $\alpha^2 \ll 1$), gives the asymptotic expression

$$\Psi \sim \text{const}\left(1 + \frac{1}{\alpha}\,|\,\mu\,|\right)\,. \tag{11.11}$$

11.2.3 The internal dissipative region

Let us consider now the neighbourhood of the point $\mu = 0$ where the condition $S \to \infty$ does not hold. Since this region is sufficiently small, the quantities $\tilde{\rho}$ and $\tilde{\eta}$ may be assumed to vary weakly inside it. On using this assumption and making the change of variables

$$\theta = \left(\frac{\alpha^2 S^2}{p}\right)^{1/4} \mu\,, \tag{11.12}$$

$$Z = \Psi''\,, \tag{11.13}$$

the set of Equations (11.2)–(11.3) results in the equation for the function $Z = Z(\theta)$

$$Z''' = \left(\nu + \theta^2\right) Z' + 4\theta Z\,. \tag{11.14}$$

This equation must be supplemented by the conditions

$$\begin{array}{l} Z(-\theta) = Z(\theta)\,, \\ Z \to 0 \quad \text{for} \quad \theta \to \infty\,. \end{array} \tag{11.15}$$

We find from (11.14)–(11.15) that the sought-after function $Z(\theta)$ has the following asymptotic behaviour for $\theta \gg 1$ $(\theta \to \infty)$:

$$Z \sim A_1 \exp\left(-\theta^2/2\right) + B\,\theta^{-4}\,. \tag{11.16}$$

For $\theta < 1$ the function $Z(\theta)$ has no singularities and can be expanded in a Taylor series.

In order to obtain the dispersion relation the integrals

$$I_0 = \int_0^{+\infty} \Psi''\, d\mu\,, \qquad I_1 = \int_0^{+\infty} \Psi''\mu\, d\mu \tag{11.17}$$

have to be evaluated. On normalizing the function $Z(\theta)$ by the condition

$$Z(0) = 1\,,$$

we find from (11.16) that

$$\tilde{I}_0 = \int_0^{+\infty} Z(\theta)\, d\theta \approx 1\,, \qquad \tilde{I}_1 = \int_0^{+\infty} Z(\theta)\,\theta\, d\theta \approx 1\,. \tag{11.18}$$

The integrals (11.17) are expressed through (11.18).

For the function $\Psi(\theta)$, we have

$$\Psi(\theta) = \int_0^{\theta} d\theta_1 \int_0^{\theta_1} Z(\theta_2)\, d\theta_2 ,$$

whence

$$\Psi(\mu) \sim \text{const} \left(1 + \frac{I_0}{(1/p) - I_1} \,|\, \mu \,| \right) \tag{11.19}$$

for $\theta \to \infty$. Here it is taken into account that

$$\Psi''_{\mu\mu}(0) = p\, \Psi(0) .$$

11.2.4 Matching of the solutions and the dispersion relation

As is seen from the asymptotic solution (11.16), the approximation $S \to \infty$ is valid once $\mu \gg \varepsilon_0$, where

$$\varepsilon_0 = \left(\frac{p}{\alpha^2 S^2} \right)^{1/4} . \tag{11.20}$$

Hence the function (11.19) must coincide with (11.12). Equating them results in the *dispersion* equation

$$\left(1 - \frac{p^{3/2}}{\alpha S} \right) - p\, \alpha \left(\frac{p}{\alpha^2 S^2} \right)^{1/4} = 0 . \tag{11.21}$$

There is no difficulty in understanding that, given the ratio

$$\frac{p^{3/2}}{\alpha S} \ll 1 , \tag{11.22}$$

the equation is reduced to

$$p \approx \left(\frac{S}{\alpha} \right)^{2/5} , \tag{11.23}$$

while given

$$p\, \alpha \left(\frac{p}{\alpha^2 S^2} \right)^{1/4} \ll 1 , \tag{11.24}$$

it reduces to

$$p = (\alpha S)^{2/3} . \tag{11.25}$$

Conditions (11.22) and (11.24) are equivalent to

$$p\,\alpha^2 \gg 1 \tag{11.26}$$

and

$$p\,\alpha^2 \ll 1\,, \tag{11.27}$$

respectively. Region (11.26) may be termed that of 'short' waves, whereas region (11.27) is that of 'long' waves. In the former the growth rate increases with the increase of the wavelength, while decreasing in the latter.

At $p\,\alpha^2 \sim 1$, i.e., when $\alpha \sim S^{1/4}$, the growth rate reaches the maximum

$$p_{\max} \sim S^{1/2}\,. \tag{11.28}$$

Recall that the dimensionless parameters

$$\alpha = ka = \frac{2\pi a}{\lambda}\,, \qquad p = \omega\,\tau_r\,.$$

Without using the condition $\alpha^2 \ll 1$, Equation (11.6) shows that $\Delta' \approx 0$ for $\alpha \approx 1$. So the tearing instability completely disappears for $\alpha \approx 1$ and exists in the region of the wave length

$$\boxed{\lambda > 2\pi a\,.} \tag{11.29}$$

That is why it is called a *long-wave* instability.

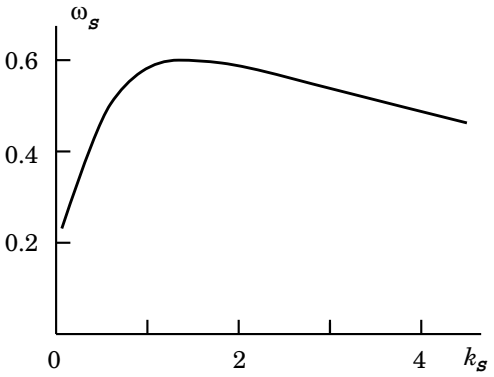

Figure 11.2: The dependence of the tearing instability increment ω_s on the wave vector k_s.

As $\alpha \to S^{-1}$, the increment tends to ${\tau_r}^{-1}$. As was mentioned earlier, in this case, i.e. in the region $\alpha < S^{-1}$, the effect of compressibility becomes dominant. It will be discussed in Section 11.5.

Expression (11.23) was obtained analitically by Furth et al. (1963); they also obtained the dependence (11.25) numerically. The results of the numerical solution of the general Equation (11.21) are given in Figure 11.2, using the notation

$$\omega_s = \omega\,\tau_r\,S^{-1/2}\,, \qquad k_s = ka\,S^{\,1/4}\,. \tag{11.30}$$

Recall that the dimensionless parameter S is the Lundquist number (6.22) but determined with respect to the current-layer thickness a.

11.3 Physical interpretation of the instability

11.3.1 Acting forces of the tearing instability

We now present another derivation of the dispersion relations, based on the consideration of the physical mechanism of the tearing instability (Furth et al., 1963). Let us make use of the absolute system of units where the speed of light $c = 1$. Besides, every coefficient of order unity will be set equal to unity.

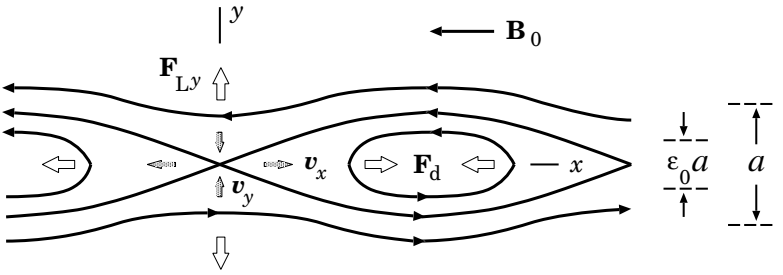

Figure 11.3: The magnetic field lines and the velocity in the course of the development of a tearing instability. The small arrows show velocity directions. Forces are shown by thick empty arrows. $\varepsilon_0 a$ is the internal region thickness. The case $\varepsilon_0 < \alpha$ is shown.

Let a small perturbation appear in the reconnecting current layer (RCL). As a consequence of the magnetic field structure (namely, antiparallel directions of reconnecting components on either side of the neutral plane), a *driving* force $\mathbf{F}_\mathrm{d}$ of the instability arises, accelerating the plasma along the x axis, i.e. along the width of the layer (see Figure 11.3). This force corresponds to a simple fact:

> parallel electric currents flowing inside the neutral layer attract each other and tend to coalesce into separate current filaments.

Thus the driving force of the instability generates plasma motions inside the RCL, directed along the x axis, with a velocity v_{1x}. As this takes place, the surrounding plasma must, by virtue of the flow continuity, flow into the internal region with a velocity v_{1y}. As a consequence, the electric current $j_{\rm s}$ arises, giving rise to the corresponding Lorentz force $F_{{\rm L}y}$, hindering the plasma from flowing into the internal region:

$$j_{\rm s} = \sigma\, v_{1y}\, \varepsilon_0 B\,, \qquad F_{{\rm L}y} = j_{\rm s}\, \varepsilon_0 B = \sigma\, v_{1y}\, (\varepsilon_0 B)^2.$$

Here we have taken into account that the reconnecting component of the field at the boundary of the internal region is equal to $B_x(y) = \varepsilon_0 B$, where $\varepsilon_0 a$ is the thickness of the internal region.

The force $F_{{\rm L}y}$ is directed against the plasma motion and is comparable in magnitude with the driving force $F_{\rm d}$ of the instability.

Hence the power with which the driving force performs work on a unit volume of the plasma is

$$P = v_{1y} F_{{\rm L}y} = \sigma\, v_{1y}^2\, (\varepsilon_0 B)^2. \tag{11.31}$$

This power goes to acceleration of the plasma; that is why

$$P = K, \tag{11.32}$$

where K is the kinetic energy acquired by the unit plasma volume in unit time:

$$K = \omega\rho\, v_{1x}^2 = \omega\rho\, \frac{v_{1y}^2}{(k\, \varepsilon_0 a)^2}\,. \tag{11.33}$$

Here use is made of the incompressibility condition $\operatorname{div} \mathbf{v} = 0$:

$$v_{1x} = \frac{v_{1y}}{k\, \varepsilon_0 a}\,.$$

On comparing (11.31) and (11.33), an expression for the thickness of the internal dissipative region is found,

$$\varepsilon_0 = \Big(\frac{\omega\rho}{k^2 a^2 B^2 \sigma}\Big)^{1/4}, \tag{11.34}$$

which coincides with expression (11.9), obtained earlier from the analytical solution.

11.3.2 Dispersion equation for tearing instability

Let us now find the dispersion relations. In the dissipative region, where the flows of plasma and field lines are relatively independent, the first addendum on the right-hand side of Ohm's law

$$\eta\,\mathbf{j} = \mathbf{E} + \mathbf{v} \times \mathbf{B}$$

dominates the second one, though these two are of the same order of magnitude. What this means is that $\varepsilon_0 a$ must be taken in such a way that

$$\eta\, j_1 \sim E_1\,. \tag{11.35}$$

However the plasma and magnetic field line motions are not completely independent, even in the internal dissipative region. The electric field perturbation E_1 is related with that of the magnetic field perturbation B_1 through

$$E_1 \sim \frac{\omega B_{1y}}{k}\,.$$

Using the Maxwell's equations

$$\operatorname{curl}\mathbf{B} = \frac{4\pi}{c}\,\mathbf{j} \quad \text{and} \quad \operatorname{div}\mathbf{B} = 0\,,$$

we obtain

$$j_1 \sim \frac{B_1''}{4\pi k} \tag{11.36}$$

once $ka < 1$. Relations (11.35) and (11.36) give rise to

$$\frac{\omega B_{1y}}{\eta} \sim \frac{B_{1y}''}{4\pi}\,. \tag{11.37}$$

Now the quantity B_{1y}'' has to be evaluated. As a consequence of a partial freezing-in, magnetic field deviations during the plasma motion along the layer in a region with a thickness

$$a\tilde{\varepsilon} \sim a^2 k\,,$$

since $a\tilde{\varepsilon}\lambda \sim a^2$. For

$$a\tilde{\varepsilon} > a\varepsilon_0 \tag{11.38}$$

this gives the estimate

$$B_{1y}'' \sim \frac{B_{1y}'}{\varepsilon_0 a} \sim \frac{B_{1y}}{\varepsilon_0 a\,\tilde{\varepsilon} a} \sim \frac{B_{1y}}{\varepsilon_0 k a^3}\,, \tag{11.39}$$

whereas for

$$a\tilde{\varepsilon} < a\varepsilon_0 \tag{11.40}$$

one has

$$B''_{1y} \sim \frac{B'_{1y}}{\varepsilon_0 a} \sim \frac{B_{1y}}{(\varepsilon_0 a)^2}\,. \tag{11.41}$$

It is a simple matter to see that the inequality (11.38) is equivalent to the inequality (11.26) determining the region of short-wave perturbations, while the inequality (11.40) is equivalent to (11.27) which corresponds to the long-wave region. Substituting the relations (11.39) and (11.41) in (11.37), with care taken of (11.34), leads to the dispersion relations:

$$\omega^5 = \frac{\eta^3 B^3}{a^{10}\rho}\,\frac{1}{k^2} \tag{11.42}$$

for the case (11.38), and

$$\omega^3 = \frac{\eta B^2}{a^2\rho}\,k^2 \tag{11.43}$$

for the case (11.40). Equations (11.42) and (11.43) are easily shown to be equivalent, respectively, to Equations (11.23) and (11.25), obtained analytically in Section 11.2.

11.4 The stabilizing effect of transversal field

While describing the effect of a transversal magnetic field, attention will be centred on the physical picture of the phenomenon. In this way we are able to understand the stabilization mechanism and easily obtain the dispersion relations for the tearing instability with a transversal field.

Given the transversal field, the plasma moves along the width of the RCL, overcoming the braking influence of the transversal field as shown in Figure 11.4. Taking this fact into account, we have instead of (11.32) to write down

$$P = K + \Pi\,. \tag{11.44}$$

The second term on the right is the work done in a unit of time against the force $F_{B\perp}$ related to the transversal field $B_\perp$, and it is given by

$$\Pi = v_{1x}\,F_{B\perp}\,. \tag{11.45}$$

Here

$$F_{B\perp} = j_{B\perp} B_\perp \quad \text{and} \quad j_{\mathrm{B}\perp} = \sigma\, v_{1x}\, B_\perp\,. \tag{11.46}$$

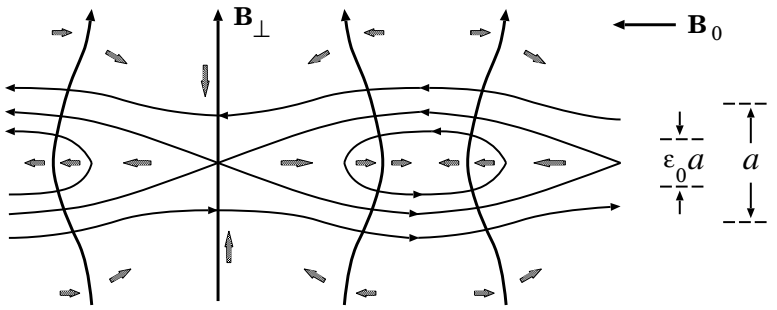

Figure 11.4: The magnetic field lines and velocities for the tearing instability in the RCL with a transversal magnetic field.

Using Equations (11.45)–(11.46) and $\operatorname{div} \mathbf{v} = 0$, the power Π is evaluated to be

$$\Pi = \sigma B_\perp^2 \, \frac{v_{1y}^2}{(k\,\varepsilon_0 a)^2} \,. \tag{11.47}$$

Substituting the relations (11.31), (11.33), and (11.46) in the relation (11.44) gives

$$\sigma\, v_{1y}^2\, (\varepsilon_0 B)^2 = \frac{\omega\rho\, v_{1y}^2}{(k\,\varepsilon_0 a)^2} + \sigma\, B_\perp^2\, \frac{v_{1y}^2}{(k\,\varepsilon_0 a)^2} \,.$$

From this there immediately follows an estimate for the thickness of the internal dissipative region with the transversal field at hand:

$$\varepsilon_0 = \left(\frac{\omega\rho}{k^2 a^2 B^2 \sigma}\right)^{1/4} \left(1 + \frac{\sigma B_\perp^2}{\omega\rho}\right)^{1/4} \tag{11.48}$$

or

$$\varepsilon_0(\xi_\perp) = \varepsilon_0(0) \left(1 + \frac{\xi_\perp^2 S^2}{p}\right)^{1/4} .$$

Here $\xi_\perp = B_\perp / B$ and the internal region thickness for $B_\perp = 0$ is designated as $\varepsilon_0(0)$. Now $\varepsilon_0(\xi_\perp)$ is implied in the expressions (11.36) to (11.41) by ε_0. Substituting (11.48) in (11.36)–(11.41) gives the dispersion relations:

$$\omega^5 = \frac{\eta^3 B^3}{a^{10}\rho}\, \frac{1}{k^2} - \frac{B_\perp^2}{\rho\eta}\, \omega^4$$

in the short-wave region

$$\varepsilon_0 < \alpha \,, \tag{11.49}$$

and

$$\omega^3 = \frac{\eta B^2}{a^2 \rho}\, k^2 - \frac{B_\perp^2}{\rho\, \eta}\, \omega^2$$

in the long-wave region

$$\varepsilon_0 > \alpha\,. \tag{11.50}$$

Let us rewrite the same dispersion relations in the dimensionless form

$$p^5 = \left(\frac{S}{\alpha}\right)^2 - \xi_\perp^2 S^2 p^4 \tag{11.51}$$

and

$$p^3 = \alpha^2 S^2 - \xi_\perp^2 S^2 p^2 \tag{11.52}$$

for the cases (11.49) and (11.50), respectively. It is easy to comprehend that

> the transversal component of magnetic field decreases the tearing mode increment over the whole wave range and also decreases the wavelength at which the increment peaks.

The rigorous analytic solution (Somov and Verneta, 1989) gives us the dispersion relation

$$\Delta^{1/4} \left(\frac{\alpha^2 S^2}{p}\right)^{1/4} \left(1 - \frac{p^{3/2}}{\alpha S}\, \Delta^{-1/2}\right) - p\, \alpha \left(\frac{\pi}{2}\right)^{1/2} = 0\,, \tag{11.53}$$

where

$$\Delta = \left(1 + \frac{\xi_\perp^2 S^2}{p}\right)^{-1}. \tag{11.54}$$

From Equation (11.53) the dispersion relations (11.51) and (11.52) follow, given the conditions (11.49) and (11.50), respectively.

The stabilizing influence of the transversal field is demonstrated by Figure 11.5 on which the graphs of the instability increment $\omega\, \tau_r$ dependence on the wave length λ/a are presented for $S = 10^8$ and three values of the transversal field: $\xi_{\perp 0} = 0$, $\xi_{\perp 1} = 10^{-4}$, and $\xi_{\perp 2} = 10^{-3}$. The solutions of the asymptotical Equations (11.51) and (11.52) are shown by the straight dotted lines, the solutions of the exact Equation (11.53) are shown by solid curves. The figure shows that,

> as the transversal magnetic field increases, the increment of the tearing instability in the reconnecting current layer (RCL) decreases and its maximum moves to the short-wave region.

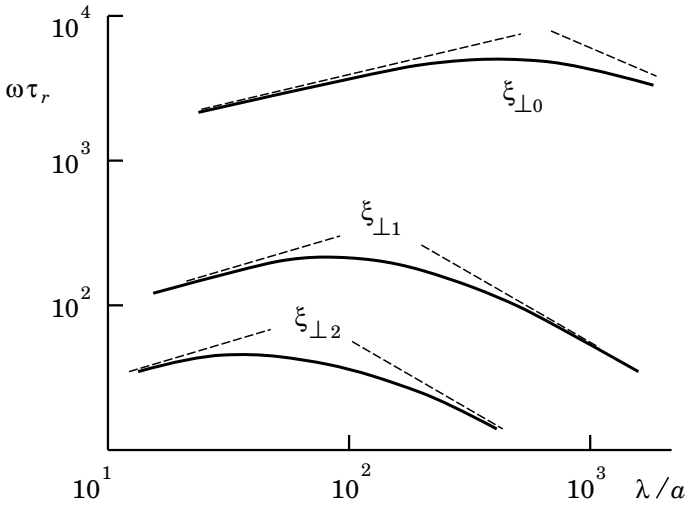

Figure 11.5: The dependence of the collisional tearing instability increment on the wavelength and the transversal component of magnetic field.

Nishikawa and Sakai (1982) have numerically solved a set of eigenmode equations in a RCL with the transversal magnetic field. The mode associated with magnetic island formation was investigated. It was found that the transversal component strongly modifies this mode and has a significant stabilizing effect on the collisional tearing mode.

11.5 Compressibility and a longitudinal field

11.5.1 Neutral current layers

Let us find the conditions under which compressibility of plasma should be taken care of and show the effect of compressibility on the tearing instability of the reconnecting current layer (RCL). For simplicity's sake, we first restrict our attention to the case $B_y = B_\perp = 0$ and $B_z = B_\parallel = 0$.

During development of the tearing instability, the plasma starts moving along the width of the layer as shown in Figure 11.3. Given the finite value of the sound velocity, V_s, the plasma in the neighbourhood $|\,\delta x\,| < V_\mathrm{s}/\omega$ of the reconnection point is drawn into the motion in a characteristic time of the instability growth ω^{-1}. Provided $V_\mathrm{s}/\omega > \lambda$, the plasma may be

considered incompressible. In the opposite case

$$\frac{V_{\rm s}}{\omega} < \lambda \tag{11.55}$$

the compressibility of the plasma must be accounted for: $\operatorname{div}\mathbf{v} \neq 0$. In this case the estimate

$$\frac{v_{1x}}{(V_{\rm s}\,/\,\omega)} \sim \frac{v_{1y}}{\varepsilon_0 a} \tag{11.56}$$

holds, where $\varepsilon_0 a$ is the internal region dimension.

Let us compare the work done by the driving instability force (Section 11.3) in unit time on unit volume,

$$P \sim \sigma v_{1y}^2\,(\varepsilon_0 B)^2\,,$$

with the kinetic energy acquired in unit time by the unit plasma volume drawn into the motion along the RCL within the neighbourhood $|\,\delta x\,| < V_{\rm s}/\omega$ of the reconnection point,

$$K \sim \omega\rho_0\, v_{1x}^2 \sim \omega\rho_0 \left(\frac{V_{\rm s}}{\omega}\,\frac{1}{\varepsilon_0 a}\right)^2 v_{1y}^2\,.$$

Here relation (11.56) is used. Equating P and K gives an estimate for ε_0:

$$\varepsilon_0 \sim \left(\frac{\rho_0 {V_{\rm s}}^2}{\omega a^2 \sigma B^2}\right)^{1/4} \sim \left(\frac{1}{\omega\tau_r}\,\frac{{V_{\rm s}}^2}{V_{{\rm A}x}^2}\right)^{1/4}, \tag{11.57}$$

where $V_{{\rm A}x} = B_x/\sqrt{4\pi\rho}$ is the Alfvén speed.

Now substituting the quantity (11.57) for ε_0 in formulae (11.37)–(11.41) immediately results in the dispersion relation

$$\omega \approx \frac{1}{\tau_r}\,\frac{V_{{\rm A}x}^2}{V_{\rm s}^2}\,.$$

Thus it is seen that

> because of compressibility of the plasma, a new branch of the tearing instability arises in the reconnecting current layer

in the long-wave region

$$\lambda > \lambda_0 \approx \frac{V_{\rm s}}{\omega} \sim 2\pi a\, S \left(\frac{V_{{\rm A}x}}{V_{\rm s}}\right)^{-3}, \tag{11.58}$$

which was absent for an incompressible plasma ($\omega \to 0$ for $\lambda > \lambda_0$). Recall that so far we have treated the case $B_\perp = 0$, $B_\parallel = 0$, i.e. the magnetically neutral current layer.

11.5.2 Non-neutral current layers

In the context of the above treatment, the role of a longitudinal field $B_z = B_\parallel \neq 0$ (along the electric current in the RCL) becomes clear. While compressing a plasma with a longitudinal magnetic field which is in fact frozen into the plasma, **the work is to be done to compress the longitudinal field** (Somov and Titov, 1985b). Thus, given the longitudinal field, the plasma pressure is supressed by the sum of the plasma pressure and the magnetic one (connected with the longitudinal field). This leads to the change

$$V_{\rm s} \to \left(V_{\rm s}^2 + V_{\rm A\parallel}^2\right)^{1/2}, \tag{11.59}$$

where $V_{\rm A\parallel} = B_\parallel/\sqrt{4\pi\rho}$, which describes the stabilizing influence of the longitudinal field. Once

$$B_\parallel > B_x(a), \tag{11.60}$$

the instability caused by the compressibility becomes suppressed.

Note that the values obtained for the growth rate of the instability are comparable with the inverse time of magnetic diffusion τ_r^{-1}. Magnetic diffusion, however, is neutralized by the plasma drift into the RCL (see Section 3.5 in Somov, 1992) and the stationary zero configuration persists for a time $t_{\rm s} \gg \tau_r$. If the condition

$$\rho_{\rm out} \ll \rho_{\rm in} \tag{11.61}$$

is satisfied, where $\rho_{\rm out}$ and $\rho_{\rm in}$ are the plasma densities inside and outside the layer, respectively, the plasma drift into the RCL cannot usually suppress the tearing instability (see, however, Pollard and Taylor, 1979). Hence the tearing instability of the RCL can play an essential role as a universal dynamic instability (Somov and Verneta, 1993).

The rigorous analytic solution of the problem concerning the compressibility effect on the tearing mode development was given by Verneta and Somov (1993).

In actual RCLs, the plasma continuously flows into the layer through its wide surfaces and flows out through the narrow side boundaries (see Figure 6.3).

> The fast outflow of plasmas from the reconnecting current layer can be of principal importance for its tearing stability

(Syrovatskii, 1981). The accelerating outflow along the main (B_x) magnetic field, which is present in the configuration with the velocity stagnation point, causes a substantial decrease in the magnitude of the linear growth rate and, for some parameter ranges, stabilization (Ip and Sonnerup, 1996).

11.6 The kinetic approach

11.6.1 The tearing instability of neutral layer

We now desribe the tearing instability in the framework of the collisionless plasma model, starting from the Vlasov equation (see vol. 1, Section 3.1.2)

$$\frac{\partial f_k}{\partial t} + \mathbf{v}\,\frac{\partial f_k}{\partial \mathbf{r}} + \frac{\mathbf{F}_k}{m_k}\,\frac{\partial f_k}{\partial \mathbf{v}} = 0\,. \tag{11.62}$$

Here

$$\mathbf{F}_k = q_k\left(\mathbf{E} + \frac{1}{c}\,\mathbf{v}\times\mathbf{B}\right)$$

and symbols $k = \mathrm{e}, \mathrm{i}$ denote electrons and ions, respectively.

As equilibrium distribution functions describing the reconnecting current layer (RCL), it is appropriate to choose (Harris, 1962)

$$f_k^{(0)}(y) = n_0\,\exp\left\{-\frac{1}{k_{\mathrm{B}}T_k}\left[\frac{1}{2}\,m_k v^2 - \vartheta_k\left(m_k v_z + \frac{1}{c}\,q_k A^{(0)}\right)\right]\right\}. \tag{11.63}$$

The notation is conventional. Here the vector potential $\mathbf{A} = \mathbf{e}_z A$ for a two-dimensional magnetic field $\mathbf{B} = \operatorname{curl}\mathbf{A}$ is introduced. The scalar potential is excluded by choosing $\vartheta_\mathrm{i}/T_\mathrm{i} = -\vartheta_\mathrm{e}/T_\mathrm{e}$. ϑ_e and ϑ_i are the flow velocities of electrons and ions.

Such distribution functions (as can be shown using Maxwell's equations) specify a current layer with the following characteristics:
(a) the equilibrium magnetic field

$$\mathbf{B} = B_0\,(y)\,\mathbf{e}_x\,,$$

where

$$\boxed{B_0\,(y) = B_0\,\tanh\,\frac{y}{a}} \tag{11.64}$$

on choosing

$$A^{(0)}\,(y) = \text{const} \times \ln\cosh\,\frac{y}{a}\,;$$

(b) the plasma density in the RCL

$$n^{(0)}\,(y) = n_0\,\cosh^{-2}\,\frac{y}{a}\,, \tag{11.65}$$

where

$$n_0 = \frac{1}{k_{\mathrm{B}}(T_\mathrm{e} + T_\mathrm{i})}\,\frac{B_0^2}{8\pi}\,;$$

(c) the RCL half-thickness

$$a = \frac{2ck_{\text{B}}(T_{\text{e}} + T_{\text{i}})}{eB_0\,(\vartheta_{\text{i}} - \vartheta_{\text{e}})}\,. \tag{11.66}$$

Therefore a magnetically-neutral one-dimemsional current layer of the Harris type is considered.

Near the plane $y = 0$ where $B_0 = 0$, particle motion is almost free inside a non-adiabatic region of thickness $2d_k$ (cf. definition (9.28)). Outside this region the particles are magnetized. The quantity d_k can be evaluated as follows (see also Section 9.1). The local Larmor radius of a particle at the boundary of the region is

$$r_{\text{L}}^{(\text{k})}\,(d_k) = \frac{V_{Tk}\,m_k\,c}{q_k\,B_0\,(d_k/a)}\,.$$

Equating it to the internal dissipative region thickness

$$r_{\text{L}}^{(\text{k})}\,(d_k) \approx d_k\,,$$

we find

$$\boxed{d_k \approx \sqrt{a r_{\text{L}}^{(\text{k})}}\,,} \tag{11.67}$$

where $r_{\text{L}}^{(\text{k})}$ is the Larmor radius in the B_0 field. Thus the motion of particles of kind k is assumed to be free inside the region $|\,y\,| < d_k$, whereas they are magnetized once $|\,y\,| > d_k$.

$\star \quad \star \quad \star$

Equations (11.62) will be solved in a *linear* approximation. The Fourier components of the perturbations are of the form

$$f^{\,(1)}(\mathbf{r}, t) = f^{\,(1)}(y)\,\exp\left(\omega t + \mathrm{i}kx\right). \tag{11.68}$$

Recall that the case $\mathbf{k} \parallel \mathbf{B}_0$ is considered. The initial Equations (11.62) give, for perturbations,

$$(\omega + \mathrm{i}kv_x)\,f_k^{\,(1)} = -\frac{1}{m_k}\,\mathbf{F}_k^{\,(1)} \cdot \frac{\partial f_k^{\,(0)}}{\partial \mathbf{v}}\,.$$

These equations determine the approximate form of the perturbed distribution function, the connection between $f_k^{\,(1)}$, $E^{\,(1)}$, and $A^{(1)}$:

$$f_k^{(1)} = \frac{q_k f_k^{\,(0)}}{k_{\text{B}} T_k}\,\left\{\vartheta_k A^{(1)} + E^{\,(1)}\,\frac{v_z}{\omega + \mathrm{i}kv_x}\right\}. \tag{11.69}$$

The first term on the right-hand side represents the influence of the magnetic field perturbation and the second one represents the interaction between the electric field of a wave and particles.

The latter contribution is negligible outside the RCL as the particle motion becomes adiabatic and there is no electric field along the magnetic field lines.

From Maxwell's equations, the perturbation electric field

$$\boxed{E^{(1)} = -\frac{1}{c}\,\omega A^{(1)}\,.} \tag{11.70}$$

Final results show that the instability growth rate complies with the condition

$$\omega < k\,\mathcal{V}_{Tk}\,, \tag{11.71}$$

where (different from the mean thermal velocity introduced in vol. 1, Section 8.1.4)

$$\mathcal{V}_{Tk} = \sqrt{\frac{2k\,T_k}{m_k}}\,. \tag{11.72}$$

Therefore we consider a low-frequency mode of the instability. This is the reason for assuming that

$$\frac{1}{v_x - \mathrm{i}\,(\omega/k)} \approx \mathrm{i}\pi\,\delta\,(v_x) + \mathrm{Vp}\left(\frac{1}{v_x}\right) \tag{11.73}$$

(the Sokhotsky formula). Here Vp is the principal value of an integral (see Vladimirov, 1971, Chapter 2, § 7).

$$\star \quad \star \quad \star$$

If W is the total kinetic energy of the particles in the perturbation, then

$$\frac{dW}{dt} = \sum_k q_k \int E^{(1)}\,v_z\,f_k^{(1)}\,d^3\mathbf{v}\,dy\,. \tag{11.74}$$

On the other hand, the energy conservation law gives

$$\frac{dW}{dt} = -\frac{1}{8\pi}\,\frac{d}{dt}\int \left(B^{(1)}\right)^2\,dy\,. \tag{11.75}$$

Substituting (11.69) and (11.73) in formula (11.74), we get

$$\frac{dW}{dt} = \frac{\pi}{k}\sum_k \frac{q_k}{k_\mathrm{B}T_k}\int\limits_{-d_k}^{+d_k}\left[\int f_k^{(0)}\,\delta\,(v_x)\left(E^{(1)}\,v_z\right)^2\,d^3\,\mathbf{v}\right]dy\,-$$

$$-\frac{1}{4\pi}\frac{d}{dt}\int\limits_{-\infty}^{+\infty}\frac{n(y)}{n(0)}\left(\frac{A^{(1)}}{a}\right)^2 dy \stackrel{\text{def}}{=} \sum_k \frac{d}{dt}W_k^{\,\mathrm{r}} - \frac{d}{dt}W^{\,\mathrm{m}}. \qquad (11.76)$$

Here $dW_k^{\,\mathrm{r}}/dt$ is the growth rate of the kinetic energy of the resonant particles of kind k in the region $|\,y\,| < d_k$, whereas $dW^{\,\mathrm{m}}/dt$ is the rate of energy decrease of the remaining particles.

The electron resonance term is $(r_{\mathrm{L}}^{(\mathrm{i})}/r_{\mathrm{L}}^{(\mathrm{e})})^{1/2}$ times greater than the ion one. Taking this fact into account, we find from formulae (11.75) and (11.76) for electrons ($k = \mathrm{e}$)

$$W^{\,\mathrm{r}} = \omega\int\limits_{-d_\mathrm{e}}^{+d_\mathrm{e}}\left[\int f_\mathrm{e}^{(0)}\,\delta\,(v_x)\left|\left(A^{(1)}\right)^2 v_z\right|^2 d^3\mathbf{v}\right] dy =$$

$$= \frac{k_\mathrm{B}T_\mathrm{e}}{8\pi e^2}\int\limits_{-\infty}^{+\infty}\left\{\left|\frac{\partial A^{(1)}}{\partial y}\right|^2 + \left|A^{(1)}\right|^2\left(k^2 - \frac{2}{a^2\,\cosh^2(y/a)}\right)\right\} dy =$$

$$= W^{\,\mathrm{m}} - \frac{1}{8\pi}\int\left(B^{\,(1)}\right)^2 dy\,. \qquad (11.77)$$

From this it follows that the *energy transfer to electrons* exists in the region

$$ka < 1 \quad \text{or} \quad \lambda > 2\pi a \qquad (11.78)$$

(cf. condition (11.29)). This process constitutes the development of the *electron* mode of the tearing instability.

> The electron mode of the teraing instability arises from the coupling of a negative energy perturbation (associated with filamentation of the original magnetically-neutral current layer) to the electron energization due to Landau resonance

(see vol. 1, Section 7.1.2).

Formula (11.77) gives us the following estimate for the growth rate of the electron tearing instability:

$$\omega \approx \left(\frac{a}{r_{\mathrm{L}}^{(\mathrm{e})}}\right)^2 \frac{d_\mathrm{e}}{\mathcal{V}_{\mathrm{Te}}}\,. \qquad (11.79)$$

Coppi et al. (1966) first proposed the *electron tearing* instability as a mechanism of explosive reconnection in the Earth magnetotail during substorm break-up (Section 11.6.3).

11.6.2 Stabilization by the transversal field

As we saw above, Landau resonance of electrons inside the neutral current layer was proposed to provide the appropriate collisionless dissipation necessary for the spontaneous reconnection in the geomagnetic tail during a substorm (Coppi et al., 1966). However Schindler (1974) showed that nonzero magnetic field component $B_\perp$ normal to the current layer *magnetizes* the electrons and restricts them from being resonant. As a result, the required dissipation relies upon the ions that are still unmagnetized. So Schindler proposed the so called *ion tearing* instability, in which the dissipation is due to ion Landau resonance. In this model the electrons act only as a charge neutralizing background.

Galeev and Zelenyi (1975, 1976) found, however, that the magnetized electrons can change the basic character of the tearing perturbation, thus making the ion energization invalid as a driver for the instability. Therefore the kinetic tearing instability can be suppressed by the transversal (i.e. perpendicular to the current layer plane) magnetic field. Let us consider this effect in some detail.

(a) We begin by considering sufficiently small values of the transversal field $B_\perp$, for which the inequality

$$\omega_{\text{L}}^{(\text{e})} = \frac{eB_\perp}{m_{\text{e}}c} < \omega \tag{11.80}$$

holds. Here $\omega_{\text{L}}^{(\text{e})}$ is the electron gyro-frequency in the transversal magnetic field $\mathbf{B}_\perp$; recall that ω is the instability increment.

In this case **electrons** in the region $|\,y\,| < d_{\text{e}}$, where the reconnecting magnetic field components tend to zero, **are in Landau resonance with the electric field perturbation** (11.70). As a consequence, the electron tearing mode develops in the reconnecting current layer (see above).

(b) As the transversal field increases, the Larmor frequency $\omega_{\text{L}}^{(\text{e})}$ increases as well. When $\omega_{\text{L}}^{(\text{e})} > \omega$ the electron resonance with the electric field perturbation breaks down and the electron mode of the instability becomes stabilized (Schindler, 1974). This takes place for

$$\frac{B_\perp}{B_0} = \xi_\perp > \left(\frac{r_{\text{L}}^{(\text{e})}}{a}\right)^{5/2} \left(1 + \frac{T_{\text{i}}}{T_{\text{e}}}\right). \tag{11.81}$$

If the electron mode of the tearing is stabilized, there remains the possibility for ions to become the resonant particles, gaining energy. However electron gyration also stabilizes the ion mode up to the values (Galeev and

Zelenyi, 1976):

$$\frac{B_\perp}{B_0} < \left(\frac{r_{\rm L}^{(\rm e)}}{a}\right)^{1/4} \left(1+\frac{T_{\rm i}}{T_{\rm e}}\right)^{-1/2} . \qquad (11.82)$$

Thus there exists a 'split' – a range of values of the magnetic field transversal component

$$\left(\frac{r_{\rm L}^{(\rm e)}}{a}\right)^{5/2} \left(1+\frac{T_{\rm i}}{T_{\rm e}}\right) < \frac{B_\perp}{B_0} = \xi_\perp < \left(\frac{r_{\rm L}^{(\rm e)}}{a}\right)^{1/4} \left(1+\frac{T_{\rm i}}{T_{\rm e}}\right)^{-1/2} . \qquad (11.83)$$

Here the **linear kinetic tearing instability becomes suppressed** (Galeev and Zelenyi, 1976). Somov and Verneta (1988) have shown that

> the transversal magnetic field effect ensures the tearing stability of high-temperature reconnecting turbulent-current layers

during the 'main' or 'hot' phase of solar flares (Somov and Verneta, 1993; see also Section 3.5 in Somov, 1992).

11.6.3 The tearing instability of the geomagnetic tail

Although the tearing instability was first proposed as a clue mechanism of magnetospheric substorms many years ago (Coppi et al., 1966), its prime role among other substorm processes was persistently challenged. The main theoretical reason was the proof by Lembege and Pellat (1982) that

> the sign of the energy of the tearing mode perturbations can be changed from negative to positive one due to the drift motion of magnetized electrons inside the reconnecting current layer (RCL.

This conclusion is similar to that one of Galeev and Zelenyi (1976) but Lembege and Pellat showed in particularly that this effect stabilizes the tearing instability under the condition

$$\xi_\perp = \frac{B_\perp}{B_0} < \frac{\pi}{4}\, ka \qquad (11.84)$$

regardless the temperature ratio $T_{\rm e}/T_{\rm i}$. Here a corresponds to the current-layer half-thickness according to the Harris formula (11.64).

Condition (11.84) shows that in the case of adiabatic electrons the tearing instability can be stabilized only for very short wavelengths

$$\lambda < \lambda_{\min} = \frac{\pi^2}{2}\,\frac{a}{\xi_\perp} . \qquad (11.85)$$

They are too short to be relevant to the underlying spontaneous reconnection process in the geomagnetic tail current layer. In fact, condition (11.85) coincides with that of the WKB approximation in the stability analysis and as a result has made the *linear* tearing instability as the substorm mechanism suspect.

There were many attempts to restore necessarily the linear ion instability as a clue substorm process. All of them look, however, pretty inconsistent with a general representation of the substorm as a relatively fast unloading process in the tail of the magnetosphere. The substorm is usually preceded and prepared by the quasi-static changes in the tail during the growth phase (Nagai et al., 1998; Kokubun and Kamide, 1998).

From a consideration of observational constraints on the onset mechanism Sitnov et al. (1997), Sitnov and Sharma (1998) concluded that

> the tearing instability must have a considerable initial stage when the equilibrium magnetic field topology is still conserved.

Moreover the instability is shown to have no linear stage. Instead, either the explicitly nonlinear or pseudolinear instability of negative energy eigenmode can develope. So the unavoidable *nonlinearity* is a key element of the substorm.

Sitnov et al. use the theory of catastrophes (Haken, 1978; Guckenheimer and Holmes, 1983) to consider a substorm as *backward bifurcation* in an open nonlinear system. In general, the *theory of catastrophes* is widely accepted as an appropriate mathematical tool to describe abrupt changes in a low-dimensional system driven by quasi-stationary evolution of a set of control parameters. The theory can be applied if we treat the tearing instability as a process for the growth of a large-scale one-mode perturbation.

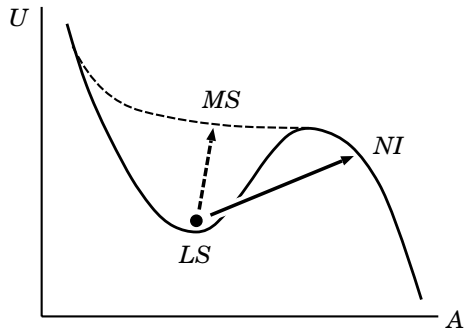

Figure 11.6: The effective potential U as a function of the state parameter A.

In Figure 11.6 the effective potential U of the geomagnetic tail current layer near the marginal state of a tearing instability is shown as a function

of the state parameter A. A process of quasi-stationary transformation of the potential minimum (LS) into the point of inflection (MS) is shown by the dashed arrow.

Being located near the bottom of the potential U well before the catastrophe, the **system is linearly stable** (LS) because of positive energy of small perturbations from the minimum. The transition to instability is possible only at the moment of the catastrophe or before the catastrophe under the influence of a *finite* amplitude perturbation (the large solid arrow) necessary to surmount the potential barrier. In both cases the destabilization of the system proves to be nonlinear.

Many difficulties of the substorm theory have arisen presumably not from the incorrect physics involved but rather from irrelevant mathematical treatment of the instability problem. Suitable treatment of the tearing instability as a backward bifurcation can resolve some long-standing problems in the theory including the consistent description of both triggered and spontaneous onsets. Much more can be done due to further elaboration of this promising approach to the magnetospheric substorm mechanism.

This page intentionally blank

Chapter 12

Magnetic Reconnection and Turbulence

The open issues focused on in this Chapter presumably will determine the nearest future as well as the most interesting perspectives of plasma astrophysics.

12.1 Reconnection and magnetic helicity

12.1.1 General properties of complex MHD systems

We are going to consider some properties of the reconnection process in complex magnetic field configurations containing many places (points or lines) where reconnection occurs. Such a situation frequently appears in space plasmas, for example in a set of *closely packed* flux tubes suggested by Parker (1972). The tubes tend to form many reconnecting current layers (RCLs) at their interfaces. This may be the case of active regions on the Sun when the field-line footpoint motions are slow enough to consider the evolution of the coronal magnetic field as a series of equilibria, but fast enough to explain coronal heating (see Sections 12.2.1 and 12.4.2).

Another example of a similar complex structure is the 'spaghetti' model of solar flares suggested by de Jager (1986) or the 'avalanche' model of them (Parker, 1988; Lu and Hamilton, 1991; Zirker and Cleveland, 1993). The last assumes that the energy release process in flares can be understood as **avalanches of many small reconnection events**. LaRosa and Moore (1993) propose that the large production rate of energetic electrons in solar flares (Section 9.1) is achieved through MHD *turbulent cascade* (see

vol. 1, Section 7.2.3) of the bulk kinetic energy of the outflows from many separate reconnecting current layers (see also Antonucci et al., 1996).

How can we estimate the rate of magnetic energy release due to reconnection in such a very complex system of flux tubes? – The inherent complexity of the field configuration which can be used as a model does not allow any optimism in an attempt to solve the dissipative MHD problem numerically.

> An alternative approach to that of solving the MHD equations as they stand is to reformulate them in terms of invariant quantities.

As we have seen in vol. 1, Section 9.4, the mass, momentum and energy are conserving quantities and can be used to construct invariants. For example, the total energy of a system before reconnection is equal to the total energy after reconnection plus dissipation. A less familiar invariant in ideal MHD is the *magnetic helicity* or, more exactly, the *global* magnetic helicity (see Exercise 12.1):

$$\mathcal{H} = \int_V \mathbf{A} \cdot \mathbf{B} \; d^3\mathbf{r} \,. \tag{12.1}$$

Here $\mathbf{A}$ is a vector potential for field $\mathbf{B}$, and V is the plasma volume bounded by a magnetic surface S, i.e.

$$\mathbf{B} \cdot \mathbf{n} \,\big|_S = 0 \,. \tag{12.2}$$

Woltjer (1958) showed that

> in ideal magnetohydrodynamic motions the global magnetic helicity $\mathcal{H}$ is conserved in any closed magnetic flux tube.

Woltjer's theorem may be extended to open-end flux tubes as well, provided the ends do not suffer any motion. In order to explain the observed toroidal field reversal in reversed-field pinches, Taylor (1974) generalized the ideal MHD result derived by Woltjer to a class of dissipative motions. Woltjer's theorem can also be used to show that the fields which minimize the magnetic energy subject to given initial and boundary conditions are in general force-free fields (Exercise 12.2).

The magnetic helicity, defined by definition (12.1), provides a measure of the *linkage* or knottedness of field lines (e.g., Berger, 1988a and 1988b). **The helicity is a topological property of a magnetic field** (see, for example, Exercise 12.1). In ideal MHD there is no reconnection. For this reason, the magnetic helicity is conserved.

If we do not have ideal MHD there is some reconnection, and helicity is not conserved. However

reconnection at a large magnetic Reynolds number generally conserves the global magnetic helicity to a great extent.

In laboratory (Taylor, 1974, 1986), solar (Berger, 1984) and magnetospheric (Wright and Berger, 1989) plasmas the fraction of helicity dissipated is normally very small.

The approximate conservation of magnetic helicity has been successful in calculating heating rates in the solar corona (Section 12.2.1). The main idea here is that the magnetic field tends to minimize its energy, subject to the constraint that its topological characteristic – helicity – is fixed. Reconnection gives the fastest way for this relaxation. The magnetic configuration in the region which is subject to reconnection should relax towards a constant-α force-free field. Such a field is also called the *linear* force-free field. Taylor (1974) used this conjecture – Taylor's hypothesis – to predict the formation of a Lundquist field in actively reconnecting fusion devices.

Interestingly, however, it is observed in some laboratory experiments that the relaxation can take place without the conservation of global magnetic helicity. Presumably such unexpected loss of helicity may be related to a *self-organization* effect in a reversed field plasma (Hirano et al., 1997). Even if the value of $\mathcal{H}$ is null at the initial stage, the plasma relaxes to a certain field configuration by producing the toroidal magnetic field and $\mathcal{H}$.

12.1.2 Two types of MHD turbulence

Turbulence in ordinary fluids has great consequences: it changes the properties of flow and changes large-scale flow pattern, even under time averaging. Turbulence introduses eddy diffusion and eddy viscosity, and it increases momentum coupling and drag forces by orders of magnitude (see Mathieu and Scott, 2000; Pope, 2000). It should obviously have a wide variety of consequences in magnetized cosmic plasmas, even in the MHD approximation.

There are at least two distinct types of MHD driven turbulence. First, when the external large-scale **magnetic field is strong**, the resulting turbulence can be described as the nonlinear interactions of Alfvén waves (e.g., Goldreich and Sridhar, 1997). Early works by Iroshnikov (1964) and Kraichnan (1965) obtained a $k^{-3/2}$ spectrum for both magnetic energy and kinetic energy in the presence of a dynamically significant magnetic field.

However these works were based on the assumption of isotropy in wavenumber space (see vol. 1, Section 7.2.2), which is difficult to justify unless the magnetic field is very weak. Goldreich and Sridhar (1997) assume a critical level of anysotropy, such that magnetic and hydrodynamic

forces are comparable, and predict a $k^{-5/3}$ spectrum for strong external field turbulence. Solar wind observations (see Leamon et al., 1998), which are well within the strong magnetized regime, and numerical studies (Cho and Vishniac, 2000a) seem to support the Kolmogorov type scaling law.

Second, when the external **magnetic field is weak**, the MHD turbulence near the scale of the largest energy-containing eddies or vortices will be more or less like ordinary hydrodynamic turbulence with a small magnetic back reaction. In this regime, the turbulent eddy turnover time at the large scale L/V is less than the Alfvénic time of the scale L/B. Here V and B are rms velocity and magnetic field strength divided by $(4\pi\rho)^{1/2}$ respectively, and L is the scale of energy injection (recall that we consider driven turbulence) or the largest energy-containing eddies.

Various aspects of the weak external field MHD turbulence have been studied both theoretically and numerically. Since large-scale magnetic fields are observed in almost all astrophysical objects, the generation and maintenance of such fields is one of the most important issues in this regime. In the mean field dynamo theory (Moffatt, 1978; Parker, 1979),

> turbulent motions at small scales are biased to create an electromotive force along the direction of the large-scale magnetic field.

This effect, called the α-effect, works to amplify and maintain large-scale magnetic fields.

Whether or not the α-effect actually works depends on the structure of the MHD turbulence, especially on the mobility of the field lines. For example, when equipartition between magnetic and kinetic energy densities occurs at any scale larger than the dissipative scale, the mobility of the field lines and the α-effect may be greatly reduced.

In the case of hydrodynamical turbulence, the energy cascades to smaller scales (see vol. 1, Figure 7.3). If we introduce an uniform **weak magnetic field**, turbulent motions will stretch the magnetic field lines and divert energy to the small-scale magnetic field.

> As the field lines are stretched, the magnetic energy density increases rapidly, untill the generation of small-scale magnetic structures is balanced by the magnetic back reaction

at some scale between L and the dissipation scale $l_{\min}$.

This will happen when the magnetic and kinetic energy densities associated with a scale l ($l > l_{\min}$) are comparable so the Lorentz forces resist further stretching at or below that scale. However stretching at scales larger than l is still possible, and the magnetic energy density will continue to grow if l ($l < L$) can increase. Eventually, a final stationary state will be reached.

What is the scale of energy equipartition? What is the magnetic field structure? – The answer to the later question depends on the nature of diffusive processes acting on the magnetic field.

Suppose that magnetic field lines are unable to smooth the tangled fields at small scales. Then, as a result of the turbulent energy cascade and the subsequent stretching of field lines,

> magnetic fields may have thin fibril structures with many polarity reversals within the energy equipartition scale l.

Consequently, magnetic structures on the equipartition scale are highly elongated along the external magnetic field direction (Batchelor, 1950). This is the kind of picture one obtains by considering passive advection of magnetic fields in a chaotic flow (for a review see Ott, 1998).

On the other hand, if we assume that MHD turbulence is always capable of relaxing tangled field lines at small scales, then we expect eddies at the final equipartition scale to be nearly isotropic (Cho and Vishniac, 2000b).

12.1.3 Helical scaling in MHD turbulence

The turbulent flows and tangled magnetic fields seem to be observed, for example, in the Earth's plasma sheet (see Borovsky and Furnsten, 2003). Here the turbulence appears to be a turbulence of eddies rather than a turbulence of Alfvén or other MHD waves. In this dynamical respect, it is similar to the turbulence observed in the solar wind. As for dissipation, two mechanisms appear to be important. One of them is electric coupling of the turbulent flows to the resistive ionosphere. The second one is a **direct cascade** of energy in the turbulence to small scales (see vol. 1, Section 7.2.2) where internal dissipation should occur at non-MHD scales.

The possibility of the self-similar cascade transfer of the hydrodynamic helicity flux over the spectrum was first introduced by Brissaud et al. (1973). The following two scenarios were analyzed from the standpoint of the dimensionality method: (a) the simultaneous transfer of energy and helicity with constant fluxes over the spectra of both parameters, (b) a constant helicity flux determining the energy distribution.

The influence of the hydrodynamic helicity is obvious from a physical standpoint:

> two helical vortices with strong axial motion in one direction have a tendency to merge because of the Bernoulli effect.

In other words, helicity should result in redistribution of the chaotic energy. Moreover a helicity flux that characterizes the variation of the mean helicity should also appear. Above all, helicity has an effect on the spectral features

of turbulence. As for the spectra, variations occur in incompressible, compressible, and stratified media, as shown by Moiseev and Chkhetiani (1996). One of the tendencies inherent in helical media is the **energy transfer to the long-wavelength region** due to the tendency of helical vortices to merge.

According to Moiseev and Chkhetiani (1996), the mechanism that generates the mean hydrodynamic helicity leads to a second cascade range in addition to the Kolmogorov range (vol. 1, Section 7.2.2). The constant that does not depend on the scale of the helicity here is its flux. Nevertheless this requirement, like the requirement that the energy flux F be constant in the Kolmogorov range, is not inflexible. The spectral characteristics undergo significant changes. They are associated, as we understand, with at least a partial **inverse cascade** into the large-scale region.

There is a broad class of effects that generate both hydrodynamic helicity itself and large helicity fluctuations under terrestrial and astrophysical conditions. In particular, the simultaneous presence of such factors as temperature and density gradients, shearing flows, and nonuniform rotation is sufficient.

Like the direct cascade in the Kolmogorov turbulence, the inverse cascade is accomplished by nonlinear interactions, suggesting that **nonlinearity is important**. However a spectral type of inverse cascade is the strongly nonlocal inverse cascade process, which is usually referred to as the α-effect (Moffatt, 1978; Krause and Rädler, 1980). This effect exists already in linear kinematic problems.

A strong indication, that the α-effect is responsible for large-scale magnetic field generation, comes from detailed analysis of three-dimensional simulations of forced MHD turbulence (Brandenburg, 2001). This may seem rather surprising at the first glance, if one pictures large-scale field generation as the result of an inverse cascade process, that (Brandenburg and Subramanian, 2000)

> the exact type of nonlinearity in the MHD equations is unessential as far as the nature of large-scale field generation is concerned.

However, magnetic helicity can only change on a resistive timescale. So the time it takes to organize the field into large scales increases with magnetic Reynolds number.

12.1.4 Large-scale solar dynamo

Magnetic activity in the Sun occurs on a wide range of spatial and temporal scales. Small-scale photospheric fields are highly intermittent (see Section 12.4). The large-scale magnetic fields display remarkably ordered

dynamics, involving cycles of activity with well-defined rules. There is an eleven year period for sunspot activity. At the beginning of a cycle, sunspot first appear in pairs at midlatitudes. Then subsequently the sites of emergence migrate towards the equator over the course of the cycle.

The magnetic orientation of the sunspot pairs reverses from one cycle to the next. So the full magnetic cycle has a mean period of 22 years. The exact period of magnetic activity varies slightly and is a useful measure of the strength of solar activity, with shorter periods corresponding to a more active Sun. The magnetic cycle is also chaotically modulated on a longer timescales and exhibits intervals of reduced sunspot activity known as grand minima with a characteristic period of about 2000 years.

Such organized dynamics on time-scales that are short compared to diffusive times requires the systematic regeneration of magnetic fields by the MHD dynamo.

The smaller scale photospheric field is believed to result from local dynamo action in the convective flows at or near the solar surface (e.g., Cattaneo, 1999; see also Section 13.5). It is likely that the large-scale (global) magnetic field is generated deeper within the Sun, probably at the interface between the solar convective zone and the radiative zone. The sunspot observations are most straightforwardly interpreted as the surface emergence of a large-scale toroidal field. The generation of such a field relies on the presence of differential rotation which stretches out poloidal field lines into strong regular toroidal field (see vol. 1, Section 20.1.5).

Helioseismology, which can assess the internal differential rotation by using frequency splitting of acoustic modes, has revealed the existence of a large radial shear below the convective zone (see vol. 1, Figure 20.4), now known as the solar *tachocline*. Here the angular velocity profile changes from being largely constant on radial lines in the convective zone to nearly solid body rotation in the radiative interior. This radial shear layer is certainly suitable for generating a strong toroidal field from any poloidal field there.

Parker (1993) postulated that the toroidal field results from the action of the shear on any poloidal component of the field in the tachocline region, while the weaker poloidal field is generated throughout the convection zone by the action of cyclonic (helical) turbulence. The key to this model is that

> the transport of magnetic fields in the convective zone is enhanced relative to that in the stable layer as a result of the turbulent convective flows.

The poloidal magnetic flux that is generated in the convective zone is readily transported by the enhanced diffusivity there, and some of it is then expelled into the region below.

However strong toroidal fields produced in the tachocline are not transported away from their region of generation because of the relatively low turbulent diffusivity there. Hence the strong toroidal field may be stored successfully in the radiative region without significantly modifying the convection in the separate layer above. Recent dynamo models have built on this interface concept.

12.2 Coronal heating and flares

12.2.1 Coronal heating in solar active regions

Heyvaerts and Priest (1984), Browning (1988) developed the model of current dissipation by reconnection, adapting Taylor's hypothesis to the conditions in a solar active region. They assumed that at any time the most relaxed accessible magnetic configuration is **a linear force-free field** which can be determined from the evolution of magnetic helicity. By so doing, Heyvaerts and Priest illustrated the role of the velocity v of photospheric motions in coronal heating. No heating is produced if these motions are very slow, and negligible heating is also produced when they are very fast. So

> coronal heating presumably results from photospheric motions which build up magnetic stresses in the corona at a rate comparable to that at which reconnection relaxes them.

The corresponding heating rate can be estimated in order of magnitude by:

$$F \approx \frac{B^2}{4\pi}\, v \left(\frac{l_b}{l_b + l_v}\right) \left(\frac{\tau_d\, v}{l_b}\right) , \tag{12.3}$$

where τ_d is the effective dissipative time, l_b and l_v are scale lengths for the magnetic field and velocity at the boundary. (Terms in brackets are limiting factors smaller than 1.) The results showed that a substantial contribution to coronal heating can come from current dissipation by reconnection.

> Reconnection with a small magnetic Reynolds number can produce significant dissipation of helicity, of course.

Wright and Berger (1991) proved that helicity dissipation in two-dimentional configurations is associated with the retention of some of the inflowing magnetic flux by the reconnection region R_r. When the reconnection site is a simple Ohmic conductor, all the field parallel to the reconnection line (the longitudinal component of magnetic field) that is swept into the region R_r

is retained (Somov and Titov, 1985a and 1985b). In contrast, the inflowing magnetic field perpendicular to the line is annihilated. Wright and Berger (1991) relate the amount of helicity dissipation to the retained magnetic flux.

12.2.2 Helicity and reconnection in solar flares

Flares in a solar or stellar atmosphere predominantly arise from the release of coronal magnetic energy. Since magnetic field lines may have fixed endpoints in the photosphere, observations of photospheric quantities such as shear and twist become important diagnostics for energy storage in the corona.

The magnetic energy of an equilibrium field in the corona can be related to measures of its net shear and twist. For example,

> the magnetic energy of a *linear* force-free field is proportional to its magnetic helicity

(see Exercise 12.2). Berger (1988b) presented a formula for the energy of a *non-linear* force-free field in terms of linking field lines and electric currents. This allows us to partition the magnetic energy among different current sources in a well-defined way. For example, energy due to reconnecting current layers (RCLs) may be compared to energy due to field-aligned currents (see Chapter 14).

Pre-flare magnetic fields are often modeled as a twisted flux tube associated with a solar prominence. Twisting can be introduced either by photospheric twisting flows (presumably due to Coriolis forces) at the locations where the base of the arch enters the photosphere (Gold and Hoyle, 1960), or by flux cancellation, i.e. by the shear flows along the photospheric neutral line and the converging flows in direction to the neutral line (e.g., Somov et al., 2002a).

If one assumes that the magnetic field of a pre-flare prominence can be modeled as a flux tube which is uniformly twisted and force-free, then it is possible to compute a relative energy, for example, the energy difference between a twisted arch and a similar arch described by a potential field. However in order to make realistic estimates of the energy available from a twisted tube for a flare, one must address the issue of the post-flare magnetic configuration. If it is assumed that the total helicity is conserved, it might be well that a linear force-free field, rather than a potential field, represents the post-flare configuration of the flux tube.

In general, estimates of the energy available in terms of the topological complexity of the magnetic field have been made by Berger (1994). The argument that the post-flare configuration should be a linear force-free field

is based on the work of Woltjer and requires that the Taylor conjecture be true (Section 12.1). The key point is that, in deriving the result that a linear force-free field is the lowest energy state that can reach when helicity is conserved, Woltier used the approximation of ideal MHD. But this means that

> the constant α or linear force-free state is topologically inaccessible from most initial configurations of a magnetic field.

While Taylor's conjecture, that the global helicity is conserved while finite diffusivity effects are invoked to allow the field to relax to a linear one, gives one way out of this conundrum, it is not entirely satisfactory from a theoretical point of view (Marsh, 1996).

It is believed that the **excess energy**, which is the energy difference between the contained energy and the minimum energy predicted by the Taylor hypothesis, **is more rapidly dissipated than the magnetic helicity**. It is also believed that reconnection may lead to the fast MHD relaxation process to the minimum energy state, creating flares. However this theoretical preposition should be subject to careful observational examination.

In principle, there may be an application in observational models of the field structure of an active region with vector magnetogram data supplying information on the force-free field parameter α. This would provide a check on the model's insight as to the true topology of the field.

Using vector magnetograms and X-ray morfology, Pevtsov et al. (1996) determine the helicity density of the magnetic field in active region NOAA 7154 during 1992 May 5–12. The observations show that a long, twisted X-ray structure retained the same helicity density as the two shorter structures, but its greater length implies a higher coronal twist. The measured length and α value combine to imply a twist that exceeds the threshold for the MHD kink instability. It appears that such simple models, which have found that the kink instability does not lead to the global dissipation, do not adequately address the physical processes that govern coronal fields.

Numerical integration of the 3D dissipative MHD equations, in those the pressure gradient force and the density variation are neglected, shows that magnetic reconnection driven by the resistive tearing instability growing on the magnetic shear inversion layer can cause the spontaneous formation of sigmoidal structure (Kusano, 2005). This process could be understood as a manifestation of the minimum energy state, which has the excess magnetic helicity compared to the bifurcation criterion for the linear force-free field (Taylor, 1974). It is also numerically demonstrated that the formation of the sigmoids can be followed by an explosive energy liberation.

12.3 Stochastic acceleration in solar flares

Modern observations of solar energetic particles (SEPs) and hard electromagnetic radiations produced by solar flares indicate that stochastic acceleration of charged particles by waves or wave turbulence, a second-order Fermi-type acceleration mechanism (see vol. 1, Section 7.2), may play an important role in understanding the energy release processes and the consequent plasma heating and particle acceleration. At first, this theory was applied to the acceleration of nonthermal electrons which are responsible for the microwave and hard X-ray emissions and for the type III radio bursts during the impulsive phase of solar flares.

12.3.1 Stochastic acceleration of electrons

LaRosa et al. (1996), Miller et al. (1996) presented a model for the acceleration of electrons from thermal to relativistic energies in solar flares. They assume that fast outflows from the sites of reconnection generate a cascading MHD turbulence. The ratio of the gas pressure to the magnetic one is presumably small in this cascade. Thus the MHD turbulence has a small parameter β (our parameter γ^2) and mainly comprises of two low-amplitude wave modes: (a) Alfvén waves and (b) *fast* magnetoacoustic waves (see vol. 1, Section 15.2). The authors do not consider a possible role of slow magnetoacoustic waves in the acceleration of protons.

LaRosa et al. assume that in the reconnection-driven turbulence there is an equipartition between these two modes. About half of the energy of the turbulence resides in Alfvén waves and about half in fast magnetoacoustic waves (FMW). The threshold speed of the resonance determines the selectivity of the wave-particle interaction. Assuming $B^{(0)} \approx 500$ G, $T^{(0)} \approx 3 \times 10^6$ K, and $n^{(0)} \approx 10^{10}$ cm^{-3}, they found that the Alfvén speed $V_{\rm A} \approx 0.036\ c$, the electron thermal speed $V_{\rm Te} \approx 0.032\ c$, and the proton thermal speed $V_{\rm Te} \approx 7.4 \times 10^{-4}\, c$. Therefore the threshold speed is far in the tail of the proton distribution, and a negligible number of protons could be accelerated by FMW or Alfvén waves. Consequently protons or other ions are a negligible dissipation source for these waves, but not for slow magnetoacoustic waves (SMW) ignored by LaRosa et al.

On the other hand, $V_{\rm A}$ is only slightly above $V_{\rm Te}$, and a significant number of the ambient electrons can resonate with the waves. Thus **FMW almost exclusively accelerate electrons** under the solar flare conditions accepted above. (They strongly differ from the conditions typical for the model of super-hot turbulent-current layers considered in Chapter 7.) The process under consideration could be called a *small-amplitude* Fermi acceleration or a resonant Fermi acceleration of second order (Miller et al., 1996)

to denote the *resonant character* of the wave-particle interaction.

> If we can ignore the gyroresonant part of the interaction, then only the parallel energy would systematically increase,

leading to a velocity-space anisotropy in the electron distribution function.

So, beyond the main question of the origin and actual properties of the turbulence under consideration, an interesting question challenging electron energization by the Fermi process is pitch-angle scattering. In the absence of ancillary scattering, acceleration by FMW would lead to a systematic decrease of particle pitch-angles. Acceleration would then become less efficient, since only those waves with very high parallel phase speed would be able to resonate with the particles. However, as a tail is formed in the parallel direction, there would appear one or another instability which excites waves (for example, the fire-hose instability; see Paesold and Benz, 1999) that can scatter the electrons back to a nearly isotropic state.

We should not forget, of course, that the usual Coulomb collisions (see vol. 1, Chapters 8 and 4), even being very rare, can well affect formation of the accelerated-electron distribution. The Coulomb scattering of anisotropic accelerated electrons leads to their isotropization. As a result, the acceleration efficiency can significantly rise like in the case of acceleration in solar-flare collapsing magnetic traps (Kovalev and Somov, 2003).

With the introduction of **isotropizing scattering of any origin**, we can avarage the momentum diffusion equation in spherical coordinates over the pitch-angle θ and obtain the isotropic momentum diffusion equation

$$\frac{\partial f}{\partial t} = \frac{1}{p^2}\,\frac{\partial}{\partial p}\left(p^2 D(p)\,\frac{\partial f}{\partial p}\right). \tag{12.4}$$

Here

$$D(p) = \frac{1}{2}\int\limits_{-1}^{+1} D_{pp}\,d\mu\,, \tag{12.5}$$

p is the magnitude of the momentum vector $\mathbf{p}$, $\mu = \cos\theta$, and D_{pp} is the μ-dependent momentum diffusion coefficient (see Miller et al., 1996). The quantity f is the phase-space distribution function, normalized such that $f(p,t)\,4\pi p^2 dp$ equals the number of particles per unit volume with momentum in the interval dp about p.

Electron acceleration and wave evolution are thus described by the two coupled partial differential equations: Equation (12.4) and the diffusion equation in the wave-number space (see vol. 1, Equation(7.28)). Their solution allows to evaluate the bulk energization of electrons by Fermi acceleration from the MHD turbulence expected in solar flares.

LaRosa et al. (1996) has found that the Fermi acceleration acts fast enough to be the damping mechanism for the FMW turbulence. This means that Fermi acceleration becomes fast enough at short enough scales $\lambda \sim \lambda_{\min}$ in the turbulent cascade of fast magnetoacoustic waves *to end* the cascade by dissipating the cascading turbulent energy into random-velocity kinetic energy of electrons. Practically all of the energy of the FMW turbulence is absorbed by the electrons while the protons get practically none.

12.3.2 Acceleration of protons and heavy ions

As we saw above, fast magnetoacoustic waves (FMW) can cascade to higher frequencies, eventually *Landau* resonate with the thermal electrons and accelerate them by the small-amplitude Fermi-type mechanism. In this Section we shall discuss the acceleration of protons and heavy ions by Alfvén waves that are a part of the same MHD turbulent cascade but *cyclotron* resonate with particles.

Let us consider for simplicity only the Alfvén waves with phase velocities parallel and antiparallel to the background field $\mathbf{B}^{(0)}$. These waves have left-hand circular polarization relative to $\mathbf{B}^{(0)}$ and occupy the frequency range below the cyclotron frequency (see Appendix 3) of Hydrogen, i.e., protons:

$$\omega < \omega_{\text{B}}^{(\text{H})} = \frac{ecB}{\mathcal{E}_{\text{H}}} \,. \tag{12.6}$$

As the waves increase in frequency, they resonate with protons of progressively lower energies.

For simplicity we also take the low-frequency limit for the dispersion relation of the Alfvén waves under consideration:

$$\omega = V_{\text{A}} \mid k_{\parallel} \mid . \tag{12.7}$$

In a multi-ion astrophysical plasma, there are resonances and cutoffs in the dispersion relation corresponding to each kind i of ions. However, because of their small abundance, Fe and the Ne group do not affect the dispersion relation. The He group will produce a resonance at $\omega_{\text{B}}^{(\text{He})}$ and a cutoff at a slightly higher frequency. We shall take, however, the Alfvén wave dispersion relation (12.7) for all

$$\omega < \omega_{\text{B}}^{(\text{He})} \,.$$

In general, a low-frequency Alfvén wave propagating obliquely with respect to the ambient field $\mathbf{B}^{(0)}$ has a linearly polarized magnetic field $\mathbf{B}^{(1)}$ normal to both $\mathbf{B}^{(0)}$ and $\mathbf{k}$ (see vol. 1, Figure 15.1). The wave electric

field $\mathbf{E}^{(1)}$ is normal to $\mathbf{B}^{(0)}$ and $\mathbf{B}^{(1)}$. A low-frequency FMW (vol. 1, Section 15.2.3) has a linearly polarized electric field $\mathbf{E}^{(1)}$ normal to both $\mathbf{B}^{(0)}$ and $\mathbf{k}$. In each case the electric field can be decomposed into left- and right-handed components. However, for parallel propagation, all Alfvén waves are left-handed, while all the FMWs are right-handed.

Since we consider the Alfvén waves which phase velocities are strictly *parallel and antiparallel* to the background field, there is only one resonant wave and it is the backward-moving Alfvén wave (Miller and Reames, 1996). Applying the cyclotron resonance condition (see vol. 1, formula (7.16)) for this wave with $s = 1$, we find its wavenumber

$$k_{\parallel} = -\frac{\omega_{\mathrm{B}}^{(\mathrm{i})}}{\gamma_{\mathrm{L}} \left(V_{\mathrm{A}} + v_{\parallel}\right)} \,. \tag{12.8}$$

Hence

> when the Alfvén wave frequency becomes close to the ion-cyclotron frequency $\omega_{\mathrm{B}}^{(\mathrm{i})}$, the thermal ions of the kind i would be accelerated out of the background energies.

The first kind of ions encountered by the Alfvén waves will be the one with the lowest cyclotron frequency, namely Fe. This is well visualized by Figure 1 in Miller and Reames. However, due to the low Fe abundance, the waves will not be completely damped and will continue to cascade up the group of ions with the next higher cyclotron frequency, namely Ne, Mg, and Si. These ions will be also accelerated but the waves will not be totally damped again. They encounter ^{4}He, C, N, and O. These ions do complitely dissipate the waves and halt the turbulent cascade.

Miller and Reames (1996) showed that abundance ratios similar to those observed in the interplanetary space after solar flares can result from the stochastic acceleration by cascading Alfvén waves in impulsive flares.

12.3.3 Acceleration of ^{3}He and ^{4}He in solar flares

The most crucial challenge to the models including the stochastic acceleration arises from the extreme enhancement of ^{3}He observed in some impulsive solar events. Nonrelativistic ^{3}He and ^{4}He ions resonate mostly with waves with frequencies close to the α-particle gyrofrequency. To study the stochastic acceleration of these ions, the exact dispersion relation for the relevant wave modes must be used, resulting in more efficient acceleration than scattering that could lead to anisotropic particle distributions. Liu et al. (2006) have carried out a quantitave study and have showed that the interplay of the acceleration, Coulomb energy loss, and the escape processes

in the stochastic acceleration of ^{3}He and ^{4}He by parallel-propagating waves can account for the ^{3}He enhancement, its varied range, and the spectral shape as observed with the *Advanced Composition Explorer* (ACE).

In general, stochastic acceleration is attractive on several points. One of them is that the stochastic interaction of particles with cascading waves in astrophysical plasma offers, in principle, the opportunity to unify electron and ion acceleration within the context of a single model. Specifically the picture that is emerging is one in which resonant wave-particle interactions are able to account for acceleration of particles out of the thermal background and to relativistic energies.

12.3.4 Electron-dominated solar flares

Hard X- and gamma-ray observations of solar flares have a wide range of energy from about 10 keV to about 10 GeV with relatively high spectral and temporal resolutions. Photon spectra over this range show significant deviations from the simple power law (e.g., Park et al., 1997). The study of these deviations can provide information about the acceleration mechanism. There is, however, some ambiguity in the analysis of the observational data because both accelerated electrons and protons contribute to the hard electromagnetic emission. Fortunately, there exist impulsive flares which have little or no evidence of nuclear exitation lines in the gamma-ray range. Such 'electron-dominated' events are uncontaminated by the proton processes and provide direct insights into the nature of the electron acceleration.

Park et al. (1997) use a model consisting of a finite-size region in the solar corona near the flare-loop top which contains a high-density of turbulence. Here the electrons are accelerated. Because of the rapid scattering by waves, the electrons trapped in this region have a nearly isotropic distribution. They emit bremsstrahlung photons which can be considered in a thin-target approximation. However electrons eventually escape this region after an escape time of $\tau_{\rm esc}(\mathcal{E})$ and lose most of their energy $\mathcal{E}$ in the chromosphere at the footpoints where they also emit hard X- and gamma-rays. This is called the *thick-target* source (see vol. 1, Section 4.4.2).

Instead of the simplified Equation (12.4), the Fokker-Planck equation (vol. 1, Section 3.1.4) re-written in energy space is used to describe the spectrum of electrons assuming isotropy and homogeneity:

$$\frac{\partial N}{\partial t} = -\frac{\partial}{\partial \mathcal{E}}\left\{\left[A(\mathcal{E}) - \left|B(\mathcal{E})\right|\right] N\right\} + \frac{\partial^2}{\partial \mathcal{E}^2}\left[D(\mathcal{E})\, N\right] - \\ - \frac{N}{\tau_{\rm es}(\mathcal{E})} + Q(\mathcal{E})\,. \tag{12.9}$$

Here $N(\mathcal{E},t)\,d\mathcal{E}$ is the number of electrons per unit volume in the energy interval $d\mathcal{E}$, $A(\mathcal{E})$ is the systematic acceleration rate, $D(\mathcal{E})$ is the diffusion coefficient, $Q(\mathcal{E})$ is a source term. The energy loss term

$$B(\mathcal{E}) = \left(\frac{d\mathcal{E}}{dt}\right)_L \tag{12.10}$$

includes both Coulomb collision and synchrotron radiation losses.

Take the Maxwellian distribution as the source term

$$Q(\mathcal{E}) = Q_0\,\frac{2}{\sqrt{\pi}}\left(\frac{\mathcal{E}}{k_{\rm B}T}\right)^{1/2}\exp\left(-\frac{\mathcal{E}}{k_{\rm B}T}\right), \tag{12.11}$$

where Q_0 is the rate at which the ambient plasma electrons of temperature T are accelerated. At steady state, the number of escaping particles is equal to the number of accelerated electrons:

$$\int \frac{N}{\tau_{\rm es}(\mathcal{E})}\,d\mathcal{E} = \int Q(\mathcal{E})\,d\mathcal{E} = Q_0\,. \tag{12.12}$$

The temperature T of about 17 MK is taken. The coefficients $A(\mathcal{E})$, $D(\mathcal{E})$, and $\tau_{\rm es}(\mathcal{E})$ of the Fokker-Planck equation are determined by the particle acceleration mechanism. They can be written in the form:

$$A(\mathcal{E}) = \mathcal{D}\,(q+2)\,(\gamma_{\rm L}\beta)^{\,q-1}, \tag{12.13}$$

$$D(\mathcal{E}) = \mathcal{D}\,\beta\,(\gamma_{\rm L}\beta)^{\,q}, \tag{12.14}$$

$$\tau_{\rm es}(\mathcal{E}) = \mathcal{T}_{\rm es}\,\frac{(\gamma_{\rm L}\beta)^{\,s}}{\beta}\,. \tag{12.15}$$

Here $\mathcal{D}$, $\mathcal{T}_{\rm es}$, q, and s are independent of the kinetic energy $\mathcal{E} = \gamma_{\rm L} - 1$ measured in units of $m_{\rm e}c^2$, and βc is the velocity of electrons.

The acceleration time τ_a, which is also the timescale for reaching the steady state in Equation (12.9), can be estimated as

$$\tau_a(\mathcal{E}) \approx \tau_{_D}(\mathcal{E}) \approx \frac{\mathcal{E}^2}{D(\mathcal{E})}\,. \tag{12.16}$$

This should be less than the rise time of a flare. For three of four flares described by Park et al. (1997), the overall rise time τ_r of the hard X-rays is about 10 s and the total duration of the flare τ_f is about 100 s. For the most impulsive flare $\tau_r < 2$ s and $\tau_f \approx 8$ s. Hence the steady state approximation is justified. After setting $\partial/\partial t = 0$, we can divide Equation (12.9) by one of the parameters, say the diffusion coefficient $\mathcal{D}$, without changing the steady state solution.

The acceleration time for an electron with energy $\mathcal{E} = 1$ is approximately $\mathcal{D}^{-1}$. Therefore, for three flares with the rise time $\tau_r \approx 10$ s, Park et al. (1997) estimate $\mathcal{D} \approx 0.15\ \mathrm{s}^{-1}$. For the shortest flare $\mathcal{D} \approx 1\ \mathrm{s}^{-1}$. Shorter rise times are possible, but these require higher values of the turbulence energy density and the magnetic field. With $\mathcal{D}$ fixed, the number of free parameters in the general stochastic model described above is reduced by one.

The numerical solutions show that the wistler wave resonant acceleration of electrons fits the observed spectra over the entire range of energy in four flares. The high-energy cutoff in the two flares can be attributed to synchrotron radiation losses in the presence of a 500 G magnetic field at the acceleration site. The observed break in the photon spectra of all four flares around 1 MeV can be attributed to a combination of the energy dependence of the escape time $\tau_{\mathrm{es}}(\mathcal{E})$ of particles out of the acceleration region and the change in the energy dependence of the bremsstrahlung cross-section between the nonrelativistic and relativistic regimes. Further steepening of the spectrum at even lower energies is caused by Coulomb losses.

12.4 Mechanisms of coronal heating

12.4.1 Heating of the quiet solar corona

The high temperature of the solar corona was originally interpreted as due to the steady dissipation of various kinds of waves coming from the lower layers (see Ulmschneider et al., 1991). Later on, heating by a myriad of very small flares releasing magnetic energy by reconnection has also been proposed (Gold, 1964; Priest, 1982; Parker, 1988). However these microflares or *nanoflares* have not yet been well identified.

It is difficult to detect the smallest flares in active regions, but in the quiet corona the background flux and stray light are smaller, and sensitive observations, for example, by the EIT (the Extreme ultraviolet Imaging Telescope) on *SOHO* can be used (Benz and Krucker, 1998). The thermal radiation of the quiet corona in high-temperature iron lines is found to fluctuate significantly, even on the shortest time scale as short as 2 min and in the faintest pixels. These observations give us an evidence that

> a significant fraction of the 'steady heating' in the quiet coronal regions is, in fact, impulsive.

The most prominent enhancements are identified with the X-ray flares above the network of the quiet chromosphere. Presumably, these X-ray flares above network elements are caused by additional plasma injected

from below and heated to slightly higher temperatures than the preexisting corona.

Magnetic flux tubes in the photosphere are subject to constant buffeting by convective motions, and as a result, flux tubes experience random walk through the photosphere. From time to time, these motions will have the effect that a flux tube will come into contact with another tube of opposite polarity. We refer to this process as reconnection in weakly-ionized plasma (Chapter 13). Another possibility is the photospheric dynamo effect (Section 13.5) which, in an initially weak field, generates thin flux tubes of strong magnetic fields. Such tubes extend high into the chromosphere and can contribute to the mass and energy balance of the quiet corona.

SOHO's MDI (the Michelson Doppler Imager) observations show that the magnetic field in the quiet network of the solar photosphere is organized into relatively small 'concentrations' (magnetic elements, small loops etc.) with fluxes in the range of 10^{18} Mx up to a few times 10^{19} Mx, and an intrinsic field strength of the order of a kilogauss. These concentrations are embedded in a superposion of flows, including the granulation and supergranulation. They *fragment* in response to sheared flows, *merge* when they collide with others of the same polarity, or *cancel* against concentrations of opposite polarity. Newly emerging fluxes replace the canceled ones.

Schrijver et al. (1997) present a quantitative statistical model that is consistent with the histogram of fluxes contained in concentrations of magnetic flux in the quiet network as well as with estimated collision frequencies and fragmentation rates. Based on the model, Schrijver et al. estimate that as much flux is cancelled as is present in quiet-network elements in 1.5 to 3 days. This time scale is close to the timescale for flux replacement by emergence in ephemeral regions. So that this appears to be the most important source of flux for the quiet network. Schrijver et al. (1997) point out that the reconnection process appears to be an important source of outer-atmosphere heating.

Direct evidence that the 'magnetic carpet' (Day, 1998), an ensemble of magnetic concentrations in the photosphere, really can heat the corona comes from the two other *SOHO* instruments, the Coronal Diagnostic Spectrometer (CDS) and the Extreme ultraviolet Imaging Telescope (EIT). Both instruments have recorded local brightenings of hot plasma that coincide with disappearaces of the carpet's elements. This indicates that just about all the elements reconnect and cancel, thereby releasing magnetic energy, rather than simply sick back beneath the photosphere.

The coronal transition region and chromospheric lines observed by *SOHO* together with centimeter radio emission of the quiet Sun simultaneously observed by the VLA show that the corona above the magnetic network has a higher pressure and is more variable than that above the in-

terior of supergranular cells. Comparison of multiwavelength observations of quiet Sun emission shows good spatial correlations between enhanced radiations originating from the chromosphere to the corona. Furthermore

> the coronal heating events follow the basic properties of regular solar flares

and thus may be interpreted as microflares and nanoflares (Benz and Krucker, 1999). The differences seem to be mainly quantitative (Krucker and Benz, 2000).

* * *

What do we need to replenish the entire magnetic carpet quickly, say 1-3 days (Schrijver et al., 1997; Moore et al., 1999) ? – A rapid replenishment, including the entire cancelation of magnetic fluxes inside the carpet, requires the fundamental assumption of a two-level reconnection in the solar atmosphere (e.g., Somov, 1999).

First, we may apply the concept of fast reconnection of electric currents as the source of energy for microflares to explain coronal heating in quiet regions (Somov and Hénoux, 1999). Second, in addition to coronal reconnection, we need an efficient mechanism of magnetic field and current dissipation in the photosphere and chromosphere. The presence of a huge amount of neutrals in the weakly ionized plasma in the temperature minimum region makes its electrodynamical properties very different from an ideal MHD medium. Dissipative collisional reconnection is very efficient here (Litvinenko and Somov, 1994b; Litvinenko, 1999; Roald et al., 2000). Presumably the same mechanism can be responsible for the heating of the chromosphere.

12.4.2 Coronal heating in active regions

The soft X-ray observations of the Sun from *Yohkoh* have revealed that roughly half of the X-ray luminosity comes from a tiny fraction (~ 2 %) of the solar disk (Acton, 1996). Virtually all of the X-ray luminosity is concentrated within active regions, where the magnetic field is the strongest. While the corona is evidently heated everywhere, there is no question that it is heated most intensively within active regions. So this Section will focus entirely on active regions.

The energy that heats the corona almost certainly propagates upward across the photosphere. Since the magnetic field plays a dominant role, the required energy flux can be expessed in terms of the electromagnetic

Poynting vector in an ideal MHD medium (see vol. 1, Exercise 13.5):

$$\mathbf{G}_{\rm P} = \frac{1}{4\pi}\,\mathbf{B}\times(\,\mathbf{v}\times\mathbf{B}\,)\;. \tag{12.17}$$

Assuming that the plasma vertical velocity v_z vanishes, we have the following expression for the vertical component of the energy flux:

$$G_z = -\frac{1}{4\pi}\;(\,\mathbf{v}\cdot\mathbf{B}\,)\;B_z\,. \tag{12.18}$$

A value of $G_z \sim 10^7$ erg cm^{-2} s^{-1} is frequently used to account for the X-ray flux from active regions.

Detailed models of coronal heating in active regions typically invoke mechanisms belonging to one of the **two broadly defined categories**: wave (AC) or stress (DC) heating.

In wave heating, the large-scale magnetic field surves essentially as a conductor for small-scale Alfvén waves propagating into the corona. So the average flux of wave energy can be written as

$$< G_z > = -\sqrt{\frac{\rho}{4\pi}}\;< v^2 >\; B_z\,. \tag{12.19}$$

Here B_z is the large-scale, stationary field, and $< v^2 >$ is the mean square velocity amplitude of the Alfvén waves. If the AC heating is the case, one expects to find some kind of correlation between the mean photospheric field strength and the heating flux.

In stress heating, the coronal magnetic field stores energy in the form of DC electric currents until it can be dissipated through, for example, nanoflares (e.g., Parker, 1988). Estimating the rate of energy storage results in a Poynting flux of the form

$$G_z = c_d\,|\,v\,|\,B_z^2\,. \tag{12.20}$$

Here the constant c_d describes the efficiency of magnetic dissipation, which might involve the random velocity v or the magnetic field geometry. Anyway, the Poynting flux in Equations (12.19) and (12.20) **scales differently** with the magnetic field B_z. While the constants of proportionality in each case may vary due to numerous other factors,

> we might expect a large enough sample to be capable of distinguishing between the two mechanisms of coronal heating.

To analyze whether active region heating is dominated by slow (DC) or rapid (AC) photospheric motions of magnetic footpoints, the so-called reduced magnetohydrodynamic (RMHD) equations are used. They describe

the dynamic evolution of the macroscopic structures of coronal loops assuming a fully turbulent state in the coronal plasma (Milano et al., 1997). The boundary condition for these equations is the subphotospheric velocity field which stresses the magnetic field lines, thus replenishing the magnetic energy that is continuously being dissipated inside the corona. In a turbulent scenario, energy is efficiently transferred by a direct cascade to the 'microscale', where viscous and Joule dissipation take place (see, however, Section 12.1.3).

Therefore, for the macroscopic dynamics of the fields, the net effect of turbulence is to produce a dramatic enhancement of the dissipation rate. Milano et al. (1997) integrated the large-scale evolution of a coronal loop and computed the effective dissipation coefficients by applying the eddy-damped closure model. They conclude that

> for broadband power-law photospheric power spectra, the heating of coronal loops is DC dominated.

Nonetheless a better knowledge of the photospheric power spectrum as a function of both frequency and wavenumber will allow for more accurate predictions of the heating rate from the theory.

12.5 Practice: Exercises and Answers

Exercise 12.1. Consider two interconnected ring-tubes C_1 and C_1 with magnetic fluxes Φ_1 and Φ_2 inside of them but without a magnetic field outside (Figure 12.1).

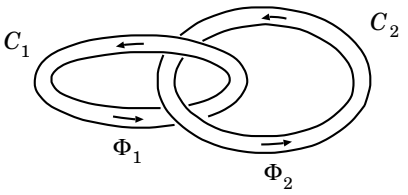

Figure 12.1: Two interconnected magnetic flux tubes.

Show that the global magnetic helicity of the system is given by the formula (Moffatt, 1978):

$$\mathcal{H} = 2\Phi_1\Phi_2\,. \tag{12.21}$$

Answer. First, we calculate the helicity of the tube C_1 by integrating formula (12.1) over the volume V_1 of the tube C_1 and replacing $\mathbf{B}\,d^3\mathbf{r}$ by

$\Phi_1\, d\,\mathbf{r}$ where $d\mathbf{r}$ is the length along the circuit C_1:

$$\mathcal{H}_1 = \int\limits_{V_1} \mathbf{A}\cdot\mathbf{B}\; d^3\mathbf{r} \;= \Phi_1 \oint\limits_{C_1} \mathbf{A}\cdot d\,\mathbf{r}\,. \tag{12.22}$$

By virtue of the Stokes theorem

$$\mathcal{H}_1 = \Phi_1 \int\limits_{S_1} \mathrm{curl}\mathbf{A}\cdot d\,\mathbf{S} = \Phi_1 \int\limits_{S_1} \mathbf{B}\cdot d\,\mathbf{S} \;= \Phi_1\Phi_2\,. \tag{12.23}$$

Since the other tube C_2 makes the same contribution to the helicity, we obtain the Moffatt formula (12.21).

Therefore

> the global magnetic helicity depends only on the fact that the two magnetic fluxes are interlinked.

The value of the helicity does not change if we deform the flux tubes as long as the linkage remains the same.

If, however, by magnetic reconnection the tubes would be cut and removed so that the linkage between them were broken, then the global helicity would go to zero. So we conclude that

> as long as the topology of magnetic fluxes does not change, the magnetic helicity is an invariant.

Exercise 12.2. Show that for the force-free fields with constant α, the magnetic energy is proportional to the global helicity (Woltjer, 1959):

$$\mathcal{M} = \alpha\,\mathcal{H}\,\frac{1}{8\pi}\,. \tag{12.24}$$

Here

$$\mathcal{M} = \int\limits_{V} \frac{B^2}{8\pi}\,dV\,, \tag{12.25}$$

V is the volume of a simply connected region bounded by a magnetic surface S where $\mathbf{B}\cdot\mathbf{n} = 0$ (see Section 12.1.1).

Discuss a kind of a surface integral which must be added to expression (12.24) in the case of a multiply connected volume such as a torus (see Reiman, 1980).

Chapter 13

Reconnection in Weakly-Ionized Plasma

Magnetic reconnection, while being well established in the solar corona, is successfully invoked for explanation of many phenomena in the low-temperature weakly-ionized plasma in the solar atmosphere.

13.1 Early observations and classical models

Magnetic reconnection, while being firmly established as a means of energy release in the high-temperature corona of the Sun during solar flares, is frequently invoked for explanation of various phenomena in the low-temperature plasma of the solar atmosphere. A particular example of these is the *prominence* phenomenon. Prominences are defined as dense ($\approx 10^{11}$ cm^{-3}) and cool ($\approx$ 6000 K) plasma 'clouds' visible in Hα above the solar surface (Tandberg-Hanssen, 1995). Pneuman (1983) suggested that both the material necessary for their formation and the magnetic field topology supporting them are the result of reconnection.

According to Pneuman (see also Syrovatskii, 1982) a neutral line of the magnetic field is produced in the corona owing to some kind of plasma flow in the photosphere. Reconnection at this line gives rise to a helical magnetic field configuration. As this takes place, chromospheric material flows into the reconnection region and is then carried up by the reconnected field lines which are concave upward. The material is thereupon radiatively cooled to form a prominence that nests in the helical field topology.

An interesting modification of this model is due to van Ballegooijen and

Martens (1989, 1990) who conjectured that the reconnection place is in fact located at the photospheric boundary. The point is that

> if reconnection takes place *deep* enough in the solar atmosphere, a sufficient quantity of material can easily be supplied to the corona,

thus facilitating the process of prominence formation. On the observational side this conjecture is substantiated by the fact (Martin, 1986) that for several hours before the formation of a filament, small-scale fragments of opposite polarity flux were seen to cancel in the region below the eventual filament.

So the model accounts for the cancelling magnetic features that are usually observed to be present in the photosphere below prominences. The scenario of the phenomenon has three phases: (a) a pre-interaction phase in which two opposite polarity photospheric magnetic fragments are unconnected magnetically, (b) an interaction phase when the fragments reconnect in the corona and create a filament, (c) a flux cancellation phase when reconnection in the photosphere produces the cancelling magnetic features.

Roumeliotis and Moore (1993) have developed a linear, analytical model for reconnection at an X-type neutral line (cf. Chapter 2). The reconnection process is assumed to be driven by converging or diverging motions applied at the photosphere. The gas pressure has been ignored (without much justifications) in the vicinity of the neutral line, and only small perturbations have been considered. The model relates the flows around the diffusion region, where dissipative effects are important, to the photospheric driving motions. The calculations based on this linear theory support the possibility of the laminar, slow reconnection occuring low in the solar atmosphere.

None of the above-mentioned authors considered the details of the reconnection process. Therefore it is still unclear whether the process can occur effectively enough in low-temperature plasma to ensure the upward flux of matter that is sufficient for prominence formation in the corona. In this Chapter we shall treat the reconnection process in the chromosphere and the photosphere in greater detail.

The reconnecting current layer (RCL) is envisaged to be formed in consequence of centre-to-boundary flows of weakly ionized plasma in convective cells. It is in such a current layer that field lines reconnect to change the field topology in the way suggested by Syrovatskii (1982) and Pneuman (1983). As distinct from the coronal case, we treat the current layer in the chromosphere and photosphere. We shall find that the reconnection efficiency is highest in the temperature minimum region, where the classical electric conductivity of weakly ionized plasma reaches its minimum.

13.2 Model of reconnecting current layer

13.2.1 Simplest balance equations

Let us consider a stationary reconnecting current layer (RCL) in the chromosphere and photosphere (Litvinenko and Somov, 1994b; Litvinenko, 1999). To find its characteristics, let us write down the order-of-magnitude relations stemming from the one-fluid equations of continuity, momentum conservation (both across and along the layer) and magnetic field diffusion into the layer:

$$n_0 v_0\, b = n v_1 a\,, \tag{13.1}$$

$$(1\,+\,x\,(T_0))\;n_0\,k_{\text{B}}T_0\,+\,\frac{{B_0}^2}{8\pi}\;=(1\,+\,x\,(T))\,n\,k_{\text{B}}T\,, \tag{13.2}$$

$$(1\,+\,x\,(T))\,n\,k_{\text{B}}T = m_p\,n\,\frac{v_1^2}{2}\;+(1\,+\,x\,(T_0))\;n_0\,k_{\text{B}}T_0\,, \tag{13.3}$$

$$\frac{c^2}{4\pi\,\sigma\,(T)\,a} = v_0\,. \tag{13.4}$$

Here a and b are the layer half-thickness and half-width. n_0 and n are the plasma concentrations outside and inside the layer, x is the ionisation degree, v_0 and v_1 are the plasma inflow and outflow velocities, m_p is the proton mass (hydrogen being assumed to be the main component of the medium), T_0 and T are the temperatures outside and inside the RCL. σ is the collisional conductivity in the layer where the magnetic field perpendicular to the electric current is zero. B_0 is the field in the vicinity of the RCL.

The set of Equations (13.1)–(13.4) should be supplemented by the energy balance equation. However it is not an easy matter to do this. On the one hand, thermal conductivity is unlikely to play a significant role in the energy balance of the low-temperature RCL. On the other hand, there are no reliable calculations for the radiative loss function $L\,(T)$ in the temperature domain $< 10^4$ K. An attempt to solve the radiative transfer equation for such a thin layer in the dense plasma of the low solar atmosphere would be an unjustified procedure given the order-of-magnitude character of the model at hand.

Let us adhere to the simplest assumption, namely that the cooling processes are effective enough to ensure the approximate equality of plasma temperatures inside and outside the RCL. Hence we postulate that

$$T \approx T_0\,. \tag{13.5}$$

This means that we do not expect an abrupt temperature enhancement in the RCL as in the fully ionized case. Note that the photospheric density is about 10^8 times as large as that of the corona. Roughly speaking, if the same amount of magnetic free energy is released in the corona and photosphere into heat in the same volume, each particle of the photosphere would receive approximately 10^{-8} of the energy given to each particle of the corona. For example, the so-called type II white-light flares (Mauas, 1990; Fang and Ding, 1995) are supposed to be the dissipation of magnetic field by reconnection in the photosphere. Such flares bring a temperature enhancement only of 150–200 K.

13.2.2 Solution of the balance equations

Now the sought-after quantities (the RCL parameters a, b etc.) can be expressed with the aid of Equations (13.1)–(13.5) via the external parameters n_0, T, x, σ, v_0, and B_0 :

$$a = \frac{c^2}{4\pi\,\sigma\,(T)\,v_0}\,, \tag{13.6}$$

$$b \;=\; (1 \,+\, \beta^{-1})\,a\,\frac{v_1}{v_0}\,, \tag{13.7}$$

$$n = n_0\,(1+\beta^{-1})\,, \tag{13.8}$$

$$v_1 = V_{\mathrm{A,s}} \equiv B_0\,\left[\,4\pi\,m_p\,n_0\,(1\,+\,\beta^{-1})\,\right]^{-1/2}\,. \tag{13.9}$$

Here

$$\beta = (1+x\,(T))\,n_0\,k_{\mathrm{B}}T\,\frac{8\pi}{{B_0}^2} \tag{13.10}$$

and $V_{\mathrm{A,s}}$ is the Alfvén speed defined by formula (6.7).

Returning to the question posed in the introduction of this Section, it is now straightforward to calculate the mass flux into the corona through the RCL, assuming the latter to be vertically orientated:

$$F = 2m_p\,nv_1\,al = 2m_p\,n_0\,(1+\beta^{-1})\,\frac{c^2\,l\,V_{\mathrm{A,s}}}{4\pi\,\sigma v_0}\,, \tag{13.11}$$

$l \sim 10^9$ cm being a typical value of the current layer length.

To find numerical values of the current layer parameters, we make use of the chromosphere model due to Vernazza et al. (1981). This model gives us the input parameters n_0, x and T as functions of the height h above the lower photospheric boundary, i.e. the level where the optical column depth in continuum $\tau_{5000} = 1$. The collisional conductivity, σ, for this model was calculated by Kubát and Karlický (1986). A typical value of the

field is assumed to be $B_0 \approx 100$ G. As for the inflow velocity, it is a free parameter. Its magnitude is of the order of the photospheric convective flow velocity ≈ 100 m/s. Table 13.1 presents the RCL characteristics predicted by our model using these data and the layer length $l \approx 10^9$ cm.

Table 13.1: Parameters of the reconnecting current layer in the chromosphere and photosphere

Height	h, km	0	0	350	350	2110	2110
Temperature	T, 10^3 K	6.4	6.4	4.5	4.5	18.5	18.5
Conductivity	σ, 10^{11} s^{-1}	6	6	1.5	1.5	140	140
Inflow velocity	v_0, 10 m s^{-1}	1	10	1	10	1	10
Half-thickness	a, 10^4 cm	10	1	50	5	0.5	0.05
Half-width	b, 10^7 cm	0.8	10^{-2}	10	0.1	3000	30
Concentration	n, 10^{16} cm^{-3}	10	10	1	1	0.02	0.02
Outflow velocity	v_1, km s^{-1}	0.6	0.6	2	2	20	20
Mass flux	F, 10^{10} g s^{-1}	300	30	300	30	0.4	0.04

13.2.3 Characteristics of the reconnecting current layer

Apart from variation of the inflow velocity, we consider three levels in the solar atmosphere, in an attempt to clarify the physical picture of the reconnection process. These are the lower photosphere ($h = 0$ km), the temperature minimum ($h = 350$ km), and the upper chromosphere ($h = 2113$ km). The properties of the reconnection process drastically differ at these levels. Different regimes of *linear* reconnection (Craig and McClymont, 1993; Priest et al., 1994) seem to be possible, including very slow (very small magnetic Reynolds number) reconnection.

The remarkable thing is that reconnection is predicted to effectively occur only in a thin layer (not thicker than several hundred km), coinciding with the temperature minimum region. Here

> a relatively thick current layer can be formed, where reconnection proceeds at a rate imposed by the converging plasma flows.

Since the magnetic field is relatively weak, the flow is practically incompressible. Magnetic energy is transformed into the thermal and kinetic energy of the resulting plasma motion. The upward flux of matter through the current layer into the corona is capable of supplying 10^{16} g of cold chromospheric material in a time of 10^4 s. This is amply sufficient for the formation of a huge prominence.

An interesting peculiarity of the solution obtained is the inverse proportionality of the mass flux to the inflow velocity. The physical reason for this is that decreasing v_0 leads to a decrease of the electric current in the current layer and hence the magnetic field gradient. Since B_0 is kept fixed, the layer thickness $2a$ has to increase, thus augmenting the matter flux.

Below the temperature minimum, the RCL does not form; $a \approx b$ because the plasma density is very high there. That diminishes the Alfvén speed and prevents the magnetic field from playing a significant role in the plasma dynamics. The overall geometry of the field is that of an X-point, so that the inflow magnetic field is highly nonuniform. This regime corresponds to the 'nonuniform' reconnection class according to classification given by Priest et al. (1994).

As for reconnection in the upper chromosphere, it is not efficient either. The reason for this is the relatively high temperature, resulting in the high conductivity (Table 13.1), which makes magnetic diffusion into the RCL too slow for any observable consequences related to the mass flux into the corona.

* * *

Several remarks are in order here, concerning our initial assumptions. First, we have assumed the RCL to be purely neutral, that is no magnetic field perpendicular to the layer has been taken into account. Allowing for a non-zero transversal field $\xi_\perp B_0$, Equation (13.1) might be rewritten as follows:

$$n_0 v_0 b = n v_1 (a + \xi_\perp b) . \tag{13.12}$$

Since our model predicts the layer to be rather thick ($a / b > 10^{-2}$) this correction is of no importance: a small transversal field does not considerably increase the effective cross-section of the matter outflow from the current layer.

Second, formula (13.5) needs some justification. By way of example, let us suppose that the influx of magnetic energy is balanced by radiative losses:

$$\frac{{B_0}^2}{4\pi}\, v_0\, b = L\,(T)\, x n^2\, ab\,. \tag{13.13}$$

A crude estimate for the loss function $L\,(T) = \chi T^{\alpha}$ has been given by, for example, Peres et al. (1982). Using this estimate together with the above RCL characteristics, one could find $T \approx 10^4$ K (for $h = 350$ km). Given the order-of-magnitude character of our model, it seems reasonable to presume that radiative losses can balance the Joule heating, so that (13.5) is valid as a first approximation. Anyway, although we expect the plasma heating to have some impact on our results, it is not likely to considerably alter the conclusions concerning reconnection efficiency. This is well supported by numerical results obtained in the more accurate model by Oreshina and Somov (1998).

Finally, we have implicitly assumed the plasma flow in the reconnection region to be well coupled. What this means is that both neutral and charged plasma components participate in the plasma flow (see, however, Section 13.4). As a consequence, the total density appears in the expression for the Alfvén speed determining the outflow velocity. If the coupling were weak, the ion Alfvén speed would have to be used in Equation (13.9), giving a faster outflow of ions.

Zweibel (1989) investigated reconnection in partially ionized plasmas and introduced the parameter Q defining the degree of coupling:

$$Q = \frac{v_0}{a\,\nu_{ni}}\,, \tag{13.14}$$

ν_{ni} being the frequency of neutral-ion collisions. The smaller Q is, the stronger is the coupling. It is easy to check that for the RCL in the temperature minimum region $Q \approx 10^{-5} - 10^{-1}$ for $v_0 = 10^3 - 10^5$ cm s^{-1}. This value of Q substantiates the assumption of **strong coupling for reasonably slow inflows**. In fact, a more self-consistent consideration of the reconnection region is necessary to take account of the generalized Ohm's law in a weakly-ionized plasma with a magnetic field near the temperature minimum.

13.3 Reconnection in solar prominences

The idea that reconnection in the dense cool plasma of the solar atmosphere is a mechanism of the so-called quiescent prominence (filament) formation was put forward many years ago. The model of prominence formation

by dint of the reconnection process was shown to predict realistic field topologies near filaments. However no investigation were performed on the value of the upward flux of plasma into the corona. As were proved in the previous Section, the flux can be high enough to explain the filament formation in a reasonable time: $F \approx 10^{11} - 10^{12}$ g s^{-1}. This seems to be a strong argument in favour of the Pneuman–van Ballegooijen–Martens model. However there were only circumstantial pieces of evidence in its favour.

Compared with the corona,

> the solar photosphere provides us with a unique place to observe the magnetic reconnection process directly,

since the magnetic fields can be measured with high resolution.

Direct indications of reconnection in the temperature minimum have been found on the basis of the study of photospheric and chromospheric magnetograms together with dopplergrams in the same spectral lines. Liu et al. (1995) have obtained magnetograms in the Hβ ($\lambda 4861.34\,A$) and FeI ($\lambda 5324.19\,A$) lines. A comparative study of such magnetograms has revealed the existence of **reverse polarity features**. The appearance and behaviour of these features can be explained by the twisting of the magnetic flux tubes and reconnection of them in the layer between the photosphere and the chromosphere, i.e. in the temperature minimum region.

Observations show that reverse polarity **cancellation** is supposed to be a slow magnetic reconnection in the photosphere. Certainly we can adjust the parameters to account for observed flux canceling. It has been also revealed (Wang, 1999) that in all well-observed events there is no connecting transversal field between two canceling component. So observation support the reconnection explanation.

We have seen that current layers can be formed in the temperature minimum region in response to photospheric flows. Reconnection efficiency is determined by the high collisinal resistivity rather than by the turbulent one, as opposed to the coronal case. As a final speculation, high-speed flows which are predicted by our model in regions of strong magnetic fields ($B_0 > 300$ G) might be identified with spicules.

* * *

Optical observations reviewed by Martin (1998) confirm the **necessary conditions** for the formation and maintenance of the filaments: (a) location of filaments at a boundary between opposite-polarity magnetic fields, (b) a system of overlying coronal loops, (c) a magnetically-defined channel beneath, (d) the convergence of the opposite-polarity network of magnetic

fields towards their common boundary within the channel, and (e) cancelation of magnetic flux at the common polarity boundary.

Evidence is put forth for **three additional conditions** associated with fully developed filaments: (A) field-aligned mass flows parallel with their fine structure, (B) a multi-polar background source of a small-scale magnetic field necessary for the formation of the filament barbs, and (C) a handedness property known as *chirality* which requires them to be either of two types, dextral or sinistral.

> In the northern hemisphere most quiescent filaments are *dextral*, and in the southern hemisphere most are *sinistral*.

This refers to the direction of the magnetic field when standing on the positive polarity and gives the two possible orientations for the axial field: namely to the right for a dextral structure and to the left for a sinistral one.

One-to-one relationships have been established between the chirality of filaments and the chirality of their filament channels and overlying coronal arcades. These findings reinforce either evidence that every filament magnetic field is separate from the magnetic field of the overlying arcade but both are parts of a larger magnetic field system. The larger system has **at least quadrupolar footprints in the photosphere** (cf. Figure 14.1) and includes the filament channel and subphotospheric magnetic fields (Martin, 1998).

To explain the hemispheric pattern, Mackay et al. (1998) consider the emergence of a sheared activity complex. The complex interacts with a remnant flux and, after convergence and flux cancellation, the filament forms in the channel. A key feature of the model is the net magnetic helicity of the complex. With the correct sign a filament channel can form, but with the opposite sign no filament channel forms after convergence because a transversal structure of the field is obtained across the polarity inversion line. This situation is quite similar to that one which will be shown in Figure 14.3.

Three-dimensional quasi-dissipative MHD simulations (Galsgaard and Longbottom, 1999) show that a thin RCL is created above the polarity inversion line. When the current becomes strong enough, magnetic reconnection starts. In the right parameter regime,

> with the correct sign of helicity, the reconnected field lines are able to lift plasma several pressure scale heights against solar gravity.

The lifted plasma forms a region with an enhanced density above the RCL along the polarity inversion line.

13.4 Element fractionation by reconnection

It is observationally established that element abundances of the solar corona and solar wind obey a systematic fractionation pattern with respect to their original photospheric abundances. This pattern is organized in such a way that elements with a low first ionization potential (FIP), the so-called low-FIP elements, are enriched by a factor of about four. Apparently the elements are enriched or depleted by a process that depends on the FIP or perhaps even more clearly on the characteristic first ionization time and the relative diffusion length for the neutrals of the minor species colliding with the dominant hydrogen atoms.

When two regions of opposite magnetic polarity come into contact with each other in a partially ionized plasma, ions drifting in response to the Lorentz force fall into the minimum of the magnetic field, and then the drifting ions force the neutrals to take part in the flow. This is the case considered by Arge and Mullan (1998). An essential aspect of reconnection in weakly-ionized plasma is that

> the atoms have no trouble flowing accross the magnetic field lines; the ions are not entirely constrained to follow the field lines as this should be in ideal MHD.

Instead, they have a significant component across the field lines. The reason is **dissipation in the form of ion-atom collisions**. In view of the fact that the atoms move across field lines freely, and in the view of the fact that collisional coupling connects the atom fluid and the ion fluid, it is not surprising that ions are *not* tied strictly to the field lines. As a result, departures from ideal MHD behaviour are an inevitable feature of the process we discuss here.

Because of the finite time required for ion-atom collisions to occur, the plasma which emerges from the RCL has an ion/atom ratio which may be altered relative to that in the ambient medium. Arge and Mullan show that in chromospheric conditions, outflowing plasma exhibits enhancements in ion/atom ratios which may be as large as a factor of ten or more. The results are relevant in the context of the Sun, where the coronal abundances of elements with low FIP are systematically enhanced in certain magnetic structures.

The first ionization potential gives the energy scale of an atomic species, hence many atomic parameters and the chemical behaviour of elements are closely related to it. Thus, in principle,

> very different physical mechanisms could be imagined which would produce an FIP dependence of elemental abundance

(see Section 13.5.3). It is important that the observed FIP enhancement varies from one type of solar magnetic features to another, ranging from unity (i.e., no enhancement) in impulsive flares to as much as 10 in diverging field structures. The last suggests that **magnetic field topology plays a role in creating the FIP effect in the Sun**.

If the magnetic field can trap the solar material and confine it (such as in a loop), the FIP effect apparently does not occur. On the other hand, if the field is such that a free outflow of material is allowed (e.g., in divergent field), then the FIP effect develops to a large amplitude. For this reason, when we model magnetic interactions in the chromosphere, for example the fine magnetic-flux tube formation (Section 13.5.3) we have to choose a topology which allows material to flow out freely.

In stars other than the Sun, EUV data have allowed to search for the FIP effect. Some stars with magnetic activity levels significantly higher than the Sun show evedence for FIP enhancement. This is consistent with a magnetic origin of FIP enhancement. Moreover the same FIP-based compositional fractionation mechanism at work in the solar atmosphere is presumably operational in the coronae of significantly more active stars (Laming and Drake, 1999).

13.5 The photospheric dynamo

13.5.1 Current generation mechanisms

In the deep photosphere, under the temperature minimum, particles are well coupled by collisions. That is why the physics of the deep photosphere, including the physics of magnetic flux tubes, is often described by the resistive *one-fluid* MHD approach. The same is valid even more for under-photospheric layers.

In the temperature minimum region, there are many neutral atoms which collide with ions and bring them into macroscopic motion. However the electrons remain frozen in the magnetic field. Therefore a treatment of this region as

> an ensemble of *three fluids* (electrons, ions and neutrals) is necessary to give a clear physical insight on the mechanisms of current generation near the temperature minimum

in the photosphere – the *photospheric dynamo* effect. Moreover, higher in the solar chromosphere, significant effects arise due to the density decrease that leads to a decoupling of the motions of ions and neutrals, that cannot be described by the one-fluid approximation.

For an axially symmetrical magnetic field, the horizontal velocities of electrons, ions and neutrals can be found analytically by solving the equations which describe the balance of the horizontal forces acting on each particle fluid (Hénoux and Somov, 1991). The horizontal velocities of ions and neutrals derived from these equations are relative to the horizontal velocities in the convective zone – the primary source of motion. It has been shown that, in an initially weak magnetic field,

> a radial inflow of neutrals can generate azimuthal DC currents, and an azimuthal velocity field can create radial DC currents leading to the circulation of vertical currents.

The effects of such velocity fields on the intensity and topology of electric currents flowing in thin magnetic flux tubes will be discussed below.

13.5.2 Physics of thin magnetic flux tubes

A schematic representation of an open flux tube S is given in Figure 13.1, which shows the location of the solar chromosphere Ch and photosphere Ph with the temperature minimum region T. Such a semi-empirical model follows, for example, from the He I ($\lambda 10830\ A$) triplet observations (Somov and Kozlova, 1998).

Let us consider the electric currents generated by azimuthal flows with the velocity v_φ in a partially ionized plasma in the region T. Since it is the relative azimuthal velocity between the magnetic field lines and the plasma, these currents can result either from azimuthal motions of the photosheric plasma around a fixed magnetic field or from the rotation around the flux tube axis of the magnetic field inserted in a static partially ionized atmosphere. Anyway the azimuthal flows generate the radial currents j_r.

An inflow of the radial current density j_r is related to the vertical current density j_z by continuity equation

$$\frac{\partial j_z}{\partial z} = -\frac{1}{r}\,\frac{\partial\,(r j_r)}{\partial r}\,. \tag{13.15}$$

The vertical electric current

$$J_z = \int 2\pi\, r j_z(r)\, dr \tag{13.16}$$

cannot be derived locally, i.e. independently of the contribution of the other neighbouring (in height z) layers in the solar atmosphere. Every layer in the temperature minimum region T acts as a current generator in a circuit that extends above and below this layer. So a circuit model is necessary to relate the total current J_z to the current densities. However, in all cases the

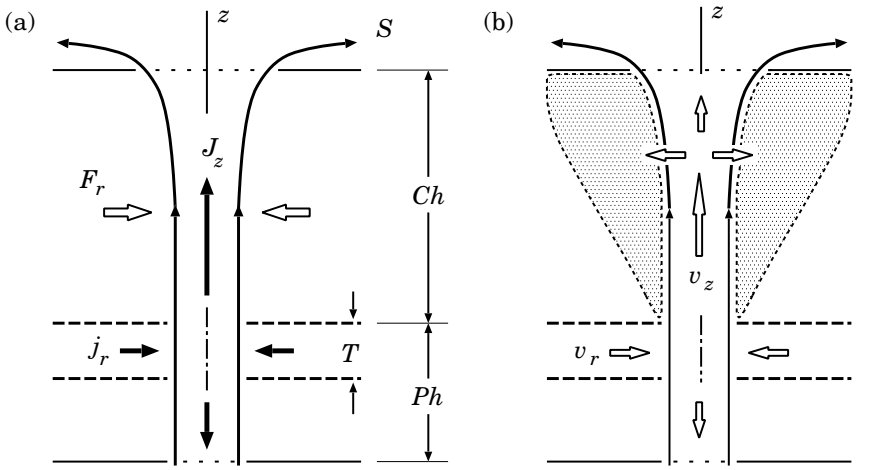

Figure 13.1: A simplified model of an open flux tube in the solar atmosphere. (a) The generation of electric currents and the pinch effect. (b) The motion of neutrals and their diffusion across the magnetic field lines in the chromosphere.

contributions of every layer to the circuit regions placed above and below it are proportional to the inverse ratio of the resistances of these parts of the circuit.

The magnetic forces produced by these currents play a significant role in the structure and dynamics of flux tubes. Even for moderate values of the azimuthal photospheric velocities v_φ, the current J_z created is strong enough to prevent by the *pinch effect* (an action of the Lorentz force component F_r) an opening of the flux tube with height (Hénoux and Somov, 1997).

> Despite the decrease of the ambient gas pressure with height, the thin magnetic flux tube extends into the solar atmosphere high above the temperature minimum.

In the internal part of the tube, the rise from the photosphere of a partially ionized plasma is found to have four effects.

First, the upflow of this plasma is associated to a leak of neutrals across the field lines as shown in Figure 13.1b and leads to an increase of the ionization degree with altitude typical for the chromosphere. Moreover the upflow brings above the temperature minimum an energy flux comparable to the flux required for chromospheric heating.

Second, the outflow of neutrals takes place at the chromospheric level

across the field lines. Here the neutrals occupy an extensive area shown by the shadow in Figure 13.1b outside the tube. This outflow of neutrals leads to ion-neutral separation and may explain the observed abundance anomalies in the corona by enhancing in the upper part of the tube the abundances of elements of a low ionization potential (Section 13.5.3).

Third, the upward motion velocities are high enough to lift the matter to an altitude characteristic of spicules or even macrospicules.

Fourth, if the footpoints of the flux tubes are twisted by the photosphere, then when they emerge into the transition region and release their magnetic energy some rotational component is retained. Strong evidence has been found from *SOHO*'s CDS (the Coronal Diagnostic Spectrometer) observations to support the hypothesis that rotation plays a role in the dynamics of transition region features. These observations are interpreted as indicating the presence of a rotating plasma, a sort of *solar tornado* (Pike and Mason, 1998).

13.5.3 FIP fractionation theory

The flux-tube model predicts the formation of closed or open structures with higher-temperature ionization state and higher low FIP to high FIP elements abundance ratios than the surrounding. A strong pressure gradient across the field lines can be present in the flux tubes where electric currents are circulating (Hénoux and Somov, 1991, 1997). Since they produce **two of the ingredients that are required for ion-neutral fractionation by magnetic fields**, i.e. small scales and strong pressure gradients perpendicular to the field lines (Hénoux and Somov, 1992), these currents can lead to the efficient ion-neutral fractionation.

Azimutal motions of the partially ionized photospheric plasma, with velocity v_φ at the boundary of the tube, $r = r_0$, generate a system of two current shells: S_{in} and S_{out} in Figure 13.2 (Hénoux and Somov, 1992, 1999). The vertical currents j_z in these shells flow in opposite directions, such that the azimutal component of the field, B_φ, vanishes at infinity. This result can be easily understood in the case of a fully ionized atmosphere where the field lines are frozen in the plasma. However the study of a partially ionized atmosphere gives insight into questions that cannot be tackled in the hypothesis of a fully ionized plasma, i.e. the possible difference in velocities perpendicular to the field lines of ions and neutrals.

The internal current system and the azimutal component of the magnetic field, B_φ, create an inward radial force $B_\varphi j_z$ that enhances, by the pinch effect discussed in Section 13.5.2, the pressure inside the internal part of the tube.

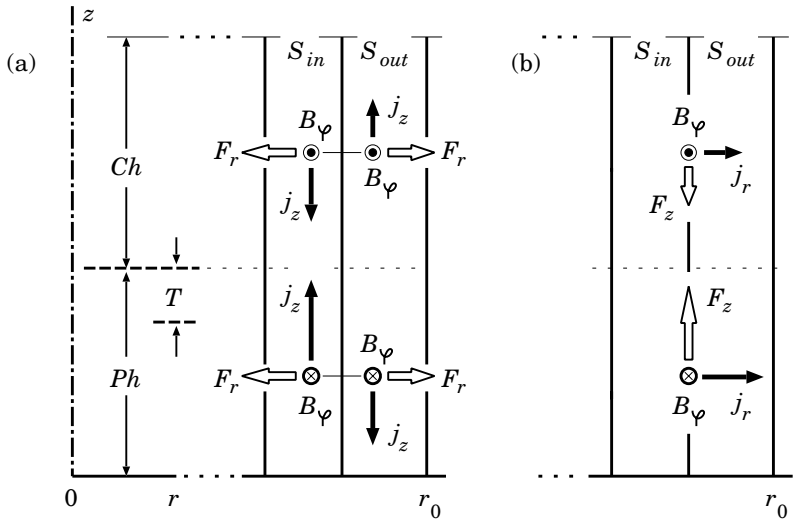

Figure 13.2: A simplified model of a thin magnetic flux tube in the solar atmosphere. (a) The vertical current density j_z and azimutal component of field B_φ create the pinch effect in the internal part of the tube. (b) The radial current density j_r and azimutal magnetic field B_φ produce the upward force in the photosphere.

The pinch effect is present from the photosphere to the chromosphere but its consequences are different in these two regions.

In the photosphere, collisions couple ions and neutrals; so they do not cross the field lines. Above the photosphere, due to the exponential decrease of the density and, as a result, of the ion-neutral friction force with height, the difference in radial velocities of neutrals and ions increases with height.

The current densities and magnetic fields in the flux tube are such that, at hydrogen densities lower than 10^{13} cm^{-3}, the collisional coupling is low enough to allow the neutrals to cross the field lines and to escape from the internal current shell with high velocities. In usual plane-parallel-atmosphere models, the fractionation starts in the temperature minimum region T in Figure 13.2a at a temperature of about 4000 K. So the population of ionized low FIP species begin to be enhanced inside the internal current shell just at heights where the usual models place the chromospheric temperature rise and where the separation between the hot and cool components of the Ayres (1996) bifurcation model starts to take place.

Between the two opposite currents flowing vertically, the upwards

Lorentz force component $B_\varphi j_r$ is present. Since the change of the direction of the vertical currents goes with the change of direction, from the photosphere to the chromosphere, of the transversal current j_r carried by ions, the $B_\varphi j_r$ force always produces a net ascending action. The intensity of this force is compatible with an ejection of matter up to heights of about 10 000 km, and therefore with the formation of spicules. This force acts in a shell, between the two neutralizing currents, where the gas pressure and collisional friction forces are reduced; it acts on ions and may then lead to a FIP effect in spicules by rising up preferentially the ionized low FIP species. A quantitative study of all these effects remains to be done.

13.6 Practice: Exercises and Answers

Exercise 13.1. Consider basic features of the magnetic flux-tube twist by a vortex-type motion of the fully ionized plasma.

Answer. Let us consider first the twisting action of a fully ionized plasma motion on a magnetic flux tube with $B_r = 0$ everywhere as this is shown in Figure 13.3a.

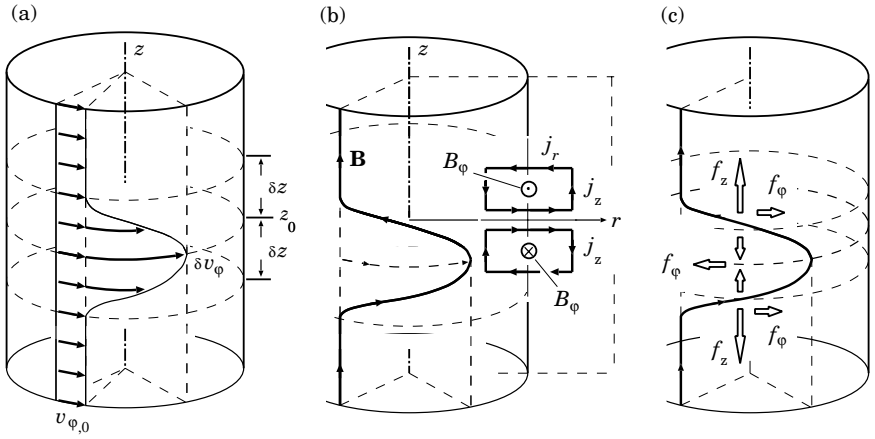

Figure 13.3: Twisting flow of a fully ionized plasma inside a flux-tube. (a) Azimutal velocity distribution at the surface $r = \text{const}$, $2\delta z$ is the thickness of a twisting zone. (b) A field line on this surface and the associated radial and vertical components of electric current densities j_r and j_z in the twisting zone. (c) The vertical component f_z of the Lorentz force compresses plasma in a central part of the twisting zone, but in outer parts it makes the twisted field line move outwards.

The tube consists of vertical magnetic field lines. Each surface $r =$ const rotates with the constant velocity $v_{\varphi,0}$ but there is an excess of the azimuthal velocity δv_φ in the layer $(z_0 - \delta z, z_o + \delta z)$ with a maximum at $z = z_0$. In this case, the radial component of electric current density, j_r, reverses twice with the height z according to formula:

$$j_r = -\frac{1}{r}\frac{\partial}{\partial z}(rB_\varphi)\,. \tag{13.17}$$

This is shown in Figure 13.3b in the plane (z, r).

The existence of a maximum of the azimutal angular velocity at a given radial distance r_0 makes the vertical component of the electric current density, j_z, to reverse also with height as well as with the radial distance r because

$$j_z = +\frac{1}{r}\frac{\partial}{\partial r}(rB_\varphi)\,. \tag{13.18}$$

A Lorentz force tends to compensate for the twist of the field lines by the detwisting motions of the plasma (Figure 13.3c). The azimuthal and vertical components of this force are respectively:

$$f_\varphi = -\,j_r B_z \quad \text{and} \quad f_z = +\,j_r B_\varphi\,. \tag{13.19}$$

The vertical component creates some compression of the plasma in the central part of the twisting zone, but it will also act in the outer parts of the twisting zone. This will preferentially result in a propagation of the twist and plasma along the tube.

Exercise 13.2. Discuss basic features of the magnetic flux-tube generation by vortex-type flows of the weakly ionized plasma near the temperature minimum in the solar atmosphere.

Answer. Let V_φ^c be the azimutal component of the velocity field at the boundary between the convective zone and the photosphere as shown in Figure 13.4.

Strong *collisional* coupling occurs in the low photosphere because of high collisional frequencies $\nu_{\rm i}$ and $\nu_{\rm e}$ in comparison with gyrofrequencies $\omega_{\rm B}^{\rm (i)}$ and $\omega_{\rm B}^{\rm (e)}$. So the electric conductivity can be considered as isotropic. Moreover at the boundary with the convective zone the conductivity is so high that the ideal MHD approximation can be accepted, and the electric field acting on particles is null:

$$E_r^c - \varepsilon V_\varphi^c\, B = 0\,. \tag{13.20}$$

So, in the steady case considered here, the radial electric field is continuous from the convective zone to the photosphere:

$$E_r = E_r^c = \varepsilon V_\varphi^c\, B\,. \tag{13.21}$$

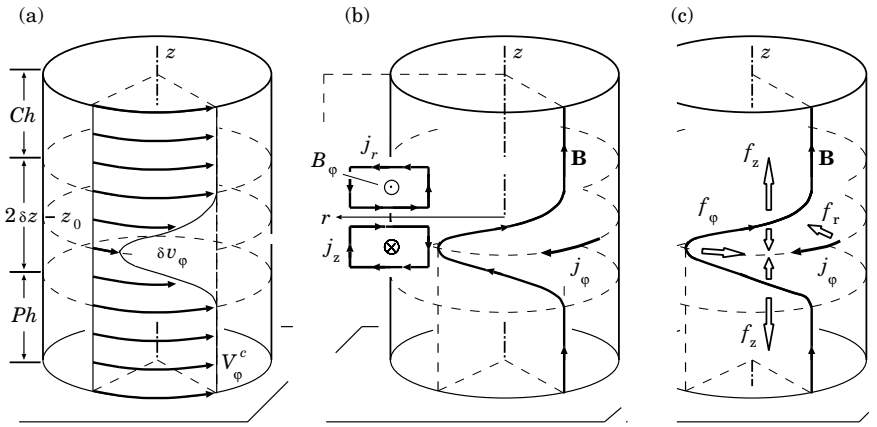

Figure 13.4: Twisting flow of a partially ionized plasma inside a magnetic flux-tube in the temperature minimum region, generated by a vortex flow in the convective zone under the photosphere. (a) Azimutal velocity distribution at the surface $r = \text{const}$, $2\delta z$ is the thickness of a generator zone. (b) A field line on this surface together with the radial and vertical components of the electric current density in the generator zone. (c) The Lorentz force components. The radial component f_r which is responsible for the pinch effect appears.

Strong *electromagnetic* coupling between electrons and ions occurs in the upper chromosphere because of low collisional frequencies $\nu_{\rm i}$ and $\nu_{\rm e}$ in comparison with gyrofrequencies $\omega_{\rm B}^{\rm (i)}$ and $\omega_{\rm B}^{\rm (e)}$. At temperatures above 10^4 K, the ideal MHD approximation can be taken again. So we can put the same boundary condition (13.21) in the upper chromosphere and lower layers.

This means that the upper part of the twisted tube in the steady case must rotate with the same azimutal velocity as the lowest part at the boundary with the convective zone (see Figure 13.4).

In the generator region, the poloidal electric current, $j_r + j_z$, is generated as well as in a fully ionized plasma, except with an opposite direction of circulation. Additionaly, another electric current is present; this is an azimuthal current j_φ. In a partially ionized plasma, the difference in the amplitude of the friction forces between neutrals and ions, between neutrals and electrons (Hénoux and Somov, 1991) leads to the generation of an azimuthal current j_φ with the same sign as the azimuthal velocity of neutrals relative to the azimuthal velocity of the electrons that are practically frozen

in the magnetic fields.

The flow of neutrals across the magnetic field **B** generates a motion of ions in the same direction. So

$$j_\varphi \approx ne\left(v_{\varphi,n} - V_\varphi^c\right) + j_\varphi^{\mathrm{H}}\,, \tag{13.22}$$

where j_φ^{H} is the Hall current related with the electric field component E_r.

This page intentionally blank

Chapter 14

Magnetic Reconnection of Electric Currents

Magnetic reconnection reconnects field lines together with field-aligned electric currents. This process may play a significant role in the dynamics of astrophysical plasma because of a topological interruption of the electric currents.

14.1 Introductory comments

We shall consider the general idea of interruption and redistribution of electric currents which are aligned with magnetic-field lines (the field-aligned currents in what follows), for example in the solar atmosphere. The currents are created under the photosphere and/or inside it, as well as they are generated in the corona. However, independently of their origin, electric currents distributed in the solar atmosphere reconnect together with magnetic field lines. So the currents are interrupted and redistributed in a topological way.

This phenomenon will be discussed in the classical example of a 2D configuration with four magnetic sources of interchanging polarity and with the 3D topological model described in Section 3.2.1. Converging or diverging flows in the photosphere create a thin reconnecting current layer (RCL) at the separator – the line where separatrix surfaces are crossing. Shearing flows generate highly concentrated currents at the separatrices. We discuss their properties and point out that

> the interruption of field-aligned electric currents by the magnetic reconnection process at the separator can be responsible for fast energy release in astrophysical plasma,

for example, in solar flares, in active regions with observed large shear as well as in quiet regions above the 'magnetic carpet' responsible for heating of the quiet corona.

14.2 Flare energy storage and release

14.2.1 From early models to future investigations

It has for a long time been clear that the energy released in flares is stored originally as magnetic energy of electric currents in the solar atmosphere. At least, there do not appear to be any other sources of energy which are adequate. Simple estimates of the *free* magnetic energy content in typical active regions (e.g., Den and Somov, 1989) show that it generally exceeds the observed energy of flares as well as the energy which is necessary for coronal heating in active regions. Free magnetic energy can, in principle, be converted into kinetic and thermal energy of the solar plasma with particle acceleration to high energies and other things that can be observed in the solar atmosphere and interplanetary space. This is the flare or, more exactly, the solar flare problem.

Jacobsen and Carlqvist (1964), Alfvén and Carlqvist (1967) were the first to suggest that

> the interruption of electric currents in the solar corona creates strong electric fields that accelerate particles during flares.

This mechanism of magnetic energy release and its conversion into thermal and supra-thermal energies of particles has been considered and well developed by many authors (e.g., Baum et al., 1978). The interruption of current was described as the formation of an electrostatic *double layer* within a current system – an electric circuit – storing the flare energy.

The formation of the double layer *locally* leads to a direct acceleration of particles. However, because the potential (which gives this acceleration) must be maintained by the external system, the *global* effects of the double layers are not small. In general, they lead to an MHD relaxation of the surrouding magnetic field-plasma configuration providing the influx of energy which is dissipated by the double layers (Raadu, 1984).

* * *

An alternative approach to the solar flare problem was introduced by Giovanelli (1946, 1947, 1948), Dungey (1958) and Sweet (1958). After them, it was believed that

> the solar flare energy can be accumulated as magnetic energy of a reconnecting current layer (RCL)

in the place of magnetic flux interaction and redistribution, more exactly, at the *separators* (Sweet, 1958). This idea was well supported by many analytical investigations, by laboratory and numerical experiments (for a review see Syrovatskii, 1981; Priest, 1982; Somov, 1992), by observations of the reconnection process in space plasmas (Hones, 1984; Berger, 1988a) and especially on the Sun (Tsuneta, 1993; Demoulin et al., 1993; Bagalá et al., 1995).

In fact, the laboratory experiment by Stenzel and Gekelman (1984) clearly indicated the appearance of double layers in the RCL. This means that local interruptions of the electric current, induced by reconnection, can exist in the place of magnetic-field line reconnection. In what follows, we will consider another effect – magnetic reconnection of electric currents – the physical phenomenon which is different from the creation of an ordinary double layer in the reconnecting current layer or in the field-aligned current.

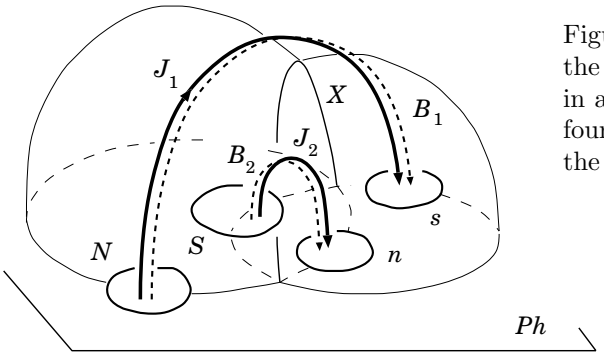

Figure 14.1: A model of the coronal magnetic field in an active complex with four magnetic sources in the photosphere.

Hénoux and Somov (1987) considered two systems of large-scale coronal currents J_1 and J_2 distributed inside two different magnetic cells interacting along the separator X as shown in Figure 14.1. Such a model for an active region complex is, in fact, the case of the magnetic topology described in Section 3.2.1. The two field lines B_1 and B_2 connect the 'old' (N, S) and 'new' (n, s) centres of activity (active regions). The coronal currents that flow from one magnetic flux region to the other (from the old region to the new one) are distributed inside the two different cells and shown

schematically as the total currents J_1 and J_2 along the field lines B_1 and B_2.

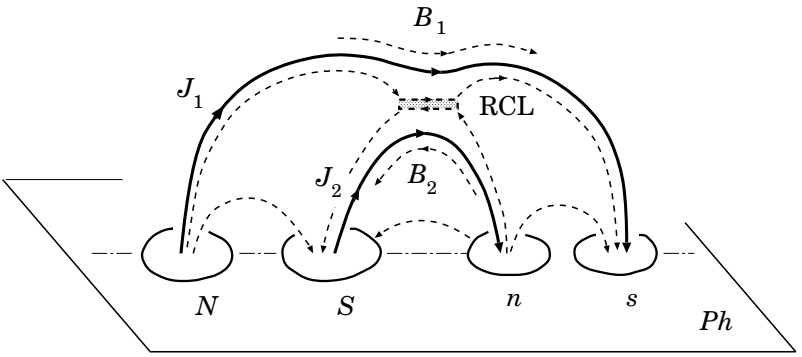

Figure 14.2: Coronal currents for the aligned old and new bipolar regions.

For simplicity, in Figure 14.2 the geometry of the same magnetic field lines and currents is illustrated in the case where the old and new bipolar regions are aligned. The field lines B_1 and B_2 near the RCL along the separator (cf. Figure 3.4) have an opposite direction and can be reconnected. The two current systems J_1 and J_2 can be close to each other near the separator. Moreover, in the case under consideration, the currents flow in the same direction. Therefore, as in Gold and Hoyle (1960), Sakai and de Jager (1996), they attract each other. So the field-aligned electric currents have to modify the equilibrium conditions for the RCL along the separator (Hénoux and Somov, 1987).

> The components of the magnetic field transversal to the separator reconnect together with electric currents flowing along them.

In this way, with a perpendicular magnetic field inside the place of interruption, magnetic reconnection creates local interruptions of the electric currents in the solar atmosphere. If these currents are highly concentrated, their interruption can give rise to strong electric fields accelerating particles and can contribute significantly to the flare energetics.

Let us consider the magnetic fields created by the currents. These additional or secondary fields are perpendicular to the currents; hence they are parallel to the separator. Therefore they play the role of the longitudinal magnetic field near the RCL (Section 6.2.2). Being superimposed on the potential magnetic field, the additional field components B_φ create two field line spirals: left-handed and right-handed (Figure 14.3a). When looking along the positive direction of the main field lines B_1 and B_2, we

see the two opposite orientations for the spirals: namely to the right for the *dextral* structure (for example, filament) and to the left for the *sinistral* one.

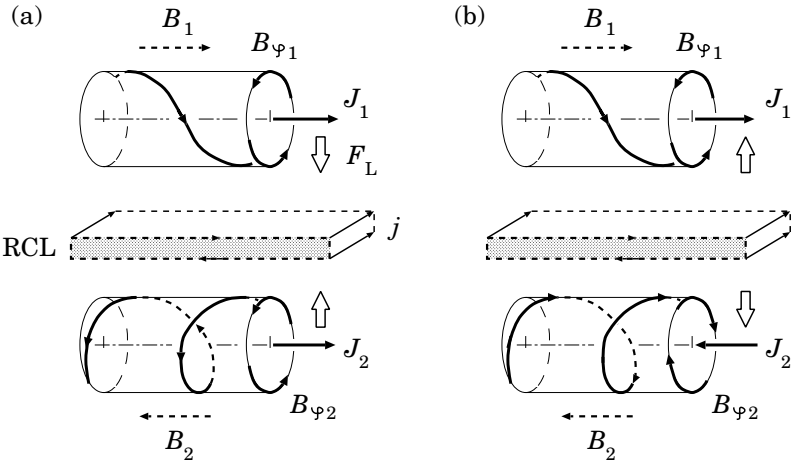

Figure 14.3: Two possible orientations of twist in two interacting magnetic flux-tubes with field-aligned electric currents.

When the currents flow in the same direction, as was shown in Figure 14.2, the azimuthal components $B_{\varphi 1}$ and $B_{\varphi 2}$ have the same direction of rotation. Being opposite inside the RCL, they reconnect well: fully or partially. At the same time, the Lorentz force F_{L} pushes the parallel currents one to another. Therefore the case shown in Figure 14.3a is the most favourable for reconnection of magnetic fields and field-aligned electric currents.

On the contrary, if the currents are antiparallel, as shown in Figure 14.3b, the azimuthal components $B_{\varphi 1}$ and $B_{\varphi 2}$ cannot be reconnected. They are compressed and they decrease the reconnection rate for the main components of the magnetic fields B_1 and B_2, as it was discussed in Section 6.2.2. Hence a handedness property known as *chirality* does influence upon the magnetic reconnection of electric currents.

This is a qualitative picture of reconnection of the field-aligned electric current according to Hénoux and Somov (1987). Physical properties of the electric current reconnection in a highly-magnitized plasma have not been investigated yet. Many of them remain to be understood, in particular, the role of Hall's and perpendicular conductivities (see Appendix 3) at the place of the electric current rupture and the role of plasma motions generated

there. However it is clear that magnetic *reconnection changes the path of an electric current circuit*. Because of large dimensions, the current circuit in the corona has a huge inductance. So a large inductive voltage can be generated locally, leading to a complex electrodynamic phenomenon with particle acceleration to high energies.

The review of the present situation in the solar flare theory will help us to understand the basic features of the electric current reconnection phenomenon in Section 14.4, see also Somov and Hénoux (1999).

14.2.2 Some alternative trends in the flare theory

A potential field in an active region contains a minimal energy which cannot be extracted from the plasma-magnetic field system. It was a question whether or not it is possible to explain the pre-flare energy storage in the force-free approximation, i.e only with electric currents aligned with the magnetic field. This idea never looked too promissing, except in some investigations (see Sturrock, 1991) that suggested that the energy of a force-free field (FFF) generated by footpoint shearing flows can exceed the energy of the 'completely open' field having the same boundary condition (the same vertical component) in the photospheric plane. If this were true, we could expect an explosive opening of such an FFF configuration with a fast release of excess energy. Then spontaneous eruptive opening could be a good model for coronal transients or coronal mass ejections (CMEs).

Aly (1984), by using the virial theorem (vol. 1, Section 19.1), as well as without it (Aly, 1991), has shown that the energy of any FFF occupying a 'coronal half-space' is either infinite or smaller than the energy of the open field. So obviously **the opening costs energy** and cannot occur spontaneously. The initial field must have free energy in excess of the threshold set by the open field limit. Only that excess is available to lift and drive the expelled plasma in CMEs or other similar phenomena (Sturrock, 1991).

This conclusion seems to be natural and could actually have important consequences for our understanding of non-steady phenomena with the opening of the coronal magnetic fields. Let us mention some of these consequences, bearing in mind, however, that coronal fields are never completely open or completely closed (see Low and Smith, 1993).

Generally, the electric currents flowing *across* the field allow the corona to have a magnetic energy in excess of the Aly's limit. These currents can be generated by any non-magnetic forces; for example, the gravity force, the gradient of gas pressure or inertia forces. The problem arises because such forces are normally relatively weak in comparison with the magnetic force in the corona. Therefore the related effects can be considered as small corrections to the FFF (see vol. 1, Section 13.1.3).

Another possibility is that the real currents in the corona comprise two different types: (i) **smoothly distributed currents** that are necessarily parallel or nearly parallel to the magnetic field lines, so that the field is locally force-free or nearly force-free; (ii) **thin current layers** of different origin, in which the gas pressure gradient or other forces are significant. If, following Aly (1984, 1991), we could recognize the low efficiency of the smooth FFF (i) in energetics and dynamics of global eruptive events in the corona, we could well replace them by potential fields in evolution and action (e.g., Syrovatskii and Somov, 1980). This means that, to some extent, it is possible to neglect the field-aligned current in (i); we may call this approximation the **minimum current corona**. However, at least one exception can be important. It will be discussed in the next Section.

If we do not consider flares or other flare-like events that open coronal fields, and if we do not investigate how to extract the accumulated energy from the FFF, then it is easy to conclude that the free magnetic energy can well be accumulated in FFFs, even if they are smoothly distributed. The basic idea here, used by many authors, is that photospheric footpoint motions stress the coronal field lines, inflate them, thereby producing free magnetic energy. For example, Porter et al. (1992) have studied the energy build-up in the stressed coronal fields possessing cylindrical symmetry. In the non-linear FFF approximation ($\alpha \neq$ const), they have shown that

> a reasonable amount of the photospheric twist can produce enough free magnetic energy to power of a typical solar flare.

The rate of the energy build-up is enhanced if the greatest twist and/or the magnetic flux is concentrated closer to the photospheric neutral line.

14.2.3 Current layers at separatrices

Analytically, by using the Grad-Shafranov equation, and numerically, by quasi-static MHD computations, Zwingmann et al. (1985) have shown the occurence of current layers near the separatrix in sheared field structures containing an X-type neutral point – the place where the separatrices cross. They interpret the break-down of the quasi-static theory near the separatrix as evidence for the appearance of a *boundary* layer with the current flowing parallel to the *poloidal* (Section 14.3) magnetic field.

Low (1991), Vekstein and Priest (1992) demonstrated analytically, in the force-free approximation, that shearing flows can produce current layers along separatrices with or without neutral points. Numerical solutions of the time-dependent MHD equations by Karpen et al. (1991), generally, confirmed the formation of currents in the frame of the line tying approximation. They concluded, however, that *true* (reconnecting) current layers

(RCL) do not form in the solar corona when a more realistic atmospheric model is considered without a null point present in the initial potential field. These authors found more distributed currents, related to plasma inertia and the absence of a *true* static equilibrium, that cannot be considered as thin current layers.

Therefore

> shearing flows in the photosphere generate highly-concentrated electric currents flowing along and near separatrices.

In this context, we suggest a new mechanism of flare energy release – the *topological interruption* of electric currents in the solar atmosphere and their redistribution (Section 14.4). We shall consider two stages of its development. In the first, the electric currents are produced by photospheric shearing motions and the magnetic energy is stored in the system of concentrated field-aligned currents. In the second stage, the flare energy release takes place because a strong electric current system is approaching the separator and disrupted by the magnetic field line reconnection process in the separator region.

14.3 Current layer formation mechanisms

14.3.1 Magnetic footpoints and their displacements

Let us discuss the topological interruption of coronal electric currents by using the classical example of a potential field in the plane (x, y) shown in Figure 14.4. Here e_i are the 'magnetic charges' placed on the x axis at

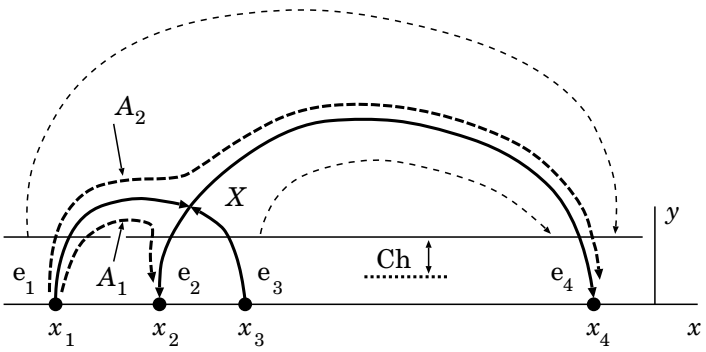

Figure 14.4: A 2D model of the magnetic field of four sources of interchanging polarities.

the points with coordinates $(x_i\,, 0)\,,\ i = 1,\ 2,\ 3,$ and 4 at the underphotospheric plane $y = 0$. For simplicity we assume that they have interchanging balanced polarities: $\mathrm{e}_1 = -\,\mathrm{e}_4 = Q$ and $-\,\mathrm{e}_2 = \mathrm{e}_3 = q$. So these are the same magnetic charges as in Figure 3.2 but placed along a straight line – the x axis. This relative position of magnetic sources corresponds to the idealized case shown in Figure 3.1.

The solid curves show two separatrices crossing at the neutral point X (cf. Figure 1.3) which is the special topological line in the z direction – the separator. Two field lines are shown by the dashed curves A_1 and A_2. They start from the magnetic charge e_1, go near the neutral point but arrive at different charges: e_2 and e_4 respectively. So they have different magnetic connectivity.

This is the *initial* configuration of a magnetic field. Just to keep the same notation as in the early works related with the controlled nuclear fusion (Morozov and Solov'ev, 1966a; Shafranov, 1966), we refer to a magnetic field in the plane (x, y) as the *poloidal* one. This part of the magnetic field $\mathbf{B}_p^{(0)}\,(x, y)$ is described by the z component of the vector potential $\mathbf{A}$:

$$\mathbf{B}_p^{(0)}\,(x, y) = \left(\frac{\partial A^{(0)}}{\partial y},\, -\frac{\partial A^{(0)}}{\partial x},\, 0\right), \tag{14.1}$$

where

$$\mathbf{A}^{(0)}\,(x, y) = \left(0,\, 0,\, A^{(0)}\,(x, y)\right).$$

In the case under consideration

$$A^{(0)}\,(x, y) = \sum_{i=1}^{4} \ln r_i\,, \tag{14.2}$$

where

$$r_i = \left[\,(x - x_i)^2 + y^2\,\right]^{1/2}$$

(see Lavrent'ev and Shabat, 1973, Chapter 3, § 2).

Near the X-type point, where the field equals zero, the vector-potential can be written as (cf. formula (2.23)):

$$A^{(0)}\,(x, y) = \frac{1}{2}\,h_0\left[\,-(x - x_0)^2 + (y - y_0)^2\,\right], \tag{14.3}$$

with x_0 and y_0 being the coordinates of the neutral point. The constant which can be added to the vector-potential is selected in such a way that $A = 0$ on the sepatrices – the lines that separate the magnetic fluxes of different linkage (or connectivity).

The main aim of our treatment is to understand the relative efficiency in generation and dissipation of electric currents of different origin. Bearing this aim in mind we will consider different motions in the photosperic plane, i.d. different displacements of field line footpoints.

Following Low (1991), we will consider **three classes of displacements**. The displacements of the first class are strictly on the line of the magnetic charges – the x axis in Figure 14.4. These displacements model the converging, diverging or emerging motions of the magnetic sources in the photosphere. They keep the magnetic field lines in the plane of the initial field – the plane (x, y).

Shearing flows in the z direction belong to the second and third classes. The displacements of the second class are only 'antisymmetric in x', i.e. the photospheric velocity in the z direction is an odd function of x. No symmetry is prescribed for the third class of displacements.

14.3.2 Classical 2D reconnection

The displacements of the *first class* defined above do not create RCLs in the absence of a neutral point X shown in Figure 14.4. The appearance of such a point on the boundary (for example, in the photosheric plane) is a necessary condition for the creation of a RCL. A sufficient condition is the existence of a non-zero electric field in this point (Section 2.1.2). The magnetic field remains potential above the photospheric plane if the boundary conditions prohibit the appearance of a neutral point. In general, however, 'a neutral point begins to appear' on the boundary surface (Somov and Syrovatskii, 1972; Low, 1991) and the reconnecting current layer is generated in it by the electric field.

Let us consider, as the simplest example, a symmetrical initial distribution of magnetic charges shown in Figure 14.5a and the small symmetrical displacements of footpoints x_2 and x_3 as follows

$$\delta x_2 = -\delta x_3 = \delta x(t)\,.$$

They are shown in Figure 14.5b. In the presence of the neutral line X, in its vicinity, the electromagnetic field can be expressed through the vector-potential (Syrovatskii, 1966a, 1971)

$$A\,(x, y, t) = A^{(0)}\,(x, y) + \delta A(t)\,. \tag{14.4}$$

Here $\delta A(t)$ is the value of the magnetic flux which has to be reconnected in the current layer at the neutral point. Then, after the reconnection time τ_r, the magnetic field will be potential one again, but with new positions

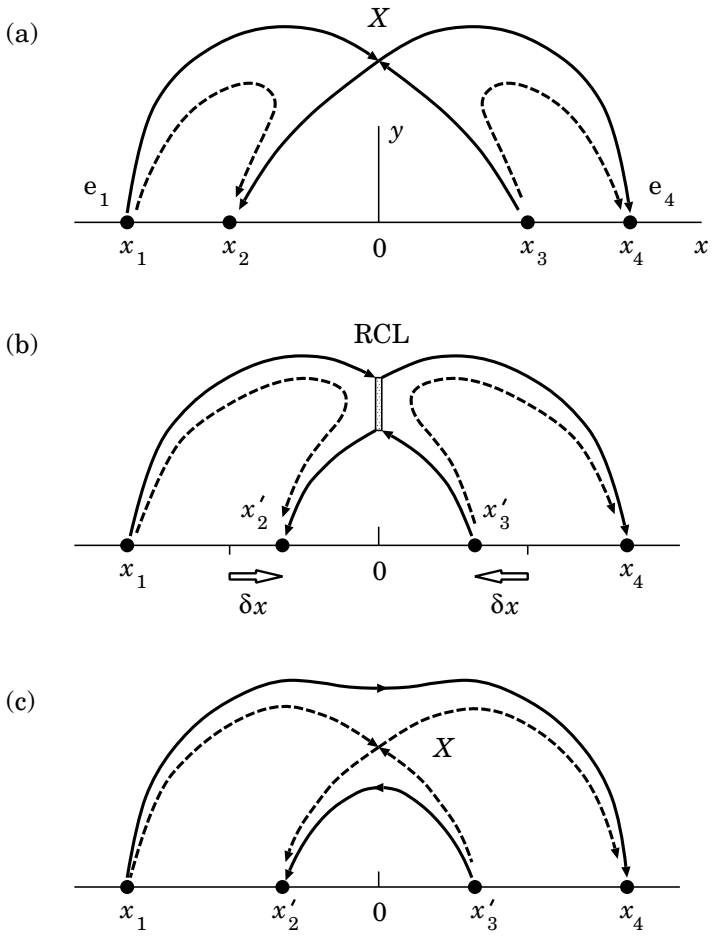

Figure 14.5: (a) The initial field configuration; (b) the formation of the reconnecting current layer RCL under the converging motion of footpoints x_2 and x_3 ; (c) the disappearance of the RCL when the field relaxes to the new potential state.

of the footpoints $x_2 + \delta x\,,\ x_3 - \delta x$. The value $\delta A(t)$ is proportional to the displacement δx.

It is clear from formula (14.4) that in the vicinity of the neutral line there is a uniform electric field directed along the line:

$$\mathbf{E} = -\frac{1}{c}\,\frac{\partial}{\partial t}\,\mathbf{A} = (\,0,\,0,\,E_z\,)\,, \tag{14.5}$$

where

$$E_z = -\frac{1}{c}\,\frac{\partial\,\delta A(t)}{\partial t}\,. \tag{14.6}$$

It is just this field which produces an electric current $\mathbf{J}$ along the neutral line (Figure 1.4b) as well as a drift motion of plasma outside the line (Figure 1.4a). In a time of the order of the Alfvén time $\tau_{\rm A}$, the current layer is formed along the neutral line.

Figure 14.5b schematically illustrates the process of the current layer formation induced by the photospheric displacements δx of the first class. The relaxation of the magnetic field which contains the current layer to the potential field corresponding to the new boundary conditions is shown in Figure 14.5c.

14.3.3 Creation of current layers by shearing flows

Let us consider some general properties of the field component B_z from the initial field (Figure 14.4) generated by a shearing displacement $\delta z\,(x)$ in the FFF approximation. To study plasma equilibrium and stability, it is convenient to use the *specific* volume of the magnetic flux tube (see vol. 1, Section 19.3.2) or simply the specific magnetic volume. This is the ratio of the geometrical volume of the flux tube $d\,V$ to the enclosed magnetic flux $d\,\Phi$, i.e.

$$U = \frac{d\,V}{d\,\Phi}\,. \tag{14.7}$$

For a field line specified by a given value of vector-potential A, by invoking the conservation of magnetic flux inside the tube, the specific volume is

$$U\,(A) = \int \frac{d\,l}{B}\,. \tag{14.8}$$

The integral in (14.8) is taken along the field line between two certain appropriate points corresponding to the beginning and the end of the tube. For the example considered in Figure 14.4, the beginning and the end of a tube are defined by the photospheric points x_1 and x_2 for all field lines

connecting these points above the photospheric plane:

$$U(A) = \int_{x_1}^{x_2} \frac{d\,l}{B_p^{(0)}(x,y)}\,. \tag{14.9}$$

By integrating the differential equation for a magnetic field line

$$\frac{dz}{B_z} = \frac{d\,l}{B_p^{(0)}(x,y)}\,, \tag{14.10}$$

taking account of (14.9), we see that the *toroidal* component B_z is given by the displacement of field line footpoints at the boundary plane $y = 0$:

$$B_z(A) = \frac{\delta z(A)}{U(A)}\,. \tag{14.11}$$

We see from (14.11) that, even if the displacement δz is a continuous function of x, a problem may arise for the following reason. In the presence of topological features like X-type points, the different field lines, by having different footpoints x_i in the photosphere and different footpoint displacements δx_i, may have the same values of A. Therefore discontinuities of B_z may appear above the photospheric plane.

Zwingmann et al. (1985) have illustrated this important feature of sheared magnetic fields analytically by considering the FFF locally near a hyperbolic X-point of the form (cf. formula (14.3)):

$$A^{(0)}(x,y) = -\frac{ax^2}{2} + \frac{by^2}{2} \quad \text{with} \quad a \neq b\,. \tag{14.12}$$

They showed that the specific volume has a logarithmic divergence for A corresponding to the separatrices that cross at the X-point, i.e. for $A = 0$. This means, first of all, that one of the diverging physical quantities is the poloidal current density

$$\mathbf{j}_p = \operatorname{curl} \mathbf{B}_z = \frac{d\,\mathbf{B}_z(A)}{dA} \cdot \mathbf{B}_p^{(0)} \propto \frac{1}{A \ln^2 A}\,. \tag{14.13}$$

The total current integrated in the direction perpendicular to the initial poloidal field $\mathbf{B}_p^{(0)}$ is finite:

$$J_t = \int_{A_1}^{A_2} \frac{d\,\mathbf{B}_z(A)}{dA}\, dA = \mathbf{B}_z(A_2) - \mathbf{B}_z(A_1)\,. \tag{14.14}$$

We are therefore led to the conclusion that

shearing flows do induce the current layers extending along the separatrices, with the current flowing parallel to the poloidal field.

This theoretical conclusion was also tested by numerical computations (Zwingmann et al., 1985) which take into account the physical effects that in real plasmas keep the current density from becoming infinitely large (see also Section 14.4).

14.3.4 Antisymmetrical shearing flows

The conclusion made above is valid even in the cases of very high symmetry, e.g. if the displacements are *antisymmetric*, and the initial potential field is symmetric (Figure 14.5) with respect to the y axis. This is clear from the following example. Let

$$x_1 = -\,x_4\,, \qquad x_2 = -\,x_3\,,$$

and

$$\delta z_1 = -\,\delta z_4 = \delta Z\,, \quad \delta z_2 = -\,\delta z_3 = \delta z\,,$$

as shown in Figure 14.6.

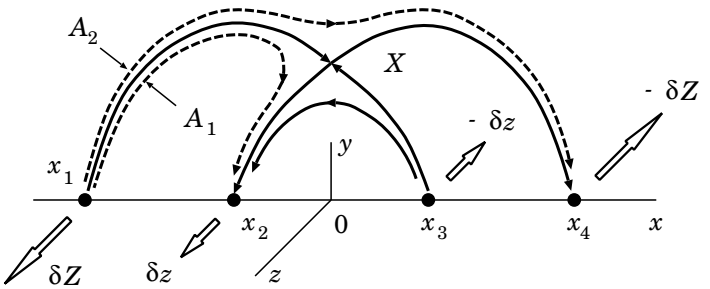

Figure 14.6: A 2D initial magnetic field configuration and the antisymmetric shearing motions of footpoints δZ and δz.

The specific volume of the magnetic flux tube which goes along the field line A_1 from the point x_1 very near the neutral X-point to the point x_2 consists of two terms

$$U\,(A_1) = \int\limits_{x_1}^{X} \frac{d\,l}{B_p^{(0)}\,(x,y)} + \int\limits_{X}^{x_2} \frac{d\,l}{B_p^{(0)}\,(x,y)} \equiv U_{1,X} + U_{X,2}\,. \qquad (14.15)$$

According to (14.11) the toroidal (or longitudinal) component of the magnetic field is equal to

$$B_z\,(A_1) = \frac{\delta z_2 - \delta z_1}{U_{1,X} + U_{X,2}}\,. \tag{14.16}$$

For the field line A_2 which goes from x_1 to x_4 very near the X-point, with account of the symmetry described above, we find the specific volume

$$U\,(A_2) = U_{1,X} + U_{X,4} = 2\,U_{1,X} \tag{14.17}$$

and the relative displacement $\delta z = \delta z_4 - \delta z_1 = -\,2\,\delta z_1$. So

$$B_z\,(A_2) = -\,\frac{\delta z_1}{U_{1X}} \neq B_z\,(A_1)\,. \tag{14.18}$$

Hence an antisymmetric shear creates the discontinuity of the toroidal field, i.e. the current layer with total current (14.14) along the separatrices, in the presence of X-type point even if the initial potential field is symmetric.

Consider another example. Let the shearing motions be antisymmetric and the initial magnetic field be symmetric, but with the neutral point placed below the level of the photosheric plane (Low, 1991). In this case the separatrix surface separates two 'magnetic islands' from each other at the point $x = 0$ and $y = 0$ as well as separating them from the surrounding field at the total separatrix surface in Figure 14.7. In this way the con-

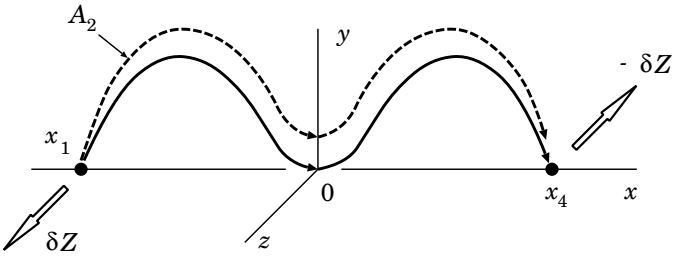

Figure 14.7: A 2D potential magnetic field of the quadrupole type without a neutral point above the photospheric plane.

nectivity of the magnetic field is discontinuous, and one may in principal expect the creation of magnetic field discontinuities. However, because of the symmetry, the specific volume is

$$U\,(A_2) = U_{1,O} + U_{O,4} = 2\,U_{1,O} \tag{14.19}$$

with a relative displacement

$$\delta z = \delta z_4 - \delta z_1 = -2\,\delta z_1\,.$$

Therefore

$$B_z\,(A_2) = B_z\,(A_1)\,. \tag{14.20}$$

We see that the second class of boundary motions cannot create current layers in the absence of neutral points (Figure 14.7). However an antisymmetric shear creates current layers with the currents flowing along separatrices in the plane (x, y) in the presence of a neutral point, even if the initial potential field is symmetrical one (Figure 14.6).

All the other shearing boundary displacements directed in the z direction are called the third class, according to the classification by Low (1991), and are discussed in the next Section.

14.3.5 The third class of displacements

Several examples of the third class displacements, including those which are symmetrical in x, were studied by Low (1991), Vekstein and Priest (1992). It was shown that these shearing displacements can create discontinuities of the B_z component which are related with electric currents along separatrices. The displacements can generate such current layers even in the absence of a neutral point, but the separatrices are necessary of course.

The general boundary displacement is a superposition of displacements from all these three classes. Titov et al. (1993) demonstrated the existence of sections of the photospheric polarity inversion line where the overlying field lines are parallel to the photosphere (like in Figure 14.7). Such sections, called 'bald patches', may exist for a wide range of fields created by four concentrated sources of magnetic flux (Gorbachev and Somov, 1989, 1990; Lau, 1993). Bald patches appear, for example, when the photospheric neutral line is bent too much in an S-like manner, because this is the case of the separator appearance (Somov, 1985; Somov and Merenkova, 1999; Somov et al., 2001). The field lines touching a patch belong to a separatrix surface along which a current layer may be formed by shearing motions of magnetic footpoints at the photosphere.

In the next Section we will discuss the mechanisms which determine the real thickness and other properties of the current layers.

14.4 The shear and reconnection of currents

14.4.1 Physical processes related to shear and reconnection

Let us start by discussing the second and third classes of displacements. Since the current density $\mathbf{j}_p$ is parallel to the poloidal field $\mathbf{B}_p^{(0)}$ (see formula (14.13)), the plasma velocity $\mathbf{v}_z$ and the total magnetic field

$$\mathbf{B}_t = \mathbf{B}_p^{(0)} + \mathbf{B}_z$$

are parallel to the discontinuity surface which coincides locally with the plane tangential to the separatrix. In this case, all the MHD boundary conditions are satisfied identically except one:

$$p_1 + \frac{\mathbf{B}_1^2}{8\pi} = p_2 + \frac{\mathbf{B}_2^2}{8\pi}\,. \tag{14.21}$$

This means that the velocity and the magnetic field may experience arbitrary jumps in magnitude and direction, being parallel to the discontinuity surface. The only requirement is that the total pressure, i.e. the sum of the gas pressure and the magnetic one, remains continuous at the discontinuity surface.

According to the general classification of MHD discontinuities given in vol. 1, Section 16.2, these discontinuities, generated by shearing flows, are usual tangetial discontinuities, except that the plasma velocities in the z direction are small in comparison with the Alfvén speed in the solar corona because the magnetic field is strong there. Therefore, until we take into account the effect discussed at the end of Section 14.4.3,

> we consider MHD tangential discontinuities as a good model for highly concentrated currents at separatrices, generated by shearing flows in the photosphere.

As treated in MHD, tangential discontinuities have several remarkable properties. One of them is important for what follows. Even in astophysical plasma of very low resistivity, such as the solar coronal plasma, a tangential discontinuity is a *non-evolutionary* discontinuity (vol. 1, Section 17.1). In contrast to the behaviour of the RCL, there is not a steady solution, the stability of which can be considered in the linear approximation.

The origin of this effect lies in the fact that the thickness of a tangential discontinuity is a continuously growing value if the electrical resistivity is finite. After its creation the $\mathbf{B}_z$ component starts to evolve in accordance

with the diffusion equation

$$\frac{\partial B_z}{\partial t} = \frac{\partial}{\partial s}\left(\nu_m \frac{\partial B_z}{\partial s}\right). \tag{14.22}$$

Here ν_m is the magnetic diffusivity, s is the coordinate ortogonal to the discontinuity surface. By virtue of Equation (14.22), the total magnetic flux of $\mathbf{B}_z$ does not change:

$$\frac{\partial}{\partial t}\int\limits_{-\infty}^{+\infty} B_z\, ds = \nu_m \left.\frac{\partial B_z}{\partial s}\right|_{-\infty}^{+\infty} = 0\,. \tag{14.23}$$

The thickness of a tangential discontinuity is increasing, but a part of the excess magnetic energy related with a tangential discontinuity is released in the continuous process in the form of Joule heating at a rate

$$\frac{\partial}{\partial t}\int\limits_{-\infty}^{+\infty} \frac{{B_z}^2}{8\pi}\, ds = -\frac{1}{4\pi}\int\limits_{-\infty}^{+\infty} \nu_m \left(\frac{\partial B_z}{\partial s}\right)^2 ds \neq 0\,. \tag{14.24}$$

Magnetic diffusion always acts to smooth out gradients in both the magnetic field and the electric current density, not to concentrate them. This property has been well demonstrated by many numerical computations.

In the RCL, however, the process of magnetic diffusion away from the discontinuity is compensated by the plasma drift motions into the layer. That is why the steady state for the RCL can exist with the layer width

$$a = \nu_m\, v_d^{-1}\,, \tag{14.25}$$

where v_d is the drift velocity, and the RCL at separator can be considered as an evolutionary discontinuity (Chapter 10). So

> there is a principal difference between the reconnecting current layer at the separator and the current layers at separatrices.

It is important that it is not possible to consider the RCL as a one-dimensional discontinuity because the plasma coming into the layer has to be compensated by plasma outflow from it. These two conditions are necessary for the existence of steady states for the RCL.

As for tangential discontinuities generated by shearing flows in the photosphere, their electric currents are always spreading out in both directions from sepatrix surfaces into the surrounding coronal plasma. By doing so, a part of the electric current flowing along the separatrices appears on the field lines which have already been reconnected (see Figure 14.4), but the remaining

> part of the electric current will be reconnected later on together with the field lines which have not been reconnected yet.

Hence we have to consider how electric currents flowing along the magnetic field lines reconnect with them.

We shall not discuss here all other mechanisms (except presumably the most important one in Section 14.4.3) which make the tangential discontinuity currents more distributed rather than concentrated. Neither will we discuss the generation of the electric currents of different origin in the solar corona, for example, currents due to variations in plasma response time (because of plasma inertia) at different heights in the solar atmosphere, nor currents related to the absence of a *true* static equilibrium (Karpen et al., 1991). We only would like to point out that electric currents of different origin, being field-aligned after their generation (Spicer, 1982), may participate in the process of magnetic field line reconnection.

14.4.2 Topological interruption of electric currents

The magnetic reconnection process does the same with electric currents as with magnetic field lines, i.e. it disrupts them and connects them in a different way. Physical consequences of the phenomenon have not yet been well investigated, but some of them look clear and unavoidable.

The first of these, an interruption of the electric current, produces an electric field. It is neccesary to note here that if reconnection of magnetic field lines would create symmetrical reconnection of currents, then one electric current, J_1 , should replace another one, J_2 , which is equal to the first current, and no electric field could be induced in such a way. Such coincidence has zero probalility.

In general, the reconnected currents are not equal among themselves; hence the current $(J_1 - J_2)$ is actually interrupted at the X point of reconnection. This process creates an electric field at the separator.

The simplest but realistic example is the case where we neglect one of the currents; e.g., $J_2 = 0$. Figure 14.8 shows such example. A new emerging magnetic flux (s, n) moves upward together with electric current J. This current is disrupted by the magnetic reconnection process in the RCL and appears to be connected into new electric circuits.

14.4.3 The inductive change of energy

The second consequence of non-symmetrical reconnection of electric currents is related to the fact that the current $(J_1 - J_2)$ is connected in another electric circuit which, in general, has another self-inductance L.

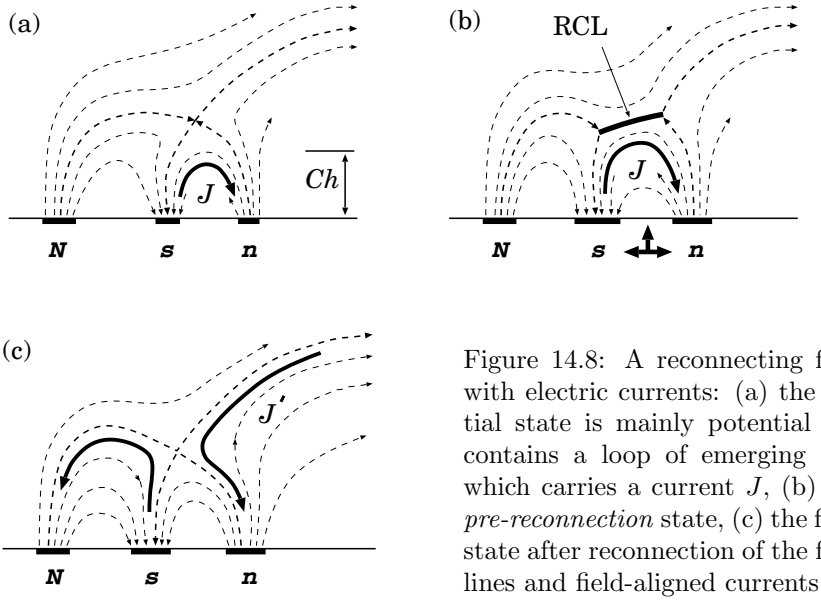

Figure 14.8: A reconnecting field with electric currents: (a) the initial state is mainly potential but contains a loop of emerging flux which carries a current J, (b) the *pre-reconnection* state, (c) the final state after reconnection of the field lines and field-aligned currents.

Hence the magnetic reconnection of the current $(J_1 - J_2)$ changes the energy of the current system

$$W_{_L} = \frac{LJ^2}{2} \tag{14.26}$$

and its inductive time scale

$$\tau_{_L} = L/R\,. \tag{14.27}$$

A larger circuit implies a larger energy but a longer inductive time scale.

Zuccarello et al. (1987) pointed out that the magnetic energy release in a flare should not be attributed to current dissipation but rather to a change in the current pattern that reduces the stored magnetic energy. They introduced an example of how self-inductance and energy storage can be changed in a sheared FFF arcade. In fact, the inductive change of energy can be reversed, with the stored energy being resupplied on the inductive time scale. In terms of MHD, the inductive energy $W_{_L}$ is the energy of the azimuthal magnetic field B_φ related to the field-aligned current J.

There is an essential advantage in our model of reconnecting electric currents. The topological interruption of large-scale electric currents flowing along and near separatrix surfaces does not require an increase of the total resistivity R everywhere the currents flow but only in the place where these

surfaces cross, i.e. along the separator line. More exactly, the plasma resistivity must be increased, for example by excitation of plasma turbulence, only inside the very thin RCL at the separator. Otherwise the reconnection process will be too slow and the rate of energy release insufficient for a typical flare.

Another important property of the model under consideration is that magnetic reconnection, when it is fast enough, restricts the current density $\mathbf{j}_p$ of electric currents flowing along the separatrix surfaces and near them. The mechanism of this restriction is the same topological one.

If the characteristic time τ_x of the δx displacements which drive reconnection is comparable with the reconnection time scale τ_r, then the field lines connecting the footpoints x_i with the X-type point (see Figure 14.5a) will not play the role of separatrices anylonger after the time τ_r. New magnetic field lines, shown by the dashed curves in Figure 14.5c, with footpoints $x_i' = x_i + \delta x_i$ will be the place where a new portion of shearing motions will produce a new portion of highly concentrated currents along these field lines, but not the previous ones. Therefore the real velocities of the footpoint displacements and the real reconnection rate determine the real distribution of concentrated electric currents generated by shearing flows in the photosphere.

14.5 Potential and non-potential fields

14.5.1 Properties of potential fields

To sum up what we can agree concerning the role of a magnetic field in solar flares, let us classify the magnetic fields in an active region, as shown in Figure 14.9. The field is divided broadly into two categories: (a) the potential or current-free part and (b) the non-potential part related to electric currents flowing in an active region.

Starting from the photosphere up to some significant height in the corona, the magnetic energy density greatly exceeds that of the thermal, kinetic and gravitational energy of the solar plasma. So the magnetic field can be considered in the strong field approximation. This means that the coronal field is mainly potential. At least, it is potential in a large scale, in which the field determines the *global* structure of an active region.

However the potential field, which satisfies the given boundary conditions in the photosphere and in the solar wind, has the minimum of energy because the potential field is current-free by definition. Two important consequences for the physics of large flares follow from this fact.

First, being disrupted, for example by an eruptive prominence, the field

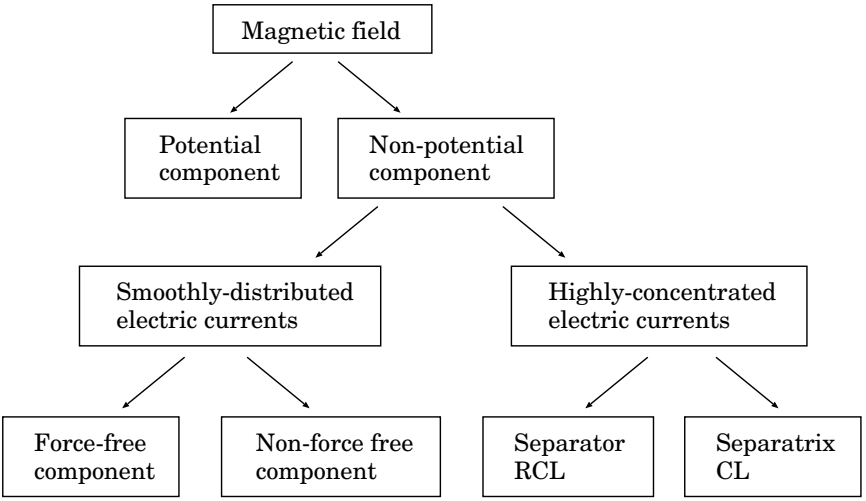

Figure 14.9: Main types of the magnetic field in an active region according to their physical properties.

lines of the potential field are connected back again via reconnection. This behaviour is important for understanding the so-called eruptive flares. In the strong field approximation, the magnetic field, changing in time, sets the solar plasma in motion. Such a motion can be described by the set of the ordinary differential equations. They are much simpler than the partial derivative equations of the usual MHD. This is a natural simplicity of the actual conditions in the solar atmosphere. In order to solve the simplified MHD equations, we have to find the potential field as a function of time. This is not difficult.

Second, since no energy can be taken from the current-free field, the current-carring components have to be unavoidably introduced in the large-flare modeling to explain accumulation of energy before a flare and its release in the flare process. We assume here that the solar flare is the phenomenon which takes its energy during the flare from some volume in the corona.

14.5.2 Classification of non-potential fields

The non-potential parts of the field are related to electric currents in the solar corona. It is of principal importance to distinguish the currents of different origin (Figure 14.9) because they have different physical proper-

ties and, as a consequence, different behaviours in the pre-flare and flare processes. The actual currents conventionally comprise two different types:

(a) the *smoothly-distributed* currents that are necessarily parallel or nearly parallel to the field lines, so the magnetic field is locally force-free (FFF) or nearly force-free;

(b) the *strongly-concentrated* electric currents like a RCL at separators and a current layer (CL) at separatrices.

It was a question whether or not it is possible to explain the pre-flare energy storage in a FFF, i.e. only with electric currents aligned with the magnetic field lines. If this could be true, we would expect an explosive opening of such a configuration with fast release of the excess energy. As mentioned above, the coronal fields can be considered as strong (and as a consequence the FFF or potential) only in some range of heights: starting from the photosphere up to a height in the corona where solar wind becomes fast enough to influence the magnetic field. Hence the corona has an upper boundary which is essential for the coronal field structure (Somov and Syrovatskii, 1972). The coronal fields are never completely open or completely closed (Low and Smith, 1993). Their energy is always lower than the Aly-Sturrock limit but higher than the energy of a potential field (Antiochos et al., 1999).

If we recognize the low efficiency of the FFF in *eruptive* solar flares, we have to assume that the currents flowing *across* the field lines allow the corona to have a magnetic energy in excess of some limit (lower than the Aly-Sturrock limit) to drive an eruptive flare. These currents can, in principle, be generated by any non-magnetic force – for example, the gravity force, the gradient of gas pressure or forces of the inertia origin.

Two problems arise, however, in this aspect: (a) in the strong magnetic field, such forces are normally relatively weak in comparison with the magnetic force in the corona, at least in large scales; (b) the smoothly-distributed currents dissipate too slowly in a low-resistivity plasma. So the highly-concentrated currents are necessary to explain an extremely high power of energy release in the impulsive phase of a flare. The RCLs may allow an active region to overcome both difficulties.

In a low-resistivity plasma, the thin CLs appear to hinder a redistribution of interacting magnetic fluxes (see the fourth line in Figure 14.9). They appear at separators in the corona, where reconnection redistributes the fluxes so that the field remains nearly potential. Since resistivity is extremely low, only very slow reconnection proceeds in such a RCL which we call it a slowly-reconnecting RCL. The wider the layer, the larger the magnetic energy is accumulated in the region of the interacting fluxes.

There is a principal difference between the RCL at a separator and the CL at separatrices. It is impossible to consider the RCL as a one-

dimensional discontinuity because the plasma coming into the RCL has to be compensated by plasma outflow from it. As for the CL generated at separatrices, it represents the current distribution typical for the MHD tangential discontinuities which are non-evolutionary; they are always spreading out in both directions from separatrix surfaces into surrounding plasma. On the contrary, the current density inside the RCL usually grows with time and reaches one or another limit. For example, wave excitation begins and wave-particle interaction becomes efficient to produce high resistivity, or the collisionless dynamic dissipation allows the fast process of collisionless reconnection.

Therefore the potential field determines a large-scale structure of the flare-active regions while the RCL at separators together with the other non-potential components of magnetic field determine energetics and dynamics of a large eruptive flare.

14.6 To the future observations by *Solar-B*

Magnetic reconnection of electric currents generated by shearing flows in the photosphere may play significant role in the energetics of solar flares related to *observed* photospheric shear. Thanks to a huge database collected by *Yohkoh*, *TRACE*, *RHESSI*, and othe satellites, it was found that an active region creates the large two-ribbon flares as well as it is the most eruptive when the active region grows in size and exhibit an S-shaped loop structure or sigmoid structure (see Sections 3.2.3 and 3.2.4). On the other hand, other flares may be not so large and may not have any significant shear. So they have a different kind of electric currents related, for example, to diverging and converging flows in the photosphere near the region of a newly emerging flux, which we called the first class displacements.

To understand the relative role of different electric currents in the energetics and dynamics of an active region,

> it is necessary to study the evolution of its magnetic structure in and above the photosphere.

This would allow us to determine not only the magnetic fluxes of certain magnetic links but also their changes – redistribution and reconnection. Such a study would also give us an information, at least qualitative, about the structure and evolution of the electric field in an active region.

Three experiments will be flown on the Japan Institute of Space and Astronautical Science (ISAS) *Solar-B* mission planned for launch in 2006. The objective of *Solar-B* is to study the origin of the corona and the coupling

between the fine magnetic structure in the photosphere and the dynamic processes occuring in the corona.

The *Solar-B* payload consists of three high-resolution solar telescopes in visible light, soft X-ray, and extreme ultra-violet (EUV) wavelengths: (a) a 50-cm optical telescope, the *Solar Optical Telescope* (SOT), with sophisticated focal plane instrumentation, the *Focal Plane Package* (FPP); (b) an X-ray telescope (XRT) for imaging the high-temperature coronal plasma with a wide field of view covering the whole Sun and with an improved angular resolution, approximately 1 arcsec, i.e. a few times better than *Yohkoh*'s SXR telescope; and (c) an EUV imaging spectrometer (EIS) for diagnosing events observed.

The telescope SOT will give quantitative measurements of the magnetic fields in features as small as 100 km in size thereby providing 10 times better resolution than other space- and ground-based magnetic field measurements. So the SOT instrument will give us opportunity to observe the Sun continuously with the level of resolution that ground-based observations can match only under exceptionally good conditions. SOT aims at measuring the magnetic field and the Doppler velocity field in the photosphere.

Placed in a sun-synchronous circular orbit with altitude 600 km and inclination 97.9 degrees, which will keep the instruments in continuous sunlight with no day/night cycle for nine months each year, the *Solar-B* satellite will carry out multi-wavelength observation in optical, EUV, and X-ray ranges. This will give an important contribution to the main goal of the *Solar-B* project: understanding the origin and dynamics of the basic magnetic structures and their effects on the solar corona. So we shall be able to understand comprehensively the solar photosphere and the corona, as a system.

This page intentionally blank

Epilogue

Most of the known matter in the Universe is in an ionized state, and many naturally occuring plasmas, such as the atmosphere of the Sun and magnetic stars, the magnetospheres of the Earth and other planets, the magnetospheres of pulsars and other relativistic objects, galactic and extragalactic jets, exibit distinctively plasma-dynamical phenomena arising from the effects of magnetic and electric forces. The science of *plasma astrophysics* was born and developed to provide an understanding of these naturally occurring plasmas and those which will be discovered and investigated in future space observations. With this aim, from the very beginning, **many of the conceptual tools** and many different approaches were introduced and developed in the course of general fundamental research on the plasma state or independently. How can we understand the interconnection between different descriptions of astrophysical plasma behavior?

I was frequently asked by my students to give them a quick introduction to the theory of astrophysical plasma. It turned out that it is not easy to do for many reasons. The most important of them is that the usual way of such an introduction is generalization. This means that we go from simple well-known things to more complicated ones, for example, we generalize the ordinary hydrodynamics to magnetohydrodynamics. Though this way certainly makes a textbook easier to read, it does not give the reader complete knowledge of the subject, the tools esspecially. For a long time, my goal was to write a book which I would myself had liked when I first took up the subject, plasma astrophysics, and which I could recommend to my students to provide them an **accessible introduction** to plasma astrophysics at least at an intuitive level of the basic concepts.

We began a long journey together, when we first started such a book, "Plasma Astrophysics. I. Fundamentals and Practice" (referred in the text as vol. 1), and we are now almost at that journey's end, book "Plasma Astrophysics. 2. Reconnection and Flares".

A unifying theme of the first book (vol. 1) was the attempt at a deeper understanding of the underlying physics. Starting from the most general

physical principles, we have seen the consecutive simplifications of them and of simplifying assumptions which allowed us to obtain a simpler description of plasma under cosmic conditions. In so doing, the boundaries of the domain of applicability for the approximation at hand were well outlined from the viewpoint of physics and possible applications.

On the basis of this approach we can find the answers to the key questions: (1) what approximation is the simplest but a sufficient one for a description of a phenomenon in astrophysical plasma; (2) how to build an adequate model for the phenomenon, for example, a solar flare.

Practice is really important in the theory of astrophysical plasma; related exercises (problems and answers supplemented to each chapter) surved to better understanding of its physics. Most of the problems for students have been used as homework in the lecture course. A particular feature of the problems is that they widely range in difficulty from fairly straightforward (useful for an exam) to quite challenging. This property is not an advantage or disadvantage of the book but rather **a current state of modern astrophysics**.

As for applications, evidently preference was given to physical processes in the solar plasma. The Sun is unique in the astrophysical realm for the great diversity of the diagnostic data that are available. Much attention to solar plasma physics was and will be conditioned by the possibility of the all-round observational test of theoretical models.

Some fourty-fourty five years ago it was still possible, as Alfvén and Fälthammar (1963) so ably demonstrated, to write a single book on cosmic plasma theory concerning practically everything worth knowing of the subject. The subsequent development has been explosive, and today a corresponding comprehensive coverage would require a hole library. The present book is an earnest attempt to a general overview of the whole area but big gaps unavoidably appear. Important and interesting effects and problems have been skipped because I either felt to go too far beyond an introductory text for students or, worse, I have not been aware of them.

> There would be infinitely more to say about new space observations, modern numerical simulations, and analytical investigations of astrophysical plasma.

Any reader who, after having read this book, would like to become acquainted with profound results of astrophysical plasma should keep this fact in mind. I hope, however, that he/she, having learned sufficiently many topics of this textbook, will willingly and easily fill the gaps. Good luck!

Appendix 1. Acronyms

Acronym	*Meaning*
ACE	Advanced Composition Explorer
CME	coronal mass ejection
CDS	Coronal Diagnostic Spectrometer
EIT	Extreme ultraviolet Imaging Telescope
FFF	force free (magnetic) field
FIP	first ionization potential
GOES	Geostationary Operational Environmental Satellite
GONG	Global Oscillation Network Group
LDE	long duration event
MDI	Michelson Doppler Imager
PNL	polarity inversion line (of the photospheric magnetic field)
RCL	reconnecting current layer
RHESSI	Reuven Ramaty High Energy Solar Spectroscopic Imager
SHTCL	super-hot turbulent-current layer
SNL	simplified neutral line (of the photospheric magnetic field)
SOHO	Solar and Heliospheric Observatory
SEPs	solar energetic particles
TRACE	Transition Region and Coronal Explorer
VLA	Very Large Array

This page intentionally blank

Appendix 2. Notation

Latin alphabet

Symbol	*Description*	*Introduced in Section (Formula)*
$\mathbf{A}$	vector potential of a magnetic field	1.1
d	thickness of non-adiabatic region	9.1
h	magnetic field gradient	1.1
H	Hamiltonian	9.2
$\mathcal{H}$	magnetic helicity	12.1
K	curvature of a magnetic field line	9.2
l	current layer length	13
$L(T)$	radiative loss function	13
$\mathbf{u}$	electric current velocity	2.3
V	velocity of the plasma flow	13
V_{a}	gradient of the Alfvén speed	2.1
x	ionisation degree	13

Greek alphabet

Symbol	*Description*	*Introduced in Section (Formula)*
ε	dimensionless electric field	9.1
ε_α	small parameter of expansion	10.3
ν_{ni}	neutral-ion mean collisional frequency	13
ξ	displacement of a current layer	10.3
$\xi_\parallel$	dimensionless longitudinal magnetic field	9.1
$\xi_\perp$	dimensionless transverse magnetic field	9.1
$\boldsymbol{\xi}$	displacement of the medium	2.1
Π	work against the Lorentz force	11.4
τ_r	reconnection time scale	14.4

Appendix 3
Useful Formulae

The most important characteristics of astrophysical plasmas (for more detail see vol. 1, Plasma Astrophysics: Fundamental and Practice)

Alfvén speed

$$V_{\rm A} = \frac{B}{\sqrt{4\pi\rho}} \approx 2.18 \times 10^{11}\, \frac{B}{\sqrt{n}}\ ,\ \ {\rm cm\ s^{-1}}\,.$$

Conductivity of magnetized plasma

$$\sigma_{\,\parallel} = \sigma = \frac{e^2 n}{m_{\rm e}}\ \tau_{\rm ei} \approx 2.53 \times 10^8\, n\,({\rm cm^{-3}})\,\tau_{\rm ei}\,({\rm s})\,,\ \ {\rm s^{-1}}\,,$$

$$\sigma_\perp = \sigma\ \frac{1}{1 + \left(\omega_{\rm B}^{\rm (e)}\,\tau_{\rm ei}\right)^2}\,, \qquad \sigma_{\rm H}\ = \sigma\ \frac{\omega_{\rm B}^{\rm (e)}\,\tau_{\rm ei}}{1 + \left(\omega_{\rm B}^{\rm (e)}\,\tau_{\rm ei}\right)^2}\,.$$

Coulomb logarithm

$$\ln\Lambda = \ln\left[\left(\frac{3k_{\rm B}^{3/2}}{2\pi^{1/2}\,e^3}\right)\left(\frac{T_{\rm e}^3}{n_{\rm e}}\right)^{1/2}\right] \approx \ln\left[1.25\times 10^4\ \left(\frac{T_{\rm e}^3}{n_{\rm e}}\right)^{1/2}\right]\,.$$

Cyclotron frequency (or gyrofrequency)

$$\omega_{\rm B} = \frac{ecB}{\mathcal{E}}\,.$$

Debye radius ($T_{\rm e} = T\,,\ T_{\rm i} = 0$ or $T_{\rm e} \gg T_{\rm i}$)

$$r_{\rm D} = \left(\frac{k_{\rm B}T}{4\pi\, ne^2}\right)^{1/2}\,.$$

Debye radius in electron-proton thermal plasma ($T_\mathrm{e} = T_\mathrm{p} = T$)

$$r_{_\mathrm{D}} = \left(\frac{k_{_\mathrm{B}} T}{8\pi\, e^2\, n}\right)^{1/2} \approx 4.9 \left(\frac{T}{n}\right)^{1/2} \ , \ \mathrm{cm}\,.$$

Dreicer electric field

$$E_{_\mathrm{Dr}} = \frac{4\pi e^3 \ln\Lambda}{k_{_\mathrm{B}}} \frac{n_\mathrm{e}}{T_\mathrm{e}} \approx 6.54 \times 10^{-8}\ \frac{n_\mathrm{e}}{T_\mathrm{e}}\,,\ \mathrm{V\,cm^{-1}}\,.$$

Drift velocity

$$\mathbf{v}_\mathrm{d} = \frac{c}{e}\ \frac{\mathbf{F}\times\mathbf{B}}{B^2}\,.$$

Electric drift velocity

$$\mathbf{v}_\mathrm{d} = c\ \frac{\mathbf{E}\times\mathbf{B}}{B^2}\,.$$

Electric field in magnetized plasma

$$E \approx \frac{1}{c}\, vB \approx 10^{-8}\ v\,(\mathrm{cm\ s^{-1}})\, B\,(\mathrm{G})\,,\ \ \mathrm{V\ cm^{-1}}\,.$$

Electron plasma frequency

$$\omega_{pl}^{(\mathrm{e})} = \left(\frac{4\pi\, e^2\, n_\mathrm{e}}{m_\mathrm{e}}\right)^{1/2} \approx 5.64 \times 10^4\ \sqrt{n_\mathrm{e}}\ ,\ \ \mathrm{rad\ s^{-1}}\,.$$

Electron-ion collision (energy exchange) time

$$\tau_{\mathrm{ei}}\,(\mathcal{E}) = \frac{m_\mathrm{e} m_\mathrm{i}\,[\,3k_{_\mathrm{B}}\,(T_\mathrm{e}/m_\mathrm{e} + T_\mathrm{i}/m_\mathrm{i})\,]^{3/2}}{e_\mathrm{e}^2\, e_\mathrm{i}^2\,(6\pi)^{1/2}\, 8\,\ln\Lambda}\,.$$

Gradient drift velocity

$$\mathbf{v}_\mathrm{d} = \frac{\mathcal{M}c}{eB}\ \mathbf{n}\times\nabla B\,.$$

Larmor frequency of a non-relativistic electron

$$\omega_{_\mathrm{B}}^{(\mathrm{e})} = \frac{eB}{m_\mathrm{e} c} \approx 1.76 \times 10^7\, B\,(\mathrm{G})\,,\ \ \mathrm{rad\ s^{-1}}\,.$$

Larmor frequency of a non-relativistic proton

$$\omega_{_\mathrm{B}}^{(\mathrm{p})} \approx 9.58 \times 10^3\ B\,(\mathrm{G})\,,\ \ \mathrm{rad\ s^{-1}}\,.$$

Larmor radius of a non-relativistic electron

$$r_{_\mathrm{L}}^{(\mathrm{e})} = \frac{cp_\perp}{eB} \approx 5.69 \times 10^{-8}\ \frac{v\,(\mathrm{cm\,s^{-1}})}{B\,(\mathrm{G})}\,,\ \ \mathrm{cm}\,.$$

Larmor radius of a non-relativistic proton

$$r_{\rm L}^{\rm (p)} \approx 1.04 \times 10^{-4}\ \frac{v\,({\rm cm\,s^{-1}})}{B\,({\rm G})}\,,\ \ {\rm cm}\,.$$

Larmor radius of a non-relativistic *thermal* electrons

$$r_{\rm L}^{\rm (e)} = \frac{V_{\rm Te}}{\omega_{\rm B}^{\rm (e)}} \approx 3.83 \times 10^{-2}\ \frac{\sqrt{T_{\rm e}\,({\rm K})}}{B\,({\rm G})}\,,\ \ {\rm cm}\,.$$

Larmor radius of a non-relativistic *thermal* protons

$$r_{\rm L}^{\rm (p)} = \frac{V_{\rm Tp}}{\omega_{\rm B}^{\rm (p)}} \approx 1.64\ \frac{\sqrt{T_{\rm p}\,({\rm K})}}{B\,({\rm G})}\,,\ \ {\rm cm}\,.$$

Lundquist number

$$N_{\rm L} = {\rm Re_m}(V_{\rm A}, L) = \frac{V_{\rm A} L}{\nu_{\rm m}}\,.$$

Magnetic diffusivity (or viscosity)

$$\nu_{\rm m} = \frac{c^2}{4\pi\sigma} \approx 7.2 \times 10^{19}\ \frac{1}{\sigma}\,,\ \ {\rm cm^2\,s^{-1}}\,.$$

Magnetic moment of a particle on the Larmor orbit

$$\mathcal{M} = \frac{1}{c}\,JS = \frac{e\,\omega_{\rm B}\,r_{\rm L}^{\,2}}{2c} = \frac{p_\perp^2}{2mB} = \frac{\mathcal{E}_\perp}{B}\,.$$

Magnetic Reynolds number

$${\rm Re_m} = \frac{L^2}{\nu_{\rm m}\,\tau} = \frac{vL}{\nu_{\rm m}}$$

Mean thermal velocity of electrons

$$V_{\rm Te} = \left(\frac{3k_{\rm B}\,T_{\rm e}}{m_{\rm e}}\right)^{1/2} \approx 6.74 \times 10^5\,\sqrt{T_{\rm e}\,({\rm K})}\,,\ \ {\rm cm\ s^{-1}}\,.$$

Mean thermal velocity of protons

$$V_{\rm Tp} \approx 1.57 \times 10^4\,\sqrt{T_{\rm p}\,({\rm K})}\,,\ \ {\rm cm\ s^{-1}}\,.$$

Sound speed in electron-proton plasma

$$V_s = \left(\gamma_g\,\frac{p}{\rho}\right)^{1/2} \approx 1.66 \times 10^4\,\sqrt{T({\rm K})}\,,\ \ {\rm cm\ s^{-1}}\,.$$

Thermal electron collisional time

$$\tau_{\rm ee} = \frac{m_{\rm e}^2}{0.714\ e^4\, 8\pi\ \ln\Lambda}\ \frac{V_{\rm Te}^3}{n_{\rm e}} \approx 4.04\times 10^{-20}\ \frac{V_{\rm Te}^3}{n_{\rm e}}\ ,\ \ {\rm s}\,.$$

Thermal proton collisional time

$$\tau_{\rm pp} = \frac{m_{\rm p}^2}{0.714\ e^4\, 8\pi\ \ln\Lambda}\ \frac{V_{\rm Tp}^3}{n_{\rm p}} \approx 1.36\times 10^{-13}\ \frac{V_{\rm Tp}^3}{n_{\rm p}}\ ,\ \ {\rm s}\,.$$

Time of energy exchange between electrons and protons

$$\tau_{\rm ep}\,(\mathcal{E}) \approx 22\,\tau_{\rm pp} \approx 950\,\tau_{\rm ee}\,.$$

Appendix 4. Constants

Fundamental physical constants

Speed of light	c	2.998×10^{10} cm s^{-1}
Electron charge	e	4.802×10^{-10} CGSE
Electron mass	m_e	9.109×10^{-28} g
Proton mass	m_p	1.673×10^{-24} g
Boltzmann constant	$k_{\rm B}$	1.381×10^{-16} erg K^{-1}
Gravitational constant	G	6.673×10^{-8} dyne cm^2 g^{-2}
Planck's constant	h	6.625×10^{-27} erg s

Some useful constants and units

Ampere (current)	A	3×10^9 CGSE
Angström (length)	A	10^{-8} cm
Electron Volt (energy)	eV	1.602×10^{-12} erg
	eV	11605 K
Gauss (magnetic induction)	G	3×10^{10} CGSE
Henry (inductance)	H	1.111×10^{-12} s^2 cm^{-1}
Ionization potential of hydrogen		13.60 eV
Joule (energy)	J	10^7 erg
Maxwell (magnetic flux)	M	3×10^{10} CGSE
Ohm (resistance)	Ω	1.111×10^{-12} s cm^{-1}
Tesla (magnetic induction)		10^4 Gauss
Volt (potential)	V	3.333×10^{-3} CGSE
Watt (power)	W	10^7 erg s^{-1}
Weber (magnetic flux)	Wb	10^8 Maxwell

Some astrophysical constants

Astronomical unit	AU	1.496×10^{13} cm
Mass of the Sun	$M_\odot$	1.989×10^{33} g
Mass of the Earth	M_E	5.98×10^{27} g
Solar radius	$R_\odot$	6.960×10^{10} cm
Solar surface gravity	$g_\odot$	2.740×10^{4} cm s^{-2}
Solar luminosity	$L_\odot$	3.827×10^{33} erg s^{-1}
Mass loss rate	$\dot{M}_\odot$	10^{12} g s^{-1}
Rotation period of the Sun	$T_\odot$	26 days (at equator)

Bibliography

Each reference is cited in the Sections of the book indicated within square brackets.

Acton, L.: 1996, Coronal structures, local and global, in *Magnetohydrodynamic Phenomena in the Solar Atmosphere: Prototypes of Stellar Magnetic Activity*, eds Y. Uchida, T. Kosugi, and H. Hudson, Dordrecht, Kluwer Academic Publ., p. 3–11. [§ 12.4]

Acton, L., Tsuneta, S., Ogawara, Y., et al.: 1992, The *Yohkoh* mission for high-energy solar physics, *Science*, v. 258, No. 5082, 618–625. [Intr., § 3.2, § 4.1]

Akimov, V.V., Ambroz, P., Belov, A.V., et al.: 1996, Evidence for prolongated acceleration in the solar flare of June 15, 1991, *Solar Phys.*, v. 166, No. 1, 107–134. [§ 9.4]

Alfvén, H. and Carlqvist, P.: 1967, Currents in solar atmosphere and a theory of flares, *Solar Phys.*, v. 1, No. 1, 220–228. [§ 14.2]

Altyntsev, A.T., Krasov, V.I., and Tomozov V.M.: 1977, Magnetic field dissipation in neutral current sheets, *Solar Phys.*, v. 55, No. 1, 69–81. [§ 3.3]

Aly, J.J.: 1984, On some properties of force-free fields in infinite regions of space, *Astrophys. J.*, v. 283, No. 1, 349–362. [§ 14.2]

Aly, J.J.: 1991, How much energy can be stored in a force-free field? *Astrophys. J.*, v. 375, No. 1, L61–L64. [§ 14.2]

Anderson, J.E.: 1963, *Magnetohydrodynamic Shock Waves*, Cambridge, Massachusetts; M.I.T. Press, p. 226. [§ 10.2]

Anosov, D.V.: 1969, *Geodesic Flows on Closed Riemannian Manifolds with Negative Curvature*, Providence, Amer. Math. Soc., p. 235. [§ 9.2]

Antiochos, S.K.: 1998, The magnetic topology of solar eruptions, *Astrophys. J.*, v. 502, L181–L184. [§ 3.2, § 3.4, § 6.4]

Antiochos, S.K., Karpen, J.T., and DeVore, C.R.: 1996, The nature of magnetic reconnection in the corona, in *Magnetic Reconnection in the*

Solar Atmosphere, eds R.D. Bentley and J.T. Mariska, Astron. Soc. of Pacific, Conf. Series, v. 111, p. 79–81. [§ 3.3, § 10.1]

Antiochos, S.K., DeVore, C.R., and Klimchuk, J.A.: 1999, A model for solar coronal mass ejections, *Astrophys. J.*, v. 510, No. 1, 485–493. [§ 5.5, § 14.5.2]

Antonucci, E., Benna, C., and Somov, B.V.: 1996, Interpretation of the observed plasma 'turbulent' velocities as a result of reconnection in solar flares, *Astrophys. J.*, v. 456, No. 2, 833–839. [§ 7.1, § 12.1]

Anwar, B., Acton, L.W., Hudson, H.S., et al.: 1993, Rapid sunspot motion during a major solar flare, *Solar Phys.*, v. 147, No. 2, 287–303. [§ 5.1.1]

Archontis, V., Moreno-Insertis, F., Galsgaard, K., et al.: 2005, The three-dimensional interaction between emerging magnetic flux and a large-scale coronal field: Reconnection, current sheets, and jets, *Astrophys. J.*, v. 635, No. 2, 1299–1318. [3.4.1]

Arge, C.N. and Mullan, D.J.: 1998, Modelling of magnetic interactions in partially-ionized gas, *Solar Phys.*, v. 182, No. 2, 293–332. [§ 13.4]

Asai, A., Ishii, T. T., Kurokawa, H., et al.: 2003, Evolution of conjugate footpoints inside flare ribbons during a great two-ribbon flare on 2001 April 10, *Astrophys. J.*, v. 586, 624–629. [5.4.1]

Aschwanden, M.J. and and Alexander, D.: 2001, Flare plasma cooling from 30 MK down to 1 MK modeled from *Yohkoh*, GOES, and TRACE observations during the Bastille day event (14 July 2000), *Solar Phys.*, v. 204, No. 1, 93–121. [§ 4.2.3, § 4.2.4, § 5.1]

Aschwanden, M.J., Kliem, B., Schwarz, U., et al.: 1998, Wavelet analysis of solar flare hard X-rays, *Astrophys. J.*, v. 505, No. 2, 941–956. [§ 7.3]

Aschwanden, M.J., Kosugi, T., Hanaoka, Y., et al.: 1999, Quadrupole magnetic reconnection in solar flares. I. Three-dimensional geometry inferred from *Yohkoh* observations, *Astrophys. J.*, v. 526, 1026-1045, [§ 6.4, § 7.2.3]

Aulanier, G., DeLuca, E.E., Antiochos, S.K., et al.: 2000, The topology and evolution of the Bastille day 1998 flare, *Astrophys. J.*, v. 540, No. 2, 1126–1142. [§ 3.4, § 5.5]

Ayres, T.R.: 1996, Thermal bifurcation of the solar chromosphere, in *Stellar Surface Structure*, eds K.G. Strassmeier and J.L. Linsky, IAU Symp. **176**, Dordrecht, Kluwer Academic Publ., p. 371–384. [§ 13.5]

Bagalá, L.G., Mandrini, C.H., Rovira, M.G., et al.: 1995, A topological approach to understand a multi-loop flare, *Solar Phys.*, v. 161, No. 1, 103–121. [Intr., § 3.4, § 6.4, § 14.2]

Bai, T. and Sturrock, P.A.: 1989, Classification of solar flares, *Ann. Rev. Astron. Astrophys.*, v. 27, 421–467. [§ 9.1, § 9.4]

Bai, T., Hudson, H.S., Pelling, R.M., et al.: 1983, First-order Fermi acceleration in solar flares as a mechanism for the second-step acceleration

of protons and electrons, *Astrophys. J.*, v. 267, No. 1, 433–441. [§ 7.3]

Barnes, G., Longcope, D.W., and Leka, K.D.: 2005, Implementing a magnetic charge topology model for solar active regions, *Astrophys. J.*, v. 629, No. 1, 561-571. [§ 3.2.3]

Barret, D., Olive, J.F., Boirin, L., et al.: 2000, Hard X-ray emission from low-mass X-ray binaries, *Astrophys. J.*, v. 533, 329-351. [§ 8.3]

Batchelor, G.K.: 1950, On the spontaneous magnetic field in a conducting liquid in turbulent motion, *Proc. Royal Soc.*, v. A201, 405–416. [§12.1]

Baum, P.J., Bratenahl, A., and Kamin, G.: 1978, Current interruption and flux transfer solar flare models, *Astrophys. J.*, v. 226, No. 1, 286–300. [§ 3.3, § 14.2]

Bednarek, W. and Protheroe, R.J.: 1999, Gamma-ray and neutrino flares produced by protons accelerated on an accretion disc surface in active galactic nuclei, *Mon. Not. Royal Astron. Soc.*, v. 302, 373–380. [§ 8.3]

Begelman, M.C., Blandford, R.D., and Rees, M.J.: 1984, Theory of extragalactic radio sorces, *Rev. Mod. Phys.*, v. 56, No. 2, 255–351. [Intr.]

Bentley, R.D., Klein, K.-L., van Driel-Gesztelyi, L., et al.: 2000, Magnetic activity associated with radio noise storms, *Solar Phys.*, v. 193, No. 1-2, 227–245. [§ 3.4]

Benz, A.: 2002, *Plasma Astrophysics: Kinetic Processes in Solar and Stellar Coronae, Second Edition*, Dordrecht, Kluwer Academic Publ., p. 299. [§ 4.2.5, § 7.4.4, § 7.5]

Benz, A. and Krucker, S.: 1998, Heating events in the quiet solar corona, *Solar Phys.*, v. 182, No. 2, 349–363. [§ 12.4]

Benz, A. and Krucker, S.: 1999, Heating events in the quiet solar corona: Multiwavelength correlations, *Astron. Astrophys.*, v. 341, No. 1, 286–295. [§ 12.4]

Benz, A.O., Lin, R.P., Sheiner, O.A., et al.: 2001, The source regions of impulsive solar electron events, *Solar Phys.*, v. 203, No. 1, 131–144. [§ 9.4]

Berger, M.A.: 1984, Rigorous limits on magnetic helicity dissipation in the solar corona, *Geophys. Astrophys. Fluid Dyn.*, v. 30, No. 1, 79–104. [§ 12.1]

Berger, M.A.: 1988a, Three-dimensional reconnection from a global viewpoint, in *Reconnection in Space Plasma*, eds T.D. Guyenne and J.J. Hunt, ESA SP-285, v. 2, p. 83–86. [§ 12.1, § 14.2]

Berger, M.A.: 1988b, An energy formula for nonlinear force-free fields, *Astron. Astrophys.*, v. 201, No. 1, 355–361. [§ 12.1, § 12.2]

Berger, M.A.: 1994, Coronal heating by dissipation of magnetic structure, *Space Sci. Rev.*, v. 68, No. 1, 3–14. [§ 12.2]

Birk, G.T. and Otto, A.: 1991, The resistive tearing instability for generalized resisitivity models, *Phys. Fluids*, v. 3, No. B7, 1746–1754. [§ 11.1]

Biskamp, D.: 1986, Magnetic reconnection via current sheets, *Phys. Fluids*, v. 29, No. 5, 1520–1531. [§ 3.2, § 10.1, § 10.5]

Biskamp, D.: 1994, Resistive and collisionless magnetic reconnection, in *Plasma Astrophysics*, eds C. Chiudery and G. Einaudi, pp. 1-29, Berlin, Springer-Verlag. [§ 6.4]

Biskamp, D.: 1997, *Nonlinear Magnetohydrodynamics*, Cambridge Univ. Press, p. 378. [§ 3.2, § 6.1, § 10.1, § 10.5]

Bogachev, S.A., Somov, B.V., and Masuda, S.: 1998, On the velocity of a hard X-ray source in the solar corona. *Astronomy Letters*, v. 24, No. 4, 543–548. [§ 7.3]

Bogachev, S.A., Somov, B.V., Kosugi, T., et al.: 2005, The motions of the hard X-ray sources in solar flares: Images and statistics, *Astrophys. J.*, v. 630, No. 1, 561–572. [§ 5.4.5]

Bogdanov, S.Yu., Frank, A.G., Kyrei, N.P., et al.: 1986, Magnetic reconnection, generation of plasma fluxes and accelerated particles in laboratory experiments, in *Plasma Astrophys.*, ESA SP-251, 177-183. [§ 3.3]

Bogdanov, S.Yu., Kyrei, N.P., Markov, V.S., et al.: 2000, Current sheets in magnetic configurations with singular X-lines, *JETP Letters*, v. 71, No. 2, 78–84. [3.3]

Borovsky, J.E. and Funsten, H.O.: 2003, MHD turbulence in the Earth's plasma sheet: Dynamics, dissipation, and driving, *J. Geophys. Res.*, v. 108, No. A7, 1284–1293. [§ 12.1.3]

Brandenburg, A.: 2001, An inverse cascade and nonlinear α-effect in simulations of isotropic helical hydromagnetic turbulence, *Astrophys. J.*, v. 550, No. 2, 824–840. [§ 12.1]

Brandenburg, A. and Subramanian, K.: 2000, Large scale dynamos with ambipolar diffusion nonlinearity, *Astron. Astrophys.*, v. 361, L33-L36. [§ 12.1]

Brissaud, A., Frisch, U., Leorat, J., et al.: 1973, Helicity cascades in fully developed isotropic turbulence, *Phys. Fluids*, v. 16, 1366-1367. [§ 12.1]

Browning, P.K.: 1988, Helicity injection and relaxation in a coronal magnetic loop with a free surface, *J. Plasma Phys.*, v. 40, No. 2, 263–280. [§ 12.2]

Brushlinskii, K.V., Zaborov, A.M., and Syrovatskii, S.I.: 1980, Numerical analysis of the current sheet near a magnetic null line, *Soviet J. Plasma Physics*, v. 6, No. 2, 165–173. [§ 3.2, § 3.3, § 10.1, § 10.5]

Büchner, J. and Zelenyi, L.: 1989, Regular and chaotic particle motion in magnetotail field reversal, *J. Geophys. Res.*, v. 94, No. A9, 11821–11842. [§ 9.2]

Canfield, R.C., Hudson, H.S., and McKenzie, D.E.: 1999, Sigmoidal morphology and eruptive solar activity, *Geophys. Res. Lett.*, v. 26, No. 6, 627–630. [§ 3.2]

Cattaneo, F.: 1999, On the origin of magnetic fields in the quiet photosphere, *Astrophys. J.*, v. 515, No. ?, L39–L42. [§ 12.1]

Chae, J., Wang, H., Qiu, J., et al.: 2001, The formation of a prominence in active region NOAA 8668. 1. SOHO/MDI observations of magnetic field evolution, *Astrophys. J.*, v. 560, No. 1, 476–489. [§ 5.3]

Chapman, S. and Kendall, P.C.: 1963, Liquid instability and energy transformation near magnetic neutral line. A soluble non-linear hydromagnetic problem, *Proc. Roy. Soc. London*, v. A271, 435–448. [§ 2.4]

Chen, J. and Palmadesso, P.J.: 1986, Chaos and nonlinear dynamics of single particle orbits in a magnetotail field, *J. Geophys. Res.*, v. 91, No. A2, 1499–1508. [§ 9.2]

Cho, J. and Vishniac, E.T.: 2000a, The anisotropy of magnetohydrodynamic Alfvenic turbulence, *Astrophys. J.*, v. 539, No. 1, 273–282. [§ 12.1]

Cho, J. and Vishniac, E.T.: 2000b, The generation of magnetic fields through driven turbulence, *Astrophys. J.*, v. 538, No. 1, 217–225. [§ 12.1]

Chupp, E.L.: 1996, in *High Energy Solar Physics*, eds R. Ramaty, N. Mandzhavidze, and X.-M. Hua, AIP Conf. Proc. 374, AIP, Woodbury, New York, 3–9, 1996. [§ 9.4]

Colgate, S.A.: 1988, Relationship between high-energy phenomena on the Sun and in astrophysics, *Solar Phys.*, v. 118, No. 1, 1–15. [§ 9.4]

Colgate, S.A. and Furth, H.P.: 1960, Stabilization of pinch discharges, *Phys. Fluids*, v. 3, No. 6, 982–1000. [§ 11.1]

Coppi, B., Laval, G., and Pellat, R.: 1966, Dynamics of the geomagnetic tail, *Phys. Rev. Lett.*, v. 6, No. 26, 1207–1210. [§ 11.1, § 11.6]

Cowley, S.W.H.: 1986, Magnetic reconnection, in *Solar System Magnetic Fields*, ed. E.R. Priest, Dordrecht, D. Reidel Publ., p. 121–134. [§ 1.2]

Cox, D.P. and Tucker, W.H.: 1969, Ionization equilibrium and radiative cooling of a low-density plasma, *Astrophys. J.*, v. 157, No. 3, 1157–1167. [§ 6.1.2]

Craig, I.J.D. and McClymont, A.N.: 1993, Linear theory of reconnection at an X-type neutral point, *Astrophys. J.*, v. 405, No. 1, 207–215. [§ 13.2.3]

Crooker, N., Joselyn, J.A., and Feynman, J. (eds): 1997, *Coronal Mass Ejections*, Washington, Amer. Geophys. Un., p. 299. [Intr.]

Crooker, N.U., Gosling, J.T., and Kahler, S.W.: 2002, Reducing heliospheric magnetic flux from coronal mass ejections without disconnection, *J. Geophys. Res.*, v. 107, No. A2, SSH 3-1. [§ 5.2.2]

Day, C.: 1998, SOHO observations implicate 'magnetic carpet' as source of coronal heating in quiet Sun, *Physics Today*, March issue, 19–21. [§ 12.4]

de Jager, C.: 1986, Solar flares and particle acceleration, *Space Sci. Rev.*, v. 44, No. 1, 43–90. [§ 12.1]

de Jager, C.: 2005, Solar forcing of climate. 1: Solar variability, *Space Sci. Rev.*, v. 120, No. 1, 197–241. [Intr., § 8.2.2]

de Kluiver, H., Perepelkin, N.F., and Hirose, A.: 1991, Experimental results on current-driven turbulence in plasmas - A survey, *Physics Reports* (Review Section of Physics Letters), v. 199, No. 6, 281-381. [§ 8.1]

Démoulin, P., van Driel-Gesztelyi, L., Schmieder, B., et al.: 1993, Evidence for magnetic reconnection in solar flares. *Astron. Astrophys.*, v. 271, No. 1, 292–307. [Intr., § 3.4, § 6.4, § 14.2]

Den, O.G. and Somov, B.V.: 1989, Magnetic field dissipation in a high-temperature plasma as a mechanism of energy release in a solar flare, *Soviet Astronomy–AJ*, v. 33, No. 2, 149–155. [§ 3.2, § 3.3, § 7.1, § 14.2]

Deng, Y., Wang, J., Yan, Y., et al.: 2001, Evolution of magnetic nonpotentiality in NOAA AR 9077, *Solar Phys.*, v. 204, No. 1, 13–28. [§ 4.2.4, § 5.1, § 5.5]

Dennis, B.R.: 1985, Solar hard X-ray bursts. *Solar Phys.*, v. 100, No. 2, 465–490. [§ 7.1]

Dennis, B.R.: 1988, Solar flare hard X-ray observations, *Solar Phys.*, v. 118, No. 1, 49–94. [§ 7.1]

Dobrowolny, M.: 1968, Instability of a neutral sheet, *Nuovo Cimento*, v. B55, No. 1, 427–438. [§ 9.3]

Domingo, V., Fleck, B., and Poland, A.A.: 1995, SOHO: the solar and heliospheric observatory, *Space Sci. Rev.*, v. 72, No. 1, 81–84. [Intr., § 4.1]

Dreicer, H.: 1959, Electron and ion runaway in a fully ionized gas, *Phys. Rev.*, v. 115, No. 2, 238–249. [§ 6.1]

Duijveman, A., Hoyng P., and Ionson, J.A.: 1981, Fast plasma heating by anomalous and inertial resistivity effects in the solar atmosphere, *Astrophys. J.*, v. 245, No. 2, 721–735. [§ 6.3]

Dungey, J.W.: 1958, *Cosmic Electrodynamics*, England, Cambridge Univ. Press, p. 183. [Intr., § 1.1, § 2.1, § 11.1, § 14.2]

Dungey, J.W.: 1961, Interplanetary magnetic field and the auroral zones, *Phys. Rev. Lett.*, v. 6, No. 2, 47–48. [§ 8.2]

Efthymiopoulos, C., Gontikakis, C., and Anastasiadis, A.: 2005, Particle dynamics in 3D reconnecting current sheets in the solar atmosphere, *Astron. Astrophys.*, v. 443, No. 2, 663–678. [§ 9.1.5]

Fang, C. and Ding, M.D.: 1995, On the spectral characteristics and atmosphere models of the two types of white-light flares, *Astron. Astrophys. Suppl.*, v. 110, No. 1, 99–106. [§ 13.2.1]

Field, G.B.: 1965, Thermal instability, *Astrophys. J.*, v. 142, No. 2, 531–567. [§ 3.3, § 6.1]

Fletcher, L.: 1995, On the generation of loop-top impulsive hard X-ray sources, *Astron. Astrophys.*, v. 303, No. 1, L9–L12. [§ 7.3.1]

Fletcher, L. and Hudson, H.: 2001, The magnetic structure and generation of EUV flare ribbons, *Solar Phys.*, v. 204, No. 1, 71–91. [§ 4.1, § 4.2.3, § 4.2.4, § 5.1]

Fletcher, L. and Hudson, H.: 2002, Spectral and spatial variations of flare hard X-ray footpoints, *Solar Phys.*, v. 210, No. 1, 307–321. [Intr., § 5.4.1]

Forbes, T.G. and Acton, L.W.: 1996, Reconnection and field line shrinkage in solar flares, *Astrophys. J.*, v. 459, No. 1, 330–341. [§ 4.1, § 4.2.4, § 5.4.1]

Froyland, J.: 1992, *Introduction to Chaos and Coherence*, Bristol, Philadelphia, Tokyo; Inst. of Phys. Publ., p. 156. [§ 9.2]

Furth, H.P.: 1961, Sheet pinch instabilities caused by finite conductivity, *Bull. Amer. Phys. Soc.*, v. 6, No. 2, p. 193. [§ 11.1]

Furth, H.P.: 1967, *Proc. ESRW Conf. of the Stability of Plane Plasmas*, Frascaty, Eur. Space Res. Inst., p. 22–25. [§ 11.1]

Furth, H.P., Killen, J., and Rosenbluth, M.N.: 1963, Finite-resistivity instabilities of a sheet pinch, *Phys. Fluids*, v. 6, No. 4, 459–484. [§ 4.2.4, § 11.1, § 11.2, § 11.3]

Galeev, A.A. and Zelenyi, L.M.: 1975, Metastable states of neutral sheet and the substorms, *JETP–Lett.*, v. 22, No. 7, 170–172. [§ 11.1, § 11.6]

Galeev, A.A. and Zelenyi, L.M.: 1976, Tearing instability in plasma configurations, *Soviet Physics–JETP*, v. 43, No. 6, 1113–1123. [§ 11.1, § 11.6]

Galeev, A.A., Rosner, R., and Vaiana, G.S.: 1979, Structured coronae of accretion discs, *Astrophys. J.*, v. 229, No. 1, 318–326. [Intr., § 8.3]

Gal'per, A.M., Zemskov, V.M., Luchkov, B.I., et al.: 1994, Temporal fine structure in hard γ radiation in solar flares, *JETP Lett.*, v. 59, No. 3, 153–157. [§ 9.4]

Galsgaard, K. and Longbottom, A.W.: 1999, Formation of solar prominences by flux convergence, *Astrophys. J.*, v. 510, No. 1, 444–459. [§ 13.3]

Giovanelli, R.G.: 1946, A theory of chromospheric flares, *Nature*, v. 158, No. 4003, 81–82. [Intr., § 1.1, § 14.2]

Giovanelli, R.G.: 1947, Magnetic and electric phenomena in the sun's atmosphere associated with sunspots, *Mon. Not. Royal Astron. Soc.*, v. 107, No. 4, 338–355. [§ 2.1, § 14.2]

Giovanelli, R.G.: 1948, Chromospheric flares, *Mon. Not. Royal Astron. Soc.*, v. 108, No. 2, 163–176. [§ 14.2]

Giuliani, P., Neukirch, T., and Wood, P.: 2005, Particle motion in collapsing magnetic traps in solar flares. 1. Kinematic theory of collapsing

magnetic traps, *Astrophys. J.*, v. 635, No. 1, 636–646. [§ 7.3.2, § 7.4.2]

Glover, A., Ranns, N.D.R., Harra, L.K., et al.: 2000, The onset and association of CMEs with sigmoidal active regions, *Geophys. Res. Lett.*, v. 27, No. 13, 2161–2164. [§ 3.2]

Gold, T.: 1964, Magnetic energy shedding in the solar atmosphere, in *AAS-NASA Symp. in the Physics of Solar Flares*, ed. W.N. Hess, NASA-SP 50, Washington DC, p. 389–396. [§ 12.4]

Gold, T. and Hoyle, F.: 1960, On the origin of solar flares, *Monthly Not. Royal Astron. Soc.*, v. 120, No. 2, 89–105. [§ 3.2, § 12.2, § 14.2]

Goldreich, P. and Sridhar, S.: 1997, Magnethydrodynamic turbulence revisited, *Astrophys. J.*, v, 485, No. 2, 680–688. [§ 12.1]

Golub, L., Bookbinder, J., DeLuca, E., et al.: 1999, A new view of the solar corona from the transition region and coronal explorer (TRACE), *Phys. Plasmas*, v. 6, No. 5, 2205–2212. [Intr.]

Gopasyuk, S.I.: 1990, Solar magnetic fields and large-scale electric currents in the active regions, *Adv. Space Res.*, v. 10, No. 9, 151–160. [§ 3.3]

Gorbachev, V.S. and Somov, B.V.: 1988, Photospheric vortex flows as a cause for two-ribbon flares: A topological model, *Solar Phys.*, v. 117, No. 1, 77–88. [§ 3.2, § 3.4, § 5.2.3]

Gorbachev, V.S. and Somov, B.V.: 1989, Solar flares of November 5, 1980, as the result of magnetic reconnection at a separator, *Soviet Astronomy–AJ*, v. 33, No. 1, 57–61. [Intr., § 3.2, § 3.4, § 5.4.2, § 6.4, § 14.3]

Gorbachev, V.S. and Somov, B.V.: 1990, Magnetic reconnection on the separator as a cause of a two-ribbon flare, *Adv. Space Res.*, v. 10, No. 9, 105–108. [Intr., § 3.2, § 3.4, § 4.2.3, § 6.4, § 14.3]

Gorbachev, V.S., Kel'ner, S.R., Somov, B.V., et al.: 1988, New topological approach to the question of solar flare trigger, *Soviet Astronomy–AJ*, v. 32, No. 3, 308–314. [§ 3.2, § 5.1]

Gosling, J.T., Birn, J., and Hesse, M.: 1995, Three-dimensional magnetic reconnection and the magnetic topology of coronal mass ejection events, *Geophys. Res. Lett.*, v. 22, No. 8, 869–872. [§ 5.2.2]

Groth, C.P.T., De Zeeuw, D.L., Gombosi, T.I., et al.: 2000, Global three-dimensional MHD simulation of a space weather event: CME formation, interplanetary propagation, and interaction with the magnetosphere, *J. Geophys. Res.*, v. 105, No. A11, 25053–25078. [§ 8.2]

Guckenheimer, J. and Holmes, P.: 1983, *Nonlinear Oscillations, Dynamical Systems and Bifurcations of Vector Fields*, New York, Springer-Verlag. [§ 11.6]

Gurevich, A.V.: 1961, On the theory of runaway electrons, *Soviet Physics–JETP*, v. 12, No. 5, 904–912. [§ 6.1]

Gurevich, A.V. and Zhivlyuk, Y.N.: 1966, Runaway electrons in a non-equilibrium plasma, *Soviet Physics–JETP*, v. 22, No. 1, 153–159. [§ 6.1]

Haisch, B.M., Strong, K.T., and Rodonò M.: 1991, Flares on the Sun and other stars, *Ann. Rev. Astron. Astrophys.*, v. 29, 275–324. [Intr.]

Haken, H.: 1978, *Synergetics*, New York, Springer-Verlag. [§ 11.6]

Hanslmeier, A.: 2002, *The Sun and Space Weather*, Dordrecht, Boston, London; Kluwer Academic Publ., p. 243. [Intr., § 8.2]

Hargreaves, J.K.: 1992, *The Solar-Terrestrial Environment*, Cambridge, UK; Cambridge Univ. Press, p. 420. [Intr.]

Harra-Murnion, L.K., Schmieder, B., van Driel-Gestelyi, L., et al.: 1998, Multi-wavelength observations of post flare loops in two long duration solar flares, *Astron. Astrophys.*, v. 337, 911–920. [§ 7.2.2]

Harris, E.G.: 1962, On a plasma sheath separating regions of oppositely directed magnetic field, *Nuovo Cimento*, v. 23, No. 1, 115–121. [§ 9.3, § 9.4, § 11.6]

Hénoux, J.-C. and Somov, B.V.: 1987, Generation and structure of the electric currents in a flaring activity complex, *Astron. Astrophys.*, v. 185, No. 1, 306–314. [§ 5.2.3, § 14.2]

Hénoux, J.-C. and Somov, B.V.: 1991, The photospheric dynamo. 1. Magnetic flux-tube generation, *Astron. Astrophys.*, v. 241, No. 2, 613–617. [§ 13.5, § 13.6]

Hénoux, J.-C. and Somov, B.V.: 1992, First ionization potential fractionation, in *Coronal Streamers, Coronal Loops, and Coronal and Solar Wind Composition*, Proc. First SOHO Workshop, ESA SP-348, p. 325–330. [§ 13.5]

Hénoux, J.-C. and Somov, B.V.: 1997, The photospheric dynamo. 2. Physics of thin magnetic flux tubes, *Astron. Astrophys.*, v. 318, No. 3, 947–956. [§ 13.5]

Hénoux, J.-C. and Somov, B.V.: 1999, Physics of thin flux tubes in a partially ionized atmosphere, in *Third Advances in Solar Physics Euroconference: Magnetic Fields and Oscillations*, eds B. Schmieder, A. Hofmann, and J. Staude, ASP Conference Series, v. 184, 55–59. [§ 13.5]

Hesse, M., Birn, J., Baker, D.N., and Slavin, J.A.: 1996, MHD simulation of the transition of reconnection from closed to open field lines, *J. Geophys. Res.*, v. 101, No. A5, 10805–10816. [§ 6.2]

Heyvaerts, J. and Priest, E.R.: 1984, Coronal heating by reconnection in DC current systems. A theory based on Taylor's hypothesis, *Astron. Astrophys.*, v. 137, No. 1, 63–78. [§ 12.2]

Hirano, Y., Yagi, Y., Maejima, Y., et al.: 1997, Self-organization and its effect on confinement in a reversed field pinch plasma, *Plasma Phys. Control. Fusion*, v. 39, No. 5A, A393–A400. [§ 12.1]

Hirose, S., Uchida, Y., Uemura, S., et al.: 2001, A quadruple magnetic source model for arcade flares and X-ray arcade formations outside active regions. II. Dark filament eruption and the associated arcade flare,

Astrophys. J., v. 551, No. 1, 586–596. [§ 5.2.2]

Hoh, F.C.: 1966, Stability of sheet pinch, *Phys. Fluids*, v. 9, 277–284. [§ 9.3]

Hones, E.W.Jr.(ed.): 1984, *Magnetic Reconnection in Space and Laboratory Plasmas*, Washington, Amer. Geophys. Un., p. 386. [§ 14.2]

Horiuchi, R. and Sato, T.: 1994, Particle simulation study of driven reconnection in a collisionless plasma, *Phys. Plasmas*, v. 1, No. 11, 3587–3597. [§ 6.1]

Horiuchi, R. and Sato, T.: 1997, Particle simulation study of collisionless driven reconnection in a sheared magnetic field, *Phys. Plasmas*, v. 4, No. 2, 277–289. [§ 6.2, § 6.4, § 7.1, § 9.2]

Horiuchi, R., Pei, W. and Sato, T.: 2001, Collisionless driven reconnection in an open system, *Earth Planets Space*, v. 53, No. 6, 439–445. [§ 6.2, § 6.4]

Horwitz, J.L., Gallagher, D.L., and Peterson, W.K. (eds): 1998, *Geospace Mass and Energy Flow*, Washington, Amer. Geophys. Un., p. 393. [Intr.]

Hudson, H. and Ryan, J.: 1995, High-energy particles in solar flares, *Ann. Rev. Astron. Astrophys.*, v. 33, 239–282. [7.3.1, § 9.1]

Hudson, H.S., Lemen, J.R., St. Cyr, O.C., et al.: 1998, X-ray coronal changes during halo CMEs, *Geophys. Res. Lett.*, v. 25, No. 14, 2481–2484. [§ 3.2]

Hurford, G.J., Schwartz, R.A., Krucker, S., et al.: 2003, First gamma-ray images of a solar flare, *Astrophys. J.*, v. 595, No. 2, L77–L80. [Intr.]

Ichimoto, K., Hirayama, T., Yamaguchi, A., et al.: 1992, Effective geometrical thickness and electron density of a flare of 1991 December 2, *Publ. Astron. Soc. Japan*, v. 44, No. 5, L117–L122. [Intr.]

Imshennik, V.S. and Syrovatskii, S.I.: 1967, Two-dimensional flow of an ideally conducting gas in the vicinity of the zero line of a magnetic field, *Soviet Physics–JETP*, v. 25, No. 4, 656–664. [§ 2.4]

Ip, J.T.C. and Sonnerup, B.U.: 1996, Resistive tearing instability in a current sheet with coplanar viscous stagnation-point flow, *J. Plasma Phys.*, v. 56, No. 2, 265–284. [§ 11.5]

Iroshnikov, P.S.: 1964, Turbulence of a conducting fluid in a strong magnetic field, *Soviet Astronomy–AJ.*, v. 7, No. 4, 566–571. [§ 12.1]

Isliker, H.: 1992, Structural properties of the dynamics in flares, *Solar Phys.*, v. 141, No. 2, 325–334. [§ 9.2]

Jacobsen, C. and Carlqvist, P.: 1964, Solar flares caused by circuit interruptions, *Icarus*, v. 3, No. 3, 270–272. [§ 14.2]

Janicke, L.: 1980, The resistive tearing mode in weakly two-dimentional neutral sheets, *Phys. Fluids*, v. 23, No. 9, 1843–1849. [§ 11.1]

Janicke, L.: 1982, Resistive tearing mode in coronal neutral sheets, *Solar Phys.*, v. 76, No. 1, 29–43. [§ 11.1]

Kan, J.R., Akasofu, S.I., and Lee, L.C.: 1983, A dynamo theory of solar flares, *Solar Phys.*, v. 84, No. 1, 153–167. [§ 3.3]

Karpen, J.T., Antiochos, S.K., and De Vore, C.R.: 1991, Coronal current sheet formation: The effect of asymmetric and symmetric shears, *Astrophys. J.*, v. 382, No. 1, 327–337. [§ 14.2, § 14.4]

Karpen, J.T., Antiochos, S.K., De Vore, C.R., et al.: 1998, Dynamic responses to reconnection in solar arcades, *Astrophys. J.*, v. 495, No. 1, 491–501. [§ 3.1, § 10.1]

Kivelson, M.G. and Russell, C.T. (eds): 1995, *Introduction to Space Physics*, Cambridge, Cambridge Univ. Press, p. 568. [Intr., § 8.2]

Klein, K.-L., Chupp, E.L., Trottet, G., et al.: 1999, Flare-associated energetic particles in the corona and at 1 AU, *Astron. Astrophys.*, v. 348, No. 1, 271–285. [§ 9.4]

Klein, K.-L., Trottet, G., Lantos, P., et al.: 2001, Coronal electron acceleration and relativistic proton production during the 14 July 2000 flare and CME, *Astron. Astrophys.*, v. 373, 1073–1082. [§ 5.2.2]

Kokubun, S. and Kamide, Y. (eds): 1998, *Substorms-4*, Dordrecht, Kluwer Academic Publ.; Tokyo, Terra Scientific Publ., p. 823. [Intr., § 11.6]

Kontorovich, V.M.: 1959, On the interaction between small perturbations and the discontinuities in MHD and the stability of shock waves, *Soviet Physics–JETP*, v. 8, No. 5, 851–858. [§ 10.2]

Kopp, R.A. and Pneuman, G.W.: 1976, Magnetic reconnection in the corona and the loop prominence phenomenon, *Solar Phys.*, v. 50, No. 1, 85-94. [§ 5.4.1]

Kosovichev, A.G., and Zharkova, V.V.: 2001, Magnetic energy release and transients in the solar flare of 2000 July 14, *Astrophys. J.*, v. 550, Part 2, L105-L108. [§ 5.1.1, § 5.3]

Kosugi, T.: 1996, Solar flare energy release and particle acceleration as revealed by *Yohkoh* HXT, in *High Energy Solar Physics*, eds R. Ramaty, N. Mandzhavidze, and X.-M. Hua, New York, American Inst. of Phys., p. 267–276. [§ 7.3.1]

Kosugi, T. and Somov, B.: 1998, Magnetic reconnection and particle acceleration in solar flares, in *Observational Plasma astrophysics: Five Years of Yohkoh and Beyond*, eds T. Watanabe, T. Kosugi, and A.C. Sterling, Dordrecht, Kluwer Academic Publ., p. 297–306. [Intr., § 9.4]

Kosugi, T., Dennis, B.R., and Kai, K.: 1988, Energetic electrons in impulsive and extended solar flares as deduced from flux correlation between hard X-rays and microwaves, *Astrophys. J.*, v. 324, 1118-1127. [§ 4.2.5, § 7.5]

Kosugi, T., Makishima, K., Murakami, T., et al.: 1991, The hard X-ray telescope (HXT) for the Solar-A mission, *Solar Phys.*, v. 136, No. 1, 17–36. [Intr., § 4.1]

Kosugi, T., Sakao, T., Masuda, S., et al.: 1994, Hard and soft X-ray observations of a super-hot thermal flare of 6 February, 1992, in *New Look at the Sun with Emphasis on Advanced Observations of Coronal Dynamics and Flares*, eds S. Enome and T. Hirayama, (Proc. Kofu Symp., Kofu, Sept. 6-10, 1993), p. 127-129. [§ 7.2.1]

Kovalev, V.A. and Somov, B.V.: 2003, The role of collisions in the particle acceleration in solar-flare magnetic traps, *Astronomy Letters*, v. 29, No. 6, 465–472. [§ 12.3.1]

Kraichnan, R.H.: 1965, Inertial-range spectrum of hydromagnetic turbulence, *Phys. Fluids*, v. 8, No. 7, 1385–1389. [§ 12.1]

Krause, F. and Rädler, K.-H.: 1980, *Mean-Field Magnetohydrodynamics and Dynamo Theory*, Oxford, Pergamon Press. [§ 12.1]

Krucker, S. and Benz, A.O.: 2000, Are heating events in the quiet solar corona small flares? Multiwavelength observations of individual events, *Solar Phys.*, v. 191, No. 2, 341–358. [§ 12.4]

Krucker, S., Benz, A.O., and Aschwanden, M.J.: 1997, *Yohkoh* observation of the source regions of solar narrowband, millisecond spike events, *Astron. Astrophys.*, v. 317, No. 2, 569–579. [§ 9.4]

Krucker, S., Hurford, G.J., and Lin, R.P.: 2003, Hard X-ray source motions in the 2002 July 23 gamma-ray flare, *Astrophys. J.*, v. 595, No. ?, L103–L106. [Intr., § 4.2.5, § 5.4.1, § 7.2.2]

Kubát, J. and Karlický, M.: 1986, Electric conductivity in the solar photosphere and chromosphere, *Bull. Astron. Inst. Czechosl.*, v. 37, No. 3, 155–163. [§ 13.2.2]

Kundt, W.: 2001, *Astrophysics: A Primer*, New York, Berlin, Heidelberg, Tokyo; Springer-Verlag, p. 183. [Intr.]

Kurths, J. and Herzel, H.: 1986, Can a solar pulsation event be characterized by a low-dimensional chaotic attractor? *Solar Phys.*, v. 10, No. 1, 39–45. [§ 9.2]

Kurths, J., Benz, A., and Aschwanden, M.J.: 1991, The attractor dimension of solar decimetric radio pulsation, *Astron. Astrophys.*, v. 248, No. 1, 270–276. [§ 9.2]

Kusano, K.: 2005, Simulation study of the formation mechanism of sigmoidal structure in the solar corona, *Astrophys. J.*, v. 631, No. 2, 1260–1269. [§ 5.5, § 12.2.2]

Kusano, K. and Nishikawa, K.: 1996, Bifurcation and stability of coronal arcades in a linear force-free field, *Astrophys. J.*, v. 461, No. 1, 415–423. [§ 3.1, § 3.3]

Laming, J.M. and Drake, J.J.: 1999, Stellar coronal abundances. VI. The FIP effect and ξ Bootis A — Solar-like anomalies, *Astrophys. J.*, v. 516, No. 1, 324–334. [§ 13.4]

Landau, L.D. and Lifshitz, E.M.: 1976, *Mechanics*, 3rd edition, Oxford, London, Paris; Pergamon Press, p. 165. [§ 9.2]

Landau, L.D., Lifshitz, E.M., and Pitaevskii, L.P.: 1984, *Electrodynamics of Continuous Media*, Oxford, New York; Pergamon Press, p. 460. [§ 10.2.2]

LaRosa, T.N. and Moore, R.L.: 1993, A mechanism for bulk energization in solar flares: MHD turbulent cascade, *Astrophys. J.*, v. 418, No. 2, 912–918. [§ 12.1]

LaRosa, T.N., Moore, R.L., Miller, J.A., et al.: 1996, New promise for electron bulk energization in solar flares: Preferential Fermi acceleration of electrons over protons in reconnection-driven MHD turbulence, *Astrophys. J.*, v. 467, No. 1, 454–464. [§ 12.3.1]

Lau, Y.-T.: 1993, Magnetic nulls and topology in a class of solar flare models, *Solar Phys.*, v. 148, No. 2, 301–324. [§ 3.2, § 14.3]

Lavrent'ev, M.A. and Shabat, B.V.: 1973, *Methods of the Theory of Complex Variable Functions*, Moscow, Nauka, p. 736 (in Russian). [§ 14.3]

Leamon, R.J., Smith, C.W., Ness, N.F., et al.: 1998, Observational constraints on the dynamics of the interplanetary magnetic field dissipation range, *J. Geophys. Res.*, v. 103, No. A3, 4775–4787, [§ 12.1]

Lembege, B. and Pellat R.: 1982, Stability of a thick two-dimensional quasineutral sheet, *Phys. Fluids*, v. 25, No. 11, 1995–2004. [§ 11.6]

Lesch, H. and Pohl, M.: 1992, A possible explanation for intraday variability in active galactic nuclei, *Astron. Astrophys.*, v. 254, No. 1, 29–38. [§ 8.3]

Li, Y.P. and Gan, W.Q.: The shrinkage of flare radio loops, *Astrophys. J.*, v. 629, No. 2, L137–L139. [§ 7.5]

Lichtenberg, A.J. and Lieberman, M.A.: 1983, *Regular and Stochastic Motion*, New York, Springer-Verlag, p. 314. [§ 9.2]

Lin, R.P., Schwartz, R.A., Pelling, R.M., et al.: 1981, A new component of hard X-rays in solar flares, *Astrophys. J.*, v. 251, No. 2, L109–L114. [§ 7.1]

Lin, R.P., Dennis, B.R., Hurford, G.J., et al.: 2002, The Reuven Ramaty High-Energy Solar Spectroscopic Imager (RHESSI), *Solar Phys.*, v. 210, No. 1, 3-32. [Intr., § 7.2.1]

Lin, R.P., Krucker, S., Hurford, G.J., et al.: 2003, *RHESSI* observations of particle acceleration and energy release in an intense solar gamma-ray line flare, *Astrophys. J.*, v. 595, No. 2, L69–L76. [Intr., § 4.2.5, § 7.2.2, § 7.5]

Lin, R.P., Larson, D., McFadden, J., et al.: 1996, Observations of an impulsive solar electron event extending down to ∼0.5 keV energy, *Geophys. Res. Lett.*, v. 23, No. 10, 1211–1214. [§ 9.4]

Lin, Y., Wei, X., and Zhang, H.: 1993, Variations of magnetic fields and electric currents associated with a solar flare, *Solar Phys.*, v. 148, No. 1, 133–138. [§ 3.1]

Litvinenko, Y.E.: 1993, Regular versus chaotic motion of particles in non-neutral current sheets, *Solar Phys.*, v. 147, No. 2, 337–342. [§ 9.2]

Litvinenko, Y.E.: 1997, Interpretation of particle acceleration in a simulation study of collisionless reconnection, *Phys. Plasmas*, v. 4, No. 9, 3439–3441. [§ 9.2]

Litvinenko, Y.E.: 1999, Photospheric reconnection and canceling magnetic features on the Sun, *Astrophys. J.*, v. 515, No. 1, 435–440. [§ 12.4, § 13.2.1]

Litvinenko, Y.E. and Somov, B.V.: 1991, Electron acceleration in current sheets in solar flares, *Soviet Astronomy Lett.*, v. 17, No. 5, 353–356. [§ 9.1]

Litvinenko, Y.E. and Somov, B.V.: 1993, Particle acceleration in reconnecting current sheets, *Solar Phys.*, v. 146, No. 1, 127–133. [§ 9.2, § 9.3]

Litvinenko, Y.E. and Somov, B.V.: 1994a, Electromagnetic expulsion force in cosmic plasma, *Astron. Astrophys.*, v. 287, No. 1, L37–L40. [§ 5.3]

Litvinenko, Y.E. and Somov, B.V.: 1994b, Magnetic reconnection in the temparature mimimum and prominence formation, *Solar Phys.*, v. 151, No. 2, 265–270. [§ 5.3, § 12.4, § 13.2.1]

Litvinenko, Y.E. and Somov B.V.: 1995, Relativistic acceleration of protons in current sheets of solar flares, *Solar Phys.*, v. 158, No. 1, 317–330. [§ 9.3.3, § 9.4]

Litvinenko, Y.E. and Somov, B.V.: 2001, Aspects of the global MHD equilibria and filament eruptions in the solar corona, *Space Sci. Rev.*, v. 95, No. 1, 67–77. [§ 5.3]

Liu, C., Deng, N., Liu, Y., et al.: 2005, Rapid change of δ spot structure associated with seven major flares, *Astrophys. J.*, v. 622, No. 1, 722–736. [§ 3.1.1, § 3.1.3]

Liu, S., Petrosian, V., and Mason, G.M.: 2006, Stochastic acceleration of ^{3}He and ^{4}He in solar flares by parallel-propagating plasma waves: General results, *Astrophys. J.*, v. 636, No. 1, 462–474. [§ 12.3.2]

Liu, Y. and Zhang, H.: 2001, Relationship between magnetic field evolution and major flare event on July 14, 2000, *Astron. Astrophys.*, v. 372, No. 3, 1019–1029. [§ 4.1, § 4.2.3, § 4.2.4, § 4.2.5, § 5.2.3, § 5.3]

Liu, Y. and Zhang, H.: 2002, Analysis of a delta spot, *Astron. Astrophys.*, v. 386, No. 2, 648–652. [§ 4.1]

Liu, Y., Srivastava, N., Prasad, D., et al.: 1995, A possible explanation of reversed magnetic field features observed in NOAA AR 7321, *Solar Phys.*, v. 158, No. 1, 249–258. [§ 13.3]

Longcope, D.W.: 1996, Topology and current ribbons: A model for current, reconnection and flaring, *Solar Phys.*, v. 169, No. 1, 91–121. [§ 3.4, § 4.2.3, § 4.2.4]

Longcope, D.W. and Cowley, S.C.: 1996, Current sheet formation along 3D magnetic separators, *Phys. Plasmas*, v. 3, No. 8, 2885–2897. [§ 3.2, § 4.2.3]

Longcope, D.W. and Silva, A.V.R.: 1998, A current ribbon model for energy storage and release with application to the flare of 7 January 1992, *Solar Phys.*, v. 179, No. 2, 349–377. [Intr., § 3.4, § 6.4]

Longcope, D.W., McKenzie, D.E., Cirtain, J., et al.: 2005, Observations of separator reconnection to an emerging active region, *Astrophys. J.*, v. 630, No. 1, 596–614. [§ 3.3.3, § 3.4.4]

Longmire, C.L.: 1963, *Elementary Plasma Physics*, New York, London; Interscience Publ., p. 296. [§ 9.3]

Low, B.C.: 1987, Electric current sheet formation in a magnetic field induced by footpoint displacements, *Astrophys. J.*, v. 323, No. 1, 358–367. [§ 2.1.2]

Low, B.C.: 1991, On the spontaneous formation of current sheets above a flexible solar photosphere, *Astrophys. J.*, v. 381, No. 1, 295–305. [§ 14.2, § 14.3]

Low, B.C. and Smith, D.F.: 1993, The free energies of partially open coronal magnetic fields, *Astrophys. J.*, v. 410, No. 1, 412–425. [§ 14.2]

Low, B.C. and Wolfson, R.: 1988, Spontaneous formation of current sheets and the origin of solar flares, *Astrophys. J.*, v. 324, No. 1, 574–581. [§ 2.1.2]

Lu, E.T. and Hamilton, R.J.: 1991, Avalanches and distribution of solar flares, *Astrophys. J.*, v. 380, No. 2, L89–L92. [§ 12.1]

Lyon J.G.: 2000, The solar wind-magnetosphere-ionosphere system, *Science*, v. 288, No. ?, 1987–1991. [§ 8.2]

Mackay, D.H., Priest, E.R., Gaizauskas, V., et al.: 1998, Role of helicity in the formation of intermediate filaments, *Solar Phys.*, v. 180, No. 1, 299–312. [§ 13.3]

Mandrini, C.H. and Machado, M.E.: 1993, Large-scale brightenings associated with flares, *Solar Phys.*, v. 141, No. 1, 147–164. [§ 3.4]

Mandrini, C.H., Demoulin, P., Hénoux, J.C., et al.: 1991, Evidence for the interaction of large scale magnetic structures in solar flares, *Astron. Astrophys.*, v. 250, No. 2, 541–547. [Intr., § 3.4]

Mandrini, C.H., Rovira, M.G., Demoulin, P., et al.: 1993, Evidence for reconnection in large-scale structures in solar flares, *Astron. Astrophys.*,

v. 272, No. 2, 609–620. [Intr., § 3.4]

Manoharan, P.K., Tokumaru, M., Pick, M., et al.: 2001, Coronal mass ejection of 2000 July 14 flare event: Imaging from near-sun to Earth environment, *Astrophys. J.*, v. 559, No. 2, 1180–1189. [§ 5.2.2]

Markovskii, S.A. and Somov, B.V.: 1996, A criterion for splitting of a reconnecting current sheet into MHD discontinuities, *J. Plasma Phys.*, v. 55, No. 3, 303–325. [§ 10.2]

Marsh, G.E.: 1996, *Force-Free Magnetic Fields: Solutions, Topology and Applications*, River Edge, London; World Scientific Publ., p. 159. [§ 12.2]

Martens, P.C.H.: 1988, The generation of proton beams in two-ribbon flares, *Astrophys. J.*, v. 330, No. 2, L131–L133. [§ 9.3, § 9.4]

Martin, S.F.: 1986, Recent observations of the formation of filaments, in *Coronal and Prominence Plasmas*, NASA CP-2442, p. 73–80. [§ 5.3, § 13.1]

Martin, S.F.: 1998, Conditions for the formation and maintenance of filaments, *Solar Phys.*, v. 182, No. 1, 107–137. [§ 5.3, § 13.3]

Martin, S.F., Livi, S.H.B., and Wang, J.: 1985, The cancellation of magnetic flux. II. In a decaying active region, *Australian J. Phys.*, v. 38, 929-959. [§ 5.3]

Masuda, S.: 1994, Ph.D. thesis, Univ. Tokyo. [§ 7.2.3]

Masuda, S.: 2002, Hard X-ray solar flares revealed with Yohkoh HXT - A review, in *Multi-wavelength Observations of Coronal Structure and Dynamics, Yohkoh 10th Anniversary Meeting*, eds P.C.H. Martens and D.P. Cauffman, Amsterdam, Pergamon, p. 351-359. [§ 7.2.1]

Masuda, S., Kosugi, T., Hara, H., et al.: 1994, A loop-top hard X-ray source in a compact solar flare as evidence for magnetic reconnection, *Nature*, v. 371, 495–497. [Intr., § 7.2.1]

Masuda, S., Kosugi, T., Hara, H., et al.: 1995, Hard X-ray sources and the primary energy-release site in solar flares, *Publ. Astron. Soc. Japan*, v. 47, 677–689. [Intr.]

Masuda, S., Kosugi, T., Sakao, T., et al.: 1998, Coronal hard X-ray sources in solar flares observed with Yohkoh/HXT, in *Observational Plasma Astrophysics: Five Years of Yohkoh and Beyond*, eds T. Watanabe, T. Kosugi, and A.C. Sterling, Dordrecht, Kluwer Academic Publ., p. 259–267. [§ 7.2.1]

Masuda, S., Kosugi, T., and Hudson, H.S.: 2001, A hard X-ray two-ribbon flare observed with *Yohkoh*/HXT, *Solar Phys.*, v. 204, No. 1, 57–69. [§ 4.1, § 4.2.3, § 4.2.5, § 5.1, § 5.4.1, § 7.5]

Mathieu, J. and Scott, J.: 2000, *An Introduction to Turbulent Flow*, New York, Cambridge Univ. Press. [§ 12.1.2]

Mauas, P.J.: 1990, The white-light flare of 1982 June 15 - Observations, *Astrophys. J. Suppl.*, v. 74, 609–646. [§ 13.2.1]

McKenzie, D.E. and Hudson, H.S.: 1999, X-ray observations of motions and structure above a solar flare arcade, *Astrophys. J.*, v. 519, L93-L96. [§ 7.3.2, § 7.3.5]

Milano, L.J., Gómez, D.O., and Martens, P.C.H.: 1997, Solar coronal heating: AC versus DC, *Astrophys. J.*, v. 490, No. 1, 442-451. [§ 12.4]

Miller, J.A. and Reames, D.V.: 1996, Heavy ion acceleration by cascading Alfvén waves in impulsive solar flares, in *High Energy Solar Physics*, eds R. Ramaty, N. Mandzhavidze, and X.-M. Hua, New York, AIP, Woodbury, 450–460. [§ 12.3.2]

Miller, J.A., LaRosa, T.N., and Moore, R.L.: 1996, Stochastic electron acceleration by cascading fast mode waves in impulsive solar flares, *Astrophys. J.*, v. 461, No. 1, 445–464. [§ 12.3.1]

Miroshnichenko, L.I.: 2001, *Solar Cosmic Rays*, Dordrecht, Boston, London; Kluwer Academic Publ., p. 480. [Intr., § 9.1]

Moffatt, H.K.: 1978, *Magnetic Field Generation in Electrically Conducting Fluids*, London, New York, Melbourne; Cambridge Univ. Press, p. 343. [§ 12.1, § 12.5]

Moiseev, S.S. and Chkhetiani, O.G.: 1996, Helical scaling in turbulence, *JETP*, v. 83, No. 1, 192–198. [§ 12.1]

Moore, R.L., Falconer, D.A., Porter, J.G., et al.: 1999, On heating the Sun's corona by magnetic explosions: Feasibility in active regions and prospects for quiet regions and coronal holes, *Astrophys. J.*, v. 526, No. 1, 505–522. [§ 12.4]

Moreton, G.E. and Severny, A.B.: 1968, Magnetic fields and flares, *Solar Phys.*, v. 3, No. 2, 282–297. [§ 3.3]

Morita, S., Uchida, Y., Hirose, S., et al.: 2001, 3D structure of arcade-type flares derived from the homologous flare series, *Solar Phys.*, v. 200, No. 1, 137–156. [§ 5.1, 6.4]

Morozov, A.I. and Solov'ev, L.S.: 1966a, The structure of magnetic fields, in: Leontovich M.A. (ed.), *Reviews of Plasma Physics*, New York, Consultans Bureau, v. 2, 1–101. [§ 14.3]

Mukerjee, K., Agrawal, P., Paul, B., et al.: 2001, Pulse characteristics of the X-ray pulsar 4U1907+09, *Atrophys. J.*, v. 548, No. 1, 368–376. [§ 8.3]

Murty, G.S.: 1961, Instabilities of a conducting fluid slab carrying uniform current in the presence of a magnetic field, *Ark. Fysik*, v. 19, No. 6, 499–510. [§ 11.1]

Nagai, T., Fuijimoto, M., Saito, Y., et al.: 1998, Structure and dynamics of magnetic reconnection for substorm onsets with Geotail observations, *J. Geophys. Res.*, v. 103, 4419–4428. [Intr., § 11.6]

Nakar, E., Piran, T., and Sari, R.: 2005, Pure and loaded fireballs in Soft Gamma-Ray repeater giant flares, *Astrophys. J.*, v. 635, No. 1, 516–521. [§ 8.4]

Nishida, A. and Nagayama, N.: 1973, Synoptic survey for the neutral line in the magnetotail during the substorm expansion phase, *J. Geophys. Res.*, v. 78, No. 19, 3782–3798. [Intr.]

Nishida, A., Baker, D.N., and Cowley, S.W.H. (eds): 1998, *New Perspectives on the Earth's Magnetotail*, Washington, Amer. Geophys. Un., p. 339. [Intr.]

Nishikawa, K.I. and Sakai, J.: 1982, Stabilizing effect of a normal magnetic field on the collisional tearing mode, *Phys. Fluids*, v. 25, No. 8, 1384–1387. [§ 11.4]

Ogawara, Y., Takano, T., Kato, T., et al.: 1991, The Solar-A mission: an overview, *Solar Phys.*, v. 136, No. 1, 1–16. [Intr., § 4.1]

Ono, Y., Yamada,M., Akao, T., et al.: 1996, Ion acceleration and direct ion heating in three-component magnetic reconnection, *Phys. Rev. Lett.*, v. 76, No. 18, 3328–3331. [§ 6.2, § 7.1]

Oreshina, A.V. and Somov, B.V.: 1998, Slow and fast magnetic reconnection. I. Role of radiative cooling, *Astron. Astrophys.*, v. 331, 1078–1086. [§ 6.1, § 13.2.3]

Ott, E.: 1998, Chaotic flows and kinematic magnetic dynamos, *Phys. Plasmas*, v. 5, No. 5, 1636-1646. [§ 12.1]

Otto, A.: 1991, The resistive tearing instability for generalized resistive models: Theory, *Phys. Fluids*, v. 3B, No. 7, 1739–1745. [§ 11.1]

Ozernoy, L.M. and Somov, B.V.: 1971, The magnetic field of a rotating cloud and magneto-rotational explosions, *Astrophys. Space Sci.*, v. 11, No. 2, 264–283. [Intr.]

Paesold, G. and Benz, A.O.: 1999, Electron firehose instability and acceleration of electrons in solar flares, *Astron. Astrophys.*, v. 351, 741–746. [§ 12.3.1]

Paesold, G., Benz, A.O., Klein, K.-L., et al.: 2001, Spatial analysis of solar type III events associated with narrow band spikes at metric wavelengths, *Astron. Astrophys.*, v. 371, 333–342. [§ 9.4]

Palmer, I.D. and Smerd, S.F.: 1972, Evidence for a two-component injection of cosmic rays from the solar flare of 1969, March 30, *Solar Phys.*, v. 26, No. 2, 460–467. [§ 9.4]

Park, B.T., Petrosian, V., and Schwartz, R.A.: 1997, Stochastic acceleration and photon emission in electron-dominated solar flares, *Astrophys. J.*, v. 489, No. 1, 358–366. [§ 12.3.4]

Parker, E.N.: 1972, Topological dissipation and the small-scale fields in turbulent gases, *Astrophys. J.*, v. 174, No. 1, 499–510. [§ 2.1.2, § 12.1]

Parker, E.N.: 1979, *Cosmic Magnetic Fields. Their Origin and Their Activity*, Oxford, Clarendon Press, p. 841. [§ 6.1, § 12.1]

Parker, E.N.: 1988, Nanoflares and the solar X-ray corona, *Astrophys. J.*, v. 330, No. 1, 474–479. [§ 12.1, § 12.4]

Parker, E.N.: 1993, A solar dynamo surface wave at the interface between convection and nonuniform rotation, *Astrophys. J.*, v. 408, No. 2, 707–719. [§ 12.1]

Peratt, A.L.: 1992, *Physics of the Plasma Universe*, New York, Berlin, Heidelberg; Springer-Verlag, p. 342. [Intr.]

Peres, G., Rosner, R., Serio, S., et al.: 1982, Coronal closed structures. 4. Hydrodynamical stability and response to heating perturbations, *Astrophys. J.*, v. 252, No. 2, 791–799. [§ 13.2.3]

Petrosian, V., Donaghy, T.Q., McTiernan, J.M.: 2002, Loop top hard X-ray emission in solar flares: Images and statistics, *Astrophys. J.*, v. 569, No. 1, 459–473. [§ 7.2.1, § 7.2.3]

Petschek, H.E.: 1964, Magnetic field annihilation, in *AAS-NASA Symp. on the Physics of Solar Flares*, ed. W.N. Hess, Washington, NASA SP-50, p. 425–439. [§ 10.1, § 10.6]

Pevtsov, A.A.: 2000, Transequatorial loops in the solar corona, *Astrophys. J.*, v. 531, No. 1, 553–560. [§ 3.4.4]

Pevtsov, A.A. and Longcope, D.W.: 1998, NOAA 7926: A kinked Ω-loop? *Astrophys. J.*, v. 508, No. 2, 908–915. [§ 3.2]

Pevtsov, A.A., Canfield, R.C., and Zirin, H.: 1996, Reconnection and helicity in a solar flare, *Astrophys. J.*, v. 473, No. 1, 533–538. [§ 3.2, § 12.2]

Pike, C.D. and Mason, H.E.: 1998, Rotating transion region features observed with the SOHO CDS, Coronal Diagnostic Spectrometer, *Solar Phys.*, v. 182, No. 2, 333–348. [§ 13.5]

Pneuman, G.W.: 1974, Magnetic structure responsible for coronal disturbances, in *Coronal Disturbances*, (IAU Symp. 57), ed. G. Newkirk, Dordrecht, Boston; D. Reidel Publ., p. 35–68. [§ 11.1]

Pneuman, G.W.: 1983, The formation of solar prominences by magnetic reconnection and condensation, *Solar Phys.*, v. 88, No. 2, 219–239. [§ 13.1]

Podgornii, A.I. and Syrovatskii, S.I.: 1981, Formation and development of a current sheet for various magnetic viscosities and gas pressures, *Soviet J. Plasma Phys.*, v. 7, No. 5, 580–584. [§ 10.1, § 10.5]

Pollard, R.K. and Taylor, Y.B.: 1979, Influence of equilibrium flows on tearing modes, *Phys. Fluids*, v. 22, No. 1, 126–131. [§ 11.5]

Pope, S.B.: 2000, *Turbulent Flows*, Cambridge, UK; Cambridge Univ. Press. [§ 12.1.2]

Porter, L.J., Klimchuk, J.A., and Sturrock, P.A.: 1992, Cylindrically symmetric force-free magnetic fields, *Astrophys. J.*, v. 385, No. 2, 738–745. [§ 14.2]

Priest, E.R.: 1982, *Solar Magnetohydrodynamics*, Dordrecht, Boston, London; D. Reidel Publ. Co., p. 472. [§ 12.4, § 14.2]

Priest, E.R. and Forbes, T.: 2000, *Magnetic Reconnection: MHD Theory and Applications*, Cambridge, Cambridge Univ. Press. [Intr.]

Priest, E.R., Titov, V.S., Vekstein, G.E., et al.: 1994, Steady linear X-point magnetic reconnection, *J. Geophys. Res.*, v. 99, No. A11, 21467–21479. [§ 13.2.3]

Qiu, J., Lee, J., and Gary, D.E.: 2004, Impulsive and gradual nonthermal emissions in an X-class flare, *Astrophys. J.*, v. 603, No. 1, 335-347. [4.2.5, 7.5]

Raadu, M.A.: 1984, Global effects of double layers, in *Second Symp. on Plasma Double Layers and Related Topics*, eds R. Schrittwieser and G. Eder; Innsbruck, p. 3–27. [§ 14.2]

Ranns, N.D.R., Harra, L.K., Matthews, S.A., et al.: 2000, Emerging flux as a driver for homologous flares, *Astron. Astrophys*, v. 360, 1163–1169. [§ 3.4]

Reiman, A.: 1980, Minimum energy state of a toroidal discharge, *Phys. Fluids*, v. 23, No. 1, 230–231. [§ 12.5]

Roald, C.B., Sturrock, P.A., and Wolfson, R.: 2000, Coronal heating: Energy release associated with chromospheric magnetic reconnection, *Astrophys. J.*, v. 538, No. 2, 960–967. [§ 12.4]

Roikhvarger, Z.B. and Syrovatskii, S.I.: 1974, Evolutionarity of MHD discontinuities with allowance for dissipative waves, *Soviet Physics–JETP*, v. 39, No. 4, 654–656. [§ 10.2]

Romanova, M.M., Ustyugova, G.V., Koldoba, A.V., et al.: 2004, Threedimentional simulations of disk accretion to an inclined dipole. II. Hot spots and variability, *Astrophys. J.*, v. 610, No. 2, 929–932. [§ 8.3]

Rose, W.K.: 1998, *Advanced Stellar Astrophysics*, Cambridge, Cambridge Univ. Press, p. 494. [Intr.]

Roumeliotis, G. and Moore, R.L.: 1993, A linear solution for magnetic reconnection driven by converging or diverging footpoint motions, *Astrophys. J.*, v. 416, No. 1, 386–391. [§ 13.1]

Rust, D.M. and Kumar, A.: 1996, Evidence for helically kinked magnetic flux ropes in solar eruptions, *Astrophys. J.*, v. 464, No. 2, L199–L202. [§ 3.2]

Sakai, J.I. and de Jager, C.: 1996, Solar flares and collisions between current-carring loops, *Space Sci. Rev.*, v. 77, No. 1, 1–192. [§ 3.2, § 14.2]

Sakao, T.: 1994, PhD Thesis, The University of Tokyo. [§ 5.4.2]

Sakao, T., Kosugi, T., and Masuda, S.: 1998, Energy release in solar flares with respect to magnetic loops, in *Observational Plasma Astrophysics: Five Years of Yohkoh and Beyond*, eds T. Watanabe, T. Kosugi, and A.C. Sterling, Dordrecht, Kluwer Academic Publ., p. 273-284. [§ 3.4, § 4.1, § 5.4.2]

Sato, J.: 1997, PhD thesis, Graduate University of Advanced Science, Tokyo. [§ 7.2.1]

Sato, J.: 2001, Obsevation of the coronal hard X-ray sources of the 1998 April 23 flare, *Astrophys. J.*, v. 558, L137–L140. [§ 7.2.1]

Sato, J., Kosugi, T., Makishima, K.: 1999, Improvement of Yohkoh hard X-ray imaging, *Publ. Astron. Soc. Japan*, v. 51, 127–150. [§ 7.2.1, § 7.2.2]

Sato, J., Sawa, M., Yoshimura, K., et al.: 2003, *The Yohkoh HXT/SXT Flare Catalogue*, Montana, Montana State Univ.; Sagamihara, Inst. of Space and Astronautical Science. [§ 7.2.3]

Schabansky, V.P.: 1971, Some processes in the magnetosphere, *Space Sci. Rev.*, v. 12, No. 3, 299–418. [§ 9.3]

Scherrer, P.H., Bogart, R.S., Bush, R.I., et al.: 1995, The solar oscillations investigation - Michelson Doppler Imager, *Solar Phys.*, v. 162, No. 1, 129–188. [Intr., § 4.1]

Schindler, K.: 1974, A theory of the substorm mechanism, *J. Geophys. Res.*, v. 79, No. 19, 2803–2810. [§ 11.1, § 11.6]

Schrijver, C.J., DeRosa M.L., Title, A.M., et al.: 2005, The nonpotentiality of active-region coronae and the dynamics of the photospheric magnetic field, *Astrophys. J.*, v. 628, No. 1, 501–513. [§ 3.3.3, § 5.2.3]

Schrijver, C.J., Title, A.M., van Ballegooijen, A.A., et al.: 1997, Sustaining the quiet photospheric network: The balance of flux emergence, fragmentation, merging, and cancellation, *Astrophys. J.*, v. 487, No. 1, 424–436. [§ 12.4]

Schuster, H.G.: 1984, *Deterministic Chaos. An Introduction*, Weinheim, Physik-Verlag, p. 220. [§ 9.2]

Severny, A.B.: 1962, The stability of plasma layer with a neutral-point magnetic field, *Soviet Astronomy–AJ*, v. 6, No. 6, 770–773. [§ 2.1]

Severny, A.B.: 1964, Solar flares, *Ann. Rev. Astron. Astrophys.*, v. 2, 363–400. [§ 3.1]

Shafranov, V.D.: 1966, Plasma equilibrium in a magnetic field, in *Reviews of Plasma Physics*, ed. M.A. Leontovich, New York, Consultants Bureau, v. 2, 103–151. [§ 14.3]

Share, G.H., Murphy, R.J., Tulka, A.J., et al.: 2001, Gamma-ray line observations of the 2000 July 14 flare and SEP impact on the Earth, *Solar Phys.*, v. 204, No. 1, 43–55. [§ 5.1]

Sheeley, N.R.Jr., Bohling, J.D., Brueckner, G.E., et al.: 1975, XUV observations of coronal magnetic fields, *Solar Phys.*, v. 40, No. 1, 103–121. [§ 3.4.4]

Shibasaki, K.: 2001, High-beta disruption in the solar atmosphere, *Astrophys. J.*, v. 557, No. 1, 326–331. [§ 5.5]

Shibata, K., Masuda, S., Shimojo, M., et al.: 1995, Hot-plasma ejections associated with compact-loop solar flares, *Astrophys. J.*, v. 451, Part 2, L83–L86. [§ 5.1]

Simnett, G.M.: 2000, Studies of the dynamic corona from SOHO, in *High Energy Solar Physics: Anticipating HESSI*, eds R. Ramaty and N. Mandzhavidze, Greenbelt, Maryland, ASP Conference Series, v. 206, 43–53. [§ 7.3]

Sitnov, M.I. and Sharma, A.S.: 1998, Role of transient electrons and microinstabilities in the tearing instability of the geomagnetotail current sheet, and the general scenario of the substorms as a catastrophe, in *Substorms-4*, eds S. Kokubun and Y. Kamide, Dordrecht, Kluwer Academic Publ.; Tokyo, Terra Sci. Publ., p. 539–542. [§ 11.6]

Sitnov, M.I., Malova, H.V., and Lui, A.T.Y.: 1997, Quasi-neutral sheet tearing instability induced by electron preferential acceleration from stochasticity, *J. Geophys. Res.*, v. 102, No. A1, 163–173. [§ 11.6]

Somov, B.V.: 1981, Fast reconnection and transient phenomena with particle acceleration in the solar corona, *Bull. Acad. Sci. USSR, Phys. Ser.*, v. 45, No. 4, 114–116. [§ 6.1, § 8.1, § 9.4.2]

Somov, B.V.: 1985, New theoretical models of solar flares, *Soviet Phys. Usp.*, v. 28, No. 3, 271–272. [§ 3.2, § 6.4, § 14.3]

Somov, B.V.: 1986, Non-neutral current sheets and solar flare energetics, *Astron. Astrophys.*, v. 163, No. 1, 210–218. [§ 3.2, § 6.4]

Somov, B.V.: 1991, A scenario for the large-scale magnetic field evolution in CMEs, *Journal of Geomag. and Geoelectricity*, v. 43 (Suppl.), 31–36. [§ 7.3]

Somov, B.V.: 1992, *Physical Processes in Solar Flares*, Dordrecht, Boston, London; Kluwer Academic Publ., p. 248. [§ 3.2, § 4.1, § 6.2, § 6.3, § 7.1, § 8.1, § 9.1, § 9.2, § 9.3, § 10.1, § 11.5, § 11.6, § 14.2]

Somov, B.V.: 1999, Cosmic electrodynamics and solar physics, *Bull. Russ. Acad. Sci., Physics*, v. 63, No. 8, 1157–1162. [§ 12.4]

Somov, B.V.: 2000, *Cosmic Plasma Physics*, Dordrecht, Boston, London; Kluwer Academic Publ., p. 652. [Intr., § 6.4]

Somov, B.V. and Bogachev, S.A.: 2003, The betatron effect in collapsing magnetic trap. *Astronomy Lett.*, v. 29, 621-628. [§ 7.4.1, § 7.4.2, § 7.4.3, § 7.4.4]

Somov, B.V. and Hénoux J.C.: 1999, Generation and interaction of electric currents in the quiet photospheric network, in *Magnetic Fields and Solar*

Processes, Proc. 9th European Meeting on Solar Physics, ESA SP-448, 659–663. [§ 12.4, § 14.2]

Somov, B.V. and Kosugi, T.: 1997, Collisionless reconnection and high-energy particle acceleration in solar flares, *Astrophys. J.*, v. 485, No. 2, 859–868. [§ 4.1, § 4.2.5, § 6.4, § 7.3, § 7.5, § 7.6, § 8.1]

Somov, B.V. and Kozlova, L.M.: 1998, Fine structure of the solar chromosphere from infrared He I line observations, *Astronomy Reports*, v. 42, No. 6, 819–826. [§ 13.5]

Somov, B.V. and Litvinenko, Yu.E.: 1993, Magnetic reconnection and particle acceleration in the solar corona, in *Physics of Solar and Stellar Coranae*, eds J. Linsky and S. Serio, Dordrecht, Kluwer Academic Publ., p. 603–606. [§ 9.1]

Somov, B.V. and Merenkova, E.Yu.: 1999, Model computations of magnetic fields in solar flares, *Bull. Russ. Acad. Sci., Physics*, v. 63, No. 8, 1186–1188. [§ 3.4, § 9.2, § 14.3]

Somov, B.V. and Oreshina, A.V.: 2000, Slow and fast magnetic reconnection. II. High-temperature turbulent-current sheet, *Astron. Astrophys.*, v. 354, 703–713. [§ 6.1, § 6.3]

Somov, B.V. and Syrovatskii, S.I.: 1972, Appearance of a current sheet in a plasma moving in the field of a two-dimensional magnetic dipole, *Soviet Phys.–JETP*, v. 34, No. 5, 992–997. [§ 2.1.2, § 6.1, § 8.3, § 14.3]

Somov, B.V. and Syrovatskii, S.I.: 1975, Electric and magnetic fields arising from the rupture of a neutral current sheet. *Bull. Acad. Sci. USSR, Phys. Series*, v. 39, No. 2, 109–111. [§ 3.3]

Somov, B.V. and Syrovatskii, S.I.: 1976a, Physical processes in the solar atmosphere associated with flares, *Soviet Physics Usp.*, v. 19, No. 10, 813–835. [§ 6.1]

Somov, B.V. and Syrovatskii, S.I.: 1976b, Hydrodynamic plasma flows in a strong magnetic field, in *Neutral Current Sheets in Plasma*, Proc. P.N. Lebedev Phys. Inst., v. 74, ed. N.G. Basov, New York and London, Consultants Bureau, p. 13–71. [§ 2.2, § 10.1]

Somov, B.V. and Syrovatskii, S.I.: 1977, Current sheets as the source of heating for solar active regions, *Solar Phys.*, v. 55, No. 2, 393–399. [§ 3.3]

Somov, B.V. and Syrovatskii, S.I.: 1982, Thermal trigger for solar flares and coronal loops formation, *Solar Phys.*, v. 75, No. 1, 237–244. [§ 6.1]

Somov, B.V. and Titov, V.S.: 1983, Magnetic reconnection as a mechanism for heating the coronal loops, *Soviet Astronomy Letters*, v. 9, No. 1, 26–28. [§ 8.1]

Somov, B.V. and Titov, V.S.: 1985a, Effect of longitudinal magnetic field in current sheets on the Sun, *Soviet Astronomy–AJ*, v. 29, No. 5, 559–563. [§ 6.2, § 12.2]

Somov, B.V. and Titov, V.S.: 1985b, Magnetic reconnection in a high-temperature plasma of solar flares. 2. Effects caused by transverse and longitudinal magnetic fields. *Solar Phys.*, v. 102, No. 1, 79–96. [§ 6.2, § 11.5, § 12.2]

Somov, B.V. and Verneta, A.I.: 1988, Magnetic reconnection in a high-temperature plasma of solar flares. 3. Stabilization effect of a transverse magnetic field in non-neutral current sheets, *Solar Phys.*, v. 117, No. 1, 89–95. [§ 11.1, § 11.6]

Somov, B.V. and Verneta, A.I.: 1989, Magnetic reconnection in a high-temperature plasma of solar flares. 4. Resistive tearing mode in non-neutral current sheets, *Solar Phys.*, v. 120, No. 1, 93–115. [§ 11.1, § 11.4]

Somov, B.V. and Verneta, A.I.: 1993, Tearing instability of reconnecting current sheets in space plasmas, *Space Sci. Rev.*, v. 65, No. 3, 253–288. [§ 11.1, § 11.5, § 11.6]

Somov, B.V., Kosugi, T., and Sakao, T.: 1998, Collisionless 3D reconnection in impulsive solar flares. *Astrophys. J.*, v. 497, No. 2, 943–956. [§ 3.4, § 4.1, § 5.1.2, § 5.2.3, § 5.4.1, § 5.5, § 6.4, § 8.1, § 9.2]

Somov, B.V., Litvinenko, Y.E., Kosugi, T., et al.: 1999, Coronal hard X-rays in solar flares: *Yohkoh* observations and interpretation, in *Magnetic Fields and Solar Processes*, Proc. 9th European Meeting on Solar Physics, ESA SP-448, 701-708. [§ 7.3, § 7.6]

Somov, B.V., Kosugi, T., Litvinenko, Y.E., et al.: 2001, Collisionless reconnection in the structure and dynamics of active regions, in *Recent Insight into the Physics of the Sun and Heliosphere: Highlights from SOHO and Other Space Missions*, Proc. IAU Symp. 203, eds P. Brekke, B. Fleck, and J.B. Gurman; Chelsea, Sheridan Books, 558-561. [§ 3.2, § 14.3]

Somov, B.V., Kosugi, T., Hudson, H.S., et al.: 2002a, Magnetic reconnection scenario of the Bastille day 2000 flare, *Astrophys. J.*, v. 579, No. 2, 863–873. [§ 4.1, § 5.2.3, § 5.4.1, § 5.4.4, § 5.5, § 6.4, § 12.2]

Somov, B.V., Kosugi, T., Litvinenko, Y.E., et al.: 2002b, Three-dimensional reconnection at the Sun: Space observations and collisionless models, *Adv. Space Res.*, v. 29, No. 7, 1035–1044. [§ 3.2]

Somov, B.V., Hénoux, J.C., and Bogachev, S.A.: 2002c, Is it possible to accelerate ions in collapsing magnetic trap? *Adv. Space Res.*, v. 30, No. 1, 55–60. [§ 7.6]

Somov, B.V., Oreshina, A.V., Oreshina, I.V., et at.: 2003a, Flares in accretion disk coronae, *Adv. Space Res.*, v. 32, No. 6, 1087–1096. [Intr., § 8.3]

Somov, B.V., Kosugi, T., Hudson, H.S., et al.: 2003b, Modeling large solar flares, *Adv. Space Res.*, v. 32, No. 12, 2439-2450. [§ 5.4.4]

Somov, B.V., Kosugi, T., Bogachev, S.A., et al.: 2005a, Motion of the HXR sources in solar flares: *Yohkoh* images and statistics, *Adv. Space Res.*, v. 35, No. 10, 1700–1706. [5.4.2]

Somov, B.V., Kosugi, T., Bogachev, S.A., et al.: 2005b, On upward motions of coronal hard X-ray sources in solar flares, *Adv. Space Res.*, v. 35, No. 10, 1690–1699. [7.2.3]

Somov, B.V., Kosugi, T., Oreshina, I.V., et al.: 2005c, Large-scale reconnection in a large flare, *Adv. Space Res.*, v. 35, No. 10, 1712–1722. [4.2.5]

Sotirelis, T. and Meng, C.-I.: 1999, Magnetopause from pressure balance, *J. Geophys. Res*, v. 104, No. A4, 6889–6898. [§ 8.2]

Speiser, T.W.: 1965, Particle trajectories in model current sheets. 1. Analytical solutions, *J. Geophys. Res.*, v. 70, No. 17, 4219–4226. [§ 1.2, § 9.1, § 9.2, § 9.3, § 9.4]

Speiser, T.W.: 1968, On the uncoupling of parallel and perpendicular particle motion in a neutral sheet, *J. Geophys. Res.*, v. 73, No. 3, 1112–1113. [§ 9.2]

Speiser, T.W. and Lyons, L.R.: 1984, Comparison of an analytical approximation for particle motion in a current sheet with precise numerical calculations, *J. Geophys. Res.*, v. 89, No. A1, 147–158. [§ 9.3]

Spicer, D.S.: 1982, Magnetic energy storage and conversion in the solar atmosphere, *Space Sci. Rev.*, v. 31, No. 1, 351–435. [§ 3.3, § 14.4]

Stenzel, R.L. and Gekelman, W.: 1984, Particle acceleration during reconnection in laboratory plasmas. *Adv. Space Res.*, v. 4, No. 2, 459–470. [§ 3.3, § 14.2]

Sterling, A.C. and Hudson, H.S.: 1997, Yohkoh SXT observations of X-ray "dimming" associated with a halo coronal mass ejection, *Astrophys. J.*, v. 491, No. 1, L55–L58. [§ 3.2]

Stewart, R.T. and Labrum, N.R.: 1972, Meter-wavelength observations of the solar radio storm of August 17–22, 1968. *Solar Phys.*, v. 27, No. 1, 192–202. [§ 9.4]

Strong, K.T., Saba, J.L.R., Haisch, B.M., et al. (eds): 1999, *The Many Faces of the Sun*, New York, Berlin, Heidelberg, Tokyo; Springer, p. 610. [Intr., § 4.1]

Sturrock, P.A.: 1991, Maximum energy of semi-infinite magnetic field configurations, *Astrophys. J.*, v. 380, No. 2, 655–659. [§ 14.2]

Sturrock, P.A.: 1994, *Plasma Physics: An Introduction to the Theory of Astrophysical, Geophysical and Laboratory Plasmas*, Cambridge, Cambridge Univ. Press, p. 335. [Intr.]

Sudol, J.J. and Harvey, J.W.: 2005, Longitudinal magnetic field changes accompanying solar flares, *Astrophys. J.*, v. 635, No. 1, 647–658. [§ 3.1.1, § 3.1.3]

Sui, L. and Holman, G.D.: 2003, Evidence for the formation of a large-scale current sheet in a solar flare, *Astrophys. J.*, v. 596, L251–L254. [§ 7.2.2, § 7.2.3]

Sui, L., Holman, G.D., and Dennis, B.R.: 2004, Evidence for magnetic reconnection in three homologous solar flares observed by RHESSI, *Astrophys. J.*, v. 612, No. 1, 546–556. [§ 7.2.2, § 7.2.3]

Svestka, Z.: 1976, *Solar Flares*, Dordrecht, D. Reidel Publ. [§ 4.1, § 5.1, § 5.4.3]

Sweet, P.A.: 1958, The production of high energy particles in solar flares, *Nuovo Cimento Suppl.*, v. 8, *Serie* 10, 188–196. [Intr., § 14.2]

Sweet, P.A.: 1969, Mechanisms of solar flares, *Ann. Rev. Astron. Astrophys.*, v. 7, 149–176. [§ 2.1, § 3.2, § 6.1, § 9.1]

Syrovatskii, S.I.: 1956, Some properties of discontinuity surfaces in MHD, *Proc. P.N. Lebedev Phys. Inst.*, v. 8, 13–64 (in Russian). [§ 10.3]

Syrovatskii, S.I.: 1962, The stability of plasma in a nonuniform magnetic field and the mechanism of solar flares, *Soviet Astronomy–AJ*, v. 6, No. 6, 768–769. [§ 2.1]

Syrovatskii, S.I.: 1966a, Dynamic dissipation of a magnetic field and particle acceleration, *Soviet Astronomy–AJ*, v. 10, No. 2, 270–276. [§ 2.1, § 2.2, § 2.3, § 3.2, § 3.4, § 6.4, § 7.1, § 14.3]

Syrovatskii, S.I.: 1966b, Dynamical dissipation of magnetic energy in the vicinity of a neutral line, *Soviet Physics–JETP*, v. 23, No. 4, 754–762. [§ 2.1, § 2.3, § 6.4]

Syrovatskii, S.I.: 1968, MHD cumulation near a zero field line, *Soviet Physics–JETP*, v. 27, No. 5, 763–766. [§ 2.4]

Syrovatskii, S.I.: 1971, Formation of current sheets in a plasma with a frozen-in strong field, *Soviet Physics–JETP*, v. 33, No. 5, 933–940. [§ 10.1, § 14.3]

Syrovatskii, S.I.: 1972, Particle acceleration and plasma ejection from the Sun, in *Solar-Terrestrial Physics 1970, Part 1*, ed. E.R. Dryer, Dordrecht, D. Reidel Publ., 119–133. [§ 3.4.1, § 5.1.1]

Syrovatskii, S.I.: 1976a, Neutral current sheets in laboratory and space plasmas, in *Neutral Current Sheets in Plasmas*, Proc. P.N. Lebedev Phys. Inst., v. 74, ed. N.G. Basov, New York, London; Consultants Bureau, p. 2–10. [§ 6.1, § 10.1]

Syrovatskii, S.I.: 1976b, Current-sheet parameters and a thermal trigger for solar flares, *Soviet Astron. Lett.*, v. 2, No. 1, 13–14. [§ 3.3, § 6.1] v2, 3.3.1, 5.1.2

Syrovatskii, S.I.: 1981, Pinch sheets and reconnection in astrophysics, *Ann. Rev. Astron. Astrophys.*, v. 19, 163–229. [§ 3.2, § 3.3, § 3.4, § 6.1, § 9.1, § 9.4, § 11.5, § 14.2]

Syrovatskii, S.I.: 1982, Model for flare loops, fast motions, and opening of magnetic field in the corona, *Solar Phys.*, v. 76, No. 1, 3–20. [§ 3.2, § 9.1, § 13.1]

Syrovatskii, S.I. and Somov, B.V.: 1980, Physical driving forces and models of coronal responses, in *Solar and Interplanetary Dynamics*, eds M. Dryer and E. Tandberg-Hanssen, IAU Symp. **91**, Dordrecht, Reidel, p. 425–441. [§ 3.2, § 14.2]

Tanaka, K.: 1987, Impact of X-ray observations from the Hinitori satellite on solar flare research, *Publ. Astron. Soc. Japan*, v. 39, No. 1, 1–45. [§ 7.1]

Tandberg-Hanssen, E.: 1995, *The Nature of Solar Prominences*, Dordrecht, Boston, London; Kluwer Academic Publ., p. 308. [§ 13.1]

Taylor, J.B.: 1974, Relaxation of toroidal plasma and generation of reverse magnetic fields. *Phys. Rev. Lett.*, v. 33, No. 19, 1139–1141. [§ 12.1, § 12.2.2]

Taylor, J.B.: 1986, Relaxation and magnetic reconnection in plasmas, *Rev. Mod. Phys.*, v. 58, No. 3, 741–763. [§ 12.1]

Tian, L., Wang, J., and Wu, D.: 2002, Non-potentiality of the magnetic field beneath the eruptive filament in the Bastille event. *Solar Phys.*, v. 209, 375–389. [4.2.4]

Titov, V.S., Priest, E.R., and Démoulin, P.: 1993, Conditions for the appearance of 'bald patches' at the solar surface, *Astron. Astrophys.*, v. 276, No. 2, 564–570. [§ 14.3]

Tsuneta, S.: 1993, Solar flares as an ongoing magnetic reconnection process, in *ASP Conf. Series*, v. 46, eds H. Zirin, G. Ai, and H. Wang, p. 239–248. [Intr., § 14.2]

Tsuneta, S.: 1996, Structure and dynamics of reconnection in a solar flare, *Astrophys. J.*, v. 456, No. 2, 840–849. [§ 4.1, § 5.1, § 6.1, § 6.4, § 7.1]

Tsuneta, S. and Naito, T.: 1996, Fermi acceleration at the fast shock in a solar flare and the impulsive loop-top hard X-ray source. *Astrophys. J.* v. 495, L67-L70. [7.4.1]

Tsuneta, S., Nitta, N., Ohki, K., et al.: 1984, Hard X-ray imaging observations of solar hot thermal flares with the *Hinotori* spacecraft, *Astrophys. J.*, v. 284, No. 2, 827–832. [§ 7.1]

Tsuneta, S., Acton, L., Bruner, M., et al.: 1991, The soft X-ray telescope for the Solar-A mission, *Solar Phys.*, v. 136, No. 1, 37–67. [Intr., § 4.1]

Tsuneta, S., Hara, H., Shimuzu, T., et al.: 1992, Observation of a solar flare at the limb with the Yohkoh soft X-ray telescope, *Publ. Astron. Soc. Japan*, v. 44, No. 5, L63–L69. [Intr.]

Tsuneta, S., Masuda, S., Kosugi, T., et al.: 1997, Hot and super-hot plasmas above an impulsive-flare loop, *Astrophys. J.*, v. 478, No. 2, 787–796. [§ 4.1, § 6.1, § 6.4, § 7.1, § 7.3]

Tsurutani, B.T., Gonzalez, W.D., Kamide, Y., et al. (eds): 1997, *Magnetic Storms*, Washington, Amer. Geophys. Un., p. 266. [Intr.]

Tsyganenko, N.A.: 1996, Effects of the solar wind conditions on the global magnetospheric configuration as deduced from data-based field models, in *Proc. of 3rd International Conf. on Substorms (ICS-3)*, Eur. Space Agency Publ., ESA SP-389, p. 181–190. [§ 8.2]

Uchida, Y., Hirose, S., Morita, S., et al.: 1998, Observations of flares and active regions from Yohkoh, and magnetohydrodynamic models explaining them, *Astrophys. Space Sci.*, v. 264, No. 1, 145–169. [§ 5.1, § 5.5]

Ulmschneider, P., Rosner, R., and Priest, E.R. (eds): 1991, *Mechanisms of Chromospheric and Coronal Heating*, Berlin, Springer-Verlag. [§ 12.4]

van Ballegooijen, A.A. and Martens, P.C.H.: 1989, Formation and eruption of solar prominences, *Astrophys. J.*, v. 343, No. 3, 971–984. [§ 5.3, § 13.1]

van Ballegooijen, A.A. and Martens, P.C.H.: 1990, Magnetic fields in quiescent prominences, *Astrophys. J.*, v. 361, No. 1, 283–289. [§ 13.1]

Vekstein, G.E. and Priest, E.R.: 1992, Magnetohydrodynamic equilibria and cusp formation at an X-type neutral line by footpoint shearing, *Astrophys. J.*, v. 384, No. 1, 333–340. [§ 14.2, § 14.3]

Vernazza, J.E., Avrett, E.H., and Loeser, R.: 1981, Structure of the solar chromosphere. 3. Models of the EUV brightness components of the quiet Sun, *Astrophys. J. Suppl.*, v. 45, 635–725. [§ 13.2.2]

Verneta, A.I. and Somov, B.V.: 1993, Effect of compressibility on the development of the tearing instability in a non-neutral current sheet in the solar atmosphere, *Astronomy Reports*, v. 37, No. 3, 282–285. [§ 11.5]

Vladimirov, V.S.: 1971, *Equations of Mathematical Physics*, New York, M. Dekker, p. 418. [§ 11.6]

Wang, H. and Qiu, J.: 2002, Relationship between flare kernels in Hα far-blue wing and magnetic fields, *Astrophys. J.*, v. 568, No. 1, 408–412. [§ 4.1]

Wang, H., Liu, C., Deng, Y., et al.: 2005, Reevaluation of the magntic structure and evolution associated with the Bastille day flare on 2000 July 14, *Astrophys. J.*, v. 627, No. 2, 1031–1039. [§ 3.1.1, § 3.1.3, § 5.1.1]

Wang, H., Qiu, J., Jing, J., et al.: 2003, Study of ribbon separation of a flare associated with a quiescent filament eruption, *Astropys. J.*, v. 593, No. 1, 564–570. [5.4.5]

Wang, J.: 1999, Vector magnetic fields and magnetic activity of the Sun, *Fundamen. Cosmic Phys.*, v. 20, No. 3, 251–382. [§ 3.1, § 13.3]

Wang, J. and Shi, Z.: 1993, The flare-associated magnetic changes in an active region. II. Flux emergence and cancelation, *Solar Phys.*, v. 143, No. 1, 119–139. [§ 4.2.4, § 5.5]

Wang, J.X., Shi, Z.X., Wang, H., et al.: 1996, Flares and the magnetic non-potentiality, *Astrophys. J.*, v. 456, No. 2, 861–878. [§ 3.3]

Wang, Y.-M. and Sheeley, N.R.: 2002, Observations of core fallback during Coronal Mass Ejections, *Astrophys. J.*, v. 567, No. 2, 1211–1224. [7.3.5]

Woltjer, L.: 1958, A theorem on force-free magnetic fields, *Proc. Nat. Acad. Sci. USA*, v. 44, No. 6, 489–491. [§ 12.1]

Woltjer, L.: 1959, Hydromagnetic equilibrium: II. Stability in the variational formulation, *Proc. Nat. Acad. Sci. USA*, v. 45, No. 6, 769–771. [§ 12.5]

Wright, A.N. and Berger, M.A.: 1989, The effect of reconnection upon the linkage and interior structure of magnetic flux tubes, *J. Geophys. Res.*, v. 94, No. A2, 1295–1302. [§ 12.1]

Wright, A.N. and Berger, M.A.: 1991, A physical description of magnetic helicity evolution in the presence of reconnection lines, *J. Plasma Phys.*, v. 46, No. 1, 179–199. [§ 12.2]

Wright, J.M.: 1997, *National Space Weather Program: The Implementation Plan*, Washington, D.C., Off. Fed. Coord. Meteorol. Serv. Supp. Res., FCM-P31. [Intr., § 8.2]

Yan, Y., Deng, Y., Karlicky, M., et al.: 2001, The magnetic rope structure and associated energetic processes in the 2000 July 14 solar flare, *Astrophys. J.*, v. 551, Part 2, L115–L118. [§ 4.1, § 5.2.3]

Zel'dovich, Ya.B. and Raizer, Yu.P.: 1966, *Physics of Shock Waves and High-Temperature Hydrodynamic Phenomena*, New York, San Francisco, London; Academic Press, v. 1, p. 464; v. 2, p. 452. [§ 2.4]

Zel'dovich, Ya.B. and Raizer, Yu.P.: 2002, *Physics of Shock Waves and High-Temperature Hydrodynamic Phenomena*, eds W.D. Hayes and R.F. Probstein, Mineola, Dover. [§ 2.4]

Zhang, H.: 1995, Configuration of magnetic shear and vertical current in the active region NOAA 5395 in 1989 March, *Astron. Astrophys. Suppl.*, v. 111, No. 1, 27–40. [§ 3.3]

Zhang, H.: 2002, Magnetic field, helicity and the 2000 July 14 flare in solar active region 9077, *Mon. Not. Royal Astron. Soc.*, v. 332, No. 2, 500–512. [§ 4.2.4, § 5.1]

Zhang, H.-Q. and Chupp, E. L.: 1989, Studies on post-flare prominence of 1981 April 27, *Astrophys. Space Sci.*, v. 153, No. 1, 95–108. [§ 9.4]

Zhang, J., Wang, J., Deng, Y., et al.: 2001, Magnetic flux cancellation associated with the major solar event on 2000 July 14, *Astrophys. J.*, v. 548, Part 2, L99–L102. [§ 4.1, § 5.2.2, § 5.3]

Zirin, H.: 1988, *Astrophysics of the Sun*, Dordrecht, D. Reidel. [§ 4.1, § 5.1]

Zirker, J.B. and Cleveland, F.M.: 1993, Avalanche models of active region heating and flaring, *Solar Phys.*, v. 145, No. 1, 119–128. [§ 12.1]

Zuccarello, F., Burm, H., Kuperus, M., et al.: 1987, Varying self-inductance and energy storage in a sheared force-free arcade, *Astron. Astrophys.*, v. 180, No. 1, 218–222. [§ 14.4]

Zweibel, E.G.: 1989, Magnetic reconnection in partially ionized gases, *Astrophys. J.*, v. 340, No. 2, 550–557. [§ 13.2.3]

Zwingmann, W., Schindler, K., and Birn, J.: 1985, On sheared magnetic field structures containing neutral points, *Solar Phys.*, v. 99, No. 1, 133–143. [§ 11.1, § 14.2, § 14.3]

Index

Color Plates

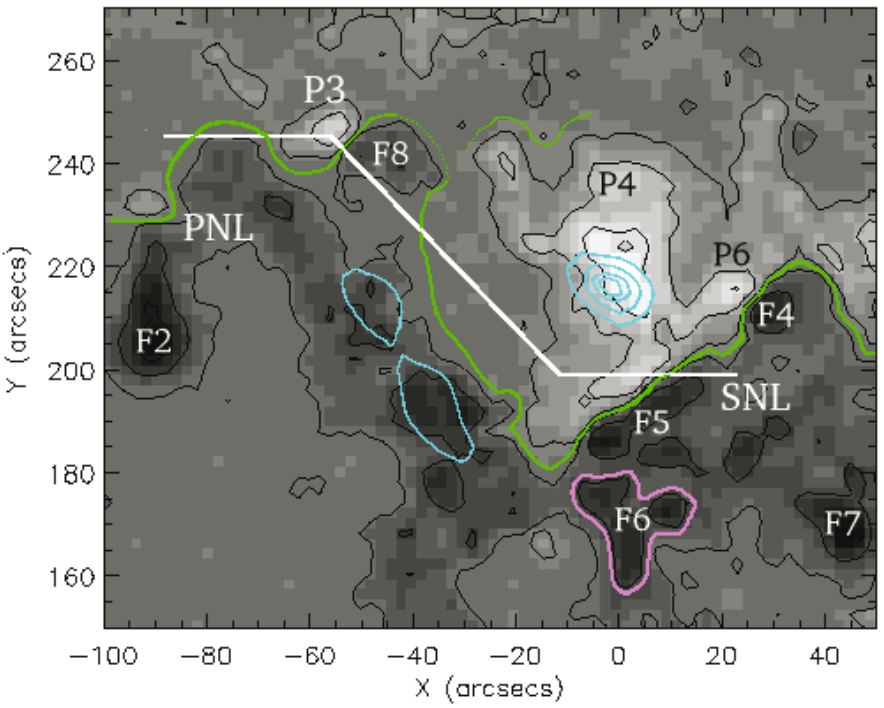

Fig. 4.2. The HXR source contours (blue curves) at the HXR maximum of the Bastille day flare overlaid on the MDI magnetogram. The green curve PNL represents the photospheric neutral line. SNL is the simplified neutral line.

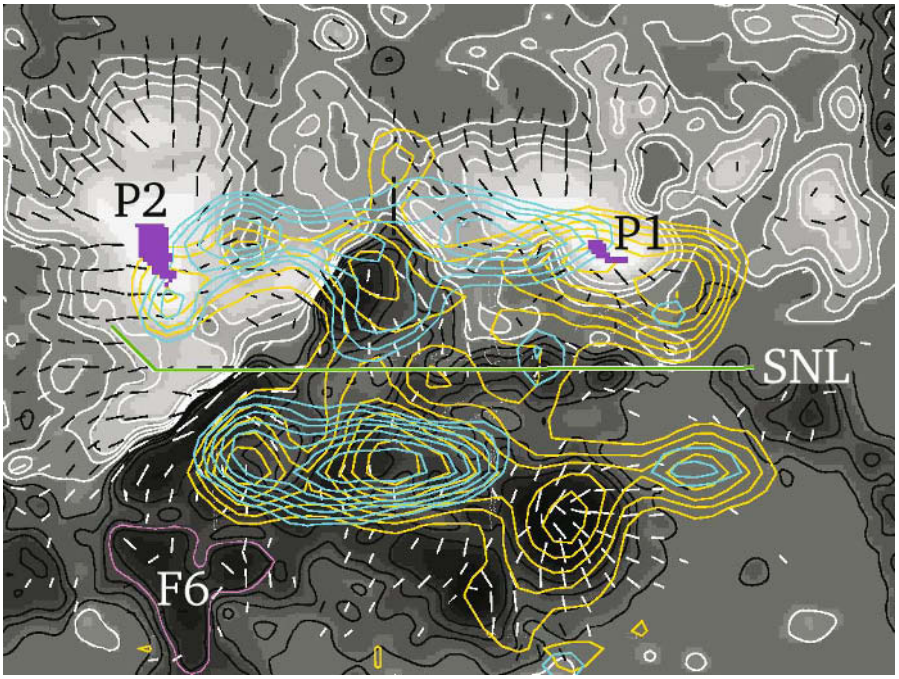

Fig. 4.3. The HXR source positions in the beginning of the first HXR spike S1 (yellow contours) and near its end (blue contours).

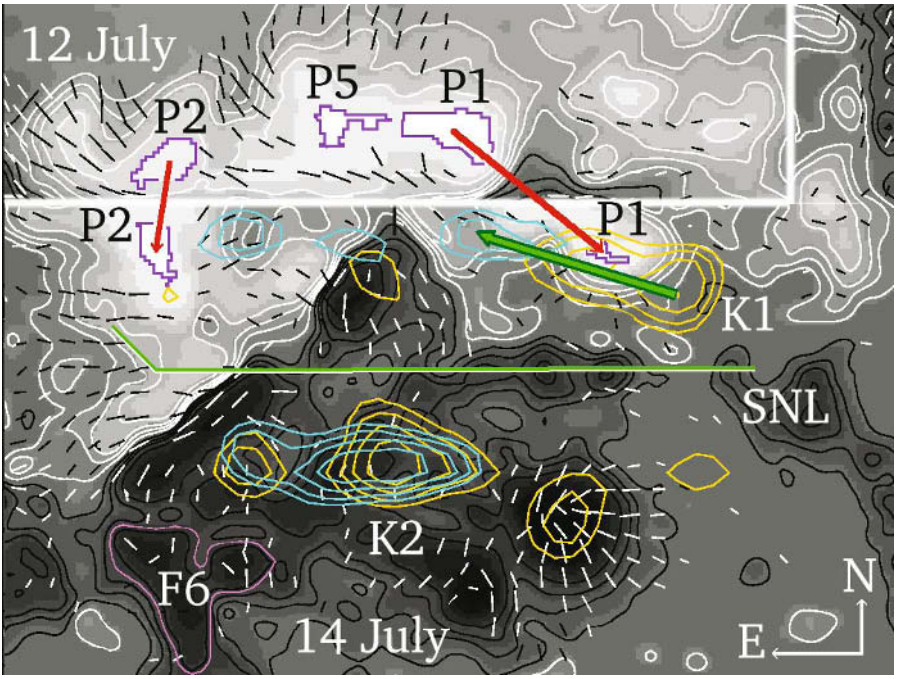

Fig. 4.4. The position and motion of the strongest HXR sources K1 and K2 relative to the SMFT magnetogram on 14 July.

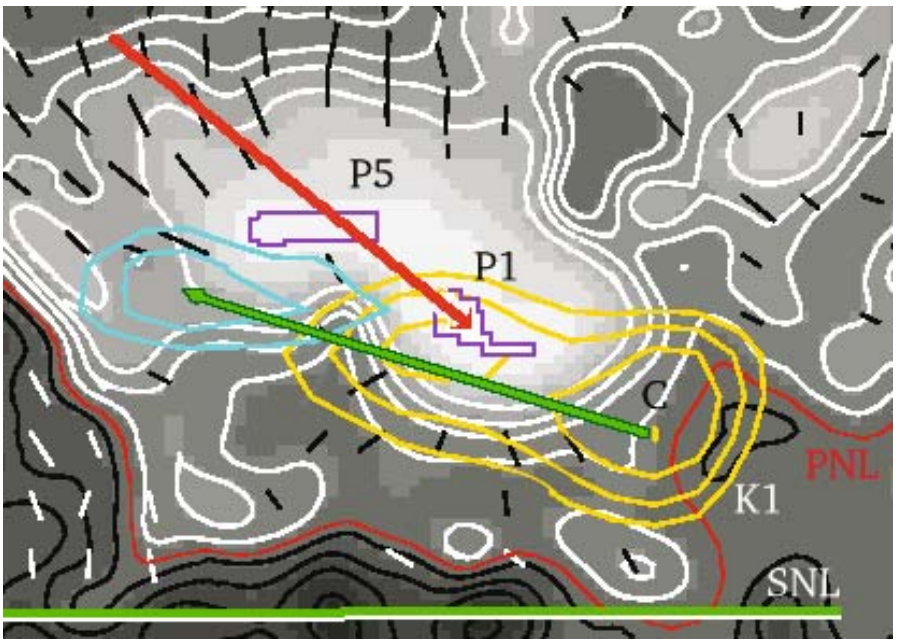

Fig. 4.5. H-band images of the brightest kernel K1 in the rise and decay of the first HXR spike S1 overlaid on the SMFT magnetogram on July 14.